VECTORS AND VECTOR-BORNE PARASITIC DISEASES: INFECTION, IMMUNITY, AND EVOLUTION

EDITED BY: Jun-Hu Chen, Emilio Luis Malchiodi, Xiao-Nong Zhou, Rachel Daniels and Banchob Sripa

PUBLISHED IN: Frontiers in Immunology and Frontiers in Microbiology

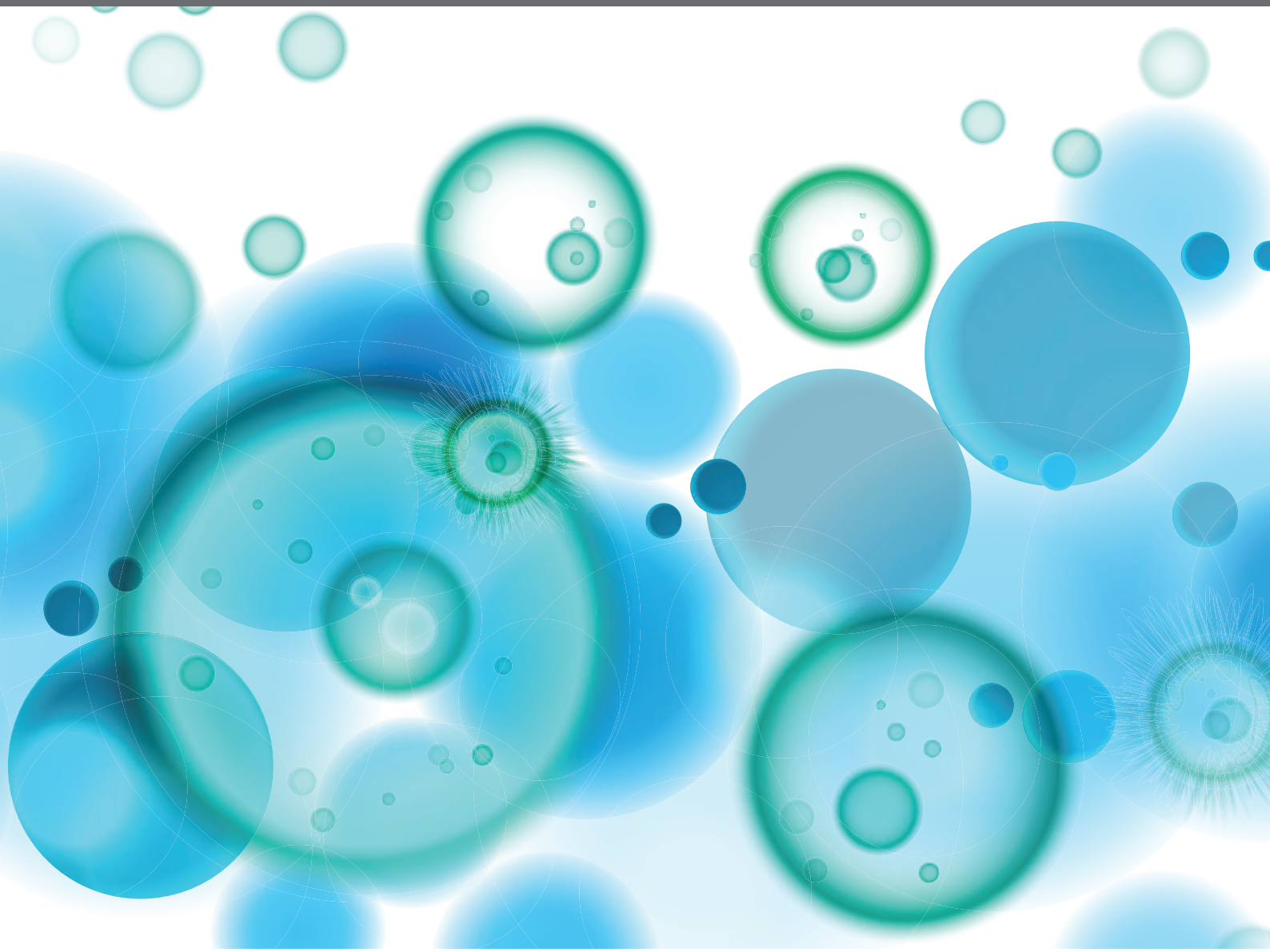

frontiers Research Topics

frontiers

ISSN 1664-8714
ISBN 978-2-88971-378-3
DOI 10.3389/978-2-88971-378-3

About Frontiers

Frontiers is more than just an open-access publisher of scholarly articles: it is a pioneering approach to the world of academia, radically improving the way scholarly research is managed. The grand vision of Frontiers is a world where all people have an equal opportunity to seek, share and generate knowledge. Frontiers provides immediate and permanent online open access to all its publications, but this alone is not enough to realize our grand goals.

Frontiers Journal Series

The Frontiers Journal Series is a multi-tier and interdisciplinary set of open-access, online journals, promising a paradigm shift from the current review, selection and dissemination processes in academic publishing. All Frontiers journals are driven by researchers for researchers; therefore, they constitute a service to the scholarly community. At the same time, the Frontiers Journal Series operates on a revolutionary invention, the tiered publishing system, initially addressing specific communities of scholars, and gradually climbing up to broader public understanding, thus serving the interests of the lay society, too.

Dedication to Quality

Each Frontiers article is a landmark of the highest quality, thanks to genuinely collaborative interactions between authors and review editors, who include some of the world's best academicians. Research must be certified by peers before entering a stream of knowledge that may eventually reach the public - and shape society; therefore, Frontiers only applies the most rigorous and unbiased reviews.
Frontiers revolutionizes research publishing by freely delivering the most outstanding research, evaluated with no bias from both the academic and social point of view. By applying the most advanced information technologies, Frontiers is catapulting scholarly publishing into a new generation.

What are Frontiers Research Topics?

Frontiers Research Topics are very popular trademarks of the Frontiers Journals Series: they are collections of at least ten articles, all centered on a particular subject. With their unique mix of varied contributions from Original Research to Review Articles, Frontiers Research Topics unify the most influential researchers, the latest key findings and historical advances in a hot research area! Find out more on how to host your own Frontiers Research Topic or contribute to one as an author by contacting the Frontiers Editorial Office: frontiersin.org/about/contact

VECTORS AND VECTOR-BORNE PARASITIC DISEASES: INFECTION, IMMUNITY, AND EVOLUTION

Topic Editors:
Jun-Hu Chen, National Institute of Parasitic Diseases, China
Emilio Luis Malchiodi, University of Buenos Aires, Argentina
Xiao-Nong Zhou, National Institute of Parasitic Diseases, China
Rachel Daniels, Harvard University, United States
Banchob Sripa, Khon Kaen University, Thailand

Citation: Chen, J.-H., Malchiodi, E. L., Zhou, X.-N., Daniels, R., Sripa, B., eds. (2021). Vectors and Vector-Borne Parasitic Diseases: Infection, Immunity, and Evolution. Lausanne: Frontiers Media SA. doi: 10.3389/978-2-88971-378-3

Table of Contents

frontiers in Immunology

EDITORIAL
published: 21 July 2021
doi: 10.3389/fimmu.2021.729415

Editorial: Vectors and Vector-Borne Parasitic Diseases: Infection, Immunity, and Evolution

Kokouvi Kassegne[1], *Xiao-Nong Zhou*[1,2] *and Jun-Hu Chen*[2*]

[1] School of Global Health, Chinese Centre for Tropical Diseases Research, Shanghai Jiao Tong University School of Medicine, Shanghai, China, [2] National Institute of Parasitic Diseases, Chinese Center for Diseases Control and Prevention (Chinese Centre for Tropical Diseases Research), National Health Commission of the People's Republic of China (NHC) Key Laboratory of Parasite and Vector Biology, WHO Collaborating Centre for Tropical Diseases, National Center for International Research on Tropical Diseases, Shanghai, China

Keywords: vector-borne parasitic diseases, malaria, schistosomiasis, Chagas disease, leishmaniasis, babesiosis, theileriosis

Editorial on the Research Topic

Vectors and Vector-Borne Parasitic Diseases: Infection, Immunity, and Evolution

The (re)emergence and burden of vector-borne parasitic diseases (VBPDs) draws attention to vectors with the parasites they carry. These include, but are not limited to: anopheles-borne diseases (e.g., caused by *Plasmodium*); tick-borne diseases (e.g., caused by *Babesia* and *Theileria*); snail-borne diseases (e.g., caused by *Schistosoma*); sand fly-borne diseases (e.g., caused by *Leishmania*); and tsetse fly- or triatomine bug-borne diseases (e.g., caused by *Trypanosoma*). Knowledge of vector and parasite biology is beginning to stimulate new concepts and tools for effective disease control. However, the mechanisms and pathways through which the development of parasites within vectors may enhance vector-mediated immune control or regulate interactions are not properly understood. In addition, the mechanisms by which hosts respond to parasite exposure and acquire immunity remain unclear. A further major challenge in combatting VBPDs is the high variability of a large repertoire of genes in the genome of a single parasite. The 14 articles of this themed Research Topic highlight the latest advances regarding vectors and VBPDs: infection, immunity, and evolution.

Understanding the immunological machinery of host-parasite interactions will advance knowledge of VBPD mechanisms to track relevant immune and parasitic molecules that ensure protection or drive disease. Induction of humoral immunity is critical for clinical protection against infection. Antibody levels targeting antigens are predictive of infection and lay the basis for the identification of biomarkers of exposure/candidate antigens for serodiagnostics or vaccines. In this collection, Hou et al. advance knowledge of B-cell epitopes of 37 erythrocyte invasion-associated antigens of *Plasmodium falciparum*, which have been tested in clinical settings as vaccine candidates. They find that most immunogenic epitopes are predominantly located in the low-complexity regions of the proteins containing repetitive and/or glutamate-rich motifs, and the epitope-derived specific antibodies could not inhibit erythrocyte invasion (Hou et al.). These indicate that immune responses could be driven away from functional domains of *P. falciparum* proteins, which is an instructive finding for the rational design of blood-stage malaria vaccine candidates. In an *in vitro* and *in vivo* study, Wang et al. evaluate the potential applications of

Edited and reviewed by:
Ian Marriott,
University of North Carolina at Charlotte, United States

****Correspondence:***
Jun-Hu Chen
chenjh@nipd.chinacdc.cn

Specialty section:
This article was submitted to Microbial Immunology, a section of the journal Frontiers in Immunology

Received: *23 June 2021*
Accepted: *07 July 2021*
Published: *21 July 2021*

Citation:
Kassegne K, Zhou X-N and Chen J-H (2021) Editorial: Vectors and Vector-Borne Parasitic Diseases: Infection, Immunity, and Evolution. Front. Immunol. 12:729415. doi: 10.3389/fimmu.2021.729415

BmSP44, an erythrocyte invasion-associated merozoite surface antigen of *Babesia microti*. The authors validate BmSP44 as a dominant immunogen candidate and demonstrate that it is a secreted protein localized in the parasite's cytoplasm. They discover that recombinant BmSP44 antisera can attenuate parasitaemia in infected mice and, more importantly, is associated with clinical protection against *B. microti* infection in immunized mice. This is reflected in a Th1/Th2 mixed immune response with significantly elevated levels of interferon-gamma (IFN-γ) and interleukin (IL)-10 during the early stage of infection (Wang et al.).

Pro- and anti-inflammatory cytokines are important mediators of cellular immunity and are associated with parasitic disease outcomes. It is a generally accepted observation that clinical symptoms develop as a result of immunopathology involving dysregulation of immune mediator balance in favor of pro-inflammatory mediators. Therefore, understanding the role of immune regulators in the establishment of protective immunity or asymptomatic infections is critical. In this regard, Frimpong et al. determine the association of pro-inflammatory mediators including tumor necrosis factor-alpha (TNF-α), IFN-γ, IL-6, IL-12p70, IL-17A and granzyme B, and the cytokines IL-4 and IL-10 with the development of asymptomatic malaria. The authors find that neither microscopic nor submicroscopic asymptomatic infection is polarized toward a pro- or "anti"-inflammatory response, but rather by a balanced inflammatory response (ratio of IFN-γ/IL-10, TNF-a/IL-10, IL-6/IL-10 as well as IFN-γ/IL-4 and IL-6/IL-4 not significantly different). This advances knowledge that asymptomatic malaria infections result in increased plasma levels of both pro- and "anti"-inflammatory cytokines relative to uninfected persons, which explains in part the lack of clinical symptoms. However, not much evidence has been forthcoming in favour of the hypothesis that IL-4 and IL-10 may be anti-inflammatory or regulatory cytokines. Unveiling the protective immune response to VBPDs is critical for a rational design of vaccines. Soto et al. add to our understanding of the role of basic leucine zipper transcription factor ATF-like 3 (Batf3) in the generation of type 1 immunity against parasitic infections. The authors demonstrate that Batf3-deficient mice are unable to control hepatic parasitosis as opposed to wild-type C57BL/6 mice. In addition, the impaired microbicide capacities of *Leishmania infantum*-infected macrophages from Batf3-deficient mice correlates with a reduction of parasite-specific IFN-γ production.

Trypanosoma cruzi is an intracellular protozoan that can reside within different tissues, evading host immunity and allowing progression towards chronic stages of infection. Such intracellular parasitism triggers strong cellular immunity that, besides being necessary to limit infection, is not sufficient to eradicate parasites from tissues. Two *in vivo* studies published in this collection provide novel insights onto vaccine candidates by *T. cruzi* infection. Antonoglou et al. explore new strategies for a differential immune response for vaccines against Chagas disease using an immunogenic chimeric molecule—NCz-SEGN24A. The authors find that NCz-SEGN24A enhances significant production of specific IgG titers in immunized mice, with significant specific cell-mediated immune responses. More importantly, the immunogen confers protection against infection in immunized mice, with 100% survival maintained in mice challenged with trypomastigotes of *T. cruzi* (Antonoglou et al.). Such a finding encourages the testing of mutated superantigens fused to specific antigens as immune modulators. In a mouse model study, Cerny et al. demonstrate that a *Salmonella*-based therapeutic DNA vaccine that combines Cruzipain (Cz) and Chagasin (Chg) provides improved protection than monocomponent therapeutic vaccines against each. The authors find that the bicomponent vaccine could significantly (i) increase the titers of antigen- and parasite-specific antibodies, and (ii) trigger a robust cellular response with IFN-γ secretion that rapidly reduces the parasitaemia during the acute phase and decreases the tissue damage in the chronic stage of the infection. Such a bicomponent vaccine strategy could be an effective tool to ameliorate the pathology associated to Chagas disease. Meanwhile, the presence of intracellular protozoa among immunocompromised HIV-infected individuals increases the incidence of severe disease. In an *in vitro* study, Urquiza et al. show that the pathogenesis of HIV-*T. cruzi* coinfection in astrocytes: (i) leads to an oxidative misbalance mechanism which increases mitochondrial and cellular reactive oxygen species (ROS) production, and (ii) boosts *T. cruzi* multiplication towards severe meningoencephalitis in the central nervous system (CNS). Findings from their study imply that ROS production drives astrocyte infection by *T. cruzi*, and involves ROS production from HIV-exposed astrocytes during coinfection, contributing to parasite persistence and CNS pathology (Urquiza et al.). These insights shed light on the pathogenesis of neurologic Chagas disease and will inform the design of future parasite control strategies.

In another *in vivo* study conducted with *L. major*, Keshavarzian et al. evaluate *Iranian Lizard Leishmania* (ILL) mixed with CpG-ODN as a bicomponent candidate vaccine against experimental murine leishmaniasis. The authors find that ILL+CpG ensures protection against the development of dermal lesions in immunized mice with a significant reduction in the parasite load in comparison to control groups. In addition, this is associated with higher production of IFN-γ, as well as a reduction in IL-4 levels and arginase activity. These findings indicate that ILL, with an appropriate adjuvant, might be suitable for use as a vaccine against leishmaniasis. Likewise, Zhang et al. utilize a recently developed humanized mouse that has been used to assess immune responses against an attenuated C9 parasite clone (C9-M) - carrying a single insertion disrupting the open reading frame of PF3D7_1305500 - of *P. falciparum*. Zhang et al. identify that the attenuated falciparum parasite induces distinct patterns of cytokine production in these humanized mice to evade residual protective non-adaptive immune responses. Their study unveils a valuable way to explore the role of C9 mutation in the growth and survival of parasite mutants and their response to the host's immune responses. This mouse might, therefore, help identify novel targets for antimalarial chemotherapy.

An *in vitro* and *in vivo* study by Huang et al. in this collection provides the first direct evidence that a natural flavonol compound—myricetin, possesses potent anti-schistosome activities. The authors find that myricetin could exhibit dose and time-dependent anthelmintic effects on *Schistosoma*

japonicum and inhibited female spawning, suggesting that it could be further explored as a therapeutic agent. Their study also offers new insights into the mechanisms of action of myricetin by revealing that it attenuates hepatic fibrosis via modulating transforming growth factor beta (TGFβ) 1 and Akt signaling, and shifting the Th1/Th2 balance in *S. japonicum*-infected mice (Huang et al.).

The high variability in the clinical course of VBPDs in patients raises fundamental questions about parasitic factors that are critical in regulating pathogenesis, disease severity, or drug resistance. In this collection, two exciting studies apply genomic approaches to dissect the genetic backgrounds of isolate parasite populations for malaria and theileriosis surveillance.

Firstly, Kassegne et al. provide the first genotyping of single nucleotide polymorphisms and local-specific signals of selection in ten clinical *P. falciparum* isolates from Togo. The authors find relatively high genome-wide diversity and recent population expansion of *P. falciparum* in Togo. Against this background, they identify a total of 383 genes under local-specific signals of selection. Importantly, host immunity is found to be the major selective agent on antigen genes, including membrane and surface proteins implicated in merozoite invasion and malaria severity, respectively. Interrestingly, they find that Togo *P. falciparum* is under no serious antimalarial drug selection (Kassegne et al.). Secondly, Roy et al. address major questions regarding the population structure and genetic diversity of *Theileria annulate* in field isolates and the impact of the theileriosis vaccine currently being used in India. Their findings highlight: (i) high transmission intensity and abundance of ticks in India in compliance with high genetic variation between the tick-borne parasite populations; and (ii) limited genetic diversity in the vaccine isolates in the country, which suggests efficacy of the schizont stage theileriosis vaccine. The authors also identify a new panel of markers that could be helpful for surveillance of this tick-borne parasite (Roy et al.). However, the low diversity in the isolates from vaccinated individuals advocates improving the current vaccine, possibly by increasing its heterozygosity.

Understanding how the mechanisms and pathways through which the development of parasites within vectors may enhance vector-mediated immune control or regulate interactions will provide critical insights into relevant molecules that secure protection in vectors.

Sharma et al. investigate how *P. vivax* alters gut-microbiota and antiplasmodial immunity and impacts tripartite *Plasmodium*-mosquito-microbiota interactions in the gut lumen. In a metagenomics and RNAseq study, Sharma et al. provide evidence that, during the preinvasive phase, *P. vivax* suppresses midgut-microbiota, which likely negates the impact of mosquito immunity and, in turn, may enhance the survival of *P. vivax*. The authors conclude that the detection of sequences matching mosquito-associated *Wolbachia* would open a new inquiry for its exploration as an agent for "paratransgenesis-based" mosquito control. Likewise, Hu et al. advance our understanding of the critical events during schistosome infection by demonstrating changes in the gut microbiome composition during schistosomiasis progression, the functional interactions between the gut bacteria and *S. japonicum* infection in mice, and the dynamic metabolite changes in the host. The authors observe a decrease in richness and diversity, as well as differed composition, of the gut microbiota in infected status versus uninfected status. They also discover metabolic biomarkers including phosphatidylcholine and colfosceril palmitate in serum, as well as xanthurenic acid, naphthalenesulfonic acid, and pimelylcarnitine in the urine (Hu et al.). These biomarkers could serve as new targets for early diagnosis and prognostic purposes following *S. japonicum* infection.

Collectively, this themed Research Topic advances our knowledge of the molecular and cellular processes involved in parasitic disease susceptibility, which may pave the way for vector control interventions as well as diagnosis, therapy, and rational design of vaccines for VBPDs.

AUTHOR CONTRIBUTIONS

KK and J-HC drafted the manuscript. All authors contributed to the article and approved the submitted version.

FUNDING

This work was supported by the National Research and Development Plan of China (Grant No. 2018YFE0121600), the National Sharing Service Platform for Parasite Resources (Grant No. TDRC-2019-194-30), and the National Natural Science Foundation of China (Grant No. 81101266). The funding bodies had no role in the design of the study, in collection, analysis, and interpretation of data, or in writing the manuscript.

Conflict of Interest: The authors declare that the research was conducted in the absence of any commercial or financial relationships that could be construed as a potential conflict of interest.

frontiers in Immunology

ORIGINAL RESEARCH
published: 15 April 2020
doi: 10.3389/fimmu.2020.00610

Low-Complexity Repetitive Epitopes of *Plasmodium falciparum* Are Decoys for Humoural Immune Responses

Nan Hou[1†], *Ning Jiang*[2,3†], *Yu Ma*[1†], *Yang Zou*[4], *Xianyu Piao*[1], *Shuai Liu*[1] and *Qijun Chen*[1,2,3*]

[1] NHC Key Laboratory of Systems Biology of Pathogens, Institute of Pathogen Biology, Chinese Academy of Medical Sciences & Peking Union Medical College, Beijing, China, [2] Key Laboratory of Livestock Infectious Diseases in Northeast China, Ministry of Education, Key Laboratory of Zoonosis, College of Animal Science and Veterinary Medicine, Shenyang Agricultural University, Shenyang, China, [3] The Research Unit for Pathogenic Mechanisms of Zoonotic Parasites, Chinese Academy of Medical Sciences, Shenyang, China, [4] Beijing Key Laboratory for Research on Prevention and Treatment of Tropical Diseases, Beijing Tropical Medicine Research Institute, Beijing Friendship Hospital, Capital Medical University, Beijing, China

OPEN ACCESS

Edited by:
Jun-Hu Chen, National Institute of Parasitic Diseases, China

Reviewed by:
Elizabeth Henny Herningtyas, Gadjah Mada University, Indonesia
Giampietro Corradin, Université de Lausanne, Switzerland
Alberto Moreno, Emory University, United States

***Correspondence:**
Qijun Chen
qijunchen759@syau.edu.cn

[†]*These authors have contributed equally to this work*

Specialty section:
This article was submitted to Microbial Immunology, a section of the journal Frontiers in Immunology

Received: *12 November 2019*
Accepted: *17 March 2020*
Published: *15 April 2020*

Citation:
Hou N, Jiang N, Ma Y, Zou Y, Piao X, Liu S and Chen Q (2020) Low-Complexity Repetitive Epitopes of Plasmodium falciparum Are Decoys for Humoural Immune Responses. Front. Immunol. 11:610. doi: 10.3389/fimmu.2020.00610

Induction of humoural immunity is critical for clinical protection against malaria. More than 100 malaria vaccine candidates have been investigated at different developmental stages, but with limited protection. One of the roadblocks constrains the development of malaria vaccines is the poor immunogenicity of the antigens. The objective of this study was to map the linear B-cell epitopes of the *Plasmodium falciparum* erythrocyte invasion-associated antigens with a purpose of understanding humoural responses and protection. We conducted a large-scale screen using overlapping peptide microarrays of 37 proteins from the *P. falciparum* parasite, most of which are invasion-associated antigens which have been tested in clinical settings as vaccine candidates, with sera from individuals with various infection episodes. Analysis of the epitome of the antigens revealed that the most immunogenic epitopes were predominantly located in the low-complexity regions of the proteins containing repetitive and/or glutamate-rich motifs in different sequence contexts. However, *in vitro* assay showed the antibodies specific for these epitopes did not show invasion inhibitory effect. These discoveries indicated that the low-complexity regions of the parasite proteins might drive immune responses away from functional domains, which may be an instructive finding for the rational design of vaccine candidates.

Keywords: ***Plasmodium falciparum*, invasion, antigen, epitope, microarray, immune escape**

INTRODUCTION

Malaria elimination efforts have yielded outstanding achievements in the past 20 years, and malaria eradication by 2050 was proposed by the Lancet Commission (1). Although more than half of the world's countries are now malaria free (2), the currently available tools and approaches will not be sufficient to achieve the optimal goal of malaria eradication.

A potent vaccine has been believed to be the most cost-effective tool for reducing the negative impact of the disease on human health and is essential for complete malaria eradication. To

date, more than 100 vaccine candidates have been investigated at different developmental stages. The world's first malaria vaccine, RTS,S/AS01, is now being deployed in a pilot roll-out in three African countries (3). However, the clinical protection obtained after immunization has not been as satisfactory as expected, although antigen-specific responses were sufficiently elicited (4, 5). Dispersion of immune responses by antigen diversity and functional compensation among family members of erythrocyte ligands have been speculated as reasons for the poor performance of the vaccine antigens. However, the immunogenic determinants of malarial antigens in connection with clinical protection are two critical aspects that have not been fully understood.

Invasion-associated antigens received wide attention as malaria vaccine candidates for invasion into erythrocytes is an essential step for the successful proliferation and transmission of plasmodial parasites (6, 7). In particular, merozoite antigens presented on the surface and that released upon contact of the merozoite with the erythrocyte are direct targets of naturally acquired humoural immunity and hence have been extensively investigated as potential candidates in vaccine development (8).

The objective of this study was to map the linear B-cell epitopes of the malaria antigens with a purpose of understanding humoural responses and protection. We conducted a large-scale linear epitope mapping using overlapped peptide microarrays to study the relationship between epitope characteristics and its antigenicity, and to find the clues resulting in high antigenicity but poor clinical protection. We screened the epitopes of 37 *Plasmodium falciparum* antigens, most of which are invasion-associated malaria vaccine candidates, with the sera of individuals of various infection histories. A clear epitope map of each antigen was generated. Epitopes containing repetitive sequences and glutamate-rich motifs were found highly antigenic and tended to be decoy epitopes that drive the host humoral immunity away from the functional domains.

MATERIALS AND METHODS

Ethical Statement

All procedures performed on human samples were carried out in line with the tenets of the Declaration of Helsinki. Informed consent was obtained from every individual involved in this study, and all human samples were anonymized. All animal procedures in this study were conducted according to the animal husbandry guidelines of the Chinese Academy of Medical Sciences. The studies in both humans and animals were reviewed and approved by the Ethical Committee and the Experimental Animal Committee of the Chinese Academy of Medical Sciences, with Ethical Clearance Numbers IPB-2016-2 and CQJ16001.

Sample Collection

A total of 289 patients suffering from falciparum malaria (FM) infection were recruited. All patients were experiencing fever (>37.5°C), blood samples were microscopically examined using Giemsa-stained thin blood smears and documented to be *P. falciparum* infection, then further confirmed by **nested** PCR (9). Among these patients, 60 were recruited in Libya from January to October 2012, 171 in Kachin state and Wa state, Burma from November 2006 to July 2011, and 58 in Beijing, Henan and Yunan, China, from September 2011 to January 2012. The sera samples of all patients were obtained before the patients received treatment. Sera samples from 144 healthy individuals (Healthy) were collected in Shenyang and Beijing, China, from September 2011 to January 2012 and were used as controls. More information about the individuals involved in this study is presented in **Supplementary Table 1**.

Proteins and Peptides

Thirty-seven *P. falciparum*-derived proteins were selected to explore the epitopes of the proteins, including apical membrane antigen (AMA)-1, cytoadherence linked asexual protein (CLAG) 3.1, 3.2, 8, and 9, erythrocyte binding antigen (EBA)-140, 165, 175, and 181, merozoite surface protein (MSP) 1, 2, 3, 4, 5, 6, 7.1, 7.2, 7.3, 7.4, 7.5, 8, 9, 10, and 11, merozoite surface protein duffy binding-like (MSPDBL), rhoptry-associated protein (Rh) 1, 2, and 3, merozoite capping protein 1 (MCP1), and endoplasmin, and a few mature parasite-derived antigens, such as *P. falciparum* 332 (PF332), histidine-rich protein (HRP) II, glutamate-rich protein (GLURP), mature-parasite-infected erythrocyte surface antigen [MESA, also called *P. falciparum* erythrocyte membrane protein 2 (PfEMP2)], serine repeat antigen (SERA) and methionine-tRNA ligase (7, 10). The amino acid sequence of each protein was derived from the protein database of NCBI (**Supplementary File 1**) and divided into consecutive peptides with a length of 30 amino acids, and each peptide had 15 amino acids overlapping with adjacent peptides (**Figures 1A**, **2A**). In total, 2,053 peptides were generated, but only 2,024 peptides (**Supplementary File 1**) were successfully synthesized (GL Biochem, Shanghai, China). Thirteen extra synthetic peptides were designed and synthesized to verify the response to repetitive sequences.

Microarray Construction

A microarray was prepared in a 100,000 grade clean room. Peptides were first dissolved to a concentration of 1 mg/ml with 30% acetonitrile solution (v/v, in Milli-Q water) as a stock solution. Then, the stock solution was diluted to 200 μg/ml with printing buffer [0.3 M phosphate-buffered saline (PBS), 0.2% glycerin, 0.01% Triton, and 1.5% mannitol] as the printing solution. SJ membranes (SJ Biomaterials, Suzhou, China) were used as supporting materials for their low background in serological assays, even without bovine serum albumin blocking (11). The membranes were first activated with the activation buffer (0.1 M 1-ethyl-3-(3-dimethylaminopropyl) carbodiimide and 0.1 M N-hydroxysuccinimide, both from Medpep, Shanghai, China) for 30 min and rinsed with Milli-Q water, then used for printing immediately. Microarrays were prepared using the non-contact printer sciFLEXARRAYER S1 (Scienion Co., Berlin, Germany) with one drop of 0.4 nL printing solution for each sample. All peptide samples were printed once to form a 7 × 7 × 4 array. For each subarray, the four corners of the square were positive controls spotted with Human IgG (DGCS-Bio, Beijing, China) at a concentration of 100 μg/ml. The first spot of the second line was a negative control with printing buffer, and the

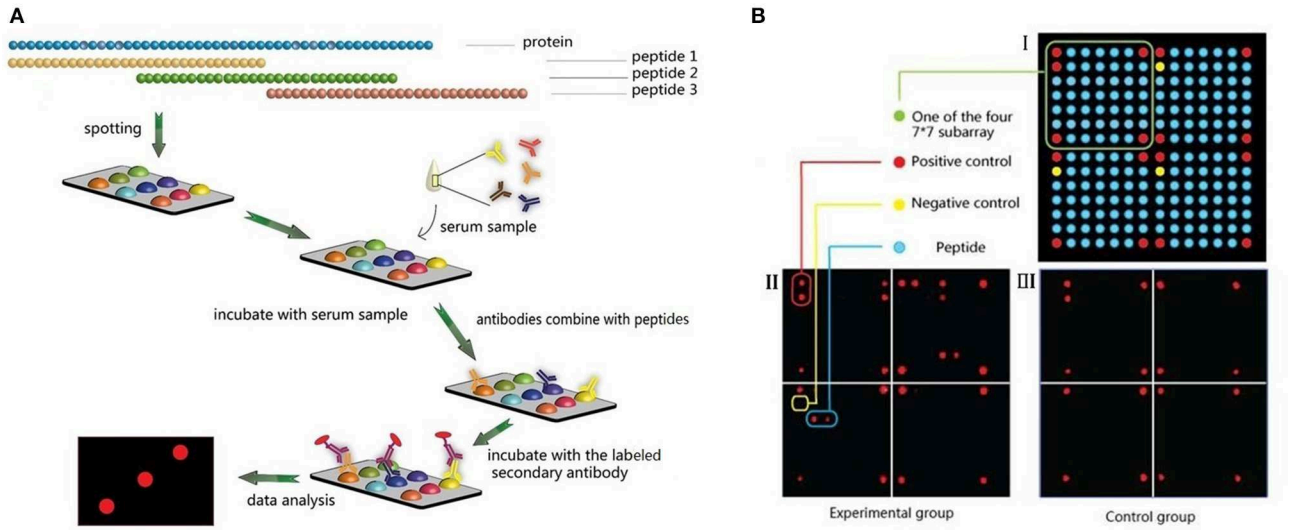

FIGURE 1 | Microarray design and experimental procedures. **(A)** Peptides design and microarray detection procedure. **(B)** Spots arrangement on the microarrays.

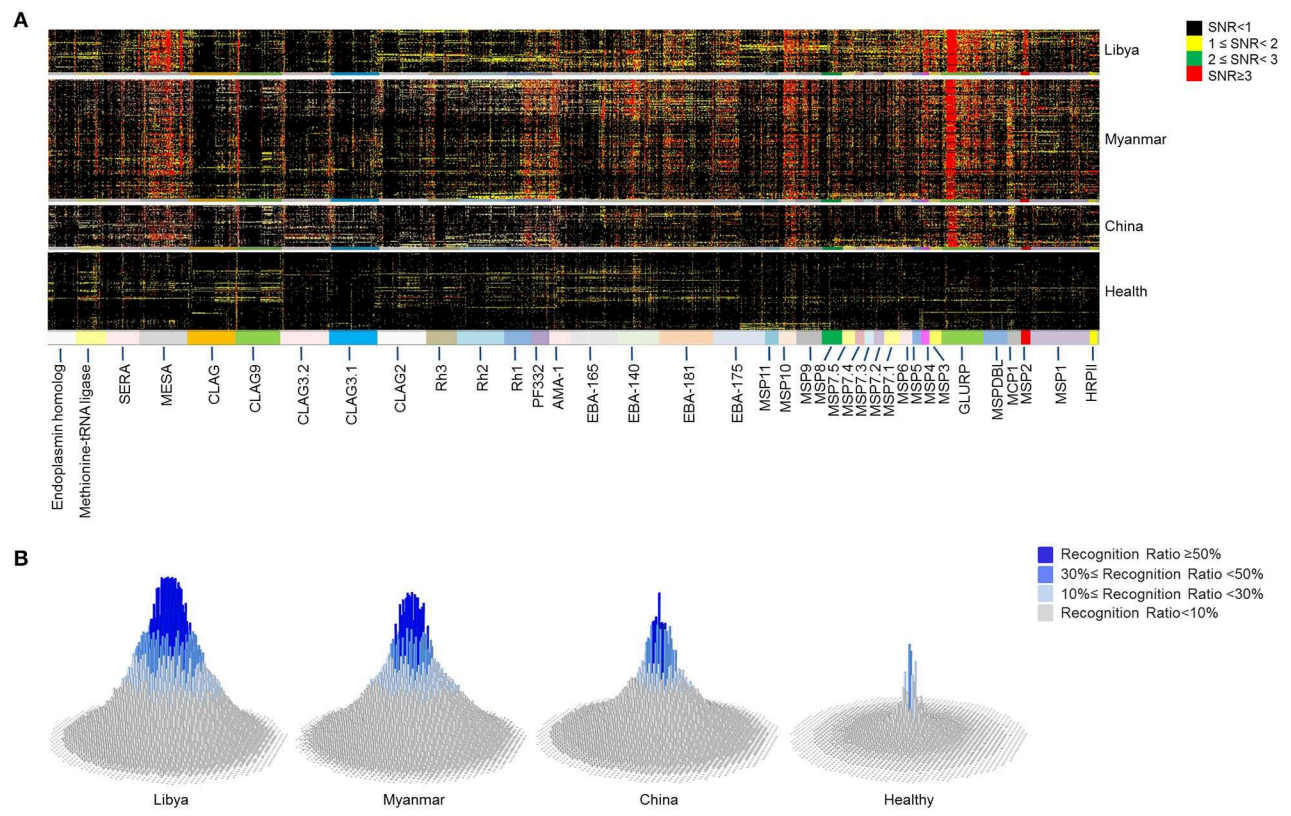

FIGURE 2 | Microarray profile analysis for immunogenic epitopes of *Plasmodium falciparum* antigens. Microarray screening was carried out with 2,024 peptides mapping to 37 proteins of *P. falciparum* 3D7 strain. Sera from naturally exposed individuals from Libya ($n = 60$), Myanmar ($n = 171$), and China ($n = 58$) and healthy individuals from China ($n = 144$) were used to detect the antibody recognition of the peptides. **(A)** The heat map depicts the breadth and intensity of antibodies reactivity across sera samples. Each dot shows a signal to noise (SNR) value of one individual. The color of the dot indicates the intensity of the reaction with SNR. **(B)** The histograms show the prevalence rate of 2,024 peptides in different regions derived from the microarray profile. The height and color of the column indicate the prevalence rate of each peptide. Each column represents one peptide.

other 176 spots were all target samples (**Figure 1B**). All samples were printed in triplicate.

Microarray Assays

Each serum sample was diluted with a dilution buffer (1% bovine serum albumin, 1% casein, 0.5% sucrose, 0.2% polyvinylpyrrolidone, and 0.5% Tween 20 in 0.01 M PBS, pH = 7.4). Then, 200 μl diluted serum was added onto each peptide microarray and incubated for 30 min on a shaker (150 rpm, 22°C). A microarray incubated with only the serum dilution buffer was included as a blank control. The microarray was then rinsed 3 times with TBST buffer (50 mM Tris, 150 mM NaCl, 0.05% Tween 20, pH 7.5) and incubated with 200 μl HRP-anti-human-IgG (1:5,000 diluted, ZSGB-Bio, Beijing, China) in Peroxidase Conjugate Stabilizer/Diluent (Thermo Fisher Scientific, Wilmington, USA) for another 30 min on the shaker (150 rpm, 22°C), followed by the same washing steps described above. Then, 15 μl SuperSignal ELISA Femto Maximum Sensitivity Substrate (Thermo Fisher Scientific) was added to the microarray to obtain chemiluminescence signals. The signal images were taken at a wavelength of 635 nm using an LAS 4000 imaging system (GE Healthcare, Uppsala, Sweden). The sera were diluted and tested for sensitivity and specificity at 1:100, 1:200, and 1:500 dilution, and 1:100 dilution was used in the eventual experiments due to its high sensitivity and low background (**Supplementary Figure 1**).

Microarray Data Acquisition, Validation, and Analysis

The microarray data were extracted from the chemiluminescence emission with AMIA Toolbox (12). R_{dot} was the readout of the human IgG/peptide dot, and R_{neg} was the readout of the negative control dot. The Signal noise ratio (SNR) was defined by the following equation: $(R_{dot} - R_{neg})/R_{neg}$. To validate the stability of the microarray, contrast experiments were carried out using the chips with the same peptides in the following groups: chips on two columns in one reactor, chips from two reactors, chips under the operation of two technicians, and chips from different lots (**Supplementary Figure 2**). The reaction intensity showed the concentration of the antibodies against the peptides in the sera. The intensity-cutoff values were determined at signal-to-noise ratio (SNR) = 2 to obtain a low level of false positives with high sensitivity. Thus, the reaction intensity was considered to be positive when the SNR $\geq$ 2.0. The prevalence rate (PR) was applied to depict the proportion of sera samples from a group that positively recognized a peptide and defined by the following equation: number of positive sera with SNR values $\geq$ 2/number of total sera from the appropriate group. Peptides with FM-PR $\geq$ 10%, Healthy-PR $\leq$ 10%, and FM-PR/Healthy-PR $\geq$ 2 ($p < 0.05$) were defined as positively recognized peptides. The peptides with FM-PR $\geq$ 50% and Healthy-PR $<$ 10% were considered to be highly antigenic peptides.

Repetitive Sequence Analysis

Sequences that contained no less than two tandem repeats with more than three amino acids per repeat were considered to be repetitive sequences. Multiple sequence alignment was used to analyse the repetitive motifs of peptides. The alignments were conducted by using Clustalx 1.83 software (Genome Campus, Cambridgeshire, UK), and the alignments were edited by using Jalview (13).

Invasion Inhibition Assays

The *P. falciparum* 3D7 strain was cultured and synchronized as previously described (14). Briefly, parasites were continuously cultured in malaria culture Media (MCM) in a candle jar at 37°C. The growth of the parasites was synchronized by treatment with 5% (w/v) D-sorbitol (Sigma, USA). Rabbit polyclonal antibodies were prepared at Beijing Protein Innovation (Beijing, China) by immunizing New Zealand white rabbits with Keyhole Limpet Hemocyanin (KHL)-coupled peptides (**Supplementary Figure 3**), which had the highest PR in the corresponding proteins or repetitive motifs. A total of 20 peptides were selected from 14 proteins that contain highly antigenic epitopes. Total IgG from sera of rabbits immunized with peptide were purified with the rProtein A Sepharose Fast Flow Kit (GE Healthcare, Uppsala, Sweden) according to the manufacturer's instructions. Total IgG from one rabbit was eventually used in each experiment with replicates. Complete culture medium (50 μl) and synchronized schizont-stage parasites (100 μl) were added to each well (0.5% parasitemia and 1% haematocrit) of 96-well U-bottom plates. Thereafter, 5 μl of test IgG was gently mixed into the indicated wells. The cultures were incubated at 37°C in a moist atmosphere of 94% N_2, 1% O_2, and 5% CO_2. After an incubation of 40–42 h, the cells were harvested and transferred to tubes for the following steps and parasitemia was determined using flow cytometry. All samples were tested in duplicate.

Measurement of Parasitemia

Thin smears of cultures were fixed in methanol and Giemsa stained for measurement of parasitemia by microscopy. The method used to detect parasitemia by flow cytometry was previously described (15). Briefly, 1–2 $\times$ 10^6 red blood cells were fixed with 1 ml of PBS containing 0.025% (v/v) glutaraldehyde at room temperature for 20 min and permeated with 0.5 ml of PBS containing 0.01% saponin at room temperature for 5 min. Then, the cells were stained with propidium iodide (PI) at a final concentration of 10 μg/ml in PBS containing 2% FCS. The cells were detected and analyzed using a FACS Canto II flow cytometer (BD Biosciences, San Jose, CA, USA).

Statistical Analysis

Data were analyzed using Excel 2010 and GraphPad Prism 5.0 (GraphPad, San Diego, CA). Two-tailed unpaired Student's *t*-tests were used to evaluate the immunoreactivity of the recognized peptides. Pearson and Spearman correlation analysis was used to calculate correlation coefficients. Values of $p < 0.05$ were considered to constitute significant differences.

TABLE 1 | The invasion-associated antigens of *Plasmodium falciparum* blood stage parasites involved in microarray screening.

Stage-association	Protein	NCBI protein ID	Description
Merozoite-associated proteins	Apical membrane antigen (AMA)-1	XP_001348015.1	An important vaccine candidate that is expressed in mature stage parasites and is essential for invasion (16–19)
	CLAG	XP_002808744.1	A strictly conserved family which play roles in merozoite invasion and infected cell adherence (20)
	CLAG3.1	XP_001351100.1	
	CLAG3.2	XP_001351099.1	
	CLAG9	XP_001352222.1	
	CLAG2	XP_001349709.1	
	Erythrocyte binding antigen (EBA) 140	XP_001349859.1	Members of erythrocyte binding-like family (EBL) of proteins involved in tight junction formation during invasion of red blood cells and as potential vaccine candidate for malaria (21–25)
	EBA165	XP_001351546.1	
	EBA175	XP_001349207.2	
	EBA181	XP_001350957.1	
	Endoplasmin homolog	XP_001350620.1	A protein with heat shock protein (Hsp) 90 domain which may serve as a molecular clamp in the binding of ligand proteins to Hsp90 (26)
	Merozoite capping protein 1 (MCP1)	XP_001347552.1	A 60-kDa protein participating in merozoite invasion of erythrocytes by facilitating attachment or movement of the junction along the parasite cytoskeletal network (26)
	Merozoite surface protein (MSP)1	XP_001352170.1	GPI-anchored proteins expressed on the merozoite surface, most of which are essential for parasite survival (10, 27). MSP-1 is the most abundant protein of GPI-anchored proteins. Vaccines with MSP-1, 2 and 3 are now being tested in clinical Phase trials (28–32)
	MSP2	XP_001349578.1	
	MSP3	XP_001347629.1	
	MSP4	XP_001349580.1	
	MSP5	XP_001349579.1	
	MSP6	XP_001347630.1	
	MSP7.1	XP_001350074.1	
	MSP7.2	XP_001350075.1	
	MSP7.3	XP_002809050.1	
	MSP7.4	XP_002809050.1	
	MSP7.5	XP_001350080.1	
	MSP8	XP_001351583.1	
	MSP9	XP_001350683.1	
	MSP10	XP_966190.1	
	MSP11	XP_001347636.1	
	Merozoite surface protein duffy binding-like (MSPDBL)	XP_001347632.1	A protein with Duffy binding-like (DBL) domain Localized on the merozoite surface and binding of merozoites with erythrocytes during invasion (33)
	Rhoptry-associated protein (RAP)1	XP_001348275.1	Rhoptry bulb proteins localsing to the parasite-host cell interface and rhoptry-associated protein complex facilitates the survival of the parasites (34)
	RAP2	XP_002808967.1	
	RAP3	XP_001351928.1	
Mature parasite-derived proteins	Glutamate-rich protein (GLURP) or	XP_001347628.1	The antigen of a blood-stage vaccine of malaria, which is an exoantigen expressed at all stages of development in the parasite life cycle in human host (35–38). Phase Ib trial of the vaccine candidate GMZ2 with Glurp and MSP has been finished (39)
	Histidine-rich protein (HRP) II	XP_002808743.1	A valuable protein for diagnosis of malaria since it is produced by ring and trophozoite-stage parasites and secreted into plasma (40, 41)
	Mature-parasite-infected erythrocyte surface antigen (MESA)	XP_001351567.1	A highly repetitive protein plays a major role in cytoadherence of infected erythrocytes by binding with erythrocyte membrane skeletal protein 4.1 (42–44)
	Methionine-tRNA ligase	XP_001347624.1	A protein with Glutathione-S-transferase (GST)-like domains which are involved in protein-protein interaction. The protein localizes to apicoplasts in asexual stages of parasites and play important roles on parasite growth (45, 46)
	P. falciparum 332 (PF332)	XP_001348162.2	A Large protein locating on the surface of mature schizonts plays critical roles in both invasion and sequestration with the Duffy-binding-like domain (47, 48)
	Serine repeat antigen (SERA)5	XP_001349586.1	An abundant late-trophozoite and schizont stage antigen with limited polymorphism which is being tested in clinical Phase trials (49, 50)

RESULTS

The Antigenic Epitopes of Critical *P. falciparum* Antigens Depicted by Peptide Microarray Screening

The proteins (**Table 1**) involved in parasite invasion of red blood cells were selected, and the sequences of these proteins were divided into consecutive peptides to explore the immunogenic epitopes. Each peptide has 30 amino acids, and 15 amino acids overlapped with adjacent peptides. The antigenicity of the epitopes was analyzed by microarray. Microarray screening of the peptide profile was carried out with 289 sera samples from patients suffering from FM and 144 healthy individuals as controls. Sixty FM patients were from Libya, while 171 were from Burma, and 58 were from China. The peptides were recognized with various reaction intensities, but most of them were poorly recognized by the sera (**Figure 2A**). Among the 2,024 peptides of the microarray profile, only 39.2% (794 peptides) were positively recognized (**Supplementary File 2**). The peptides that showed high reaction intensity tended to have a high prevalence of specific antibodies (**Figure 2** and **Supplementary Figure 4**).

Furthermore, the reaction intensity (**Figure 2A**) and prevalence (**Figure 2B**) of the antibodies to the specific epitopes varied with the intensity of malaria transmission. For most of the peptides, the antibody reaction intensity and prevalence gradually decreased from high-endemicity areas to low-endemicity areas. These findings are consistent with previous studies (51). However, a large number of peptides had higher antibody reaction intensity and prevalence in Burma, the relatively low-endemic area, than in Libya. These peptides were mainly attributed to AMA-1, CLAG family members, EBA family members, MSP family members, PF332, Rh1, Rh2, and SERA5 (**Supplementary File 3**). Thus, the humoural response is not always related to the transmission intensity.

Among the 37 proteins, only 14 proteins, GLURP, MESA, AMA-1, CLAG, EBA-181, endoplasmin homolog, MCP1, MSP4, 5, 9, and 10, MSPDBL, PF332, and Rh1, contained peptides with FM-PR $\geq$ 50%, Healthy-PR $<$ 10% and FM-PR/Healthy-PR $\geq$ 2 ($p < 0.05$, **Figure 3**). These peptides with high PR tended to have high reaction intensity with the third quartile of SNR (Q3); thus, they were considered to contain highly antigenic epitopes. Among the 14 proteins, only GLURP and PfEMP2/MESA contained highly antigenic epitopes with a relatively wider distribution in the molecules, whereas the reactivity of the other proteins was restricted to only one or a few peptides (**Figure 3**).

Repetitive Sequences With Distinct Amino Acid Contexts Were Predominantly Immunogenic

The sequences of positively reactive peptides were analyzed to reveal the characteristics of the immunogenic determinants of the antigens. Surprisingly, most of the immunodeterminants were located in the low-complexity regions composed of distinct repetitive amino acid motifs (**Table 2**). The proportion of repetitive peptides rose perpendicularly with the increase in PR, and 11 peptides (91.7%) were repetitive peptides among the 12 peptides with a PR $\geq$ 80%. Although most of the highly antigenic peptides were repetitive peptides, not all of the repetitive sequences were highly antigenic. Among the 2,024 peptides of the 37 proteins, 139 peptides from 17 proteins contained repetitive motifs (**Figure 4A** and **Supplementary File 4**). Of those repetitive motifs, 6 repetitive motifs, -HEIVEVEEILPED-, -ENIENNEN-, KKKQEEE, -EDDD, G(/D)ESKET, and NKNK were located in peptides with high antigenicity (**Figure 4A**). Different peptides with the tandem repeat motif -HEIVEVEEILPED- were most immunogenic, with a PR value of 83.2 $\pm$ 2.5%, while the peptides with repeating motif ENEDND had a PR value of only 1.7 $\pm$ 0.0% for sera samples from malaria-exposed individuals.

To determine the significance of the amino acids within or surrounding the motif in their effect on the antigenicity, different peptides were constructed containing at least one GESKET motif and a decreased number of non-repetitive amino acids according to the peptide sequence of the MESA protein, RPRKH VNVMG ESKET GESKE TGESK ETGES, or with decreased tandem repeats of GESKET, and then screened with the same set of patient sera. The addition of any amino acids to the core repetitive sequence did not obviously alter the antibody recognition rate or reaction intensity (**Figure 4B**), and additional units beyond two repeats did not add any power for recognition (**Figure 4C**). Thus, a sequence containing two tandem repeats of the motif will be sufficient to form a B cell epitope and can elicit strong humoural immune responses.

Another feature of the highly immunogenic polypeptides was the enrichment of glutamic acid. Among the 2,024 peptides, 94 were glutamate-rich, in which glutamic acid accounted for over 30% of the amino acid composition, and 23 (24.5%) glutamate-rich peptides were recognized by over 50% of sera samples from malaria-exposed individuals (**Supplementary File 5**). Furthermore, the proportion of glutamate-rich peptides increased to 83.3% when the PR was over 80% (**Table 2**). Among the 11 repetitive polypeptides with a PR over 80% in sera samples from the FM patients, 10 (90.9%) were glutamate-rich (**Table 2**). For all 2,024 peptides, the content of glutamic acid was positively correlated with the PR in sera samples from malaria-exposed individuals (Pearson $r = 0.1090$, $p < 0.0001$, **Supplementary Figure 5**).

The Antibodies Specific for the Highly Antigenic Epitopes Failed to Interfere With Parasite Invasion

To determine whether the epitope-specific antibodies are protective, invasion inhibition assays were undertaken to investigate the neutralization effect of the total IgG from peptide-immunized rabbits. In total, 20 peptides from 14 proteins that contain highly antigenic epitopes were selected as immunogens for generation of specific antibodies. Peptide-specific polyclonal antibodies were generated, and total IgG was purified. Antibodies specific to the peptide (MESA-008) from the red blood cell-binding sites of MESA with low antigenicity were also applied to compare the neutralization activity of the antibodies specific for the functional domain with that of the antibodies specific for

FIGURE 3 | Immunoreactivity profiles of the 14 proteins that contained highly antigenic peptides. The reaction intensity and prevalence rate (PR) of the specific antibodies against peptides from the antigens were detected by microarray with sera from falciparum patients (FM) and healthy individuals (Healthy). The PR for the

(Continued)

FIGURE 3 | appropriate group (left Y axis) and the reaction intensity with the third quartile of signal noise ratio (Q3, right Y axis) were showed. Each pair of columns or dots represents one peptide. Peptides with prevalence rates ≥50% in FM patients, <10% in healthy individuals and FM-PR/Healthy-PR ≥ 2 ($p < 0.05$) were highlighted in red. The upper columns or dots represent FM patients (FM-PR or FM-Q3), and the below represent healthy individuals (Healthy-PR or Healthy-Q3). The profiles of proteins were represented in the name order.

TABLE 2 | Characteristics of positively recognized peptides.

Prevalence rate (PR)	No. peptides	Repetitive peptides		E-rich peptides		E-rich repetitive peptides	
		No.	Proportion of total peptides (%)	No.	Proportion of total peptides (%)	No.	Proportion of repetitive peptides (%)
≥80%	12	11	91.7	10	83.3	10	90.9
<80%, ≥60%	16	9	56.3	8	50.0	7	77.8
<60%, ≥50%	29	10	34.5	5	17.2	3	30.0
<50%, ≥40%	46	15	32.6	7	15.2	5	33.3
<40%, ≥30%	116	27	23.3	17	14.7	12	44.4
<30%, ≥20%	211	25	11.8	15	7.1	7	28.0
<20%, ≥10%	364	21	5.8	19	5.2	9	42.9
Total	794	118	1.5	81	1.0	53	44.9

Peptides with FM-PR ≥ 10%, Healthy-PR < 10%, and FM-PR/Healthy-PR ≥ 2 were considered to be positively recognized peptides. Glutamic (E)-rich cutoff = 30%.

immunodeterminants. Normal rabbit IgG was used as a negative control. Only antibodies specific for AMA-1-040, GLURP-027, GLURP-078, and MESA-008 showed invasion inhibitory effect (**Figure 5**), and the three antibodies specific for AMA-1-040, GLURP-027, and GLURP-078 showed a weaker effect than the antibodies specific for MESA-008. Most of the antibodies specific for the highly antigenic peptides showed no inhibitory effect on parasite invasion (**Supplementary Figure 6**).

DISCUSSION

Invasion into erythrocytes by extracellular merozoites is an essential step in the development and proliferation of malarial parasites (6, 7). In recent decades, various antigens have been explored for the development of blood-stage vaccines. However, progress has been limited, which has been attributed to antigen polymorphisms, antigenic variation and functional complementation (7, 10). In previous studies, the criteria for vaccine candidate selection have been mainly based on the immunogenicity of antigens in eliciting high antibody titres, and CSP-based vaccines are the best example (52, 53). Lessons have indicated that apart from the importance of cellular immune responses, antibodies that can neutralize the infectivity of the parasite are critical. In this study, we used overlapping peptide microarrays to investigate the immunogenic epitopes of 37 *P. falciparum* antigens, most of which are essential proteins in parasite invasion and have been extensively explored in malaria vaccine development.

To date, epitopes analyses have either been based on limited structural data or sequence data alone. The structural studies located the position of epitopes within the protein conformation (54). However, studies on discontinuous B-cell epitopes are laborious, time consuming and provide limited information. The overlapping peptide array in our study, with 2,024 peptides derived from 37 malaria antigens, presented abundant information in one study and present a fine map of linear B-cell epitopes that elicit humoral immune responses.

Here, surprisingly, of the highly immunogenic regions of the well-recognized antigens, most of the epitopes were located in the low-complexity regions composed of repetitive amino acid motifs (**Table 2**). The proportion of repetitive peptides sharply increased and reached 91.7% when the antibody PR was over 80% (**Table 2**). Tandemly repeated amino acid sequences are characteristic of many malaria parasite proteins, and a multitude of other higher eukaryotic parasites, such as *Toxoplasma*, *Leishmania*, *Trypanosoma*, and *Schistosoma*, share this common feature, and it has been proposed that antigens with sequence repeats are dominant natural immunogens (55).

Enrichment of glutamic acid was another feature of the highly immunogenic polypeptides. Most peptides with a high antibody reaction intensity and PR were glutamate-rich sequences, and the proportion of glutamate-rich peptides sharply increased and reached 83.3% when the PR was over 80% (**Table 2**). Furthermore, the repetitive and glutamate-rich characteristics were strongly correlated with the immunogenicity of the peptides (**Table 2** and **Supplementary Figures 4**, **5**). Some glutamate-rich proteins of *Plasmodium* were found to be antigenic and had a serological cross-reaction. GLURP, the glutamate-rich protein of *P. falciparum*, is expressed in both liver and blood stage parasites (35). Previous studies have found a strong correlation between the levels of GLURP-specific IgGs and protection against malaria attacks (36, 37). The human immune response is primarily directed to R2 (aa 705-1178), where the highly immunogenic repeats are located, and this region of GLURP has been developed primarily as a blood-stage vaccine (38). In addition to *Plasmodium*, many other pathogens, such as *Babesia*

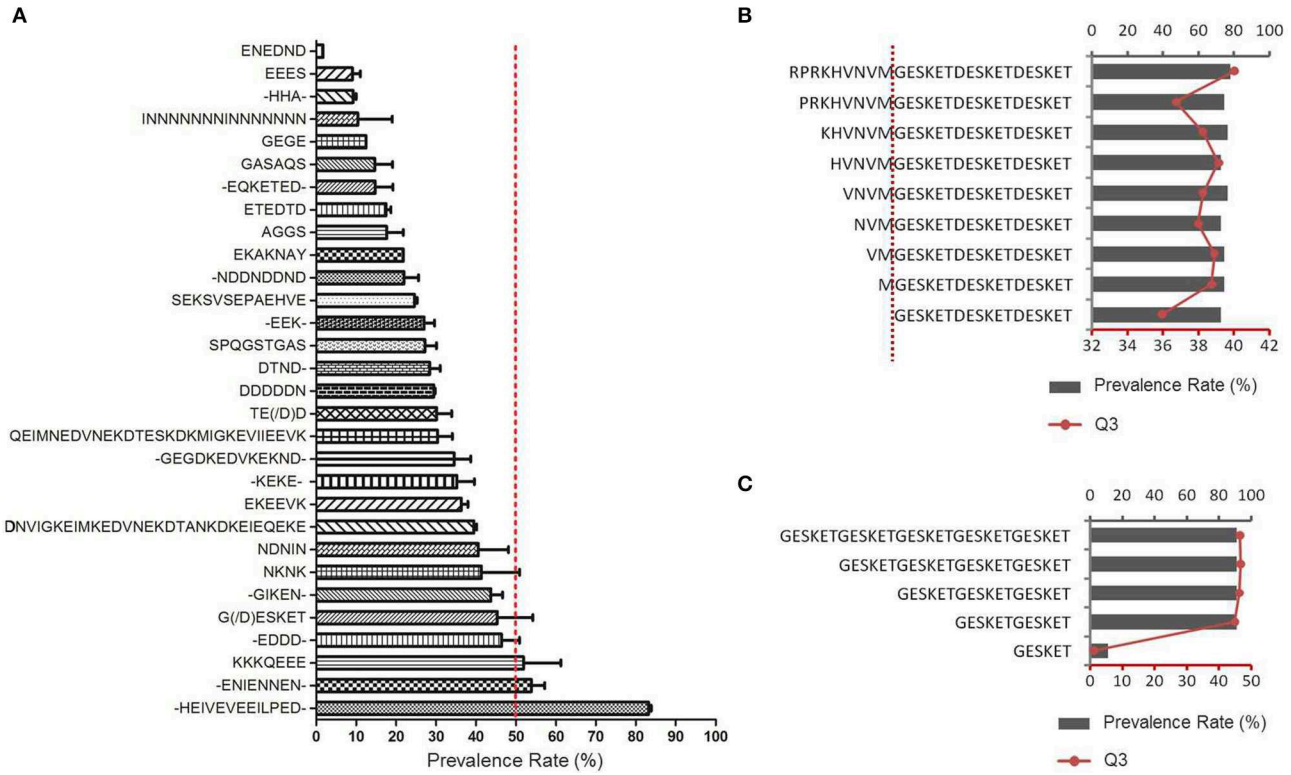

FIGURE 4 | Antigenicity of repetitive peptides. **(A)** The prevalence rates of antibodies recognizing different peptides with the repetitive motifs were derived from the microarray profile. The 30 types of repetitive sequences were represented in rows in ascending order of the average PR of all the peptides containing the motif (Mean ± SD). - indicates varied amino acid. The red dotted line indicates the 50% prevalence rate. **(B,C)** Thirteen extra synthetic peptides were printed onto the microarray chips and detected by sera from African FM patients. **(B)** Influence of the adjacent amino acids on the immunoreactivity of peptides with the G(D)ESKET motif **(C)** The number of G(D)ESKET required for eliciting optimal humoral responses. The prevalence rate for appropriate group (columns, up X axis) and the reaction intensity with the third quartile of signal noise ratio (Q3, red dot, low X axis) were showed.

gibsoni (56), *Entamoeba histolytica* (57), *Pneumocystis carinii,* and *Mycobacterium tuberculosis* (58), also have immunogenic glutamate-rich proteins, and some of them were evaluated as new diagnostic tools or vaccine candidates. Additionally, many allergens from plants (59–61) and some self-antigens that lead to autoimmune disease (62, 63) were also glutamate-rich antigens. Thus, it is likely that there are many glutamate-rich proteins that are highly immunogenic in various pathogen species, especially in parasites.

The function of conserved, tandemly repeated regions within proteins has been discussed for decades and is still not clear (64, 65). Proteins with repetitive structures have already been used for vaccines. These proteins, including the circumsporozoite protein (CSP), were initially spotted by immune-screening of cDNA libraries and later included in vaccine development (52, 53). However, except for the most advanced pre-erythrocytic vaccine candidate RTS,S, the progress of vaccines based on these antigens has not been very satisfactory. Hypotheses such as antigenic variation and functional complementation with alternative proteins that allow the parasite to evade the protective immune responses of the host have been proposed (5, 66), but could not explain the failures of vaccines targeting the early-stage parasite.

A direct invasion inhibitory effect of antibodies on the functional domains of malaria antigens has been observed in many studies. Anti-AMA1 polyclonal and monoclonal antibodies block parasite invasion *in vitro* (16–18). Monoclonal antibodies against the epitope mapped to the receptor binding sites of EBA-175 could block *P. falciparum* erythrocyte invasion (25). Our results also found that antibodies against the erythrocyte binding site of PfEMP2/MESA could inhibit parasite invasion. MESA has been recognized as a membrane-anchored protein that is expressed in the trophozoite stage of the parasite and contains 7 distinct repeat regions that cover over 60% of the protein (42, 43). The distribution of the repeats in the molecule is highly conserved [**Figure 4B** and **Supplementary Figure 7**; (67)]. The binding domain of MESA with the erythrocytic protein 4.1 was mapped to a 19-residue region near the N-terminus of the protein (44).

However, antibodies against the high-antigenicity and low-complexity epitopes represented by the microarray seemed to have no neutralizing effect. Since the sera used in this study were derived from patients, particularly the Chinese patients returning from African regions who were suffering from *P. falciparum* infection with at least one malaria episode, the antibodies specific for the repetitive antigenic motifs were

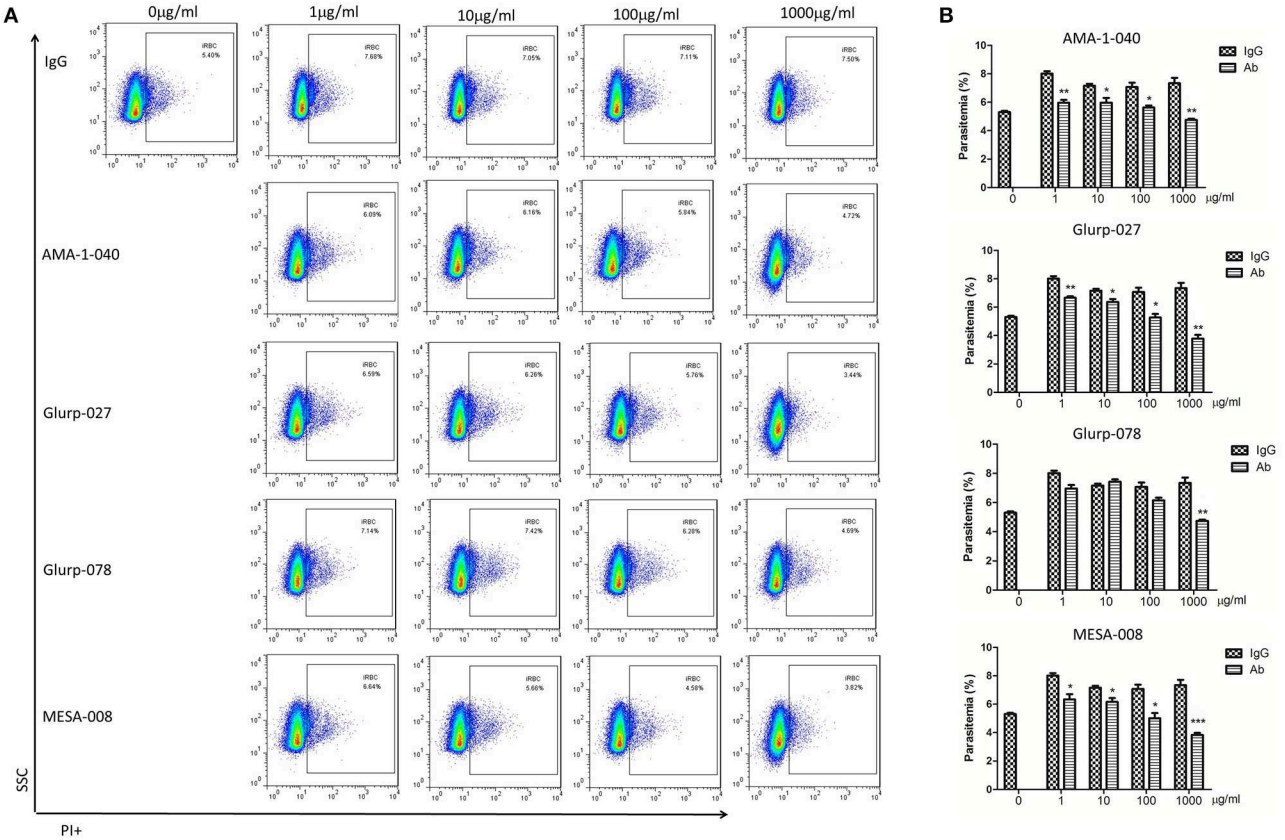

FIGURE 5 | Invasion inhibition assays with total IgG containing peptide-specific antibodies. Highly synchronized schizont-stage parasites of PF3D7 strain were cultured in the presence of total IgG containing polyclonal antibodies (Ab) and IgG control derived from naïve rabbits. Parasitemia was determined using flow cytometry after 40–42 h of cultivation. **(A)** Representative dot plots showing the frequency of PI+ infected red blood cells (iRBC). **(B)** Histograms comparing the parasitemia between antibody-treated group and IgG control group. The results are representative of 3 independent experiments, with data indicating the mean + SD. $^{*}p < 0.05$, $^{**}p < 0.01$, and $^{***}p < 0.0001$. *Comparison to the corresponding naïve IgG group.

obviously not protective. The *in vitro* assay revealed that most antibodies to the highly antigenic epitopes showed no inhibitory effect on parasite invasion (**Supplementary Figure 6**). The antibodies of AMA-1-040, GLURP-027, and GLURP-078, which displayed slight invasion inhibition effect, were all located outside the low-complexity region of the protein sequences (**Figure 5**). When trying to build three-dimensional structures of these proteins with SWISS-MODEL [https://swissmodel.expasy.org/interactive; (68)] to predict the location of the highly antigenic epitopes, however, these epitopes were all located in the regions without homolog models, indicating that these regions are likely within the non-functional domains. Thus, it is hypothesized that antibodies to the low-complexity regions might not be able to interfere with the functionality of the host molecules. Furthermore, these highly antigenic peptides had very low polymorphism in different isolates of *P. falciparum* (**Supplementary Figure 7**), indicating these sequences may serve as decoy epitopes to attract host humoural immunity.

Previous studies reported that antibodies of highly antigenic epitopes could block parasite invasion through an antibody-dependent cell inhibition (ADCI) mechanism (69, 70). However, most of these studies were carried out *in vitro* with monocytes from healthy individuals. Our study with *P. berghei* ANKA (PbANKA)-infected C57BL/6 mice revealed that although monocytes/macrophages facilitated parasite clearance in the early stage of infection, their activity and quantity declined soon post-infection (71). Some parasite antigens were even reported to suppress monocyte/macrophage activation (72). Furthermore, phagocytic receptors of non-opsonic phagocytosis, such as CD36 and ICAM-1, were sharply decreased post-infection or even deficient in malaria-endemic regions (73–75). Thus, even though these antibodies could interfere with parasite invasion through ADCI *in vitro*, their effect *in vivo* remains uncertain, considering the very short extracellular period of time before parasite invasion.

Collectively, we found that *P. falciparum* antigens that contain repetitive sequences and glutamate-rich motifs are highly antigenic. The motifs with a confined sequence context drove humoural responses to the protein regions that are likely not functional. Thus, malaria parasites, especially *P. falciparum*, may have developed a mechanism of immune evasion with the decoy epitopes that drive the host humoural immunity away from the

recognition of the functional domains of these antigens (64, 65). These findings highlight the importance of determination of antigens that can elicit protective immune responses.

DATA AVAILABILITY STATEMENT

All datasets generated for this study are included in the article/**Supplementary Material**.

ETHICS STATEMENT

All procedures performed on human samples were carried out in line with the tenets of the Declaration of Helsinki. Informed consent was obtained from every individual involved in this study, and all human samples were anonymized. All animal procedures in this study were conducted according to the animal husbandry guidelines of the Chinese Academy of Medical Sciences. The studies in both humans and animals were reviewed and approved by the Ethical Committee and the Experimental Animal Committee of the Chinese Academy of Medical Sciences, with Ethical Clearance Numbers IPB-2016-2 and CQJ16001. The patients/participants provided their written informed consent to participate in this study.

AUTHOR CONTRIBUTIONS

QC conceived and designed experiments. NH, NJ, and YM performed the majority of the experiments. NH and QC analyzed the data and wrote the manuscript. YZ, XP, and SL performed some experiments.

FUNDING

This work was supported by the National Natural Science Foundation of China (Grant Nos. 81672050 and 81420108023), CAMS Innovation Fund for Medical Sciences (CIFMS) (Grant Nos. 2017-I2M-3-016 and 2019-I2M-5-042), and National Science and Technology Major Project (Grant Nos. 2018ZX10101001 and 2018ZX10711001).

ACKNOWLEDGMENTS

We thank Professor Klavs Berzins at Stockholm University very much for providing the archived patient sera from Africa. We appreciate very much the technical assistance from experts of Nano-Bio-Chem Centre, Suzhou Institute of Nano-Tech and Nano-Bionics, Chinese Academy of Sciences. We appreciate the kind assistance from Professor Jian Yang in the bioinformatic analysis of the data.

SUPPLEMENTARY MATERIAL

The Supplementary Material for this article can be found online at: https://www.frontiersin.org/articles/10.3389/fimmu.2020.00610/full#supplementary-material

REFERENCES

1. Feachem RGA, Chen I, Akbari O, Bertozzi-Villa A, Bhatt S, Binka F, et al. Malaria eradication within a generation: ambitious, achievable, and necessary. *Lancet*. (2019) 394:1056–112. doi: 10.1016/S0140-6736(19)31139-0
2. World Health Organization. *WHO World Malaria Report 2012*. (2012). Available online at: https://www.who.int/malaria/publications/world_malaria_report_2012/en/
3. World Health Organization. *Malaria Vaccine Pilot Launched in Malawi*. (2019). Available online at: https://www.who.int/news-room/detail/23-04-2019-malaria-vaccine-pilot-launched-in-malawi (accessed April 23, 2019).
4. Schwartz L, Brown GV, Genton B, Moorthy VS. A review of malaria vaccine clinical projects based on the WHO rainbow table. *Malar J*. (2012) 11:11. doi: 10.1186/1475-2875-11-11
5. Riley EM, Stewart VA. Immune mechanisms in malaria: new insights in vaccine development. *Nat Med*. (2013) 19:168–78. doi: 10.1038/nm.3083
6. Dvorak JA, Miller LH, Whitehouse WC, Shiroishi T. Invasion of erythrocytes by malaria merozoites. *Science*. (1975) 187:748–50. doi: 10.1126/science.803712
7. Cowman AF, Crabb BS. Invasion of red blood cells by malaria parasites. *Cell*. (2006) 124:755–66. doi: 10.1016/j.cell.2006.02.006
8. Narula AK, Azad CS, Nainwal LM. New dimensions in the field of antimalarial research against malaria resurgence. *Eur J Med Chem*. (2019) 181:111353. doi: 10.1016/j.ejmech.2019.05.043
9. Kimura M, Kaneko O, Liu Q. Indentification of the four species of human malaria parasites by nested PCR that targets variant sequences in the small subunit rRNA gene. *Parasitol Int*. (1997) 46:91–5. doi: 10.1016/S1383-5769(97)00013-5
10. Beeson JG, Drew DR, Boyle MJ, Feng G, Fowkes FJ, Richards J, et al. Merozoite surface proteins in red blood cell invasion, immunity and vaccines against malaria. *FEMS Microbiol Rev*. (2016) 40:343–72. doi: 10.1093/femsre/fuw001
11. Ma H, Wu Y, Yang X, Liu X, He J, Fu L, et al. Integrated poly(dimethysiloxane) with an intrinsic nonfouling property approaching absolute zero background in immunoassays. *Anal Chem*. (2010) 82:6338–42. doi: 10.1021/ac101277e
12. White AM, Daly DS, Willse AR, Protic M, Chandler DP. Automated microarray image analysis toolbox for MATLAB. *Bioinformatics*. (2005) 21:3578–9. doi: 10.1093/bioinformatics/bti576
13. Waterhouse AM, Procter JB, Martin DM, Clamp M, Barton GJ. Jalview version 2–a multiple sequence alignment editor and analysis workbench. *Bioinformatics*. (2009) 25:1189–91. doi: 10.1093/bioinformatics/btp033
14. Trager W, Jensen JB. Human malaria parasites in continuous culture. 1976. *J Parasitol*. (2005) 91:484–6. doi: 10.1645/0022-3395(2005)0910484:HMPICC2.0.CO;2
15. Barkan D, Ginsburg H, Golenser J. Optimisation of flow cytometric measurement of parasitaemia in plasmodium-infected mice. *Int J Parasitol*. (2000) 30:649–53. doi: 10.1016/S0020-7519(00)00035-7
16. Thomas AW, Deans JA, Mitchell GH, Alderson T, Cohen S. The Fab fragments of monoclonal IgG to a merozoite surface antigen inhibit *Plasmodium knowlesi* invasion of erythrocytes. *Mol Biochem Parasitol*. (1984) 13:187–99. doi: 10.1016/0166-6851(84)90112-9
17. Thomas AW, Trape JF, Rogier C, Goncalves A, Rosario VE, Narum D, et al. High prevalence of natural antibodies against *Plasmodium falciparum* 83-kilodalton apical membrane antigen (PF83/AMA-1) as detected by capture-enzyme-linked immunosorbent assay using full-length baculovirus recombinant PF83/AMA-1. *Am J Trop Med Hyg*. (1994) 51:730–40. doi: 10.4269/ajtmh.1994.51.730
18. Harris KS, Casey JL, Coley AM, Masciantonio R, Sabo JK, Keizer DW, et al. Binding hot spot for invasion inhibitory molecules on *Plasmodium falciparum* apical membrane antigen 1. *Infect Immun*. (2005) 73:6981–9. doi: 10.1128/IAI.73.10.6981-6989.2005
19. Sheehy SH, Duncan CJ, Elias SC, Biswas S, Collins KA, O'Hara GA, et al. Phase Ia clinical evaluation of the safety and immunogenicity of the *Plasmodium*

falciparum blood-stage antigen AMA1 in ChAd63 and MVA vaccine vectors. *PLoS ONE*. (2012) 7:e31208. doi: 10.1371/journal.pone.0031208
20. Gupta A, Thiruvengadam G, Desai SA. The conserved clag multigene family of malaria parasites: essential roles in host-pathogen interaction. *Drug Resist Updates*. (2015) 18:47–54. doi: 10.1016/j.drup.2014.10.004
21. Orlandi PA, Sim BK, Chulay JD, Haynes JD. Characterization of the 175-kilodalton erythrocyte binding antigen of *Plasmodium falciparum*. *Mol Biochem Parasitol*. (1990) 40:285–94. doi: 10.1016/0166-6851(90)90050-V
22. Maier AG, Baum J, Smith B, Conway DJ, Cowman AF. Polymorphisms in erythrocyte binding antigens 140 and 181 affect function and binding but not receptor specificity in *Plasmodium falciparum*. *Infect Immun*. (2009) 77:1689–99. doi: 10.1128/IAI.01331-08
23. Lopaticki S, Maier AG, Thompson J, Wilson DW, Tham WH, Triglia T, et al. Reticulocyte and erythrocyte binding-like proteins function cooperatively in invasion of human erythrocytes by malaria parasites. *Infect Immun*. (2011) 79:1107–17. doi: 10.1128/IAI.01021-10
24. Zerka A, Rydzak J, Lass A, Szostakowska B, Nahorski W, Wroczynska A, et al. Studies on immunogenicity and antigenicity of baculovirus-expressed binding region of *Plasmodium falciparum* EBA-140 merozoite ligand. *Arch Immunol Ther Exp*. (2016) 64:149–56. doi: 10.1007/s00005-015-0367-5
25. Ambroggio X, Jiang L, Aebig J, Obiakor H, Lukszo J, Narum D, et al. The epitope of monoclonal antibodies blocking erythrocyte invasion by *Plasmodium falciparum* map to the dimerization and receptor glycan binding sites of EBA-175. *PLoS ONE*. (2013) 8:e56326. doi: 10.1371/journal.pone.0056326
26. Klotz FW, Hadley TJ, Aikawa M, Leech J, Howard RJ, Miller L, et al. A 60-kDa *Plasmodium falciparum* protein at the moving junction formed between merozoite and erythrocyte during invasion. *Mol Biochem Parasitol*. (1989) 36:177–85. doi: 10.1016/0166-6851(89)90190-4
27. Gilson PR, Nebl T, Vukcevic D, Moritz RL, Sargeant T, Speed TP, et al. Identification and stoichiometry of glycosylphosphatidylinositol-anchored membrane proteins of the human malaria parasite *Plasmodium falciparum*. *Mol Cell Proteomics*. (2006) 5:1286–99. doi: 10.1074/mcp.M600035-MCP200
28. Lawrence G, Cheng QQ, Reed C, Taylor D, Stowers A, Cloonan N, et al. Effect of vaccination with 3 recombinant asexual-stage malaria antigens on initial growth rates of *Plasmodium falciparum* in non-immune volunteers. *Vaccine*. (2000) 18:1925–31. doi: 10.1016/S0264-410X(99)00444-2
29. Stoute JA, Gombe J, Withers MR, Siangla J, McKinney D, Onyango M, et al. Phase 1 randomized double-blind safety and immunogenicity trial of *Plasmodium falciparum* malaria merozoite surface protein FMP1 vaccine, adjuvanted with AS02A, in adults in western Kenya. *Vaccine*. (2007) 25:176–84. doi: 10.1016/j.vaccine.2005.11.037
30. Hu J, Chen Z, Gu J, Wan M, Shen Q, Kieny MP, et al. Safety and immunogenicity of a malaria vaccine, *Plasmodium falciparum* AMA-1/MSP-1 chimeric protein formulated in montanide ISA 720 in healthy adults. *PLoS ONE*. (2008) 3:e1952. doi: 10.1371/journal.pone.0001952
31. McCarthy JS, Marjason J, Elliott S, Fahey P, Bang G, Malkin E, et al. A phase 1 trial of MSP2-C1, a blood-stage malaria vaccine containing 2 isoforms of MSP2 formulated with Montanide(R) ISA 720. *PLoS ONE*. (2011) 6:e24413. doi: 10.1371/journal.pone.0024413
32. Hoffman SL, Vekemans J, Richie TL, Duffy PE. The march toward malaria vaccines. *Vaccine*. (2015) 33(Suppl. 4):D13–23. doi: 10.1016/j.vaccine.2015.07.091
33. Wickramarachchi T, Cabrera AL, Sinha D, Dhawan S, Chandran T, Devi YS, et al. A novel *Plasmodium falciparum* erythrocyte binding protein associated with the merozoite surface, PfDBLMSP. *Int J Parasitol*. (2009) 39:763–73. doi: 10.1016/j.ijpara.2008.12.004
34. Ghosh S, Kennedy K, Sanders P, Matthews K, Ralph SA, Counihan NA, et al. The *Plasmodium* rhoptry associated protein complex is important for parasitophorous vacuole membrane structure and intraerythrocytic parasite growth. *Cell Microbiol*. (2017) 19:e12733. doi: 10.1111/cmi.12733
35. Hogh B, Thompson R, Zakiuddin IS, Boudin C, Borre M. Glutamate rich *Plasmodium falciparum* antigen (GLURP). *Parassitologia*. (1993) 35(Suppl.):47–50.
36. Theisen M, Vuust J, Gottschau A, Jepsen S, Hogh B. Antigenicity and immunogenicity of recombinant glutamate-rich protein of *Plasmodium falciparum* expressed in *Escherichia coli*. *Clin Diagn Lab Immunol*. (1995) 2:30–4. doi: 10.1128/CDLI.2.1.30-34.1995
37. Oeuvray C, Theisen M, Rogier C, Trape JF, Jepsen S, Druilhe P. Cytophilic immunoglobulin responses to *Plasmodium falciparum* glutamate-rich protein are correlated with protection against clinical malaria in Dielmo, Senegal. *Infect Immun*. (2000) 68:2617–20. doi: 10.1128/IAI.68.5.2617-2620.2000
38. Lyke KE. Steady progress toward a malaria vaccine. *Curr Opin Infect Dis*. (2017) 30:463–70. doi: 10.1097/QCO.0000000000000393
39. Belard S, Issifou S, Hounkpatin AB, Schaumburg F, Ngoa UA, Esen M, et al. A randomized controlled phase Ib trial of the malaria vaccine candidate GMZ2 in African children. *PLoS ONE*. (2011) 6:e22525. doi: 10.1371/journal.pone.0022525
40. Namsiripongpun V, Wilde H, Pamsandang P, Tiersansern P. Field study of an antigen-detection ELISA specific for *Plasmodium falciparum* malaria. *Trans R Soc Trop Med Hyg*. (1993) 87:32–4. doi: 10.1016/0035-9203(93)90410-R
41. Desakorn V, Silamut K, Angus B, Sahassananda D, Chotivanich K, Suntharasamai P, et al. Semi-quantitative measurement of *Plasmodium falciparum* antigen PfHRP2 in blood and plasma. *Trans R Soc Trop Med Hyg*. (1997) 91:479–83. doi: 10.1016/S0035-9203(97)90292-3
42. Coppel RL. Repeat structures in a *Plasmodium falciparum* protein (MESA) that binds human erythrocyte protein 4.1. *Mol Biochem Parasitol*. (1992) 50:335–47. doi: 10.1016/0166-6851(92)90231-8
43. Kun JF, Waller KL, Coppel RL. *Plasmodium falciparum*: structural and functional domains of the mature-parasite-infected erythrocyte surface antigen. *Exp Parasitol*. (1999) 91:258–67. doi: 10.1006/expr.1998.4374
44. Bennett BJ, Mohandas N, Coppel RL. Defining the minimal domain of the *Plasmodium falciparum* protein MESA involved in the interaction with the red cell membrane skeletal protein 4.1. *J Biol Chem*. (1997) 272:15299–306. doi: 10.1074/jbc.272.24.15299
45. Wolf YI, Aravind L, Grishin NV, Koonin EV. Evolution of aminoacyl-tRNA synthetases–analysis of unique domain architectures and phylogenetic trees reveals a complex history of horizontal gene transfer events. *Genome Res*. (1999) 9:689–710.
46. Hussain T, Yogavel M, Sharma A. Inhibition of protein synthesis and malaria parasite development by drug targeting of methionyl-tRNA synthetases. *Antimicrob Agents Chemother*. (2015) 59:1856–67. doi: 10.1128/AAC.02220-13
47. Moll K, Chene A, Ribacke U, Kaneko O, Nilsson S, Winter G, et al. (2007). A novel DBL-domain of the *P. falciparum* 332 molecule possibly involved in erythrocyte adhesion. *PLoS ONE* 2:e477. doi: 10.1371/journal.pone.0000477
48. Nilsson S, Moll K, Angeletti D, Albrecht L, Kursula I, Jiang N, et al. Characterization of the Duffy-binding-like domain of *Plasmodium falciparum* blood-stage antigen 332. *Malar Res Treat*. (2011) 2011:671439. doi: 10.4061/2011/671439
49. Perrin LH, Merkli B, Loche M, Chizzolini C, Smart J, Richle R. Antimalarial immunity in Saimiri monkeys. Immunization with surface components of asexual blood stages. *J Exp Med*. (1984) 160:441–51. doi: 10.1084/jem.160.2.441
50. Palacpac NM, Ntege E, Yeka A, Balikagala B, Suzuki N, Shirai H, et al. Phase 1b randomized trial and follow-up study in Uganda of the blood-stage malaria vaccine candidate BK-SE36. *PLoS ONE*. (2013) 8:e64073. doi: 10.1371/journal.pone.0064073
51. Nebie I, Tiono AB, Diallo DA, Samandoulougou S, Diarra A, Konate AT, et al. Do antibody responses to malaria vaccine candidates influenced by the level of malaria transmission protect from malaria? *Trop Med Int Health*. (2008) 13:229–37. doi: 10.1111/j.1365-3156.2007.01994.x
52. Burkot TR, Da ZW, Geysen HM, Wirtz RA, Saul A. Fine specificities of monoclonal antibodies against the *Plasmodium falciparum* circumsporozoite protein: recognition of both repetitive and non-repetitive regions. *Parasite Immunol*. (1991) 13:161–70. doi: 10.1111/j.1365-3024.1991.tb00272.x
53. Soe S, Theisen M, Roussilhon C, Aye KS, Druilhe P. Association between protection against clinical malaria and antibodies to merozoite surface antigens in an area of hyperendemicity in Myanmar: complementarity between responses to merozoite surface protein 3 and the 220-kilodalton glutamate-rich protein. *Infect Immun*. (2004) 72:247–52. doi: 10.1128/IAI.72.1.247-252.2004
54. Morris GE. Epitope mapping. *Methods Mol Biol*. (2005) 295:255–68. doi: 10.1385/1-59259-873-0:255

55. Schofield L. The circumsporozoite protein of Plasmodium: a mechanism of immune evasion by the malaria parasite? *Bull World Health Organ.* (1990) 68(Suppl.):66–73.
56. Mousa AA, Cao S, Aboge GO, Terkawi MA, El Kirdasy A, Salama A, et al. Molecular characterization and antigenic properties of a novel *Babesia gibsoni* glutamic acid-rich protein (BgGARP). *Exp Parasitol.* (2013) 135:414–20. doi: 10.1016/j.exppara.2013.08.005
57. Carrero JC, Petrossian P, Acosta E, Sanchez-Zerpa M, Ortiz-Ortiz L, Laclette J, et al. Cloning and characterization of *Entamoeba histolytica* antigens recognized by human secretory IgA antibodies. *Parasitol Res.* (2000) 86:330–4. doi: 10.1007/s004360050052
58. Smulian AG, Sullivan DW, Theus SA. Immunization with recombinant *Pneumocystis carinii* p55 antigen provides partial protection against infection: characterization of epitope recognition associated with immunization. *Microbes Infect.* (2000) 2:127–36. doi: 10.1016/S1286-4579(00)00275-6
59. Thakur IS. Fractionation and analysis of allergenicity of allergens from *Prosopis juliflora* pollen. *Int Arch Allergy Appl Immunol.* (1989) 90:124–9. doi: 10.1159/000235013
60. Fowler MR, Gartland J, Norton W, Slater A, Elliott MC, Scott N, et al. RS2: a sugar beet gene related to the latex allergen Hev b 5 family. *J Exp Bot.* (2000) 51:2125–6. doi: 10.1093/jexbot/51.353.2125
61. de Souza CR, Carvalho LJ. Glutamic acid-rich proteins in cassava (*Manihot esculenta* Crantz) storage roots. *Mol Nutr Food Res.* (2013) 57:934–5. doi: 10.1002/mnfr.201370055
62. Stodulkova E, Pohl J, Man P, Votruba J, Capkova J, Sedlackova M, et al. Comparison of amino acid compositions of peptides eluted from HLA-B27 molecules of healthy individuals and patients with ankylosing spondylitis. *Immunol Lett.* (2006) 103:135–41. doi: 10.1016/j.imlet.2005.10.017
63. Winkler PA, Ekenstedt KJ, Occelli LM, Frattaroli AV, Bartoe JT, Venta PJ, et al. A large animal model for CNGB1 autosomal recessive retinitis pigmentosa. *PLoS ONE.* (2013) 8:e72229. doi: 10.1371/journal.pone.0072229
64. Anders RF. Multiple cross-reactivities amongst antigens of *Plasmodium falciparum* impair the development of protective immunity against malaria. *Parasite Immunol.* (1986) 8:529–39. doi: 10.1111/j.1365-3024.1986.tb00867.x
65. Schofield L. On the function of repetitive domains in protein antigens of *Plasmodium* and other eukaryotic parasites. *Parasitol Today.* (1991) 7:99–105. doi: 10.1016/0169-4758(91)90166-L
66. Arama C, Troye-Blomberg M. The path of malaria vaccine development: challenges and perspectives. *J Intern Med.* (2014) 275:456–66. doi: 10.1111/joim.12223
67. Saul A, Yeganeh F, Howard RJ. Conservation of repeating structures in the PfEMP2/MESA protein of *Plasmodium falciparum*. *Immunol Cell Biol.* (1992) 70:353–5. doi: 10.1038/icb.1992.45
68. Waterhouse A, Bertoni M, Bienert S, Studer G, Tauriello G, Gumienny R, et al. SWISS-MODEL: homology modelling of protein structures and complexes. *Nucleic Acids Res.* (2018) 46:W296–303. doi: 10.1093/nar/gky427
69. Bouharoun-Tayoun H, Attanath P, Sabchareon A, Chongsuphajaisiddhi T, Druilhe P. Antibodies that protect humans against *Plasmodium falciparum* blood stages do not on their own inhibit parasite growth and invasion *in vitro*, but act in cooperation with monocytes. *J Exp Med.* (1990) 172:1633–41. doi: 10.1084/jem.172.6.1633
70. Theisen M, Soe S, Oeuvray C, Thomas AW, Vuust J, Danielsen S, et al. The glutamate-rich protein (GLURP) of *Plasmodium falciparum* is a target for antibody-dependent monocyte-mediated inhibition of parasite growth *in vitro*. *Infect Immun.* (1998) 66:11–7. doi: 10.1128/IAI.66.1.11-17.1998
71. Hou N, Jiang N, Zou Y, Piao X, Liu S, Li S, et al. Down-regulation of Tim-3 in monocytes and macrophages in *Plasmodium* infection and its association with parasite clearance. *Front Microbiol.* (2017) 8:1431. doi: 10.3389/fmicb.2017.01431
72. Sampaio NG, Eriksson EM, Schofield L. *Plasmodium falciparum* PfEMP1 modulates monocyte/macrophage transcription factor activation and cytokine and chemokine responses. *Infect Immun.* (2018) 19:86. doi: 10.1128/IAI.00447-17
73. Lee K, Godeau B, Fromont P, Plonquet A, Debili N, Bachir D, et al. CD36 deficiency is frequent and can cause platelet immunization in Africans. *Transfusion.* (1999) 39:873–9. doi: 10.1046/j.1537-2995.1999.39080873.x
74. Aitman TJ, Cooper LD, Norsworthy PJ, Wahid FN, Gray JK, Curtis BR, et al. Malaria susceptibility and CD36 mutation. *Nature.* (2000) 405:1015–6. doi: 10.1038/35016636
75. Chua CL, Brown G, Hamilton JA, Rogerson S, Boeuf P. Monocytes and macrophages in malaria: protection or pathology? *Trends Parasitol.* (2013) 29:26–34. doi: 10.1016/j.pt.2012.10.002

Conflict of Interest: The authors declare that the research was conducted in the absence of any commercial or financial relationships that could be construed as a potential conflict of interest.

frontiers in Immunology

ORIGINAL RESEARCH
published: 16 April 2020
doi: 10.3389/fimmu.2020.00593

Myricetin Possesses Anthelmintic Activity and Attenuates Hepatic Fibrosis *via* Modulating TGFβ1 and Akt Signaling and Shifting Th1/Th2 Balance in *Schistosoma japonicum*-Infected Mice

Ping Huang[1,2,3], *Minyu Zhou*[1,2,3], *Shaoyun Cheng*[1,2,3], *Yue Hu*[1,2,3], *Minzhao Gao*[4], *Yubin Ma*[1,2,3], *Yanin Limpanont*[5], *Hongli Zhou*[1,2,3], *Paron Dekumyoy*[5], *Yixin Cheng*[1,2,3] *and Zhiyue Lv*[1,2,3,4]*

[1] Joint Program of Pathobiology, Fifth Affiliated Hospital, Zhongshan School of Medicine, Sun Yat-sen University, Guangzhou, China, [2] Ministry of Education, Key Laboratory of Tropical Disease Control, Sun Yat-sen University, Guangzhou, China, [3] Key Laboratory of Tropical Translational Medicine of Ministry of Education, Hainan Medical University, Haikou, China, [4] Guangdong Provincial Key Laboratory of Biomedical Imaging, Fifth Affiliated Hospital, Sun Yat-sen University, Zhuhai, China, [5] Faculty of Tropical Medicine, Mahidol University, Bangkok, Thailand

OPEN ACCESS

Edited by:
Jun-Hu Chen,
National Institute of Parasitic Diseases, China

Reviewed by:
Jilong Shen,
Anhui Medical University, China
Theerakamol Pengsakul,
Prince of Songkla University, Thailand

***Correspondence:**
Zhiyue Lv
lvzhiyue@mail.sysu.edu.cn

Specialty section:
This article was submitted to Microbial Immunology, a section of the journal Frontiers in Immunology

Received: 24 February 2020
Accepted: 13 March 2020
Published: 16 April 2020

Citation:
Huang P, Zhou M, Cheng S, Hu Y, Gao M, Ma Y, Limpanont Y, Zhou H, Dekumyoy P, Cheng Y and Lv Z (2020) Myricetin Possesses Anthelmintic Activity and Attenuates Hepatic Fibrosis via Modulating TGFβ1 and Akt Signaling and Shifting Th1/Th2 Balance in Schistosoma japonicum-Infected Mice. Front. Immunol. 11:593. doi: 10.3389/fimmu.2020.00593

Schistosomiasis is a zoonotic and debilitating parasitic disease caused by *Schistosoma japonicum*. Praziquantel remains the choice for treating schistosomiasis, but its efficacy could be hampered by emergence of resistance. In this study, using large-scale drug screening, we selected out myricetin, a natural flavonol compound, having a good anti-schistosome effect. We found that myricetin exhibited dose and time-dependent insecticidal effect on *S. japonicum in vitro*, with an LC_{50} of 600 μM for 24 h, and inhibited female spawning. The drug mainly destroyed the body structure of the worms and induced apoptosis of the worm cells, which in turn led to death. In addition, oral administration of myricetin in mice infected with *S. japonicum* showed a deworming effect *in vivo*, as evidenced by a significant reduction in the liver egg load. H&E staining, quantitative RT-PCR, and Western blotting assays showed that myricetin significantly alleviated liver fibrosis in mice infected with *S. japonicum*. Myricetin also effectively inhibited the expression of TGFβ1, Smad2, phospho-Smad2, Smad3, phospho-Smad3, ERK, phospho-ERK, Akt, and phospho-Akt in the liver of infected mice, suggesting that myricetin attenuated liver fibrosis in mice *via* modulating TGFβ1 and Akt signaling. Flow cytometric analysis of Th subtypes (Th1/Th2/Th17/Treg) in the mouse spleen further revealed that myricetin significantly increased the percentage Th1 cells in infected mice and reduced the proportion of Th2 cells and Th17 cells. Immunology multiplex assay further showed that myricetin attenuated *S. japonicum*-induced rise in the plasma levels of IL-4, IL-5, IL-10, IL-13, and IL-17A in infected mice while increasing the plasma contents of IFN-γ, IL-12, and IL-7. In conclusion, our study provides

the first direct evidence that myricin possesses potent anti-schistosome activities *in vitro* and *in vivo*, and offers new insights into the mechanisms of action by myricetin. The present findings suggest that myricetin could be further explored as a therapeutic agent for *S. japonicum*.

Keywords: *Schistosoma japonicum*, myricetin, Th1/Th2 balance, TGFβ1/Smad, Akt

INTRODUCTION

Schistosomiasis is a parasitic disease caused by parasites of the genus *Schistosom*a. According to a World Health Organization survey, schistosomiasis, one of the neglected tropical diseases, is endemic in 78 countries and regions, infecting ∼230 million people and posing a health threat to ∼780 million people worldwide. Among them, 120 million infections are symptomatic, and nearly 300,000 deaths occur due to schistosomiasis annually in the sub-Saharan Africa area (1–3). There are mainly six species of schistosomiasis that are related to humans, of which *Schistosoma* (*S.*) *mansoni*, *S. haematobium*, and *S.japonicum* are the most prevalent (4). The life expectancy of adult schistosomes is on the average 3–10 years in the human host, and in some cases, it can be as long as 40 years (5, 6). Although schistosomiasis cannot proliferate in the final host, it can produce a large number of eggs deposited in the liver or other organs. Mature females can lay hundreds (*S. mansoni*, *S. haematobium*) to thousands (*S. japonicum*) of eggs per day. Long-term parasitism and massive egg production leads to infection and disease transmission.

In the absence of effective vaccines, chemotherapy is an important measure for schistosomiasis control. Currently, the drug of choice for clinical use is praziquantel, which is effective against all schistosome species in humans and has low toxicity (7–9). However, the application of praziquantel has some limitations. For example, it can kill early schistosomula (3–6 h) that have just penetrated into the skin and adult worms, but it has a weak effect on schistosomula and no preventive effect (10). Repeated infections after treatment is another major problem in schistosomiasis control. Meanwhile, due to the long-term and large-scale repeated uses of praziquantel in endemic areas, resistance to praziquantel may be emerging (11, 12). British scholars have induced a praziquantel-resistant *S. manoni* strain using sub-dose praziquantel to treat infected mice (13), so it is urgent to develop an alternative drug.

Currently, there are three ways to develop praziquantel alternatives (14): synthesis of new praziquantel derivatives, design of new pharmacophores and large-scale screening of new compounds. In this study, we obtained myricetin (3, 3′, 4′, 5, 5′, 7-hexahydroxy flavone), a compound with potential effects on *S. japonicum*, through large-scale screening of small-molecule compound libraries. Myricetin is a natural flavonol compound and widely exists in many natural plants, fruits, and vegetables (15), and has a wide range of pharmacological activities, including anti-oxidant, anti-tumor, anti-inflammatory, anti-microbial, anti-allergic, cardiovascular, and neuronal protection effects (15). Recent studies have revealed that myricetin can improve CCl4-induced liver fibrosis in mice (16), but its effect on liver disease caused by *S. japonicum* infection is yet to be determined.

In this study, we observed the anti-*S. japonicum* adult effect of myricetin *in vitro*, and then a mouse model of *S. japonicum* cercariae infection was established and treated with myricetin. Pathological damage and expression of liver fibrosis factors in infected mice before and after treatment were detected and its underlying mechanism was explored in order to evaluate the potential value of myricetin as a novel anti-*S. japonicum* drug.

MATERIALS AND METHODS

Ethics Statement

The Institutional Animal Care and Use Committee of Sun Yat-sen University approved all animal experiments in this study (No. 2019-2663 and No. 2019-070). Animals were maintained under specific pathogen-free conditions with unrestricted access to sterilized food and water.

Animals

S. japonicum-infected *Oncomelania* (*O.*) *hupensis* were supplied by the National Institute of Parasitic Diseases, Chinese Center for Disease Control and Prevention, Shanghai, China. New Zealand rabbits (2.0–2.5 kg) and BALB/c mice (6–8 weeks) (Charles River, Beijing, China) were maintained in a specific pathogen-free environment and had *ad libitum access* to water and food.

The study protocol for all animal experiments was approved by The Institutional Animal Care and Use Committee of Sun Yat-sen University. Animal studies were carried out in strict accordance with institutional and state guidelines on the use of experimental animals.

Drugs

The small molecule compound library was donated by Dr. Kai Deng at Sun Yat-sen University. Myricetin and dimethyl sulfoxide (DMSO) were purchased from Sigma-Aldrich (St. Louis, MO, USA), and RPMI 1,640 medium, penicillin/streptomycin and fetal bovine serum were purchased from Gibco (California, USA). Praziquantel tablets (Nanjing Pharmaceutical Factory Co., Ltd., Nanjing, China) were gifts from Dr. Shouyi Chen at Guangzhou Center for Disease Control and Prevention, China.

Animal Infection

At an ambient temperature of 25 ± 1°C, *O. hupensis* were put into a 12-well plate, and after addition of dechlorinated water to a

2/3 volume, they were placed under an incandescent lamp for 2 h for cercaria escape. Then, the abdominal fur of rabbits and mice was shaved and the skin moistened with dechlorinated water. The cercariae were counted on a cover slip and then attached to the depilated skin of the animals. After 20 min, the slide was removed. Each New Zealand rabbit was infected with 1000–1200 cercariae, and each mouse was infected with 30 ± 2 cercariae.

In vitro Insecticidal Experiments

Drug Screening

At 8 weeks post-infection, New Zealand rabbits were sacrificed by air embolization after blood was taken from the heart, and adult *S. japonicum* worms parasitizing in the mesenteric vein and hepatic portal vein were collected after dissection. After wash with normal saline, the worms were put into a 24-well plate, and each well-contained 3 pairs of adults/1 mL complete medium (RPMI 1,640 medium containing 100 U/ml penicillin, 100 μg/ml streptomycin and 10% heat-inactivated serum), and then placed in the incubator (37°C, 5% CO_2) for 4 h. Then, different small-molecule drugs (1,000 μM) were added, with 100 μM praziquantel and 1% DMSO as positive and negative control, respectively. At 24, 48, and 72 h of incubation, the survival status of the parasites was evaluated under an inverted microscope and its viability was scored (17) to screen out the drug with obvious insecticidal effect.

Activity of Myricetin Against *S. japonicum in vitro*

Like the drug screening method, in each well with 6 males or females, 1 mL complete medium containing myricetin at different concentrations (300, 400, 500, 600, 700, and 800 μM) was added, with 100 μM praziquantel and 1% DMSO as positive and negative control, respectively. At different time points (24, 48, 72, and 96 h), the survival status of the worms was observed under the microscope and their viability was scored. The culture medium of each group was collected after 96 h incubation, and then centrifuged. The supernatant was discarded, and 1 ml pre-chilled PBS (pH 7.4) was added to resuspend the precipitates. The number of eggs in each group was counted. Three independent experiments were performed; unless otherwise stated, after incubation with the half-lethal dose (LC_{50}) of myricetin, 100 μM praziquantel (positive group) and 1% DMSO (negative group) for 24 h, the worms were collected for subsequent experiments after wash with normal saline, such as acetocarmine-fast green staining, scanning electron microscopy (SEM), transmission electron microscopy (TEM), real-time quantitative polymerase chain reaction (RT-qPCR) and flow cytometric analysis.

Acetocarmine-Fast Green Staining

Adult worms were fixed with 95% ethanol, 3% formalin and 2% glacial acetic acid solution overnight, followed by transfer to acetic acid magenta solution for 1–2 h at room temperature, and separation with 1% HCl. The worms were dehydrated with 80 and 90% ethanol for 5 min, respectively, and then transferred to a solid green staining solution for several seconds. Finally, the worms were transparentized with methyl salicylate for 24 h, and was sealed with neutral gum, and observed under an inverted microscope and photographs were taken (Leica, Heidelberg, Germany).

Scanning Electron Microscope

Adult worms were fixed with 2.5% glutaraldehyde for 24 h. The fixed specimens were dehydrated in gradient ethanol (50, 70, 85, and 100%) for 5–10 min, respectively, and replaced with pure acetone for 15–20 min, and then with isoamyl acetate for 15–30 min. The worms were transferred carefully to the sample cage, dried at critical point, coated with gold on surface, and observed by HITACH2S570 (HITACHI, Tokyo, Japan).

Transmission Electron Microscope

After washing of the worms three times with PBS, the middle part of worms was taken using a surgical blade under a stereo microscope (SZ650, Cnoptec, Chongqing, China), and put in 2.5% glutaraldehyde overnight at 4°C, and then fixed with 1% osmic acid for 1 h. After gradient acetone dehydration, the specimen was dehydrated twice with pure acetone and embedded in 812 epoxy resin (Ted Pella Inc., Redding, USA). After ultra-thin sectioning (60 nm), the slices were immersed in uranyl acetate-lead citrate for double staining and viewed under a Tecnai G2 Spirit Twin electron microscope (FEI, Hillsboro, USA) operated at 80 kV.

In addition, after anesthesia by intraperitoneal sodium pentobarbital, mouse heart in each group was perfused with normal saline, and then fixed with a mixture of 2.5% glutaraldehyde and 4% paraformaldehyde, and then the left lobe of the liver was morselized (1 mm × 1 mm × 1 mm) and immersed in the fixative solution, and then viewed with a transmission electron microscope.

Real-Time Quantitative RT-PCR

Total RNA of *S. japonicum* was extracted using TRIzol Reagent (Thermo Fisher Scientific, Waltham, USA) as instructed by the manufacturer. Then, cDNA was synthesized from total RNA using the RevertAid First Strand cDNA Synthesis kit (Thermo Fisher Scientific). The primers of 13 apoptosis-related genes are displayed in **Table 1**. *NADH* was used as the internal reference gene. In addition, total RNA of liver tissues was extracted. Liver fibrosis-related gene primers are shown in **Table 2**. *GAPDH* served as the internal reference gene. Real time quantitative PCR (RT-qPCR)was performed using SYBR® Premix Ex Taq ™ (Takara, Tokyo, Japan) in a 20- μL volume. The PCR was run on a real-time quantitative PCR system (Bio-Rad, California, USA) at 95°C for 30 s, followed by 95°C for 5 s and 60°C for 34 s for 40 cycles. Next, the melting curve was analyzed (95°C for 15 s and 65°C for 15 s.). The relative expression of each gene was calculated using the $2^{-\Delta\Delta Ct}$ method (18).

Flow Cytometry

For examination of apoptosis of *S. japonicum*, male and female *S. japonicum* were collected separately, and digested with 4% trypsin-EDTA for 4 h at 4°C, and the mixture was gently suspended every 30 min, and then filtered through a 70 μm cell sieve. After centrifugation at 600 g for 10 min, the supernatant was discarded and the pellet was resuspended into a single cell suspension with pre-chilled PBS (pH 7.4).

TABLE 1 | The primer sequences of *Schistosoma japonicum* apoptosis-associated genes used for quantitative real-time PCR.

Gene	Forward primer sequence	Reverse primer sequence
Bak	GCATCAGCCAAGGCATCTTCACAA	TCAACACTATGTGGTTC AGCCCGA
Bax	GGAGACAATGGAGACCGAAA	CGACCAATTAGGGCTTG TGT
Bcl-2	TGACTGTTACTACTCGCTCTG	TGACTCACAATCTCGC ATG
CYC	CCACACAAAACAGGACCCAA	CCTTCTTCAAACCAGCA AATACC
Caspase 2	TGCTAGCTGGGAAACCCAAG	TTCACGAGAATTCGAC GGCA
Caspase 3	ATCGCTGTCCTTCCCTGATTGGAA	ATTACATCATCGCCTGCA TCGGCA
Caspase 7	TGACGTGCAAAATATTAAGAGAGCC	CCACCTTCATCACCAT GAGAAA
Caspase 9	GGGTGAAGAACGCAATCATAAC	CCAAGAAACAAATCCA GGCAAA
APAF	TCTGGATCCCACCGTTTACCAACT	AGCACTCGTCCAACTTCA ACATCC
CIAP	GCGGCCGTTTCCACTCATGTTAAA	ACCACCGGGTTGTAAAC AGGATGA
IAP	TCCGCCTACAAAGTCAATCTAC	TCACTACCTTCGCTCAA TGC
AIF	TGCCGAATTAGCCTACTGGTGTCT	TGGTGGTGGTGTAGAAT CCTTGT
API	TCTGTGCTGTCAACTTGG	GCGTAATCTTGTGCTAA CTG
NADH	CGAGGACCTAACAGCAGAGG	TCCGAACGAACTTTGA ATCC

TABLE 2 | The primer sequences of liver fibrosis related genes (mice) used for quantitative real-time PCR.

Gene	Forward primer sequence	Reverse primer sequence
α-SMA	CACAGCCCTGGTGTGCGACAAT	TTGCTCTGGGCTTCAT CCCCCA
Collagen I	GGAGACAATGGAGACCGAAA	CGACCAATTAGGGCTTG TGT
Collagen IV	ATGCCCTTTCTCTTCTGCAA	GAAGGAATAGCCGATCC ACA
TGF-β1	CAACAATTCCTGGCGTTACCTTGG	GAAAGCCCTGTATTCCGT CTCCTT
TGF-β1RII	TACGAGCCCCCATTTGGTTC	CCAGCACTCGGTCAAAG TCT
Smad2	GTATGGACACAGGCTCTCCG	ACCAGAATGCAGGTTCC GAG
Smad3	CTCCAAACCTCTCCCCGAAT	GAGTTGGAGGGGTCAGT GAA
ERK	ACCACATTCTAGGTATCTTGGGT	AGTTTCGGGCCTTCATGTT AAT
GAPDH	CAGATCCACAACGGATATATTGGG	CATGACAACTTTGGCA TTGTGG

S. japonicum was stained using FITC-Annexin V/propidium iodide (BD Biosciences, Franklin Lakes, USA) and apoptosis was examined using a CytoFLEX flow cytometer (Beckman Coulter, Atlanta, USA).

For examination of cytokine production, mouse spleen was harvested and rendered into single cell suspensions. Red blood cells were lysed and the cell suspension was adjusted to an appropriate concentration. Lymphocytes were stimulated with phorbol myristate acetate/ionomycin (Multisciences, Hangzhou, China) for 4 h, and then Golgi inhibitor brefeldin A/monensin (Multisciences) was added to prevent the exocytosis of cytokines. FITC-conjugated anti-CD3e and V450-conjugated anti-CD8 antibody (BD Biosciences) were added for surface staining, and then the cells were resuspended with fixation/permeabilization buffer (BD Biosciences) and PE-conjugated anti-IFN-γ, IL-17A, APC-conjugated anti-IL-4 antibodies (BD Biosciences) were added for intracellular cytokine staining.

For detection of Treg cells, V450-conjugated anti-CD4 and BB515-conjugated anti-CD25 antibodies (BD Biosciences) were added for surface staining, and then fixed and permeabilized with foxp3 staining buffer (Invitrogen) according to the instructions. Cells were incubated for 30 min at 4°C in the dark for 40–50 min with AF647-conjugated anti-Foxp3 antibody, and then detected with a CytoFLEX S flow cytometer.

Anti-Schistosome Effect *in vivo*

Schistosome-infected mice treated with myricetin in vivo

BALB/c mice were randomly divided into four groups: the control group, the infected group, the praziquantel-treated group and the myricetin-treated group (8 mice in each group). Except for the control group, the remaining mice were infected with 30 ± 2 *S. japonicum* cercariae as described above. Thirty-six to 42 days after infection, the mice in the praziquantel-treated and me-treated groups were administered with praziquantel 500 mg/kg and myricetin 250 mg/kg (dissolved in 0.9% normal saline) daily, and the other two groups received the same volume of saline by gastric lavage. At week 7 post *S. japonicum* infection (wpi), the mice in each group were weighed, and then anesthetized with pentobarbital sodium intraperitoneally, and blood samples were drawn from the orbit. The adult worms were collected from the hepatic portal vein and mesenteric vein *via* cardiac perfusion, and liver and spleen tissues were collected, weighed and then kept according to different experimental needs. All the worms were placed in a 60 mm Petri dish containing normal saline, and the total number of worms, the number of females and males were counted under a stereo microscope (19, 20).

Egg count

The median liver lobe in mice of each group was partially cut out, weighed and placed in an Eppendorf tube, and morsellized, and then added with 4% potassium hydroxide solution, and shaken in a 37°C constant temperature shaker overnight till the liver tissue was completely digested. After centrifugation at 1,500 g for 5 min, the supernatant was removed, and the precipitates were dissolved in 1 mL normal saline and 10 μl of the resuspension with eggs

was counted manually on a microscopic slide. The experiment was repeated 5–7 times. The number of worm eggs per gram of liver tissue was calculated (21).

Enzyme-Linked Immunosorbent Assay (ELISA)

Whole blood was collected from the mice and kept at room temperature for 30 min, and after coagulation, it was centrifuged at 4,000 rpm for 20 min. The serum was harvested, and type III procollagen (PC III), collagen IV, laminin and hyaluronidase were measured by ELISA Kit (Cusabio, Wuhan, China).

Histopathological examination

The left liver tissue of the mice was partially collected and immersed in 4% paraformaldehyde for 24 h, and then the tissue was embedded in paraffin and sectioned. Tissue sections were dewaxed in xylene, and then dehydrated in gradient alcohol, and stained according to haematoxylin-eosin (H&E) and Masson staining instructions (Biosharp, Wuhan, China). Pathological changes were observed under a full automatic upright microscope (Olympus, Tokyo, Japan). The area of granulomas was calculated as previously described (22), and the area of liver fibrosis was measured using Image Pro plus 6.0 software (MEDIA CYBERNETICS image technology Inc., Maryland, USA).

Western blotting assay

Liver tissues were lyzed with RIPA lysis buffer (Thermo Fisher Scientific) or NP40 lysis buffer (Beyotime, Shanghai, China). The lysates were resolved by 12% SDS-polyacrylamide gel electrophoresis. The detection of Collagen I and Collagen IV molecules needs to be performed under non-denaturing conditions. Primary antibodies against the following proteins were used: TGFβ1, SMA, collagen I and IV, Smad2 and phospho-Smad2, Smad3 and phospho-Smad3, ERK1/2 and phospho-ERK1/2, and GAPDH (Abcam, Cambridge, UK). After incubation with a HRP-conjugated goat anti-rabbit IgG (Abcam), the protein bands were detected using Pierce Enhanced Chemiluminescence Detection Reagent (Millipore, Burlington, USA) on a chemiluminescence imaging system (Bio-Rad) and quantified using Image J (National Institutes of Health, Bethesda, USA).

Immunology multiplex assay

Levels of cytokines in mouse serum were determined using Mouse High Sensitivity T Cell Magnetic Bead Panel as instructed by the manufacturer (Millipore, Massachusetts, USA).

Data analysis

Quantitative data was expressed as means ± standard deviation (SD). Differences between groups were analyzed by one-way analysis of variance (ANOVA) using SPSS 19.0 (SPSS Inc, New York, USA). All histograms were drawn by GraphPad Prism 7.0 (GraphPad Software, San Diego, USA). $P < 0.05$ was considered statistically significant.

RESULTS

Myricetin Exhibits Dose- and Time-Dependent Insecticidal Effect on *S. japonicum in vitro* and Inhibits Female Spawning

Totally 480 small-molecule compounds in the compound library (**Supplementary Table 1**) were screened to determine their effects on the viability of *S. japonicum*. The initial detection concentration was 1,000 μM. In this compound library, myricetin had obvious helminthicidal effect *in vitro* (**Figure 1A**). To further delineate the effect of myricetin on schistosomes, we examined the effect of myricetin at different concentrations on the worms over time under a microscope. Myricetin exhibited a time- and dose-dependent helminthicidal effect on adult *S. japonicum in vitro*, with an LC_{50} of 600 μM for 24 h. All the worms died by 8 h post-treatment with myricetin (1,000 μM) or praziquantel while about 80% of the untreated worms were still alive at 96 h (**Figure 1B**, **Table 3**).

Schistosoma eggs are recognized as the leading cause of liver damage in the host (23). When adult worms were incubated with myricetin at different concentrations for 96 h (end point), the number of eggs in each group was counted. When the concentration of myricetin was <500 μM, egg production by females did not significantly differ from that of the normal control group ($P > 0.05$). Meanwhile, egg production decreased to 394.3 ± 136.6 with 500 μM myricetin [$F_{(9,20)} = 50.26$, $P < 0.001$] and 24.67 ± 19.4 with 800 μM myricetin [$F_{(9,20)} = 50.26$, $P < 0.001$], showing a dose-dependent decrease in the female spawning rate (**Figure 1C**).

Myricetin Damages the Integrity of the Tegument of *S. japonicum*

The male worm body became stiff with wrinkles on the tegument, and the intestinal branches became disordered. Vesicle-like protrusions appeared on tegument of the female worm, and the intestine ruptured leaking its contents. Some worms' ovaries were irregular in shape and stained unevenly (**Figures 2A,B**). SEM further revealed that upon treatment with myricetin, the male worms showed a depressed oral and ventral sucker with a swollen margin, and its surface displayed irregular contraction and protuberances deformation. Ridges were arranged irregularly, with loss of cilia and collapse of sensory papillae. Necrosis and rupture appeared at the edge of the male worms' oral sucker and ventral sucker adhering to a lump. The ridges fused together to form a mass in the middle and caudal portion of the integument with decreased sensory papillae. These results indicated that myricetin can damage the integrity of the tegument of *S. japonicum* (**Figures 2C,D**).

Myricetin Promotes Apoptosis of the Worms

TEM revealed tegument peeling, disorganized tegument structure and vesicles between the tegument matrix and

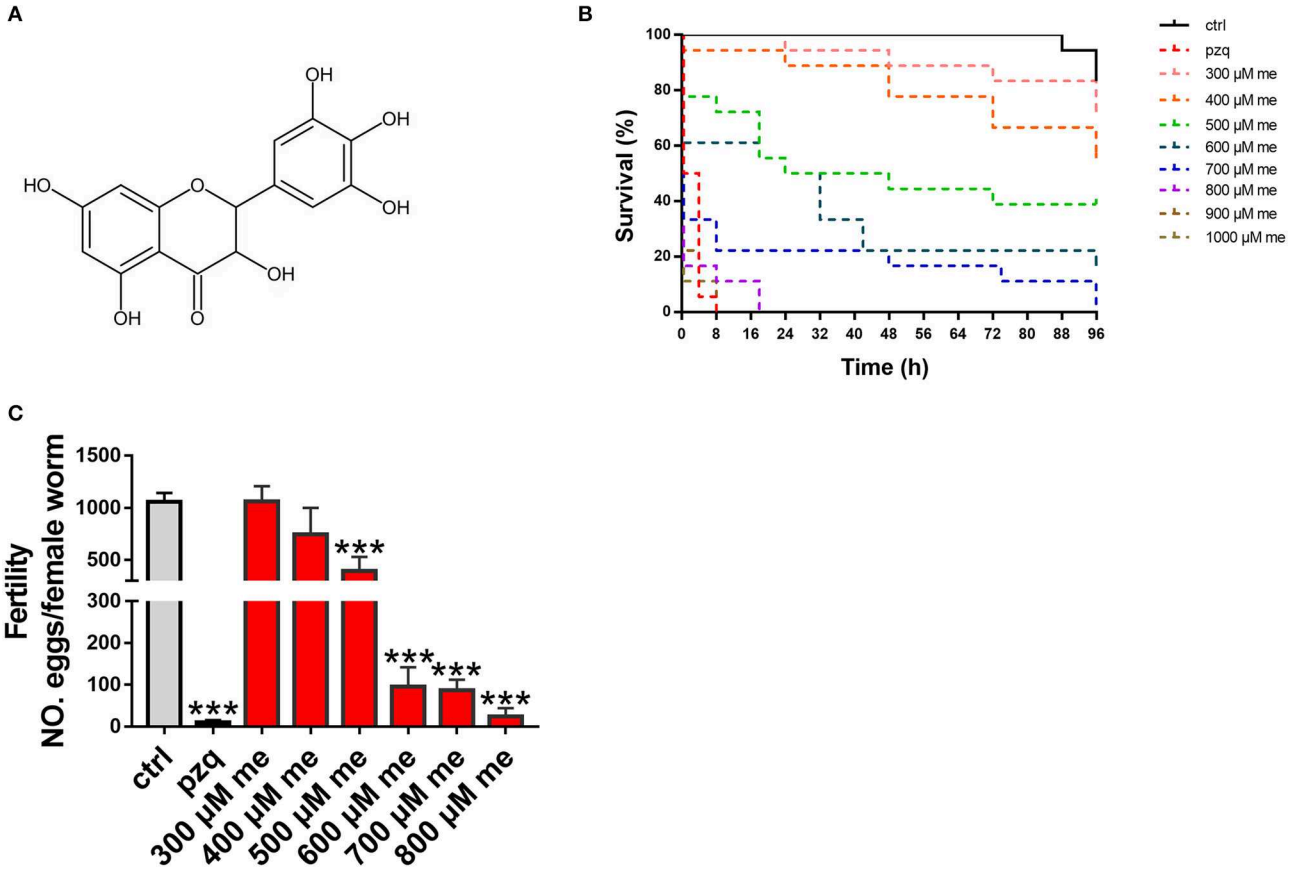

FIGURE 1 | *In vitro* effects of myricetin on the activity of *S. japonicum.* **(A)** Chemical structure of myricetin ($C_{15}H_{10}O_8$, MW318.24) **(B)** Insecticidal activity myricetin against *S. japonicum* in different time intervals and concentrations in the laboratory **(C)** Pairs of adult worms were treated with myricetin in different concentrations (300, 400, 500, 600, 700, and 800 μM) for 96 h, and the number of eggs laid in culture was counted under an inverted microscope. As positive pzq and negative control ctrl group, adult worms were incubated in RPMI 1,640 medium with praziquantel (100 μM) or 1% DMSO, respectively. Data were shown as the means ± SD ($n = 3$). ***$P < 0.001$, compared with the negative ctrl group.

parenchymal cells in male worms in the myricetin-treated group, and a rough outer plasma membrane and swollen myofilaments in female worms. Worm cells treated with myricetin exhibited apoptosis related morphological changes, mainly including karyorrhexis, pyknosis, cytoplasm concentration and increased compactness and cytoplasmic vacuolation (**Figure 3A**). Flow cytometry further revealed that treatment with myricetin for 24 h caused a 5.8- and 4.0- fold increase in the percentage of apoptotic cells of the male (myricetin: 42.7 ± 6.5% *vs.* control: 7.4 ± 2.6%; $t = 8.776$, $P = 0.0009$) and the female worms (myricetin: 11.3 ± 2.3% vs. control: 2.82 ± 0.3; $t = 3.730$, $P = 0.0203$), respectively. These findings suggest that both male and female worms are sensitive to myricetin (**Figures 3B,C**).

Our quantitative RT-PCR assays demonstrated that compared with the control group, the expression of *Bak*, cytochrome c (*CYC*) and apoptotic protease activating factor 1 (*APAF*) in males increased 4-fold ($t = 2.836$, $P = 0.022$), 2.8-fold ($t = 3.231$, ($P = 0.012$) and 10-fold ($t = 2.521$, $P = 0.036$), respectively, while the expression of *Bak*, *CYC*, *caspase 7*, *APAF*, *AIF*, and *API* in females increased 9-fold ($t = 7.566$, $P < 0.001$), 5.8-fold ($t = 8.509$, $P < 0.001$), 4.2-fold ($t = 5.363$, $P = 0.001$), 22.8-fold ($t = 5.101$, $P = 0.001$), 15.8-fold ($t = 6.952$, $P < 0.001$) and 3.5-fold ($t = 5.15$, $P = 0.001$), respectively. The expression of anti-apoptotic gene *Bcl-2* decreased 4-fold ($t = 7.122$, $P < 0.0001$) and 6.7-fold ($t = 7.982$, $P < 0.001$) in males and females, respectively (**Figure 3D**). The results confirmed that myricetin induces apoptosis of *S. japonicum*.

Myricetin Reduces Egg Production of *S. japonicum* and Adult Worm Load in Mice

Mice were treated with 500 mg/kg praziquantel or 250 mg/kg myricetin daily after infection with *S. japonicum* by intragastric lavage for 35–42 days. The mice were euthanized at 7 weeks after infection. The results showed that myricetin significantly reduced the adult worm load in mice [infected: 14.4 ± 2.6; myricetin: 5.6 ± 2.1; $F_{(3, 16)} = 83.32$, $P < 0.001$]. Interestingly, the egg load in the mouse liver in each group indicated that myricetin effectively inhibited egg production of *S. japonicum*

TABLE 3 | The time- and dose- dependent effects of myricetin on *S. japonicum* adult worms.

C (μmol/L)	Number of worms	24 h	48 h	72 h	96 h
		score/VDR (%)	score/VDR (%)	score/VDR (%)	score/VDR (%)
Male					
Ctrl	6	18.0 ± 0.0/0.0	18.0 ± 0.0/0.0	18.0 ± 0.0/0.0	16.7 ± 1.2/7.0
Pzq	6	0.0 ± 0.0/100.0	0.0 ± 0.0/100.0	0.0 ± 0.0/100.0	0.0 ± 0.0/100.0
me (300)	6	16.7 ± 1.2/7.0	16.7 ± 1.2/7.0	16.7 ± 1.2/7.0	14.0 ± 2.0/22.0
me (400)	6	12.7 ± 1.2/30.0	12.7 ± 1.2/30.0	10.0 ± 2.0/44.0	8.0 ± 3.5/56.0
me (500)	6	8.7 ± 1.2/52.0	7.3 ± 1.2/59.0	3.3 ± 1.2/81.0	0.3 ± 0.6/98.0
me (600)	6	7.3 ± 1.2/59.0	3.3 ± 2.3/81.0	0.7 ± 1.2/96.0	0.0 ± 0.0/100.0
me (700)	6	5.3 ± 1.2/70.0	4.7 ± 1.2/74.0	1.0 ± 1.0/94.0	0.0 ± 0.0/100.0
me (800)	6	0.0 ± 0.0/100.0	0.0 ± 0.0/100.0	0.0 ± 0.0/100.0	0.0 ± 0.0/100.0
Female					
Ctrl	6	18.0 ± 0.0/0.0	18.0 ± 0.0/0.0	18.0 ± 0.0/0.0	16.3 ± 1.5/9.0
Pzq	6	0.0 ± 0.0/100.0	0.0 ± 0.0/100.0	0.0 ± 0.0/100.0	0.0 ± 0.0/100.0
me (300)	6	18.0 ± 0.0/0.0	16.7 ± 2.3/7.0	16.0 ± 2.0/11.0	14.7.0 ± 1.2/19.0
me (400)	6	14.7 ± 1.2/19.0	12.7 ± 2.3/30.0	11.3 ± 1.2/37.0	10.7 ± 3.1/41.0
me (500)	6	12.0 ± 0.0/33.0	10.7 ± 1.2/41.0	9.3 ± 3.1/48.0	2.7 ± 1.2/85.0
me (600)	6	10.0 ± 0.0/44.0	9.3 ± 5.0/48.0	4.7 ± 1.2/74.0	0.7 ± 1.2/96.0
me (700)	6	9.3 ± 1.2/48.0	4.0 ± 2.0/78.0	2.7 ± 1.2/85.0	0.0 ± 0.0/100.0
me (800)	6	0.0 ± 0.0/100.0	0.0 ± 0.0/100.0	0.0 ± 0.0/100.0	0.0 ± 0.0/100.0

Adult worms were incubated with myricetin in different concentrations. The viability of worms were scored at 24, 48, 72, and 96 h under inverted microscope using a viability scale of 0–3 (3, normally active; 2, slow activity; 1, minimal activity, occasional movement of head or tail; 0, total absence of mobility). ctrl, adult worms were incubated in RPMI 1,640 medium with 1% DMSO. pzq, praziquantel (100 μM) was used as positive control groups. VDR, Vitality Decrease Rate.

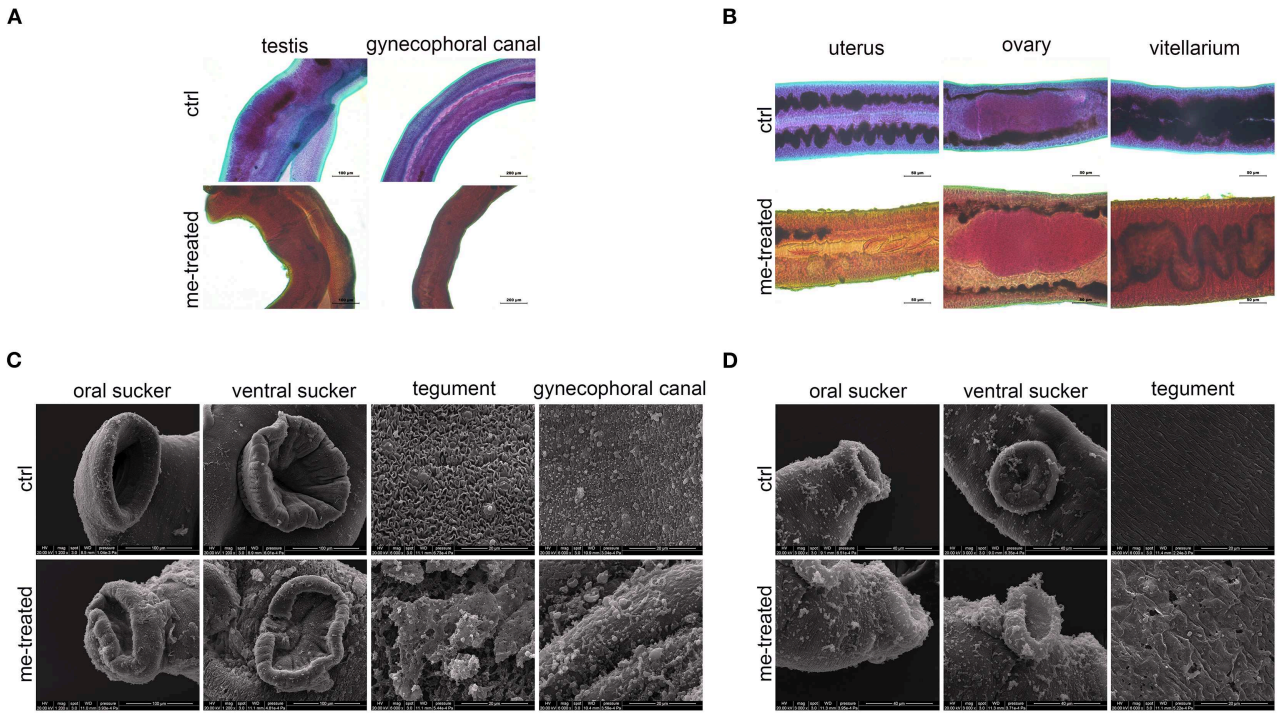

FIGURE 2 | Morphological changes in male and female of *S. japonicum in vitro*. Adult worm pairs were incubated with myricetin (me) at 600 μM for 24 h, and female and male worms were separated for analysis. Adult male **(A)** and female **(B)** were stained with acetocarmine-fast green and observed under Leica microscope. **(C)** Scanning electron microscopy (SEM) analysis of the oral sucker, ventral sucker, tegument and the special structure of male worms, gynecophoral canal of *S. japonicum* following treatment with myricetin. Scale bars: **(A)** upper left row, 100 μm; lower right row, 200 μm **(B)** 50 μm and **(C)** The oral sucker and ventral sucker of male worms, 100 μm; **(D)** The oral sucker and ventral sucker of female worms, 40 μm; The tegument and gynecophoral canal, 20 μm. ctrl, adult worms were incubated in RPMI 1,640 medium with 1% DMSO; me-treated, adult worms treated with myricetin.

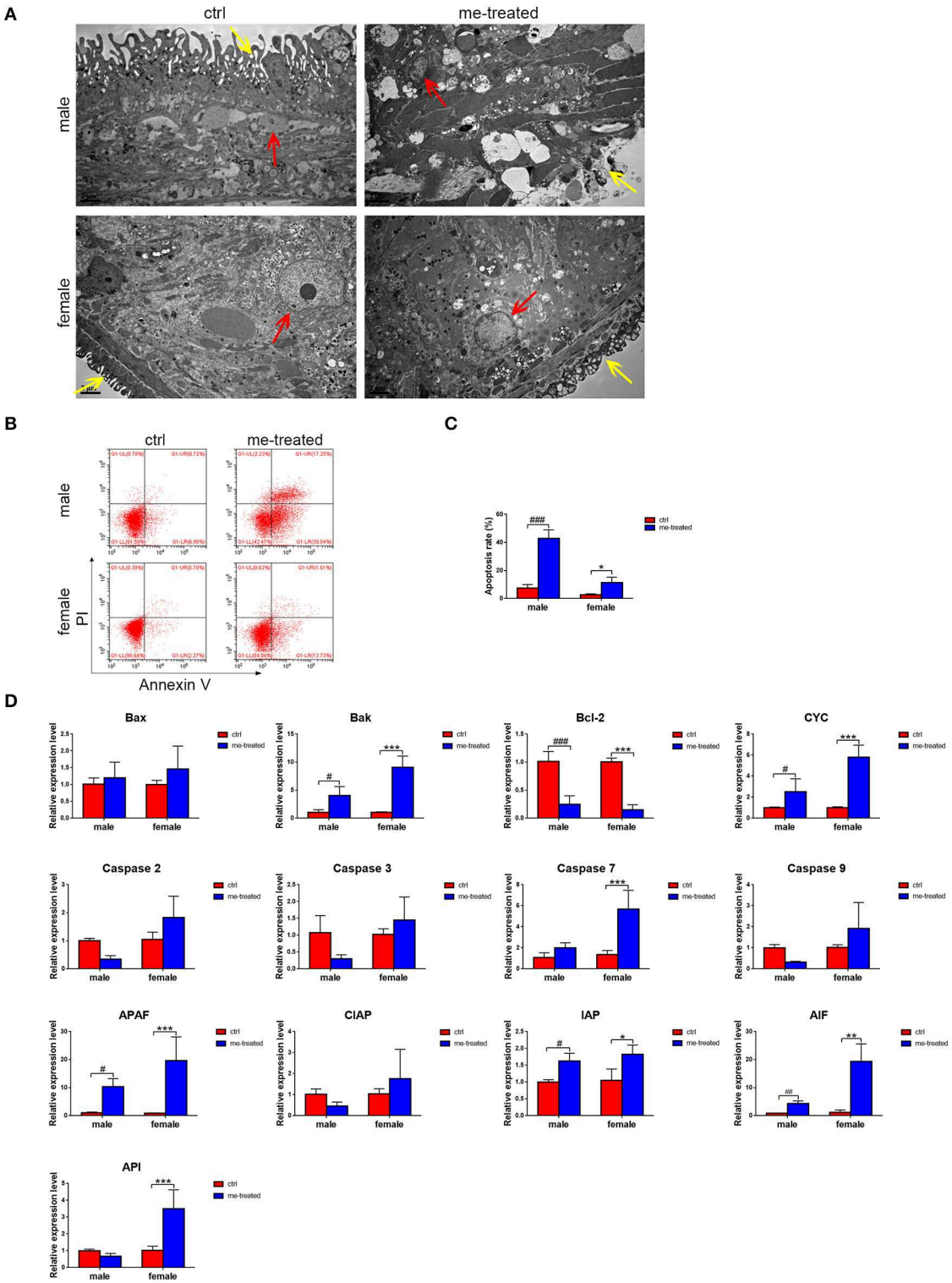

FIGURE 3 | Myricetin induces the apoptosis process and destroy the tegument architecture of *S. japonicum* adult worms *in vitro*. **(A)** Adult worms following treatment with myricetin were observed by transmission electron micrographs (TEM). The yellow and red arrows indicate tegument and cell nucleus, respectively. (Scale bars: 2 μm) **(B)** Apoptosis induced with myricetin was detected using Flow cytometry in worms. **(C)** Apoptosis induced with myricetin was statistical analyzed in worms. **(D)** Relative expression levels of 13 apoptosis associated genes after treatment with myricetin measured by Real-time qPCR. Data were shown as the means ± SD. $^{\#}P < 0.05$, $^{\#\#}P < 0.01$, $^{\#\#\#}P < 0.001$, compared with the negative ctrl group of male worms; $^{*}P < 0.05$, $^{**}P < 0.01$, $^{***}P < 0.001$, compared with the negative ctrl group of female worms. Data are representative results from at least 15 worms investigated in three independent experiments. ctrl, adult worms were incubated in RPMI 1,640 medium with 1% DMSO; me-treated, adult worms treated with myricetin.

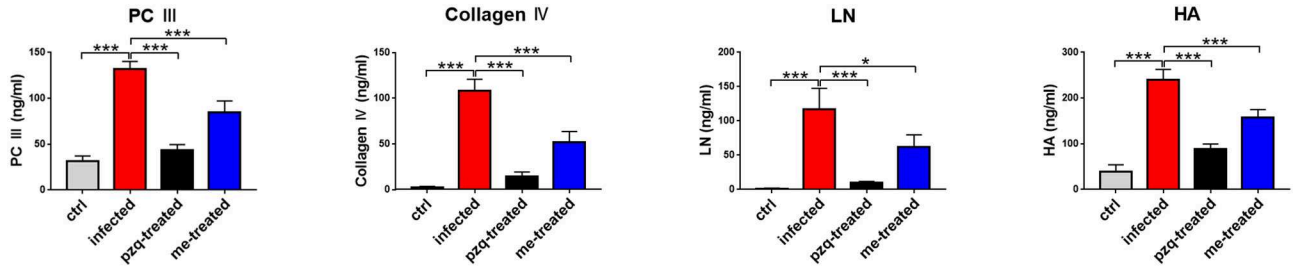

FIGURE 4 | Detection of hepatic fibrosis in *S. japonicum* cercaria infected BALB/c mice with 500 mg/kg praziquantel or 250 mg/kg myricetin for 7days. All mice were randomly divided into four groups: ctrl, the control group; infected: *S. japonicum* infected group; the pzq-treated, the praziquantel-treated group; me-treated, the myricetin-treated group. Levels of type III procollagen (PC III), type IV collagen (collagen IV), laminin (LN) and hyaluronidase (HA) are shown. Data are reported as the mean ± SD ($n = 3$). $^{*}P < 0.05$, $^{***}P < 0.001$, compared with the infected group.

TABLE 4 | Worm and egg burden in liver after treatment of *S. japonicum* infected BALB/c mice with praziquantel or myricetin.

Group	Total worms	Male worms	Female worms	No. of eggs found in liver, per gram
Ctrl	neg	neg	neg	neg
Infected	14.4 ± 2.61	7.6 ± 1.14	6.8 ± 1.64	19626.81 ± 3226.05
pzq-treated	neg	neg	neg	1238.09 ± 1495.85***
me-treated	5.6 ± 2.07***	3.8 ± 1.79**	1.8 ± 0.45***	5727.63 ± 1786.04***

*Balb/c mice were infected percutaneously with 30 ± 2 cercariae of S. japonicum. Worm and egg burdens were determined at 7 weeks post-infection. Data are expressed as the mean ± SD (n = 5), **P < 0.01, ***P < 0.001 compared with the infected group. ctrl, the control group; infected: S. japonicum-infected group; pzq-treated: the praziquantel-treated group; me-treated: the myricetin-treated group. neg, negative, indicating that no worms or eggs detected.*

[eggs per gram of liver tissue: infected: 19626.8 ± 3226.1 *vs.* myricetin: 5727.6 ± 1786.0; $F_{(3, 16)} = 102.2$, $P < 0.001$], and their inhibitory effects were not significantly different ($P > 0.05$) (**Table 4**).

Myricetin Lessens *S. japonicum*-Induced Pathological Changes in Mouse Liver

The livers of infected mice became gray-black-colored and had a rough surface with numerous irregular whitish micro- and macro-nodules, which were alleviated by myricetin and praziquantel. H&E staining showed that after infection, worm eggs were deposited in the liver surrounded by a large number of inflammatory cells, accompanied by collagen deposition, which formed diffuse egg granulomas. Consistently, ELISA revealed that PC III in mouse serum increased from 31.42 ± 5.58 ng/mL to 131.6 ± 8.75 ng/mL, collagen IV from 2.13 ± 1.47 ng/mL to 108.3 ± 12.58 ng/mL, laminin from 1.13 ± 0.84 ng/mL to 117.3 ± 30.3 ng/mL and hyaluronidase from 39.12 ± 14.89 ng/mL to 239.8 ± 22.89 ng/mL after schistosome infection, indicating obvious liver fibrotic lesions in the mouse liver. An obvious reduction was observed after treatment with myricetin in the serum levels of PC III (84.72 ± 12.32 ng/mL), collagen IV (51.55 ± 12.14 ng/mL), laminin (62.02 ± 17.79 ng/mL) and hyaluronidase (158 ± 16.92 ng/mL) compared to the infected mice [PC III: $F_{(3, 20)} = 164.3$, $P < 0.001$; collagen IV: $F_{(3, 20)} = 164.4$, $P < 0.001$; laminin: $F_{(3, 8)} = 28$, $P = 0.125$and hyaluronidase: $F_{(3, 20)} = 158.9$, $P < 0.001$, respectively], suggesting that myricetin has an inhibitory effect on liver fibrosis caused by *S. japonicum* infection (**Figure 4**). Furthermore, the size of liver tissue granulomas in the myricetin group was significantly lower vs. the infected group [myricetin: 11.43 ± 2.89% *vs.* infected control: 19.67 ± 1.58%, $F_{(3, 8)} = 79.74$, $P = 0.0007$]. Masson staining further showed that in the infected group, a large amount of collagen fiber was deposited around granulomas and diffusely distributed in the liver tissue, and the size of liver fibrosis area was 13.40 ± 1.64%. Myricetin significantly lessened hepatic fibrosis compared with the control group [8.37 ± 1.40%, $F_{(3, 8)} = 79.49$, $P = 0.002$] (**Figure 5**).

Additionally, TEM revealed that *S. japonicum* infection could induce cell apoptosis, proliferation of endoplasmic reticulum in hepatocytes, mitochondrial abnormalities such as decreased or absent cristae and membrane disorganization, and formation of fibrous tissue in the mouse liver. In some cases, remarkable hepatocyte apoptosis occurred, showing nuclear shrinkage and pyknosis. The liver pathological damage in infected mice were alleviated after treatment with praziquantel and myricetin (**Figure 6**).

Myricetin Shifts Th1/Th2 Balance in *S. japonicum*-Infected Mice

Flow cytometric analysis of Th subtypes (Th1/Th2/Th17/Treg) in the mouse spleen revealed that *S. japonicum* infection caused no significant change in Th1 cells (2.14 ± 0.274%) in mice, but resulted in an increased in the percentage of Th2 cells from 1.20 ± 0.07% to 4.14 ± 0.46%, and Th17 cells from 1.43 ± 0.40% to 2.25 ± 0.10%, and Treg cells from 0.52 ± 0.051% to 3.05 ± 1.34%. Myricetin significantly up-regulated Th1 cells in infected mice [4.56 ± 0.87%, $F_{(3, 8)} = 18.81$, $P < 0.001$] and reduced the proportion of Th2 cells [1.89 ± 0.62%, $F_{(3, 8)} = 19.65$, $P = 0.001$] and Th17 cells [1.527 ± 0.1973%, $F_{(3, 8)} = 7.398$, $P = 0.015$]. In addition, myricetin did not significantly reduced the proportion of Treg in infected mice (1.39 ± 0.44%) ($P > 0.05$) (**Figure 7**). We further examined whether myricetin induced changes in serum cytokines in *S. japonicum*-infected mice. ELISA showed that

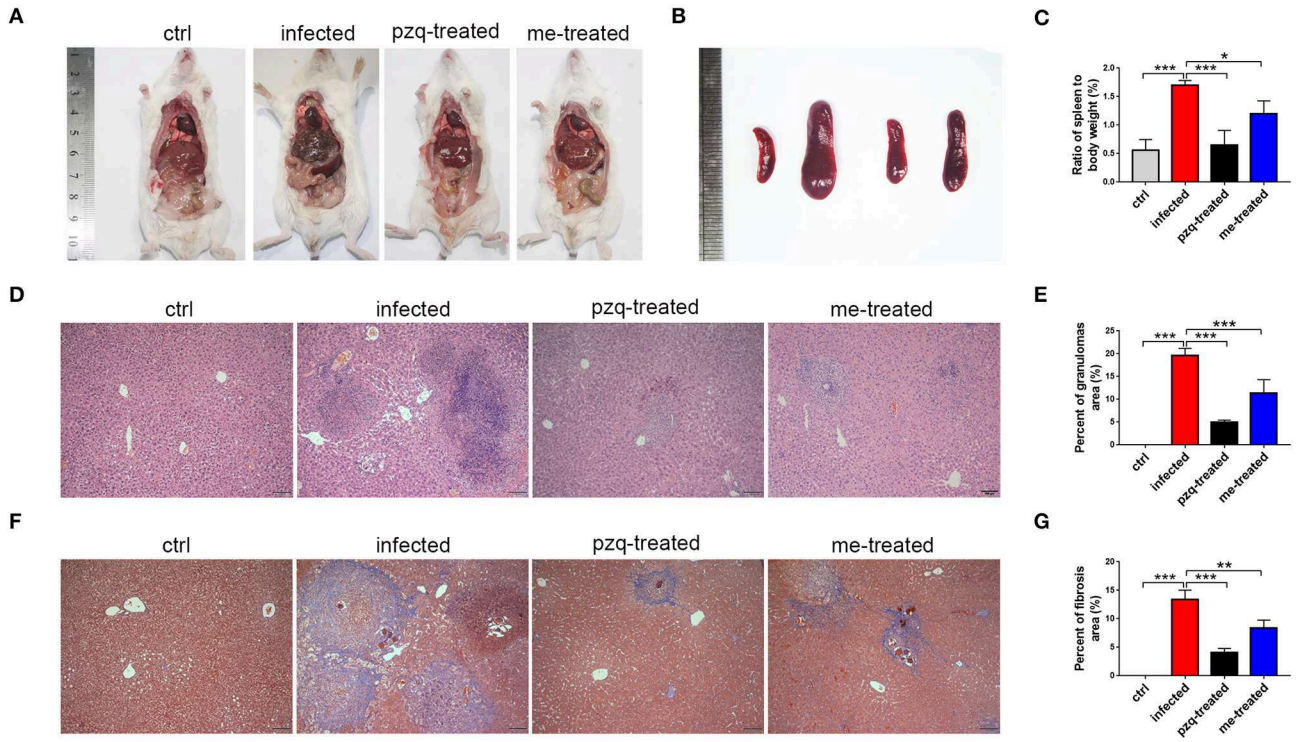

FIGURE 5 | Comparison of the granulomatous inflammation in the liver and pathological changes in the spleen. **(A)** Anatomy images of liver were taken by Nikon DSLR Camera. **(B)** Pathological changes of spleen in different groups (From left to right: ctrl, infected, treated with praziquantel, and treated with myricetin. **(C)** The ratio of spleen to body weight of mice infected with *S. japonicum* cercariae at 7 weeks. **(D)** Representative H&E staining images of hepatic granulomas at 7 weeks post infection with 30 *S. japonicum* cercariae (Scale bars: 100 μm). **(E)** Percent of granulomas in liver were analyzed with Image pro plus 6.0 software. **(F)** Fibrosis changes of liver at 7 weeks post infection with *S. japonicum* were observed by Masson staining (Scale bars: 100 μm). **(G)** The percent of fibrosis area was measured by Image pro plus 6.0. The data are expressed as the mean ± SD ($n = 3$). $^{**}P < 0.01$, $^{***}P < 0.001$, compared with the infected group. ctrl, the control group; infected: *S. japonicum* infected group; pzq-treated, the praziquantel-treated group; me-treated, the myricetin-treated group.

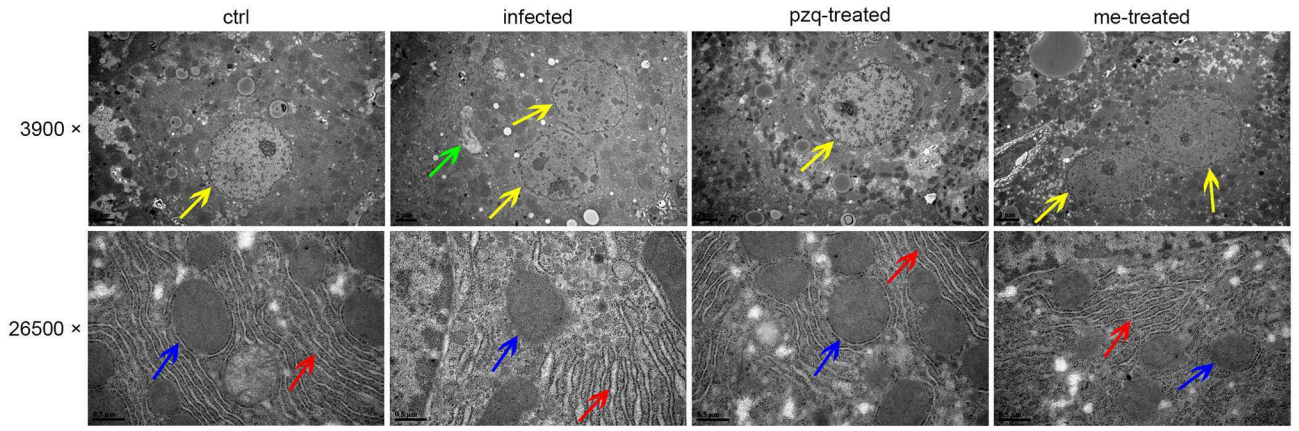

FIGURE 6 | Representative TEM images of pathological changes of liver after treatment of *S. japonicum* infected mice with praziquantel or myricetin. The yellow, green, red and blue arrows indicate cell nucleus, fiber, endoplasmic reticulum and mitochondria, respectively. Scale bars: upper row, 2 μm; lower row, 0.5 μm. ctrl, the control group; infected: *S. japonicum* infected group; the pzq-treated, the praziquantel-treated group; me-treated, the myricetin-treated group.

S. japonicum infection caused apparent increase in the plasma levels of IL-12, IL-2, TNF-α, IL-4, IL-5, IL-10, IL-13, IL-17A, IL-6, and MIP-2. Myricetin attenuated the rise in the plasma levels of IL-4, IL-5, IL-10, IL-13, and IL-17A in infected mice while increasing the plasma contents of IFN-γ, IL-12, and IL-7 (**Figure 8**).

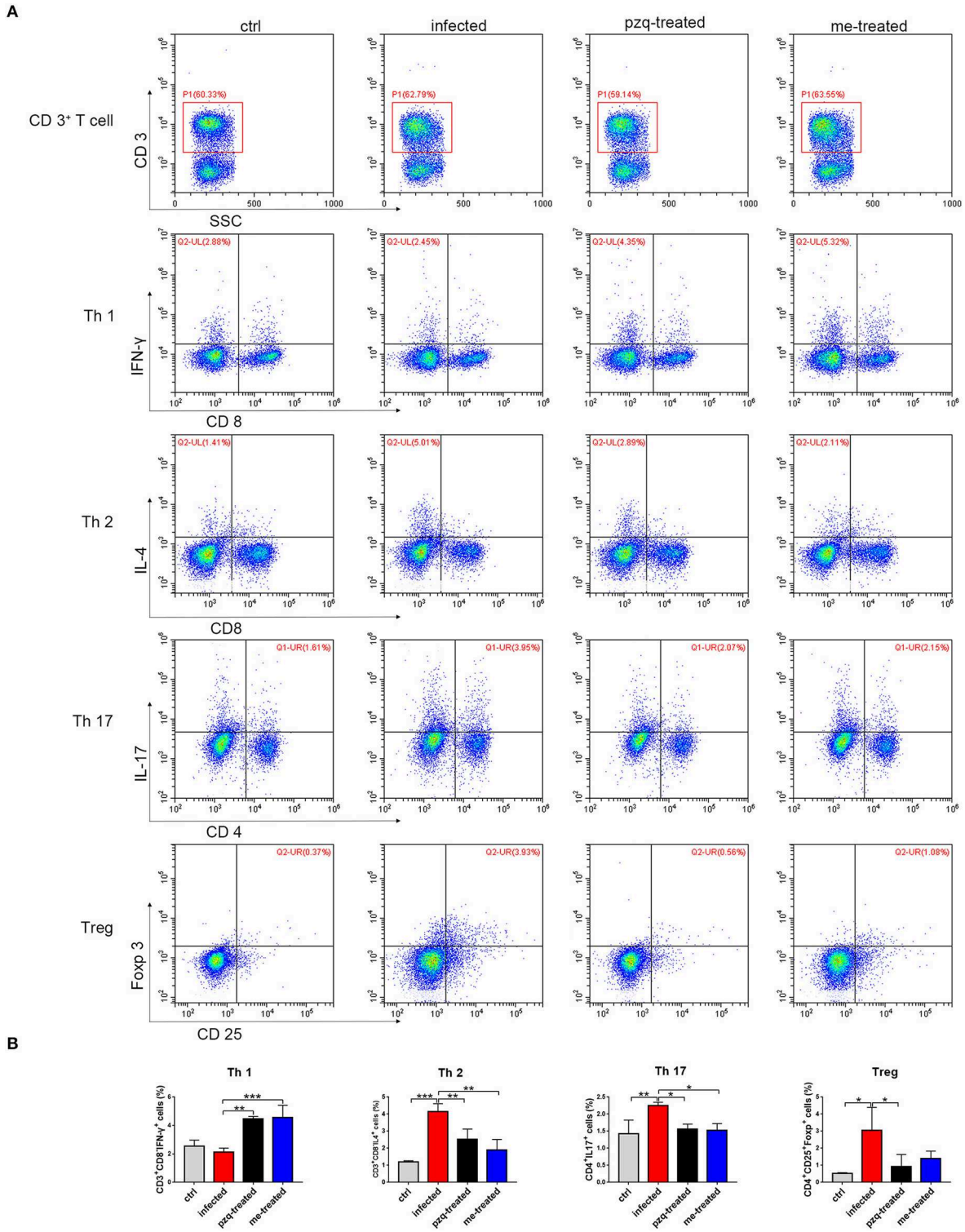

FIGURE 7 | Expression of Th subtypes (Th1/Th2/Th17/Treg) in spleen after treatment of *S. japonicum* infected BALB/c mice with praziquantel or myricetin. **(A)** Flow cytometry results of $CD3^+CD8^-IFN^-\gamma^+$, $CD3^+CD8^-IL^-4^+$, $CD4^+IL^-17^+$ and $CD4^+CD25^+Foxp^+$ cells in different groups. **(B)** The percentages of $CD3^+CD8^-IFN^-\gamma^+$ (Th1), $CD3^+CD8^-IL^-4^+$ (Th2), $CD4^+IL^-17^+$ (Th17) and $CD4^+CD25^+Foxp^+$ (Treg) cells were analyzed by flow cytometry. Data were shown as the means ± SD ($n = 3$). $^*P < 0.05$, $^{**}P < 0.01$, $^{***}P < 0.001$, compared with the infected group. ctrl, the control group; infected: *S. japonicum* infected group; the pzq-treated, the praziquantel-treated group; me-treated, the myricetin-treated group.

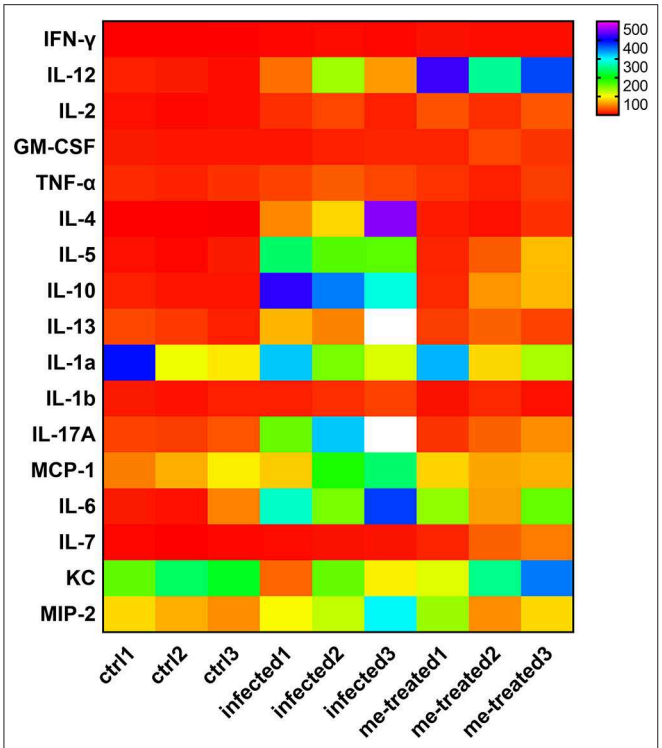

FIGURE 8 | Analysis of serum cytokine changes in *S. japonicum* infected mice after treated with myricetin. The heat map was performed by comparing the serum cytokine levels of different groups, data are representative of three independent experiments. ctrl, the control group; infected: *S. japonicum* infected group; me-treated, the myricetin-treated group.

Myricetin Attenuates *S. japonicum*-Induced Liver Fibrosis by Regulating TGFβ1/Smad/ERK Signaling

We further examined the expression of α-SMA, collagen I and IV in liver tissue. Our RT-PCR assays showed that myricetin caused a 10-, 6-, and 4.6-fold reduction in the mRNA transcript levels of α-SMA, collagen I and IV in infected mice compared to non-treated infected mice [$F_{(3, 8)} = 19.81$, $P < 0.001$]; $F_{(3, 8)} = 5.63$, $P = 0.04$ and $F_{(3, 8)} = 15.5$, $P = 0.002$, respectively) (**Figure 9A**). Consistent findings were also found in Western blotting assays [α-SMA: $F_{(3, 8)} = 19.81$, $P = 0.002$; collagen I: $F_{(3, 8)} = 27.44$, $P = 0.022$; collagen IV: $F_{(3, 8)} = 63.82$, $P < 0.001$] (**Figures 9B,C**), indicating that myricetin can effectively inhibit schistosome-induced upregulation of hepatic fibrosis-related proteins in mice.

TGFβ1 signaling is important in activating hepatic stellate cells and implicated in hepatic fibrosis. Our RT-qPCR assays showed that schistosome infection caused a 6.3-, 4.9-, 2.5-, 3.5-, and 2.2-fold increase in the mRNA transcript levels of TGFβ1, TGFRII, Smad2, Smad3, and ERK in mouse liver tissues. Meanwhile, myricetin effectively suppressed schistosome-induced upregulation of the mRNA transcript levels of TGFβ1 [$F_{(3, 8)} = 10.86$, $P = 0.004$], TGFR II [$F_{(2, 6)} = 36.32$, $P < 0.001$], Smad2 [$F_{(2, 6)} = 21.74$, $P = 0.007$], Smad3 [$F_{(2, 6)} = 51.01$, $P < 0.001$], and ERK1/2 [$F_{(2, 6)} = 7.719$, $P = 0.041$] in the liver tissues of infected mice. Western blotting assays further showed that myricetin effectively inhibited the protein expression of TGFβ1 [$F_{(2, 6)} = 33.9$, $P = 0.009$], ERK [$F_{(2, 6)} = 6.797$, $P = 0.041$], phospho-ERK [$F_{(2, 6)} = 28.58$, $P = 0.022$], Smad2 [$F_{(2, 6)} = 10.13$, $P = 0.044$], phospho-Smad2 [$F_{(2, 6)} = 7.862$, $P = 0.026$], Smad3 [$F_{(2, 6)} = 11.78$, $P = 0.019$], p-Smad3 [$F_{(2, 6)} = 6.107$, $P = 0.050$], Akt [$F_{(2, 6)} = 12.37$, $P = 0.015$], phospho-Akt [$F_{(2, 6)} = 15.32$, $P = 0.023$] in the liver tissues of infected mice (**Figure 10**). Thus, we inferred that myricetin may reduce liver fibrosis induced by *S. japonicum* infection by regulating the TGFβ1/Smad/ERK and PI3K/Akt signaling pathway.

DISCUSSION

Praziquantel has been widely used as an anti-schistosome drug, which was hailed as a breakthrough in the chemotherapy of schistosomiasis and has greatly promoted the prevention and control of schistosomiasis. However, whether repeated uses of praziquantel for large-scale chemotherapy would lead to the occurrence of resistance has received widespread attention. For *S. japonicum*, no evidence shows reduced sensitivity to praziquantel (12), but long-term reliance on a drug may have the potential risk of resistance. In this study, large-scale screening of the small-molecule compound library revealed that myricetin has a good helminthicidal effect on *S. japonicum in vitro*. We demonstrated that myricetin attenuated liver fibrosis in mice *via* modulating TGFβ1 and Akt signaling and shifting Th1/Th2 balance. Our study provides the first piece of direct experimental evidence that myricetin possesses potent anti-schistosome activities *in vitro* and *in vivo* and offers new insights into the mechanisms of action by myricetin, indicating that myricetin could be further explored as a therapeutic agent for *S. japonica*.

Myricetin is a common natural flavonol compound which can be detected in *Myrica rubra*, *Vaccinium macrocarponl Ait*, *Ribes nigrum L.*, *Vaccinium uliginosum Linn.* and *Semen Trigonellae* (24). Myricetin possesses a variety of pharmacological activities such as anti-oxidation, anti-tumor, anti-inflammatory, anti-microbial, anti-allergy, protection of cardiovascular and neurons (25–27) and has little toxic side effects (28). In addition, myricetin possesses hepatoprotective effects (29). At present, the effects of myricetin on parasites and hosts have not been reported yet. In this paper, we found that myricetin has good anti-*S. japonicum* activity. The findings of *in vitro* experiments illustrated that with the prolongation of the incubation time and the increase of drug concentration, the mortality of adult *S. japonicum* was increased and the activity of the worms decreased, indicating that the effect of myricetin on *S. japonicum* adult worms was time- and concentration-dependent. The entire worm is surrounded by a continuous cytoplasmic membrane, or syncytium, known as the tegument, composed of surface membrane, matrix and basal membrane, which is a unique structure of all trematodes. This structure is closely related to immune escape, nutrient uptake, excretion of catabolites, targeted drug absorption and other physiological processes (30–32), and most effective drugs against schistosomes would

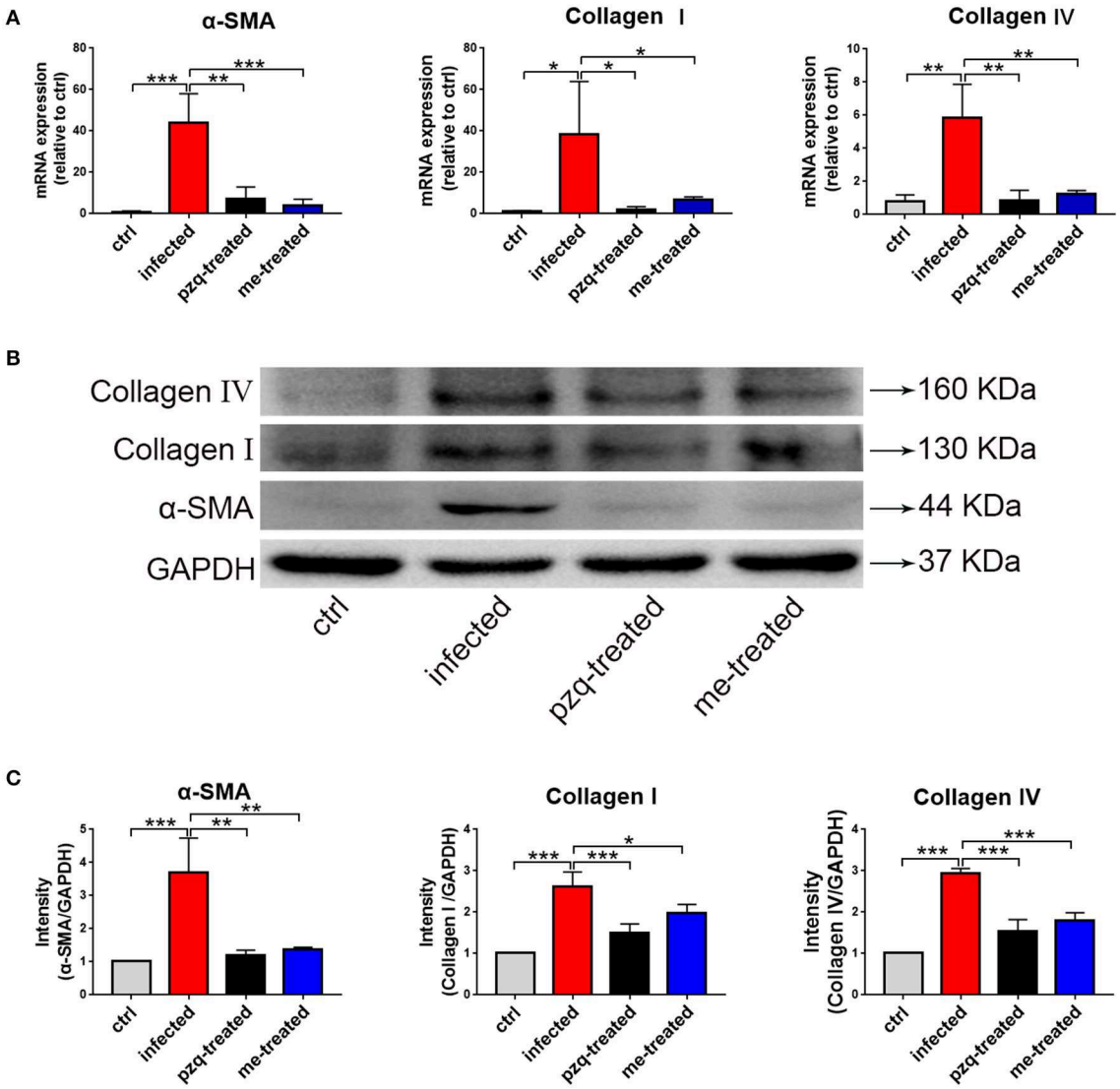

FIGURE 9 | RT-qPCR and western blot analyses of alpha-smooth muscle actin (α-SMA), Collagen I and Collagen IV in liver of *S. japonicum* infected mice after treated with praziquantel or myricetin. **(A)** RT-qPCR products obtained with the total RNA of liver with α-SMA-, Collagen I- or Collagen IV-specific primers. **(B)** The expression levels of α-SMA, Collagen I and Collagen IV in liver were confirmed by western blot. **(C)** Densitometric analysis of α-SMA, Collagen I and Collagen IV normalized to the endogenous control (GAPDH) and expressed as fold change. Data are expressed as the mean ± SD (n=3). $^{*}P < 0.05$, $^{**}P < 0.01$, $^{***}P < 0.001$, compared with the infected group. ctrl, the control group; infected: *S. japonicum* infected group; the pzq-treated, the praziquantel-treated group; me-treated, the myricetin-treated group.

damage the tegument, including praziquantel (33), oxamycin (34) and artemisinin (35). After treatment with myricetin, *S. japonicum*'s oral and abdominal suckers, sensory sensory papillae and on the surface, tegument and the reproductive organs were damaged to some extent, which may be due to the disruption of the osmotic pressure balance of the worm body, leading to changes in the body structure of the worm and eventually death.

Apoptosis is a normal process in growth and development of many organisms. Excessive activation or inhibition of apoptotic signals may result in the occurrence and development of many diseases, especially cancer (36). The levels of apoptosis of *S. japonicum* adult worms in different definite hosts are different, and are significantly higher in rats than mice (37). Under TEM, typical apoptotic phenomena were seen in both male and female worms treated with myricetin, including cell shrinkage, and pyknosis, but no mitochondrial damage was observed. The caspase family, the Bcl-2 family, cytokine-induced apoptosis inhibitor and apoptosis inhibitory factor (IAP) are involved in the apoptosis of *S. japonicum* (38–40). Our RT-qPCR assays showed that the expression of caspase 7, CYC and APAF in males and Bak, CYC, caspase 7, APAF, AIF and API in females elevated, while the anti-apoptotic gene bcl-2 decreased in both sexes, suggesting that the reduction of

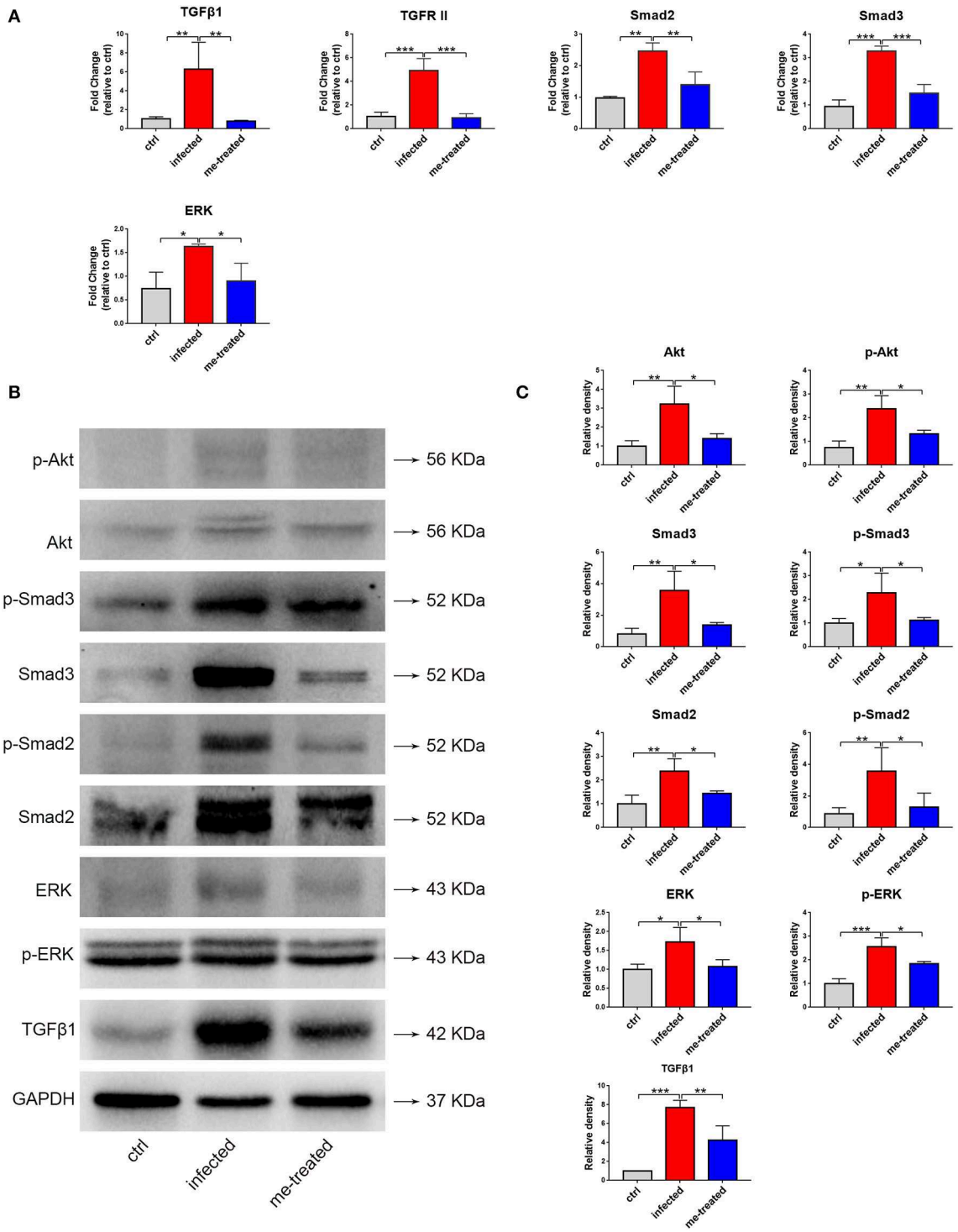

FIGURE 10 | Effects of myricetin on the TGF-β1-induced signaling pathway in *S. japonicum* infected mice model. **(A)** The mRNA expression of TGFβ1, TGFR II, smad2, smad3 and ERK was detected by RT-qPCR. **(B)** Western blot analysis for TGFβ1, ERK, p-ERK, Smad2, p-Smad2, Smad3, p-Smad3, Akt and p-Akt. **(C)** The relative densitometry of TGFβ1, ERK, p-ERK, Smad2, p-Smad2, Smad3, p-Smad3, Akt and p-Akt (relative to the endogenous control, GAPDH) and expressed as fold change. The values are expressed as the mean ± SD. $^{*}P < 0.05$, $^{**}P < 0.01$, $^{***}P < 0.001$ compared with the infected group. ctrl, the control group; infected: *S. japonicum* infected group; me-treated, the myricetin-treated group.

the worm's vitality and even death may be due to the drug *via* modulating the transcription level of the apoptotic genes of the worm. Additionally, flow cytometry revealed that the percentage of apoptotic cells in males was significantly higher than that in females after the action of myricetin, which is probably due to differences in the tegument structure and function between the male and female worms. The males are more sensitive to the stimulation of the surrounding environment with a loose tegument. In summary, *in vitro* results showed that myricetin had a good helminthicidal effect, and the damage to the tegument and the occurrence of worm cell apoptosis provide a basis for myricetin's helminthicidal action mechanism.

In the animal model of schistosome infection, Th1 type immune response is dominated in the acute phase, and produce cytokines such as IFN-γ, IL-12, and TNF-α, which can inhibit the invasion of pathogens by killing them (41). Th1 type immune response also has a certain inhibitory effect on granuloma and liver fibrosis. After 4 weeks of infection, the host's immune response shifts to a Th2 type, producing cytokines such as IL-4, IL-10, and IL-13. As the infection enters the chronic phase, the egg granuloma size becomes smaller, and Treg cells are activated, and Th1/Th2 immune balance is regulated and maintained, thereby inhibiting the development of liver fibrotic lesions (42, 43). Additionally, Th17 cells are positively correlated with liver pathological damage, and the use of IL-17 neutralizing antibodies can effectively lessen egg granulomatous lesions (44). By detecting $CD4^+$ T cell subtypes from spleen cells of mice infected with *S. japonicum* after 7 weeks of infection, we found that myricetin increased the proportion of Th1 cells but decreased the proportion of Th2 and Th17 cells, and ELISA also demonstrated elevations in plasma IFN-γ, IL-12, and IL-7 with concurrent reductions in plasma IL-4, IL-5, IL-10, IL-13, and IL-17A, indicating that myricetin modulates the immune response in schistosome-infected mice. Furthermore, we found that myricetin significantly reduced the area of liver granulomas and alleviated liver fibrosis. Egg granuloma is the basis of development of liver fibrosis induced by schistosome infection. Soluble egg antigens stimulate the production by macrophages and lymphocytes of various cytokines such as PDGF and TGFβ1 to induce the activation and proliferation of hepatic stellate cells (HSCs), which then transform into myofibroblasts capable of producing collagen. The activation of HSC is key to the formation of liver fibrosis (45). Activation of HSCs leads to increased expression of profibrotic factors such as α-SMA, collagen I and IV, cytoplasmic expansion, excessive synthesis and less degradation of ECM, leading to fibrosis. The main components of the ECM include hyaluronidase, PC III, collagen IV and laminin, which are commonly used as indicators of liver fibrosis clinically (46). Myricetin effectively inhibited *S. japonicum*-induced upregulation of liver fibrosis factor α-SMA, collagen I and IV and plasma hyaluronidase, PC III, collagen IV and laminin in mice, indicating that myricetin significantly lessened liver fibrosis in mice.

TGFβ1 signaling is the main regulatory mechanism in liver fibrosis. In TGFβ1-Smad signaling, TGFβ1 first activates intracellular signals by binding to TGFβ II, and then TGFβ1 activates TGF-β receptor type I (TβRI) kinase, resulting in phosphorylation of Smad2 and Smad3. Subsequently, activated Smad2 and Smad3 form a hetero-oligomer with Smad4, and then the Smad complex translocates to the nucleus, where it regulates transcription of target genes (47, 48). TGFβ1-Smad continues to activate ERK1/2 signaling (49, 50). TGFβ1/Smad/ERK signaling can promote liver fibrosis (51). In addition, TGFβ1 has been reported to activate PI3K/Akt signaling (52). Activation of Akt can not only promote the proliferation and migration of HSCs, but also promote the production of ECM by HSCs (53). Our study showed that myricetin suppressed the expression of TGFβ1, phospho-Smad2, phospho-Smad3, phosph-ERK1/2, Akt, phospho-Akt in schistosome-infected mice, revealing that myricetin may reduce liver fibrosis in schistosome-infected mice by inhibiting TGFβ1/Smad/ERK and PI3K/Akt signaling.

In conclusion, our study provides evidence for the first time that myricetin has anti-*S. japonicum* effects *in vitro* and *in vivo*. Meanwhile, myricetin has a significant effect on reducing liver fibrosis in schistosome-infected hosts, suggesting that myricetin with low toxicity may be explored as a novel therapeutic drug against *S. japonicum*.

DATA AVAILABILITY STATEMENT

All datasets generated for this study are included in the article/**Supplementary Files**.

ETHICS STATEMENT

The animal study was reviewed and approved by The Institutional Animal Care and Use Committee of Sun Yat-sen University.

AUTHOR CONTRIBUTIONS

ZL conceived and designed the study. ZL and PH drafted the manuscript. PH, MZ, and SC carried out the experiments. YH, MG, YM, and YL participated in data analysis. HZ, PD, and YC participated in study design, technological guidance and coordination. The final manuscript was read and approved by all authors.

FUNDING

This work was supported by the National Natural Science Foundation of China (Grant Nos. 81572023 and 81371836), Science and Technology Planning Project of Guangdong Province (Grant No. 2019B030316025), the National Key Research and Development Program of China (Grant Nos. 2016YFC1202000 and 2016YFC1200500), the Project of Basic Platform of National Science and Technology Resources of the Ministry of Sciences and Technology of China (Grant No. TDRC-2019-194-30), the Undergraduates Innovation Training Program of Guangdong Province (Grant No. 201601084), the 111 Project

(Grant No. B12003) and Teaching Reform Project of Guangdong Province (Grant No. 2017001).

ACKNOWLEDGMENTS

We thank Prof. Kai Deng provided the drug library; Mrs. Yuanjun Guan, Mrs. Juan Li, Mrs. Yaqiong Wang and Prof. Jinlang Wu for their technical advice for microscopy, SEM and TEM observation. And we would like to kindly offer our gratitude for reviewing the manuscript by Dr. Bo Cui.

SUPPLEMENTARY MATERIAL

The Supplementary Material for this article can be found online at: https://www.frontiersin.org/articles/10.3389/fimmu.2020.00593/full#supplementary-material

REFERENCES

1. Steinmann P, Keiser J, Bos R, Tanner M, Utzinger J. Schistosomiasis and water resources development: systematic review, meta-analysis, and estimates of people at risk. *Lancet Infect Dis*. (2006) 6:411–25. doi: 10.1016/S1473-3099(06)70521-7
2. Colley DG, Bustinduy AL, Secor WE, King CH. Human schistosomiasis. *Lancet*. (2014) 383:2253–64. doi: 10.1016/S0140-6736(13)61949-2
3. Hotez PJ, Fenwick A. Schistosomiasis in Africa: an emerging tragedy in our new global health decade. *PLoS Negl Trop Dis*. (2009) 3:e485. doi: 10.1371/journal.pntd.0000485
4. McManus DP, Dunne DW, Sacko M, Utzinger J, Vennervald BJ, Zhou XN. Schistosomiasis. *Nat Rev Dis Primers*. (2018) 4:13. doi: 10.1038/s41572-018-0013-8
5. Warren KS, Mahmoud AA, Cummings P, Murphy DJ, Houser HB. Schistosomiasis mansoni in Yemeni in California: duration of infection, presence of disease, therapeutic management. *Am J Trop Med Hyg*. (1974) 23:902–9. doi: 10.4269/ajtmh.1974.23.902
6. Chabasse D, Bertrand G, Leroux JP, Gauthey N, Hocquet P. Developmental bilharziasis caused by *Schistosoma mansoni* discovered 37 years after infestation. *Bull Soc Pathol Exot Filiales*. (1985) 78:643–7.
7. Fenwick A, Savioli L, Engels D, Robert Bergquist N, Todd MH. Drugs for the control of parasitic diseases: current status and development in schistosomiasis. *Trends Parasitol*. (2003) 19:509–15. doi: 10.1016/j.pt.2003.09.005
8. Wiest PM, Li Y, Olds GR, Bowen WD. Inhibition of phosphoinositide turnover by praziquantel in *Schistosoma mansoni*. *J Parasitol*. (1992) 78:753–5.
9. Ribeiro F, Coelho PM, Vieira LQ, Watson DG, Kusel JR. The effect of praziquantel treatment on glutathione concentration in *Schistosoma mansoni*. *Parasitology*. (1998) 116:229–36. doi: 10.1017/s0031182097002291
10. King CH, Olbrych SK, Soon M, Singer ME, Carter J, Colley DG. Utility of repeated praziquantel dosing in the treatment of schistosomiasis in high-risk communities in Africa: a systematic review. *PLoS Negl Trop Dis*. (2011) 5:e1321. doi: 10.1371/journal.pntd.0001321
11. Ismail M, Botros S, Metwally A, William S, Farghally A, Tao LF, et al. Resistance to praziquantel: direct evidence from *Schistosoma mansoni* isolated from Egyptian villagers. *Am J Trop Med Hyg*. (1999) 60:932–5. doi: 10.4269/ajtmh.1999.60.932
12. Wang W, Dai JR, Li HJ, Shen XH, Liang YS. Is there reduced susceptibility to praziquantel in *Schistosoma japonicum*? Evidence from China. *Parasitology*. (2010) 137:1905–12. doi: 10.1017/S0031182010001204
13. Fallon PG, Doenhoff MJ. Drug-resistant schistosomiasis: resistance to praziquantel and oxamniquine induced in *Schistosoma mansoni* in mice is drug specific. *Am J Trop Med Hyg*. (1994) 51:83–8. doi: 10.4269/ajtmh.1994.51.83
14. Ronketti F, Ramana AV, Chao-Ming X, Pica-Mattoccia L, Cioli D, Todd MH. Praziquantel derivatives I: modification of the aromatic ring. *Bioorg Med Chem Lett*. (2007) 17:4154–7. doi: 10.1016/j.bmcl.2007.05.063
15. Salvamani S, Gunasekaran B, Shaharuddin NA, Ahmad SA, Shukor MY. Antiartherosclerotic effects of plant flavonoids. *Biomed Res Int*. (2014) 2014:1–11. doi: 10.1155/2014/480258
16. Geng Y, Sun Q, Li W, Lu ZM, Xu HY, Shi JS, et al. The common dietary flavonoid myricetin attenuates liver fibrosis in carbon tetrachloride treated mice. *Mol Nutr Food Res*. (2017) 61:1600392. doi: 10.1002/mnfr.201600392
17. Manneck T, Haggenmuller Y, Keiser J. Morphological effects and tegumental alterations induced by mefloquine on schistosomula and adult flukes of *Schistosoma mansoni*. *Parasitology*. (2010) 137:85–98. doi: 10.1017/S0031182009990965
18. Ji PY, Hu HL, Yang XY, Wei XX, Zhu CC, Liu JC, et al. AcCystatin, an immunoregulatory molecule from Angiostrongylus cantonensis, ameliorates the asthmatic response in an aluminium hydroxide/ovalbumin-induced rat model of asthma. *Parasitol Res*. (2015) 114:613–24. doi: 10.1007/s00436-014-4223-z
19. Lewis F, Tucker M. Schistosomiasis. *Curr Protoc Immunol*. (2001) 19:19111. doi: 10.1002/0471142735.im1901s28
20. Mann VH, Morales ME, Rinaldi G, Brindley PJ. Culture for genetic manipulation of developmental stages of *Schistosoma mansoni*. *Parasitology*. (2010) 137:451–62. doi: 10.1017/S0031182009991211
21. Cioli D, Knopf PM, Senft AW. A study of *Schistosoma mansoni* transferred into permissive and nonpermissive hosts. *Int J Parasitol*. (1977) 7:293–7. doi: 10.1016/0020-7519(77)90038-8
22. Amiri P, Locksley RM, Parslow TG, Sadick M, Rector E, Ritter D, et al. Tumour necrosis factor alpha restores granulomas and induces parasite egg-laying in schistosome-infected SCID mice. *Nature*. (1992) 356:604–7. doi: 10.1038/356604a0
23. Hang LM, Warren KS, Boros DL. *Schistosoma mansoni*: antigenic secretions and the etiology of egg granulomas in mice. *Exp Parasitol*. (1974) 35:288–98. doi: 10.1016/0014-4894(74)90035-6
24. Hakkinen SH, Karenlampi SO, Heinonen IM, Mykkanen HM, Torronen AR. Content of the flavonols quercetin, myricetin, and kaempferol in 25 edible berries. *J Agric Food Chem*. (1999) 47:2274–9. doi: 10.1021/jf9811065
25. Jayaraman P, Sakharkar MK, Lim CS, Tang TH, Sakharkar KR. Activity and interactions of antibiotic and phytochemical combinations against *Pseudomonas aeruginosa in vitro*. *Int J Biol Sci*. (2010) 6:556–68. doi: 10.7150/ijbs.6.556
26. Kang NJ, Jung SK, Lee KW, Lee HJ. Myricetin is a potent chemopreventive phytochemical in skin carcinogenesis. *Ann N Y Acad Sci*. (2011) 1229:124–32. doi: 10.1111/j.1749-6632.2011.06122.x
27. Lee SE, Park YS. Gene expression profiling of human umbilical vein endothelial cells exposed to myricetin. *Biochip J*. (2013) 7:335–43. doi: 10.1007/s13206-013-7404-4
28. Yang Y, Choi JK, Jung CH, Koh HJ, Heo P, Shin JY, et al. SNARE-wedging polyphenols as small molecular botox. *Planta Medica*. (2012) 78:233–6. doi: 10.1055/s-0031-1280385
29. Matic S, Stanic S, Bogojevic D, Vidakovic M, Grdovic N, Dinic S, et al. Methanol extract from the stem of *Cotinus coggygria Scop*., and its major bioactive phytochemical constituent myricetin modulate pyrogallol-induced DNA damage and liver injury. *Mutat Res*. (2013) 755:81–9. doi: 10.1016/j.mrgentox.2013.03.011
30. Jones MK, Gobert GN, Zhang L, Sunderland P, McManus DP. The cytoskeleton and motor proteins of human schistosomes and their roles in surface maintenance and host-parasite interactions. *Bioessays*. (2004) 26:752–65. doi: 10.1002/bies.20058
31. Van Hellemond JJ, Retra K, Brouwers JF, van Balkom BW, Yazdanbakhsh M, Shoemaker CB, et al. Functions of the tegument of schistosomes:

clues from the proteome and lipidome. *Int J Parasitol*. (2006) 36:691–9. doi: 10.1016/j.ijpara.2006.01.007
32. Pereira AS, Padilha RJ, Lima-Filho JL, Chaves ME. Scanning electron microscopy of the human low-density lipoprotein interaction with the tegument of *Schistosoma mansoni*. *Parasitol Res*. (2011) 109:1395–402. doi: 10.1007/s00436-011-2386-4
33. Shaw MK, Erasmus DA. *Schistosoma mansoni*: dose-related tegumental surface changes after *in vivo* treatment with praziquantel. *Z Parasitenkd*. (1983) 69:643–53. doi: 10.1007/bf00926674
34. Fallon PG, Fookes RE, Wharton GA. Temporal differences in praziquantel- and oxamniquine-induced tegumental damage to adult *Schistosoma mansoni*: implications for drug-antibody synergy. *Parasitology*. (1996) 112:47–58. doi: 10.1017/s0031182000065069
35. Xiao S, Binggui S, Chollet J, Tanner M. Tegumental changes in 21-day-old *Schistosoma mansoni* harboured in mice treated with artemether. *Acta Trop*. (2000) 75:341–8. doi: 10.1016/s0001-706x(00)00067-x
36. Elmore S. Apoptosis: a review of programmed cell death. *Toxicol Pathol*. (2007) 35:495–516. doi: 10.1080/01926230701320337
37. Wang T, Guo X, Hong Y, Han H, Cao X, Han Y, et al. Comparison of apoptosis between adult worms of *Schistosoma japonicum* from susceptible (BALB/c mice) and less-susceptible (Wistar rats) hosts. *Gene*. (2016) 592:71–7. doi: 10.1016/j.gene.2016.07.054
38. Luo R, Zhou C, Shi Y, Zhao J, Cheng G. Molecular characterization of a cytokine-induced apoptosis inhibitor from *Schistosoma japonicum*. *Parasitol Res*. (2012) 111:2317–24. doi: 10.1007/s00436-012-3086-4
39. Kumar S, Biswal DK, Tandon V. In-silico analysis of caspase-3 and−7 proteases from blood-parasitic Schistosoma species (Trematoda) and their human host. *Bioinformation*. (2013) 9:456–63. doi: 10.6026/97320630009456
40. Lee EF, Clarke OB, Evangelista M, Feng Z, Speed TP, Tchoubrieva EB, et al. Discovery and molecular characterization of a Bcl-2-regulated cell death pathway in schistosomes. *Proc Natl Acad Sci USA*. (2011) 108:6999–7003. doi: 10.1073/pnas.1100652108
41. Caldas IR, Campi-Azevedo AC, Oliveira LF, Silveira AM, Oliveira RC, Gazzinelli G. Human schistosomiasis mansoni: immune responses during acute and chronic phases of the infection. *Acta Trop*. (2008) 108:109–17. doi: 10.1016/j.actatropica.2008.05.027
42. Wilson MS, Mentink-Kane MM, Pesce JT, Ramalingam TR, Thompson R, Wynn TA. Immunopathology of schistosomiasis. *Immunol Cell Biol*. (2007) 85:148–54. doi: 10.1038/sj.icb.7100014
43. Chuah C, Jones MK, Burke ML, McManus DP, Gobert GN. Cellular and chemokine-mediated regulation in schistosome-induced hepatic pathology. *Trends Parasitol*. (2014) 30:141–50. doi: 10.1016/j.pt.2013.12.009
44. Wang Q, Chou X, Guan F, Fang Z, Lu S, Lei J, et al. Enhanced Wnt Signalling in Hepatocytes is associated with *Schistosoma japonicum* infection and contributes to liver fibrosis. *Sci Rep*. (2017) 7:230. doi: 10.1038/s41598-017-00377-4
45. Friedman SL. Mechanisms of disease: Mechanisms of hepatic fibrosis and therapeutic implications. *Nat Clin Pract Gastroenterol Hepatol*. (2004) 1:98–105. doi: 10.1038/ncpgasthep0055
46. Zhang Q, Shang MM, Ling QF, Wu XP, Liu CY. Hepatoprotective effects of loach (*Misgurnus anguillicaudatus*) lyophilized powder on dimethylnitrosamine-induced liver fibrosis in rats. *Arch Pharm Res*. (2014). doi: 10.1007/s12272-014-0445-y. [Epub ahead of print].
47. Conidi A, Cazzola S, Beets K, Coddens K, Collart C, Cornelis F, et al. Few Smad proteins and many Smad-interacting proteins yield multiple functions and action modes in TGFbeta/BMP signaling *in vivo*. *Cytokine Growth Factor Rev*. (2011) 22:287–300. doi: 10.1016/j.cytogfr.2011.11.006
48. Meng XM, Chung AC, Lan HY. Role of the TGF-beta/BMP-7/Smad pathways in renal diseases. *Clin Sci (Lond)*. (2013) 124:243–54. doi: 10.1042/CS20120252
49. Hayashida T, Decaestecker M, Schnaper HW. Cross-talk between ERK MAP kinase and Smad signaling pathways enhances TGF-beta-dependent responses in human mesangial cells. *FASEB J*. (2003) 17:1576–8. doi: 10.1096/fj.03-0037fje
50. Wang M, Chen DQ, Wang MC, Chen H, Chen L, Liu D, et al. Poricoic acid ZA, a novel RAS inhibitor, attenuates tubulo-interstitial fibrosis and podocyte injury by inhibiting TGF-beta/Smad signaling pathway. *Phytomedicine*. (2017) 36:243–53. doi: 10.1016/j.phymed.2017.10.008
51. El-Tanbouly DM, Wadie W, Sayed RH. Modulation of TGF-beta/Smad and ERK signaling pathways mediates the anti-fibrotic effect of mirtazapine in mice. *Toxicol Appl Pharmacol*. (2017) 329:224–30. doi: 10.1016/j.taap.2017.06.012
52. Lechuga CG, Hernandez-Nazara ZH, Dominguez Rosales JA, Morris ER, Rincon AR, Rivas-Estilla AM, et al. TGF-beta1 modulates matrix metalloproteinase-13 expression in hepatic stellate cells by complex mechanisms involving p38MAPK, PI3-kinase, AKT, and p70S6k. *Am J Physiol Gastrointest Liver Physiol*. (2004) 287:G974–987. doi: 10.1152/ajpgi.00264.2003
53. Reif S, Lang A, Lindquist JN, Yata Y, Gabele E, Scanga A, et al. The role of focal adhesion kinase-phosphatidylinositol 3-kinase-akt signaling in hepatic stellate cell proliferation and type I collagen expression. *J Biol Chem*. (2003) 278:8083–90. doi: 10.1074/jbc.M212927200

Conflict of Interest: The authors declare that the research was conducted in the absence of any commercial or financial relationships that could be construed as a potential conflict of interest.

frontiers in Immunology

ORIGINAL RESEARCH
published: 14 May 2020
doi: 10.3389/fimmu.2020.00609

Altered Gut Microbiota and Immunity Defines *Plasmodium vivax* Survival in *Anopheles stephensi*

*Punita Sharma[1], Jyoti Rani[1,2], Charu Chauhan[1], Seena Kumari[1], Sanjay Tevatiya[1], Tanwee Das De[1], Deepali Savargaonkar[1], Kailash C. Pandey[1] and Rajnikant Dixit[1]**

[1] Laboratory of Host-Parasite Interaction Studies, ICMR-National Institute of Malaria Research, New Delhi, India, [2] Bio and Nanotechnology Department, Guru Jambheshwar University of Science and Technology, Haryana, India

Blood-feeding enriched gut-microbiota boosts mosquitoes' anti-*Plasmodium* immunity. Here, we ask how *Plasmodium vivax* alters gut-microbiota, anti-*Plasmodial* immunity, and impacts tripartite *Plasmodium*-mosquito-microbiota interactions in the gut lumen. We used a metagenomics and RNAseq strategy to address these questions. In naïve mosquitoes, *Elizabethkingia meningitis* and *Pseudomonas* spp. are the dominant bacteria and blood-feeding leads to a heightened detection of *Elizabethkingia*, *Pseudomonas* and *Serratia 16S rRNA*. A parallel RNAseq analysis of blood-fed midguts also shows the presence of *Elizabethkingia-related* transcripts. After, *P. vivax* infected blood-meal, however, we do not detect bacterial 16S rRNA until circa 36 h. Intriguingly, the transcriptional expression of a selected array of antimicrobial arsenal cecropins 1–2, defensin-1, and gambicin remained low during the first 36 h—a time frame when ookinetes/early oocysts invaded the gut. We conclude during the preinvasive phase, *P. vivax* outcompetes midgut-microbiota. This microbial suppression likely negates the impact of mosquito immunity which in turn may enhance the survival of *P. vivax*. Detection of sequences matching to mosquito-associated *Wolbachia* opens a new inquiry for its exploration as an agent for "paratransgenesis-based" mosquito control.

Keywords: *Anopheles stephensi*, midgut, microbiome, *Plasmodium vivax*, tripartite interactions

OPEN ACCESS

Edited by:
Rachel Daniels, Harvard University, United States

Reviewed by:
Gislane Lelis Vilela de Oliveira, São Paulo State University, Brazil
Diling Chen, Guangdong Academy of Science, China

***Correspondence:**
Rajnikant Dixit
dixitrk@mrcindia.org

Specialty section:
This article was submitted to Microbial Immunology, a section of the journal Frontiers in Immunology

Received: *19 November 2019*
Accepted: *17 March 2020*
Published: *14 May 2020*

Citation:
Sharma P, Rani J, Chauhan C, Kumari S, Tevatiya S, Das De T, Savargaonkar D, Pandey KC and Dixit R (2020) Altered Gut Microbiota and Immunity Defines Plasmodium vivax Survival in Anopheles stephensi. Front. Immunol. 11:609. doi: 10.3389/fimmu.2020.00609

INTRODUCTION

A blood meal is an essential requirement for the reproductive success of adult female mosquitoes. Immediately after blood meal uptake, mosquitoes' gut physiology undergoes complex modulation to facilitate rapid blood meal digestion and activation of the vitellogenesis process (1, 2). The blood-meal also triggers proliferation of gut microbiome eliciting immune response (3, 4), and once the blood meal digestion is completed within first 30 h, the immune response apparently ceases to basal level (5, 6).

This mosquito's gut immune response may indirectly affect the early development of *Plasmodium* when mosquitoes take infected blood (7–9). Removal of gut microbes by antibiotic treatment enhances *Plasmodium* survival, however, our understanding of how *Plasmodium* manages its safe journey to the gut and succeeds to develop in the susceptible mosquitoes remains unclear (10). A tripartite interaction of gut-microbes-parasites during earlier or pre-invasive phase of the malaria infection is expected to play a vital role in the success of the parasite's journey through the gut lumen (11–15). But a great deal of understanding that how a parasite manages its survival during acute gut-microbe interaction is still limited (4). Once the gut epithelial is invaded, the

Plasmodium population undergoes several bottlenecks reducing the oocysts load either to zero in naturally selected refractory mosquito strains, or a few oocysts in a susceptible mosquito vector species (16, 17).

Within 8–9 days post-infection, the surviving oocysts rupture to millions of sporozoites, released in the hemolymph (11). During free circulation, sporozoites compete to invade the salivary glands, and if not successful are rapidly cleared by the mosquito immune blood cells "hemocytes" (6, 16–18). The invaded sporozoites reside in clusters in the salivary glands till they get a chance to invade the vertebrate host (19, 20). Though studies targeting individual tissues such as midgut or salivary glands are valuable, the genetic basis of *Plasmodium* population alteration is not well-understood (21).

We hypothesized that for its survival *Plasmodium* must overcome at least two levels of competitive challenges (**Figure 1**). The first one follows a 24–30 h pre-invasive phase of interaction initiated immediately after a blood meal influencing: (a) parasite development and adaptation to physiologically distinct but hostile gut environment than vertebrate host; (b) nutritional resources competition against exponentially proliferating gut microbes, and (c) the barrier(s) infringement of gut epithelial prior maturation of peritrophic matrix, a unique but unresolved mechanism of self-protection. A second phase follows post-gut invasion of ookinetes which encompasses a direct interaction of (d) developing and maturing oocysts within midgut (8–10 days); (e) free circulatory sporozoites and hemocytes; and (f) salivary invaded sporozoites within salivary glands (10–16 days).

Thus, to decode the tissue-specific molecular complexity/nature of interactions, we designed and carried out a system-wide investigation. In this report, we followed changes (1) in the gut microbiota under naïve, blood-fed and *Plasmodium* infected blood fed conditions, and (2) changes in the expression of selected immune markers. Our data demonstrates how an early suppression of gut microbiome proliferation, and hence gut immunity may support *P. vivax* survival during the pre-invasive phase of development. While in the second complimentary report, we demonstrate that post-gut invasion, a smart molecular relationship with individual tissues such as midgut, hemocytes, salivary glands, and strategic changes in the genetic makeup of *P. vivax* favor its survival in the mosquito host [see (22)].

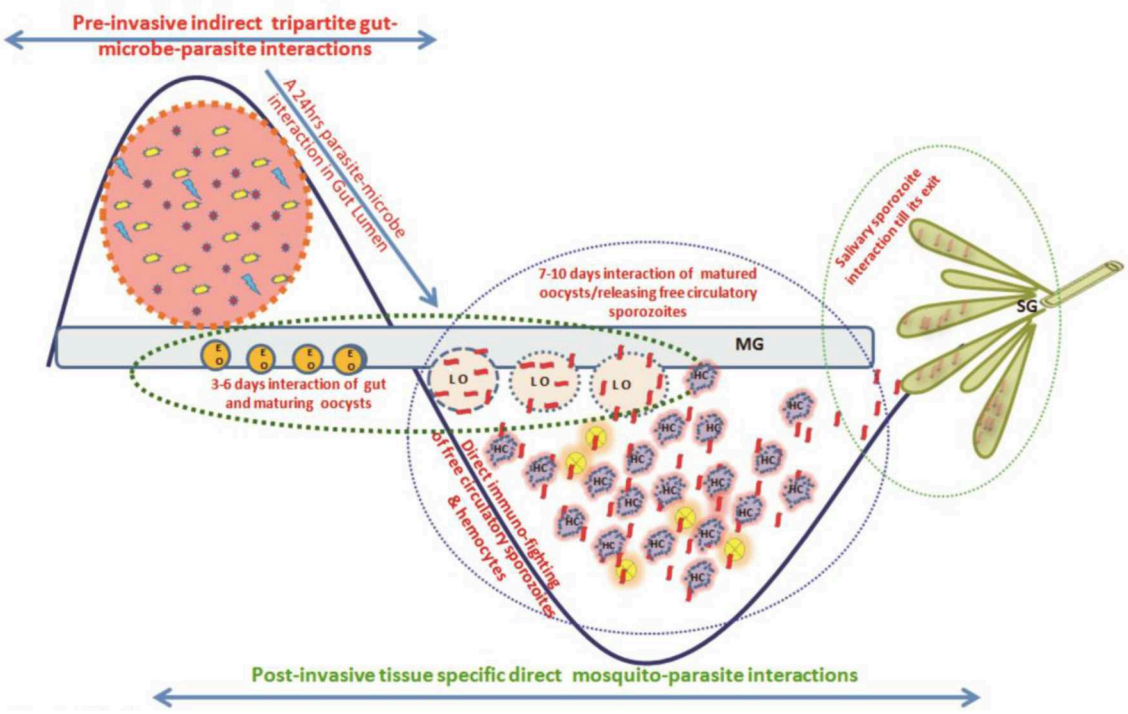

FIGURE 1 | A proposed working hypothesis to decode a system-wide pre and post-gut invasive phases of *P. vivax*-mosquito interactions: Immediately after an infected blood meal, sexual developmental physiology of *Plasmodium* rapidly change to adapt mosquitoes' hostile gut-lumen environment and progressively faces gut-microbiota boosted anti-*Plasmodium* immunity. Though the mechanism that how *Plasmodium* manages safe journey and survival from gut lumen → gut epithelium → hemolymph → salivary gland → vertebrate host is not fully known, but we propose and decode (i) a 24–30 h of pre-invasive phase of an indirect gut-microbe-parasite interaction in the gut lumen for ookinetes invasion; and (ii) a longer post-gut invasive, a direct parasite-tissues such as midgut (MG), hemocyte (HC), and salivary gland (SG) interactions, are crucial for the *Plasmodium* survival (22). Schematically, , represents *Plasmodium* gametocytes; and , different bacterial species; , the mustard yellow circle represents early gut invaded maturing oocysts (EO); , peach circle with blue dotted boundary is Late rupturing oocysts (LO); , red ribbon is sporozoite; , salivary lobes; , the purple cloudy structure is hemocyte.

MATERIALS AND METHODS

Technical overview presented in **Figure S1**.

Mosquito Rearing

Anopheles stephensi colonies were reared in the central insectary facility at ICMR-National Institute of Malaria Research (NIMR). A constant 28 ± 2°C temperature and relative humidity of ∼80% was maintained in the insectarium. A live rabbit was offered as a blood meal for egg maturation and gonotrophic cycle maintenance (6, 23).

Metagenomic Study

Tissue Dissection and Sample Preparation

For the study, *A. stephensi* pupae ($n = 200$) were reared in ethanol sterilized plastic cages fitted with autoclaved mesh cloth on the top. Ten percent sterile, fresh sugar solution was provided daily with a sterile cotton swab fitted in a test tube throughout the experiment. For metagenomics studies, we collected the guts from 4 to 5 days old either sugar-fed or blood-fed ∼50 adult female mosquitoes. Dissections were performed after surface sterilization of the mosquitoes using 75% ethanol for 1 min in 50 µl 1X Saline-Tris-EDTA (STE) buffer. Total DNA from pooled gut samples was extracted under aseptic conditions of the laminar airflow, as described earlier (24). In brief, the tissue was homogenized using handheld battery run homogenizer and contaminating protein was digested by proteinase K treatment. For DNA quality assessment ∼5 µl of gDNA was loaded on 0.8% agarose gel and run through standard agarose gel electrophoresis to visualize the single intact band as the quality mark (**Figure S2**). Quantification was performed using Qubit dsDNA BR Kit (Thermo Fisher Scientific Inc.) after checking the $A_{260/280}$ ratio of 1 µl of each sample using Nanodrop 8000.

16S rRNA Based Metagenomic Sequencing and Analysis

Using Nextera XT Index Kit (Illumina Inc.), the amplicon libraries were prepared from the qualified DNA samples. Primers were designed and synthesized using the V3-V4 hyper-variable region of 16S rDNA gene (**Table ST1**). The Illumina adaptors ligated amplicons were amplified by using i5 and i7 primers for multiplex indexing. Purification of the amplicon libraries was performed on 1X AMpureXP beads and checked for its quality with Bioanalyzer 2100 Agilent using a DNA1000 chip and quantification was done on fluorometer by Qubit dsDNA HS Assay kit (Life Technologies) (**Figure S3**). A Paired-End (PE) sequencing was done with MiSeq technology and generated data was stitched into single-end reads. Final clean reads were subjected for Operational Taxonomic Units (OTUs) clustering and analysis using Quantitative Insights into Microbial Ecology (QIIME version 1.9.1) software package comprising of tools and algorithms such as FastTree for heuristic based maximum-likelihood phylogeny inference (25). The taxomic assignment to the final OTUs was done by RDP classifier data using a naïve Bayesian classifier, raw data output as .biom files were further analyzed through MEGAN software (26).

Gut RNAseq Analysis

Approximately one microgram purified total RNA from pooled 24–48 h post-blood-fed ∼20 adult female mosquitoes guts, was subjected to double-stranded cDNA library preparation (Clontech SMART^{TM}) and sequencing (Illumina Technology), as described earlier (23, 27–29). Briefly, the purified ds cDNA sample (∼200 ng) was sheared using the Covaris sonication method and the overhangs so generated were end-repaired before further processing. The paired-end cDNA libraries were generated through Illumina TruSeq Nano DNA HT Library Preparation Kit using 2 × 150 PE chemistry on NextSeq for generating ∼1 GB data as per the described protocol. The end-repaired fragments were subjected to enrichment by a limited number of PCR cycles after adding a poly A-tail and adapter ligation. Library quantitation and qualification were performed using DNA high Sensitivity Assay Kit. The sequencing of whole transcriptomes was performed on Illumina NextSeq. Trimmomatic v0.30 software was used to filter the raw reads. After removing adaptor sequences and low quality (QV < 20) reads, high-quality clean reads were used to make *de novo* assembly using Trinity software (release r2013-02-25). CD-HIT-EST (Version 4.6) was used to remove the shorter redundant transcripts. All CDS were predicted from transcript using Transdecoder and selected longest frame transcripts were subjected for functional annotation using BLASTX against NR database and BLAST2GO program [see also (22)].

Artificial Membrane Feeding and *P. vivax* Infection

The collection of the *P. vivax* infected patients' blood samples was approved by the Ethics committee of NIMR, Delhi (ECR/NIMR/EC/2012/41). Prior collection of blood samples, a written informed consent (IC) was obtained from donors visiting to institutional clinic. Venous blood was drawn into heparin-containing tubes and kept at 37°C till feeding. Overnight starved 4–5 days old female *A. stephensi* mosquitoes were fed using pre-optimized artificial membrane feeding assay (AMFA). Only full-fed mosquitoes were maintained at optimal insectarium conditions and positive infection was confirmed by standard mercurochrome staining of gut oocysts readily observed under a compound microscope. Desired tissue samples such as midgut, salivary glands, hemocytes were collected from ∼20 infected or uninfected adult female mosquitoes for subsequent analysis as reported in Tevatiya et al. (22). However, we excluded mosquito samples which showed poor/negative oocysts development in their gut.

RNA Isolation and Differential Gene Expression Analysis

Total RNA from different tissues was isolated (30) from naïve, blood-fed or *Plasmodium*-infected *A. stephensi* mosquitoes ($n = 20$) and cDNA was synthesized using Verso cDNA synthesis kit (Thermo Fisher Scientific, #AB1453A) as per manufacturer protocol. Routine laboratory optimized RT-PCR and agarose gel electrophoresis processes were followed for differential expression of the selected genes. Relative gene expression was performed by QuantiMix SYBR green dye (Thermo scientific

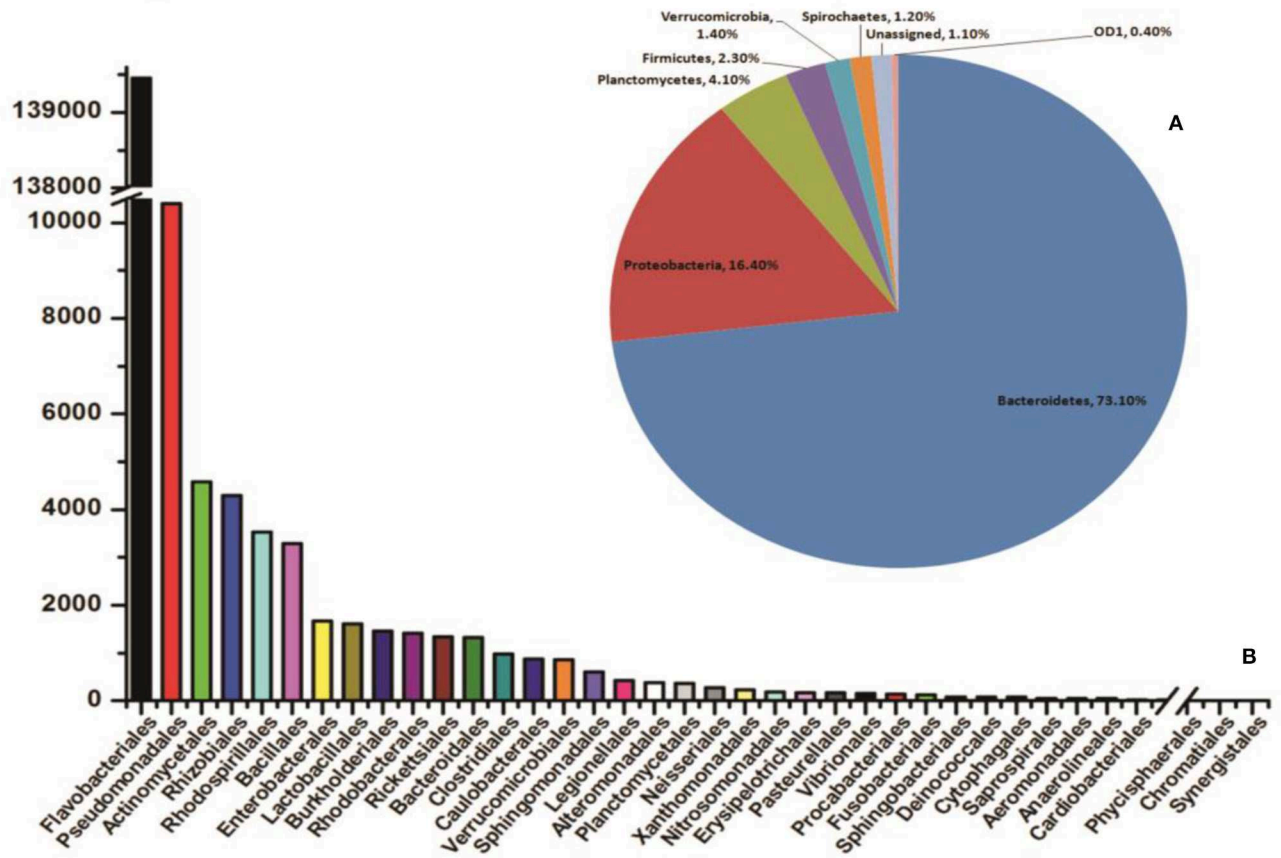

FIGURE 2 | QIIME analysis based gut microbial community structure in naïve mosquitoes ($n = 40$). **(A)** Diversity of the microbiota in the mosquito gut, at phylum level showing dominant association of Bacteroidetes and Proteobacteria followed by Planctomycetes; Firmicutes, Verrucomicrobia, Spirochaetes; **(B)** The bar graph representing abundance of different bacteria at order level based on number of gut metagenomics reads, where Flavobacteriales and Pseudomonadales are the most abundant orders to which *Elizabethkingia* and *Pseudomonas* belong, respectively. Enterobacterales are also among the top ten abundant orders which include Serratia.

2X DyNAmo Color Flash Sybr Green Master Mix Cal. No. F-416) in Eco-Real Time (Illumina, USA; Cat. No. EC-101-1001) or CFX-96 (Biorad, USA), Real-Time PCR machine. PCR cycle parameters included initial denaturation at 95°C for 15 min, followed by 44 cycles of 10 s at 95°C, 20 s at 55°C, and 22 s at 72°C with a final extension of 15 s at 95°C, 15 s at 55°C, and 15 s at 95°C. All qPCR measurements were performed with two technical replicates to rule out any possibility of biases. At least three independent biological replicates were tested for better evaluation. Differential gene expression was evaluated using the *ddCT* method and statistically analyzed by the student *"t"* test. List of primers presented in the **Table ST2**.

RESULTS

Elizabethkingia and *Pseudomonas* Predominate Mosquito Gut

To identify and catalog gut-associated bacteria, we sequenced and analyzed a total of 3,68,138 Illumina raw reads originating from naive mosquito gut metagenomic library. Diversity richness indices such as Shannon-Weaver (1.662 ± 0.02) and Simpson reciprocal (1.667 ± 0.001) showed an optimal estimation and even distribution of species. A QIIME analysis at phylum level showed that mosquitoes gut dominantly harbors Bacteroidetes (73.13%); Proteobacteria (16.4%); Planctomycetes (4.10%); Firmicutes (2.3%), Verrucomicrobia (1.4%), Spirochaetes (1.2%), OD1 (0.4%), and 1.10% 16S reads remained unassigned (**Figure 2A**). At the class level, the Flavobacteria and Gammaproteobacteria where *Elizabethkingia meningoseptica* and *Pseudomonas* sp. were the most abundant gram-negative bacteria, respectively (**Figure 2B**).

Blood Meal Alters the Gut Microbiome Community Structure

In coherence with previous studies, we also observed that blood meal gradually enriched the total bacterial population in the gut till 24 h, which restored to their basal level within 48 h of blood meal (**Figure S4**). To further clarify that how blood meal influences individual bacterial population we cataloged and compared gut microbiome of naïve and 24 h blood-fed

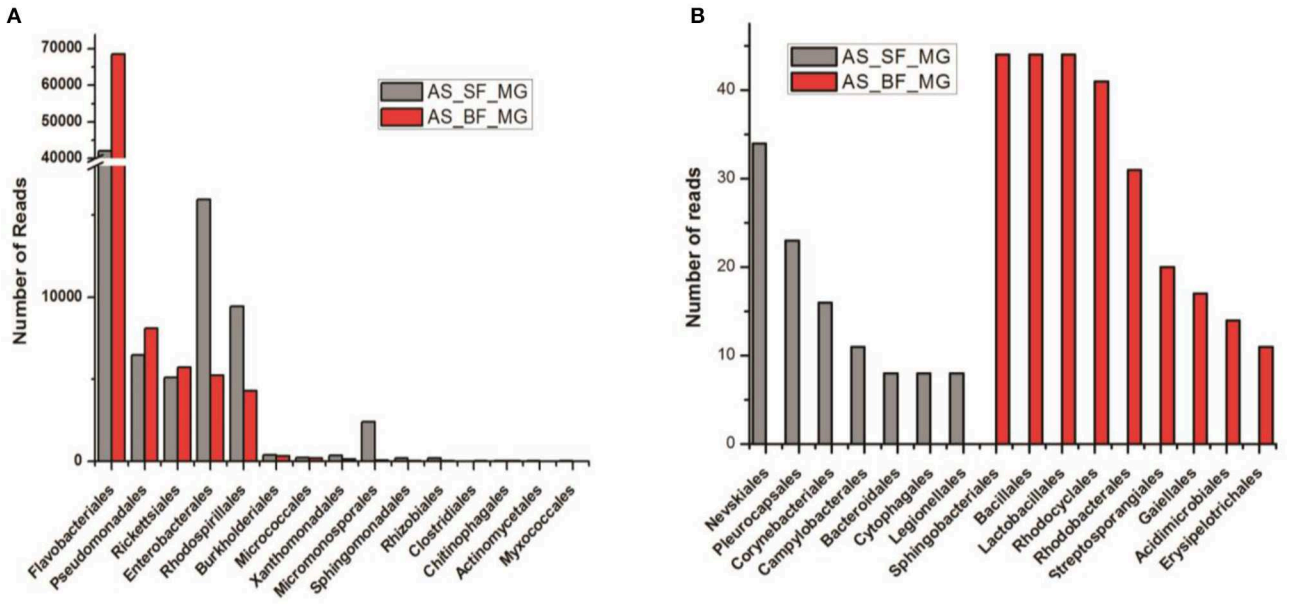

FIGURE 3 | Blood-meal alters gut community structure (order level). **(A)** Comparative analysis of common bacterial community abundances among naïve and blood-fed mosquitoes gut ($n = 50$); **(B)** bar graph represents unique bacterial orders showing association with either sugar-fed (SF) or blood-fed (BF) mosquitoes gut. AS, *A. stephensi*.

adult female mosquito guts. Alpha-diversity rarefaction curves estimate the full extent of phylotype richness and quantifiable diversity estimation (**Figure S5**). A normalized read count data comparison showed that blood meal not only enriched gut-associated dominant Flavobacteria but also favored modest enrichment of unique bacteria such as Bacillales, Lacto-bacillales, Spinghobacteriales, Rohocyclales (**Figures 3A,B**).

To validate the above observation, we examined relative abundances of selected bacterial species, by Real-time PCR assay, using bacterial species-specific primers (see **Table ST2**). We observed a relatively higher abundance of bacteria such as *Pseudomonas*, *Elizabethkingia,* and *Serratia*, in the ovary and midgut than other tissues. However, within midgut, *Elizabethkingia* showed higher abundance than the *Pseudomonas* and *Serratia*, corroborating the metagenomic data (**Figures 4A–D**, **Table ST3**). Individual bacterial species such as *Elizabethkingia* (Flavobacteria), *Pseudomonas* and *Serratia* (Enterobacteriaceae) also showed a gradual enrichment until 24 h post-blood-feeding. However, post 30 h blood meal digestion the bacterial population restored to the basal level of naïve mosquito midgut (**Figures 5A–C**).

RNAseq Recovers Molecular Signatures of Gut-Microbe Interaction

To establish a molecular/ functional relation of gut-microbe interaction, we analyzed a total of 46,73,408 Illumina reads originating from 24 h post blood-fed gut RNAseq library (**Table ST4**). Surprisingly, a species distribution analysis of 5,041 full-length transcripts predicted that at least 90% of transcripts sequences matched to insects, but ∼10% transcripts i.e., 479 CDS showed significant homology to microbial proteins (**Table ST5**). Transcripts homolog to insects dominantly matched to *A. gambiae* (∼72%), *A. sinensis* (∼13%), *A. darlingi* (∼7%), *Aedes aegypti* (∼1.6%), and *Culex* (∼1.1%) (**Figure 6A**). A close examination of BLASTx analysis of microbial sequences/transcripts further identified that at least 8% of transcripts encode proteins homologous to *Elizabethkingia* (EK) (**Figure 6A**), strengthening our finding that EK constitutes a major gut endosymbiotic bacteria in *A. stephensi.* While remaining 2% of transcripts showed significant homology to other microbes such as *Annacalia alegera*; *Wolbachia* and viruses (**Table ST5**).

A comprehensive GO annotation of 391 putative transcripts indicated that EK bacterial species encodes the diverse nature of proteins (**Figure 6B**, **Table ST5**). Transcriptional profiling of selected bacterial transcripts encoding LEM A, Ton-B dependent receptor, FecR, ABC transporter, SusC/Rag family protein showed enriched expression in response to blood feeding and digestion (**Figure 6C**, **Table ST6**).

Early *Plasmodium vivax* Infection Suppresses Gut Microbiota and Immunity

We observed a significant loss in the gut bacterial population in *Plasmodium*-infected mosquitoes which remained below the detection limit until 36 h (**Figure 7A**). However, surprisingly, after 36 h the total bacterial population followed a gradual enrichment to multifold level till 10 days of gut infection (**Figure 7A**). Interestingly, *Elizabethkingia* and *Serratia* also showed a similar pattern of enrichment, except *Pseudomonas* whose population level remains least affected (**Figures 7B–D**).

Since the blood meal-induced gut microbiota also boosts gut immunity, we tested whether *P. vivax* infection influences

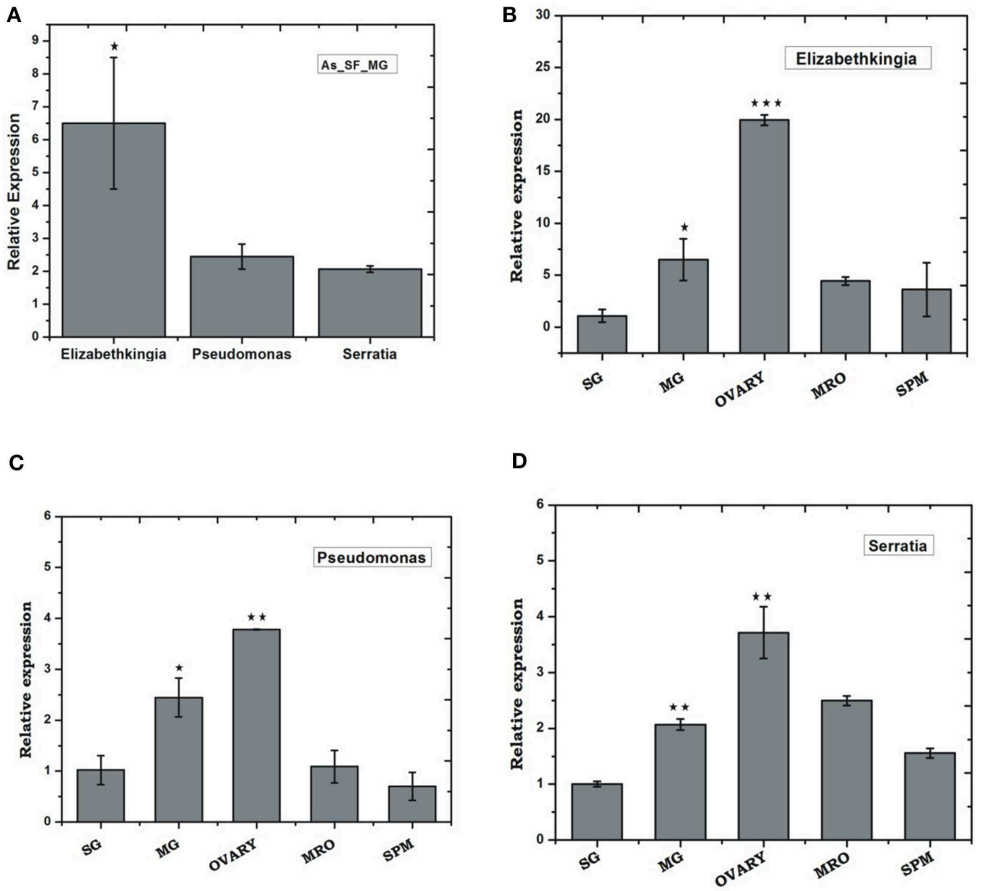

FIGURE 4 | Tissue-specific relative distribution of dominant endo-symbiotic bacteria in the naïve mosquitoes: **(A)** Relative abundance of *Elizabethkingia* ($p \leq 0.05$), *Pseudomonas*, *Serratia* in the naïve mosquito gut; tissue-specific relative abundance of **(B)** *Elizabethkingia* (MG $p \leq 0.033$; Ovary $p \leq 0.00045$); **(C)** *Pseudomonas* (MG $p \leq 0.025$; Ovary $p \leq 0.0026$); and **(D)** *Serratia* (MG $p \leq 0.0025$; Ovary $p \leq 0.0072$); AS, *A. stephensi*; SF, sugar fed; SG, salivary gland; MG, midgut; MRO, male reproductive organ; SPM, Spermathecae. Data was statistically analyzed considering SG expression as control sample for "*t*" test. $^{*}p < 0.05$; $^{**}p < 0.005$; $^{***}p < 0.0005$.

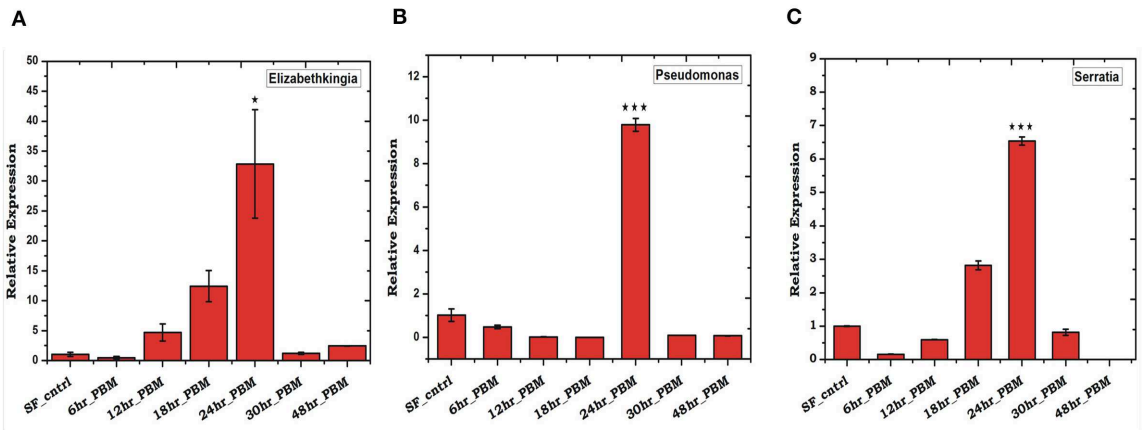

FIGURE 5 | Blood feeding and species-specific distribution of gut microbes: Time-dependent relative abundance of **(A)** *Elizabethkingia* ($p \leq 0.001$); **(B)** *Pseudomonas* ($p \leq 0.0005$); and **(C)** *Serratia* ($p \leq 0.0001$); in the blood-fed mosquitoes gut. The gut tissue was collected at different time intervals of 6, 12, 18, 24, 30, and 48 h post-blood-feeding. Data were statistically analyzed using student *"t"* test, where naïve sugar fed (SF) mosquito gut samples were considered as control against selected test sample. $^{*}p < 0.05$; $^{***}p < 0.0005$.

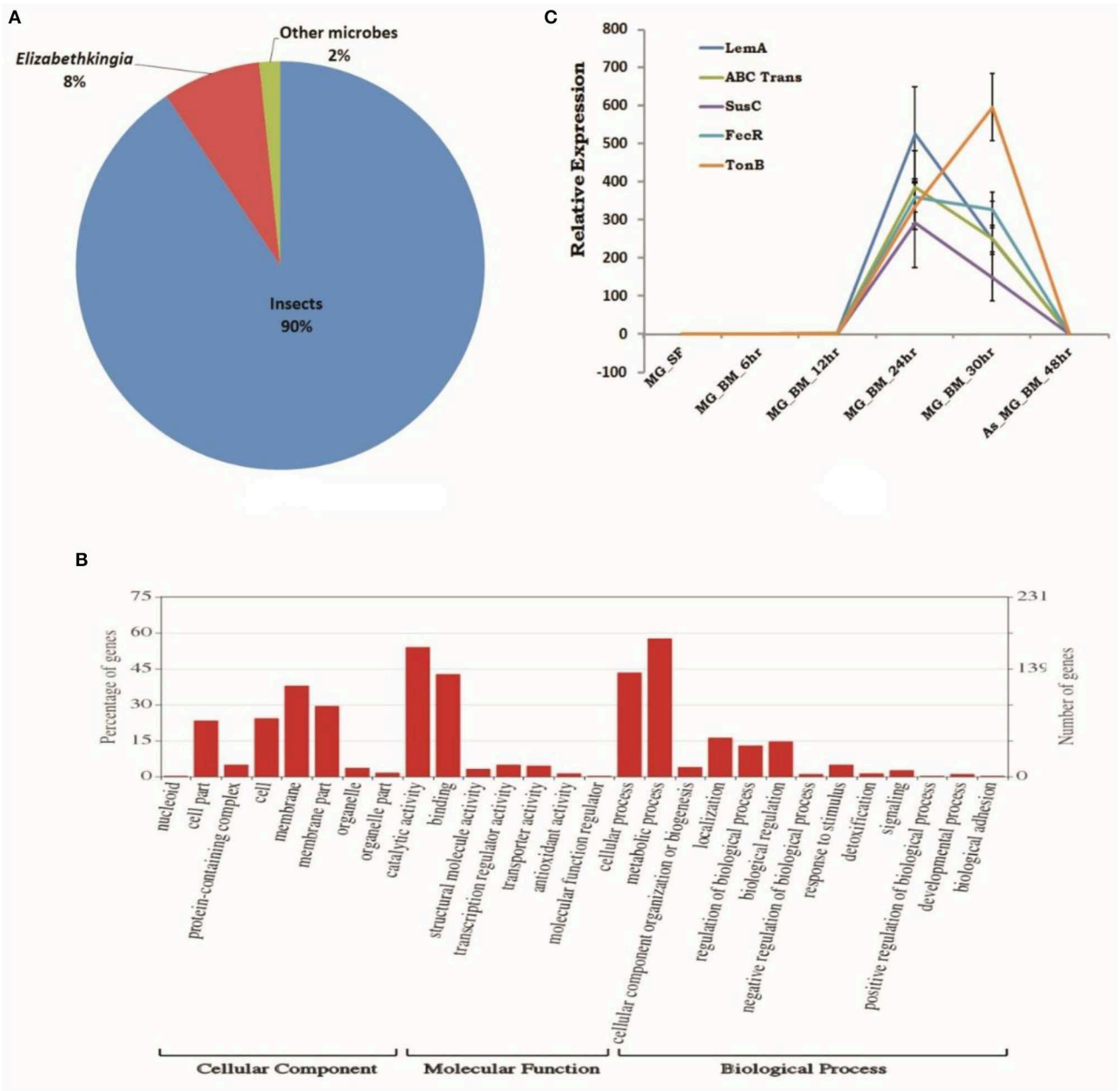

FIGURE 6 | RNAseq identified microbial transcripts signatures. **(A)** Pie chart showing species distribution analysis of gut RNAseq data identifying transcripts having BLASTX homology to Insects (90%), *Elizabethkingia* as dominant gut endosymbiont bacteria (8%), and other microbes (2%); **(B)** molecular catalog of identified EK transcripts; and **(C)** transcriptional profiling of bacterial EK specific transcripts in response to blood meal.

gut immune response. Time-dependent transcriptional profiling of all the selected anti-microbial peptides [also see (22)] showed a unique pattern of immunosuppression during the pre-invasive phase of ookinetes to early oocysts development (**Figure 8**). All the tested immune transcripts showed expression enrichment only 36 h post-infection. But, exceptionally, gambicin showed higher response than cecropin (C1, C2) and defensin (D1) (**Figure 8**), suggesting its unique role against late oocysts development of *P. vivax*.

Laboratory Reared *Anopheles stephensi* Harbor *Wolbachia* Bacteria

Surprisingly, a qualified subset of 250 bp long metagenomic sequencing reads (6,532 blood-fed and 6,154 naïve mosquitoes gut) showed 100% identity to *Wolbachia* endosymbiont of *Chrysomya megacephala* (Accession #CP021120.1; **Figure S6A**, also see FASTA **File S8**). Also, identification of at least 7 mRNA transcripts, originating from distinct gut RNAseq libraries and encoding different *Wolbachia* homolog proteins (**Figure S6B**, **Table ST7**), further predicts the novel

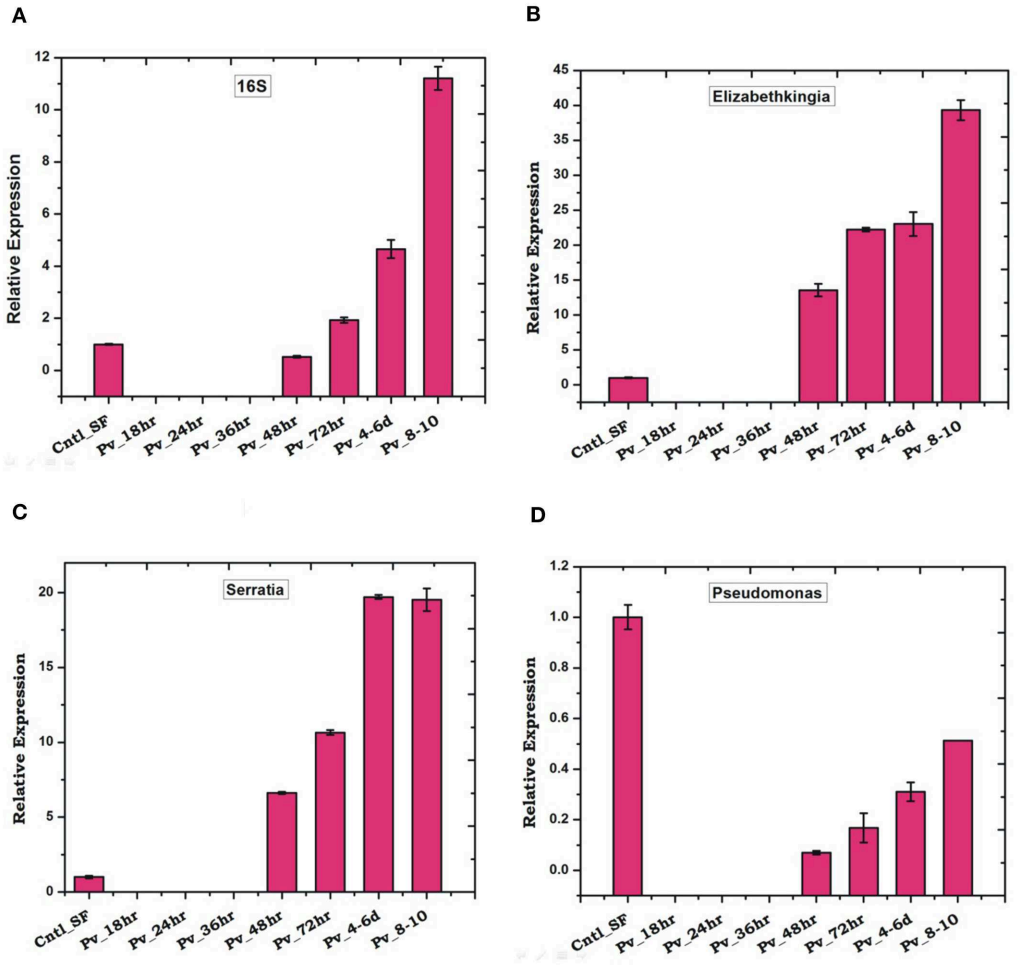

FIGURE 7 | *P. vivax* infection cause early suppression and late restoration/enrichment of gut bacterial population: A time dependent relative quantification of gut microbiota in response to *Plasmodium vivax* (Pv) infection showing enrichment 48 h post-infection (PI) of **(A)** *Total bacteria* (16S): $p \leq 0.002$/4-6DPI, $p \leq 0.0004$/8-10DPI; **(B)** *Elizabethkingia* $p \leq 0.001$/48hPI, $p \leq 4.69E\text{-}05$/72hPI, $p \leq 0.001$/4-6DPI, $p \leq 0.0003$/8-10DPI; **(C)** (*Serratia* $p \leq 0.0001$/48hPI, $p \leq 8.73E\text{-}05$//72hPI, $p \leq 1.85E\text{-}05$/4-6DPI, $p \leq 0.0004$)/8-10DPI; and **(D)** *Pseudomonas*. DPI, days post-infection.

Wolbachia association. An ongoing similar comparative gut metagenomic analysis of Indian vector *A. culicifacies* (unpublished), reared in the same insectarium environment, did not yield a single sequence of *Wolbachia* origin, supporting that *A. stephensi* may exclusively harbor novel *Wolbachia* bacterial species.

DISCUSSION

Using a meta-transcriptomic strategy, we targeted to decode the molecular basis of tripartite gut-microbe-*P. vivax* interaction in the mosquito host *A. stephensi*. Our metagenomic study identifies *Elizabethkingia* and *Pseudomonas* as dominant gut-inhabiting bacteria in the laboratory-reared naïve adult female mosquitoes. In response to the blood meal, we observed a significant alteration of gut microbial community structure and enrichment of dominant bacterial species e.g., *Elizabethkingia* sp. (Flavobacteriales), *Pseudomonas* (Pseudomonadales), and *Serratia* (Enterobacteriales). Previous several studies have also reported a similar pattern of gut microbe enrichment (31, 32), but the nature of gut-microbe interactions, especially microbial proteins facilitating blood meal digestion, remains unclear (33). Available draft genome sequence of cultured bacterial species predicts several metabolic pathways, but no functional relation has been established (34, 35).

Functional annotation of at least ∼391 *Elizabethkingia* transcripts identified from blood-fed mosquitoes gut-RNAseq data provide direct evidence of "*in vivo*" metabolically active proteins, which may have a role in blood meal digestion. Until 30 h of post-blood meal, an enriched expression of transcripts such as LEM-A, Ton-B dependent receptor, FecR, ABC transporter suggested their important role in iron metabolism (**Table ST6**). Possibly this is accomplished through siderophore uptake and oxidative stress management, a possible mechanism benefiting mosquito's survival and reproductive outcome (36–38).

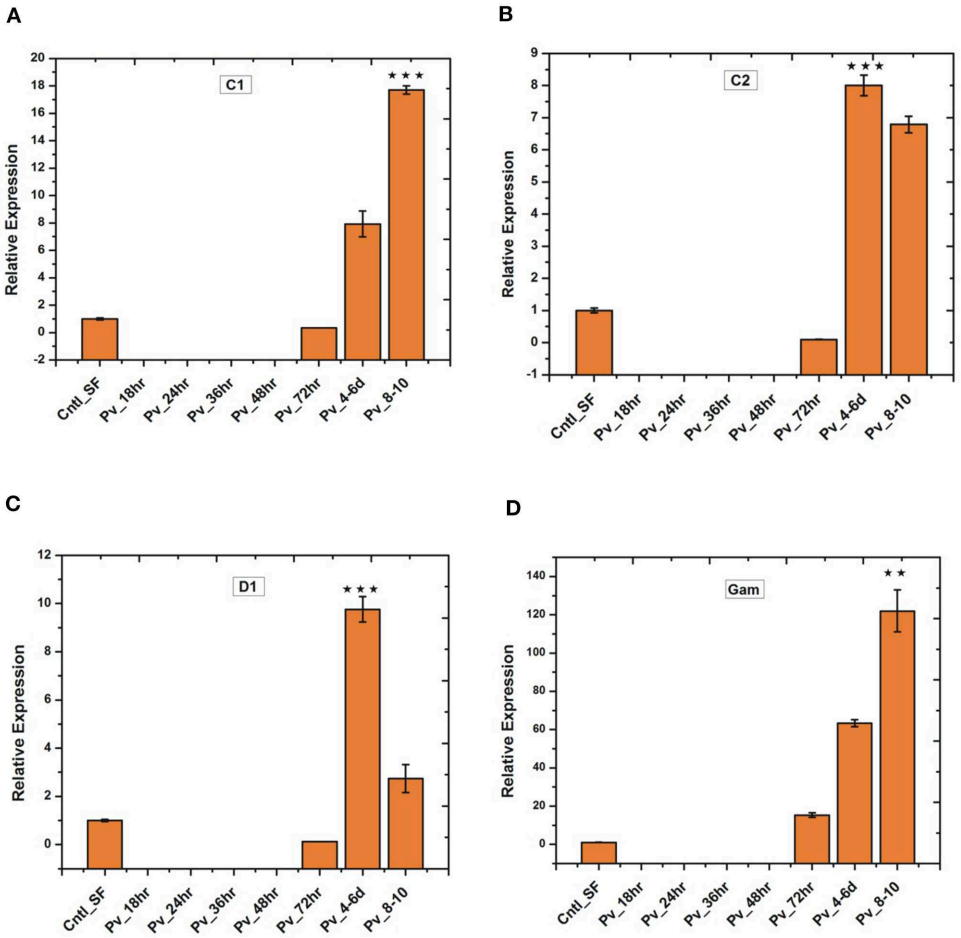

FIGURE 8 | Relative quantification of gut immune transcripts in response to *Plasmodium vivax* infection: Transcriptional profiling of antimicrobial peptides (AMPs) C1 ($p \leq 9.00674E-05$), C2 ($p \leq 0.0005$), D1 ($p \leq 0.0008$), Gambicin ($p \leq 0.002$) showing early suppression of gut immunity which restored after 3 days of *P. vivax* infected blood meal. C1-C2, cecropin1 and cecropin2; D1, defensin1; Gam, Gambicin. $^{**}p < 0.005$; $^{***}p < 0.0005$.

It is known that gut endosymbionts also serve as potent modulators of sexual development and transmission of the malaria parasite in *Anopheles* mosquitoes (39, 40). This antagonistic relationship of gut bacteria has been observed in the sporogonic development of *Plasmodium* in several *Anopheline* mosquitoes (7, 40, 41). Introduction of *E. coli*, *Pseudomonas,* and *Serratia* by oral feeding reduces the gut oocyst load in *A. gambiae* (40), but species-specific interaction of the *Plasmodium* and bacteria remains unclarified. In our infectivity assay, we observed that *P. vivax* disables bacterial proliferation to keep an immunosuppression till invasion to the gut epithelium.

Though it is unknown how sexual stages of *Plasmodium* utilize ingested iron in the blood into the mosquito gut, an earlier study in *Anopheline* mosquitoes suggests that iron-depleted blood inhibits *P. falciparum* gametocyte activation, and hence the infectivity (42, 43). Thus, we hypothesized the first 24 h of gut-microbe-*Plasmodium* interaction in the gut lumen are crucial for *Plasmodium* survival, where it may limit the availability of iron/nutrients required for bacterial growth (44). Corroborating to earlier studies, we also observed that mosquitoes were able to restore the basal levels of gut microbiota within 30 h of uninfected blood meal digestion (6). However, surprisingly, *P. vivax* infection caused a major shift in gut microbiota restoration to an enriched state after 48 h of infection. Interestingly, this shift of bacterial enrichment boosted a similar pattern of gut immunity induction, till late oocysts exited gut epithelium (**Figure 8**). Together, we hypothesized that in the gut lumen, gut-microbe-*P. vivax* interaction undergoes a unique "flip-show" where an early suppression of gut bacteria may favor *Plasmodium* survival, but the late phase gut immunity activation may restrict gut oocysts population. A late phase anti-*Plasmodium* immunity has also been suggested in other mosquito-parasite interaction studies (45). Since we observed this pattern repeatedly for at least four independent experiments, thus it is very unlikely that it may be an undisclosed confounding effect of a blood sample originating from the patient having antibiotic treatment before diagnosis (46).

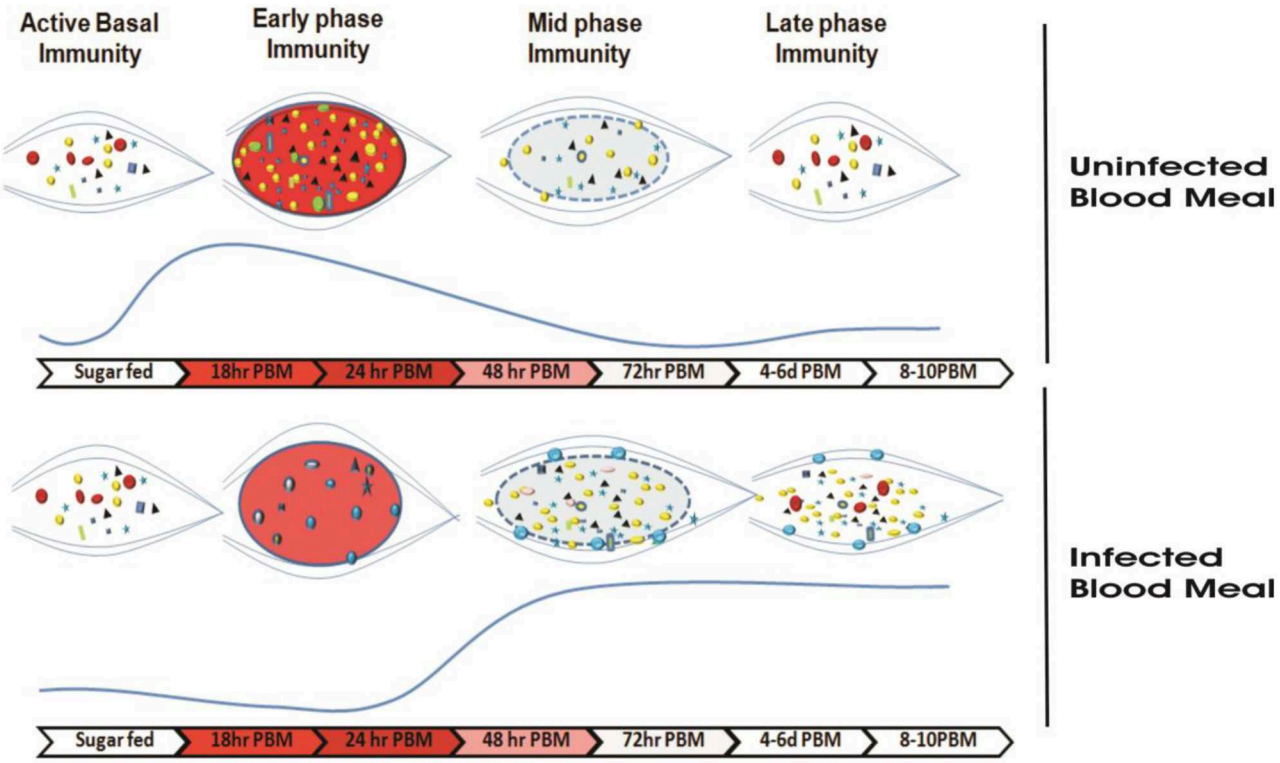

FIGURE 9 | Survival strategy model of *P. vivax* during the pre-invasive phase of development inside the mosquito gut: A schematic representation of the microbial distribution in response to blood-feeding vs. *Plasmodium*-infected blood meal. In absence of *Plasmodium*, after a normal blood-feeding rapid proliferation of gut bacteria occurs in a nutrient-rich medium (of which Fe is indispensable to bacterial growth) during a time window of 18–24 h. Mosquito induces an innate immune response (via the production of various AMPs) to this incremental bacterial growth in order to tame the bacterial load and restore it to a basal level by 48 h. In presence of *Plasmodium*, *Plasmodium vivax* suppresses the proliferation of the gut bacteria possibly by altering Fe metabolism or nutrition physiology during initial hours (18–24 h) in a bid to dampen the mosquito innate immune response and to shore up ookinete invasion. In a direct competition for nutritional resources within the gut lumen between the parasite and bacteria, the parasite overcomes the bacteria. The parasite leaves the lumen and encysts beneath the basal lamina. After 48 h post-blood meal, in absence of competition with the parasite in the gut lumen allows the bacteria to proliferate possibly by feeding on undigested food left in the lumen. As the bacterial load rises, it leads to activation of mosquito innate immune responses followed by synthesis of various AMPs which not only limit the bacterial load but also limit the medium and late oocyst development. , different bacteria residing the gut; , *Elizabethkingia*, , *Pseudomonas*, , *Serratia*; , *Plasmodium viva;* , midgut; , blood bolus after normal blood-feeding, , blood bolus after *Plasmodium*-infected blood uptake; , peritrophic matrix after blood digestion.

Paratransgenesis approaches for manipulating gut endosymbionts such as *Elizabethkingia*, *Serratia* to block parasite development are under progress (47–49). A dominant association of tested *Elizabethkingia*, *Pseudomonas*, *Serratia* with mosquito ovaries/eggs, and subsequent validation of transovarian transfer from F1, F2, and F3 generation (see **Figure S7**) supports an idea to select and target them for future manipulation. Alternatively, by manipulating intracellular endosymbiont such as *Wolbachia* induced male sterility and pathogen development inhibition, is rapidly gaining much attention for vector-borne disease control program (50, 51). Trial releases of *Wolbachia* inhabiting mosquitoes is now being proved as a tool to reduce dengue cases in several countries (52, 53). Laboratory validation of a similar strategy in *Anopheline* mosquitoes for malaria control is also in progress (54).

A surprising finding of at least ∼6% metagenomic sequences and *Wolbachia* homolog protein-encoding transcripts, further established a natural association of a novel *Wolbachia* bacteria in laboratory-reared mosquitoes. Thus, we believe a systemic evaluation and validation of *Wolbachia* interaction influencing *Plasmodium* development and cytoplasmic incompatibility in *A. stephensi*, may be valuable to design a novel tool to fight malaria in India.

CONCLUSION

Several studies prove that immediately after blood feeding, a vital tripartite interaction occurs among mosquito-microbe-parasite in the mosquito's gut lumen. But the molecular basis that how *Plasmodium* manages its survival, development, and transmission is not well-known. For the first time, we establish that *P. vivax* causes an early suppression of gut microbial population, possibly by altering iron metabolism and nutritional physiology. And by this strategy, the parasite not only weakens gut immunity, but also favors successful invasion

and development in the mosquito *A. stephensi* (**Figure 9**). With current data, we further propose that late oocysts/bursting oocysts releasing sporozoites alters gut bacterial susceptibility to boost late-phase immunity, a plausible mechanism to restrict the *Plasmodium* population [see (22); https://www.biorxiv.org/content/10.1101/774166v1].

DATA AVAILABILITY STATEMENT

The sequence data have been submitted to the NCBI SRA database under the following accession number: SAMN10496496- DNA_AS_SF_MG; SAMN10439711-AS_MG_BF_DNA for individual samples of metagenomics data described in the article. The sequences of Blood fed midgut RNASeq data is submitted with accession number-SRR8580010. All other data is included as **Supplementary Material**.

ETHICS STATEMENT

The studies involving human participants were reviewed and approved by the Institutional Ethics Committee of NIMR (Ref#ECR/NIMR/EC/2012/41). The patients/participants provided their written informed consent to participate in this study.

AUTHOR'S NOTE

Successful malaria transmission relies on the competitive interactions of *Plasmodium* and mosquito's tissue-specific immune potential. Within 24 h of a blood meal, gut-microbiota grows exponentially and spikes a mosquito's immune response, which is detrimental to parasite development and survival. How *Plasmodium* manages to evade this pre-invasive immune barrier in the gut remains elusive. We investigated the influence of tripartite gut-microbiome-parasite interaction on human malaria parasite *Plasmodium vivax* in its natural/native vector *Anopheles stephensi*. Surprisingly, we found that infectious blood meal leads to dramatic suppression in the gut-bacteria population, a plausible strategy of *P. vivax* ookinetes to avoid immune responses. These findings provide a newer perspective on how *Plasmodium* may impact microbiota for its own survival. Disruption and manipulation of this gut-microbe-interaction may help to design new paratransgenesis molecular tools for malaria control.

AUTHOR CONTRIBUTIONS

PS, RD, and KP contributed idea and hypothesis generation, conceived, and designed the experiments. PS, CC, SK, JR, ST, TD, and DS contributed to design and performing the experiments, data acquisition, writing and editing. PS, KP, and RD data analysis and interpretation, data presentation, contributed reagents, materials, analysis tools, wrote, reviewed, edited, and finalized manuscript. All authors read and approved the final manuscript.

FUNDING

Work in the laboratory was supported by the Indian Council of Medical Research (ICMR), Government of India [3/1/3PDF(13)/2016-HRD]. RD was a recipient of a DBT sponsored Ramalingaswami Fellowship.

ACKNOWLEDGMENTS

Authors thanks to NIMR-clinical facility support. Authors thanks Dr. Neena Valecha and Dr. Mayur Kajla for reviewing and valuable comments on the manuscript. The authors also thank ICMR-NIMR for basic infrastructure and instrumentation support. We thank Kunwarjeet Singh for technical assistance and mosquito rearing. We are thankful to Xcelris Labs Limited Ahmedabad, Gujarat, India, and NGB Patparganj, Delhi for the meta-transcriptomic sequencing services. This manuscript has been released as a Pre-Print @www.Biorxiv.org; https://www.biorxiv.org/content/10.1101/774075v1.

SUPPLEMENTARY MATERIAL

The Supplementary Material for this article can be found online at: https://www.frontiersin.org/articles/10.3389/fimmu.2020.00609/full#supplementary-material

REFERENCES

1. Attardo GM, Hansen IA, Raikhel AS. Nutritional regulation of vitellogenesis in mosquitoes: implications for anautogeny. *Insect Biochem Mol Biol.* (2005) 35:661–75. doi: 10.1016/j.ibmb.2005.02.013
2. Richards SL, Anderson SL, Yost SA. Effects of blood meal source on the reproduction of *Culex pipiens* quinquefasciatus (Diptera: Culicidae). *J Vector Ecol.* (2012) 37:1–7. doi: 10.1111/j.1948-7134.2012.00194.x
3. Gaio ADO, Gusmão DS, Santos AV, Berbert-Molina MA, Pimenta PF, Lemos FJ. Contribution of midgut bacteria to blood digestion and egg production in aedes aegypti (diptera: culicidae) (L.). *Parasit Vectors.* (2011) 4:105. doi: 10.1186/1756-3305-4-105
4. Romoli O, Gendrin M. The tripartite interactions between the mosquito, its microbiota and Plasmodium. *Parasit Vectors.* (2018) 11:200. doi: 10.1186/s13071-018-2784-x
5. Pumpuni CB, Demaio J, Kent M, Davis JR, Beier JC. Bacterial population dynamics in three *Anopheline* species: the impact on *Plasmodium sporogonic* development. *Am J Trop Med Hyg.* (1996) 54:214–8. doi: 10.4269/ajtmh.1996.54.214
6. Das De T, Sharma P, Thomas T, Singla D, Tevatiya S, Kumari S, et al. Interorgan molecular communication strategies of local and systemic innate immune responses in mosquito *Anopheles stephensi*. *Front Immunol.* (2018) 9:148. doi: 10.3389/fimmu.2018.00148
7. Dong Y, Manfredini F, Dimopoulos G. Implication of the mosquito midgut microbiota in the defense against malaria parasites. *PLoS Pathog.* (2009) 5:e1000423. doi: 10.1371/journal.ppat.1000423
8. Smith RC, Vega-Rodríguez J, Jacobs-Lorena M. The Plasmodium bottleneck: malaria parasite losses in the mosquito vector. *Mem Inst Oswaldo Cruz.* (2014) 109:644–61. doi: 10.1590/0074-0276130597
9. Rodgers FH, Gendrin M, Wyer CAS, Christophides GK. Microbiota-induced peritrophic matrix regulates midgut homeostasis and prevents systemic

infection of malaria vector mosquitoes. *PLoS Pathog.* (2017) 13:e1006391. doi: 10.1371/journal.ppat.1006391
10. Noden BH, Vaughan JA, Pumpuni CB, Beier JC. Mosquito ingestion of antibodies against mosquito midgut microbiota improves conversion of ookinetes to oocysts for *Plasmodium falciparum*, but not *P. yoelii. Parasitol Int.* (2011) 60:440–6. doi: 10.1016/j.parint.2011.07.007
11. Simonetti AB. The biology of malarial parasite in the mosquito–a review. *Mem Inst Oswaldo Cruz.* (1996) 91:519–41. doi: 10.1590/S0074-02761996000500001
12. Chavshin AR, Oshaghi MA, Vatandoost H, Pourmand MR, Raeisi A, Enayati AA, et al. Identification of bacterial microflora in the midgut of the larvae and adult of wild caught *Anopheles stephensi*: a step toward finding suitable paratransgenesis candidates. *Acta Trop.* (2012) 121:129–34. doi: 10.1016/j.actatropica.2011.10.015
13. Chavshin AR, Oshaghi MA, Vatandoost H, Pourmand MR, Raeisi A, Terenius O. Isolation and identification of culturable bacteria from wild *Anopheles culicifacies*, a first step in a paratransgenesis approach. *Parasit Vectors.* (2014) 7:419. doi: 10.1186/1756-3305-7-419
14. Anglero-Rodriguez YI, Blumberg BJ, Dong Y, Sandiford SL, Pike A, Clayton AM, et al. A natural *Anopheles*-associated *Penicillium chrysogenum* enhances mosquito susceptibility to *Plasmodium* infection. *Sci Rep.* (2016) 6:34084. doi: 10.1038/srep34084
15. Saraiva RG, Kang S, Simoes ML, Anglero-Rodriguez YI, Dimopoulos G. Mosquito gut antiparasitic and antiviral immunity. *Dev Comp Immunol.* (2016) 64:53–64. doi: 10.1016/j.dci.2016.01.015
16. Drexler AL, Vodovotz Y, Luckhart S. Plasmodium development in the mosquito: biology bottlenecks and opportunities for mathematical modeling. *Trends Parasitol.* (2008) 24:333–6. doi: 10.1016/j.pt.2008.05.005
17. Bennink S, Kiesow MJ, Pradel G. The development of malaria parasites in the mosquito midgut. *Cell Microbiol.* (2016) 18:905–18. doi: 10.1111/cmi.12604
18. Belachew EB. Immune response and evasion mechanisms of *Plasmodium falciparum* parasites. *J Immunol Res.* (2018) 2018:6529681. doi: 10.1155/2018/6529681
19. Rosenberg R, Wirtz RA, Schneider I, Burge R. An estimation of the number of malaria sporozoites ejected by a feeding mosquito. *Trans R Soc Trop Med Hyg.* (1990) 84:209–12. doi: 10.1016/0035-9203(90)90258-G
20. Ghosh AK, Jacobs-Lorena M. Plasmodium sporozoite invasion of the mosquito salivary gland. *Curr Opin Microbiol.* (2009) 12:394–400. doi: 10.1016/j.mib.2009.06.010
21. Simões ML, Mlambo G, Tripathi A, Dong Y, Dimopoulos G. Immune regulation of plasmodium is *Anopheles* species specific and infection intensity dependent. *MBio.* (2017) 8:e01631-17. doi: 10.1128/mBio.01631-17
22. Tevatiya S, Kumari S, Chauhan C, Singla D, De TD, Sharma P, et al. Genetic changes of *P. vivax* tempers host tissue-specific responses in *Anopheles stephensi*. *bioRxiv.* (2019) 774166. doi: 10.1101/774166
23. Sharma P, Sharma S, Mishra AK, Thomas T, Das De T, Rohilla SL, et al. Unraveling dual feeding associated molecular complexity of salivary glands in the mosquito *Anopheles culicifacies*. *Biol Open.* (2015) 4:1002–15. doi: 10.1242/bio.012294
24. Sharma P, Sharma S, Maurya RK, Das De T, Thomas T, Lata S, et al. Salivary glands harbor more diverse microbial communities than gut in *Anopheles culicifacies*. *Parasit Vectors.* (2014) 7:235. doi: 10.1186/1756-3305-7-235
25. Price MN, Dehal PS, Arkin AP. FastTree 2–approximately maximum-likelihood trees for large alignments. *PLoS ONE.* (2010) 5:e9490. doi: 10.1371/journal.pone.0009490
26. Wang Q, Garrity GM, Tiedje JM, Cole JR. Naive Bayesian classifier for rapid assignment of rRNA sequences into the new bacterial taxonomy. *Appl Environ Microbiol.* (2007) 73:5261–7. doi: 10.1128/AEM.00062-07
27. Zhu YY, Machleder EM, Chenchik A, Li R, Siebert PD. Reverse transcriptase template switching: a SMART approach for full-length cDNA library construction. *Biotechniques.* (2001) 30:892–7. doi: 10.2144/01304pf02
28. Thomas T, De TD, Sharma P, Lata S, Saraswat P, Pandey KC, et al. Hemocytome: deep sequencing analysis of mosquito blood cells in Indian malarial vector *Anopheles stephensi*. *Gene.* (2016) 585:177–90. doi: 10.1016/j.gene.2016.02.031
29. Das De T, Thomas T, Verma S, Singla D, Chauhan C, Srivastava V, et al. A synergistic transcriptional regulation of olfactory genes drives blood-feeding associated complex behavioral responses in the mosquito *Anopheles culicifacies*. *Front Physiol.* (2018) 9:577. doi: 10.3389/fphys.2018.00577
30. Dixit R, Rawat M, Kumar S, Pandey KC, Adak T, Sharma A. Salivary gland transcriptome analysis in response to sugar feeding in malaria vector *Anopheles stephensi*. *J Insect Physiol.* (2011) 57:1399–406. doi: 10.1016/j.jinsphys.2011.07.007
31. Tchioffo MT, Boissière A, Abate L, Nsango SE, Bayibéki AN, Awono-Ambéné PH, et al. Dynamics of bacterial community composition in the malaria mosquito's epithelia. *Front Microbiol.* (2015) 6:1500. doi: 10.3389/fmicb.2015.01500
32. Muturi EJ, Dunlap C, Ramirez JL, Rooney AP, Kim CH. Host blood-meal source has a strong impact on gut microbiota of *Aedes aegypti*. *FEMS Microbiol Ecol.* (2019) 95:fiy213. doi: 10.1093/femsec/fiy213
33. Chen S, Blom J, Walker ED. Genomic, physiologic, and symbiotic characterization of serratia marcescens strains isolated from the mosquito *Anopheles stephensi*. *Front Microbiol.* (2017) 8:1483. doi: 10.3389/fmicb.2017.01483
34. Kukutla P, Lindberg BG, Pei D, Rayl M, Yu W, Steritz M, et al. Draft genome sequences of elizabethkingia anophelis strains R26T and Ag1 from the midgut of the malaria mosquito *Anopheles gambiae*. *Genome Announc.* (2013) 1:e01030-13. doi: 10.1128/genomeA.01030-13
35. Pei D, Hill-Clemons C, Carissimo G, Yu W, Vernick KD, Xu J. Draft genome sequences of two strains of *Serratia* spp. from the midgut of the malaria mosquito *Anopheles gambiae*. *Genome Announc.* (2015) 3:e00090-15. doi: 10.1128/genomeA.00090-15
36. Köster W. ABC transporter-mediated uptake of iron, siderophores, heme and vitamin B12. *Res Microbiol.* (2001) 152:291–301. doi: 10.1016/S0923-2508(01)01200-1
37. Mettrick KA, Lamont IL. Different roles for anti-sigma factors in siderophore signalling pathways of *Pseudomonas aeruginosa*. *Mol Microbiol.* (2009) 74:1257–71. doi: 10.1111/j.1365-2958.2009.06932.x
38. Wang R, Xu H, Du L, Chou SH, Liu H, Liu Y, et al. A TonB-dependent receptor regulates antifungal HSAF biosynthesis in Lysobacter. *Sci. Rep.* (2016) 6:26881. doi: 10.1038/srep26881
39. Weiss B, Aksoy S. Microbiome influences on insect host vector competence. *Trends Parasitol.* (2011) 27:514–22. doi: 10.1016/j.pt.2011.05.001
40. Tchioffo MT, Boissiere A, Churcher TS, Abate L, Gimonneau G, Nsango SE, et al. Modulation of malaria infection in *Anopheles gambiae* mosquitoes exposed to natural midgut bacteria. *PLoS ONE.* (2013) 8:e81663. doi: 10.1371/annotation/d8908395-a526-428c-b9ed-4430aaf8f7d7
41. Pumpuni CB, Beier MS, Nataro JP, Guers LD, Davis JR. *Plasmodium falciparum*: inhibition of sporogonic development in *Anopheles stephensi* by gram-negative bacteria. *Exp Parasitol.* (1993) 77:195–9. doi: 10.1006/expr.1993.1076
42. Ke H, Sigala PA, Miura K, Morrisey JM, Mather MW, Crowley JR, et al. The heme biosynthesis pathway is essential for *Plasmodium falciparum* development in mosquito stage but not in blood stages. *J Biol Chem.* (2014) 289:34827–37. doi: 10.1074/jbc.M114.615831
43. Ferrer P, Vega-Rodriguez J, Tripathi AK, Jacobs-Lorena M, Sullivan DJ. Antimalarial iron chelator FBS0701 blocks transmission by *Plasmodium falciparum* gametocyte activation inhibition. *Antimicrob Agents Chemother.* (2015) 59:1418–26. doi: 10.1128/AAC.04642-14
44. Clark MA, Goheen MM, Cerami C. Influence of host iron status on *Plasmodium falciparum* infection. *Front Pharmacol.* (2014) 5:84. doi: 10.3389/fphar.2014.00084
45. Clayton AM, Dong Y, Dimopoulos G. The *Anopheles* innate immune system in the defense against malaria infection. *J Innate Immun.* (2014) 6:169–81. doi: 10.1159/000353602
46. Gendrin M, Rodgers FH, Yerbanga RS, Ouédraogo JB, Basáñez MG, Cohuet A, et al. Antibiotics in ingested human blood affect the mosquito microbiota and capacity to transmit malaria. *Nat Commun.* (2015) 6:5921. doi: 10.1038/ncomms6921
47. Chen S, Bagdasarian M, Walker ED. Elizabethkingia anophelis: molecular manipulation and interactions with mosquito hosts. *Appl Environ Microbiol.* (2015) 81:2233–43. doi: 10.1128/AEM.03733-14
48. Wang S, Dos-Santos ALA, Huang W, Liu KC, Oshaghi MA, Wei G, et al. Driving mosquito refractoriness to *Plasmodium falciparum*

with engineered symbiotic bacteria. *Science.* (2017) 357:1399–402. doi: 10.1126/science.aan5478
49. Koosha M, Vatandoost H, Karimian F, Choubdar N, Oshaghi MA. Delivery of a genetically marked serratia AS1 to medically important arthropods for use in RNAi and paratransgenic control strategies. *Microb Ecol.* (2018) 78:185–94. doi: 10.1007/s00248-018-1289-7
50. Bourtzis K, Dobson SL, Xi Z, Rasgon JL, Calvitti M, Moreira LA, et al. Harnessing mosquito-Wolbachia symbiosis for vector and disease control. *Acta Trop.* (2014) 132(Suppl.):S150–63. doi: 10.1016/j.actatropica.2013.11.004
51. Jayakrishnan L, Sudhikumar AV, Aneesh EM. Role of gut inhabitants on vectorial capacity of mosquitoes. *J Vector Borne Dis.* (2018) 55:69–78. doi: 10.4103/0972-9062.242567
52. Dorigatti I, McCormack C, Nedjati-Gilani G, Ferguson NM. Using *Wolbachia* for dengue control: insights from modelling. *Trends Parasitol.* (2018) 34:102–13. doi: 10.1016/j.pt.2017.11.002
53. Garcia GA, Sylvestre G, Aguiar R, da Costa GB, Martins AJ, Lima JBP, et al. Matching the genetics of released and local *Aedes aegypti* populations is critical to assure *Wolbachia* invasion. *PLoS Negl Trop Dis.* (2019) 13:e0007023. doi: 10.1371/journal.pntd.0007023
54. Bian G, Joshi D, Dong Y, Lu P, Zhou G, Pan X, et al. Wolbachia invades *Anopheles stephensi* populations and induces refractoriness to *Plasmodium* infection. *Science.* (2013) 340:748–51. doi: 10.1126/science.1236192

Conflict of Interest: The authors declare that the research was conducted in the absence of any commercial or financial relationships that could be construed as a potential conflict of interest.

frontiers in Immunology

ORIGINAL RESEARCH
published: 30 June 2020
doi: 10.3389/fimmu.2020.01279

Heterologous Chimeric Construct Comprising a Modified Bacterial Superantigen and a Cruzipain Domain Confers Protection Against *Trypanosoma cruzi* Infection

María Belén Antonoglou[1,2], *Andrés Sánchez Alberti*[1,2,3], *Daniela María Redolfi*[1,2], *Augusto Ernesto Bivona*[1,2,3], *María Julieta Fernández Lynch*[1,2], *Sofía Noli Truant*[1,2], *María Belén Sarratea*[1,2], *Laura Valeria Iannantuono López*[2], *Emilio Luis Malchiodi*[1,2,3] *and Marisa Mariel Fernández*[1,2*]

[1] Cátedra de Inmunología, Departamento de Microbiología, Inmunología, Biotecnología y Genética, Facultad de Farmacia y Bioquímica, Universidad de Buenos Aires, Buenos Aires, Argentina, [2] Instituto de Estudios de la Inmunidad Humoral "Prof. Ricardo A. Margni" (IDEHU), UBA-CONICET, Universidad de Buenos Aires, Buenos Aires, Argentina, [3] Departamento de Microbiología, Parasitología e Inmunología, Facultad de Medicina and Instituto de Microbiología y Parasitología Médica (IMPaM), UBA-CONICET, Universidad de Buenos Aires, Buenos Aires, Argentina

OPEN ACCESS

Edited by:
Fabiano Oliveira,
National Institutes of Health (NIH),
United States

Reviewed by:
Mariana Dominguez,
University of São Paulo, Brazil
Paola Lasso,
Pontifical Javeriana
University, Colombia

***Correspondence:**
Marisa Mariel Fernández
mmfernan@ffyb.uba.ar

Specialty section:
This article was submitted to Vaccines and Molecular Therapeutics, a section of the journal Frontiers in Immunology

Received: 31 March 2020
Accepted: 20 May 2020
Published: 30 June 2020

Citation:
Antonoglou MB, Sánchez Alberti A, Redolfi DM, Bivona AE, Fernández Lynch MJ, Noli Truant S, Sarratea MB, Iannantuono López LV, Malchiodi EL and Fernández MM (2020) Heterologous Chimeric Construct Comprising a Modified Bacterial Superantigen and a Cruzipain Domain Confers Protection Against Trypanosoma cruzi Infection. Front. Immunol. 11:1279. doi: 10.3389/fimmu.2020.01279

Chagas disease is an endemic chronic parasitosis in Latin America affecting more than 7 million people. Around 100 million people are currently at risk of acquiring the infection; however, no effective vaccine has been developed yet. *Trypanosoma cruzi* is the etiological agent of this parasitosis and as an intracellular protozoan it can reside within different tissues, mainly muscle cells, evading host immunity and allowing progression towards the chronic stage of the disease. Considering this intracellular parasitism triggers strong cellular immunity that, besides being necessary to limit infection, is not sufficient to eradicate the parasite from tissues, a differential immune response is required and new strategies for vaccines against Chagas disease need to be explored. In this work, we designed, cloned and expressed a chimeric molecule, named NCz-SEGN24A, comprising a parasite antigen, the N-terminal domain of the major cysteine protease of *T. cruzi*, cruzipain (Nt-Cz), and a non-toxic form of the staphylococcal superantigen (SAg) G, SEG, with the residue Asn24 mutated to Ala (N24A). The mutant SAg SEGN24A, retains its ability to trigger classical activation of macrophages without inducing T cell apoptosis. To evaluate, as a proof of concept, the immunogenicity and efficacy of the chimeric immunogen vs. its individual antigens, C3H mice were immunized intramuscularly with NCz-SEGN24A co-adjuvanted with CpG-ODN, or the recombinant proteins Nt-Cz plus SEGN24A with the same adjuvant. Vaccinated mice significantly produced Nt-Cz-specific IgG titers after immunization and developed higher IgG2a than IgG1 titers. Specific cell-mediated immunity was assessed by *in-vivo* DTH and significant responses were obtained. To assess protection, mice were challenged with trypomastigotes of *T. cruzi*. Both schemes reduced the parasite

load throughout the acute phase, but only mice immunized with NCz-SEGN24A showed significant differences against control; moreover, these mice maintained 100% survival. These results encourage testing mutated superantigens fused to specific antigens as immune modulators against pathogens.

Keywords: cruzipain, chimeric immunogen, immune modulators, *Trypanosoma cruzi*, mutant superantigen

INTRODUCTION

Pathogens have evolved a diverse range of strategies to subvert the host immune system and survive. These strategies include evasion and modulation of the immune response, among others. Most of the intracellular parasites constitute a perfect example of this situation. *Trypanosoma cruzi* is the intracellular protozoan that causes Chagas disease, which affects 7 million people in America (1, 2) and leaves 100 million people in endemic areas at risk of acquiring the infection (3). The infection is contracted when the infective form of the parasite, the metacyclic trypomastigote, presents in the feces of hematophagous triatomines and penetrates a skin wound or an intact mucosa of the host. The acute phase of the disease exhibits non-specific symptoms, except for a periorbital eye inflammation denominated Romaña's sign, which usually occurs when the inoculation site is the conjunctiva. Although an important immune response is detected during this phase, it is inefficient to eradicate the parasite, allowing the development of the disease chronic period, which extends for decades. This stage is characterized by a low or undetectable parasitemia and most of the patients remain asymptomatic. After this period, around 30% of the infected people develop serious cardiac or digestive pathologies (4, 5). In addition to the worsening of the health, Chagas disease has also a high economic impact since it mostly affects economically active people (6). With the aim to develop an effective vaccine against *T. cruzi* to prevent or treat the infection, many antigens have been tested in preclinical studies in combination with different adjuvants [Reviewed in Cazorla et al. (7)]. In many of these studies, after experimental challenge vaccinated mice achieved 100% survival rates; however, clinical trials in humans were not performed with these formulations. In the last 20 years, recombinant proteins or DNA were employed as immunogens and, in combination with the latest generation of adjuvants, new vaccination strategies were developed with promising results [Reviewed in Bivona et al. (8)]. Cruzipain (Cz), the major cysteine protease of *T. cruzi,* has been studied by many authors as a fine antigen to evoke protective immune responses (9–16). In 2010, Cazorla et. al. described that the N-terminal domain of Cz (Nt-Cz) displayed the highest protective role during immunization, bypassing ineffective responses towards the C-terminal domain (17). In previous work from our laboratory, an engineered chimeric immunogen named Traspain was designed containing Nt-Cz as one of the key parasitic molecules, with very promising results (18, 19).

The development of effective prophylactic or therapeutic vaccines against *T. cruzi* requires the use of adjuvants and diverse delivery systems which promote a differential immune response. Bacterial Superantigens (SAgs) are enterotoxins which engage the T cell receptors (TCR) on the surface of T cells and the major histocompatibility complex (MHC) class II molecules on antigen presenting cells (APC) as non-processed molecules, eliciting an unregulated immune response characterized by a strong proinflammatory profile and a non-effective immune response. The idea of using this important immune modulatory characteristic of the SAgs for health care, gave rise to the construction of biotherapeutic tools for cancer treatment (20–22). Based on the capacity of SAgs to induce cross-presentation, modified SAgs were also used as adjuvants to improve the vaccination process (23).

The staphylococcal enterotoxin G (SEG) is a non-classical SAg which belongs to the group II or SEB family (24, 25). In the absence of T cells, SEG interacts with human monocytic/macrophagic cells inducing a strong M1 immune response with proinflammatory cytokines, which would eventually lead to a further T cell differentiation toward Th1/Th17 profiles (26). SAgs are also able to interact with dendritic cells without affecting their viability or migration to the secondary lymphoid organs. In a previous study (27), we demonstrated that SEG is phagocytized by murine dendritic cells, is found in sequential vesicles and afterwards released in the lymph node as a native and active molecule able to interact with TCR and MHC-II.

SAgs can stimulate T cells bearing certain variable β chain isoforms. The SAgs of group II are very well-characterized by their interaction with the mouse variable β chain 8.2 (mVβ). Classical SAgs, such as SEB and SEC3, bind the mVβ8.2 chain establishing three hydrogen bonds with residues located in the β chain through Asn24, with an affinity in the micromolar range. The affinity between SEG and mVβ8.2, which is in the nanomolar range, is the highest reported for staphylococcal superantigens (28). The complex SEG-Vβ8.2 has been crystallized, and the residues involved in the direct contact between these molecules are very well-documented (29). As it was also described for classical SAgs, the Asn24 on SEG surface is crucial for the interaction with the TCR and promotion of the T cell proliferation and further exhaustion (30).

These previous works prompted us to develop a mutant version of SEG, SEGN24A, which would be non-toxic but would maintain SAg's properties at innate level without exhaustion of the T cell responses. In addition, we designed, expressed, and tested as a proof of concept, a heterologous chimeric immunogen between the mutated bacterial SAg, SEGN24A, and the N-terminal domain of the major parasite antigen, Cz, with the aim to control *T. cruzi* infection in mice. The idea behind the

design was that SEGN24A would contribute with its immune modulatory properties at the innate immune response, while Nt-Cz would confer specific protection to the immunized host. We demonstrated that the chimeric antigen, named NCz-SEGN24A adjuvanted with CpG-ODN, was able to protect against infection with *T. cruzi*, improving the performance of the administration of non-conjugated Nt-Cz and SEGN24A antigens.

MATERIALS AND METHODS

Mice, Parasites and Cells

Different groups of inbred mice from the C3H/HeN strain were used in this work for immunization protocols. Mice breeding was carried out in the animal facilities of the "Instituto de Microbiología y Parasitología Médica" (IMPaM, UBA-CONICET). Experiments with animals were approved by the Review Board of Ethics of the School of Medicine (UBA, Argentina) and conducted in accordance with the guidelines established by the National Research Council (CONICET), CD resolution #: 3381-18.

Trypanosoma cruzi bloodstream trypomastigotes (from strains RA, Tulahuen-expressing β-galactosidase or K98 clone) were obtained from blood of CF1 infected mice.

Vero cells (ATCC CCL-81) were used for *T. cruzi in-vitro* infection and cultured in RPMI-1640 medium (Gibco) supplemented with 10% fetal bovine serum (FBS). RAW 264.7 cells (ATCC TIB-71) were used for evaluation of SAgs-mediated inhibition of proliferation and were cultured in DMEM medium (Hyclone) supplemented with 10% FBS. Both cell lines were regularly tested for *Mycoplasma* spp. infection with DAPI staining.

Superantigens and Nt-Cz Recombinant Expression and Purification

Staphylococcal SEGwt was produced and purified as previously described (28). Briefly, SEGwt was cloned in pET-26b (Novagen, Merck), expressed in *Escherichia coli* BL21 (DE3) and purified by Ni^{++}-NTA affinity chromatography (GE Healthcare), followed by *Superdex 200* molecular exclusion (GE Healthcare).

Hot spot punctual mutation on the TCR-binding site of SEGwt was introduced by site-directed mutagenesis (QuikChange™ Site-Directed Mutagenesis Kit, Stratagene). Asn24, which is essential for TCR binding and T cell activation (29), was replaced by Ala, generating the mutant SEGN24A. pET-26b plasmid encoding the *segn24a* gene was used to transform competent *E. coli* BL21 (DE3). SEGN24A protein was expressed in *E. coli* BL21 (DE3) as inclusion bodies, *in-vitro* refolded by drip dialysis method and furthered purified under native conditions by Ni^{++}-NTA.

The N-terminal domain of Cz (Nt-Cz) was produced as previously described (17). Briefly, Nt-Cz was cloned in pET-23a, expressed in *Escherichia coli* BL21 (DE3) and purified by Ni^{++}-NTA affinity chromatography, followed by *in vitro*-folding by dialysis. Purity levels of proteins were determined by SDS-PAGE.

Proteins were treated with agarose-polymixin B (Sigma Aldrich) to remove endotoxin traces and absence of LPS was assessed by Limulus test. In addition, the amount of remaining endotoxin was evaluated by the Pierce LAL chromogenic endotoxin quantitation Kit (Thermo Scientific) following the manufacturers' instructions. For all recombinant proteins, it was verified that <0.1 EU/ml of endotoxin was present.

Flow Cytometry for *in-vivo* Stimulation of T Cells Bearing TCR Vβ8.1/8.2

Female C3H/HeN mice 6 to 8 weeks-old ($n = 3$/group) were inoculated subcutaneously into the footpad with 30 μg of SEGwt or SEGN24A, or sterile PBS (control). After 48 h, mice were sacrificed, and their popliteal and inguinal lymph nodes were removed. Single cell suspensions were obtained from each node by mechanical dislodging. Cells were immunolabeled with e-Fluor 660-conjugated anti-mouse CD3 antibody (e-Bioscience Inc.) and FITC-conjugated anti- Vβ8.1/8.2 TCR (e-Bioscience, Inc.). To perform suitable data acquisition and analysis, autofluorescence and single-stained controls were included. Stained cells were passed through the BD FACSCanto flow cytometer. Data were analyzed using the FlowJo v10 software (Tree Star, Inc.).

Surface Plasmon Resonance Assay (SPR)

SPR assays were performed using a BIAcore T100 instrument (GE Healthcare). SEGwt or SEGN24A (ligands) were immobilized on a CM5 chip (GE Healthcare) surface by amine coupling according to the manufacturer's instructions. Soluble TCR β chain Vβ8.2 protein (analyte) was diluted in PBS, pH 7.4 running buffer, and injected over chip surfaces at a flow rate of 30 $\mu l \times min^{-1}$ for 60 s at 25°C. The data were analyzed with the BIA evaluation software (GE Healthcare). To avoid conformational restrictions due to the immobilization procedure, the assay was also performed immobilizing TCR β chain Vβ8.2 over the chip surface and using SEGwt or SEGN24A as analyte (31).

Cell Inhibition Assays

To evaluate the ability of SAgs to inhibit macrophage proliferation, RAW 264.7 cells (2×10^4/well) were cultured in the presence of SEGwt, SEGN24A (10 μg/ml) or medium (control) for 48 h at 37°C in 5% (v/v) CO_2. During the last 8 h, 0.5 μCi [^{3}H]-thymidine/well was added and then harvested onto glass fiber filters. Incorporation of radioactivity was then measured using a Liquid Scintillation Analyzer Tri–Carb 2810 TR (Perkin Elmer). All measurements were made in triplicate.

Nitrite Assay

Nitrites production was evaluated in culture supernatants by Griess reaction. Briefly, RAW 264.7 cells (1×10^5/well) were cultured in the presence of SEGwt, SEGN24A (10 μg/ml) or medium (control). At 48 h supernatants were recovered, mixed with same volume of A + B Griess reagent (Laboratorios Britania) and then incubated in the dark for 10 min at room temperature.

The absorbance of the reaction mixture was measured at 540 nm and the nitrites concentration in the samples was determined using a sodium nitrite ($NaNO_2$) standard curve.

NCz-SEGN24A Construction, Recombinant Expression and Characterization

The heterologous chimeric *ncz-segn24a* gene was constructed using splicing by overlap extension PCR (SOE-PCR) (32, 33). **Supplementary Figure 1** provides details on the PCRs that were performed in order to fuse *nt-cz* and *segn24a* genes. The resultant fused chimeric gene was *ncz-segn24a*. *Bam*HI restriction site was included in PF_1, and PR_4 included *Eco*RI restriction site as well as a 6 his tag coding sequence. Cloning was done in a pET-32a(+) vector, which allowed fusion to thioredoxin (Trx). Gene sequencing was performed to confirm the chimeric gene.

NCz-SEGN24A (MW 69 kDa) protein was expressed in *E. coli* BL21 (DE3) as inclusion bodies, purified under denaturing conditions by Ni^{++}-NTA, *in-vitro* refolded by dialysis method and furthered purified by *Superdex 200* molecular exclusion (GE Healthcare). Purity levels were determined by SDS-PAGE. LPS absence was determined by the Pierce LAL chromogenic endotoxin quantitation Kit (Thermo Scientific) following the manufacturers' instructions.

Immunoblotting was performed in order to verify NCz-SEGN24A identity. Briefly, 10 μg of NCz-SEGN24A, Nt-Cz (MW 23 kDa) and SEGN24A (MW 27 kDa) were separated by 12.5% SDS-PAGE and transferred to polyvinylidene difluoride (PVDF) membrane. As primary antibodies, sera from mice immunized with the recombinant protein Nt-Cz or SEG superantigen were used (1/500 dilution). As secondary antibody, rabbit anti-mouse IgG conjugated with peroxidase (Jackson ImmunoResearch, 1/1000 dilution) was used; the reaction was revealed using 4-chloro-1-naphtol and H_2O_2.

Immunization Protocols

As a proof of concept, different immunization protocols were tested in this work. Inbred C3H/HeN mice from 6 to 8 weeks old (n = 5-6 animals per group) were used. In all cases, animals were immunized with 4 doses of each formulation separated by 15 days, intramuscularly in the quadriceps muscles.

To initially prove properties of NCz-SEGN24A as an immunogen, two experimental groups were designed: (i) 10 μg of recombinant protein NCz-SEGN24A and (ii) control with PBS (control group in each protocol).

Secondly, the chimeric protein was proved in parallel with its individual antigens, using the adjuvant CpG-ODN 1826 (Invivogen). In this case, three experimental groups were designed: (i) NCz-SEGN24A protein+CpG, (ii) Nt-Cz protein+SEGN24A+CpG, (iii) control. Each group received 10 μg of each component, with the exception of group (ii) that received 5 μg of each antigen.

In the last part of this work, NCz-SEGN24A was evaluated against the single *T. cruzi* specific antigen; in order to achieve this, three experimental groups were immunized: (i) NCz-SEGN24A protein+CpG, (ii) Nt-Cz protein+CpG, (iii) control. Each group received 10 μg of each component.

ELISA for Determination of Antigen-Specific IgG Antibodies

Sera from immunized mice were collected 15 days after the last dose for the determination of antigen-specific IgG, IgG1, IgG2a by indirect ELISA, as previously described (34). Plates were coated with Nt-Cz protein in all cases, and horseradish peroxidase-labeled anti-mouse IgG antibody (Jackson ImmunoResearch), or biotin-conjugated anti-mouse IgG1 or anti-mouse IgG2a (Pharmingen Becton Dickinson), were used as secondary antibodies.

Cell Infection Inhibition by Specific Immune Sera

The ability of sera from immunized mice to inhibit parasite infection was assessed. Vero cells (5×10^3 cells/well) were infected with blood trypomastigotes expressing β-galactosidase at a MOI of 10:1 for 24 h at 37°C. Trypomastigotes were pre-incubated in triplicate with diluted serum (1/10) from mice immunized with NCz-SEGN24A+CpG. After overnight incubation, cells were washed and treated for 4 days. CPRG was added to determine the levels of parasites as previously described (35). Uninfected cells were used as blanks, and additional controls were performed with sera from mice before immunization (pre-immune) and sera from non-immunized mice.

Delayed-Type Hypersensitivity Test (DTH)

A DTH assay was performed 15 days after the last immunization by intradermal challenge with 10 μg of Nt-Cz in the right footpad of the animals. Footpad thickness was measured before and 72 h after antigen inoculation using a Vernier caliper. Results are expressed as the increased millimeters in footpad thickness induced by inoculation.

Challenge With *T. cruzi* Bloodstream Trypomastigotes

Fifteen days after the last immunization, animals (n = 5-6 per group) were infected intraperitoneally with 10^4 *T. cruzi* blood trypomastigotes of the virulent RA strain, for analysis of the acute phase. Parasitemia was monitored by counting blood parasites every 2–3 days in a Neubauer chamber. For this purpose, a 1/5 dilution of blood in lysis buffer (0.75% NH_4Cl, 0.2% Tris, pH 7.2) was made.

Alternatively, vaccine efficacy was evaluated in a sub-lethal challenge. For this purpose, after the last immunization animals were challenged with 3×10^5 blood trypomastigotes of the less virulent K98 clone (from CA-I strain) by intraperitoneal injection. Parasitemias were recorded weekly during the acute phase (19, 35).

Statistical Analysis

Statistical analysis was carried out with GraphPad Prism 6.0 software (San Diego, CA, USA), using one-way or two-way ANOVA along with the post-tests indicated in each trial, unless otherwise specified in figure legends.

The statistical analyses were referred to the control group of each experiment, except when indicated. Values of $p < 0.05$ were considered significant.

RESULTS

Mutant SEGN24A Neither Binds Mouse TCR Variable β Chain nor Stimulates *in-vivo* Vβ8.1/8.2 Bearing T Cells

Taking into account the high resolution X-ray structure of SEGwt-mVβ8.2 (pdb 3MC0) as a template (29), selective mutation of Asn24, crucial residue for binding to the TCR in related SAgs (30), resulted in the generation of SEGN24A. Structural studies strongly suggested that higher affinity of SEG-mVβ8.2 complex is due to the presence of five hydrogen bonds established between SEGN24 and different residues of the TCR variable β chain. Due to the nature of the Ala side chain, hydrogen bonds cannot be established with the TCR residues since they are outside of the interaction sphere (distances higher than 3.4 Å) (**Figure 1A**). In order to evaluate the resultant ability of mutant SEGN24A to bind mVβ8.2 chain, surface plasmon resonance (SPR) assays were performed. Direct binding of soluble SEGwt or SEGN24A to mVβ8.2 was analyzed. SEGN24A failed to bind mVβ8.2 specifically. On the contrary, the interaction between SEGwt and mVβ8.2 showed a high affinity with a dissociation constant (K_D) of 3.7×10^{-7} M (**Figure 1B**), in accordance with our previous results (29).

We next analyzed whether SEGN24A would be able to induce stimulation of T cells bearing Vβ8.1/8.2 *in-vivo*. SEGwt and SEGN24A were subcutaneously injected into C3H mice footpad. After 48 h, mice were sacrificed, and their popliteal and inguinal lymph nodes removed and pooled for analysis of Vβ8.1/8.2 T cell populations. FACS analysis showed a significant increase in the frequency of Vβ8.1/8.2$^+$ T cells in lymph nodes stimulated with SEGwt, while SEGN24A was unable to stimulate Vβ8.1/8.2$^+$ T cells (**Figure 1C**).

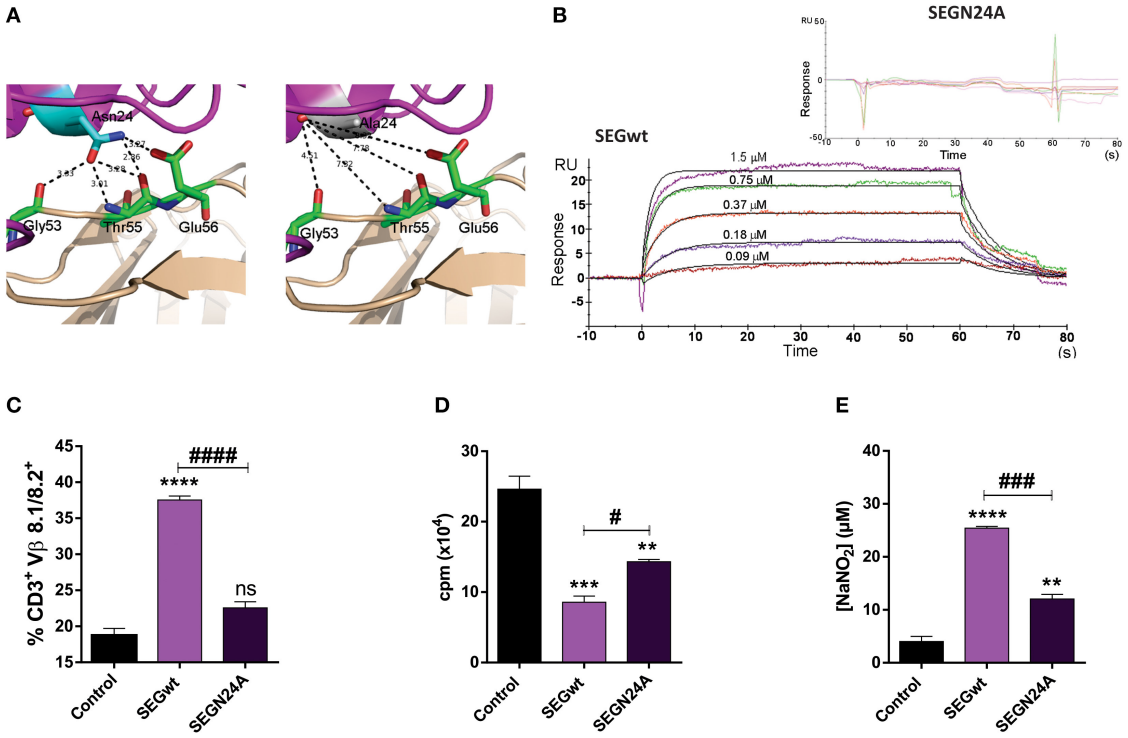

FIGURE 1 | Superantigen mutant SEGN24A shows no effect on T cells but retains ability to induce a proinflammatory profile in RAW 264.7 macrophages. **(A)** Comparison of the TCR mVβ8.2 and SEGwt (pdb 1XXG) or SEGN24A interfaces. mVβ8.2 and SEG are colored wheat and magenta, respectively. Residues of mVβ8.2 involved in the interaction with residue 24 of SEGwt or SEGN24A are colored green. SEG N24 (left side) or A24 (right side) are colored cyan or white, respectively. Hydrogen bonds established between Asn24 and mVβ8.2 are shown as black dashes. Since hydrogen bonds must be calculated with a cut-off distance of 2.5–3.4 Å, Ala24 is not able to establish hydrogen bonds with mVβ8.2. **(B)** SPR analysis of SEG-mVβ8.2 interaction. SPR sensorgrams show the interactions between SEGwt (800 RU immobilized, lower panel) with mVβ8.2 (1.50–0.09 μM), or SEGN24A (900 RU immobilized, upper panel) with mVβ8.2 (60–0.8 μM) after correction for nonspecific binding. Apparent K_D for binding of mVβ8.2 to immobilized SEGwt was 3.7×10^{-7} M by kinetic analysis using a 1:1 binding model. SEGN24A showed no specific binding to mVβ8.2. **(C)** C3H/HeN mice were inoculated subcutaneously with 30 μg of SEGwt, SEGN24A or PBS (control) into the mice footpad. After 48 h, cells were isolated from popliteal and inguinal lymph nodes and T cell stimulation was evaluated by flow cytometry with anti-CD3$^+$ and anti-Vβ8.1/8.2$^+$. **(D)** RAW 264.7 cells (2×10^4/well) were incubated with wild-type or mutant superantigens (10 μg/ml) for 48 h, 0.5 μCi [3H]-thymidine/well was added for the last 8 h. DNA was harvested and counts per minute were determined as a measure of cell proliferation. **(E)** Supernatants of RAW 264.7 cells (1×10^5/well) were collected after 48 h of stimulation with SAgs and the nitrites level was measured using the Griess reagent. Data are expressed as the mean ± SEM of three independent experiments. Asterisks represent statistical significance respect to control. $^{**}p < 0.01$, $^{***}p < 0.001$, $^{****}p < 0.0001$, ns, non-significant. Hashes represent statistical significance between stimulation with wild-type and mutant SAg, $^{\#}p < 0.05$, $^{\#\#\#}p < 0.001$, $^{\#\#\#\#}p < 0.0001$. One-way ANOVA plus Tukey's post-test **(C–E)**.

SEGN24A Retains, in a Lesser Extent, SEGwt Effects on Macrophages

To verify if SEGN24A retained the ability to induce a M1 profile on macrophages, a mouse macrophagic cell line RAW 264.7 was cultured in presence of SEGN24A or SEGwt. Although in a lesser extent, the mutated SAg was able to mimic the effect of SEGwt. Both wild type and mutant SAgs induced an inhibition of macrophagic proliferation in absence of T cells (**Figure 1D**). This phenomenon was previously related to apoptotic and necrotic death with an early activation and secretion of proinflammatory cytokines (26). The cell death process would be of interest considering that other adjuvants such as aluminum salts mediate their adjuvant-properties in part through the release of damage associated molecular pattern (DAMPs) after exerting cytotoxicity (36, 37). Moreover, SEGN24A induced a significant increment in nitrites production (**Figure 1E**), characteristic of classical macrophage activation.

These results confirm that while SEGN24A has no TCR binding function (**Figure 1B**), it keeps the ability to interact with macrophagic cells, an essential feature to exert an adjuvant effect.

Construction, Expression and Characterization of the Heterologous Chimeric Antigen NCz-SEGN24A

The heterologous chimera between a parasite antigen domain and a bacterial mutated superantigen, NCz-SEGN24A, was engineered fusing the Nt-Cz domain directly to the mutant SEGN24A. The construct also possesses a thioredoxin N-terminal tag, to facilitate folding and stability due to disulfide bonds formation, and a 6 his tag to allow purification (**Figure 2A**). NCz-SEGN24A was successfully expressed in *E. coli* BL21 (DE3) and purified by Ni^{2+}-NTA affinity chromatography. Refolding of recombinant NCz-SEGN24A was performed *in-vitro,* followed by molecular exclusion chromatography (**Figure 2B**). A single 69 kDa band was obtained by SDS-PAGE (**Figure 2C**). Final yield of NCz-SEGN24A protein was ∼5 mg per liter of culture.

The immunochemical identity of the construct was furthered determined by Western Blot. NCz-SEGN24A was recognized by polyclonal antibodies specific for both domains (**Figure 2D**).

Immunization With NCz-SEGN24A Elicits a Humoral and Cellular Specific Immune Response

With the aim to evaluate the immunogenicity of adjuvantless NCz-SEGN24A, C3H mice were immunized with four doses of the recombinant protein and 15 days after last boost, Nt-Cz-specific antibody titers in sera were determined by ELISA. We observed that mice immunized with NCz-SEGN24A elicited antibody titers considerably higher than control group ($p < 0.01$) (**Figure 3A**). To estimate the developed T cell profile, we analyzed the titers of the IgG1 and IgG2a isotypes specific against Nt-Cz. Antibodies isotypes reflected a Th1-biased response since IgG2a levels were higher than IgG1 ($p < 0.0001$) (**Figure 3B**).

A delayed-type hypersensitivity test was performed to evaluate the specific cellular immune response. Mice developed a tendency of swelling regarding a cellular response, 72 h after the injection of Nt-Cz in the footpad (0.13 ± 0.03 for NCz-SEGN24A vs. 0.07 ± 0.01 for control) (**Figure 3C**).

These results were encouraging since a parasite homologous chimeric immunogen, Traspain (18), was not able to promote specific humoral or cellular immune responses (Sanchez Alberti, unpublished results).

NCz-SEGN24A Immunization Displays a Tendency of Parasite Load Reduction After *T. cruzi* Challenge

To evaluate if immunization with NCz-SEGN24A was able to confer protection, 15 days after last dose mice were challenged with bloodstream trypomastigotes of the K98 clone, from *T. cruzi* CA-I strain. As it is shown in **Figure 3D**, immunization with NCz-SEGN24A resulted in a reduction of the number of circulating parasites. Furthermore, at the peak of parasitemia (35 dpi) there was a significant reduction of parasites compared against control (PBS) ($p<0.05$). We also calculated the area under the parasitemia concentration-time curve (AUC) to assess the ability of the vaccination to reduce the total parasite load. In this case, we observed a reduction of the total parasite load conferred by immunization with NCz-SEGN24A, although there was not a significant difference compared to control (AUC: 112.5 ± 36.9 vs. 132.8 ± 41.0, respectively) (**Figure 3E**).

Co-administration of NCz-SEGN24A With CpG-ODN Evokes Specific Humoral Responses and Develops Neutralizing Antibodies

Taking into account the well-known capacity of CpG-ODN to stimulate Th1-responses (38, 39), we combined them with the chimeric NCz-SEGN24A. Considering that the protective effect could be due to the administration of one molecule that would function as an immune modulator and another that would serve as the specific immunogenic antigen (40, 41), we also developed an immunization protocol that included the individual proteins Nt-Cz and SEGN24A co-administered with CpG-ODN. Immunization groups through the intramuscular route included: Nt-Cz+SEGN24A+CpG, or the chimeric NCz-SEGN24A+CpG, all the antigens in equal molar mass. Analysis of the specific antibody response obtained after the last dose showed that both groups developed high and significant IgG anti-Nt-Cz specific titers ($p < 0.01$ and $p < 0.05$, respectively), which did not differ from each other (**Figure 4A**). Interestingly, immunization with both, the individual antigens and the chimeric antigen plus CpG-ODN elicited significant IgG2a specific antibodies, reflecting a Th1-biased response (**Figure 4B**). We observed an unbalanced ratio IgG2a/IgG1 for the immunization with the separated proteins, suggesting a more balanced immunity when NCz-SEGN24A plus CpG-ODN is used as immunogen (**Figure 4C**). As expected, antibodies specific

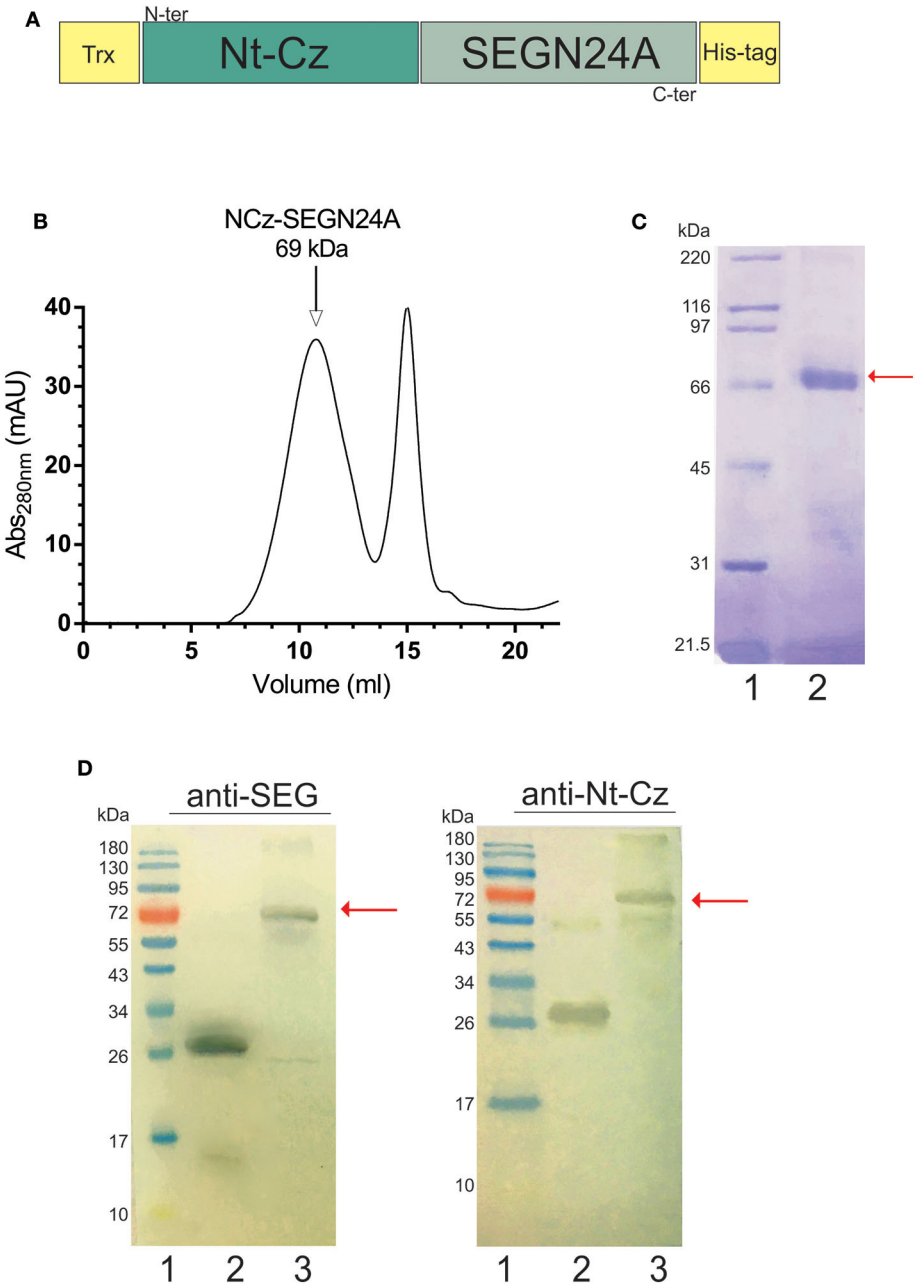

FIGURE 2 | Construction and characterization of heterologous chimeric antigen NCz-SEGN24A. **(A)** Schematic representation of NCz-SEGN24A. Bacterial SAg mutant SEGN24A was fused to the C-terminal of the N-terminal domain of parasite cruzipain (Nt-Cz). A thioredoxin (Trx) tag was added to fused NCz-SEGN24A in its N-terminal, and histidine tag (His-tag) was added at the C-terminal. **(B)** Chromatogram of the NCz-SEGN24A purification with Superdex 200 molecular exclusion (SEC). **(C)** Analysis of recombinant NCz-SEGN24A by SDS-PAGE. The 69-kDa protein was detected using Coomassie blue staining after purification by Ni^{2+}-NTA column followed by SEC (Lane 2). Arrow indicates NCz-SEGN24A band. **(D)** Immunochemical identity by Western blot. Domain-specific polyclonal antibodies were used as primary antibodies. SDS-PAGE gels were loaded as follows, lines: 1- MWM, 2- SEGN24A (left, 27 kDa) or Nt-Cz (right, 23 kDa), 3- NCz-SEGN24A (69 kDa), arrows point at NCz-SEGN24A band.

titers resulted about 10-fold higher when immunization was performed with CpG-ODN compared to adjuvantless injection (**Figure 3A**).

More importantly, Nt-Cz-specific antibodies proved to be functional and neutralizing, since incubation of trypomastigotes of Tulahuen strain with serum of NCz-SEGN24A-vaccinated mice significantly decreased *in-vitro* invasion of non-phagocytic Vero cells (**Figure 4D**).

Moreover, when analyzing cellular *in-vivo* responses, a significant increase in DTH assay was

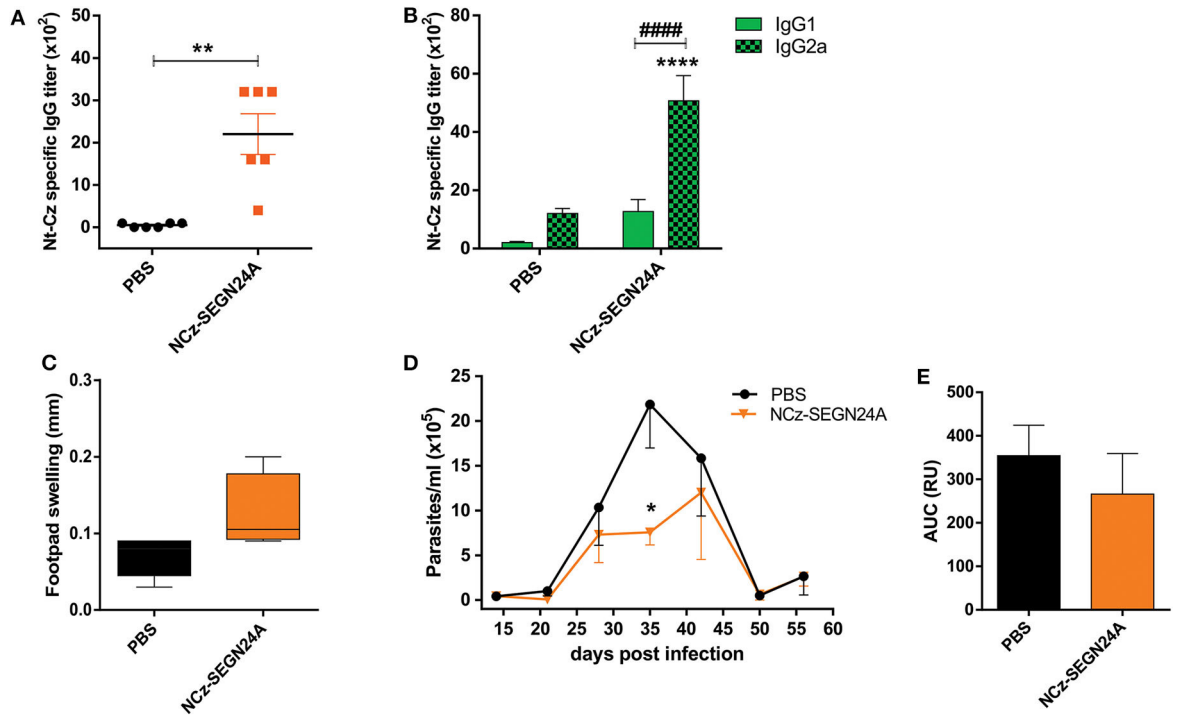

FIGURE 3 | NCz-SEGN24A develops a strong and Th1-directed humoral response and decreases parasite loads after *T. cruzi* challenge. **(A)** Nt-Cz-specific IgG antibodies response. Titers were determined by ELISA in sera samples from C3H/HeN mice vaccinated with either NCz-SEGN24A, by the intramuscular route, or saline (PBS) at 15 days post vaccination. **(B)** Nt-Cz specific IgG1 and IgG2a titers, determined by indirect ELISA using an isotype-specific secondary antibody. **(C)** Delayed-type hypersensitivity (DTH) test. Footpad thickness in vaccinated mice was measured before and 72 h after inoculation of 10 μg of Nt-Cz. Results are expressed as the difference in footpad thickness before and after inoculation. **(D)** Protection against a *T. cruzi* challenge. Fifteen days after the last immunization, mice were challenged with 3×10^5 K98 clone bloodstream trypomastigotes. Parasitemia after infection was monitored weekly during its acute phase. **(E)** Area under the parasitemia curve (AUC). Data are expressed as the mean ± SEM of two independent experiments. Asterisks represent statistical significance respect to saline group: $^*p < 0.05$; $^{**}p < 0.01$; $^{****}p < 0.0001$. Hashes represent statistical significance between IgG1 and IgG2 isotypes: $^{\#\#\#\#}p < 0.0001$. Mann-Whitney test **(A)**, two-way ANOVA plus Sidak's post-test **(B)**, Student's *t*-test **(C,E)**.

observed for both immunization with individual proteins or NCz-SEGN24A ($p < 0.01$ and $p < 0.001$, respectively) (**Figure 4E**).

NCz-SEGN24A Plus CpG-ODN but Not Its Individual Antigens Confer Protection Against *T. cruzi* Challenge

To determine whether chimeric NCz-SEGN24A adjuvanted with CpG-ODN possessed superior protective capacity against *T. cruzi* infection compared to its individual domains, 2 weeks after immunization mice were challenged with blood trypomastigotes from the virulent RA strain, belonging to the discrete type unit (DTU) TcVI. Throughout the acute phase of the parasitemia, NCz-SEGN24A+CpG showed the ability to reduce the level of circulating parasites (**Figure 5A**). We observed that on the early acute phase (9 dpi) NCz-SEGN24A+CpG group achieved the highest control of parasitemia. Moreover, when the area under the parasite-load curves were analyzed (**Figure 5B**), NCz-SEGN24A+CpG showed a significant reduction on the total parasite load compared with the control group, whereas the individual antigens Nt-Cz plus SEGN24A+CpG conferred less protection.

More importantly, mice vaccinated with chimeric NCz-SEGN24A+CpG showed an increase in the survival rate compared to PBS group. Specifically, this group was the only one to maintain 100% survival rates, showing clear differences against the group of mice immunized with the individual antigens (60% survival for both Nt-Cz+SEGN24A+CpG and control) (**Figure 5C**).

These results taken together manifest a clear advantage of administration of the chimeric NCz-SEGN24A plus CpG-ODN rather than immunizing with its individual domains, in terms of protection and survival against infection with *T. cruzi*.

Chimeric NCz-SEGN24A Improves Protection Elicited by Nt-Cz Antigen

As it was previously reported, immunization of mice with Nt-Cz plus CpG-ODN enhances protection conferred by vaccination with the full-length cruzipain or its C-terminal domain (17). To evaluate if vaccination with chimeric NCz-SEGN24A antigen would improve protection over the single *T. cruzi* antigen, we performed an immunization protocol where a group of

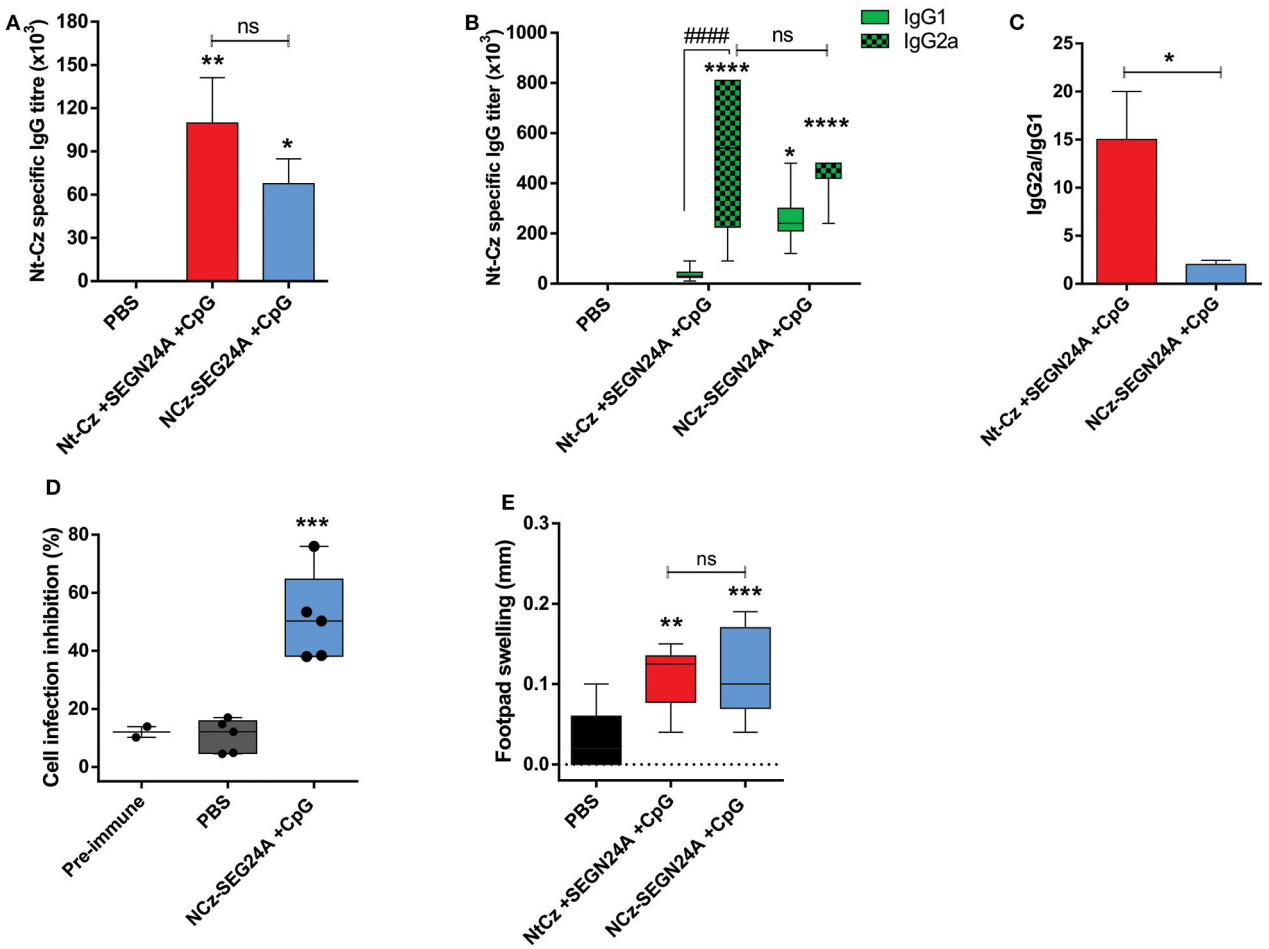

FIGURE 4 | Co-administration of NCz-SEGN24A with CpG-ODN evokes specific humoral responses and develops neutralizing antibodies. Mice were either immunized with chimeric protein NCz-SEGN24A+CpG or with individual antigens Nt-Cz+SEGN24A+CpG intramuscularly, or saline. **(A)** Nt-Cz specific IgG antibodies determined by ELISA in sera samples, 15 days after last immunization. **(B)** Nt-Cz specific IgG1 and IgG2a isotypes titers, determined by ELISA. **(C)** IgG2a/IgG1 ratio **(D)** Neutralization of *T. cruzi* non-phagocytic cell infection by sera from immunized mice. **(E)** DTH test, results are expressed as the difference in footpad thickness before and after 72 h inoculation with Nt-Cz antigen. Data are expressed as the mean ± SEM of three independent experiments. Asterisks represent statistical significance respect to saline group, except indicated otherwise: $^{*}p < 0.05$, $^{**}p < 0.01$, $^{***}p < 0.001$, $^{****}p < 0.0001$, ns, non-significant difference. Hashes represent statistical significance between IgG1 and IgG2 isotypes: $^{\#\#\#\#}p < 0.000$. Kruskal–Wallis plus Dunn's post-test **(A)**, two-way ANOVA plus Sidak's post-test **(B)**, one-way ANOVA plus Tukey's post-test **(C,D)**.

mice received Nt-Cz+CpG, and other group received NCz-SEGN24A+CpG (10 μg of each in both schemes).

After the last dose, animals were challenged with blood trypomastigotes of K98 clone, which belongs to a different DTU, TcI. On the acute phase of the infection, mice of both groups presented much lower amounts of circulating parasites (**Figure 6A**); at the peak of parasitemia (35 dpi), there were significant differences on the number of parasites for both groups against control ($p < 0.05$). However, when analyzing the areas under the total parasitemia curve, only mice immunized with NCz-SEGN24A+CpG presented significant reductions against control group in the total parasite loads ($p < 0.05$), with a 3-fold reduction of AUC (**Figure 6B**). Even though there was not a significant difference between AUC of Nt-Cz and NCz-SEGN24A groups, these results suggest an improvement in protection of the chimeric antigen vaccination over immunization with the single Nt-Cz antigen, which would be due to the inclusion of the superantigen domain in the chimera design.

DISCUSSION

Vaccination has proven to be the most successful strategy to stimulate systemic immune responses protecting against infection (42, 43). However, up to date, there are still many diseases for which there are no effective vaccines available. Among them, parasitic infections and particularly Chagas disease does not count yet with a vaccine generating sterilizing immunity (44).

In this work, with the aim to elicit a protective differential immune response against *T. cruzi*, we described a novel

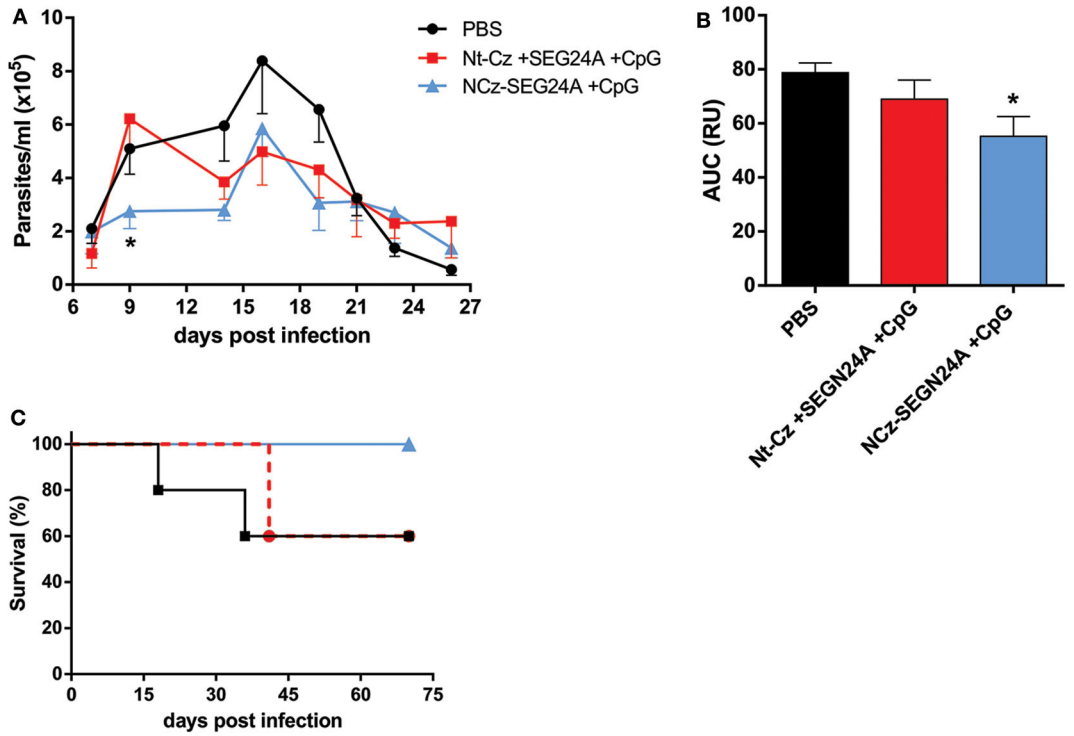

FIGURE 5 | NCz-SEGN24A+CpG, but not its individual antigens, confers protection against *T. cruzi* infection. Immunized mice with NCz-SEGN24A+CpG, individual antigens Nt-Cz+SEGN24A+CpG or saline ($n = 5$/group) were challenged intraperitoneally 15 days after the last dose with 1×10^4 trypomastigotes from the RA strain. **(A)** Parasitemia levels were monitored during the acute phase of the infection in 5 μl of blood taken every 2 days. **(B)** AUC of the parasitemia curve. **(C)** Survival rates were monitored daily over an extended period of the acute phase. Data are expressed as the mean ± SEM of three independent experiments. Asterisks represent statistical significance respect to saline group. *$p < 0.05$. One-way ANOVA plus Tukey's post-test **(B)**.

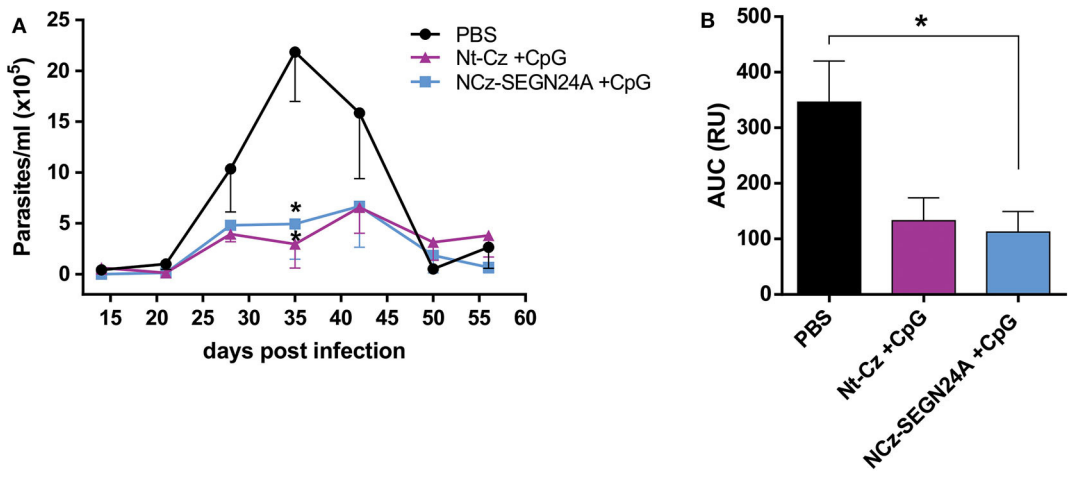

FIGURE 6 | NCz-SEGN24A improves protection conferred by the single Nt-Cz antigen. Mice were either immunized with chimeric NCz-SEGN24A+CpG or with *T. cruzi* antigen Nt-Cz+CpG intramuscularly. Fifteen days after the last dose, mice were challenged with 3×10^5 bloodstream trypomastigotes of K98 clone. **(A)** Parasitemia after infection was monitored weekly during its acute phase. **(B)** AUC of the parasitemia curve. Data are expressed as the mean ± SEM of two independent experiments. Asterisk represents statistical significance respect to saline group; *$p < 0.05$, and ns: non-significant difference. One-way ANOVA plus Tukey's post-test **(B)**.

immunogen for vaccination purposes. We used a chimeric molecule that included a detoxified bacterial superantigen, which lacks its ability to bind to the TCR but retains the interaction with APCs, and an immunogenic domain of the *T. cruzi* antigen Cz. Thus, by mutation of one residue of major energetic contribution to TCR binding site (29), we obtained SEGN24A which showed

non-significant increase in the frequency of mVβ8.2-bearing T cells *in-vivo*. In addition, by performing SPR assays, we observed a complete lack of interaction between SEGN24A and mVβ8.2. These results are in line with other authors' publications, where removal of the ability of different SAgs to bind the TCR alone is enough to ablate the recruitment of T cells bearing particular Vβ TCRs, and thus, cell proliferative activities responsible for SAgs toxicity (45, 46).

Although SEGN24A lost its ability to stimulate T cells, as it was expected, it retained its capability to interact with macrophages similarly as SEGwt did. In accordance with this, SEGN24A would be able to promote a proinflammatory profile, which could determine a Th1 environment without the elimination of the T cell effective pool. With the aim to determine if SEGN24A induced a M1 profile when interacting with macrophagic cells, we performed assays using the murine cell line RAW 264.7. We observed that, both wild-type and mutant SEG reduced the proliferation rate of a macrophagic cell line and significantly stimulated nitrites secretion on the supernatant of these cells, characteristic of classical macrophagic activation. These results agree with previous publications (26), where different non-classical SAgs, including SEG, inhibited proliferation of human THP-1 cell line differentiated to macrophages, associated with cell death. As it was stated before, cell death could result in DAMPs release, favoring immune response stimulation, as it was previously described for other adjuvants (36, 37). Noli Truant et. al. (26) also reported that SAgs promoted on macrophages a proinflammatory cytokines response of M1 profile that also included nitrites production. Our results suggest that the mutant SEGN24A maintains the MHC-II binding capacity, activating biological responses on macrophages, though in a lesser extent compared to SEGwt. In a previous work, we demonstrated that SEG does not interfere with the viability of murine DCs (27) and the present results allow us to hypothesize that SEGwt and SEGN24A display similar behavior with mouse DCs, which needs to be further confirmed.

In the design of the heterologous chimeric construct were included the bacterial mutant SAg SEGN24A and the N-terminal domain of cruzipain (Cz), the major cysteine protease of *T. cruzi*. Our choice was based on previous publications of our group, where we demonstrated that Nt-Cz is the catalytic and protective domain of the enzyme. During natural infection with the parasite, C-terminal domain of Cz is immunodominant, eliciting high titers of specific antibodies. When immunizations are performed with the full-length Cz, immune responses are mostly directed against the C-terminal domain, which is poorly protective. In contrast, immunization with Nt-Cz redirects the immune response to the protective domain, avoiding distraction of the immune system, thereby enhancing protection (17). Other chimeric molecules have already been designed including the Nt-Cz domain, showing very promising results in terms of protection conferred against *T. cruzi* infection (18, 19).

As a proof of concept, the heterologous chimeric antigen NCz-SEGN24A was tested with different immunization protocols. First, we analyzed whether NCz-SEGN24A has intrinsic immunogenic properties. By immunizing mice with NCz-SEGN24A without the addition of adjuvants, systemic-antibody titers were obtained against the parasite antigen. However, for a parasite homologous chimeric immunogen that also included Nt-Cz, Traspain, no specific antibodies responses were evoked without the addition of adjuvants (Sanchez Alberti, unpublished results). Moreover, the profile of elicited antibodies in NCz-SEGN24A immunized mice indicated higher IgG2a than IgG1 specific profiles, indicating that the immune response was predominantly oriented by the Th1 subset, which is desirable in the design of vaccines against intracellular pathogens. Modest cellular responses were also elicited. These results suggest that NCz-SEGN24A could have self-adjuvanting properties which could be mediated by direct targeting to MHC-II on APCs, conferred by the superantigenic domain. Previous reports are in line with these findings, since conjugation of antigens to modified-superantigens promotes targeting to APCs by MHC-II binding and this improves antigen-specific immune responses (23, 46, 47). Nevertheless, further studies should be performed with NCz-SEGN24A, in order to prove this hypothesis.

The humoral and cellular responses triggered by NCz-SEGN24A immunization were translated into a tendency of reduction on parasite loads throughout the acute phase of the infection, after challenging mice with *T. cruzi* trypomastigotes. NCz-SEGN24A-immunized mice showed significant differences at the peak of parasitemia (35 dpi) compared to control, although the area under the total parasitemia curve (AUC) did not evidence statistical differences. Data points out that humoral responses toward the parasitic antigen are primed by immunization with NCz-SEGN24A alone. Nonetheless, since stronger cellular inductions are needed to control *T. cruzi* infection, the addition of adjuvants improves these responses.

Unmethylated synthetic CpG-ODNs have been widely used as adjuvants to improve humoral and cellular responses toward vaccine antigens, evidenced by several preclinical and clinical trials (48–50). In the current study, the inclusion of CpG-ODN potentiated humoral responses by inducing a ten-fold increase in IgG anti-Nt-Cz specific titers in mice immunized with NCz-SEGN24A; similar responses were obtained in mice immunized with both Nt-Cz and SEGN24A proteins. In addition, these immunizations displayed an IgG2a predominating isotype, accordingly with a Th1-oriented profile, and cellular responses were augmented when compared to adjuvantless NCz-SEGN24A immunization. Similar patterns of responses have been consistently reported by utilizing CpG-ODN for other antigens, including *T. cruzi* (13, 17, 35, 51–53). More importantly, sera samples from NCz-SEGN24A immunized mice were able to dramatically reduce the infection of Vero cells, compared with samples from PBS-vaccinated animals. These findings are in correspondence with former data showing highly significant inhibition of cell-invasion by sera from Nt-Cz+CpG immunized mice, whereas immunization with the C-terminal domain of Cz did not elicit a detectable inhibition (17). Thus, it could be inferred that subdominant B-cell epitopes capable of developing a high neutralizing activity are indeed retained in the chimeric NCz-SEGN24A protein. The promising results obtained using NCz-SEGN24A+CpG

prompted us to analyze the cellular immune response induced by this chimeric immunogen. Preliminary results, obtained with four immunizations of NCz-SEGN24A+CpG, showed production of intracellular cytokines by $CD4^+$ T cells. We observed differential intracellular levels of IFN-γ, TNF-α and IL-2 when compared with the control group immunized with PBS (unpublished results). Even though no specific $CD8^+$ T cells activity was measured in this manuscript, a rich microenvironment in IL-2 would facilitate $CD8^+$ T cell proliferation which would be essential to eradicate the infected cells. Since the dysfunction of the $CD8^+$ T cell is a key to the persistence of *T. cruzi* in the murine model (54), functional $CD8^+$ T cells (55, 56) could contribute to control the parasitemia in the chronic phase of the disease. Preliminary results carried out during the chronic phase of the disease suggest that mice immunized with four doses of NCz-SEGN24A+CpG displayed an undetectable parasitemia, determined by quantitative real time PCR (unpublished data).

After *T. cruzi* challenge, both immunization groups reduced the parasite loads throughout the acute phase of the infection. Nonetheless, mice vaccinated with the chimeric antigen conferred significant differences against control when comparing the areas under the total parasitemia curve. NCz-SEGN24A-immunized mice were also able to control parasitemia in the early days of the infection (9 dpi), which would be of particular relevance given the silent entry of the parasite and the consequent delayed generation of proper immune responses that allow the establishment of the infection (2, 57). Additionally, the NCz-SEGN24A-immunized group maintained 100% survival until 75 dpi, showing a better performance in protection than Nt-Cz plus SEGN24A group. We hypothesize that one of the reasons could be related to NCz-SEGN24A differential intracellular pathway inside APCs, as it was previously shown for SEGwt (27), which would allow longer times of exposure of the parasitic antigen to T cells. Importantly, when immunizations were performed with the individual antigens, the molar doses of Nt-Cz and SEGN24A were higher than those in chimeric NCz-SEGN24A (10 μg of total protein were administered in each protocol), meaning that vaccination with NCz-SEGN24A+CpG was more efficient at controlling parasitemia with lower amount of molecules of the specific parasite antigen.

When we compared NCz-SEGN24A+CpG immunization vs. Nt-Cz+CpG, by performing a challenge with trypomastigotes from a different strain and DTU than the one we had used in the former experiment, NCz-SEGN24A was the only group to show statistical differences in AUC against control. The chimeric antigen showed a clear protection in the assay performed, meaning that the inclusion of the SAg domain could indeed result advantageous. Furthermore, NCz-SEGN24A was able to show a significant protection with lower molar doses of the Nt-Cz antigen, considering that in fact in the Nt-Cz+CpG group the molar dose was even double than in Nt-Cz+SEGN24A+CpG group.

As a general conclusion, we were able to develop a novel heterologous immunogen including a bacterial superantigen which proved to be protective during the acute phase of the infection against *T. cruzi*. Protection was even extended toward *T. cruzi* strains belonging to different DTUs, although further analysis should be performed to better characterize immune response evoked by NCz-SEGN24A antigen as well as extension of protection during the chronic phase. Our results highlight the importance of developing chimeric molecules and multicomponent vaccines against *T. cruzi* infection, with the aim of reducing parasitemia from the first stages of the infection, and we strongly believe that inclusion of modified bacterial superantigens are very promising in this field.

DATA AVAILABILITY STATEMENT

The raw data supporting the conclusions of this article will be made available by the authors, without undue reservation.

ETHICS STATEMENT

The animal experiments (antisera production) were performed in accordance with the School of Medicine, Animal Ethics Committee (University of Buenos Aires) CD resolution #: 3381-18 Authorities for Animal Health of IMPaM, School of Medicine.

AUTHOR CONTRIBUTIONS

MA, AS, AB, EM, and MMF conceived and designed experiments. MA, AS, DR, AB, MJF, LI, SN, and MS performed the experiments. MA, AS, EM, and MMF analyzed the data. MA, EM, and MMF wrote the paper. All authors contributed to the article and approved the submitted version.

FUNDING

This work was supported by the Grants from the Universidad de Buenos Aires (2018-2021 # 20020170100323BA) and Fundación Bunge & Born (2015-2017) destined to support neglected diseases studies.

ACKNOWLEDGMENTS

We thank Carla Pascuale (Flow Cytometry unit, INBIRS, UBA-CONICET, Facultad de Medicina, UBA) and Sabrina Soldavini, Valeria Cardozo and Marianela Lewicki (Animal facilities and care IMPaM, Facultad de Medicina, UBA) for all the technical assistance.

SUPPLEMENTARY MATERIAL

The Supplementary Material for this article can be found online at: https://www.frontiersin.org/articles/10.3389/fimmu.2020.01279/full#supplementary-material

REFERENCES

1. Ribeiro AL, Nunes MP, Teixeira MM, Rocha MOC. Diagnosis and management of Chagas disease and cardiomyopathy. *Nat Rev Cardiol.* (2012) 9:576–89. doi: 10.1038/nrcardio.2012.109
2. Nardy AF, Freire-de-lima CG, Morrot A. Immune evasion strategies of *Trypanosoma cruzi*. *J Immunol. Res.* (2015) 2015:178947. doi: 10.1155/2015/178947
3. Sales PA, Molina I, Murta SMF, Sánchez-Montalvá A, Salvador F, Corrêa-Oliveira R, et al. (2017). Experimental and clinical treatment of Chagas disease: a review. *Am J Trop Med Hyg.* 97, 1289–303. doi: 10.4269/ajtmh.16-0761
4. Bilate AM, Cunha-Neto E. Chagas disease cardiomyopathy: current concepts of an old disease. *Rev Inst Med Trop Sao Paulo*. (2008) 50:67–74. doi: 10.1590/S0036-46652008000200001
5. Gascon J, Bern C, Pinazo MJ. Chagas disease in Spain, the United States and other non-endemic countries. *Acta Trop*. (2010) 115:22–7. doi: 10.1016/j.actatropica.2009.07.019
6. Hotez P. A handful of "antipoverty" vaccines exist for neglected diseases, but the world's poorest billion people need more. *Health Aff*. (2011) 30:1080–7. doi: 10.1377/hlthaff.2011.0317
7. Cazorla SI, Frank FM, Malchiodi EL. Vaccination approaches against *Trypanosoma cruzi* infection. *Expert Rev Vaccines*. (2009) 8:921–35. doi: 10.1586/erv.09.45
8. Bivona AE, Sanchez Alberti A, Cerny N, Trinitario S, Malchiodi EL. Chagas disease vaccine discovery. The search for a different immune reaction to protect against *Trypanosoma cruzi* infection. *Biochem Biophys Acta-Mol Basis Dis.* (2020) 1866:165658. doi: 10.1016/j.bbadis.2019.165658
9. Laderach D, Cerban F, Motran C, De Cima EV, Gea S. *Trypanosoma cruzi:* The major cysteinyl proteinase (cruzipain) is a relevant immunogen of parasite acidic antigens (FIII). *Int J Parasitol*. (1996) 26:1249–54. doi: 10.1016/S0020-7519(96)00099-9
10. Zúñiga E, Montes C, Barbieri G, Gruppi A. Antibodies against *Trypanosoma cruzi* alkaline antigens are elicited in sera from acute but not chronic human chagasic patients. *Clin Immunol.* (1999) 93:81–9. doi: 10.1006/clim.1999.4744
11. Schnapp AR, Eickhoff CS, Scharfstein J, Hoft DF. Induction of B- and T-cell responses to cruzipain in the murine model of *Trypanosoma cruzi* infection. *Microbes Infect*. (2002) 4:805–13. doi: 10.1016/S1286-4579(02)01600-3
12. Schnapp AR, Eickhoff CS, Sizemore D, Curtiss R, Hoft DF. Cruzipain induces both mucosal and systemic protection against *Trypanosoma cruzi* in mice. *Infect Immun*. (2002) 70:5065–74. doi: 10.1128/IAI.70.9.5065-5074.2002
13. Frank FM, Petray PB, Cazorla SI, Muñoz MC, Corral RS, Malchiodi EL. Use of a purified *Trypanosoma cruzi* antigen and CpG oligodeoxynucleotides for immunoprotection against a lethal challenge with trypomastigotes. *Vaccine*. (2003) 22:77–86. doi: 10.1016/S0264-410X(03)00541-3
14. Guiñazú N, Pellegrini A, Carrera-Silva EA, Aoki MP, Cabanillas AM, Gìronés N, et al. Immunisation with a major *Trypanosoma cruzi* antigen promotes pro-inflammatory cytokines, nitric oxide production and increases TLR2 expression. *Int J Parasitol*. (2007) 37:1243–54. doi: 10.1016/j.ijpara.2007.03.010
15. Cazorla SI, Becker PD, Frank FM, Ebensen T, Sartori MJ, Corral RS, et al. Oral vaccination with salmonella enterica as a cruzipain-DNA delivery system confers protective immunity against *Trypanosoma cruzi*. *Infect Immun*. (2008) 76:324–33. doi: 10.1128/IAI.01163-07
16. Cazorla SI, Frank FM, Becker PD, Corral RS, Guzmán CA, Malchiodi EL. Prime-boost immunization with cruzipain co-administered with MALP-2 triggers a protective immune response able to decrease parasite burden and tissue injury in an experimental *Trypanosoma cruzi* infection model. *Vaccine*. (2008) 26:1999–2009. doi: 10.1016/j.vaccine.2008.02.011
17. Cazorla SI, Frank FM, Becker PD, Arnaiz M, Mirkin GA, Corral RS, et al. Redirection of the immune response to the functional catalytic domain of the cystein proteinase cruzipain improves protective immunity against *Trypanosoma cruzi* infection. *J Infect Dis*. (2010) 202:136–44. doi: 10.1086/652872
18. Sanchez Alberti A, Bivona AE, Cerny N, Schulze K, Weißmann S, Ebensen T, et al. Engineered trivalent immunogen adjuvanted with a STING agonist confers protection against *Trypanosoma cruzi* infection. *NPJ Vaccines*. (2017) 2:9. doi: 10.1038/s41541-017-0010-z
19. Sanchez Alberti A, Bivona AE, Matos MN, Cerny N, Schulze K, Weißmann S, et al. Mucosal heterologous prime/boost vaccination induces polyfunctional systemic immunity, improving protection against *Trypanosoma cruzi*. *Front Immunol*. (2020) 11:128. doi: 10.3389/fimmu.2020.00128
20. Ma W, Yu H, Wang Q, Jin H, Solheim J, Labhasetwar V. A novel approach for cancer immunotherapy: tumor cells with anchored superantigen SEA generate effective antitumor immunity. *J Clin Immunol*. (2004) 24:294–301. doi: 10.1023/B:JOCI.0000025451.41948.94
21. Liu X, Zeng L, Zhao Z, Xie Y, Wang S, Zhang J, et al. Construction, expression, and characterization of rSEA-EGF and *in vitro* evaluation of its antitumor activity against nasopharyngeal cancer. *Technol Cancer Res Treat*. (2018) 17:1533033818762910. doi: 10.1177/1533033818762910
22. Golob-Urbanc A, Rajčević U, Strmšek Ž, Jerala R. Design of split superantigen fusion proteins for cancer immunotherapy. *J Biol Chem*. (2019) 294:6294–305. doi: 10.1074/jbc.RA118.006742
23. Dickgreber N, Stoitzner P, Bai Y, Price KM, Farrand KJ, Manning K, et al. Targeting antigen to MHC class II molecules promotes efficient cross-presentation and enhances immunotherapy. *J Immunol.* (2009) 182:1260–9. doi: 10.4049/jimmunol.182.3.1260
24. Jarraud S, Cozon G, Vandenesch F, Bes M, Etienne J, Lina G. Involvement of enterotoxins G and I in staphylococcal toxic shock syndrome and staphylococcal scarlet fever. *J Clin Microbiol*. (1999) 37:2446–9. doi: 10.1128/JCM.37.8.2446-2449.1999
25. Jarraud S, Peyrat MA, Lim A, Tristan A, Bes M, Mougel C, et al. egc, A highly prevalent operon of enterotoxin gene, forms a putative nursery of superantigens in *Staphylococcus aureus. J Immunol.* (2001) 166:669–77. doi: 10.4049/jimmunol.166.1.669
26. Noli Truant S, De Marzi MC, Sarratea MB, Antonoglou MB, Meo AP, Iannantuono López LV, et al. egc superantigens impair monocytes/macrophages inducing cell death and inefficient activation. *Front Immunol.* (2020) 10:3008 doi: 10.3389/fimmu.2019.03008
27. Ganem MB, De Marzi MC, Fernández-Lynch MJ, Jancic C, Vermeulen M, Geffner J, et al. Uptake and intracellular trafficking of superantigens in dendritic cells. *PLoS ONE*. (2013) 8:e66244. doi: 10.1371/journal.pone.0066244
28. Fernández MM, De Marzi MC, Berguer P, Burzyn D, Langley RJ, Piazzon I, et al. Binding of natural variants of staphylococcal superantigens SEG and SEI to TCR and MHC class II molecule. *Mol Immunol*. (2006) 43:927–38. doi: 10.1016/j.molimm.2005.06.029
29. Fernández MM, Cho S, De Marzi MC, Kerzic MC, Robinson H, Mariuzza RA, et al. Crystal structure of staphylococcal enterotoxin G (SEG) in complex with a mouse T-cell receptor β chain. *J Biol Chem*. (2011) 286:1189–95. doi: 10.1074/jbc.M110.142471
30. Leder L, Llera A, Lavoie PM, Lebedeva MI, Li H, Sekaly RP, et al. A mutational analysis of the binding of staphy- lococcal enterotoxins B and C3 to the T-cell receptor β chain and major histocompatibility complex class II. *J Exp Med*. (1998) 187:823–33. doi: 10.1084/jem.187.6.823
31. Fernández MM, Bhattacharya S, De Marzi MC, Brown P, Kerzick M, Schuck P, et al. Superantigen natural affinity maturation revealed by the crystal structure of staphylococcal enterotoxin G and its binding to T-cell receptor Vβ8.2. *Proteins*. (2007) 68:389–402. doi: 10.1002/prot.21388
32. Warrens AN, Jones MD, Lechler RI. Splicing by over-lap extension by PCR using asymmetric amplification: an improved technique for the generation of hybrid proteins of immunological interest. *Gene*. (1997) 186:29–35. doi: 10.1016/S0378-1119(96)00674-9
33. Wurch T, Lestienne F, Pauwels PJ. A modified overlap extension PCR method to create chimeric genes in the absence of restriction enzymes. *Biotechnol Tech*. (1998) 12:653–7. doi: 10.1023/A:1008848517221
34. Matos MN, Cazorla SI, Bivona AE, Morales C, Guzmán CA, Malchiodi L. Tc52 amino-terminal-domain DNA carried by attenuated salmonella enterica serovar typhimurium induces protection against a *Trypanosoma cruzi* lethal challenge. *Infect Immun*. (2014) 82:4265–75. doi: 10.1128/IAI.02190-14
35. Bivona AE, Sánchez Alberti A, Matos MN, Cerny N, Cardoso AC, Morales C, et al. *Trypanosoma cruzi* 80 kDa prolyl oligopeptidase (Tc80) as a novel immunogen for chagas disease vaccine. *PLoS Negl Trop Dis*. (2018) 12:e0006384. doi: 10.1371/journal.pntd.0006384
36. Miyaji EN, Carvalho E, Oliveira MLS, Raw I, Ho PL. Trends in adjuvant development for vaccines: DAMPs and PAMPs as

potential new adjuvants. *Braz J Med Biol Res.* (2011) 44:500–13. doi: 10.1590/S0100-879X2011000600003
37. Svensson A, Sandberg T, Siesjö P, Eriksson H. Sequestering of damage-associated molecular patterns (DAMPs): a possible mechanism affecting the immune-stimulating properties of aluminium adjuvants. *Immunol Res*. (2017) 65:1164–75. doi: 10.1007/s12026-017-8972-5
38. Bode C, Zhao G, Steinhagen F, Kinjo T, Klinman DM. CpG DNA as a vaccine adjuvant. *Expert Rev Vaccines*. (2011) 10:499–511. doi: 10.1586/erv.10.174
39. Scheiermann J, Klinman DM. Clinical evaluation of CpG oligonucleotides as adjuvants for vaccines targeting infectious diseases and cancer. *Vaccine*. (2014) 32:6377–89. doi: 10.1016/j.vaccine.2014.06.065
40. Ibañez AE, Coria LM, Carabajal MV, Delpino MV, Risso GS, Cobiello PG, et al. A bacterial protease inhibitor protects antigens delivered in oral vaccines from digestion while triggering specific mucosal immune responses. *J Control Release*. (2015) 220:18–28. doi: 10.1016/j.jconrel.2015.10.011
41. Coria LM, Ibañez AE, Tkach M, Sabbione F, Bruno L, Carabajal MV, et al. A brucella spp. protease inhibitor limits antigen lysosomal proteolysis, increases cross-presentation, and enhances CD8+ T cell responses. *J Immunol.* (2016) 196:4014–29. doi: 10.4049/jimmunol.1501188
42. Rueckert C, Guzmán CA. Vaccines: from empirical development to rational design. *PLoS Pathog*. (2012) 8:e1003001. doi: 10.1371/journal.ppat.1003001
43. Andreano E, D'Oro U, Rappuoli R, Finco O. Vaccine evolution and its application to fight modern threats. *Front Immunol*. (2019) 10:1722. doi: 10.3389/fimmu.2019.01722
44. Beaumier CM, Gillespie PM, Hotez PJ, Bottazzi ME. New vaccines for neglected parasitic diseases and dengue. *Transl. Res.* (2013) 162:144–55. doi: 10.1016/j.trsl.2013.03.006
45. Hu D-L, Omoe K, Sasaki S, Sashinami H, Sakuraba H, Yokomizo Y, et al. Vaccination with nontoxic mutant toxic shock syndrome toxin 1 protects against *Staphylococcus aureus* infection. *J Infect Dis.* (2003) 188:743–52. doi: 10.1086/377308
46. Radcliff FJ, Loh JMS, Ha B, Schuhbauer D, McCluskey J, Fraser JD. Antigen targeting to major histocompatibility complex class II with streptococcal mitogenic exotoxin Z-2 M1, a superantigen-based vaccine carrier. *Clin Vaccine Immunol.* (2012) 19:574–86. doi: 10.1128/CVI.05446-11
47. McIntosh JD, Manning K, Chokshi S, Naoumov NV, Fraser JD, Dunbar PR, et al. An engineered non-toxic superantigen increases cross presentation of hepatitis B virus nucleocapsids by human dendritic cells. *PLoS ONE*. (2014) 9:e93598. doi: 10.1371/journal.pone.0093598
48. Halperin SA, Van Nest G, Smith B, Abtahi S, Whiley H, Eiden JJ. A phase I study of the safety and immunogenicity of recombinant hepatitis B surface antigen co-administered with an immunostimulatory phosphorothioate oligonucleotide adjuvant. *Vaccine*. (2003) 21:2461–7. doi: 10.1016/S0264-410X(03)00045-8
49. Hopkins RJ, Daczkowski NF, Kaptu PE, Muse D, Sheldon E, LaForce C, et al. Randomized, double-blind, placebo-controlled, safety and immunogenicity study of 4 formulations of anthrax vaccine adsorbed plus CPG 7909 (AV7909) in healthy adult volunteers. *Vaccine*. (2013) 23:1–7. doi: 10.1016/j.vaccine.2013.04.063
50. Rynkiewicz D, Rathkopf M, Sim I, Waytes AT, Hopkins RJ, Giri L, et al. Marked enhancement of the immune response to BioThrax® (anthrax vaccine adsorbed) by the TLR9 agonist CPG 7909 in healthy volunteers. *Vaccine*. (2011) 29:6313–20. doi: 10.1016/j.vaccine.2011.05.047
51. Corral RS, Petray PB. CpG DNA as a Th1-promoting adjuvant in immunization against *Trypanosoma cruzi*. *Vaccine*. (2000) 19:234–42. doi: 10.1016/S0264-410X(00)00172-9
52. Matos MN, Sánchez Alberti A, Morales C, Cazorla SI, Malchiodi EL. A prime-boost immunization with Tc52 N-terminal domain DNA and the recombinant protein expressed in *Pichia pastoris* protects against *Trypanosoma cruzi* infection. *Vaccine.* (2016) 34:3243–51. doi: 10.1016/j.vaccine.2016.05.011
53. Matos MN, Cazorla SI, Schulze K, Ebensen T, Guzmán CA, Malchiodi EL. Immunization with Tc52 or its amino terminal domain adjuvanted with c-di-AMP induces Th17+Th1 specific immune responses and confers protection against *Trypanosoma cruzi. PLoS Negl Trop Dis.* (2017) 11:e0005300. doi: 10.1371/journal.pntd.0005300
54. Pack AD, Collins MH, Rosenberg CS, Tarleton RL. Highly competent, non-exhausted CD8+ T cells continue to tightly control pathogen load throughout chronic *Trypanosoma cruzi* infection. *PLoS Pathog.* (2018) 14:e1007410. doi: 10.1371/journal.ppat.1007410
55. Bachmann MF, Wolint P, Walton S, Schwarz K, Oxenius A. Differential role of IL-2R signaling for CD8+ T cell responses in acute and chronic viral infections. *Eur J Immunol*. (2007) 37:1502–12. doi: 10.1002/eji.200637023
56. Badovinac VP, Porter BB, Harty JT. CD8+ T cell contraction is controlled by early inflammation. *Nat Immunol*. (2004) 5:809–17. doi: 10.1038/ni1098
57. Padilla AM, Simpson LJ, Tarleton RL, Padilla AM, Simpson LJ, Tarleton RL. Insufficient TLR activation contributes to the slow development of CD8 + T cell responses in *Trypanosoma cruzi* infection. *J Immunol.* (2009) 183:1245–52. doi: 10.4049/jimmunol.0901178

Conflict of Interest: The authors declare that the research was conducted in the absence of any commercial or financial relationships that could be construed as a potential conflict of interest.

frontiers in Immunology

ORIGINAL RESEARCH
published: 07 July 2020
doi: 10.3389/fimmu.2020.01437

Babesia microti Protein *Bm*SP44 Is a Novel Protective Antigen in a Mouse Model of Babesiosis

Hui Wang[1†], *Yao Wang*[1†], *Jilei Huang*[2], *Bin Xu*[2], *Junhu Chen*[2], *Jianfeng Dai*[3*] and *Xia Zhou*[1*]

[1] School of Biology and Medical Science, Soochow University Medical College, Suzhou, China, [2] Key Laboratory of Parasite and Vector Biology of the Chinese Ministry of Health, Chinese Center for Disease Control and Prevention, WHO Collaborating Center for Tropical Diseases, National Center for International Research on Tropical Diseases, National Institute of Parasitic Diseases, Shanghai, China, [3] Jiangsu Key Laboratory of Infection and Immunity, Institutes of Biology and Medical Sciences, Soochow University, Suzhou, China

Babesiosis caused by *Babesia* species imposes an increasing threat to public-health and so far, there is no effective vaccine to prevent *Babesia* infections. *Babesia* surface antigen may participate in the invasion of erythrocytes. In our previous study, a surface antigen of *B. microti* merozoites, named as *Bm*SP44 was identified as a dominant reactive antigen by protein microarray screening. To evaluate its potential applications in diagnosis and prevention of Babesiosis, the open reading frame encoding *Bm*SP44 was cloned and the recombinant protein was expressed. In consistent with the protein microarray result, recombinant *Bm*SP44 (r*Bm*SP44) can be recognized by sera from *B. microti* infected mice. Immunofluorescence assays (IFA) confirmed that *Bm*SP44 is a secreted protein and localized principally in the cytoplasm of the parasites. The parasitemia and *Babesia* gene copies were lower in mice administered r*Bm*SP44 antisera compared with normal controls. Active immunization with r*Bm*SP44 also afforded protection against *B. microti* infection. The concentrations of hemoglobin in r*Bm*SP44 immunization group were higher than those in the control group. Importantly, vaccination of mice with r*Bm*SP44 resulted in a Th1/Th2 mixed immune response with significantly elevated IL-10 and IFN-γ levels during the early stage of infection. Taken together, our results indicated that r*Bm*SP44 can induce a protective immune response against *Babesia* infection. Thus, *Bm*SP44 can be used as both a diagnosis marker and a vaccine candidate.

Keywords: *Babesia microti*, secreted protein, vaccine, antigens, diagnosis marker

OPEN ACCESS

Edited by:
Fabiano Oliveira, National Institutes of Health (NIH), United States

Reviewed by:
Estrella Montero, Carlos III Health Institute, Spain
Reginaldo G. Bastos, Washington State University, United States

***Correspondence:**
Jianfeng Dai
daijianfeng@suda.edu.cn
Xia Zhou
zhouxia@suda.edu.cn

[†] *These authors have contributed equally to this work*

Specialty section:
This article was submitted to Vaccines and Molecular Therapeutics, a section of the journal Frontiers in Immunology

Received: *26 February 2020*
Accepted: *03 June 2020*
Published: *07 July 2020*

Citation:
Wang H, Wang Y, Huang J, Xu B, Chen J, Dai J and Zhou X (2020) Babesia microti Protein BmSP44 Is a Novel Protective Antigen in a Mouse Model of Babesiosis. Front. Immunol. 11:1437. doi: 10.3389/fimmu.2020.01437

INTRODUCTION

Babesia is a tick-borne intraerythrocytic protozoan parasite belonging to the phylum Apicomplexa. *B. microti* causes babesiosis in animals and humans worldwide. Although most human babesiosis cases were reported in the United States (1), babesiosis is regarded as an emerging vector-borne parasitic disease in other countries during recent years (2, 3). Babesiosis is normally a benign infection and most of the cases can be asymptomatic or present with mild symptoms. But in populations of neonates or immunocompromised patients, the infection of *Babesia* can be fatal (4, 5). Currently, no vaccine is available to control *Babesia* infection, and drugs for babesiosis are limited, suggesting the importance and necessity to explore potential vaccine based on relative antigen molecules (6, 7).

In recent years, several proteins involved in cell invasion and immunity have been developed as vaccine candidates and their protections against *Babesia* infection in animal models have been evaluated (8–13). But all these candidates as vaccines exhibited limited protection from the infection of *Babesia*. Thus, more work is required for identification of novel targets which can induce stronger protection against babesiosis.

The process of parasite invasion and enveloping within host cells is highly dependent on the interaction between the parasite and host-surface molecules (14, 15). The surface proteins produced by *Babesia* parasite enable it to adhere to and invade the erythrocytes, where it survives and grows (16, 17). Surface secreted proteins usually play a key role in facilitating parasite invasion, host cell remodeling and can be targeted or activated by the humoral immune response in the host (18–21). The surface proteins present in early infective stages may be useful for developing a diagnostic test for babesiosis as well as vaccine.

In our previous study, protein microarray screening was performed using a *Babesia* genomic expression library against murine sera from different stages of infection. Ten *B. microti* antigens were identified as targets of host humoral immune responses (22). However, the antigenicity, immunogenicity, function, and subcellular localization of these surface antigens are not clearly understood.

In the current study, the functions of a dominant *Babesi*a antigen *Bm*SP44 was evaluated in a mouse model of babesiosis. *Bm*SP44 was confirmed as a secretory protein in the parasite of *B. microti*. The protection effect of this antigen against *Babesia* infection in a mouse model was examined by passive and active immunization strategies. Meanwhile, the changes of cytokine expressions after active immunization were examined to systematically evaluate the function of the protein. Our results suggested that *Bm*SP44 may serve as a potential vaccine candidate as well as a diagnostic antigen.

MATERIALS AND METHODS

Ethics Statement

All animal procedures were conducted in compliance with the principle for the Care and Use of Medical Laboratory Animals (Ministry of Health, People's Republic of China) and approved by the Institutional Animal Care and Use Committee (IACUC) of Soochow University for the use of laboratory animals (Permit Number: ECSU-201800091). All efforts were made to minimize suffering.

Animals and *Babesia* Infections

Six-to-eight-week-old female BALB/c mice were provided by the Experimental Animal Center of Soochow University (Suzhou, China), and kept under specific pathogen-free conditions. The Peabody strain (ATCC, PRA-99) of *B. microti* was obtained from ATCC. One mouse was initially infected via intraperitoneal injection and blood from the mouse (5 days post infection, the parasitemia is approximately 60%) was taken from the eyelids, anticoagulated with ethylenediaminetetraacetic acid (EDTA), mixed with sterile 0.9% physiological saline in a ratio of 1:2, and infected by 100 μl per BALB/c mouse via intraperitoneal injection. The infections were performed with this strain of *Babesia* by intraperitoneal (i.p.) injection with 1×10^7 *B. microti*-infected red blood cells (iRBCs). Totally, 6 mice equally divided into two groups, 3 mice in the immunized group, and 3 ones set as the control were use in the passive experiments. And there were totally 10 mice in the active immunized experiment, each group with 5 mice and the same protocols were applied in independently.

Preparing Secreted Protein Microarray and Acquiring Immunoreactivity Profiles

Based on the SignalP software (http://www.cbs.dtu.dk/services/SignalP/) and EuPathDB database (http://piroplasmadb.org/piro/), ORFs encoding *Babesia* proteins containing signal peptides were selected and cloned in-frame into the pEU-E01-His-TEVMCS-N2 (pEU, Cell Free Sciences, Matsuyama, Japan) vector. The cell-free protein synthesis system, wheat germ cell-free (WGCF) system was applied in the high throughput expression assay. The ORF sequences were amplified from cDNA of *B. microti* PRA99 strain and the recombinant protein r*Bm*SA1 (23) expressed in *E. coli* DH5α strain was used as the positive control. The wheat germ lysate with expression of an empty vector served as the negative control. Detailed protocols with the high throughput assay were described in our previously study (22).

Bioinformatic Analysis of the Gene Coding for *Bm*Sp44

Antigenic epitopes were predicted using ABCPred (http://www.imtech.res.in/raghava/abcpred/). The hydrophobicity and the signal peptide were predicted using Expasy (http://www.expasy.org/) and the SignalP4.1 server (http://www.cbs.dtu.dk/services/SignalP/), respectively.

Expression and Purification of Recombinant Protein *Bm*SP44

Expression of *Bm*SP44 with glutathione S-transferase (GST) fusion proteins was conducted using the pGEX vector system. ORF of *Bm*SP44 was amplified with the proof-reading Polymerase (Pfu) (Transgene, Beijing) from the cDNA of *B. microti* using gene-specific primers (forward-TTCCAGGG GCCCCTGGGATCCATGCATATCAACTACAAATTAAT TA and reverse- TCACGATGCGGCCGCTCGAGTTAA GCAGCATTAGGTGTGTGAT). The fragment was then cloned into pGEX-6P-2 (Invitrogen, Carlsbad, NM) vector by digestion with *BamHI* and *XhoI* (Vazyme, USA). Validated pGEX constructs were re-transfected into *E. coli* strain BL21 (DE3) for recombinant protein expression. Briefly, 1,000 ml of LB medium containing 1 ml of ampicillin were incubated with bacterium in constant temperature shaker. After 4 h, protein expression was induced with 0.5 mM Isopropyl β-D-1-thiogalactopyranoside (IPTG). Then, the soluble recombinant GST-tagged fusion proteins were purified using GST affinity agarose (GE Healthcare, Sweden) and the GST tag was

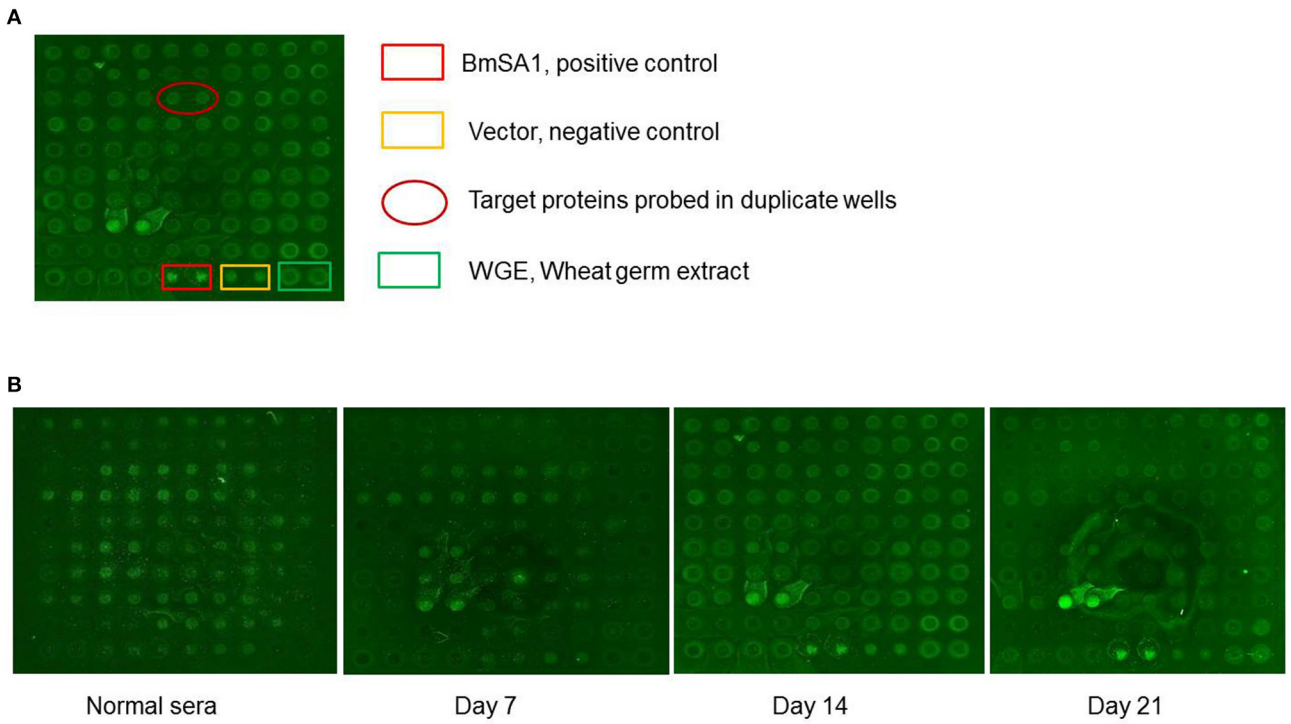

FIGURE 1 | *B. microti* proteins detected by sera from infected BALB/c mice. **(A)** Normal: the sera from the normal BALB/c mouse; the sera from the BALB/c mice infected on day 7, 14, and 21 p.i. pEU-His vector, Wheat germ extract (WGE) and *Bm*SA1 were used as negative and positive controls, respectively. **(B)** The protein arrays probed with mouse sera from 3 different infection stages.

removed by on-column enzyme digestion of Prescission Protease (Sigma).

Preparing Rabbit Antisera Against r*Bm*SP44

For generation of Rabbit antisera against r*Bm*SP44, NZW rabbit was immunized with 100 μg of r*Bm*SP44 together with complete Freund's adjuvant (Sigma-aldrich, USA). The rabbit was received 2 boosts (400 μg r*Bm*SP44) at 2-week intervals in incomplete Freund's adjuvant. Two weeks after the final boost, sera were collected and the antibody titers were evaluated with the standard ELISA procedures described above.

Western Blot Analysis

Total protein samples were separated on 10% sodium dodecyl sulfate polyacrylamide gel electrophoresis (SDS-PAGE), and transferred to a 0.45 μm polyvinylidene difluoride (PVDF) membranes. The blot was blocked with 5% skim milk diluted in TBS containing 0.05% Tween (TBST) for 1 h at room temperature. The *B. microti* hyperimmune sera were diluted (1:5,000) in TBST containing 2% skim milk and incubated overnight at 4°C. The blot was washed with TBST three times and then incubated in an HRP-conjugated goat anti-mouse IgG (H+L) secondary antibody (Bioworld, USA) (1:10,000) for 1 h at room temperature. After three washes with TBST, the signal was detected with an enhanced chemiluminescence ECL Plus kit (Thermo, USA).

Evaluation of r*Bm*SP44 as a Diagnostic Antigen

Enzyme-linked immunosorbent assay (ELISA) plates were coated with the r*Bm*SP44 protein (to the final concentration of 5 μg/ml) and incubated overnight at 4°C. After three washes with PBST, the plates were blocked with 2% BSA. One hundred microliters of sera from different infection stages (7, 14, and 21 days post infection), and negative mouse sera (from healthy mice) were diluted (1:2,000) in 2% BSA and incubated for 30 min. After incubating with peroxidase-conjugated rabbit anti-mouse IgG antibody, the reaction was examined with 3, 3, 5, 5′-Tetramethylbenzidine–hydrogen peroxide substrate (TMB) (Biolegend, USA) according to standard protocols.

Immunofluorescent Assay (IFA) and Confocal Microscopy

Anticoagulated blood collected from mice infected with *B. microti* with approximately 30% parasitemia was smeared on slides using cytospin centrifugation (Thermo Fisher Scientific) and fixed with 4% PFA-PBS for 10 min. After washed three times with PBS, the slides were permeabilized with 0.4% Triton X100 for 10 min, and then treated with protease K (20 μg/ml) for 5 min. After washes, the slides were blocked with 5% FBS for 30 min to reduce non-specific binding and then incubated overnight at 4°C with a 1:300 dilution of

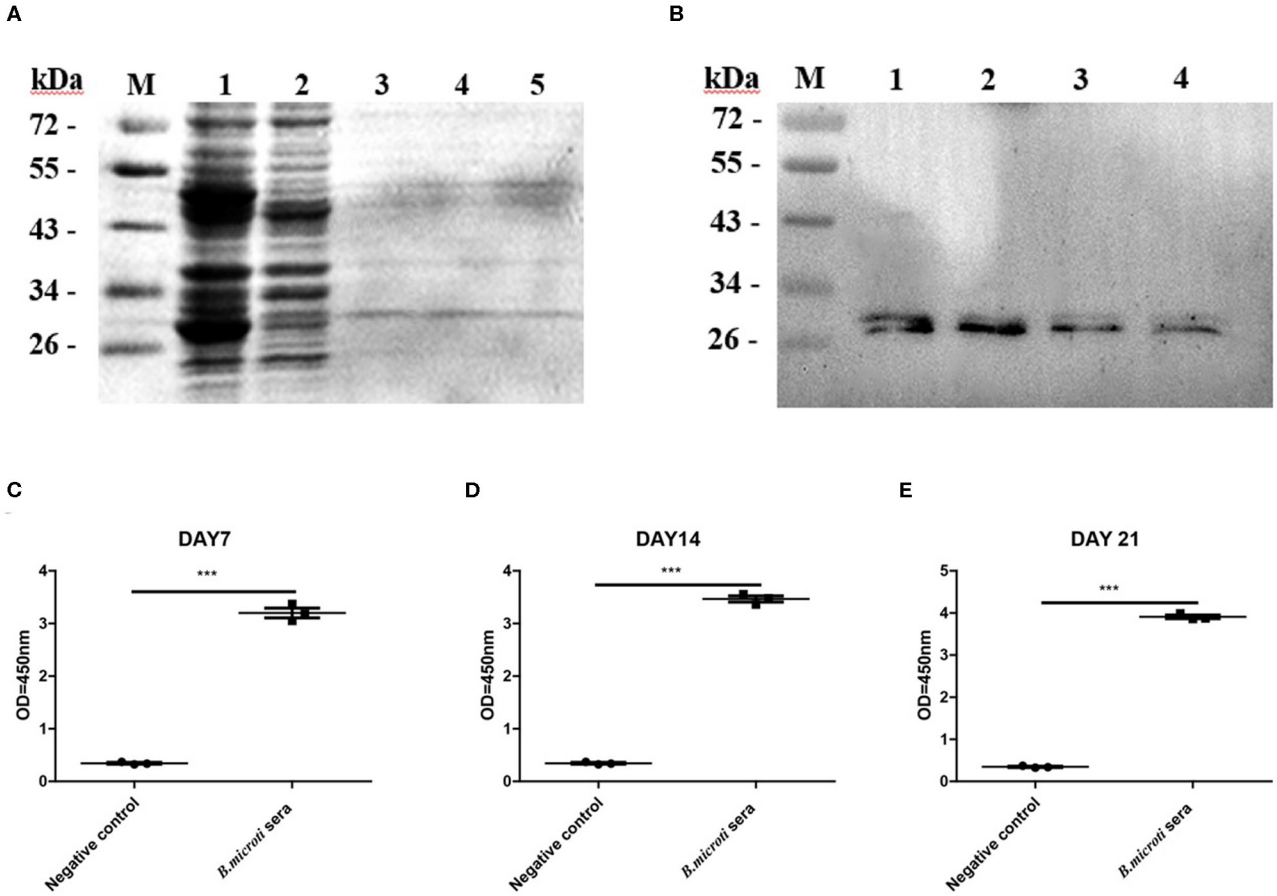

FIGURE 2 | Recombinant antigen production and evaluation of r*Bm*SP44 as a diagnostic antigen. **(A)** SDS-PAGE analysis of bacterial lysate as stained by Coomassie blue. Lane 1: induced protein; Lane 2: non-induced control; Lane 3 and 5: The purification of r*Bm*SP44 after cleavage of GST tag; **(B)** Western blot analysis of r*Bm*SP44; M: Protein marker; Lane 1–4: The recombinant proteins; Protein incubated with an anti-r*Bm*SP44 monoclonal antibody (~24 kDa); **(C–E)** r*Bm*SP44 recognized by sera from *B. microti* infected mice [Sera from day7 **(C)**, 14 **(D)**, and 21 **(E)** p.i.] Significant differences are as follows: ***$P < 0.001$, compared to non-infected control sera, *t*-test. The data shown are representative of at least 3 independent experiments.

mouse anti-BmSP44 serum. After washing three times again, the slides were incubated with Alexa Fluor488 goat anti-mouse IgG for 1 h (Invitrogen) diluted at 1:500 in PBS for 1 h at room temperature. After washes, the slides were incubated with 0.5 μg/ml 6-diamidino-2-phenylindole (DAPI) for 15 min and imaged using a Nikon C2 Confocal microscope system (Nikon, Tokyo, Japan).

Passive Immunization

The rabbit was immunized with r*Bm*SP44 100 μg mixed with complete Freund's adjuvant (Sigma-aldrich, USA) in ratio of 2:1 and boosted twice at 2-week intervals by injection of 200 μg protein mixed with incomplete Freund's adjuvant also in ratio of 2:1. Two weeks after the final boost, sera were collected and the antibody titers were evaluated with the standard ELISA procedures described above. For passive immunization, mice were administered of r*Bm*SP44 rabbit antisera (200 μl each) or control antisera (5 per group). Twenty-four hours later, the animals were challenged with intraperitoneal inoculation of 1×10^7 *B. microti*-parasitized red blood cells (iRBCs).

Active Immunization

For active immunization, mice (5 per group) were immunized with r*Bm*SP44 (20 μg/each) mixed with complete Freund's adjuvant while the control group receiving Freund's adjuvant only. Animals were received 2 boosts (40 μg r*Bm*SP44) at 2-week intervals in incomplete Freund's adjuvant. Two weeks after the final boost, sera were collected and evaluated with the standard ELISA procedures described above.

Parasitemia and *Babesia* Load

The concentration of parasites in the blood was determined by blood smears examination and quantitative RT-PCR (qRT-PCR). Thin films from the peripheral blood were prepared every third days after *B. microti* inoculation, and stained with Giemsa's solution. The numbers of infected and non-infected erythrocytes were counted per 50 microscopic fields to calculate

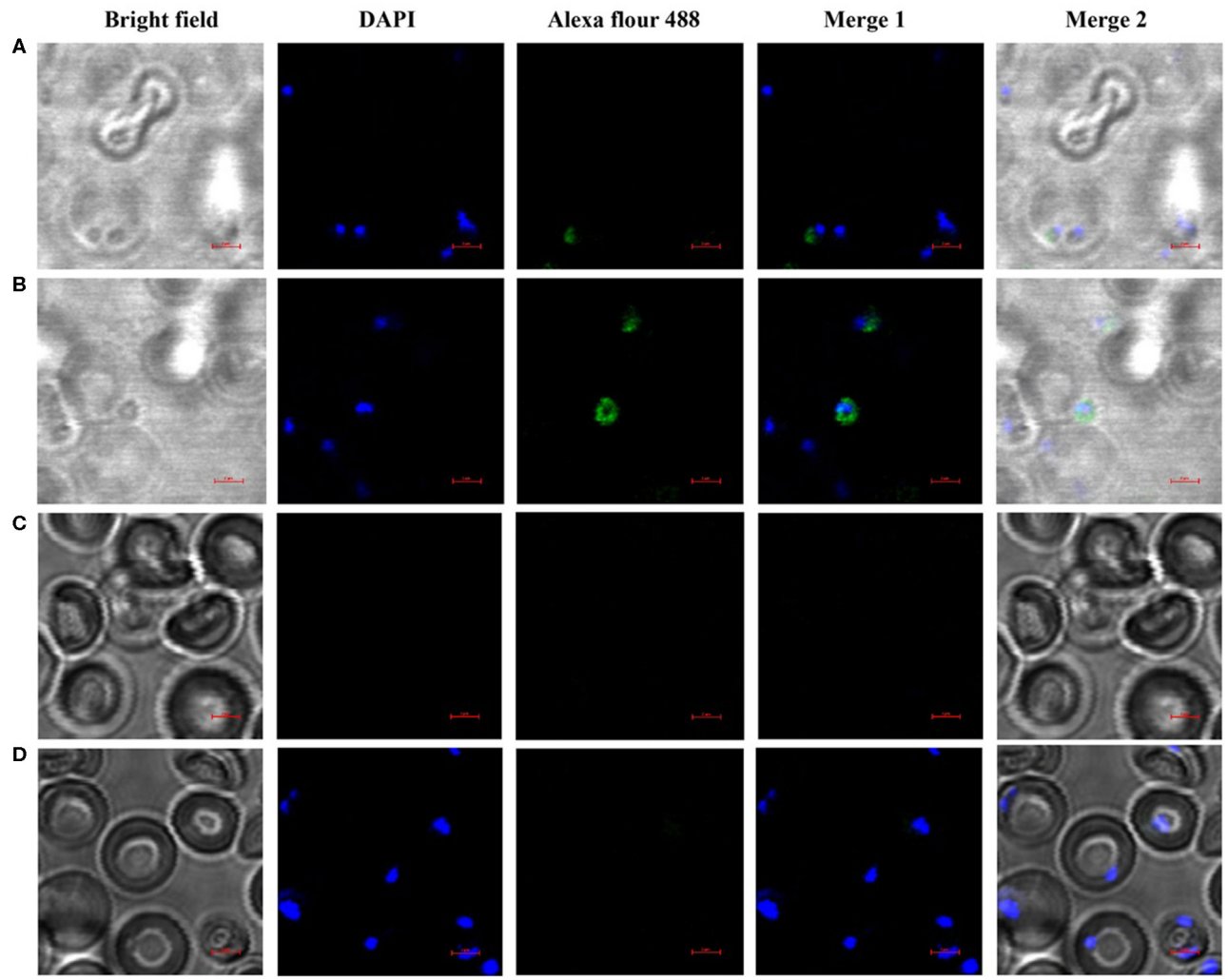

FIGURE 3 | *Bm*SP44 is a secreted protein pf *B. microti.* The immunolocalization of *Bm*SP44 on the membrane of the *B. microti* and the cytoplasm of the iRBCs were examined by IFA with anti-*Bm*SP44 sera. The obvious green fluorescent staining is observed on the membrane of the parasite and the cytoplasm of the iRBCs. **(A)** iRBCs incubated with mouse anti- r*Bm*SP44 serum, the parasite taking residence in RBCs; **(B)** iRBCs incubated with mouse anti- r*Bm*SP44 serum, the parasite outside the RBCs; **(C)** Normal RBCs incubated with mouse anti-r*Bm*SP44 serum; **(D)** iRBCs incubated with normal mouse serum; Bars, 2 μm.

parasitemia. The degree of infection in each group is presented as the geometric mean of the parasitemia percentage. The blood RNA was extracted used for using the blood RNA kit (OMEGA, USA). Briefly, the blood RNA was reverse-transcribed using the PrimeScript Master Mix kit (TaKaRa, Japan). PCR was performed by using iTaq SYBR Green Supermix (Monad, China) on a CFX96 real time PCR system (Eppendorf, USA) and involved an initial denaturation at 95°C for 30 s, 40 cycles of 5 s at 95°C, and 30 s at 60°C. At the end of each reaction, a melting curve (70–95°C) was checked to confirm the identity of the PCR product. *B. microti 18S rRNA* primers: forward- AGCGTTTTCGAAGGTA TGTTGC and reverse-AGCAGATACATCCTTACTAGGGAAA. Mouse GAPDH (control): forward- GGCCTTCCGTGTTCCT ACC and reverse – AGCCCAAGATGCCCTTCAGT were applied during the amplification. And the mouse GAPDH gene was amplified as an internal control.

Severity of the Disease

Besides the parasitemia and *Babesia* load, the weight, temperature, and hemoglobin level of mice were also measured to evaluate the severity of the disease. The weight and the temperature were monitored daily post *B. microti* infection. To measure the hemoglobin (Hb) concentration, 10 μl of blood was diluted in 2,490 μl of Drabkin's reagent (Sigma-Aldrich, St. Louis, MO, USA) and quantified at 540 nm using a biophotometer (Eppendorf, USA). The absorbance and hemoglobin concentration (Hb) were counted using a commercial Hb standard curve.

Detection of Cytokine Levels in Serum

After receiving active immunization with the recombinant protein, mice were challenge with 1×10^7 *B. microti* infected erythrocytes. Sera samples were prepared from each immunized

or control mouse on day 0, 3, 6, and 9 after challenge. The concentration of cytokines such as IFN-γ, TNF-α, and IL-10 were determined by ELISA assay according to the manufacturer's instructions (Biolegend, USA).

Statistical Analysis

GraphPad Software of Prism 7 software was used in charts and statistical analyses. Statistical differences were analyzed by Student's *t*-test and ANOVA. A value of $p < 0.05$ was considered statistically significant.

RESULTS

High-Throughput Screening of Secreted Proteins by Protein Arrays

A total of 55 proteins containing signal peptides from *B. microti* were selected and screened by sera collected from *B. microti* infected mice at different stages of infection. One secreted protein, named *Bm*SP44, showed a higher immune reactivity with the sera collected on day 7, 14, and 21 post infection compared to other antigens tested (**Figures 1A,B**).

Molecular Characterization and Sequence Analysis of *Bm*SP44

The nucleotide sequence coding *Bm*SP44 was 654 bp long and predicted to encode a protein of 218 amino acid residues (**Supplementary File 1** with a predicted molecular weight and isoelectric point of 24 kDa and 5.39. Signal peptide sequence was found in *Bm*SP44 protein based on SignalP4.1 and antigenic epitopes were predicted using ABCPred bioinformatic serves (**Supplementary Figures 1A,B**. However, no homologous genes were identified in other species of *Babesia* based on the current genome sequences available from NCBI database.

Evaluation of *Bm*SP44 as a Diagnostic Antigen

To investigate the characteristics of *Bm*SP44, a recombinant protein without the GST tag (∼24 kDa) was produced in the *E.coli* expression system (**Figure 2A**) and used to immunize mice. Western blot suggested that r*Bm*SP44 reacted with the sera from r*Bm*SP44-immunized mice but not from the controls (**Figure 2B**).

To validate the potential of r*Bm*SP44 as a diagnostic antigen, an indirect ELISA was set to detect *Bm*SP44 specific antibodies from sera of *B. microti* infected mice. The results suggested that r*Bm*SP44 can be detected with mouse serum collected on day 7, 14, and 21 p.i. (**Figures 2C–E**), which were consistent with the data from high throughput protein microarray. Thus, *Bm*SP44 can be used as a diagnostic antigen since it can be detected with host serum at different stages of infection.

Localization of *Bm*SP44 in *B. microti*

The localization of *Bm*SP44 in *B. microti* and infected RBCs was detected by IFA using mouse anti-*Bm*SP44 sera. *Bm*SP44 appeared to localize on the surface of *B. microti*, supporting that it is a potential secreted antigen of *B. microti* (**Figures 3A,B**). As negative controls, red blood cells from non-infected mice did not show any specific fluorescent signals (**Figures 3C,D**).

Passive Immunization With Antisera Against r*Bm*SP44 Interferes With *B. micoti* Infection

In order to examine whether r*Bm*SP44 antiserum thwarts infection with *B. microti*, r*Bm*SP44 antisera were administered into the mice 24 h before *B. microti* challenge. The titers of the rabbit antisera against r*Bm*SP44 were confirmed by ELISA before inoculation (**Supplementary Figure 2**). qRT-PCR analysis suggested that *Babesia* gene copies in mice receiving rabbit antisera against r*Bm*SP44 were reduced on day 3, 6, and 9 p.i. compared with that in control animals (**Figure 4A**). The results from the blood smears also showed a decrease parasitemia in passive immunization group compared with the control group (**Figures 4B–H**).

Active Immunization With r*Bm*SP44 Reduces *Babesia* Infection in Mice

We then examined whether active immunization of mice with r*Bm*SP44 influenced *Babesia* infection. Following active immunization, high levels of r*Bm*SP44 antibodies were detected in mouse sera (**Figure 5A**). After challenged with *B. microti*, mice immunized with r*Bm*SP44 displayed reduced *Babesia* gene copies in whole blood samples on day 3, 6, and 9 p.i. compared with controls (**Figure 5B**). A reduced *Babesia* parasitemia also observed in blood smears from r*Bm*SP44 immunized mice compared to controls (**Figures 5C–I**). Therefore, active immunization with r*Bm*SP44 also protects against *B. microti* infection of mice.

Parasitemia is a major indicator for evaluating the severity of the disease. Meanwhile, weight, body temperature, and concentration of hemoglobin were also introduced to evaluate the severity of Babesiosis. Our results showed that the concentrations of hemoglobin in r*Bm*SP44 immunized mice were significantly higher than that of controls, while there are no obvious differences regarding the weight and the temperature between the two groups (**Figures 6A–F**).

Cytokine Profiles of r*Bm*SP44 Immunized Mice

In order to analyze the levels of Th1 and Th2 cytokines in infected mouse sera, the expressions of IFN-γ, TNF-α, and IL-10 were determined by ELISA kits. Compared with the control groups, serum IFN-γ, and IL-10 expression were significantly higher in mice immunized with r*Bm*SP44 on day 6 p.i. Serum TNF-α was also slightly higher in the immunized group than the controls on day 6 and 9 p.i., but the differences were not significant. These data suggested that a Th1/Th2-mixed immune response was induced in r*Bm*SP44 immunized mice during the early stage of infection. This Th1/Th2-mixed immune response may contribute to the protective efficacy of r*Bm*SP44 against *Babesia* parasites infection (**Figures 7A–C**).

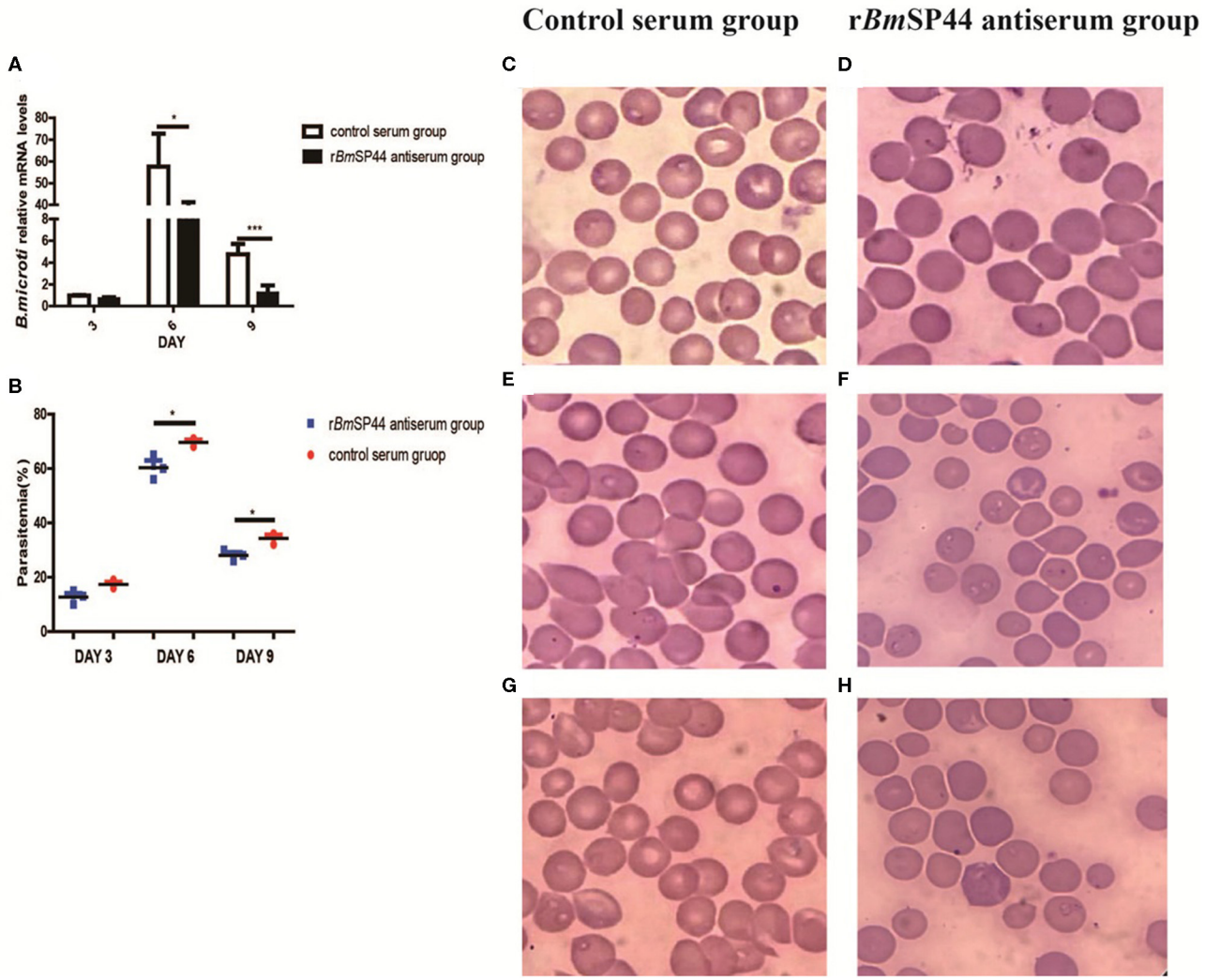

FIGURE 4 | The Parasitemia were reduced in *Bm*SP44 antisera passive immunized mice. **(A)** Revervse transcription qPCR analysis of the expression of *B. microti* at different developmental stages. After reverse transcription, the cDNA was used as a template for qPCR using SYBR Green. Each reaction was performed in triplicate. All fold changes were relative to the different stage. Significant differences are as follows: $^{*}P < 0.05$, $^{***}P < 0.001$. **(B)** Parasitemia of the immunized group is lower than that of the control group, which is quantified as the percentage of iRBCs by blood smears on day 3, 6, and 9 p.i. The degree of parasitemia were 16, 70, and 32% in normal rabbit sera passive immunized group ($n = 3$) and 10, 56, and 18% in r*Bm*SP44-antiserum immunized group ($n = 3$), respectively. The values shown for each group are the mean + SEM of the parasitemia. Significant differences are as follows: $^{*}P < 0.05$. **(C–H)** Giemsa staining of blood smears from group **(C,E,G)** and r*Bm*SP44-antiserum group **(D,F,H)**. Sections obtained on day 3 **(C,D)**, 6 **(E,F)**, and 9 **(G,H)** p.i.

DISCUSSION

B. microti, a major etiological agent of tick-borne babesiosis invading only erythrocytes in human has been sequenced to have the smallest nuclear genome among all apicomplexan parasites (24). Several novel antigens of the parasite were characterized using protein microarrays (25–27). Some of them can trigger host immune response and be associated with genes encoding the secretome and the surface proteome of the parasite (28–30). These studies provide candidates for the development of improved diagnostic assays and vaccines.

A panel of secreted proteins containing signal peptides were identified in previous studies (12, 22), some of which have been characterized as diagnostic antigens of babesiosis. Relative fewer were considered as candidates in vaccine development (31–33). What's more, increased drug resistance of *Babesia* and modest effect of new vaccine candidates were reported (34, 35). In this study, the gene encoding *Bm*SP44 was cloned and characterized in *B. microti*. Bioinformatics analysis suggested that *Bm*SP44 has no homologous genes in other species of *Babesia*; in addition, *Bm*SP44 does not contain any conserved domains, making it difficult to predict its function. *Bm*SP44 is a secreted protein that can be recognized by the host's immune system and therefore considered as an attractive vaccine candidate and a diagnostic marker. Our microarray and ELISA data all indicated that r*Bm*SP44

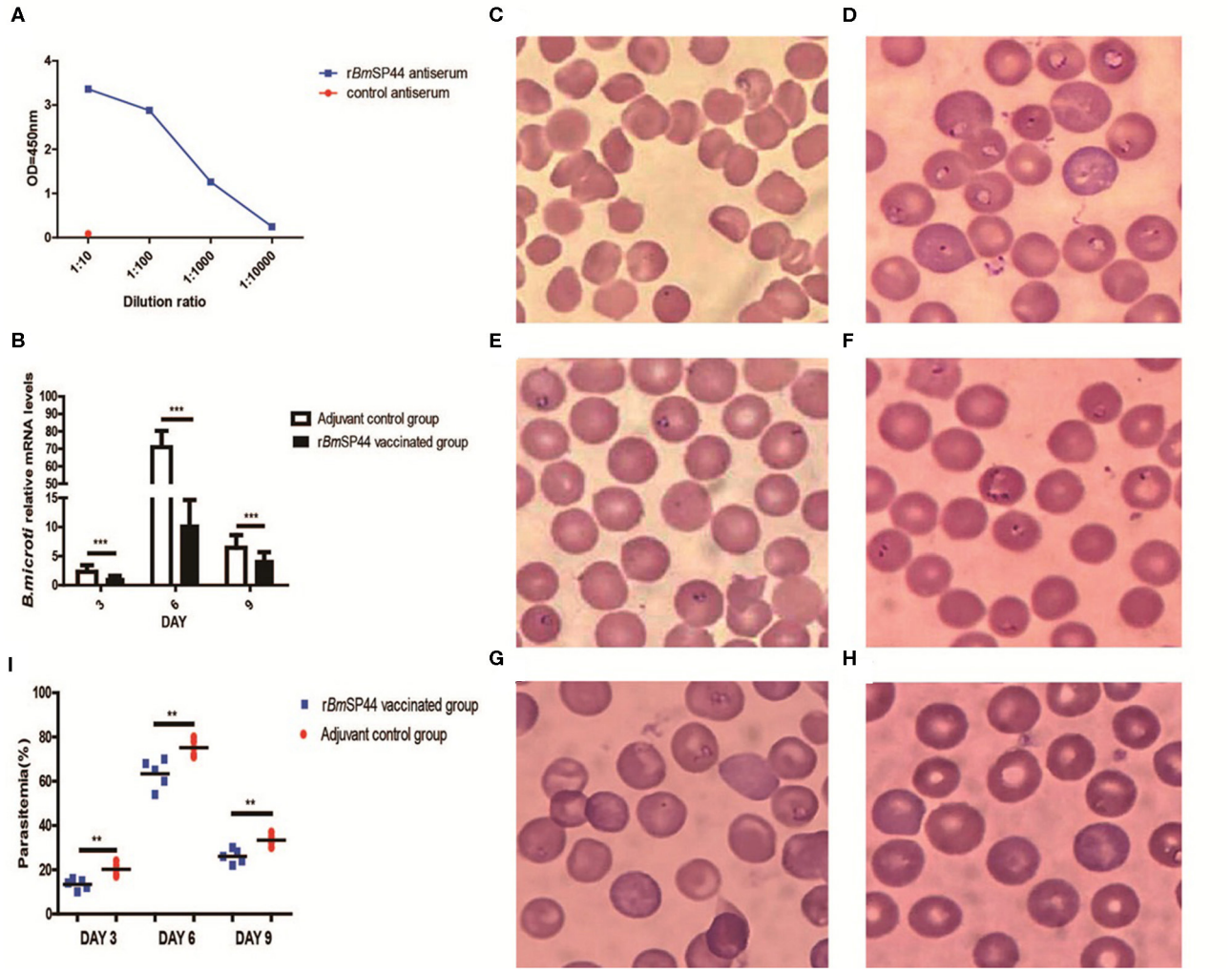

FIGURE 5 | r*Bm*SP44 active immunization protects against *B. microti* infection in BALB/c mice. **(A)** The levels of anti-*Bm*SP44 antibody in the sera of immunized mice or control (adjuvant) mice were measured by ELISA at different time points. **(B)** Active immunization with r*Bm*SP44 or adjuvant control BALB/c mice were challenged with 1×10^7 erythrocytes with *B. microti* and blood samples were obtained on day 3, 6, and 9 p.i. Revervse transcription qPCR analysis of the expression of *B.microti* at different developmental stages. After reverse transcription, the cDNA was used as a template for qPCR using SYBR Green. Each reaction was performed in triplicate. All fold changes were relative to the different stage. Significant differences are as follows: $^{***}P < 0.001$. **(C–I)** Parasitaemia is quantified as the percentage of iRBCs by blood smears on day 3, 6, and 9 p.i. Giemsa staining of blood smears from control **(C,E,G)** and r*Bm*SP44 immunized group **(D,F,H)**. Sections obtained on day 3 **(C,D)**, 6 **(E,F)**, and 9 **(G,H)** p.i. **(I)** Parasitemia of the immunized group and that of the control group caculated by blood smears observed under microscope. The degree of infection were 20, 75, and 35% in control Adjuvant-vaccinated group ($n = 5$) and 12, 60, and 24% in r*Bm*SP44 vaccinated group ($n = 5$), respectively. The values shown for each group are the mean + SEM of the parasitemia. Significant differences are as follows: $^{**}P < 0.01$.

could be an antigen for serological diagnostics marker for human babesiosis.

As *Bm*SP44 elicits strong immunoreactions, we extended the study to test the role of r*Bm*SP44 in altering *Babesia* infection. In our active immunization experiments, the mice immunized with r*Bm*SP44 demonstrated significant protection against *Babesia* infection. The passive immunization with r*Bm*SP44 rabbit antiserum also delivered protection in immunized mice; however the protection rates were lower than that of active immunization experiments. Although rabbit antibodies have the advantages of recognizing small epitopes (36, 37), the antibody titer of passive immunization was lower than that of active immunization in our study. Also, active immunization may result in cellular immunity in addition to humoral immunity. This may explain why the passive immunization inducing relatively weak protection compared to the active immunization.

As apicomplexan protozoa, the protective immunity induced by *Babesia* proteins like *Bm*MetAP1, *Bm*HSP70 involves mainly cell-mediated responses with high level of IgG1 and Th1

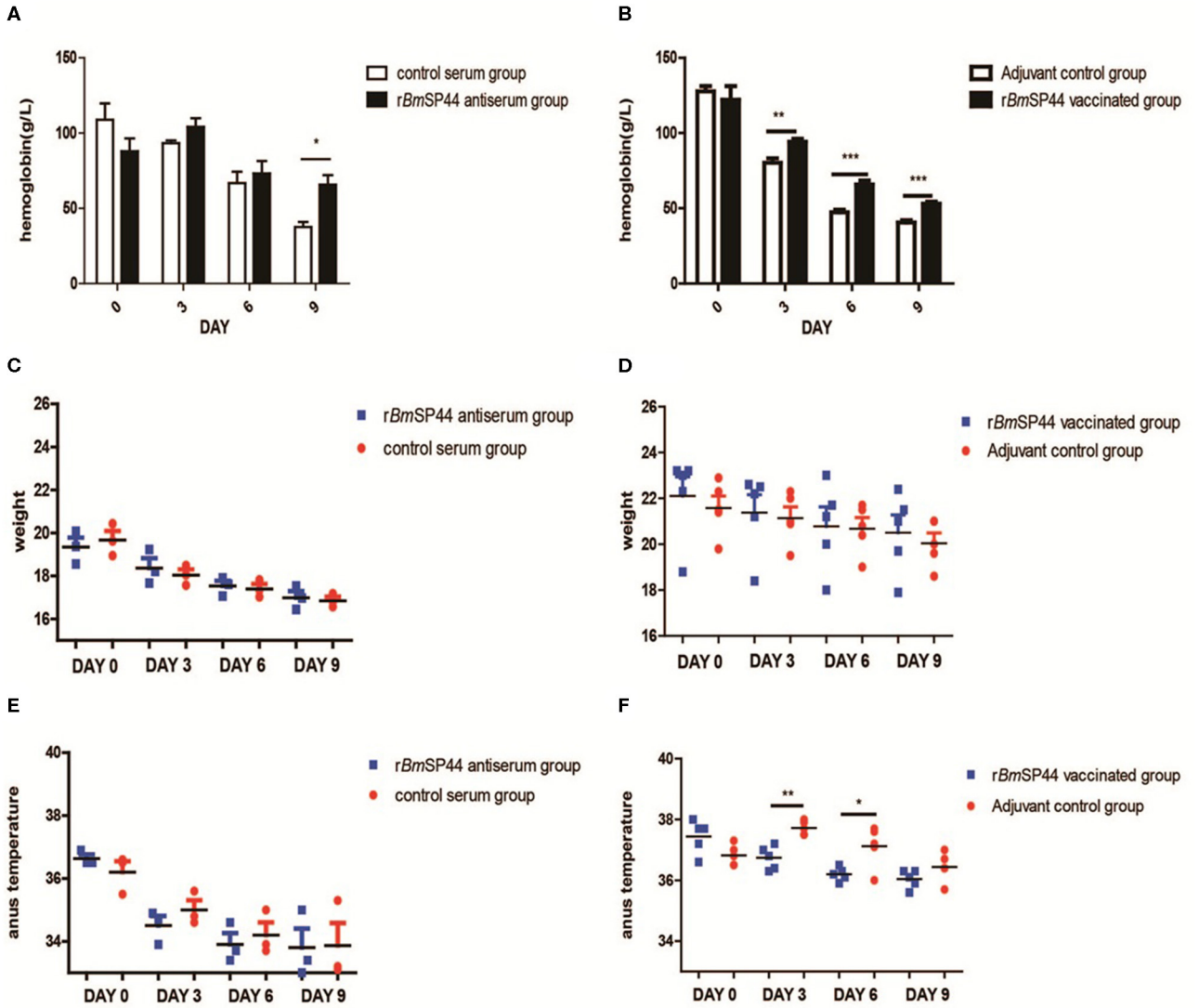

FIGURE 6 | The hemoglobin level, weight, and temperature of *B. microti* infected mice. **(A,B)** The hemoglobin was measured in peripheral blood by Drabkin's reagent on Day 0, 3, 6, and 9 p.i. The concentrations of hemoglobin were 118, 92, 68, and 38 g/l in the normal rabbit sera passive immunized group ($n = 3$); 88, 100, 73, and 72 g/l in r*Bm*SP44-antiserum immunized group ($n = 3$). The data in the active immunized groups are as following: 125, 80, 48, and 41 g/l in control Adjuvant-vaccinated group ($n = 5$) and 118, 92, 63, and 53 g/l in r*Bm*SP44 vaccinated group ($n = 5$), respectively. The values shown for each group are the mean + SEM of the hemoglobin. Significant differences were as follows: $^{*}P < 0.05$,$^{**}P < 0.01$, $^{***}P < 0.001$. **(C,D)** The change in weight was not discernible on day 0, 3, 6, and 9 p.i. The weight were 19.6, 18.1, 17.3, and 16.8 g in normal rabbit sera passive immunized group ($n = 3$), 19.4, 18.2, 17.6, and 17.0 g in r*Bm*SP44-antiserum immunized group ($n = 3$). The data in the active immunized group are as following: 21.5, 21.0, 20.8, and 20.0 g in control Adjuvant-vaccinated group ($n = 5$) and 23.0, 22.2, 21.2, and 21.0 g in r*Bm*SP44 vaccinated group ($n = 5$), respectively. **(E,F)** The temperatures of the r*Bm*SP44 immunized mice were significantly lower than that of the control mice on day 3 and 6 p.i. The degree of weight were 36.5, 34.8, 33.9, and 33.2°C in normal rabbit sera passive immunized group ($n = 3$); 36.5, 34.7, 33.7, and 33.4°C in r*Bm*SP44-antiserum immunized group ($n = 3$). The data in the active immunized groups were 36.8, 37.7, 37.2, and 36.4°C in control Adjuvant-vaccinated group ($n = 5$) and 37.7, 36.8, 36.2, and 36.1°C in r*Bm*SP44 vaccinated group ($n = 5$), respectively. The starting point of the ordinate in the scatter plot is 33.0°C and the values shown for each group are the mean + SEM of the temperature levels. Significant differences were as follows: $^{**}P < 0.01$, $^{*}P < 0.05$. The representative results of at least 3 independent experiments are shown, with 3–5 mice per group.

cytokines, such as IFN-γ and IL-12 (38, 39). The interaction between the erythrocyte receptors and MSP1 was critical for the invasion process of *Plasmodium,* another important intraerythrocytic protozoon. Thus, MSP1 is a major malaria vaccine candidate which protects malaria parasites in mouse models (40). Humoral immune responses may also contribute to the protections in these parasite infections. Classically, the Th1 cytokines responses are characterized by the production of IFN-γ, IL-2, and TNF-α, while Th2 responses are represented by cytokine IL-4, IL-6, and IL-10. It was confirmed that cytokines such as IL-12, TNF-α, IFN-γ, and IL-2 play an important role in controlling the proliferation of *Babesia* in

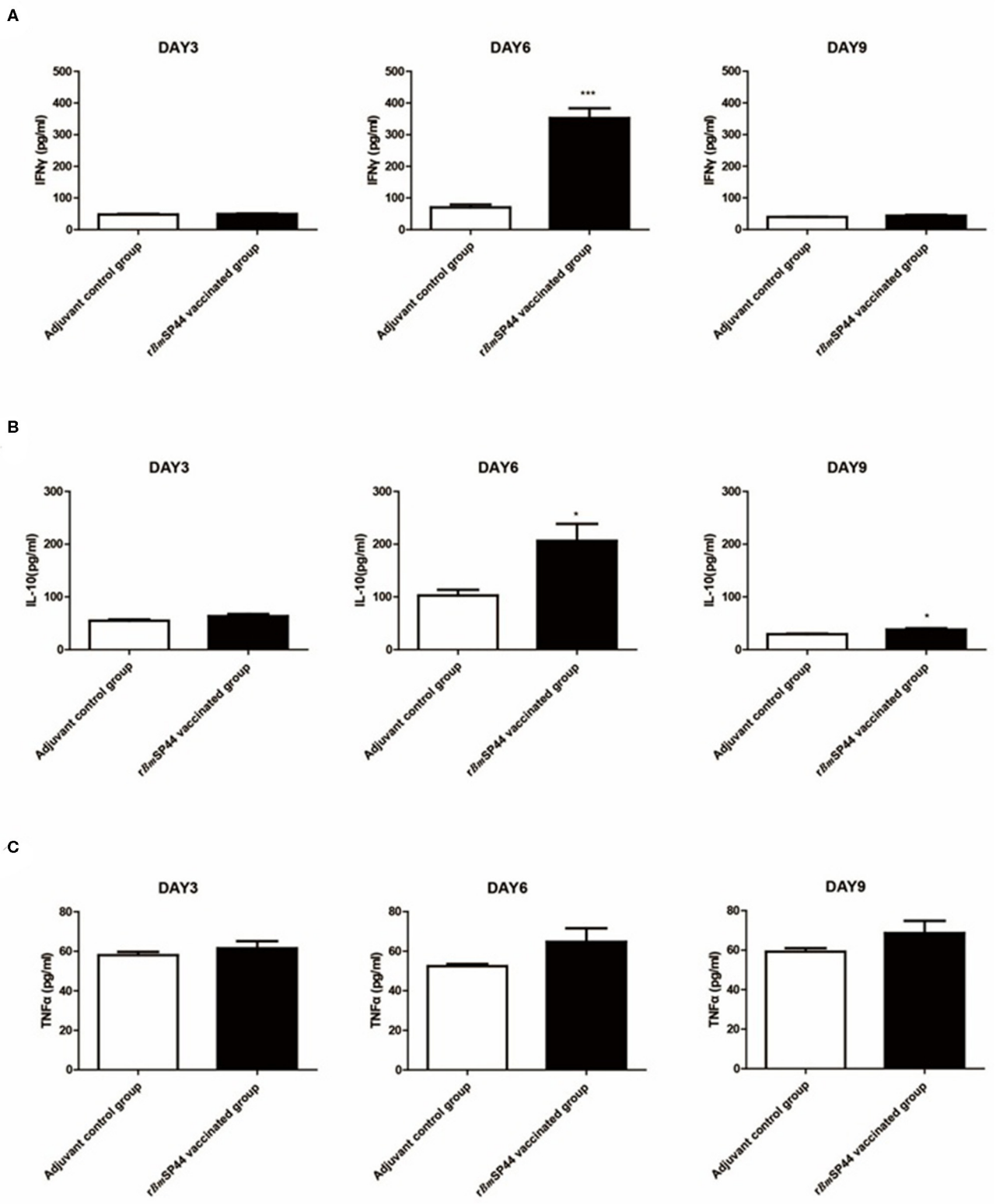

FIGURE 7 | Cytokine levels in sera of r*Bm*SP44 immunized or mice after infection of *B. microti.* BALB/c mice of the *Bm*SP44 vaccinated or adjuvant treated control groups were followed by a challenge with 1×10^7 erythrocytes infected with *B. microti* and the samples were taken on Day 3, 6, and 9 p.i. **(A)** The concentrations of

(Continued)

FIGURE 7 | IFN-γ in sera were 45.4, 60.5, and 40.0 pg/ml in Adjuvant-vaccinated control group ($n = 5$) and 52.3, 231.9, and 43.5 pg/ml in r*Bm*SP44 vaccinated group ($n = 5$), respectively. Results are presented as the mean ± SEM. The asterisks (*) indicate that the levels of IFN-γ by immunized mice was significantly higher (***$P < 0.001$) than those of the adjuvant control group. **(B)** The concentrations of IL-10 in sera were 53.9, 101.5, and 28.8 pg/ml in Adjuvant-vaccinated control group ($n = 5$) and 64.4, 193.2, and 40.9 pg/ml in r*Bm*SP44 vaccinated group ($n = 5$), respectively. Results are presented as the mean ± SEM. The asterisks (*) indicate that the levels of IL-10 by immunized mice were significantly higher (*$P < 0.05$) than those of the adjuvant control group. **(C)** The concentrations of TNF-α in sera were 57.2, 51.9, and 57.9 pg/ml in Adjuvant-vaccinated control group ($n = 5$) and 60.3, 62.3, and 68.5 pg/ml in r*Bm*SP44 vaccinated group ($n = 5$), respectively. Results are presented as the mean ± SEM. The data represent two individual experiments. All the levels of cytokine in sera were measured by ELISA kits.

the early and acute stages of infection, while IL-10, IL-4, IL-5, and IL-6 may involve in chronic and low parasitemia stages of infections (41–45). Our current study suggested that immunization with r*Bm*SP44 elicits IFN-γ, TNF-α, and IL-10 expression and results in a Th1/Th2 mixed humoral and cellular immune response, which may contribute to protect mice from *Babesia* infection.

The clinical manifestations of *Babesia* infections are diverse and the declining concentration of hemoglobin induced by babesiosis is considered to be a major feature of the infection (42). In our current study, the concentration of hemoglobin in the immunization group was slightly higher than that in controls, while changes in weight and temperature were not discernible. We only observed the condition within 2 weeks after infection, and the increment of temperature is not only associated directly to the concentration of parasites but also related to the immune status of the hosts.

In conclusion, our study indicated that *Bm*SP44 is a secreted protein and localized principally in the cytoplasm of the parasites. *Bm*SP44 can elicit immune responses in a mouse model of Babesiosis and can be recognized by immune serum from different stages of infection. Both active and passive immunization with r*Bm*SP44 (or antisera) can afford protection to mice against *Babesia* infection. Thus, *Bm*SP44 can be used as both a diagnosis marker and a vaccine candidate to combat Babesiosis.

DATA AVAILABILITY STATEMENT

The datasets generated for this study can be found in the Protein ID: CCF73510.

ETHICS STATEMENT

All animal procedures were conducted in compliance with the principle for the Care and Use of Medical Laboratory Animals (Ministry of Health, People's Republic of China) and approved by the Institutional Animal Care and Use Committee (IACUC) of Soochow University for the use of laboratory animals (Permit Number: ECSU-201800091).

AUTHOR CONTRIBUTIONS

XZ and JD conceived the study, collected and analyzed the data, and drafted the manuscript. HW, YW, and JH carried out the whole experiments and revised the manuscript. BX and JH conceived the project and provided technical support for data collection and analysis. All authors read and approved the final manuscript. Written consent to publish was obtained.

FUNDING

This research was supported by the National Natural Science Foundation of China (Grant Nos. 81601784, 81971917), and the Priority Academic Program Development of Jiangsu Higher Education Institutions. This project was also supported by the Key Laboratory of Parasite and Vector Biology, Ministry of Health with Grant No. WSBKFKT-201710.

ACKNOWLEDGMENTS

We would like to thank Dr. Kezhen Wang, Wen Pan, and Zhenyu Song for technical assistance.

SUPPLEMENTARY MATERIAL

The Supplementary Material for this article can be found online at: https://www.frontiersin.org/articles/10.3389/fimmu.2020.01437/full#supplementary-material

Supplementary File 1 | The amino acid sequences of *Bm*SP44.

Figure S1 | Predicated signal peptide and antigenic epitopes of *Bm*SP44 **(A)** Signal peptide was detected in *Bm*SP44 based on SignalP4.1 software; **(B)** Antigenic epitopes of *Bm*SP44 were predicted by ABCPred bioinformatic serves.

Figure S2 | Quantification of the antibody titers in sera of rabbits immunized with r*Bm*SP44. Rabbits immunized with 100 μg **(A)** or 500 μg **(B)** r*Bm*SP44, respectively and the antibody tiers were examined by ELISA. Normal rabbit serum was served as a control.

REFERENCES

1. Vannier E, Krause PJ. Human babesiosis. *N Engl J Med.* (2012) 366:2397–407. doi: 10.1056/NEJMra1202018
2. Zhou X, Xia S, Huang JL, Tambo E, Zhuge HX, Zhou XN. Human babesiosis, an emerging tick-borne disease in the People's Republic of China. *Parasite Vectors.* (2014) 7:509. doi: 10.1186/PREACCEPT-1503099832120211
3. Vannier E, Krause PJ. Babesiosis in China, an emerging threat. *Lancet Infect Dis.* (2015) 15:137–9. doi: 10.1016/S1473-3099147 1062-X
4. Asensi V, González LM, Fernández-Suárez J, Sevilla E, Navascués RÁ, Suárez ML, et al. A fatal case of *Babesia divergens* infection in Northwestern Spain. *Ticks Tick Borne Dis.* (2018) 9:730–4. doi: 10.1016/j.ttbdis.2018.02.018

5. Chen Z, Li H, Gao X, Bian A, Yan H, Kong D, et al. Human Babesiosis in China: a systematic review. *Parasitol Res.* (2019) 118:1103–12. doi: 10.1007/s00436-019-06250-9
6. Wormser GP, Prasad A, Neuhaus E, Joshi S, Nowakowski J, Nelson J, et al. Emergence of resistance to azithromycin-atovaquone in immunocompromised patients with *Babesia microti* infection. *Clin Infect Dis.* (2010) 50:381–6. doi: 10.1086/649859
7. Krause PJ. Human babesiosis. *Int J Parasitol.* (2019) 49:165–74. doi: 10.1016/j.ijpara.2018.11.007
8. Morahan BJ, Wang L, Coppel RL. No TRAP, no invasion. *Trends Parasitol.* (2009) 25:77–84. doi: 10.1016/j.pt.2008.11.004
9. Moreau E, Bonsergent C, Al Dybiat I, Gonzalez LM, Lobo CA, Montero E, et al. *Babesia divergens* apical membrane antigen-1 (*Bd*AMA-1): a poorly polymorphic protein that induces a weak and late immune response. *Exp Parasitol.* (2015) 155:40–5. doi: 10.1016/j.exppara.2015.04.024
10. Ord RL, Rodriguez M, Cursino-Santos JR, Hong H, Singh M, Gray J, et al. Identification and characterization of the rhoptry neck protein 2 in *Babesia divergens* and *B. microti*. *Infect Immun.* (2016) 84:1574–84. doi: 10.1128/IAI.00107-16
11. Wang G, Efstratiou A, Adjou Moumouni PF, Liu M, Jirapattharasate C, Guo H, et al. Expression of truncated *Babesia microti* apical membrane protein 1 and rhoptry neck protein 2 and evaluation of their protective efficacy. *Exp Parasitol.* (2017) 172:5–11. doi: 10.1016/j.exppara.2016.11.001
12. Xu B, Liu XF, Cai YC, Huang JL, Zhang RX, Chen JH, et al. Screening for biomarkers reflecting the progression of *Babesia microti* infection. *Parasite Vectors.* (2018) 11:379. doi: 10.1186/s13071-018-2951-0
13. Nathaly Wieser S, Schnittger L, Florin-Christensen M, Delbecq S, Schetters T. Vaccination against babesiosis using recombinant GPI-anchored proteins. *Int J Parasitol.* (2019) 49:175–81. doi: 10.1016/j.ijpara.2018.12.002
14. Nyalwidhe J, Maier UG, Lingelbach K. Intracellular parasitism: cell biological adaptations of parasitic protozoa to a life inside cells. *Zoology.* (2003) 106:341–8. doi: 10.1078/0944-2006-00127
15. Piña-Vázquez C, Reyes-López M, Ortíz-Estrada G, de la Garza M, Serrano-Luna J. Host-parasite interaction: parasite-derived and -induced proteases that degrade human extracellular matrix. *J Parasitol Res.* (2012) 2012:748206. doi: 10.1155/2012/748206
16. Lobo CA, Rodriguez,M, Cursino-Santos JR. *Babesia* and red cell invasion. *Curr Opin Hematol.* (2012) 19:170–5. doi: 10.1097/MOH.0b013e328352245a
17. Parker ML, Penarete-Vargas DM, Hamilton PT, Guérin A, Dubey JP, Perlman SJ, et al. Dissecting the interface between apicomplexan parasite and host cell: Insights from a divergent AMA-RON2 pair. *Proc Natl Acad Sci USA.* (2016) 113:398–403. doi: 10.1073/pnas.1515898113
18. Frolich S, Entzeroth R, Wallach M. Comparison of protective immune responses to apicomplexan parasites. *J Parasitol Res.* (2012) 2012:852591. doi: 10.1155/2012/852591
19. Man S, Fu Y, Guan Y, Feng M, Qiao K, Li X, et al. Evaluation of a major surface antigen of *Babesia microti* merozoites as a vaccine candidate against *Babesia* infection. *Front Microbiol.* (2017) 8:2545. doi: 10.3389/fmicb.2017.02545
20. Rodríguez-Galán A, Salman AM, Bowyer G, Collins KA, Longley RJ, Brod F, et al. An *in vitro* assay to measure antibody-mediated inhibition of *P. berghei* sporozoite invasion against *P falciparum* antigens. *Sci Rep.* (2017) 7:17011. doi: 10.1038/s41598-017-17274-5
21. Hidalgo-Ruiz M, Suarez CE, Mercado-Uriostegui MA, Hernandez-Ortiz R, Ramos JA, Galindo-Velasco E, et al. *Babesi*a *bovis* RON2 contains conserved B-cell epitopes that induce an invasion-blocking humoral immune response in immunized cattle. *Parasite Vectors.* (2018) 11:575. doi: 10.1186/s13071-018-3164-2
22. Zhou X, Huang JL, Shen HM, Xu B, Chen JH, Zhou XN. Immunomics analysis of *Babesia microti* protein markers by high-throughput screening assay. *Ticks Tick Borne Dis.* (2018) 9:1468–74. doi: 10.1016/j.ttbdis.2018.07.004
23. Luo Y, Jia H, Terkawi MA, Goo YK, Kawano S, Ooka H, et al. Identification and characterization of a novel secreted antigen 1 of *Babesia microti* and evaluation of its potential use in enzyme-linked immunosorbent assay and immunochromatographic test. *Parasitol Int.* (2011) 60:119–25. doi: 10.1016/j.parint.2010.11.001
24. Cornillot E, Hadj-Kaddour K, Dassouli A, Noel B, Ranwez V, Vacherie B, et al. Sequencing of the smallest Apicomplexan genome from the human pathogen *Babesia microti*. *Nucleic Acids Res.* (2012) 40:9102–14. doi: 10.1093/nar/gks700
25. Xu X, Zhang Y, Lin D, Zhang J, Xu J, Liu YM, et al. Serodiagnosis of *Schistosoma japonicum* infection: genome-wide identification of a protein marker, and assessment of its diagnostic validity in a field study in China. *Lancet Infect Dis.* (2014) 14:489–97. doi: 10.1016/S1473-30991470067-2
26. Carmona SJ, Nielsen M, Schafer-Nielsen C, Mucci J, Altcheh J, Balouz V, et al. Towards high-throughput immunomics for infectious diseases: use of next-generation peptide microarrays for rapid discovery and mapping of antigenic determinants. *Mol Cell Proteomics.* (2015) 14:1871–84. doi: 10.1074/mcp.M114.045906
27. Cornillot E, Dassouli A, Pachikara N, Lawres L, Renard I, Francois C, et al. A targeted immunomic approach identifies diagnostic antigens in the human pathogen *Babesia microti*. *Transfusion.* (2016) 56:2085–99. doi: 10.1111/trf.13640
28. Silva JC, Cornillot E, McCracken C, Usmani-Brown S, Dwivedi A, Ifeonu OO, et al. Genome-wide diversity and gene expression profiling of *Babesia microti* isolates identify polymorphic genes that mediate host-pathogen interactions. *Sci Rep.* (2016) 6:35284. doi: 10.1038/srep35284
29. Elton CM, Rodriguez M, Ben Mamoun C, Lobo CA, Wright GJ. A library of recombinant *Babesia microti* cell surface and secreted proteins for diagnostics discovery and reverse vaccinology. *Int J Parasitol.* (2019) 49:115–25. doi: 10.1016/j.ijpara.2018.10.003
30. Magni R, Luchini A, Liotta L, Molestina RE. Analysis of the *Babesia microti* proteome in infected red blood cells by a combination of nanotechnology and mass spectrometry. *Int J Parasitol.* (2019) 49:139–44. doi: 10.1016/j.ijpara.2018.08.004
31. Jia H, Terkawi MA, Aboge GO, Goo YK, Ma L, Zhou J, et al. Identification of secreted antigen 3 from *Babesia gibsoni*. *Clin Vaccine Immunol.* (2009) 16:944–8. doi: 10.1128/CVI.00087-09
32. Goo YK, Aboge GO, Terkawi MA, Jia H, Yamagishi J, Sunaga F, et al. Four promising antigens, *Bg*P32, *Bg*P45, *Bg*P47, and *Bg*P50, for serodiagnosis of *Babesia gibsoni* infection were classified as B. *gibsoni* merozoite surface protein family. *Parasitol Int.* (2012) 61:364–8. doi: 10.1016/j.parint.2011.11.007
33. Zhan X, Yu L, An X, Liu Q, Li M, Nie Z, et al. Evaluation of *Babesia gibsoni* GPI-anchored protein 47 (BgGPI47-WH) as a potential diagnostic antigen by enzyme-linked immunosorbent assay. *Front Vet Sci.* (2019) 6:333. doi: 10.3389/fvets.2019.00333
34. Lubin AS, Snydman DR, Miller KB. Persistent babesiosis in a stem cell transplant recipient. *Leuk Res.* (2011) 35:e77–8. doi: 10.1016/j.leukres.2010.11.029
35. Szymczak J, Kozłowska J, Doligalska M. Evaluation of inhibitory effect of redox-active antimalarial drug against *Babesia microti* in mice. *Ann Parasitol.* (2017) 63:223–7. doi: 10.17420/ap6303.109
36. Vilches-Moure JG, Ramos-Vara JA. Comparison of rabbit monoclonal and mouse monoclonal antibodies in immunohistochemistry in canine tissues. *J Vet Diagn Invest.* (2005) 17:346–50. doi: 10.1177/104063870501700407
37. Seeber S, Ros F, Thorey I, Tiefenthaler G, Kaluza K, Lifke V, et al. A robust high throughput platform to generate functional recombinant monoclonal antibodies using rabbit B cells from peripheral blood. *PLoS ONE.* (2014) 9:e86184. doi: 10.1371/journal.pone.0086184
38. Terkawi MA, Aboge G, Jia H, Goo H, Ooka YK, Yamagishi J, et al. Molecular and immunological characterization of *Babesia gibsoni* and *Babesia microti* heat shock protein-70. *Parasite Immunol.* (2009) 31:328–40. doi: 10.1111/j.1365-3024.2009.01109.x
39. Munkhjargal T, Aboge GO, Ueno A, Aboulaila M, Yokoyama N, Igarashi I. Identification and characterization of profilin antigen among *Babesia* species as a common vaccine candidate against babesiosis. *Exp Parasitol.* (2016) 166:29–36. doi: 10.1016/j.exppara.2016.03.024
40. Renia L, Goh YS. Malaria Parasites: The Great Escape. *Front Immunol.* (2016) 7:463. doi: 10.3389/fimmu.2016.00463
41. Chen D, Copeman DB, Burnell J, Hutchinson GW. Helper T cell and antibody responses to infection of CBA mice with *Babesia microti*. *Parasite Immunol.* (2000) 22:81–8. doi: 10.1046/j.1365-3024.2000.00279.x
42. Brown AL, Shiel RE, Irwin PJ. Clinical, haematological, cytokine and acute phase protein changes during experimental *Babesia gibsoni* infection of beagle puppies. *Exp Parasitol.* (2015) 157:185–96. doi: 10.1016/j.exppara.2015.08.002

43. Roussilhon C, Bang G, Bastaert F, Solhonne B, Garcia-Verdugo I, Peronet R, et al. The antimicrobial molecule trappin-2/elafin has anti-parasitic properties and is protective *in vivo* in a murine model of cerebral malaria. *Sci Rep.* (2017) 7:42243. doi: 10.1038/srep42243
44. Djokic V, Akoolo L, Parveen N. *Babesia microti* infection changes host spleen architecture and is cleared by a Th1 immune response. *Front Microbiol.* (2018) 9:85. doi: 10.3389/fmicb.2018.00085
45. Zhou X, Wang H, Xue JB, Xia S, Zhou XN. [Epidemic and research progress of babesiosis]. *Zhongguo Xue Xi Chong Bing Fang Zhi Za Zhi.* (2019) 31:63–70. doi: 10.16250/j.32.1374.2018293

Conflict of Interest: The authors declare that the research was conducted in the absence of any commercial or financial relationships that could be construed as a potential conflict of interest.

frontiers in Immunology

ORIGINAL RESEARCH
published: 11 September 2020
doi: 10.3389/fimmu.2020.01801

Attenuated *P. falciparum* Parasite Shows Cytokine Variations in Humanized Mice

Lei-lei Zhang[1], *Jin-Long Li*[2], *Ming-Xin Ji*[1], *Dan Tian*[1], *Li-Yan Wang*[3], *Chen Chen*[3] *and Miao Tian*[4]*

[1] Department of Anesthesiology, The Second Hospital of Jilin University, Changchun, China, [2] Department of Gastrointestinal Surgery, The Second Hospital of Jilin University, Changchun, China, [3] Department of Operating Room, The Second Hospital of Jilin University, Changchun, China, [4] Department of Gynecology and Obstetrics, The Second Hospital of Jilin University, Changchun, China

A recently developed humanized mouse has been used to assess the immune response evoked against the isolated attenuated C9 parasite clone (C9-M; carrying a single insertion disrupting the open reading frame (ORF) of PF3D7_1305500) of *Plasmodium falciparum*. Significant human RBC engraftment was achieved by ameliorating the residual non-adaptive immune response using clodronate-loaded liposome treatment. Controlled reactive professional phagocytic leukocytes in immunodeficient mice allowed for sizeable human blood chimerism and injected huRBCs acted as *bona fide* host cells for *P. falciparum*. huRBC-reconstituted immunodeficient mice received infectious challenge with attenuated *P. falciparum* C9 parasite mutants (C9-M), complemented (C9-C), and wild type (NF54) progenitors to study the role of immune effectors in the clearance of the parasite from mouse circulation. C9-M and NF54 parasites grew and developed in the huRBC-reconstituted humanized NSG mice. Further, the presence of mutant parasites in deep-seated tissues suggests the escape of parasites from the host's immune responses and thus extended the survival of the parasite. Our results suggest an evasion mechanism that may have been employed by the parasite to survive the mouse's residual non-adaptive immune responses. Collectively, our data suggest that huRBCs reconstituted NSG mice infected with attenuated *P. falciparum* is a valuable tool to explore the role of C9 mutation in the growth and survival of parasite mutants and their response to the host's immune responses. This mouse might help in identifying novel chemotherapeutic targets to develop new anti-malarial drugs.

Keywords: humanized mice, clodronate-loaded liposomes, NOD/SCID/IL-2rg^{-}/ (NSG) growth mutants, TK/NOG, cytokine, PF3D7_1305500, C9 parasite mutants (C9-M), complemented parasites (C9-C)

OPEN ACCESS

Edited by:
Xiao-Nong Zhou, National Institute of Parasitic Diseases, China

Reviewed by:
Gaurav Gupta, NIIT University, India
Sunil Joshi, University of Miami, United States

****Correspondence:***
Miao Tian
tmiaolook@zoho.com.cn

Specialty section:
This article was submitted to Microbial Immunology, a section of the journal Frontiers in Immunology

Received: *24 April 2020*
Accepted: *06 July 2020*
Published: *11 September 2020*

Citation:
Zhang L-l, Li J-L, Ji M-X, Tian D, Wang L-Y, Chen C and Tian M (2020) Attenuated P. falciparum Parasite Shows Cytokine Variations in Humanized Mice. Front. Immunol. 11:1801. doi: 10.3389/fimmu.2020.01801

INTRODUCTION

The human malaria parasite was accountable for 4,45,000 deaths in the 2016 (1). The *in vitro* findings do not replicate the *in vivo* findings and therefore a laboratory animal model is indeed needed. However, the study of human malaria parasites in animal models is severely limited by ethical and technical constraints, since only a few primate species have been found to be receptive to *P. falciparum* infection (2–4). Currently, the majority of *in vivo* investigations to understand malaria biology are dependent upon rodent malaria species (*P. berghei* and *P. yoelii*) which are

used as surrogates to study human malaria (3–6). Therefore, humanized mice capable of harboring the human malaria infection are urgently needed to understand the parasite biology. A human blood chimeric mouse could serve to harmonize *in vitro P. falciparum* cultivation and *in vivo* studies carried out in rodent animal models. Introduction of several mouse strains with genetic immune deficiencies has greatly benefited the development of a small laboratory animal model (7–15) to study the asexual blood stage infection of *P. falciparum*. Recently, an immunodeficient mouse (16) was reconstituted with uninfected and infected huRBCs. This NSG mouse, depleted with γ-chain of the IL-2 receptor, has been shown to better tolerate a variety of human transplanted cells (17–24). The reduction in the residual innate immune effectors (mainly cells of monocytes and macrophages lineage) and co-administration of huRBCs supplied with decomplemented human serum through an intravenous route led to the development of a reproducible humanized mouse. The disruption of PF3D7_1305500 in C9-M parasites showed 50% attenuation as compared to the wild type parasites (NF54) (25). Therefore, C9-M and C9-C (Rescued phenotype of wild-type growth by genetic complementation) parasites (26) showed the attenuation in PF13_0027 knock-out parasites (C9-M) growth, which in turn resulted in the irregular cell cycle. The late entry into the S/M phase coincides with the timing for the peak expression of PF13_0027, suggesting that the deficiency in the mutant cycle can be correlated with the gene expression pattern (26).

Low parasitemia of the C9-M parasite in mouse circulation and extended survival of the C9-M parasite in deep-seated tissues suggests that the parasite may have employed a mechanism to escape the host's residual immunity. This parasitologically altered behavior of C9-M parasites was confirmed by the serum estimation of pro-inflammatory cytokines from the C9-M infected mice when compared to the NF54 and C9-C parasites.

Thus, the present study was designed to create an improved understanding of host–parasite interactions to bridge the gap between *in vivo* and clinical studies. The growth mutant (C9-M) parasites grafted in humanized mice showed nearly similar parasitemia patterns to that of NF54. Further, the C9-M parasite seems to have employed a mechanism to evade the host's immune responses and resides/sequesters in the deep-seated tissues. Our study showed the importance of human RBC reconstituted NSG mouse model to study the behavior of generated attenuated and complement parasites (25, 27). This humanized mouse may prove to be an important tool to study the immune mechanism(s) employed by the parasite to develop an indepth understanding on the sequestration-like phenomenon of human malaria parasite, *P. falciparum*. In brief, the present study showed the variation in the cytokines and parasitologically altered behavior of C9-M parasite upon engrafted in huRBC reconstituted NSG mice for its extended survival.

Abbreviations: ORF, open reading frame; Clo-lip, Clodronate-loaded liposomes; NSG, NOD/SCID/IL-2rg$^{-/}$; huRBC, Human Red Blood Cells; TK/NOG, Thymidine kinase-NOD/SCID/IL-2rg^{-}/; C9 mutant, PF3D7_1305500; MCV, mean corpuscular volume; hDHFR, human dihydrofolate reeducates; BSD, Blasticidin.

MATERIALS AND METHODS

Animal Ethics Committee Approval

All animal procedures were carried out in compliance with The Second Hospital of Jilin University, Changchun. The procedures were reviewed and approved by The Second Hospital of Jilin University, Changchun, China.

Mice

Four- to 6-week-old male and female NOD/SCIDIL-2Rγ$^{-/-}$ (NSG/NOG) mice were procured from Jackson Laboratory, USA. The transgenic thymidine kinase-NOG (TK/NOG) strain was procured from Taconic, USA. The immunodeficient/transgenic mice were housed in sterile isolators and supplied with autoclaved tap water with a γ-irradiated pelleted diet *ad libitum*. Animals were manipulated under pathogen free conditions using a laminar flow-hood cabinet. One hundred and ten animals were used in the study. Six animals were allocated for each experimental group, except for the giemsa staining assay wherein four animals were used. Animal allocation was randomized, and mice receiving treatment were monitored daily and weighed three times (Monday, Wednesday, Fridays) per week. *P. falciparum* infected mice were treated with the analgesic ketoprofen to alleviate pain caused by the malaria infection.

Human Erythrocytes

The huRBCs are the *bona fide* host cells for the development of *P. falciparum* in *in vitro* cultivation and huRBCs reconstituted mice. The packed huRBCs were provided by the Interstate Blood Bank (Chinese blood bank). Blood was taken from donors with no history of malaria. The huRBCs were suspended in SAGM (Saline, Adenine, Glucose, Mannitol solution) and stored at 4°C for a maximum of 2 weeks. Before injection, huRBCs were washed three times in RPMI-1640 medium (Gibco-BRL, Grand Island, New York), supplemented with 1 mg of hypoxanthine per liter (Sigma-Aldrich, St. Louis, Missouri), and warmed for 10 min at 37°C. Blood samples drawn from mice were used to determine the percentage of huRBC in mice's peripheral blood at regular intervals by flow cytometer (Accuri cytometers) using FITC labeled anti-human glycophorin antibody (ebiosciences, USA).

P. falciparum Parasites Culture

C9 mutant, complement parasites (Gene complementation of the C9 mutant to rescue the wild-type phenotype) and wild type *P. falciparum* line (NF54) were employed in the study. C9-M and C9-C parasites were generated by the interstional mutagenesis by others (26). *P. falciparum* strains were cryopreserved using the glycerol/sorbitol method as described elsewhere (28). The parasites were cultured *in vitro* at 5% hematocrit, at 37°C with 5% CO_2, using RPMI-1640 medium (Gibco/BRL), 35 mM HEPES (Sigma), 0.25% $NaHCO_3$, 0.5% albumax II (Gibco/BRL), and 0.01 mg/ml gentamicin.

In vivo Replication of *P. falciparum* in the NSG-IV Model

P. falciparum was maintained in huRBCs reconstituted NSG (immunocompromised) mice undergoing additional modulation

of innate immune-defenses using the clodronate-containing liposomes, as described earlier (16). huRBC administered and intravenously infected humanized mouse is referred to "NSG-IV model." The proportion of huRBCs in the mouse's blood was measured at 3-day intervals until the end of the study by the flow cytometer (Accuri C6 flow cytometry, BD Biosciences, USA) using FITC labeled anti-human glycophorin monoclonal antibody (ebiosciences, CA, USA). Seventy to Ninety percentage of circulating huRBCs were quantified in the mice circulation. Mice were intravenously inoculated with 300 μl asynchronous *P. falciparum* culture maintaining 1% parasitemia. Following *P. falciparum* infection, thin blood films were drawn daily from the tail vein on infected humanized mice. Parasitemia has been expressed as a percentage of all erythrocytes found in mouse periphery; the real percentage of parasitized huRBCs is higher in humanized mice, proportional to the level of chimerism, since murine erythrocytes do not receive infection but were included in counts.

Estimates of the total parasite biomass in each mouse were calculated based on the mean corpuscular volume (MCV) of mouse erythrocytes (45fL), MCV of human erythrocytes (86fL), hematocrit in the mice of 0.7, weight of NSG mice (25 grams), and a conservative estimate of 5.5 ml of blood per 100 grams of mouse weight using the following equation:

Number of infected RBCs = (0.055 ml/g) (25 g) (0.7) × (huRBC parasitemia)

[86fL + (mouse Chimerism/human Chimerism) 45fL]

Sorbitol Synchronization of *Plasmodium falciparum*

Parasite cultures at 5% parasitemia, predominantly ring stages, were synchronized to remove late stage parasites using pre-warmed (37°C) 5% sorbitol. After harvesting culture at 1600 RPM for 6 min, medium was removed and replaced with 10 volumes of pre-warmed 5% sorbitol (29). The re-suspended culture was incubated at 37°C for 15 min, and parasites were pelleted down by the centrifugation; sorbitol was then removed and replaced with fresh complete medium.

Giemsa Staining and Parasite Count

P. falciparum infected mice were euthanized to extract organs (Kidney, liver, spleen, lung, and brain). These extracted organs were perfused, and cells collected from the organs were placed on the glass slides. Briefly, cells were fixed with methanol and stained with Giemsa, and examined at 100X magnification to perform differential counts of each stage (200 parasites from each organ counted). The analysis of deep-seated organs for parasite count in NSG mice infected with C9-M and C9-C parasites was carried out.

Genotyping of Growth Attenuated (Mutant) and Complemented *P. falciparum* Parasites

The original parasites C9-M and C9-C were harvested from *in vitro* cultures as well as from humanized mouse (huRBCNSG-IV) infected with C9-M, C9-C, and wild type parasites. The specific primers (F5′ATGGTTGGTTCGCTAAACTG3′, R5′TTAATCATTCTTCTCATATACTTCAAA3′) and (F:CTTC ACTATCGCTTTGATCC, RTCGCTATCCCATAAATTACAA) were used to identify the presence of hDHFR and BSD from *in vitro* cultures and *P. falciparum*-harboring humanized mice. The genomic DNA was extracted from parasite cultures and tail snips of mice infected with *P. falciparum* strains using a DNA mini-kit (Qiagen). DNA was amplified in 20 μl reaction mixture by adopting the following PCR conditions: 1 cycle at 45°C for 30 min and 94°C for 2 min, followed by 35 cycles of 94°C for 15 s, 45°C for 30 s, and 65°C for 3 min. The amplified DNA showed the product band of 563 and 393 bp on 0.8% agarose gel of hDHFR and BSD, respectively.

Plasmodium falciparum Growth Assay

Growth assays were carried out by maintaining asynchronous cultures of *P. falciparum* wild-type and mutant parasites at 0.5–2% parasitemia in 96-well plates and diluting every 48 h for 168 h. The parasite cultures were plated in triplicate at time zero and end point of the assay, and for each time point samples were taken at every 24 h for 7 days and fixed with 0.05% glutaraldehyde after the removal of culture medium. Flow cytometer was used to estimate the parasitemia as described elsewhere (30, 31) and parasites were stained with ethidium bromide. The stained parasites were analyzed through Accuri C6 flow cytometry system (Accuri, USA). A total of 100,000 cells were counted for each sample and data were analyzed using C Flow Plus software (Accuri). Growth rate (defined as the change in parasite numbers every 24 h over a period of 7 days) analyses were performed using Microsoft Excel and (Microsoft) and SAS 9.3.

Serum Estimation of Cytokines and Chemokines

Hundred microliter blood samples were collected through the submandibular puncture of mice, and sera were stored at−80°C. Cytokines and chemokines (IL-6, MCP-1, IFNγ, TNFα, IL-12p70, and IL-10) were quantified using the BD^{TM} Cytometric Bead Array mouse inflammatory kit (BD biosciences) following the manufacturer's recommendations.

Genotyping of TK/NOG Mice by Diagnostic PCR

Transgenic offspring were genotyped and identified by PCR (annealing temperature 59°C) using HTKF1 forward primer, 5′-CACGTCTTTATCCTGGATTACG-3′ and hGHR1 reverse primer, 5′-CACTGGAGTGGCAACTTCCA-3′. The genomic DNA was extracted from tail snips by DNA mini-kit (Qiagen), and amplified in a 20 μl reaction mixture using the PCR conditions: 2 min at 94°C, then 30 cycles of 30 s at 94°C, 30 s at 59°C, and 30 s at 72°C, and finally 3 min at 72°C. The transgene DNA showed an amplified product band of 236 bp on 1% agarose gel (32).

Statistical Analysis

Each growth assay data was analyzed using C Flow Plus software (Accuri). Growth rate and statistical analysis was carried out by Student's *t*-test using Prism software (Graph Pad 5 Demo) and data was expressed as the mean ± standard deviation (S.D.) of the mean ($^{*}p < 0.05$, $^{**}p < 0.01$, and $^{***}p < 0.001$). A value of *P*

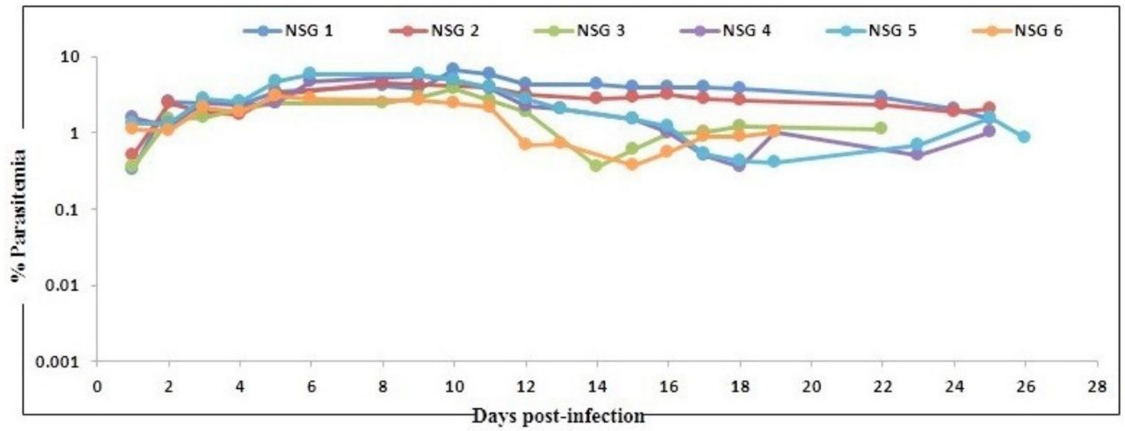

FIGURE 1 | Evolution of *P. falciparum* (NF54) parasitemia in six untreated mice. Mice were intravenously inoculated with 0.3 ml of asynchronous cultures at 1% parasitemia of *P. falciparum* on day 0. Mice were supplied with huRBC every 3 days. Parasitemia in mice was expressed as the percentage of *P. falciparum*-huRBC in the total RBC observed on thin blood smears. Data shown are from the first day of detectable parasitemia up to the day the mice were used for other malaria studies.

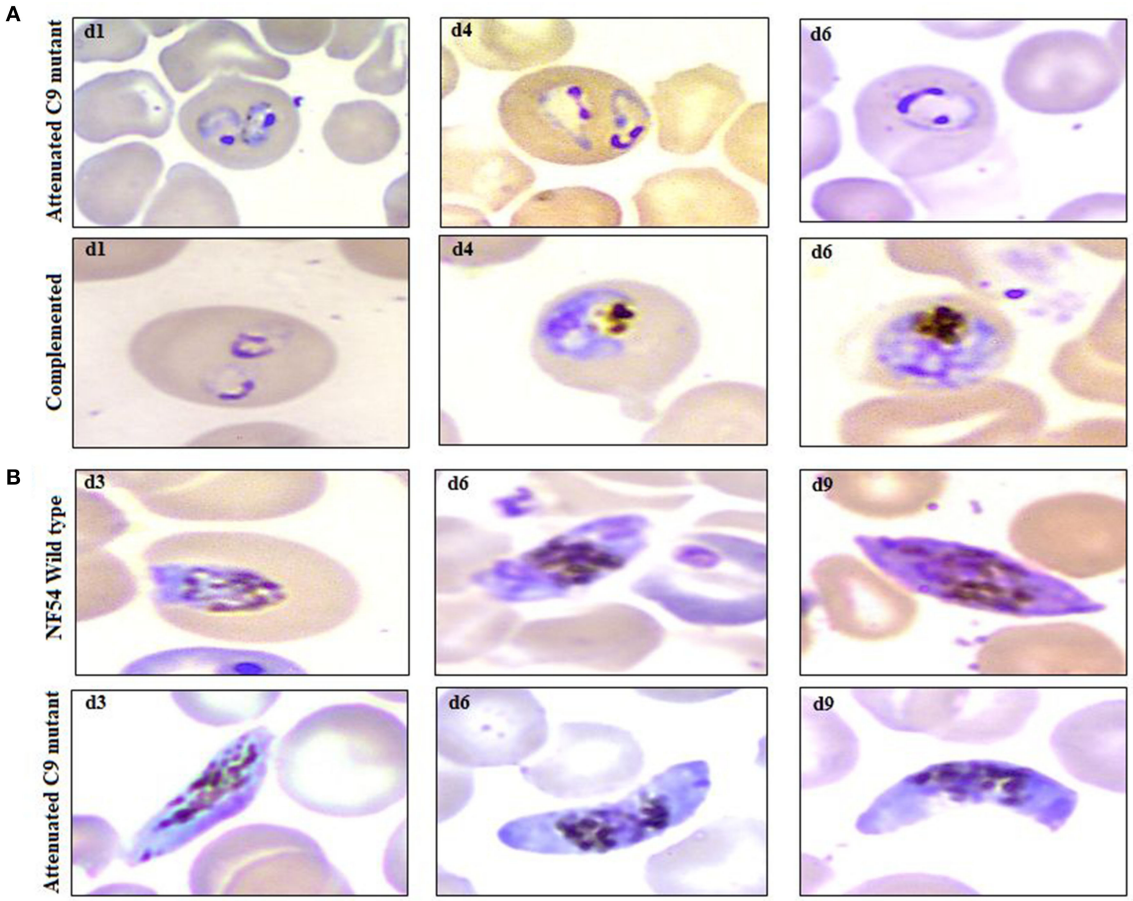

FIGURE 2 | Example of parasitemia obtained from highly attenuated C9-M and complemented C9-C parasites in humanized mice (NSG-IV), **(A)** upper row (attenuated C9 mutant) and lower row (complemented) depicts the dominance of ring stage parasites along with the presence of trophozoites with frequent poly-parasitism seen on thin blood smears drawn from NSG mice infected with C9-M and C9-Cparasites, respectively, on day 1, 4, and 6 post-infection, **(B)** occurrence of mature gametocytes (stage V) in peripheral blood of NSG mice infected with NF54 (upper row) and attenuated C9 mutant (lower row) *P. falciparum*.

< 0.05 was considered statistically significant. The evaluation of inflammatory mediators' results are presented as mean SEM from the experiment performed using three mice per group.

RESULTS

Growth and Replication of *P. falciparum* in PfhuRBC-NSG-IV Mice

In agreement with the previous findings (16), we used a slightly modified protocol for reconstituting NSG immunodeficient mice with huRBCs (PfhuRBC-NSG) for sustained *P. falciparum* growth. Experiments were performed in NSG mice using 650 μl of huRBC pellets mixed with 25% de-complemented human serum intravenously injected three times every week, and reconstituted NSG mice were infected with *P. falciparum* through an intravenous route. Codronate-loaded liposome (clo-lip) suspension was injected intraperitoneally, and clo-lip and huRBCs were administered the same day. This mouse model is called "Pf-NSG IV" model. With this IV protocol 100% of NSG mice, as reported earlier (16), were seen parasitized by day 1 post-inoculation. As shown in **Figure 1**, low to moderate levels of parasitemia were obtained. In fact, parasites could persist as long as un-infected huRBC were co-administered with human serum along with the immunomodulatory agent, clo-lip. Furthermore, despite individual variations in the maximal parasitemia reached, the parasitemia observed were found stable to determine *in vivo* effect of C9-M *P. falciparum* parasites. Thus, we sought to better understand the individual variations in the parasitemia in mouse circulation which could be explained due to the varying levels of blood chimerism. However, significant ($p < 0.05$) numbers of huRBCs in mouse periphery supported rapid and optimum growth of *P. falciparum* (**Figure 1**) with abundant and healthy-looking parasites showing frequent poly-parasitism of huRBC (**Figure 2A**).

Three mice for each group were infected with NF54 (**Figure 3A**), C9-M (**Figure 3B**), and C9-C (**Figure 3C**) parasites. Interestingly, all NSG-IV mice showed 100% infection and supported the replication of all *P. falciparum* strains employed (**Figure 3**). However, we did not see significant ($p < 0.05$) differences in parasite growth in NF54, C9-M, and C9-C parasites in these humanized NSG mice. The short-term human blood chimerism in mouse circulation led to the clearance of NF54 infected erythrocytes on day 13 and 14 post-infection (**Figure 3A**). However, sufficient numbers of circulating huRBCs allowed C9-M (**Figure 3B**) and C9-C parasites (**Figure 3C**) to stay in the periphery until day 22 post-infection. Low standing parasitemia seen with C9-M is attributed to the knock-out of PF3D7_1305500, which may have modulated the host immune response due to the higher secretion of immunoregulatory and anti-inflammatory cytokine, IL-10.

Humanized Mice Support the Development of Attenuated C9-M *P. falciparum*

Based on the successful development and replication of different strains of *P. falciparum* (NF54, C9-M, and C9-C) (**Figure 3**), we next carried out the growth assays to detect the effect of engraftment on the attenuation attributes of mutant parasites. Therefore, a library of unique mutant clones was created from a laboratory line of *P. falciparum* (NF54) using random insertional mutagenesis with a *piggyBac* transposon (33). Fifty percentage attenuation in the *in vitro* culture of intra-erythrocytic C9-M mutant parasites was seen and compared with the wild type (NF54) parasites (**Figure 4A**). The mutation responsible for attenuation in the growth of C9-M parasite *in vitro* slowed down the parasite growth and replication. As with others (26), the mean number of calculated merozoites remained the same as those seen with the parent parasites (NF54). Interestingly, C9-M parasite did not retain its phenotype when grafted in huRBC-reconstituted NSG mice. Also, we did not see significant differences in the parasitemia pattern of C9-M and wild type (**Figures 3A,B**) parasites, or in their morphology (**Figure 2A**). Growth assays were carried out on the blood drawn from the mice harboring C9-M and NF54 parasites (**Figure 4B**). The growth phenotype (50% growth attenuation) of C9-M parasite in parasite culture and grafted in huRBC-reconstituted humanized mice exhibited a different pattern. The humanized NSG mice supported *P. falciparum* infection and allowed for replication of the C9-M parasite. These attenuated growth mutants survived the residual innate immune responses of the host. Therefore, humanized mice will be useful to study the genotypic and phenotypic characteristics of mutant parasites.

In vitro and *in vivo* Typing of C9-Mutant and C9-Complement Parasite

We did not see much difference in the growth pattern of wild type and mutant (C9-M) parasite when growth assays were conducted on parasites from culture and grafted humanized mice. Therefore, we decided to characterize both mutant and complement parasite strains. Parasite strains grafted in humanized mice (Pf-huRBC/NSG-IV) were typed for the attenuated C9-M and C9-C phenotype by PCR (**Figure 5**). Both strains were thawed, cultured, and kept under Blasticidin (BSD) pressure *in vitro* (**Figure 5B**), and the presence of human-DHFR and BSD selection markers were confirmed with the genomic DNA extracted from C9-M and C9-C parasites from culture and *P. falciparum* infected humanized NSG mice (**Figures 5A,B**). hDHFR (**Figure 5A**) and BSD (**Figure 5B**) showed an amplified product band of 536 and 393 bp of DNA extracted from C9-M and C9-C parasites from culture and mice harboring the parasite, respectively.

Putative Phosphatase (PF3D7_1305500) Knock-Down Is Correlated With Cytokine Variations in *P. falciparum* Infected Humanized NSG Mice

The idea of the present work is to validate the role of knock-down effect of ribosomal binding protein (PF3D7_1305500) in huRBCs reconstituted humanized mice. Following the confirmation of the development and replication of typed mutant (PF3D7_1305500) parasite in humanized mice, upon

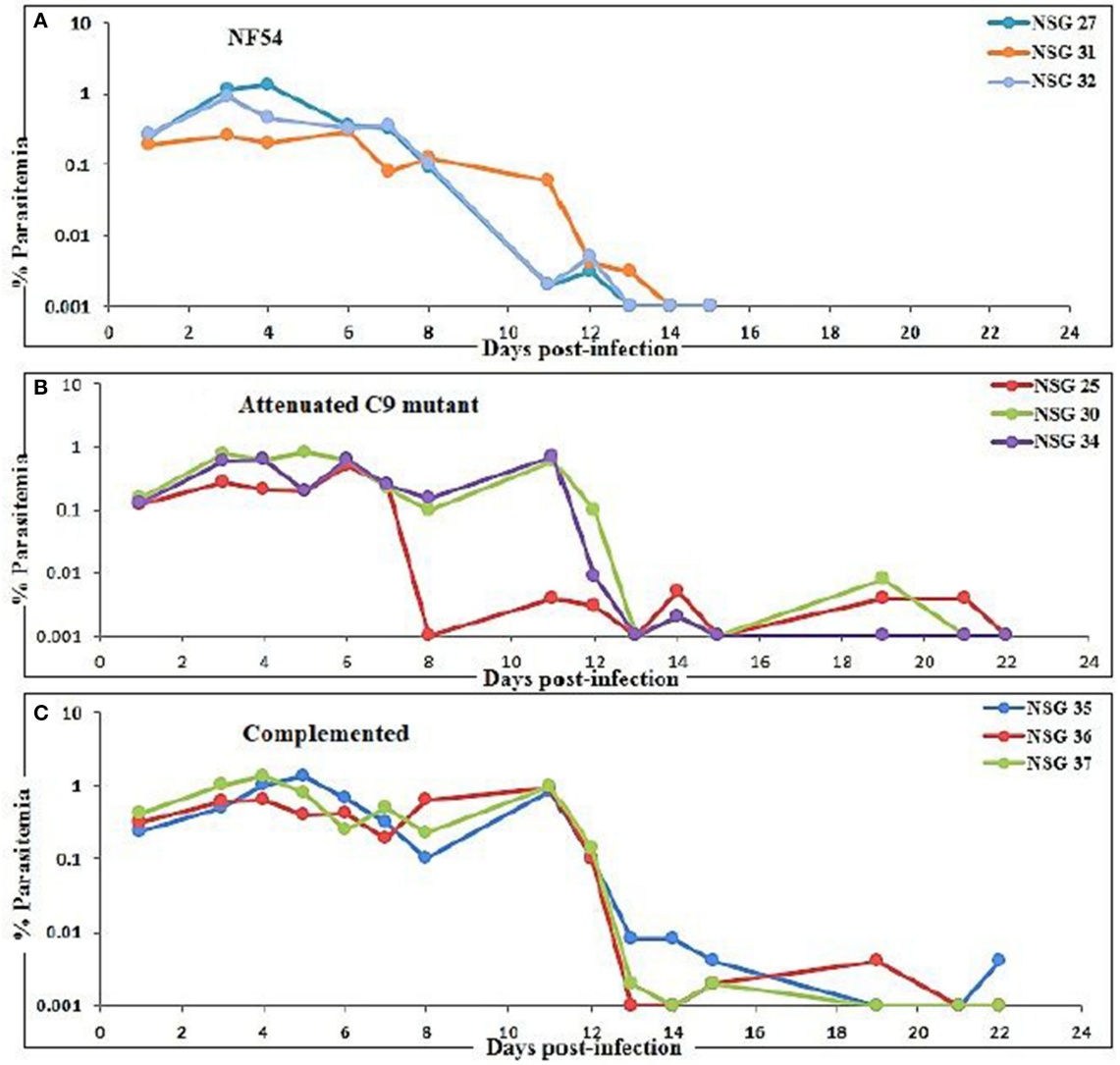

FIGURE 3 | Evolution of *P. falciparum* parasitemia of mice treated with **(A)** NF54 (wild type), **(B)** attenuated C9 mutant, and **(C)** complemented *P. falciparum*. All mice were infected through an intravenous route with 0.3 ml of asynchronous cultures at 1% parasitemia of NF54, C9 mutant (C9-M), and complemented parasite (C9-C) of *P. falciparum*. The PfNSG-IV mice supported the grafting of highly attenuated parasites without needing the adaptation of the parasite to the host.

injection with 650 μl of huRBC, our results showed the significant ($p < 0.05$) human blood chimerism (proportion of huRBC in mouse's periphery) ranging from 60 to 70% of total erythrocytes. This blood-chimerism was stable over a month and supported rapid and optimal growth of *P. falciparum* (**Figures 1**, **3**) with abundant and very healthy-looking parasites (**Figure 2A**). Total hematocrit in mouse's periphery showed an average of 55–60% of huRBCs in this protocol (data not shown).

Furthermore, the use of a lower dose (450 μl) of huRBC showed an initial establishment of human blood chimerism followed by a decrease, which is most likely due to the inflammation induced by parasites (16). Therefore, we used human RBCs reconstituted NSG-IV mice to analyze inflammatory markers to investigate the role of PF3D7_1305500 RNA binding protein in the intra-erythrocytic development of the parasite. Three mice in each group were reconstituted with huRBCs, given the infectious challenge with NF54, C9-M, and C9-C parasites, and sera were collected at different time-points. The raised levels of IL-6 (632 ± 526Vs 17 ± 8 pg/ml, day 15 post-infection) and IL-10 (88 ± 60 vs. 30 ± 27.41 pg/ml, day 12 post-infection) were quantified in the mice infected with C9-M parasites and compared with NF54 wild type *P. falciparum* (**Figure 6**). The higher inflammation mounted by the host against the parasite infection is correlated with the clearance of infected and uninfected huRBC from the mouse's periphery. A greater increase in the chemokine MCP-1 (1129 ± 435 vs. 277 ± 16 pg/ml day 9 PI) in NF54 infected mice and the level

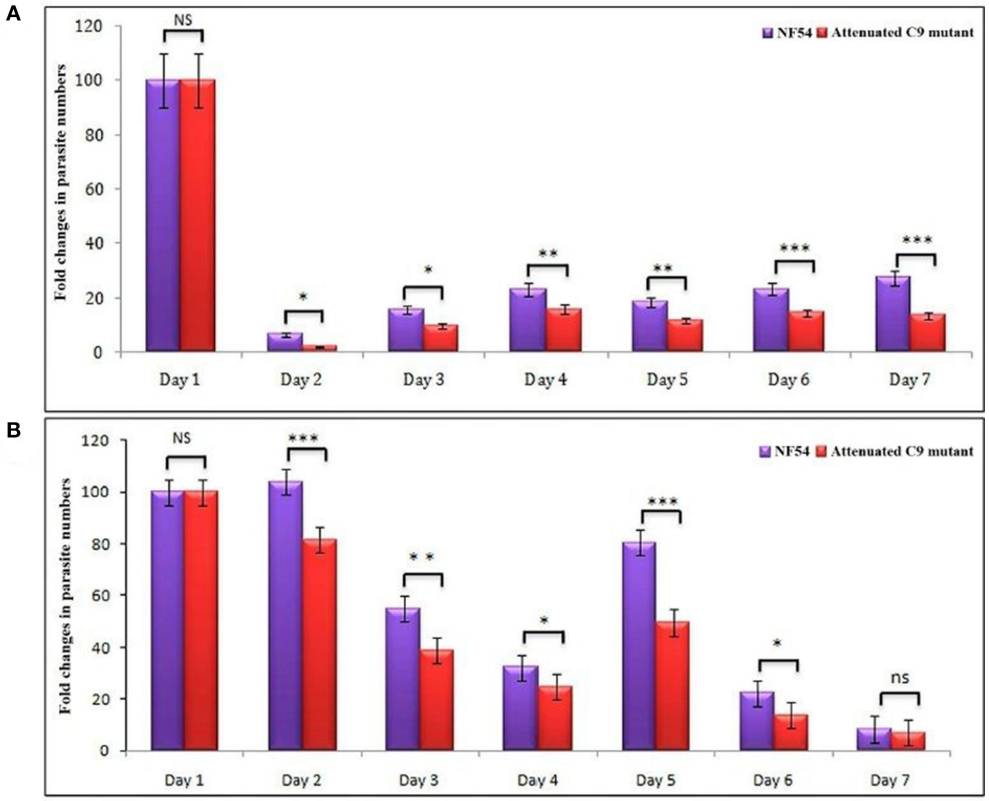

FIGURE 4 | (A) *In vitro* and, **(B)** *in vivo* phenotypic characterization of attenuated growth mutants. A bar graph of fold changes in parasite numbers for 7 days of growth revealed a spectrum of attenuated growth phenotypes in C9-M*P. falciparum* parasite until day 6 in comparison to their wild type progenitors. The growth assays were carried-out on the samples collected from *in vitro* cultures and mice infected with wild type and C9-M *P. falciparum*. *$p < 0.05$; **$p < 0.01$; ***$p < 0.001$.

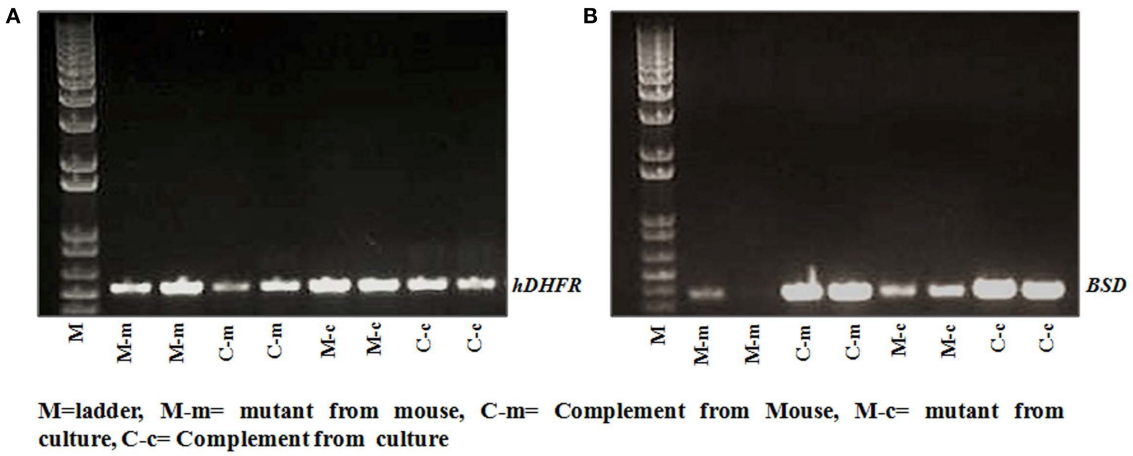

FIGURE 5 | Genotyping of parasite strain(s) used in the study. The presence of **(A)** hDHFR, and **(B)** BSD cassette in integrated parasite genome from cultures, and NSG mice infected with C9-M and C9-C parasites was confirmed in both the strains tested. Lane 2 and 3: C9-M parasites from mouse; lane 4 and 5: C9-C parasite from mouse; lane 6 and 7: C9-M parasite from culture, and lane 8 and 9: C9-C parasite from culture.

of IFN-γ (158 ± 73 vs. 1.65 ± 5 pg/ml day 15 PI) in C9-M parasites than NF54 was found to be significant ($p > 0.05$). Interestingly, a greater increase in TNF-α (422 ± 50.63 vs. 49 ± 21.76 pg/ml day, 21 PI) and IL-12 (128 ± 69 vs. 110 ± 56 pg/ml, day 15 PI) was seen in the mice infected with C9-C parasites than those seen with NF54 infected mice (**Figure 6**).

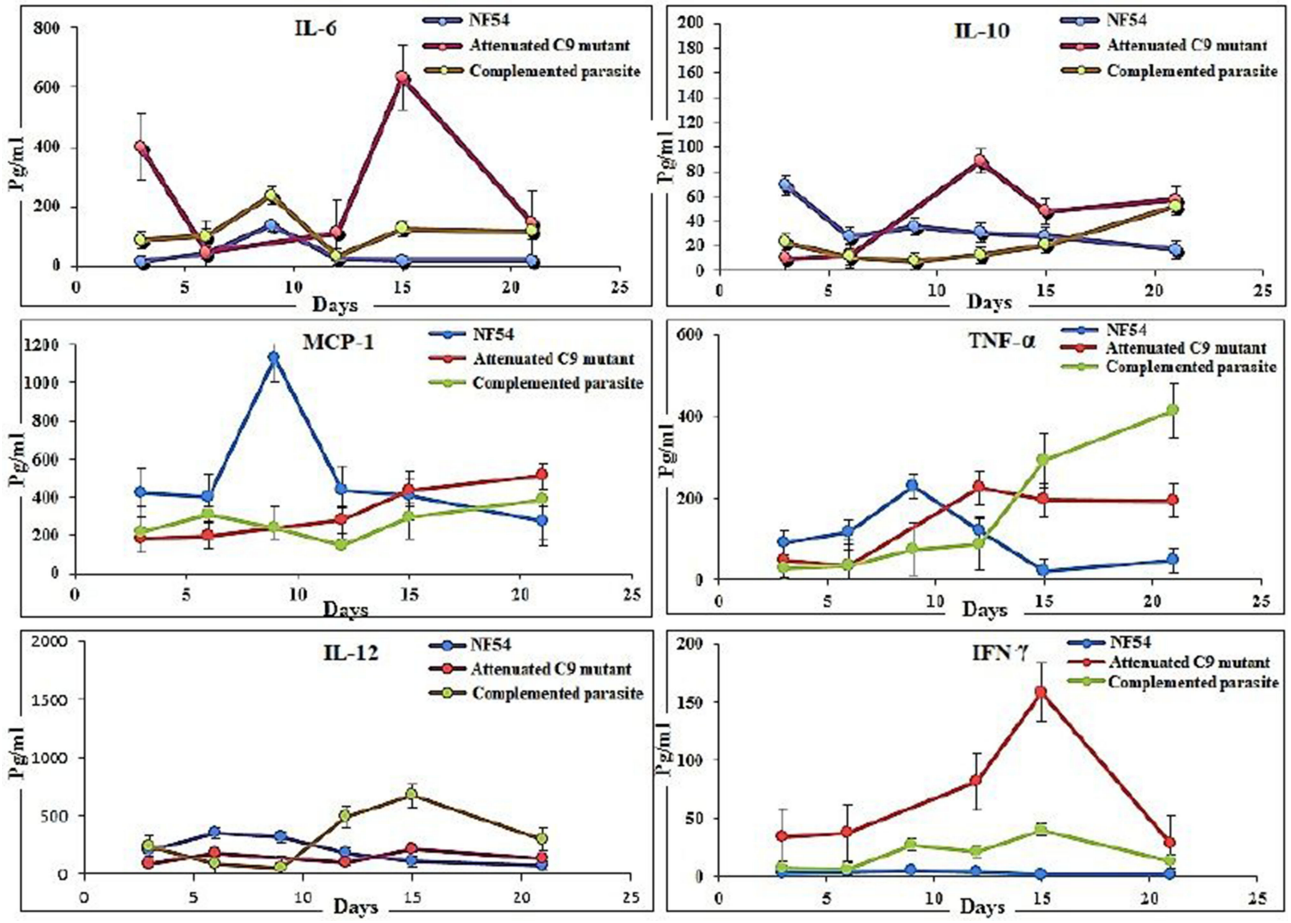

FIGURE 6 | Putative phosphatase (PF3D7_1305500) knock-down is correlated with the reduction in the inflammation in *P. falciparum* infected humanized mice. The determination of cytokines (IL-6, IL-10, MCP-1, TNF-α, IFN-γ, and IL-12) in the serum collected from mice infected with wild type NF54, attenuated C9 mutant, complemented parasites. Results represent the mean of experiment performed using three mice per group, and the standard error was calculated.

The sub-optimal dose of huRBC grafting resulted in the reduced human blood chimerism and resulting parasitemia. Consistent with other's findings (16), the initial rise of IL6, followed by an increase of IL-12p70 and moderate changes in TNF-α and MCP-1 that are temporally associated with anemia, may play a role in its etiology.

C9 Mutant *P. falciparum* Partially Escapes the Residual Innate Immunity of Host

Cells of monocyte-macrophage lineage are continuously recruited and play an important role in the clearance of the parasite from mouse circulation, but mutant parasites reside for long periods of time. Therefore, we next decided to confirm the importance of monocyte/macrophage in the clearance of parasites. The macrophages are the main subsets recruited all over the course of infection, and found to be more active than other phagocytes at ingesting infected and uninfected huRBCs in the peritoneum (9, 34–36) (**Supplementary Figure 1**). C9-M parasite showed 100% infectivity and slow growth upon being grafted in humanized NSG mice, and parasitemia was seen to decrease by day 12 post-infection (**Figure 3B**). These mutant parasites were found sequestered in the liver, kidney, and brain to survive the host's residual innate immune responses (**Figures 7A,B**). The phagocytosis of uninfected and infected huRBCs and subsequent release of pigment suggested that complete escape of parasite from host's non-adaptive immune response was not possible (**Figure 7A**). Furthermore, our results suggest that the C9-M parasite may have employed evasion mechanism(s) to survive the residual innate immune response of the host. Our findings describe the role of macrophages (MP) in the rejection of both uninfected and infected huRBC by two mechanisms: the release of inflammatory mediators for the activation of monocytes, that then result in increased erythro-phagocytosis. The role of macrophages in xenograft rejection is shown by the infiltration of leukocytes during the rejection of pig-to-primate xenografts (37, 38). Furthermore, selective macrophage depletion in immunocompetent rodents showed significant delays in cellular infiltration and xenograft rejection (39, 40).

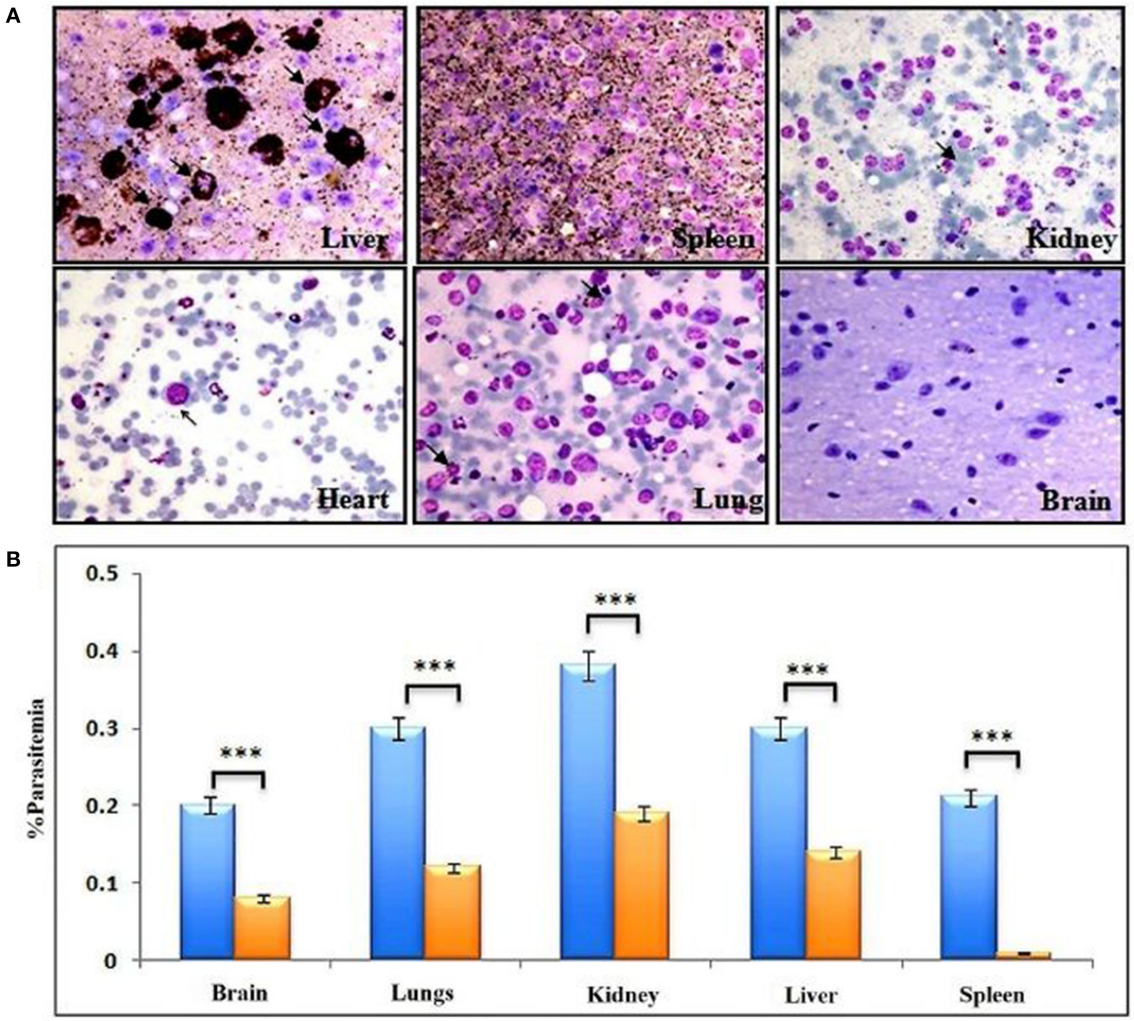

FIGURE 7 | Complete escape from mouse's residual non-adaptive immunity is not possible by C9-M parasite. **(A)** Representative Giemsa staining of smears drawn from various organs 11 days post-infection from three different NSG mice (upper panels: liver, spleen, and kidney, lower panels: heart, lungs, and brain). Arrows indicate C9-M parasitized huRBCs. The presence of parasites in different organs, their phagocytosis, and subsequent release of pigment from active phagocytes, mainly macrophages, is an example of active residual innate immune effectors, **(B)** parasite count in different organs, blue bars; C9-M, red bars; C9-C parasites. ***$p < 0.001$.

NSG-IV Mice Supported the C9-M *P. falciparum* for the Development of Gametocytes (Propagation Carriers)

The propagation of the parasite from one host to another is important to confirm the replication of the parasite. NF54-wild type strain is known to develop gametocyte *in vitro* culture, which was supported by the humanized mice to induce the production of gametocytes (**Figure 2B**, lower panel, 1st row; d3, d6, d9). In addition to the remarkable growth and development of C9-M parasites seen in NSG-IV mice, gametocytes were developed in humanized mice (**Figure 2B**, lower panel, 2nd row; d3, d6, d9). These sexual forms (**Figure 2B**, lower panel) were frequently seen up to stage V. The observation of stage V gametocytes implies that infected huRBC are able to survive in mouse's circulation for at least 9 days without suffering any immune-mediated insult when NSG-IV protocol was used. We tried to feed mosquitoes on the developed gametocytes to demonstrate their infectivity, but failed to see the development of oocyte on day 11 followed by the development of sporozoites on day 16 or 17. We think more efforts are needed to demonstrate the infectivity of gametocytes developed in Pf-NSG-IV mice.

huRBC Reconstituted TK/NOG Mouse: A Better Strain for Humanization

We wanted to study the transgenic strain (32, 41–54) (expressing the thymidine kinase transgene on mouse's hepatocyte) primarily dedicated for developing the human liver-chimeric mice to examine the inflammatory disorders and liver metabolism of drugs. Since this strain is of NOG background, we thought it could support the reconstitution of huRBCs and *P. falciparum*

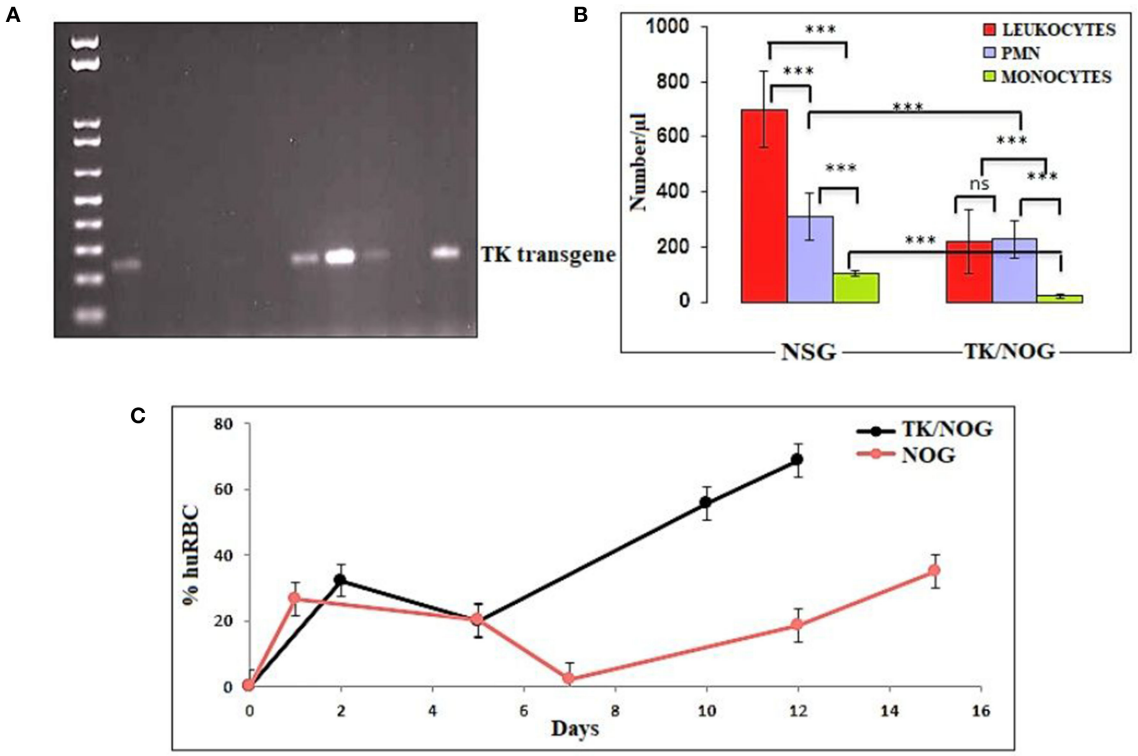

FIGURE 8 | Thymidine kinase transgene expression and enhanced huRBC grafting. **(A)** All litters were genotyped with gDNA samples extracted from tail snips by PCR, and amplified transgene DNA (Thymidine Kinase, 236 bp) was visualized at 1% agarose, **(B)** The reduction in the number of innate immune cells of TK/NOG and NSG mice was compared **(C)** the greater human blood chimerization (huRBC grafting) is seen in TK/NOG mice than NSG mice. ***$p < 0.001$.

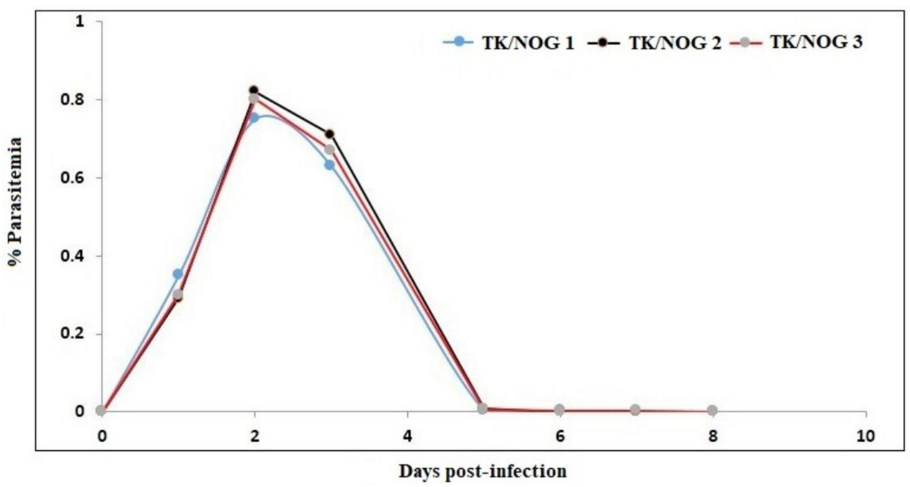

FIGURE 9 | Determination of the half-life of huRBC in mouse's circulation. Mice were intravenously inoculated with 0.3 ml of asynchronous cultures at 1% parasitemia of NF54 strain of *P. falciparum* on day 0. The parasitemia in mice was expressed as the percentage of *P. falciparum*-huRBC in the total RBC observed on thin smears. The data shown is from the first day of detectable parasitemia up to the day the mice had huRBCs in their circulation.

infection. Thus, this mouse strain was deployed in the present study, set to breed, and littermates were genotyped by the established PCR method (32). DNA transgene showed an amplified band of thymidine kinase (**Figure 8A**) on the agarose gel. The absolute numbers of innate immune effectors (Leukocytes, monocytes, and polymorphonuclears) in TK/NOG were observed to be lesser than in NSG mice (**Figure 8B**). Next, we wanted to assess the importance of thymidine

kinase transgene expression in TK/NOG mice. Therefore, TK/NOG and NSG mice were treated with clodronate-loaded liposomes to check the production of excessively recruited monocytes/macrophages, and animals were intravenously reconstituted with huRBCs. TK/NOG mice supported the significant and long-term huRBC chimerization as compared to NSG mice (**Figure 8C**). We went on to estimate the half-life (4–5 days) of huRBC to determine the survival of huRBC in mouse periphery (**Figure 9**). The human blood chimerism was found better (75%) in TK/NOG mice than NSG mice (15–20%) by day 12 post-huRBCs injections (**Figure 8C**).

huRBC reconstituted TK/NOG received infection with parental NF54, C9-M, C9-C, and 3D7 (three mice each) strain of *P. falciparum* (**Figure 10**). All mice receiving infection were seen parasitized by day 1 post-inoculation using IV protocol.

The stable blood-chimerism was seen with huRBs reconstituted TK/NOG (**Figure 8C**). These mice supported rapid and optimal growth of all *P. falciparum* strains tested (**Figure 10**). Except for 3D7, all strains (NF54, C9-M, C9-C) showed consistency in parasitemia pattern. Lack in the adaptation of the parasite to the host was attributed to variations seen in the pattern of 3D7 parasitemia. The 3D7 strain made attempts to accommodate with the host's immune system in TK/NOG mice for nearly 2 weeks, and adapted parasites exhibited normal growth and development of 3D7 by day 17 post-infection (**Figure 10**).

DISCUSSION

This study is part of our efforts to develop understanding on experimental mouse model(s) to study unknown asexual blood stage genes/RNA binding proteins of *P. falciparum*. As with others (25), our *in vitro* study showed that attenuated C9-M did not lead the normal cell cycle due to knock-down of PF3D7_1305500. This study suggests the importance of this atypical phosphatase in the regulation of the *P. falciparum* cell cycle. The attenuated C9 knock-out created by random insertional mutagenesis was used in this study to attest the *in vitro* studies (26). Moreover, the importance of PF3D7_1305500 playing a crucial role in the growth and development of asexual blood stage *P. falciparum* was confirmed in humanized mice (**Figure 11**).

We succeeded to implement a reproducible infection by using different *P. falciparum* strains in a PfhuRBC-NSG-IV humanized mouse (16) to understand the development and replication of attenuated C9-M parasites. Consistent with the previously published findings (16), we confirm that employing an intravenous route for both parasite and huRBC delivery, clodronate-loaded liposomal suspension for macrophage suppression, and the IL-2R-γ mutation on NOD/SCID genetic background, helped in achieving a model with greater reproducibility which supported the infection with different strains, including the severely attenuated C9-M.

The present study shows that *P. falciparum* huRBC/NSG-IV model (huRBC-reconstituted NSG mice infected with NF54, C9-M, and C9-C parasites) may be useful to study the immune responses evoked against the grafted parasite, and possible survival mechanisms employed by the parasites. The additional defects in the innate immune system of NSG mice are most likely related to the defective activation of phagocytes which led to the reduced *P. falciparum* selection pressure (11).

Our results show that: (1) *P. falciparum* induces strain dependent moderate inflammation characterized by the release of inflammatory cytokines in the serum; (2) evolution of parasitemia in mouse's periphery remained stable but short-term blood chimerization (insufficient huRBCs) in the circulation leads to the clearance of parasites driven by the pro-inflammatory cytokines; (3) growth and development of all *P. falciparum* strains was supported by the developed humanized mice, indicating that, in contrast to Aotus, Saimiri, and previous mouse models, there is no requirement for the preliminary adaptation of the parasite to PfhuRBC-NSG-IV host. The slower growth of C9-M indicated that the parasite could retain the mutant phenotype upon being grafted in human RBCs reconstituted humanized mice. However, there was no difference seen in the parasitemia patterns of grafted parental NF54, C9-M, and C9-C parasites. This shows the relevance of this mouse as it helps in understanding the behavior and relevance of C9 mutation in the growth and replication of the asexual blood stage infection of *P. falciparum* without tampering its genotype and phenotype; (4) migration of parasites from the mouse's periphery to deep-seated organs with the extended residence indicated that C9-M parasites may have employed molecular mechanism(s) to partially evade the host's innate immune response; (5) humanized mouse supported the development of the sexual stage of *P. falciparum*. Stage III, IV, and V gametocytes were seen in the peripheral blood but their infectivity could not be demonstrated; and (6) transgenic/immunodeficient (TK/NOG) mice were shown to better control the non-adaptive immune response as compared to NSG mice, and therefore higher human blood chimerism was seen when reconstituted with huRBCs in the mouse prepared by clo-lip treatment. huRBCs grafted TK/NOG mice showed greater susceptibility toward infection with stable parasitemia in all *P. falciparum* strains tested (**Figure 10**).

Results obtained with the humanized mouse model, as reported earlier (9, 13, 16), concur to suggest that the model is closer to events recorded in humans (for instance, the receptivity shown toward non-adapted parasites and gametocyte production).

The disruption of any biochemical process affects the normal pattern of metabolic events which leads to the completion of the asexual blood stage development of *P. falciparum*. The *in vitro* findings (26) showed the significance of PF3D7_1305500 (C9-M) in the regulation of the asexual blood stage cell cycle of *P. falciparum*. The delayed transition of pre-S trophozoite to S/M schizonts showed the checkpoint of the parasite growth cycle. The rescue of C9-M phenotype by the genetic complementation confirmed the requirement of PF3D7_1305500 for normal growth and development of *P. falciparum in vitro* (26). Further, the *in vivo* selection process led to the variants of *P. falciparum* carrying potential rearrangements to variable molecules encoding antigenic determinants (55). The engraftment of C9-M in humanized mice shows the elicitation

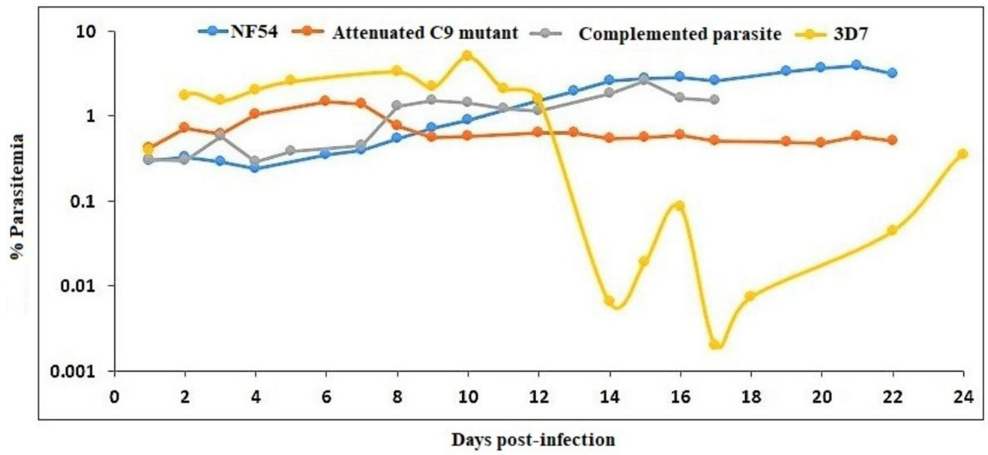

FIGURE 10 | NF54 (wild type), attenuated C9-M, complemented C9-C, and 3D7 parasite strains are supported by TK/NOG mice. The trend of parasitemia is the mean of three mice each of all parasite strains tested. Mice were intravenously inoculated with 0.3 ml of asynchronous cultures at 1% *P. falciparum* parasitemia on day 0. Mice were supplied with huRBC every 3 days. Parasitemia in the mice was expressed as the percentage of *P. falciparum* parasitized huRBCs in total RBC counted on thin blood smears. The presented data is from the first day of detectable parasitemia.

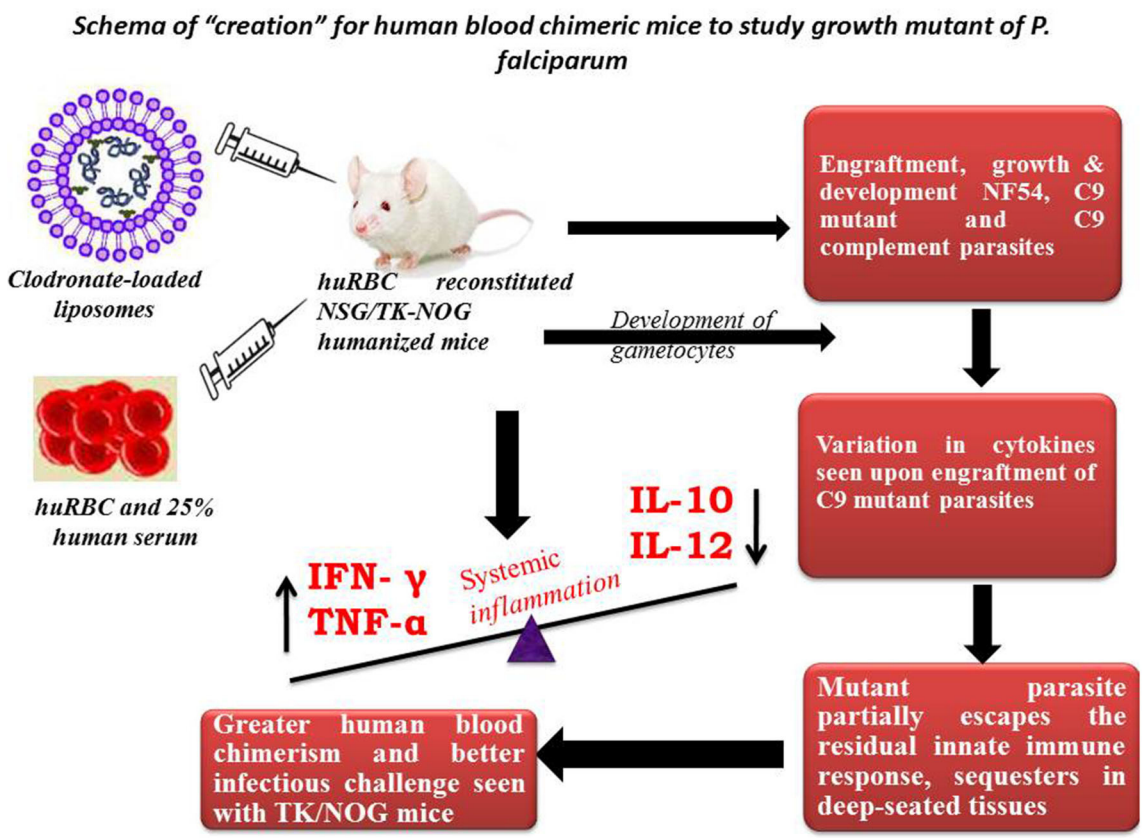

FIGURE 11 | Schema of "creation" for human blood chimeric mice to study the growth mutant of *P. falciparum*. huRBCs reconstituted NSG mice showing variation in the cytokine levels of C9-mutant and C9-complement parasites as compared to wild type NF54. This model indicates the escape-mechanism-like phenomenon since mutant parasites reside for longer in the deep-seated tissues and evade the residual innate immunity of the host.

of active residual innate immune responses. The detailed analysis better defined the role of each cytokines/chemokines produced against the grafted C9-M and C9-C *P. falciparum*. And, our findings contribute to understanding the delicate balance between inflammation control and *P. falciparum* survival in humanized mice (**Supplementary Figure 1**).

The relationship between the knock-out effect of putative phosphatase and the mouse's ability to both tolerate the graft and produce fewer inflammatory mediators is an interesting finding. A marginal increase in the inflammatory mediator (IL-6) and immune-suppressor (IL-10) than their wild type progenitors was seen. We believe that improved survival of infected and uninfected huRBCs is associated with a decrease in the inflammatory cytokine and a slight increase in the production of IL-10 by the cells of myeloid origin in C9-M harboring mice. Therefore, controlled pro-inflammatory cytokines allowing the sustained parasite development in deep-seated organs indicate that *P. falciparum* might be employing the escape mechanisms to survive the host's residual innate immunity (55). We measured increased levels of TNF-α and IL-12 in C9-M and C9-C parasites in infected humanized mice. In addition, we saw an increase in serum levels of MCP-1 in NF54 infected humanized mice. These results are in agreement with earlier findings (16). The increase of IL-12p70, TNF-α, and MCP-1 are temporally associated with anemia which might play a role in its etiology and inflammation. Lastly, we introduced a very promising transgenic/immunodeficient strain (32, 41–45, 47–51, 56, 57), primarily dedicated for developing human liver chimeric mice to study human liver physiology, drug metabolism, and liver pathogenesis of viral etiology or liver regeneration. However, we reconstituted TK/NOG mice with huRBC and saw better blood chimerism to allow *P. falciparum* replication. The better control of residual non-adaptive immune effectors such as leukocytes, PMNs, and monocytes/macrophages (49, 58) also contributed to the parasite's growth and development. The monocytes/macrophage bears their most critical function in the clearance of parasitized or un-parasitized huRBCs from mouse's periphery (9). The significant human blood chimerization supported by the TK/NOG mice when grafted with huRBC advocates for better replication of *P. falciparum* (49).

CONCLUSION AND FUTURE PERSPECTIVES

The emergence of resistance to frontline drugs and the lack of diverse therapeutic agents necessitates the finding of effective anti-malarial drugs and the identification of new drug targets (7, 59–65). Our *P. falciparum*-NSG-IV model may allow the study of asexual blood stage growth mutant(s) and their effect on the human system. This mouse shows reproducibility of both huRBC grafting and parasite survival, less day to day variation in parasitemia, does not require preliminary adaptation of parasite strains to the mouse, and supports the development of even attenuated *P. falciparum*. The evasion mechanisms employed by the parasites help survive against the host's residual immune responses and raises the possibility of partial sequestration of parasites in deep-seated organs, which are key findings of the present work. The delineation of *in vivo* function and behavior of attenuated C9-M parasites gene (PF3D7_130550) in a humanized mouse might give insights into this unknown protein, important for the growth and development of the asexual blood stage of *P. falciparum*.

DATA AVAILABILITY STATEMENT

The raw data supporting the conclusions of this article will be made available by the authors, without undue reservation.

ETHICS STATEMENT

The animal study was reviewed and approved by The Second Hospital of Jilin University, Changchun, China.

AUTHOR CONTRIBUTIONS

LZ and MT conceived and designed the experiments, analyzed the data, and wrote the paper. LZ, J-LL, M-XJ, DT, L-YW, and CC performed the experiments and contributed materials/analysis tools. All authors contributed to the article and approved the submitted version.

FUNDING

Authors express their gratitude toward The Second Hospital of Jilin University, Changchun, China for funding the proposed study.

ACKNOWLEDGMENTS

The instrumentation facility of The Second Hospital of Jilin University, Changchun, China is duly acknowledged.

SUPPLEMENTARY MATERIAL

The Supplementary Material for this article can be found online at: https://www.frontiersin.org/articles/10.3389/fimmu.2020.01801/full#supplementary-material

Supplementary Figure 1 | (a) HuRBCs are massively engulfed by macrophages in the peritoneum of mice administered with human RBCs. **(b)** Sizable rafting of huRBCs was seen when co-injected with clodronate loaded liposomes (9). Black Square-HuRBC, Plain circle- HuRBC+ Clo-lip, Open circle- HuRBC+ NIMP.

REFERENCES

1. WHO. *World Malaria Report*. World Health Organization (2017). p. 1–196.
2. Murray CJ, Rosenfeld LC, Lim SS, Andrews KG, Foreman KJ, Haring D, et al. Global malaria mortality between 1980 and 2010: a systematic analysis. *Lancet*. (2012) 379:413–31. doi: 10.1016/S0140-6736(12)60034-8
3. Druilhe P, Hagan P, Rook GA. The importance of models of infection in the study of disease resistance. *Trends Microbiol.* (2002) 10(Suppl. 10):S38–46. doi: 10.1016/S0966-842X(02)02437-X
4. White NJ, Turner GD, Medana IM, Dondorp AM, Day NP. The murine cerebral malaria phenomenon. *Trends Parasitol.* (2010) 26:11–15. doi: 10.1016/j.pt.2009.10.007

5. Druilhe P, Barnwell JW. Pre-erythrocytic stage malaria vaccines: time for a change in path. *Current Opin Microbiol.* (2007) 10:371–8. doi: 10.1016/j.mib.2007.07.009
6. Siu E, Ploss A. Modeling malaria in humanized mice: opportunities and challenges. *Ann N Y Acad Sci.* (2015) 1342:29–36. doi: 10.1111/nyas.12618
7. Dondorp AM, Yeung S, White L, Nguon C, Day NP, Socheat D, et al. Artemisinin resistance: current status and scenarios for containment. *Nat Rev Microbiol.* (2010) 8:272–80. doi: 10.1038/nrmicro2331
8. Shanks GD. Treatment of falciparum malaria in the age of drug resistance. *J Postgrad Med.* (2006) 52:277–80.
9. Arnold L, Tyagi RK, Mejia P, Van Rooijen N, Pérignon JL, Druilhe P. Analysis of innate defences against *Plasmodium falciparum* in immunodeficient mice. *Malaria J.* (2010) 9:197. doi: 10.1186/1475-2875-9-197
10. Badell E, Oeuvray C, Moreno A, Soe S, van Rooijen N, Bouzidi A, et al. Human malaria in immunocompromised mice: an *in vivo* model to study defense mechanisms against *Plasmodium falciparum*. *J Exp Med.* (2000) 192:1653–660. doi: 10.1084/jem.192.11.1653
11. Angulo-Barturen I, Jiménez-Díaz MB, Mulet T, Rullas J, Herreros E, Ferrer S, et al. A murine model of falciparum-malaria by *in vivo* selection of competent strains in non-myelodepleted mice engrafted with human erythrocytes. *PloS ONE.* (2008) 3:e2252. doi: 10.1371/journal.pone.0002252
12. Druilhe P, Spertini F, Soesoe D, Corradin G, Mejia P, Singh S, et al. A malaria vaccine that elicits in humans antibodies able to kill *Plasmodium falciparum*. *PLoS Med.* (2005) 2:e344. doi: 10.1371/journal.pmed.0020344
13. Moreno A, Badell E, Van Rooijen N, Druilhe P. Human malaria in immunocompromised mice: new *in vivo* model for chemotherapy studies. *Antimicrob Agents Chemother.* (2001) 45:1847–53. doi: 10.1128/AAC.45.6.1847-1853.2001
14. Vaughan AM, Kappe SH, Ploss A, Mikolajczak SA. Development of humanized mouse models to study human malaria parasite infection. *Fut Microbiol.* (2012) 7:657–65. doi: 10.2217/fmb.12.27
15. McCarthy JS, Marquart L, Sekuloski S, Trenholme K, Elliott S, Griffin P, et al. Linking murine and human *Plasmodium falciparum* challenge models in a translational path for antimalarial drug development. *Antimicrob Agents Chemother.* (2016) 60:3669–75. doi: 10.1128/AAC.02883-15
16. Arnold L, Tyagi RK, Meija P, Swetman C, Gleeson JG, Pérignon JL, et al. Further improvements of the *P. falciparum* humanized mouse model. *PloS ONE.* (2011) 6:e18045. doi: 10.1371/journal.pone.0018045
17. King M, Pearson T, Shultz LD, Leif J, Bottino R, Trucco M, et al. Development of new-generation HU-PBMC-NOD/SCID mice to study human islet alloreactivity. *Ann N Y Acad Sci.* (2007) 1103:90–93. doi: 10.1196/annals.1394.011
18. Watanabe S, Terashima K, Ohta S, Horibata S, Yajima M, Shiozawa Y, et al. Hematopoietic stem cell-engrafted NOD/SCID/IL2Rgamma null mice develop human lymphoid systems and induce long-lasting HIV-1 infection with specific humoral immune responses. *Blood.* (2007) 109:212–8. doi: 10.1182/blood-2006-04-017681
19. Ito M, Hiramatsu H, Kobayashi K, Suzue K, Kawahata M, Hioki K, et al. NOD/SCID/gamma(c)(null) mouse: an excellent recipient mouse model for engraftment of human cells. *Blood.* (2002) 100:3175–82. doi: 10.1182/blood-2001-12-0207
20. Ito M, Kobayashi K, Nakahata T. NOD/Shi-scid IL2rgamma(null) (NOG) mice more appropriate for humanized mouse models. *Curr Top Microbiol Immunol.* (2008) 324:53–76. doi: 10.1007/978-3-540-75647-7_3
21. Kenney LL, Shultz LD, Greiner DL, Brehm MA. Humanized mice and tissue transplantation. *Am J Transpl.* (2016) 16:389. doi: 10.1111/ajt.13520
22. Audigé A, Rochat MA, Li D, Ivic S, Fahrny A, Muller CKS, et al. Long-term leukocyte reconstitution in NSG mice transplanted with human cord blood hematopoietic stem and progenitor cells. *BMC Immunol.* (2017) 18:28. doi: 10.1186/s12865-017-0209-9
23. Herndler-Brandstetter D, Shan L, Yao Y, Stecher C, Plajer V, Lietzenmayer M, et al. Humanized mouse model supports development, function, and tissue residency of human natural killer cells. *Proc Natl Acad Sci USA.* (2017) 114:E9626–34. doi: 10.1073/pnas.1705301114
24. Brehm M, Bortell R, Verma M, Shultz L, Greiner D. Humanized mice in translational immunology. *Transl Immunol Mech Pharmacol Approach.* (2016) 2016:285–326. doi: 10.1016/B978-0-12-801577-3.00012-5
25. Balu B, Singh N, Maher SP, Adams JH. A genetic screen for attenuated growth identifies genes crucial for intraerythrocytic development of *Plasmodium falciparum*. *PloS ONE.* (2010) 5:e13282. doi: 10.1371/journal.pone.0013282
26. Balu B, Campbell C, Sedillo J, Maher S, Singh N, Thomas P, et al. Atypical mitogen-activated protein kinase phosphatase implicated in regulating transition from pre-S-Phase asexual intraerythrocytic development of *Plasmodium falciparum*. *Eukaryot Cell.* (2013) 12:1171–178. doi: 10.1128/EC.00028-13
27. Balu B, Chauhan C, Maher SP, Shoue DA, Kissinger JC, Fraser MJ, et al. piggyBac is an effective tool for functional analysis of the *Plasmodium falciparum* genome. *BMC Microbiol.* (2009) 9:83. doi: 10.1186/1471-2180-9-83
28. Rowe AW, Eyster E, Kellner A. Liquid nitrogen preservation of red blood cells for transfusion; a low glycerol-rapid freeze procedure. *Cryobiology.* (1968) 5:119–28. doi: 10.1016/S0011-2240(68)80154-3
29. Lambros C, Vanderberg JP. Synchronization of *Plasmodium falciparum* erythrocytic stages in culture. *J Parasitol.* (1979) 65:418–20. doi: 10.2307/3280287
30. Li Q, Gerena L, Xie L, Zhang J, Kyle D, Milhous W. Development and validation of flow cytometric measurement for parasitemia in cultures of *P. falciparum* vitally stained with YOYO-1. *Cytometry Part A.* (2007) 71:297–307. doi: 10.1002/cyto.a.20380
31. Persson KE, Lee CT, Marsh K, Beeson JG. Development and optimization of high-throughput methods to measure *Plasmodium falciparum*-specific growth inhibitory antibodies. *J Clin Microbiol.* (2006) 44:1665–73. doi: 10.1128/JCM.44.5.1665-1673.2006
32. Hasegawa M, Kawai K, Mitsui T, Taniguchi K, Monnai M, Wakui M, et al. The reconstituted 'humanized liver' in TK-NOG mice is mature and functional. *Biochem Biophys Res Commun.* (2011) 405:405–10. doi: 10.1016/j.bbrc.2011.01.042
33. Balu B, Shoue DA, Fraser MJ, Adams JH. High-efficiency transformation of *Plasmodium falciparum* by the lepidopteran transposable element piggyBac. *Proc Natl Acad Sci USA.* (2005) 102:16391–16396. doi: 10.1073/pnas.0504679102
34. Silva MT, Correia-Neves M. Neutrophils and macrophages: the main partners of phagocyte cell systems. *Front Immunol.* (2012) 3:174. doi: 10.3389/fimmu.2012.00174
35. Cassado Ados A, D'Império Lima MR, Bortoluci KR. Revisiting mouse peritoneal macrophages: heterogeneity, development, and function. *Front Immunol.* (2015) 6:225. doi: 10.3389/fimmu.2015.00225
36. de Back DZ, Kostova EB, van Kraaij M, van den Berg TK, Van Bruggen R. Of macrophages and red blood cells; a complex love story. *Front Physiol.* (2014) 5:9. doi: 10.3389/fphys.2014.00009
37. Itescu S, Kwiatkowski P, Artrip JH, Wang SF, Ankersmit J, Minanov OP, et al. Role of natural killer cells, macrophages, and accessory molecule interactions in the rejection of pig-to-primate xenografts beyond the hyperacute period. *Hum Immunol.* (1998) 59:275–86. doi: 10.1016/S0198-8859(98)00026-3
38. Lin Y, Vandeputte M, Waer M. Natural killer cell- and macrophage-mediated rejection of concordant xenografts in the absence of T and B cell responses. *J Immunol.* (1997) 158:5658–67.
39. Fox A, Koulmanda M, Mandel TE, van Rooijen N, Harrison LC. Evidence that macrophages are required for T-cell infiltration and rejection of fetal pig pancreas xenografts in nonobese diabetic mice. *Transplantation.* (1998) 66:1407–16. doi: 10.1097/00007890-199812150-00002
40. Wu GS, Korsgren O, Zhang JG, Song ZS, Van Rooijen N, Tibell A. Role of macrophages and natural killer cells in the rejection of pig islet xenografts in mice. *Transplant Proc.* (2000) 32:1069. doi: 10.1016/S0041-1345(00)01127-1
41. Kosaka K, Hiraga N, Imamura M, Yoshimi S, Murakami E, Nakahara T, et al. A novel TK-NOG based humanized mouse model for the study of HBV and HCV infections. *Biochem Biophys Res Commun.* (2013) 441:230–5. doi: 10.1016/j.bbrc.2013.10.040
42. Higuchi Y, Kawai K, Yamazaki H, Nakamura M, Bree F, Guguen-Guillouzo C, et al. The human hepatic cell line HepaRG as a possible cell source for the generation of humanized liver TK-NOG mice. *Xenobiotica.* (2014) 44:146–53. doi: 10.3109/00498254.2013.836257
43. Tsukada A, Suemizu H, Murayama N, Takano R, Shimizu M, Nakamura M, et al. Plasma concentrations of melengestrol acetate in humans extrapolated from the pharmacokinetics established in *in vivo* experiments with rats and chimeric mice with humanized liver and physiologically

based pharmacokinetic modeling. *Regul Toxicol Pharmacol.* (2013) 65:316–24. doi: 10.1016/j.yrtph.2013.01.008
44. Yamazaki H, Suemizu H, Murayama N, Utoh M, Shibata N, Nakamura M, et al. *In vivo* drug interactions of the teratogen thalidomide with midazolam: heterotropic cooperativity of human cytochrome P450 in humanized TK-NOG mice. *Chem Res Toxicol.* (2013) 26:486–9. doi: 10.1021/tx400008g
45. Kim M, Choi B, Joo SY, Lee H, Lee JH, Lee KW, et al. Generation of humanized liver mouse model by transplant of patient-derived fresh human hepatocytes. *Transplant Proc.* (2014) 46:1186–90. doi: 10.1016/j.transproceed.2013.11.098
46. Xu D, Wu M, Nishimura S, Nishimura T, Michie SA, Zheng M, et al. Chimeric TK-NOG mice: a predictive model for cholestatic human liver toxicity. *J Pharmacol Exp Ther.* (2015) 352:274–80. doi: 10.1124/jpet.114.220798
47. Kamimura H, Ito S, Nozawa K, Nakamura S, Chijiwa H, Nagatsuka S, et al. Formation of the accumulative human metabolite and human-specific glutathione conjugate of diclofenac in TK-NOG chimeric mice with humanized livers. *Drug Metab Dispos.* (2015) 43:309–16. doi: 10.1124/dmd.114.061689
48. Xu D, Michie SA, Zheng M, Takeda S, Wu M, Peltz G. Humanized thymidine kinase-NOG mice can be used to identify drugs that cause animal-specific hepatotoxicity: a case study with furosemide. *J Pharmacol Exp Ther.* (2015) 354:73–8. doi: 10.1124/jpet.115.224493
49. Soulard V, Bosson-Vanga H, Lorthiois A, Roucher C, Franetich JF, Zanghi G, et al. *Plasmodium falciparum* full life cycle and *Plasmodium ovale* liver stages in humanized mice. *Nat Commun.* (2015) 6:7690. doi: 10.1038/ncomms8690
50. Kai Y, Hikita H, Tatsumi T, Nakabori T, Saito Y, Morishita N, et al. Emergence of hepatitis C virus NS5A L31V plus Y93H variant upon treatment failure of daclatasvir and asunaprevir is relatively resistant to ledipasvir and NS5B polymerase nucleotide inhibitor GS-558093 in human hepatocyte chimeric mice. *J Gastroenterol.* (2015) 50:1145–51. doi: 10.1007/s00535-015-1108-6
51. Uchida T, Hiraga N, Imamura M, Tsuge M, Abe H, Hayes CN, et al. Human cytotoxic T lymphocyte-mediated acute liver failure and rescue by immunoglobulin in human hepatocyte transplant TK-NOG mice. *J Virol.* (2015) 89:10087–96. doi: 10.1128/JVI.01126-15
52. Fomin ME, Beyer AI, Muench MO. Human fetal liver cultures support multiple cell lineages that can engraft immunodeficient mice. *Open Biol.* (2017) 7:170108. doi: 10.1098/rsob.170108
53. Suzuki E, Koyama K, Nakai D, Goda R, Kuga H, Chiba K. Observation of clinically relevant drug interaction in chimeric mice with humanized livers: the case of valproic acid and carbapenem antibiotics. *Eur J Drug Metab Pharmacokinet.* (2017) 42:965–72. doi: 10.1007/s13318-017-0413-2
54. Shimizu M, Suemizu H, Mitsui M, Shibata N, Guengerich FP, Yamazaki H. Metabolic profiles of pomalidomide in human plasma simulated with pharmacokinetic data in control and humanized-liver mice. *Xenobiotica.* (2017) 47:844–8. doi: 10.1080/00498254.2016.1247218
55. Lavazec C, Sanyal S, Templeton TJ. Hypervariability within the Rifin, Stevor and Pfmc-2TM superfamilies in *Plasmodium falciparum*. *Nucleic Acids Res.* (2006) 34:6696–707. doi: 10.1093/nar/gkl942
56. Xu D, Nishimura T, Nishimura S, Zhang H, Zheng M, Guo YY, et al. Fialuridine induces acute liver failure in chimeric TK-NOG mice: a model for detecting hepatic drug toxicity prior to human testing. *PLoS Med.* (2014) 11:e1001628. doi: 10.1371/journal.pmed.1001628
57. Xu D, Huang P, Yu Z, Xing DH, Ouyang S, Xing G. Efficacy and safety of panax notoginseng saponin therapy for acute intracerebral hemorrhage, meta-analysis, and mini review of potential mechanisms of action. *Front. Neurol.* (2015) 5:274. doi: 10.3389/fneur.2014.00274
58. Moreno-Sabater A, Pérignon JL, Mazier D, Lavazec C, Soulard V. Humanized mouse models infected with human *Plasmodium* species for antimalarial drug discovery. *Expert Opin Drug Discov.* (2018) 13:131–40. doi: 10.1080/17460441.2018.1410136
59. Hyde JE. Drug-resistant malaria. *Trends Parasitol.* (2005) 21:494–8. doi: 10.1016/j.pt.2005.08.020
60. Haldar K, Bhattacharjee S, Safeukui I. Drug resistance in *Plasmodium*. *Nat Rev Microbiol.* (2018) 16:156–70. doi: 10.1038/nrmicro.2017.161
61. Thu AM, Phyo AP, Landier J, Parker DM, Nosten FH. Combating multi-drug resistant *Plasmodium falciparum* malaria. *FEBS J.* (2017) 284:2569–78. doi: 10.1111/febs.14127
62. Menard D, Dondorp A. Antimalarial drug resistance: a threat to malaria elimination. *Cold Spring Harbor Perspect Med.* (2017) 7:a025619. doi: 10.1101/cshperspect.a025619
63. Arie S. Researchers and WHO clash over global threat of drug resistant malaria. *BMJ.* (2017) 359:j5127. doi: 10.1136/bmj.j5127
64. Cui L, Mharakurwa S, Ndiaye D, Rathod PK, Rosenthal PJ. Antimalarial drug resistance: literature review and activities and findings of the ICEMR network. *Am J Trop Med Hyg.* (2015) 93:57–68. doi: 10.4269/ajtmh.15-0007
65. Amolegbe SA, Hirano Y, Adebayo JO, Ademowo OG, Balogun EA, Obaleye JA, et al. Mesoporous silica nanocarriers encapsulated antimalarials with high therapeutic performance. *Sci Rep.* (2018) 8:3078. doi: 10.1038/s41598-018-21351-8

Conflict of Interest: The authors declare that the research was conducted in the absence of any commercial or financial relationships that could be construed as a potential conflict of interest.

frontiers in Immunology

ORIGINAL RESEARCH
published: 08 October 2020
doi: 10.3389/fimmu.2020.569727

Alterations of Gut Microbiome and Metabolite Profiling in Mice Infected by *Schistosoma japonicum*

Yue Hu[1,2,3†], *Jiansong Chen*[4†], *Yiyue Xu*[1,2], *Hongli Zhou*[1,2], *Ping Huang*[1,2], *Yubin Ma*[1,2], *Minzhao Gao*[5], *Shaoyun Cheng*[1,2], *Haiyun Zhou*[4] *and Zhiyue Lv*[1,2,3,6*]

[1] *Key Laboratory of Tropical Disease Control (Sun Yat-sen University), Ministry of Education, Guangzhou, China,* [2] *Key Laboratory of Tropical Translational Medicine of Ministry of Education, Hainan Medical University, Haikou, China,* [3] *Joint Program of Pathobiology, Fifth Affiliated Hospital, Zhongshan School of Medicine, Sun Yat-sen University, Guangzhou, China,* [4] *Instrumental Analysis and Research Center, Sun Yat-sen University, Guangzhou, China,* [5] *Department of Gastroenterology, The Fifth Affiliated Hospital of Sun Yat-sen University, Zhuhai, China,* [6] *Provincial Engineering Technology Research Center for Biological Vector Control, Zhongshan School of Medicine, Sun Yat-sen University, Guangzhou, China*

OPEN ACCESS

Edited by:
Jun-Hu Chen, National Institute of Parasitic Diseases (China), China

Reviewed by:
Wanchai Maleewong, Khon Kaen University, Thailand
Guillaume Sarrabayrouse, Vall d'Hebron Research Institute (VHIR), Spain
Jilong Shen, Anhui Medical University, China

***Correspondence:**
Zhiyue Lv
lvzhiyue@mail.sysu.edu.cn

† These authors have contributed equally to this work

Specialty section:
This article was submitted to Microbial Immunology, a section of the journal Frontiers in Immunology

Received: *04 June 2020*
Accepted: *24 August 2020*
Published: *08 October 2020*

Citation:
Hu Y, Chen J, Xu Y, Zhou H, Huang P, Ma Y, Gao M, Cheng S, Zhou H and Lv Z (2020) Alterations of Gut Microbiome and Metabolite Profiling in Mice Infected by Schistosoma japonicum. Front. Immunol. 11:569727. doi: 10.3389/fimmu.2020.569727

Schistosoma japonicum (*S. japonicum*) is one of the etiological agents of schistosomiasis, a widespread zoonotic parasitic disease. However, the mechanism of the balanced co-existence between the host immune system and *S. japonicum* as well as their complex interaction remains unclear. In this study, *16S* rRNA gene sequencing, combined with metagenomic sequencing approach as well as ultraperformance liquid chromatography–mass spectrometry metabolic profiling, was applied to demonstrate changes in the gut microbiome community structure during schistosomiasis progression, the functional interactions between the gut bacteria and *S. japonicum* infection in BALB/c mice, and the dynamic metabolite changes of the host. The results showed that both gut microbiome and the metabolites were significantly altered at different time points after the infection. Decrease in richness and diversity as well as differed composition of the gut microbiota was observed in the infected status when compared with the uninfected status. At the phylum level, the gut microbial communities in all samples were dominated by Firmicutes, Bacteroidetes, Proteobacteria, and Deferribacteres, while at the genus level, *Lactobacillus*, *Lachnospiraceae NK4A136 group*, *Bacteroides*, *Staphylococcus*, and *Alloprevotella* were the most abundant. After exposure, *Roseburia,* and *Ruminococcaceae UCG-014* decreased, while *Staphylococcus*, *Alistipes*, and *Parabacteroides* increased, which could raise the risk of infections. Furthermore, LEfSe demonstrated several bacterial taxa that could discriminate between each time point of *S. japonicum* infection. Besides that, metagenomic analysis illuminated that the AMP-activated protein kinase (AMPK) signaling pathway and the chemokine signaling pathway were significantly perturbed after the infection. Phosphatidylcholine and colfosceril palmitate in serum as well as xanthurenic acid, naphthalenesulfonic acid, and pimelylcarnitine in urine might be metabolic biomarkers due to their promising diagnostic potential at the early stage of the infection. Alterations of glycerophospholipid and purine metabolism were also discovered in the infection. The present study might provide further understanding of the mechanisms during schistosome infection in aspects of

gut microbiome and metabolites, and facilitate the discovery of new targets for early diagnosis and prognostic purposes. Further validations of potential biomarkers in human populations are necessary, and the exploration of interactions among *S. japonicum*, gut microbiome, and metabolites is to be deepened in the future.

Keywords: *Schistosoma japonicum*, gut microbiome, metagenomics, metabolomics, *16S* rRNA, UPLC-MS 3

INTRODUCTION

Schistosomiasis is a zoonotic parasitic disease mainly caused by the infection of *Schistosoma japonicum* (*S. japonicum*), *Schistosoma mansoni (S. mansoni)*, and *Schistosoma haematobium (S. haematobium)*, which seriously damages human and animal health and hinders socio-economic development. This neglected tropical disease affects ∼200 million people, and ∼779 million are at risk of infection worldwide (1). *S. japonicum* is distributed principally in East Asia, especially in China, the Philippines, and Indonesia, with more than 1 million people infected and ∼46 million people at risk (2). In China, *S. japonicum* is endemic in mainly 12 provinces along the middle and the lower reaches of the Yangtze River and regions south of it. The life cycle of *S. japonicum* is complex and consists of asexual generation in the intermediate host and sexual generation in the definitive host, including the seven developmental stages of egg, miracidium, mother sporocyst, daughter sporocyst, cercaria, juvenile schistosomulum, and adult worm (3). Different stages of *S. japonicum* cause various damages to the host, and complex immune pathological reactions lead to diverse clinical symptoms. Larval worms induce Th1 responses with elevated levels of the inflammatory cytokines IFN-γ, IL-12, and TNF-α in the early phase of schistosomiasis and cause diarrhea, fatigue, and anemia, while adult worms become mature and lay eggs; parasite eggs that deposit in the liver and colon of infected hosts elicit Th2 responses and then upregulate the serum cytokine levels of IL-4, IL-5, IL-13, and TGF-β, leading to portal vein hypertension syndrome, ascites, and liver fibrosis (2, 4, 5). During *S. japonicum* infection, egg deposits in the tissues are a determining factor that shifts the Th1 response to the Th2 response (5). To protect against eggs, delayed-type hypersensitivity reactions of the host are triggered but lead to the formation of circumoval granuloma in livers and colons, followed by fibrosis, which is the main cause of death (5). Immunological downregulation occurs to both, protecting the host from inflammatory damage and preventing the parasites from being eliminated during late chronic infection (4). However, the mechanism of this balanced co-existence between the host's immune system and *S. japonicum* as well as their complex interaction remains unclear.

At present, schistosomiasis is diagnosed by a clinical history of contact with fresh water from endemic foci, followed by both direct methods and indirect tests in the clinical laboratory. The former includes using the Kato–Katz technique to examine the feces under light microscopy for detection of eggs, while the latter includes using immunological approaches, such as detecting soluble antigens secreted from eggs *via* the antigen–antibody reaction (2, 6, 7). Imaging methods, for instance, ultrasonography (US), CT scan and MR, scan, are established to inspect the presence of periportal fibrosis (7). Nevertheless, these diagnostic methods are not sensitive or specific enough and are not suitable for early diagnosis; therefore, a well-suited approach with high sensitivity and specificity is urgently required to detect acute stage infection.

Metabolomics is a quantitative measurement of multi-parametric metabolic responses of multi-cellular systems and aims to identify and quantify numerous small molecules (<1,200 Da) present in various biological samples or specific physiological states; metabolomics can provide a comprehensive systems-level study of the relationships between host genetic and environmental factors with high-density data and multivariate mathematical modeling (8–10). Nuclear magnetic resonance (NMR) spectroscopy, liquid chromatography–mass spectrometry (LC–MS), and gas chromatography–mass spectrometry are the most widely used analytical techniques for metabolomic analyses. Due to the main advantages of much better sensitivity and resolution, more coverage of metabolites, and high-throughput capacity (11), MS-based techniques have been implemented more frequently than NMR. Metabolomics has already been widely applied in parasitological studies, with comprehensive characterizations of the host metabolic responses to infections by several parasites, such as *Plasmodium falciparum* (12–14), *Trypanosoma brucei* (15–17), *Toxoplasma gondii* (18–20), and *S. japonicum* (2, 6, 21). Hence, metabolomics is a suitable diagnostic tool to provide novel insights into the mechanisms underlying the progression of schistosomiasis, clearly revealing the resistance mechanism between the host and *S. japonicum* and thus leading to the discovery of potential metabolic biomarkers that are useful for early diagnosis.

The gut microbiota, consisting of diverse microbial communities, has a profound impact on influencing host physiology by the composition, density, and activities of colonizing microorganisms as well as on animal evolution through the interplay between host and microbial communities (22). Once the balance in proportions among core bacterial communities breaks down, dysbiosis occurs, which may alter host interactions and lead to numerous diseases, such as inflammatory gut disorders, diabetes, and obesity (23). *S. japonicum* adult worms live in the mesenteric veins of the host and can cause intestinal schistosomiasis with symptoms of mucosal granulomatous inflammation, superficial bleeding, and pseudopolyposis (24). However, the interaction between the host, *S. japonicum*, and the microbiota and the potential effects of helminths on shaping the host–microbiota composition and structure are unclear; therefore, further investigation is warranted.

Previous studies have shown that infection with *S. japonicum* modified both bacterial richness and bacterial community composition (25), reduced the levels of tricarboxylic acid cycle intermediates, increased the levels of amino acids, choline, and urinary 3-ureidopropionate, and perturbed lipid metabolism, glycolysis stimulation, tricarboxylic acid cycle, and a series of microbial-related metabolites (2, 6). Nevertheless, the alterations of microbiome and metabolome in the time course of infection progression have not been described yet; therefore, the aim of the current study is to investigate the dynamic alteration of gut microbiome community structure and the metabolite profile of the hosts infected with *S. japonicum*, and the correlations between host metabolism and gut microbiome after the infection by omics-based and systems-level approaches involving metabolic profiling with ultraperformance liquid chromatography–mass spectrometry (UPLC–MS), *16S* rRNA gene sequencing, and shotgun metagenomics sequencing. To our knowledge, employing metagenomic sequencing and untargeted metabolic profiling to investigate the effects of infection with *S. japonicum* in BALB/c mice would allow a better understanding of the mechanisms during schistosomiasis development and potentially reveal new targets for early diagnosis and prognosis.

MATERIALS AND METHODS

Ethics Statement

All animal experiments were conducted strictly in accordance with the guidelines of the National Institutes of Health on animal care and the ethical guidelines. The protocol was approved by the Animal Care and Use Committee of Sun Yat-sen University [permit no. SYXK (Guangdong) 2017-0081]. All efforts were made to minimize the suffering of the animals.

Mice and Cercariae

Seventy specific-pathogen-free 6- to 8-week-old female BALB/c mice (18 ± 2 g body weight) were purchased from the Animal Experiment Center at Sun Yat-sen University (Guangzhou, China) and were housed in plastic cages with free access to autoclaved chow and water under controlled temperature and humidity and a 12-h light/12-h dark cycle. The animals were randomly divided into seven groups, with 10 mice in each group. After the mice acclimated to the new environment, 60 of them were infected with 30 ± 2 *S. japonicum* cercariae per individual *via* the shaved abdominal skin. The cercariae were obtained from infected *Oncomelania*, which were provided by the National Institute of Parasitic Diseases, Chinese Center for Disease Control and Prevention (Shanghai, China), that were placed in dechlorinated water and exposed to artificial light for more than 2 h. The other mice were left uninfected and served as controls.

Sample Collection

The mice in each group were sacrificed by chloral hydrate asphyxiation and cervical dislocation either before infection or at 3, 7, 14, 21, 28, and 42 days post-infection (dpi). Blood samples were drawn from orbital veins and centrifuged at 3,000 $\times g$ for 10 min to collect the serum after clotting. The serum was stored at−80°C until further analysis. Urine and feces samples were collected the day before the mice were sacrificed by placing them individually in metabolic cages, which can separate feces from urine using different small plastic tubes embedded at the bottom of the cages. Dry ice was placed around the collection tubes to prevent oxidation or degradation of metabolites. At least 0.5 ml of urine and 1 g of feces were obtained; then, the samples were transferred into Eppendorf tubes and stored in a freezer at−80°C for further testing.

Genomic DNA Extraction and *16S* rRNA Gene Sequencing

Nucleic acid extraction of thirty fecal samples of the 0, 7, 14, 21, 28, and 42 dpi groups (five samples per group) was carried out using a QIAamp Fast DNA Stool Mini kit (cat. no. 51604, QIAGEN, Hilden, Germany), following the manufacturer's instructions. The concentration of DNA was measured on a NanoDrop (Thermo Scientific, Waltham, MA, USA), and 1% agarose gel electrophoresis was used to assess the integrity and the purity of DNA. After that, extracted DNA was diluted to a concentration of 1 ng/μl and used as a template to amplify the V3–V4 regions of the *16S* rRNA gene, utilizing the primers 343F (5′-TACGGRAGGCAGCAG-3′) and 798R (5′-AGGGTATCTAATCCT-3′) with barcodes in combination with HiFi Hot Start Ready Mix (cat. no. KK2501, Kapa Biosystems, Boston, MA, USA). Polymerase chain reaction (PCR) amplicon product quality was demonstrated through agarose gel electrophoresis, and PCR amplicons were purified with Agencourt AMPure XP beads (cat. no. A63881, Beckman Coulter, Brea, CA, USA), followed by another round of PCR amplification. The final amplicons were quantified with a Qubit® dsDNA HS Assay Kit (cat. no. Q32854, Life Technologies, Waltham, MA, USA) after a subsequent clean-up, as described above. Afterwards, the purified amplicons from each sample were pooled in equal amounts for subsequent *16S* rRNA sequencing on the Illumina MiSeq platform.

Metagenome Sequencing

Two microliters of DNA (10 ng/μl) from nine fecal samples of the 0, 21, and 42 dpi groups (three samples per group) was fragmented to ∼300–500 bp with a Covaris S220 (Covaris, Woburn, MA, USA) individually. Subsequently, library construction was performed using a TruSeq Nano DNA LT Sample Preparation Kit (cat. no. FC-121-4001, Illumina, San Diego, CA, USA) according to the manufacturer's instructions, and then a TruSeq PE Cluster Kit v3-cBot-HS (cat. no. PE-401-3001, Illumina, San Diego, CA, USA) was used for bridge PCR. The resulting DNA was then pooled and quantified by Kapa Library Quantification Kits (cat. no. KK4824, Kapa Biosystems, Boston, MA, USA) and sequenced using the Illumina HiSeq platform with a TruSeq SBS Kit v3-HS (cat. no. FC-401-3001, Illumina, San Diego, CA, USA).

16S rRNA Gene Analysis

Paired-end reads were reprocessed using Trimmomatic software (26) to detect and cut off ambiguous bases from the N terminal. Low-quality sequences with an average quality score lower than

20 were removed by the sliding window trimming approach. After trimming, the paired-end reads were assembled using Fast Ligation-based Automatable Solid-phase High-throughput software (version 1.2.11) (27). Only sequences with 10 base pairs (bp) of minimal overlapping, 200 bp of maximum overlapping, and 20% of maximum mismatch rate were assembled according to their overlap sequence. Reads with ambiguous, homologous sequences and a total length of <200 bp were abandoned, while reads with 75% of bases above Q20 were retained. Next, the sequences were checked by Quantitative Insights Into Microbial Ecology (QIIME) software (version 1.8.0) (28) for the following criteria: the maximum length of a homopolymer run was six, the maximum number of mismatches in the primer was two, the maximum number of errors in the barcode was zero, and reads with chimeras were detected and removed. After that, clean reads were obtained, followed by subjecting to primer sequence removal and clustering to generate operational taxonomic units (OTUs) using UPARSE software (version 6.1.351) with 97% sequence similarity cutoff (equal to bacterial species level) (29). All representative reads were chosen from each OTU by selecting the most abundant sequence with the QIIME package. High-quality representative sequences were annotated and blasted against the Silva database (version 123) on the basis of the Ribosomal Database Project classifier (the confidence threshold was set as 70%) (30).

Alpha diversity (within-sample diversity) was estimated for each group using the number of observed species, Chao1 richness estimator, Shannon–Wiener index, and phylogenetic diversity index, while beta diversity (between-sample diversity) was monitored with two-dimensional and three-dimensional principal coordinate analysis (PCoA) plots on the basis of weighted UniFrac distance metrics. Bar plots were generated to visualize the relative abundances and alterations over time in bacterial communities for fecal samples from each group. To distinguish significant differences in microbial communities at different taxonomic levels between healthy mice and *S. japonicum*-infected mice, one-way analysis of variance (ANOVA) was performed; statistical significance level was set at $p < 0.05$. Linear discriminant analysis (LDA) coupled with effect size (LEfSe) measurement[1] was implemented to illuminate microbial taxa that were differentially represented between the groups, in order to discover the potential markers at different time points. Pearson correlation coefficients between the top 30 dominant gut bacteria at the genus level were calculated, and bacterial genera with high correlations and $p < 0.05$ were used to build an associated network with Cytoscape software (version 3.6.1) to find correlations between gut microbiota changes and explore the ecological significance related to each other. Unless otherwise stated, statistical analyses and plots were carried out using R software (version 3.5.1).

Metagenomic Analysis

Next-generation sequencing quality control (QC) Toolkit (version 2.3.2) (31) was used to discard raw metagenomic reads with 70% of bases below Q20 and remove reads from the 3′ end until reaching the first nucleotide with a minimum quality score cutoff of 20 and if either read was shorter than 70 bp or contained "N" bases or ambiguous bases. Afterwards, sequences of *Mus musculus*[2] were filtered out by Burrows–Wheeler Alignment (version 0.7.9a) (32). After the scaffold sequences from all samples were assembled with Short Oligonucleotide Analysis Package *Denovo*[3] (version 4.5.4) (33), open reading frames (ORFs) were predicted and translated into amino acid sequences by prodigal[4] (version 2.6.3) (34). Cluster Database at High Identity with Tolerance[5] (version 4.5.4) was implemented to build non-redundant gene sets for all predicted genes and to cluster ORFs with more than 95% identity and more than 90% coverage. The gene with the longest full length from each cluster was selected as the representative read of each gene set. For further analysis, annotations were performed with the gene set representative reads by using Blastp[6] (Blast version 2.2.28+) alignment (E-value < 0.00001) between ORFs and the protein databases of the Kyoto Encyclopedia of Genes and Genomes[7].

Metabolic Profiling

Sample Processing for Metabolomics

Each 10-μl serum sample was thawed on ice and diluted 1:10 in methanol. After that, the mixture was vortexed briefly and incubated overnight at 4°C to precipitate proteins thoroughly, followed by centrifugation at 10,000 ×*g* for 10 min, and ∼80-μl aliquots of the supernatant were then transferred to a vial for analysis. The urine samples were prepared by diluting 50 μl of urine with 450 μl of Milli-Q water and centrifuging for 10 min at 10,000 ×*g* at 4°C to remove particulates. A 200-μl volume of supernatant was collected and transferred into a glass vial afterwards. Liver and colon samples were processed following a modified version of the method of Elizabeth et al. (35). Briefly, frozen tissue (50 ± 0.5 mg) was added to 1.5 ml of prechilled methanol/water (1:1, v:v) solvent, which was subsequently completely homogenized in an ice bath. The suspension was centrifuged at 16,000 ×*g* for 10 min, and the resulting supernatant was transferred into an Eppendorf tube and then processed through vacuum freeze-drying to obtain an aqueous extract. The dried residue was redissolved in 120 μl of methanol/water (1:1, v:v) and centrifuged at 13,000 ×*g* for 10 min to remove particulates. Thereafter, the clear supernatant was transferred to a sampling vial. For each type of specimen, QC samples were prepared by mixing an equal volume of all individuals into the vial to ensure the repeatability and the stability of the analysis.

Ultraperformance Liquid Chromatography Conditions

An ACQUITY UPLC-I Class System (Waters Ltd., Milford, MA, USA) was used to perform chromatographic separations. Each sample was injected onto an ACQUITY UPLC C18 BEH column (2.1 × 100 mm, 1.7 μm; Waters, Milford, MA, USA) in a

[1]http://huttenhower.org/galaxy

[2]http://www.ncbi.nlm.nih.gov/assembly/GCF_000001635.23

[3]http://soap.genomics.org.cn/

[4]https://github.com/hyattpd/Prodigal

[5]http://www.bioinformatics.org/cd-hit/

[6]http://blast.ncbi.nlm.nih.gov/Blast.cgi

[7]http://www.genome.jp/kegg/pathway.html (KEGG)

random order at 38°C, while QC samples were detected every 10 specimens throughout the injection.

For the serum samples, mobile phase A was water mixed with 0.1% formic acid, while mobile phase B was 70% isopropanol and 30% acetonitrile containing 0.1% formic acid. The serum samples were eluted under gradient conditions at a flow rate of 400 μl/min with 1% B, which was held for 1 min and then was ramped up from 1 to 40% B for 2 min, from 40 to 75% B for 5 min, from 75 to 85% B for 4 min, and from 85 to 99% B for 6 min, held at 99% B over 4 min, and then returned to 1% B for 3 min. The volume of the sample injected onto the column was 1.000 μl.

For the urine samples, the gradient solvent system included water (A) and acetonitrile (B), each containing 0.1% formic acid. The injection volume of the urine samples was set to 0.300 μl; the separation gradient was held at 3% B for 1.2 min, ramped up from 3 to 45% B over 8.8 min and from 45 to 98% B for 4 min, held at 98% B over 2 min, and then returned to 3% B for 3 min, with a flow rate of 400 μl/min.

For the liver supernatant, the injection volume was 0.400 μl; the mobile phase was held at 2% B for 2 min, increased from 2 to 45% B over the next 8 min, followed by 45 to 98% B over 3 min, held at 98% B for 2 min, and decreased to 2% B, which was held for 2 min, at a flow rate of 400 μl/min. However, the injection volume of the colon supernatant was set to 1.500 μl; the separation gradient was held at 25% B for 0.5 min, ramped from 25 to 50% B over 4.5 min, from 50 to 65% B for 7 min, and from 65 to 95% B for 4 min, held 95% B for 2 min, and then returned to 25% B over 3 min, with a flow rate of 400 μl/min. The gradient solvent systems used for the liver and the colon supernatants were the same as that used for the urine samples.

Quadrupole-Time-of-Flight Mass Spectrometry Conditions

Mass spectrometry data were collected by a SYNAPT G2-Si High-Definition Mass Spectrometer with an electrospray ionization (ESI) source (Waters Ltd., Milford, MA, USA) in both positive and negative ion modes for the serum and the urine samples, whereas only negative ion mode was used for the liver and colon aqueous extracts due to the limited valuable compounds detected in the positive ion mode. Nitrogen gas was set as desolvation and cone gas. The capillary voltage was set at 2.5 kV, nebulizer gas at 6 bar, cone voltage at 35 kV, cone gas flow at 30 L/h, source temperature at 110°C, desolvation gas temperature at 350°C, and desolvation gas flow at 700 L/h. The eluted compounds were scanned from mass/charge (*m/z*) 50 to *m/z* 1,200 at a rate of 0.3 s per scan for both MS mode and MS^E mode. The collision energy was set from 20 to 50 eV for MS^E mode. To ensure mass accuracy and reproducibility, leucine enkephalin was used to correct data (*m/z* 556.2720 in positive mode and *m/z* 554.2615 in negative mode) at a concentration of 1 ng/μl and a flow rate of 5 μl/min continuously.

Data Analysis

The raw data were acquired by Masslynx (version 4.1, Waters, Manchester, UK) and imported into Progenesis QI (version 2.1, Nonlinear Dynamics, Waters, Manchester, UK) for data preprocessing, including peak alignment, picking, and normalization as well as compound identification. Normalized and scaled datasets were imported into SIMCA-P (version 13.0, Umetrics, Umea, Sweden) and MetaboAnalyst 4.0[8] (36, 37) to carry out statistical analyses. The statistical significance between experimental groups was determined by one-way ANOVA, with $p < 0.05$. Principal component analysis (PCA) and partial least squares-discriminatory analysis (PLS-DA) were used to visualize natural separation and trends among the groups by score plots, while orthogonal partial least squares-discriminatory analysis (OPLS-DA) was conducted to find the maximum separation between healthy mice and *S. japonicum*-infected mice. Advanced statistical and visualization tools, such as variable importance in projection (VIP) and S-plots, were performed to reveal underlying trends in data. The discriminated metabolites were selected based on significant changes, including VIP scores that were taken from comparisons in OPLS-DA models >2, $p < 0.05$, and QC samples' coefficient of variation (CV) <30 and were putatively identified by searching databases such as the Human Metabolome Database[9] (38) and METLIN[10] (39) with accurate mass spectral data and MS/MS spectra. Furthermore, receiver operating characteristic (ROC) curve analysis was carried out to evaluate the early diagnostic capability of identified potential biomarkers. Metabolite set enrichment analysis (MSEA) and pathway analysis were performed by MetaboAnalyst 4.0 to investigate the most significant metabolic pathways involved in *S. japonicum* infection. Finally, correlations between the dominant gut bacteria changes and shifted metabolites were calculated in R software (version 3.5.1) by a hierarchical clustering algorithm to determine the relationships between them.

RESULTS

Gut Microbiome Community Structure Changes in Mice Infected by *S. japonicum*

High-throughput sequencing of the *16S* rRNA gene was implemented to illustrate the alterations in the gut bacterial compositions of BALB/c mice associated with *S. japonicum* infection. A total of 1,210,516 valid reads were retained from 30 fecal samples, with an average of 40,350 sequences per sample, for further processing after filtering, which generated 19,868 OTUs at 97% similarity level (**Supplementary Table 1**) and 56 OTUs shared among all samples (**Supplementary Figure 1**). Most of the shared OTUs are members of the families Lachnospiraceae, Ruminococcaceae, and Bacteroidales S24-7 group. The four different alpha diversity estimators mentioned above increased over time among all groups but to a lesser extent in the infected mice than in the uninfected mice, whereas the least diversity presented at 21 dpi, indicating that the infection of *S. japonicum* reduced the alpha diversity of host gut bacteria, especially at 21 dpi (**Supplementary Figure 2**). However, the differences were not statistically significant ($p > 0.05$). A three-dimensional PCoA plot based on weighted UniFrac distances (**Supplementary Figure 3**) showed the variations of the gut

[8]http://www.metaboanalyst.ca
[9]http://www.hmdb.ca
[10]http://metlin.scripps.edu

bacterial communities of BALB/c mice, with 49.84, 18.29, and 7.12% variation explained by principal component (PC) 1, PC2, and PC3, respectively. The difference was observed between the 0-dpi group and the 42-dpi group, which demonstrated that the effect of *S. japonicum* infection in the late stage on the gut microbiome composition of the host was relatively stronger.

Perturbed Gut Bacteria in Mice With *S. japonicum* Infection

To observe *S. japonicum* infection effects on the gut microbiome of BALB/c mice, bar plots were generated according to the relative abundance of the 15 most abundant gut bacterial phyla (**Figure 1A**) and genera in different groups (**Figure 1B**). Subsequently, one-way ANOVA was applied to identify significant alterations in the composition of the host gut microbiota at the phylum and the genus levels during infection. It is obvious that Firmicutes and Bacteroidetes were the most abundant gut bacterial phyla, with total average relative abundances over 90% in all groups, and the abundances of Proteobacteria and Deferribacteres were altered according to the time of infection but with no statistical significance ($p > 0.05$, **Supplementary Table 2**). At the genus level, *Lactobacillus*, *Lachnospiraceae NK4A136* group, *Bacteroides*, *Staphylococcus*, and *Alloprevotella* were the most prevalent gut microbiome in BALB/c mice, but only alterations of the relative abundances of *Staphylococcus*, *Parabacteroides*, *Alistipes*, *Roseburia*, and *Ruminococcaceae UCG-014* showed statistical significance in the top 15 most important gut genera ($p < 0.05$, **Supplementary Table 3**). Notably, *Staphylococcus*, with a relative abundance of 14.46% in the 21-dpi group, was almost undetectable in other groups (**Figure 2A**). Furthermore, the average relative abundance of *Parabacteroides* was decreased before 7 dpi, but it was increased after that (**Figure 2B**); *Alistipes* was significantly more abundant in the infected groups than in the uninfected group (**Figure 2C**). In contrast, *Roseburia* and *Ruminococcaceae UCG-014* (**Figures 2D,E**) were reduced after infection with *S. japonicum,* while the average relative abundance of the latter increased approximately twofold at 7 dpi.

To determine the taxa ranging from the phylum to the genus level that discriminated between each time point of *S. japonicum* infection, LEfSe, with an adjusted $p < 0.05$ and LDA score threshold >6.0, was performed. Bacteria from the phyla Firmicutes and Saccharibacteria, in addition to *Alistipes* and other taxa, were significantly associated with the 7-dpi group, while only *Parabacteroides* and *Lachnospiraceae UCG-005* were significantly related to the 14-dpi group. Some members of the phyla Firmicutes and Proteobacteria were significantly enriched in the 21-dpi group, but the most significant was *Staphylococcus*. The Gammaproteobacteria class significantly distinguished the 28-dpi group from the other groups. Over-abundances of other members from the phyla Firmicutes, Bacteroidetes, and Proteobacteria were significantly linked to the 42-dpi group. However, no discriminative gut flora was found in the 0-dpi group. It is worth noting that *Lachnospiraceae UCG-005* was related to the 14-dpi group, whereas *Lachnospiraceae UCG-010* was associated with the 42-dpi group (**Figure 3**). The cladogram in **Figure 4** showed the most relevant clades among each group, which was in accordance with the above mentioned results.

Correlations between the top 30 dominant bacterial genera are demonstrated in **Figure 5**, with either a positive or a negative Pearson correlation coefficient ($p < 0.05$). The gut bacteria were divided into four clusters, and the most connected bacteria were *Anaerotruncus*, *Coprococcus 1*, *Parabacteroides*, *Bacteroides*, *Erysipelatoclostridium*, and *Odoribacter*, while *Odoribacter* had the maximum connections with other genera. It is interesting that significant negative correlations were only found in *Odoribacter* and *Lachnoclostridium*, as well as *Enterorhabdus* and *Lachnospiraceae UCG-001*, whereas the remaining bacteria were significantly positively related to each other.

S. japonicum Infection-Induced Metagenome Changes

Metagenomic analysis was used in this study to identify genes of host gut microbiota involved in specific pathways or functions during *S. japonicum* infection. An average of 56,686,511 valid reads per sample was obtained after removing sequences of the host, and then a non-redundant gene catalog that contained 1,048,575 clusters assembled into bacterial genes was constructed for further annotation. Afterwards, annotated metagenomic data were obtained by mapping to KEGG orthologs (kos), and the ko number was implemented to correspond to the KEGG pathway to indicate which genes were associated with specific metabolic pathways or functions (**Supplementary Table 4**). A hierarchical clustering heat map constructed based on the results from analysis of KEGG at level 3 demonstrated a remarkable ability to discriminate between healthy mice and infected mice in 14 different KEGG pathways (**Figure 6**). The 0-dpi group showed seven enriched pathways including transport and catabolism (regulation of mitophagy—yeast ko04139, regulation of autophagy ko04140), signal transduction (mTOR signaling pathway ko04150), immune system (RIG-I-like receptor signaling pathway ko04622), metabolism of terpenoids and polyketides (sesquiterpenoid and triterpenoid biosynthesis ko00909), xenobiotic biodegradation and metabolism (steroid degradation ko00984), and biosynthesis of other secondary metabolites (aflatoxin biosynthesis ko00254) ($p < 0.05$). Additionally, signal transduction (AMPK signaling pathway ko04152), immune system (chemokine signaling pathway ko04062), metabolism of terpenoids and polyketides (biosynthesis of vancomycin group antibiotics ko01055), metabolism of other amino acids (beta-alanine metabolism ko00410), biosynthesis of other secondary metabolites (penicillin and cephalosporin biosynthesis ko00311), and substance dependence (cocaine addiction ko05030) were significantly perturbed in the 42-dpi group ($p < 0.05$), whereas biosynthesis of other secondary metabolites (betalain biosynthesis ko00965) was altered significantly in the 21-dpi group, with $p < 0.05$.

Multivariate Statistical Analysis of Metabolite Profiling

In PCA score plots, QC samples that applied to test analytical repeatability and instrument performance and stability were

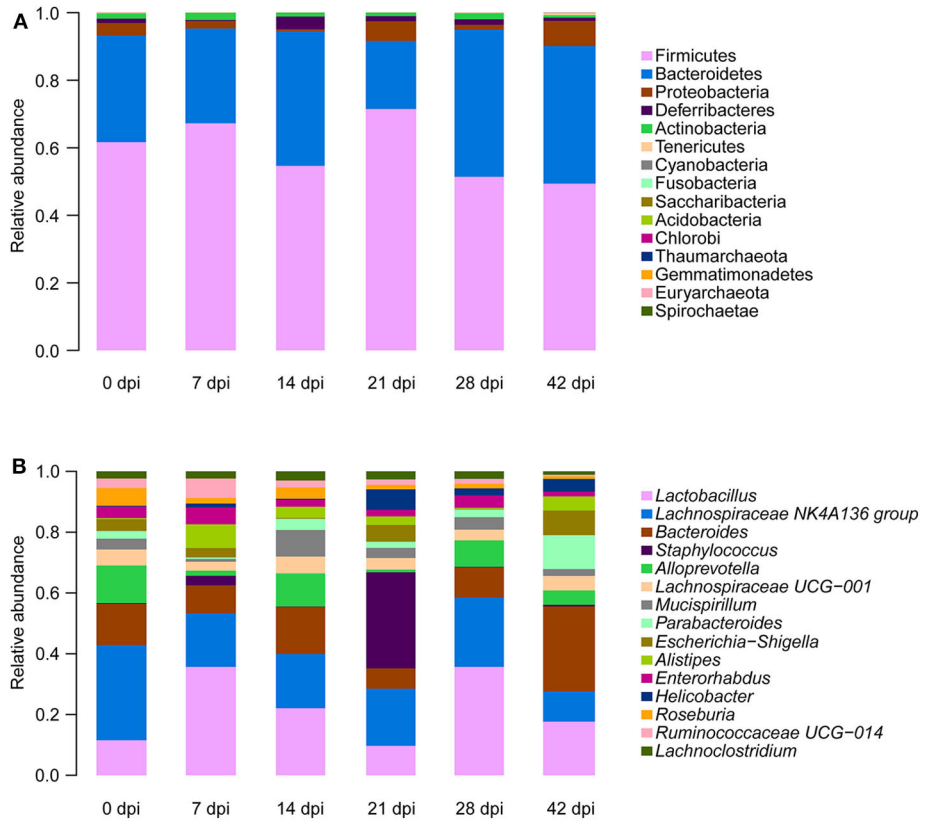

FIGURE 1 | Relative abundances of the top 15 most important gut microbiota constituents at the phylum level **(A)** and genus level **(B)** across different time points as assessed by *16S* rRNA sequencing. Each column represents the composition of the microbial taxa in one group.

tightly clustered, which demonstrated high reproducibility of the instrument (**Supplementary Figure 4**). Representative base peak intensity chromatograms of all types of specimens at seven time points are shown in **Supplementary Figures 5–8**. Differences in peaks and peak heights were observed among all groups, which indicated that the composition of metabolite profiles of BALB/c mice was changed during *S. japonicum* infection.

Initially, PCA, which is an unsupervised method of pattern recognition aiming to identify the overall clustering patterns and trends in a data set without considering groups, was implemented to obtain a global view and determine whether the metabolites from these seven groups of mice differed. Based on the top three principal components, the PCA results showed distinguished classifications between the control mice and the mice with different statuses of *S. japonicum* infection from serum and urine samples separately in both ESI modes, indicating that *S. japonicum* infection had significant effects on mouse metabolism (**Figure 7**). However, the 0-dpi group and early infection groups appeared to be partially overlapping, and the latter were closer than the late infection groups to the controls in the PCA score plots, whereas the most profound differences were found between the 0-dpi group and the late infection groups, which illustrate that the changes in metabolite profiles were miniscule at the early stage of infection and then became significant in the later stage. However, samples derived from liver and colon aqueous extracts demonstrated unclear classifications between healthy mice and infected mice of different time periods of *S. japonicum* infection with PCA in negative ion mode. This finding is evident in the PCA score plots in **Figure 7F**, which revealed that the effects of *S. japonicum* infection on mouse metabolism were not as evident in tissue as they were in body fluids.

Subsequently, in order to enhance the separation among the different classes of samples, a supervised method, PLS-DA was performed. For serum, urine, and liver aqueous extracts, PLS-DA models were constructed for all time points of *S. japonicum* infection separately, and all groups could be readily clearly differentiated from each other by PLS1, PLS2, and PLS3 in both ESI modes; high values of R^2 and Q^2 of each model reflected the data stability and the good fit of the model parameters (**Figure 8**, **Supplementary Table 5**). These results revealed that the biochemical perturbations and the metabolic profiles of the infected groups were distinct from those of the uninfected group. Furthermore, notable separation was found between control mice and infected mice during the process of schistosomiasis. Nevertheless, colon aqueous extract samples from all groups still clustered together in the PLS-DA score plot.

Finally, OPLS-DA was applied to reduce the dimension and produce the clearest separation between two groups as

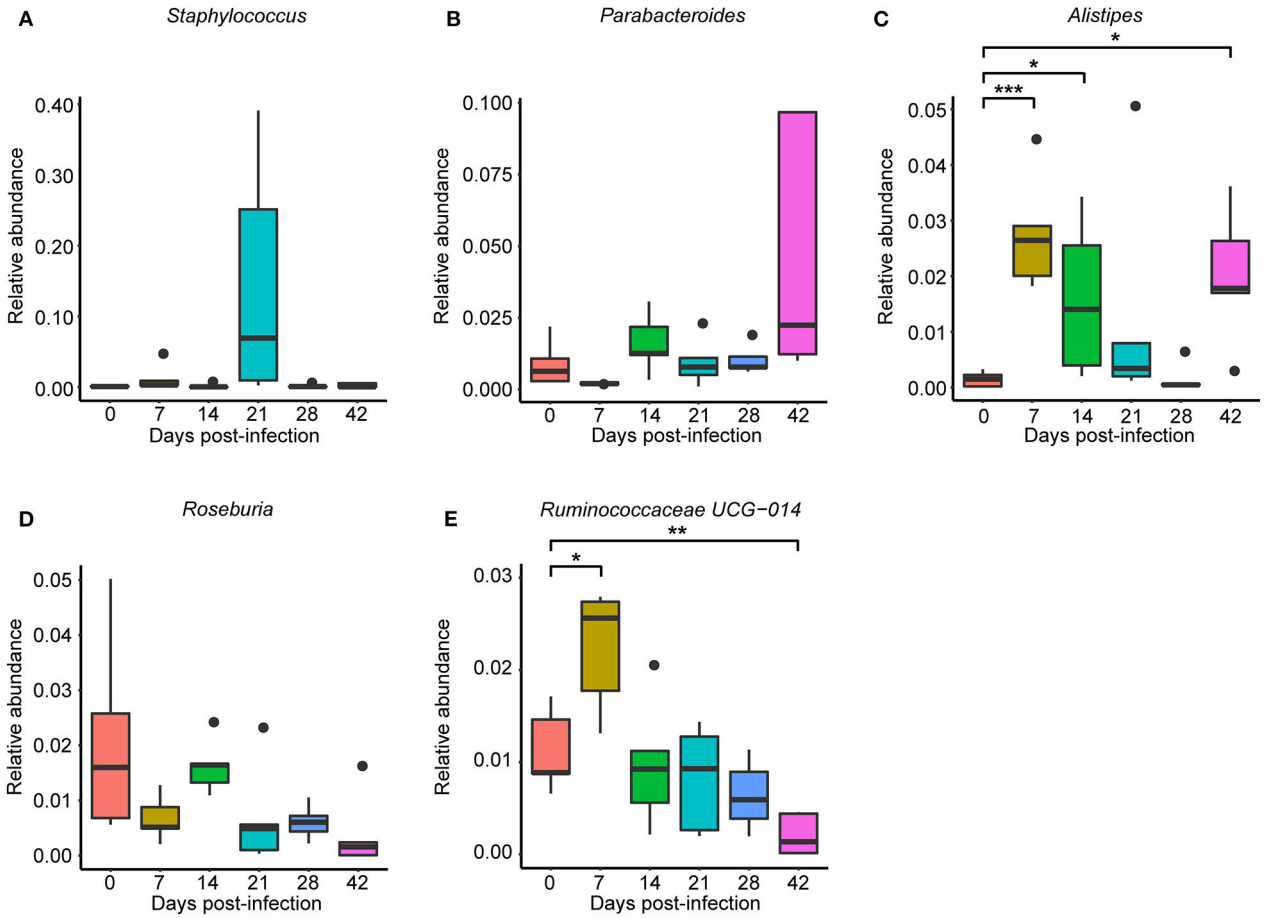

FIGURE 2 | Relative abundances of significantly altered top 15 most important gut genera associated with *Schistosoma japonicum* infection. Each column represents one group. **(A)** *Staphylococcus*. **(B)** *Parabacteroides*. **(C)** *Alistipes*. **(D)** *Roseburia*. **(E)** *Ruminococcaceae UCG-014*. The top and the bottom whiskers indicate the maximum and the minimum values, respectively, and the hyphen represents the median value (*$p < 0.05$, **$p < 0.01$, ***$p < 0.001$).

well as identifying metabolites that drive group distinction with one predictive and one orthogonal component (**Supplementary Figures 9–14**). The S-plots obtained from OPLS-DA were used to find out the meaningful and reliable variables that were attributable to the separation between two groups; the ions farther from the origin in the plot represent higher VIP values and were selected as potential metabolite biomarkers (**Supplementary Figures 9–14**).

Biomarker Identification and Analysis

A total of 42 unique compounds were identified in serum extracts, 53 unique compounds were identified in urine samples, and 24 unique compounds were identified from liver and colon aqueous extracts on the basis of the S-plot, VIP scores >2, $p < 0.05$, and QC samples' CV <30 (**Supplementary Table 6**). The majority of these metabolites were lipids, glucose, organic acids, nucleic acids, and amino acids. As shown in **Supplementary Figure 15**, hierarchical cluster analysis demonstrated the trends of significantly identified compounds for seven time points from all individuals. Most of the lipids were downregulated persistently during *S. japonicum* infection, while some phospholipids were upregulated in medium-term infection or late infection. However, several phospholipids were altered in only early- and medium-term infection, with downregulation. In addition, glucose and some organic acids were increased at 3 dpi but dropped to the uninfected levels after that. We picked out five potential biomarkers related to the early diagnosis of schistosomiasis (at 3 dpi) based on VIP value >5 and the value of the area under the ROC curve (AUC) >0.9. Phosphatidylcholine (PC) (22:6/18:0) and colfosceril palmitate in serum as well as xanthurenic acid, naphthalenesulfonic acid, and pimelylcarnitine in urine demonstrated promising diagnostic potential between the uninfected group and the 3-dpi group, with an AUC value of 0.9–1, while xanthurenic acid and naphthalenesulfonic acid exhibited the most discriminatory power since the sensitivity and the specificity were both 100% (**Figure 9B**). Therefore, xanthurenic acid and naphthalenesulfonic acid may be the most powerful targets for early diagnosis of schistosomiasis. The abundance of xanthurenic acid, PC (22:6/18:0), and colfosceril palmitate were significantly reduced at 3 dpi, whereas naphthalenesulfonic acid and pimelylcarnitine levels rose extremely at 3 dpi (**Figure 9A**).

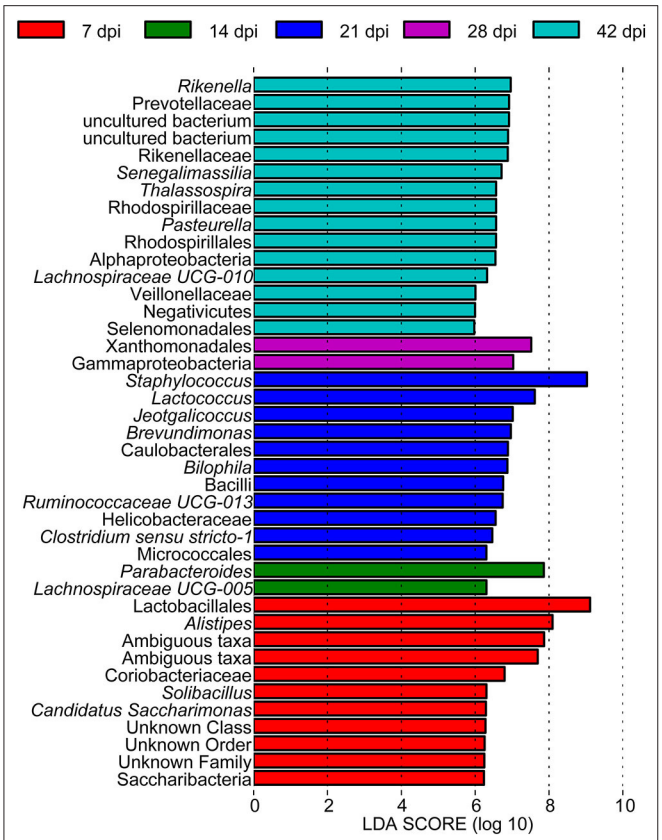

FIGURE 3 | A histogram with linear discriminant analysis scores showing differentially abundant gut bacteria during the course of *Schistosoma japonicum* infection. Taxa highlighted in different colors indicate over-representation in the corresponding groups.

MSEA and Pathway Analysis

The MSEA results indicated that two sets of identified metabolites extracted from serum (**Figure 10A**) and six sets of identified metabolites in liver aqueous extracts (**Figure 10C**) were different between the uninfected group and the infected groups; among these, purine metabolism, caffeine metabolism, pyrimidine metabolism, and galactose metabolism were significantly enriched ($p < 0.05$). Moreover, the metabolites were grouped based on the KEGG database by pathway analysis, while purine metabolism (ko00230), sphingolipid metabolism (ko00600), and glycerophospholipid metabolism (ko00564) were significantly related to the process of schistosomiasis ($p < 0.05$) (**Figures 10B,D**). Among pathways of serum metabolites, glycerophospholipid metabolism and purine metabolism showed the impact factors of 0.18 and 0.04, respectively (**Figure 10B**), while purine metabolism demonstrated the impact factor of 0.03 in pathways of liver aqueous metabolites (**Figure 10D**), which indicated that these two pathways were disturbed mostly during *S. japonicum* infection.

Relationships Between Host Metabolome and Gut Microbiome

To investigate the functional correlation between the altered metabolites from the colon and fecal flora alterations, correlation analysis was conducted by calculating the Pearson's correlation coefficient. As shown in **Figure 11**, clear correlations between altered metabolic profiles and gut microbiome were observed; however, more metabolites were negatively correlated with fecal flora, whereas two compounds exhibited significant positive correlations with some bacterial groups ($p < 0.05$). Of particular note is that LysoPC (20:1), which decreased in the colon of *S. japonicum*-infected BALB/c mice, was positively correlated with the reduction of *Lachnospiraceae NK4A136* group and *Roseburia*. Additionally, cortolone, which increased in the colon of *S. japonicum*-infected BALB/c mice, was positively correlated with the elevation of *Bacteroides* as well as *Parabacteroides*. In summary, *S. japonicum* infection induced significant perturbation in both the gut microbiome and the metabolomic profile of the host, which were interactive during the process of schistosomiasis.

DISCUSSION

Parasitic infection can impact the gut microbiota composition of the host, and the underlying mechanism is its effect on the host immune system, which could break the balance between the gut microbiome and the host that has already been established (40). In this study, *16S* rRNA sequencing was applied to demonstrate the dynamic alteration in the gut microbiome of BALB/c mice in response to *S. japonicum* infection and to identify bacteria that are crucial in the complex host-parasite interplay. The result of diversity analysis showed an overall reduction in alpha diversity and a relative increase in beta diversity of host gut bacteria after *S. japonicum* infection; beta diversity analysis also demonstrated strong associations between the gut microbiota composition and stage of infection, especially in the late stage, which was in conformity with previous studies of *S. japonicum* and *S. mansoni* (25, 41). As we have known, the schistosomula enter the venous blood vessels and are transported to the lungs where they become lung schistosomula at 3 dpi. At 7 dpi, the schistosomula enter the arterial circulation and then migrate to the mesenteric veins of the liver and become mature a week later. At 21 dpi, the worms migrate to the mesenteric veins of the bowel, and gametes of both the female and the male worms occur. Then, the female worm produces immature eggs at 28 dpi. At 42 dpi, mature eggs deposit in the liver of the host through the bloodstream or pass through the intestinal wall and are excreted in the feces. Thus, the gut microbiome community structures of the host are altered variously by *S. japonicum* infection due to the varying parasitic sites of the worm at different time points, and the gut microbiota of each individual respond differently according to the degree of homeostasis disruption. While the decrease in richness of the gut microbiota is harmful to the healthy individual who is infected by the parasite because the gut microbiome is crucial in providing a protective environment (42), for the individual with autoimmune diseases, such as Crohn's disease, ulcerative colitis (UC), and coeliac disease, parasites may actively contribute to reinstating gut homeostasis with quantitative and qualitative modifications of the gut microbiota, which can profoundly influence immune cell development and function in the intestine (43–46).

Firmicutes, Bacteroidetes, Proteobacteria, and Deferribacteres, which are common in the mouse (47), were also

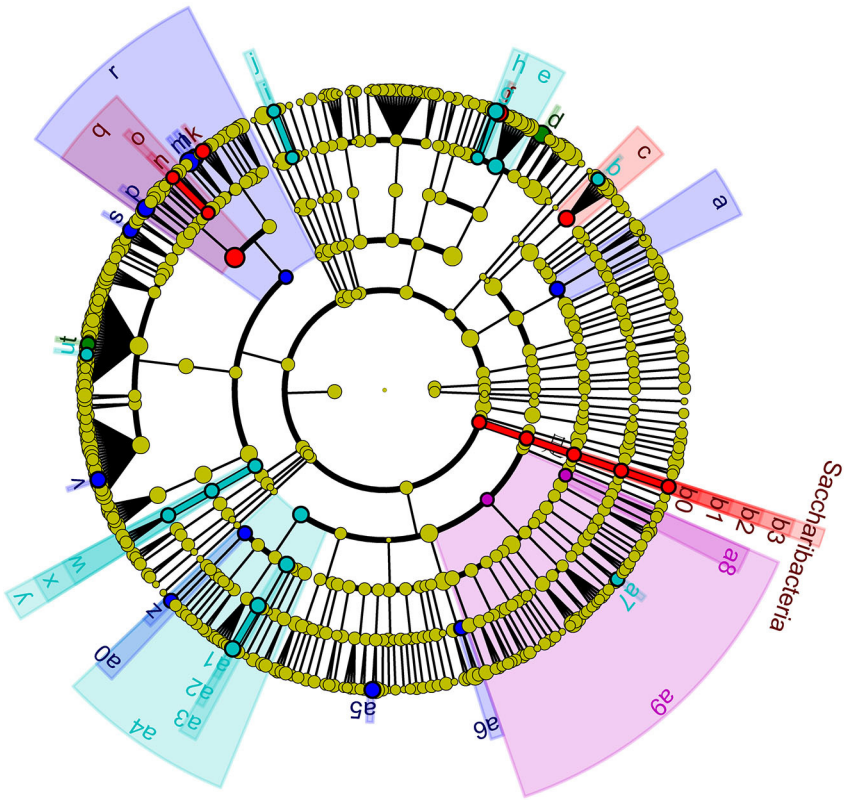

FIGURE 4 | A cladogram showing the discriminated taxa in different groups. Regions with different colors represent different groups. Differently colored nodes in the branches represent the microbial groups that play an important role in the corresponding groups, whereas yellow nodes indicate bacterial groups that are insignificant in all groups.

the dominant gut bacterial phyla in both infected and uninfected BALB/c mice, but no statistically significant differences were observed during the infection. Similarly, previous research has shown that Firmicutes decreased relatively and Bacteroidetes and Proteobacteria increased relatively in response to *S. japonicum* infection in C57BL/6 mice, whereas the same variations were not found in BALB/c mice (25). These results illustrated that the alteration in gut microbiome composition after *S.*

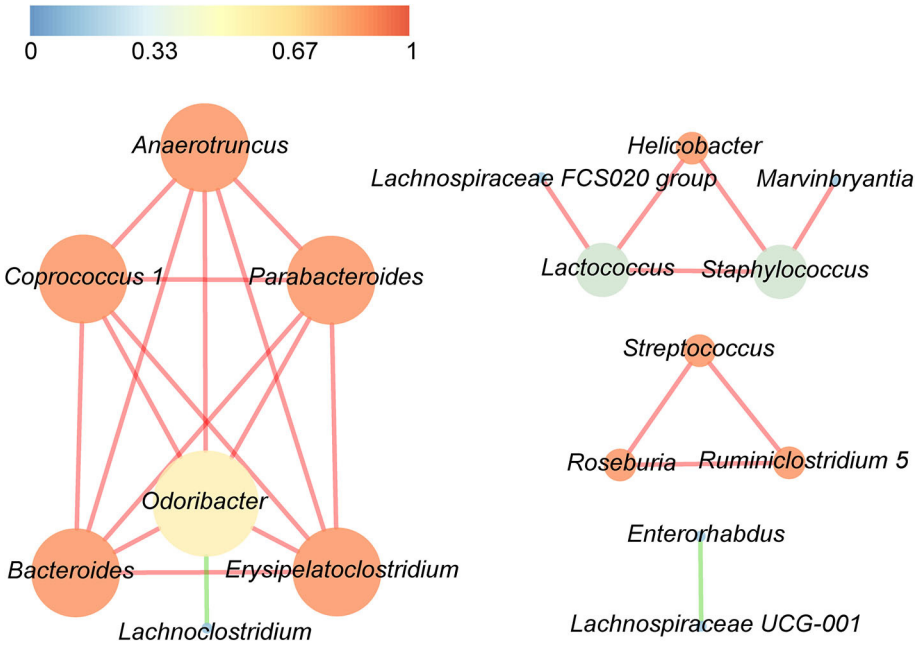

FIGURE 5 | Significant relationships among the top 30 abundant bacterial genera were detected by Pearson correlation coefficient ($p < 0.05$). The nodes in the interaction network represent the dominant genus, the connection between them shows an association between the two genera, and the red line indicates a positive correlation, whereas the green line indicates a negative correlation. The size of a node is proportionally positive to the degree of the node, and the color of the node is related to the clustering coefficient, that is, the color gradient from dark colors to bright colors corresponds to the value of the aggregation coefficient from low to high.

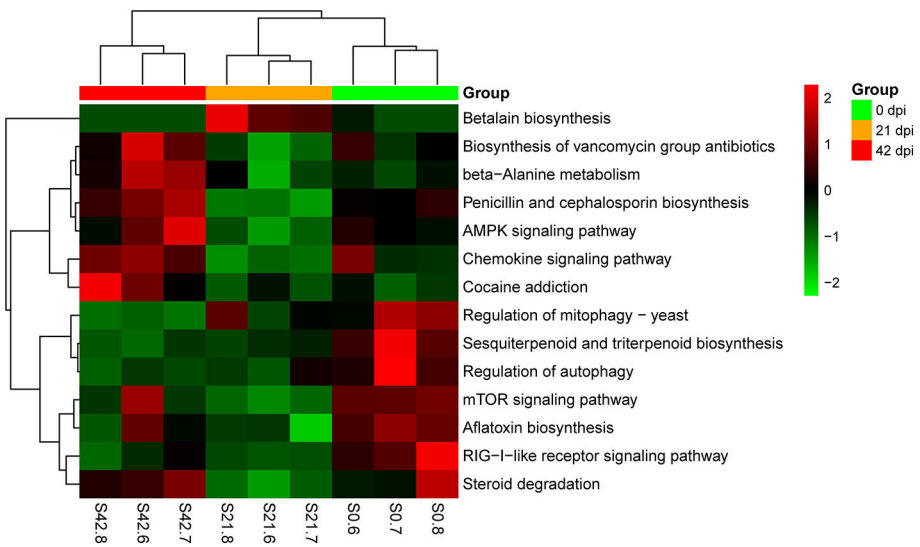

FIGURE 6 | Hierarchical clustering heat map constructed using annotated metagenomic data on the basis of the Kyoto Encyclopedia of Genes and Genomes (KEGG). Samples are shown in columns, and KEGG pathways are shown in rows.

japonicum infection was closely related to the host itself. The abundance of some prevalent genera, including *Staphylococcus*, *Parabacteroides*, *Alistipes*, *Roseburia*, and *Ruminococcaceae UCG-014*, was changed significantly during the infection. Both *Parabacteroides* and *Alistipes* are members of Bacteroidetes and were relatively abundant in response to infection, while members of Firmicutes, *Roseburia*, and *Ruminococcaceae UCG-014* were decreased after the infection, which indicated that although no significant differences were found at the phylum level, significant differences were observed at the genus level, and the change trend of different genera from the same phylum was consistent in the course of the infection. Earlier studies have illustrated

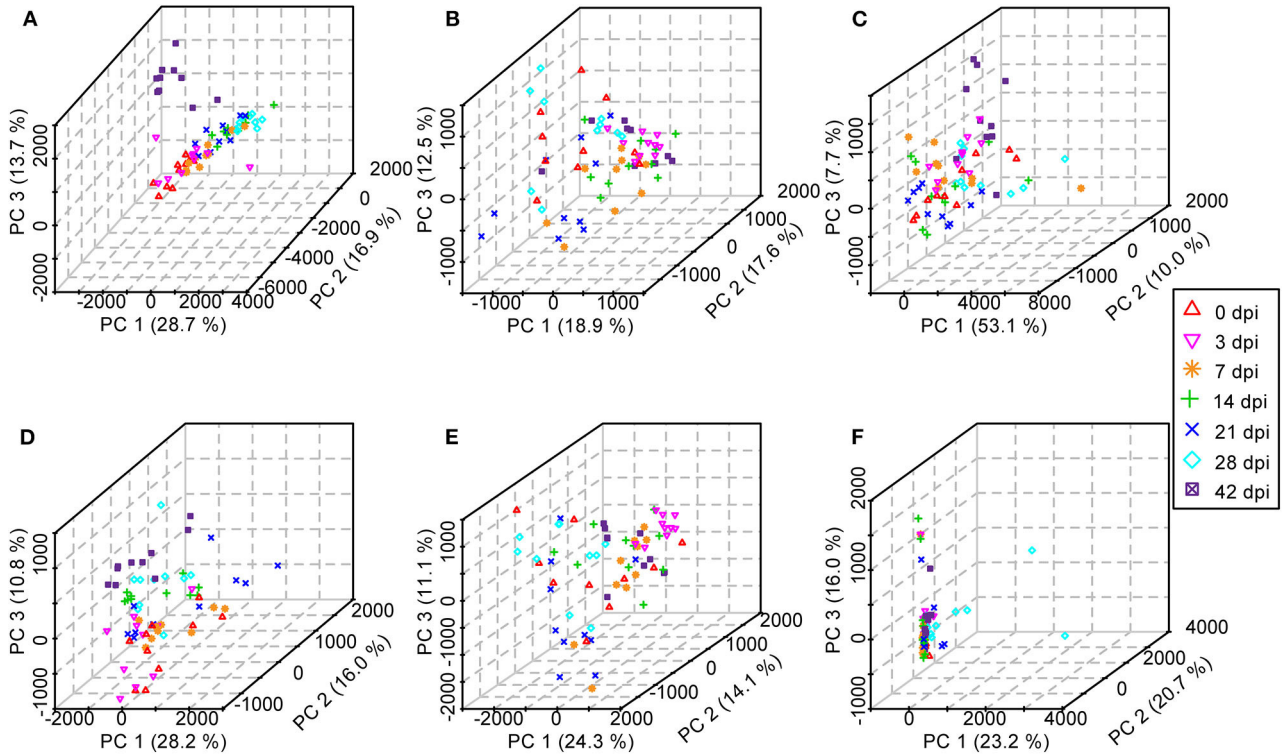

FIGURE 7 | Three-dimensional score plots of principal component analysis from healthy mice and infected mice at different time points. Each point represents an individual. **(A)** Serum samples in positive electrospray ionization (ESI+) mode. **(B)** Urine samples in ESI+ mode. **(C)** Liver aqueous extracts in negative electrospray ionization (ESI-) mode. **(D)** Serum samples in ESI- mode. **(E)** Urine samples in ESI- mode. **(F)** Colon aqueous extracts in ESI- mode.

that *Alistipes* can produce anti-inflammatory metabolites, which would promote the differentiation of anti-inflammatory Treg/Tr1 cells in the gut of mice, and *Alistipes* can also protect mice suffering from the effects of dextran sulfate sodium (48, 49). Hence, depletion of *Alistipes* was found in *Salmonella*-infected mice, porcine epidemic diarrhea virus-infected piglets, and chronic hepatitis B patients (50–52). Nevertheless, *Alistipes* was reported to result in the increase of trimethylamine N-oxide and the decrease of short-chain fatty acids (SCFA) production, which led to the destruction of the intestinal barrier (51, 53). The enhanced abundance of *Alistipes* during *S. japonicum* infection may be caused by the stress reaction of the hosts. Furthermore, as probiotic-type bacteria, which are able to prevent pathogen infection, a reduction in the diversity and the abundance of *Parabacteroides* was observed in mice infected with intestinal helminth parasites in an earlier study (54), which was found at only 7 dpi of *S. japonicum*; however, the increased abundance of *Parabacteroides* after 7 dpi might be a consequence of stress response because some bacteria belonging to *Parabacteroides* were involved in the metabolism of amino acid. Consistently, previous studies have suggested that *Roseburia*, one kind of SCFA-producing bacteria that is essential for maintaining the gut function of humans and animals (55), was significantly decreased both in chronic kidney disease and in end-stage renal disease patients (56, 57), so the intestinal homeostasis was broken. Similarly, some members of Ruminococcaceae were butyrate producers, and the abundance of *Ruminococcaceae UCG-014* reduced in a UC carcinogenesis model and even in a hypertriglyceridemia-related acute necrotizing pancreatitis model (58, 59). Interestingly, *Staphylococcus*, a classical non-enteric pathogen, was also found in the gut microbiome and increased in cystic fibrosis patients (60, 61), which was evident at 21 dpi of *S. japonicum*.

Using LEfSe, we noted that *Alistipes* (phylum Bacteroidetes) showed great abundance at 7 dpi and that another member from Bacteroidetes, *Parabacteroides*, was significantly associated with 14 dpi of *S. japonicum*. Furthermore, LEfSe identified a greater differential abundance of *Staphylococcus* (phylum Firmicutes) at 21 dpi, before the female adults laid eggs, while the greater differential abundance of Gammaproteobacteria was highlighted by LEfSe at 28 dpi, after the female adults laid eggs. Conversely, a significant over-representation of the class Gammaproteobacteria (phylum Proteobacteria) was identified in *Clostridium difficile* infection patients and children with acute diarrhea (62, 63). However, since we did not study bacteria with low abundance, we cannot draw a more precise conclusion based on the results of LEfSe. Correlation analysis of the top 30 dominant genera in the course of *S. japonicum* infection illustrated that most genera were positively related to each other, which showed that the co-occurrence relation was general in

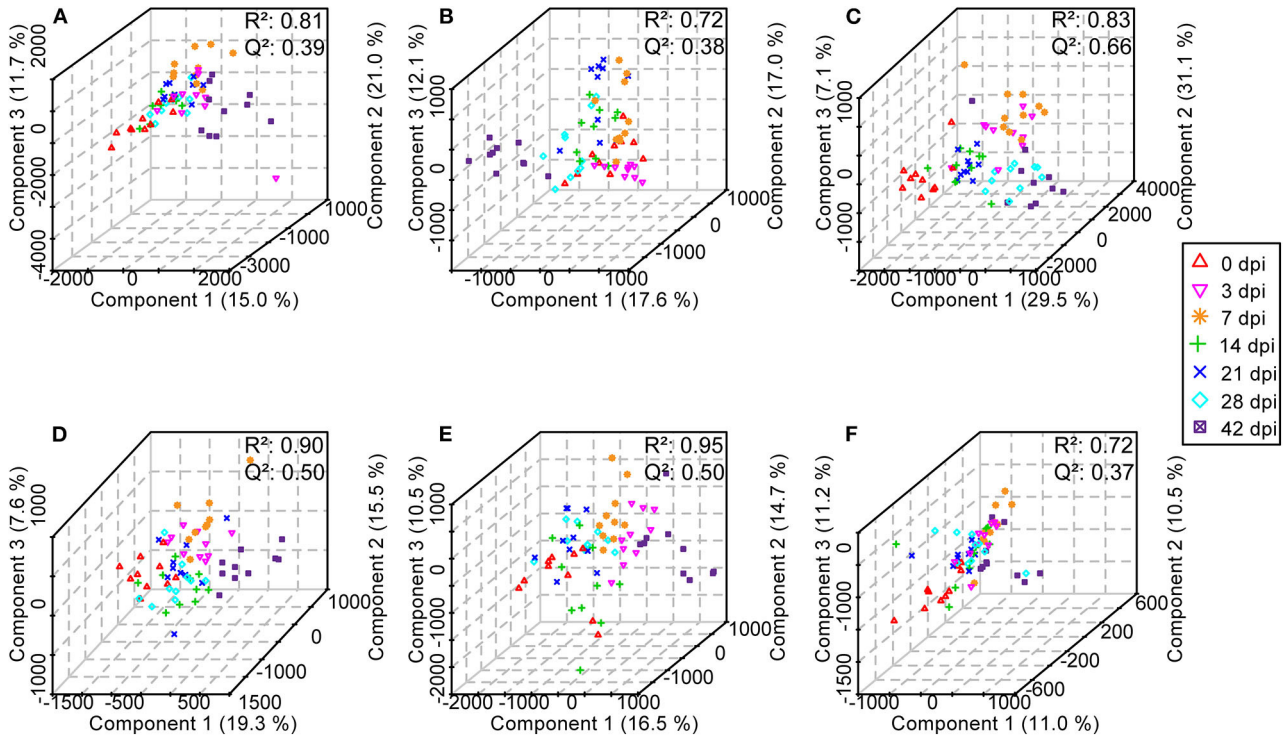

FIGURE 8 | Three-dimensional score plots of partial least squares-discriminatory analysis from healthy mice and infected mice at different time points. Each point represents an individual. **(A)** Serum samples in positive electrospray ionization (ESI+) mode. **(B)** Urine samples in ESI+ mode. **(C)** Liver aqueous extracts in negative electrospray ionization (ESI-) mode. **(D)** Serum samples in ESI- mode. **(E)** Urine samples in ESI- mode. **(F)** Colon aqueous extracts in ESI- mode.

the gut microbiome for those who would work together even though they may belong to different phyla. Regardless, co-exclusion relationships were observed in *Odoribacter* (phylum Bacteroidetes) and *Lachnoclostridium* (phylum Firmicutes) as well as in *Lachnospiraceae UCG-001* (phylum Firmicutes) and *Enterorhabdus* (phylum Actinobacteria). *Odoribacter* and *Lachnospiraceae UCG-001* became more abundant, while the others became relatively less abundant during *S. japonicum* infection.

The results of the *16S* rRNA gene-based analysis clarified the dynamic changes in the host gut microbiome in response to *S. japonicum* infection and the interactions between dominant genera. Subsequently, metagenomics sequencing was performed to search for altered pathways or functions at 0, 21, and 42 dpi of *S. japonicum*, which might enable us to generate hypotheses about the mechanisms underlying the infection. Consistent with the alterations in the gut microbiota, the functional metagenome was also changed significantly. In particular, the only ko category significantly enriched among the microbiome of BALB/c mice at 21 dpi was the biosynthesis of betalain, and the involved gene was tyrosinase (K00505), a kind of oxidoreductase. Betalain biosynthesis plays a crucial part in response to osmotic adjustment and salt resistance, and betaine is vital to enhance stress resistance (64), so the activation of betalain biosynthesis was helpful to the gut microbiome to resist stress while *S. japonicum* migrates to the mesenteric veins. Other particularly notable signaling pathways associated with *S. japonicum* infection at 42 dpi were the AMPK and the chemokine signaling pathways. The former was activated by calcium/calmodulin-dependent protein kinase exclusion β (CaMKK β, K07359), one of the upstream kinases, which reflected the elevated AMP/ATP ratio in response to the infection. Once activated, AMPK would lead to a concomitant inhibition of energy-consuming biosynthetic pathways, including the synthesis of glycogen and cholesterol. Chemokines play an important role in protective host response, and the upregulation of the chemokine signaling pathway at 42 dpi showed that the gut microbiota was sensitive to the infection and chemokine receptors were activated to produce an inflammatory immune response. In summary, we hypothesize that the gut microbiota in the host provide signals that resist the parasites and enhance the immune response of the host. These findings from the functional metagenome analysis offered a more detailed view of specific microbiome-encoded functions that are associated with *S. japonicum* infection and may facilitate further studies on the interaction between specific genes.

To describe the metabolic profile of BALB/c mice after *S. japonicum* infection, an untargeted UPLC–MS/MS-based high-resolution metabolomics analysis was performed in the present study. Both PCA and PLS-DA revealed differences between uninfected and infected mice, and the differences increased over time; however, more obvious variances were observed in body fluids than in tissues, which indicated that body fluids were

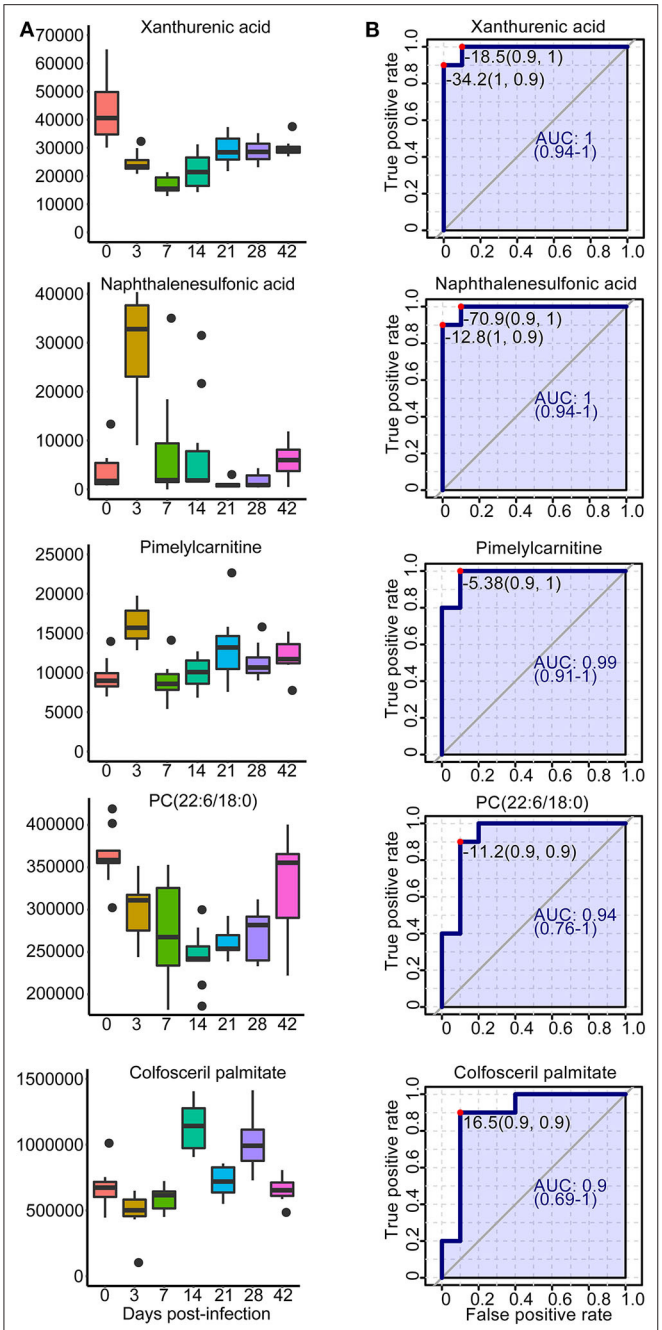

FIGURE 9 | Overview of selected representative metabolites from serum and urine associated with schistosomiasis. **(A)** Box plots showing the abundance of selected biomarkers. Each column represents a time point. **(B)** The receiver operating characteristic curve for selected biomarkers. The x-axis represents the specificity, while the y-axis represents the sensitivity.

affected more severely than cells during *S. japonicum* infection and that is why more differential metabolites were obtained in the former than in the latter. This result is expected because *S. japonicum* does not parasitize the host cell.

In response to *S. japonicum* infection, the significantly different metabolites were lipids, and the result is consistent with the prior study on *S. japonicum* and *T. brucei rhodesiense* (*T. b. rhodesiense*) (2, 16). Lipids are the major constituents of membranes and are important in reserving energy; they are also highly biologically active metabolites that are involved or even play a part in signaling and a range of inflammatory processes (65). As the major structural lipids that form cellular membranes, phospholipids participate in the regulation of nutrient transport as well as toxic host-cell effector molecules; they are synthesized to support the growth of cells in the course of infection, and phospholipid biosynthetic pathways are the targets of drugs (66–68). Our results demonstrated that most of the altered lipids belonged to glycerophospholipids, which are structural components of biological membranes (69), followed by sphingolipids and diacylglycerol. The majority of glycerophospholipids were significantly reduced in response to the infection, such as PC, phosphatidylethanolamine (PE), phosphatidylserine, phosphatidylinositol, and LysoPC. However, the concentration of some PCs was elevated in *S. japonicum*-infected mice, which was different from the results in *S. haematobium*-infected patients, where high levels of PC and PE were found (70). It is believed that the abundance of PC and PE in bladder endothelial cells may be one of the mechanisms for inducing cancer in chronic urogenital schistosomiasis (70); nevertheless, the different variations presented in PC after *S. japonicum* infection remain unclear, and future studies should address this question.

An endogenous phospholipid, LysoPC, which is derived from PC, has various stimulating or modulating effects on immune cells and possesses pro-inflammatory activities as well as anti-inflammatory properties; a heightened level of LysoPC in the plasma was considered as a marker for cell membrane injury (71, 72). Besides that, LysoPC participates in the elimination of dead eukaryotic and prokaryotic cells and controlling bacterial growth during infection (72, 73). Earlier studies have proven that LysoPC has direct antibacterial activities against methicillin-resistant *Staphylococcus aureus* as well as the ability to enhance neutrophil antimicrobial ability to remove ingested bacteria (74–76); however, our results illustrated that LysoPC does not inhibit all bacteria because LysoPC (20:1) was positively correlated with *Lachnospiraceae NK4A136* group and *Roseburia*, the genera that are beneficial to the host during *S. japonicum* infection.

It cannot be ignored that some sphingomyelin (SM) species were reduced after infection, while the concentration of ceramide (Cer) was elevated, especially at the late stage of infection; the variation trend of SM and Cer was also observed in *T. b. rhodesiense* human African trypanosomiasis patients (16). Sphingolipids not only are components of the membrane that are able to protect the cell from harmful environmental factors but also are involved in cellular signaling as a second messenger (77, 78); the significant observations in sphingolipids (SM and Cer) may offer the basis and foundation for revealing the resistance mechanism between hosts and *S. japonicum* since infection can trigger the generation of Cer, which is generated in part by sphingomyelinase enzymes, leading to cell autophagy and apoptosis, additional pro-inflammatory cytokines, and chemokine synthesis, as well as other metabolic disorders (16, 79, 80). It is more interesting to note that the metagenomic analysis

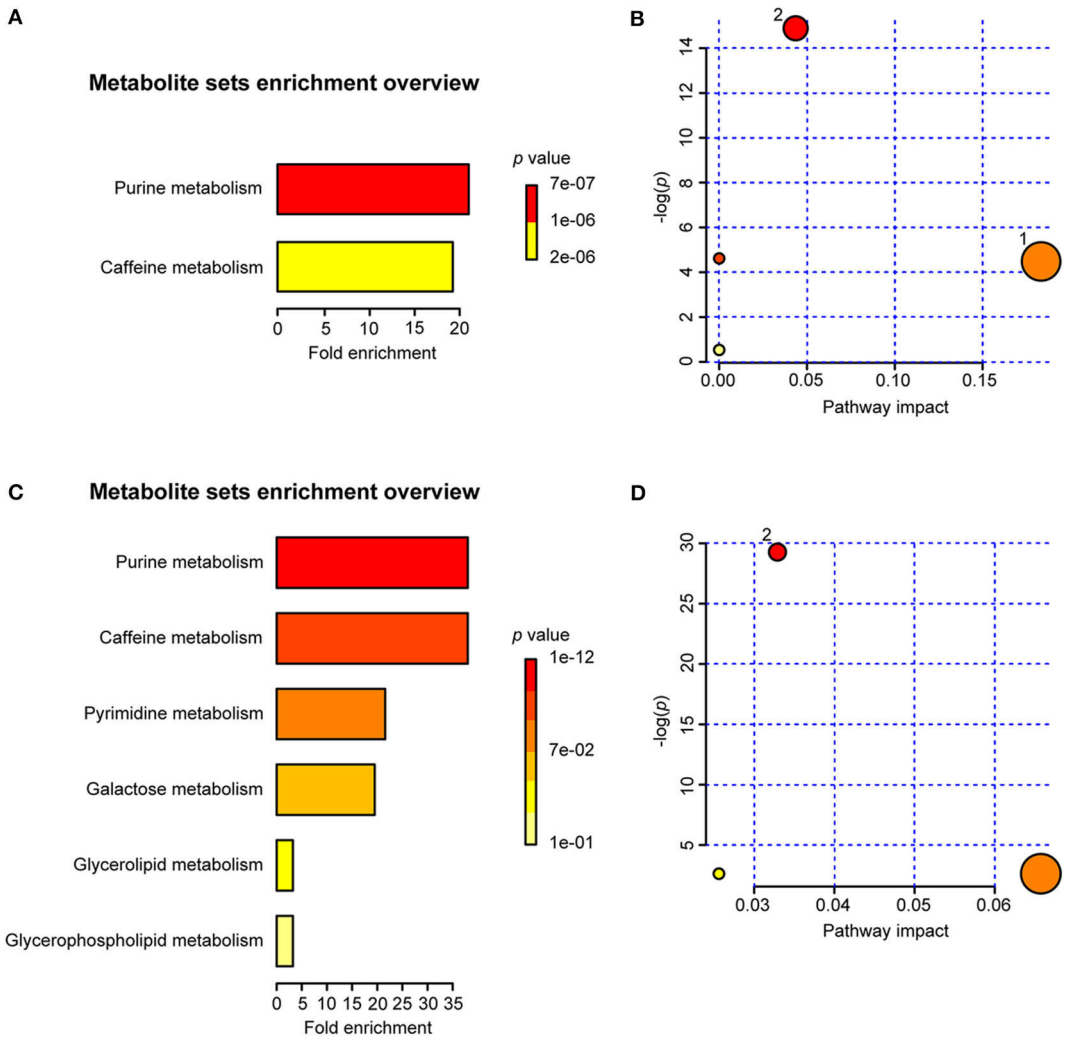

FIGURE 10 | Summary of metabolite set enrichment analysis (MSEA) and pathway analysis. **(A)** Summary plot for MSEA in serum is ranked according to Holm *p*-value. **(B)** Pathway analysis of serum metabolites shows key nodes in metabolic pathways that have been significantly changed during an infection. The x-axis represents increasing metabolic pathway impact from pathway topology analysis, whereas the y-axis represents unadjusted *p*-value by pathway enrichment analysis. Greater pathway enrichment and higher pathway impact values are exhibited in larger sizes and darker colors, respectively. **(C)** Summary plot for MSEA in liver aqueous extracts is ranked according to Holm *p*-value. **(D)** Pathway analysis of liver aqueous metabolite shows key nodes in metabolic pathways that have been significantly changed during an infection. 1, glycerophospholipid metabolism; 2, purine metabolism.

revealed that the chemokine signaling pathway was upregulated at 42 dpi, which suggests that inflammatory effects existed in gut bacteria also; the host and the gut microbiota collaborate with each other to eliminate the parasites.

Surprisingly, the levels of two kinds of carnitine species (acetylcarnitine and oleoylcarnitine) were significantly lower in infected mice than in uninfected mice, while another two kinds of carnitine species (hydroxyisovaleroyl carnitine and pimelylcarnitine) were increased at 3 dpi. Carnitine plays a crucial role in fat metabolism and energy production in mammals, and it can support the production of $CD4^+$ and $CD8^+$ T cells during infection (81, 82); a prior study has shown that the levels of carnitine and several acylcarnitines were elevated in *S. japonicum*-infected *Microtus fortis* (*M. fortis*) and C57BL/6 mice, but the phenomenon was more obvious in *M. fortis* (21). Hence, we suggest that host responses to *S. japonicum* infection vary and that the protective reaction against *S. japonicum* is relatively less strong in BALB/c mice.

Pathway analysis illuminated that both sphingolipid metabolism and glycerophospholipid metabolism were altered in the process of schistosomiasis, which is consistent with an earlier study of *S. haematobium* (70). In fact, sphingolipids and their derivatives have recently presented as promising drug targets for controlling infectious and inflammatory disease; however, how sphingolipid-mediated pathologies and how the host modifies sphingolipid metabolism to benefit itself remain unclear, and a better understanding of these mechanisms may provide new insights into new therapeutic strategies (83).

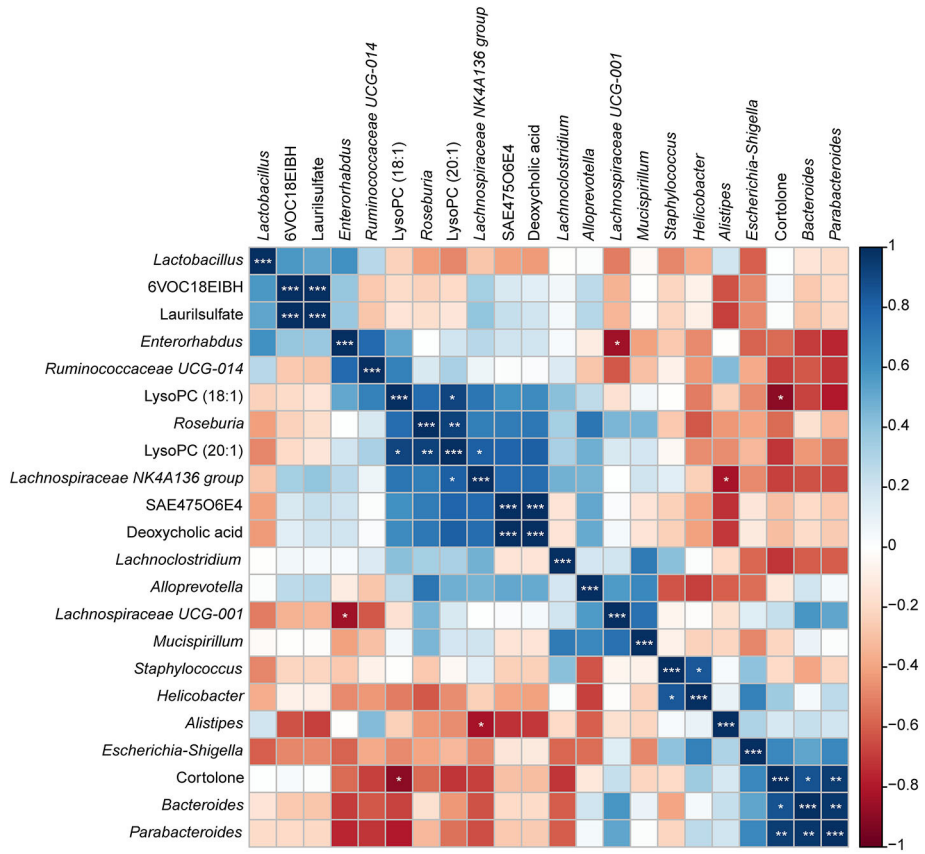

FIGURE 11 | Correlation plot showing the relationship between the altered metabolites from the colon and the top 15 abundant gut bacteria. The correlations between them are exhibited by colors; blue indicates a positive correlation, red indicates a negative correlation, and a darker color illustrates a stronger correlation (*$p < 0.05$, **$p < 0.01$, ***$p < 0.001$).

Nevertheless, because of the absence of age-matched uninfected BALB/c mice in this study, the alterations of gut microbiome and metabolites could be partially related to the age effect rather than the progression of *S. japonicum* infection alone.

CONCLUSIONS

In the present study, we applied *16S* rRNA gene sequencing combined with a metagenomic sequencing approach and UPLC–MS metabolic profiling to highlight three aspects of the interrelationships between *S. japonicum*, the gut microbiome, and metabolites. We demonstrated that both the gut microbiome and the metabolites were significantly altered in *S. japonicum*-infected BALB/c mice; moreover, they were also associated with the time course of *S. japonicum* infection. In response to *S. japonicum* infection, not only the richness and diversity of gut microbiota were decreased but also the composition of the microbiota which differed obviously from that present during the uninfected status. In summary, the abundance of some bacteria that could produce SCFA was decreased, while those of some opportunistic pathogens that could raise the risk of infections were increased. In addition, metagenomic analysis revealed that the AMPK and chemokine signaling pathways were significantly perturbed after infection. The metabolic biomarkers that we identified in this study were found in serum or urine, with little or no invasiveness, and could distinguish *S. japonicum* infection from non-infection at 3 dpi with high sensitivity and specificity. Additionally, alterations in glycerophospholipid and purine metabolism were discovered in *S. japonicum* infection. As a result, these findings may provide a novel understanding of the mechanisms during schistosomiasis development regarding aspects of the gut microbiome and metabolites and facilitate the discovery of new targets for early diagnosis and prognosis. Nevertheless, further validations of potential biomarkers in human populations are essential, and the exact mechanisms of interactions between *S. japonicum*, the gut microbiome, and metabolites also await future research.

DATA AVAILABILITY STATEMENT

The sequencing data of 16S rRNA gene and metagenome have been deposited in the NCBI Sequence Read Archive under the project number PRJNA602960 and PRJNA602878.

ETHICS STATEMENT

The animal study was reviewed and approved by the Animal Care and Use Committee of Sun Yat-sen University.

AUTHOR CONTRIBUTIONS

ZL conceived and designed the study. ZL, YH, and JC drafted the manuscript. YH and JC carried out the experiments. YX, HoZ, PH, YM, MG, SC, and HaZ participated in data analysis. HaZ participated in study design, technological guidance, and coordination. All authors contributed to the article and approved the submitted version.

FUNDING

This work was supported by grants from the National Natural Science Foundation of China (grant nos. 81572023 and 81371836), the Science and Technology Planning Project of Guangdong Province (grant no. 2019B030316025), the Natural Science Foundation of Guangdong Province (grant no. 2019A1515011541), the National Key Research and Development Program of China (grant nos. 2016YFC1202000 and 2016YFC1200500), the Project of Basic Platform of National Science and Technology Resources of the Ministry of Sciences and Technology of China (grant no. TDRC-2017-22), the 111 Project (grant no. B12003), the Undergraduates Innovation Training Program of Guangdong Province (grant no. 201601084), and the Teaching Reform Project of Guangdong Province (grant no. 2017001).

ACKNOWLEDGMENTS

We would like to thank Mrs. Tingchan Liang for polishing the manuscript.

SUPPLEMENTARY MATERIAL

The Supplementary Material for this article can be found online at: https://www.frontiersin.org/articles/10.3389/fimmu.2020.569727/full#supplementary-material

Supplementary Figure 1 | A flower plot showing unique and common operational taxonomic units among all samples.

Supplementary Figure 2 | Rarefaction plots of *16S* rRNA gene sequences obtained from fecal samples across multiple time points based on alpha diversity analyses. Lines represent the means, and the standard deviations are shown by error bars. **(A)** Observed species. **(B)** Chao1. **(C)** Shannon–Wiener index. **(D)** Phylogenetic diversity index.

Supplementary Figure 3 | Principal coordinate analysis (PCoA) plots showing beta diversity differences on the basis of *16S* rRNA gene sequencing during *S. japonicum* infection. Figures were calculated using weighted UniFrac distance, and each point represents an individual. **(A)** Two-dimensional PCoA plot. **(B)** Three-dimensional PCoA plot.

Supplementary Figure 4 | Three-dimensional score plots of principal component analysis from quality control and samples. **(A)** Serum samples in positive electrospray ionization (ESI+) mode. **(B)** Urine samples in ESI+ mode. **(C)** Liver aqueous extracts in negative electrospray ionization (ESI-) mode. **(D)** Serum samples in ESI- mode. **(E)** Urine samples in ESI- mode. **(F)** Colon aqueous extracts in ESI- model.

Supplementary Figure 5 | Base peak intensity chromatograms of serum samples from different time points in ESI+ mode **(A)** and ESI- mode **(B)** as analyzed by quadrupole-time-of-flight mass spectrometry with a full scan.

Supplementary Figure 6 | Base peak intensity chromatograms of urine samples from different time points in ESI+ mode **(A)** and ESI- mode **(B)** as analyzed by quadrupole-time-of-flight mass spectrometry with a full scan.

Supplementary Figure 7 | Base peak intensity chromatograms of liver aqueous extracts from different time points in ESI- mode as analyzed by quadrupole-time-of-flight mass spectrometry with a full scan.

Supplementary Figure 8 | Base peak intensity chromatograms of colon aqueous extracts from different time points in ESI- mode as analyzed by quadrupole-time-of-flight mass spectrometry with a full scan.

Supplementary Figure 9 | Orthogonal partial least squares-discriminatory analysis (OPLS-DA) of serum extracts in ESI+ mode at different stages of *Schistosoma japonicum* infection. Each point represents one sample in score plots. OPLS-DA loadings S-plot combined with the covariance and the correlation loading profile indicate the variable importance. Each point represents a variable.

Supplementary Figure 10 | Orthogonal partial least squares-discriminatory analysis (OPLS-DA) from serum extracts in ESI- mode at different stages of *Schistosoma japonicum* infection. Each point represents one sample in score plots. OPLS-DA loadings S-plot combined with the covariance and the correlation loading profile indicate the variable importance. Each point represents a variable.

Supplementary Figure 11 | Orthogonal partial least squares-discriminatory analysis (OPLS-DA) from urine extracts in ESI+ mode at different stages of *Schistosoma japonicum* infection. Each point represents one sample in score plots. OPLS-DA loadings S-plot combined with the covariance and the correlation loading profile indicate the variable importance. Each point represents a variable.

Supplementary Figure 12 | Orthogonal partial least squares-discriminatory analysis (OPLS-DA) from urine extracts in ESI- mode at different stages of *Schistosoma japonicum* infection. Each point represents one sample in score plots. OPLS-DA loadings S-plot combined with the covariance and the correlation loading profile indicate the variable importance. Each point represents a variable.

Supplementary Figure 13 | Orthogonal partial least squares-discriminatory analysis (OPLS-DA) from liver aqueous extracts in ESI- mode at different stages of *Schistosoma japonicum* infection. Each point represents one sample in score plots. OPLS-DA loadings S-plot combined with the covariance and the correlation loading profile indicate the variable importance. Each point represents a variable.

Supplementary Figure 14 | Orthogonal partial least squares-discriminatory analysis (OPLS-DA) from colon aqueous extracts in ESI- mode at different stages of *Schistosoma japonicum* infection. Each point represents one sample in score plots. OPLS-DA loadings S-plot combined with the covariance and the correlation loading profile indicate the variable importance. Each point represents a variable.

Supplementary Figure 15 | Heat map visualization for the significantly different identified metabolites at different time points. Each column represents a sample, and each row represents a metabolite. The scaled intensity of the metabolites is reflected by the color key; higher intensity levels, when compared to the mean metabolite intensity value, are colored red, while lower intensity levels are colored green. Branch height represents the similarity between two metabolites, and metabolites with the shortest vertical difference indicate the closest connection.

Supplementary Table 1 | Operational taxonomic unit tables and taxonomic classifications of the *16S* rRNA gene.

Supplementary Table 2 | One-way ANOVA of relative abundances of gut microbiome constituents at the phylum level.

Supplementary Table 3 | One-way ANOVA of relative abundances of gut microbiome constituents at the genus level.

Supplementary Table 4 | KEGG annotation of metagenomic data.

Supplementary Table 5 | Q^2 and R^2 values are provided to show partial least squares-discriminatory analysis (PLS-DA) classification performance with different number of components.

Supplementary Table 6 | Statistically significantly changed metabolites identified in serum samples, urine samples, liver aqueous extracts and colon aqueous extracts ($p < 0.05$).

REFERENCES

1. Li Q, Zhao N, Liu M, Shen H, Huang L, Mo X, et al. Comparative analysis of proteome-wide lysine acetylation in juvenile and adult *Schistosoma japonicum*. *Front Microbiol.* (2017) 8:2248. doi: 10.3389/fmicb.2017.02248
2. Wu J, Xu W, Ming Z, Dong H, Tang H, Wang Y. Metabolic changes reveal the development of schistosomiasis in mice. *PLoS Negl Trop Dis.* (2010) 4:e807. doi: 10.1371/journal.pntd.0000807
3. Liu S, Zhou X, Piao X, Wu C, Hou N, Chen Q. Comparative analysis of transcriptional profiles of adult *Schistosoma japonicum* from different laboratory animals and the natural host, water buffalo. *PLoS Negl Trop Dis.* (2015) 9:e0003993. doi: 10.1371/journal.pntd.0003993
4. Ke XD, Shen S, Song LJ, Yu CX, Kikuchi M, Hirayama K, et al. Characterization of *Schistosoma japonicum* CP1412 protein as a novel member of the ribonuclease T2 molecule family with immune regulatory function. *Parasit Vectors.* (2017) 10:89. doi: 10.1186/s13071-016-1962-y
5. Qiu S, Fan X, Yang Y, Dong P, Zhou W, Xu Y, et al. *Schistosoma japonicum* infection downregulates house dust mite-induced allergic airway inflammation in mice. *PLoS ONE.* (2017) 12:e0179565. doi: 10.1371/journal.pone.0179565
6. Wang Y, Utzinger J, Xiao SH, Xue J, Nicholson JK, Tanner M, et al. System level metabolic effects of a *Schistosoma japonicum* infection in the Syrian hamster. *Mol Biochem Parasitol.* (2006) 146:1–9. doi: 10.1016/j.molbiopara.2005.10.010
7. Gouveia LR, Santos JC, Silva RD, Batista AD, Domingues ALC, Lopes EPA, et al. Diagnosis of coinfection by schistosomiasis and viral hepatitis B or C using 1H NMR-based metabonomics. *PLoS ONE.* (2017) 12:e0182196. doi: 10.1371/journal.pone.0182196
8. Martin FP, Wang Y, Sprenger N, Yap IK, Lundstedt T, Lek P, et al. Probiotic modulation of symbiotic gut microbial-host metabolic interactions in a humanized microbiome mouse model. *Mol Syst Biol*. (2008) 4:157. doi: 10.1038/msb4100190
9. Feng Q, Liu Z, Zhong S, Li R, Xia H, Jie Z, et al. Integrated metabolomics and metagenomics analysis of plasma and urine identified microbial metabolites associated with coronary heart disease. *Sci Rep*. (2016) 6:22525. doi: 10.1038/srep22525
10. Li N, Liu Y, Li W, Zhou L, Li Q, Wang X, et al. A UPLC/MS-based metabolomics investigation of the protective effect of ginsenosides Rg1 and Rg2 in mice with Alzheimer's disease. *J Ginseng Res.* (2016) 40:9–17. doi: 10.1016/j.jgr.2015.04.006
11. Nassar AF, Wu T, Nassar SF, Wisnewski AV. UPLC-MS for metabolomics: a giant step forward in support of pharmaceutical research. *Drug Discov Today*. (2017) 22:463–70. doi: 10.1016/j.drudis.2016.11.020
12. Olszewski KL, Morrisey JM, Wilinski D, Burns JM, Vaidya AB, Rabinowitz JD, et al. Host-parasite interactions revealed by Plasmodium falciparum metabolomics. *Cell Host Microbe*. (2009) 5:191–9. doi: 10.1016/j.chom.2009.01.004
13. MacRae JI, Dixon MW, Dearnley MK, Chua HH, Chambers JM, Kenny S, et al. Mitochondrial metabolism of sexual and asexual blood stages of the malaria parasite Plasmodium falciparum. *BMC Biol*. (2013) 11:67. doi: 10.1186/1741-7007-11-67
14. Orikiiriza J, Surowiec I, Lindquist E, Bonde M, Magambo J, Muhinda C, et al. Lipid response patterns in acute phase paediatric Plasmodium falciparum malaria. *Metabolomics*. (2017) 13:41. doi: 10.1007/s11306-017-1174-2
15. Creek DJ, Mazet M, Achcar F, Anderson J, Kim DH, Kamour R, et al. Probing the metabolic network in bloodstream-form Trypanosoma brucei using untargeted metabolomics with stable isotope labelled glucose. *PLoS Pathog*. (2015) 11:e1004689. doi: 10.1371/journal.ppat.1004689
16. Lamour SD, Gomez-Romero M, Vorkas PA, Alibu VP, Saric J, Holmes E, et al. Discovery of infection associated metabolic markers in human african trypanosomiasis. *PLoS Negl Trop Dis*. (2015) 9:e0004200. doi: 10.1371/journal.pntd.0004200
17. Vincent IM, Daly R, Courtioux B, Cattanach AM, Bieler S, Ndung'u JM, et al. Metabolomics identifies multiple candidate biomarkers to diagnose and stage human african trypanosomiasis. *PLoS Negl Trop Dis*. (2016) 10:e0005140. doi: 10.1371/journal.pntd.0005140
18. Ramakrishnan S, Docampo MD, MacRae JI, Ralton JE, Rupasinghe T, McConville MJ, et al. The intracellular parasite Toxoplasma gondii depends on the synthesis of long-chain and very long-chain unsaturated fatty acids not supplied by the host cell. *Mol Microbiol*. (2015) 97:64–76. doi: 10.1111/mmi.13010
19. Chen XQ, Zhou CX, Elsheikha HM, He S, Hu GX, Zhu XQ. Profiling of the perturbed metabolomic state of mouse spleen during acute and chronic toxoplasmosis. *Parasit Vectors*. (2017) 10:339. doi: 10.1186/s13071-017-2282-6
20. Zhou CX, Cong W, Chen XQ, He SY, Elsheikha HM, Zhu XQ. Serum metabolic profiling of oocyst-induced *Toxoplasma gondii* acute and chronic infections in mice using mass-spectrometry. *Front Microbiol*. (2017) 8:2612. doi: 10.3389/fmicb.2017.02612
21. Hu Y, Sun L, Yuan Z, Xu Y, Cao J. High throughput data analyses of the immune characteristics of Microtus fortis infected with *Schistosoma japonicum*. *Sci Rep*. (2017) 7:11311. doi: 10.1038/s41598-017-11532-2
22. Douglas AE. Lessons from studying insect symbioses. *Cell Host Microbe*. (2011) 10:359–67. doi: 10.1016/j.chom.2011.09.001
23. Schwarz RS, Moran NA, Evans JD. Early gut colonizers shape parasite susceptibility and microbiota composition in honey bee workers. *Proc Natl Acad Sci USA*. (2016) 113:9345–50. doi: 10.1073/pnas.1606631113
24. McManus DP, Dunne DW, Sacko M, Utzinger J, Vennervald BJ, Zhou XN. Schistosomiasis. *Nat Rev Dis Primers*. (2018) 4:13. doi: 10.1038/s41572-018-0013-8
25. Zhao Y, Yang S, Li B, Li W, Wang J, Chen Z, et al. Alterations of the Mice Gut Microbiome via *Schistosoma japonicum* Ova-Induced Granuloma. *Front Microbiol*. (2019) 10:352. doi: 10.3389/fmicb.2019.00352
26. Bolger AM, Lohse M, Usadel B. Trimmomatic: a flexible trimmer for Illumina sequence data. *Bioinformatics*. (2014) 30:2114–20. doi: 10.1093/bioinformatics/btu170
27. Reyon D, Tsai SQ, Khayter C, Foden JA, Sander JD, Joung JK. FLASH assembly of TALENs for high-throughput genome editing. *Nat Biotechnol*. (2012) 30:460–5. doi: 10.1038/nbt.2170
28. Caporaso JG, Kuczynski J, Stombaugh J, Bittinger K, Bushman FD, Costello EK, et al. QIIME allows analysis of high-throughput community sequencing data. *Nat Methods*. (2010) 7:335–6. doi: 10.1038/nmeth.f.303
29. Edgar RC. UPARSE: highly accurate OTU sequences from microbial amplicon reads. *Nat Methods*. (2013) 10:996–8. doi: 10.1038/nmeth.2604
30. Wang Q, Garrity GM, Tiedje JM, Cole JR. Naive Bayesian classifier for rapid assignment of rRNA sequences into the new bacterial taxonomy. *Appl Environ Microbiol*. (2007) 73:5261–7. doi: 10.1128/AEM.00062-07
31. Patel RK, Jain M. NGS QC Toolkit: a toolkit for quality control of next generation sequencing data. *PLoS ONE*. (2012) 7:e30619. doi: 10.1371/journal.pone.0030619
32. Li H, Durbin R. Fast and accurate long-read alignment with Burrows-Wheeler transform. *Bioinformatics*. (2010) 26:589–95. doi: 10.1093/bioinformatics/btp698
33. Luo R, Liu B, Xie Y, Li Z, Huang W, Yuan J, et al. SOAPdenovo2: an empirically improved memory-efficient short-read *de novo* assembler. *Gigascience*. (2012) 1:18. doi: 10.1186/2047-217X-1-18
34. Hyatt D, Chen GL, Locascio PF, Land ML, Larimer FW, Hauser LJ. Prodigal: prokaryotic gene recognition and translation initiation site identification. *BMC Bioinform*. (2010) 11:119. doi: 10.1186/1471-2105-11-119
35. Want EJ, Masson P, Michopoulos F, Wilson ID, Theodoridis G, Plumb RS, et al. Global metabolic profiling of animal and human tissues via UPLC-MS. *Nat Protoc*. (2013) 8:17–32. doi: 10.1038/nprot.2012.135

36. Xia J, Wishart DS. Web-based inference of biological patterns, functions and pathways from metabolomic data using MetaboAnalyst. *Nature Protocols*. (2011) 6:743–60. doi: 10.1038/nprot.2011.319
37. Chong J, Soufan O, Li C, Caraus I, Li S, Bourque G, et al. MetaboAnalyst 4.0: towards more transparent and integrative metabolomics analysis. *Nucleic Acids Res.* (2018) 46:W486–94. doi: 10.1093/nar/gky310
38. Wishart DS, Jewison T, Guo AC, Wilson M, Knox C, Liu Y, et al. HMDB 3.0–the human metabolome database in 2013. *Nucleic Acids Res.* (2013) 41(Database issue):D801–7. doi: 10.1093/nar/gks1065
39. Tautenhahn R, Cho K, Uritboonthai W, Zhu Z, Patti GJ, Siuzdak G. An accelerated workflow for untargeted metabolomics using the METLIN database. *Nat Biotechnol*. (2012) 30:826–8. doi: 10.1038/nbt.2348
40. Guernier V, Brennan B, Yakob L, Milinovich G, Clements AC, Soares Magalhaes RJ. Gut microbiota disturbance during helminth infection: can it affect cognition and behaviour of children? *BMC Infect Dis*. (2017) 17:58. doi: 10.1186/s12879-016-2146-2
41. Jenkins TP, Peachey LE, Ajami NJ, MacDonald AS, Hsieh MH, Brindley PJ, et al. Schistosoma mansoni infection is associated with quantitative and qualitative modifications of the mammalian intestinal microbiota. *Sci Rep*. (2018) 8:12072. doi: 10.1038/s41598-018-30412-x
42. Van den Abbeele P, Van de Wiele T, Verstraete W, Possemiers S. The host selects mucosal and luminal associations of coevolved gut microorganisms: a novel concept. *FEMS Microbiol Rev*. (2011) 35:681–704. doi: 10.1111/j.1574-6976.2011.00270.x
43. Broadhurst MJ, Ardeshir A, Kanwar B, Mirpuri J, Gundra UM, Leung JM, et al. Therapeutic helminth infection of macaques with idiopathic chronic diarrhea alters the inflammatory signature and mucosal microbiota of the colon. *PLoS Pathog*. (2012) 8:e1003000. doi: 10.1371/journal.ppat.1003000
44. Boyett D, Hsieh MH. Wormholes in host defense: how helminths manipulate host tissues to survive and reproduce. *PLoS Pathog*. (2014) 10:e1004014. doi: 10.1371/journal.ppat.1004014
45. Lee SC, Tang MS, Lim YA, Choy SH, Kurtz ZD, Cox LM, et al. Helminth colonization is associated with increased diversity of the gut microbiota. *PLoS Negl Trop Dis*. (2014) 8:e2880. doi: 10.1371/journal.pntd.0002880
46. Giacomin P, Croese J, Krause L, Loukas A, Cantacessi C. Suppression of inflammation by helminths: a role for the gut microbiota? *Philos Trans R Soc Lond B Biol Sci*. (2015) 370:1675. doi: 10.1098/rstb.2014.0296
47. Deng H, Yang S, Zhang Y, Qian K, Zhang Z, Liu Y, et al. Bacteroides fragilis prevents *Clostridium difficile* infection in a mouse model by restoring gut barrier and microbiome regulation. *Front Microbiol*. (2018) 9:2976. doi: 10.3389/fmicb.2018.02976
48. Dziarski R, Park SY, Kashyap DR, Dowd SE, Gupta D. Pglyrp-regulated gut microflora *Prevotella falsenii*, *Parabacteroides distasonis* and *Bacteroides eggerthii* enhance and *Alistipes finegoldii* attenuates colitis in mice. *PLoS ONE*. (2016) 11:e0146162. doi: 10.1371/journal.pone.0146162
49. Li J, Sung CY, Lee N, Ni Y, Pihlajamaki J, Panagiotou G, et al. Probiotics modulated gut microbiota suppresses hepatocellular carcinoma growth in mice. *Proc Natl Acad Sci USA*. (2016) 113:E1306–15. doi: 10.1073/pnas.1518189113
50. Borton MA, Sabag-Daigle A, Wu J, Solden LM, O'Banion BS, Daly RA, et al. Chemical and pathogen-induced inflammation disrupt the murine intestinal microbiome. *Microbiome*. (2017) 5:47. doi: 10.1186/s40168-017-0264-8
51. Wang J, Wang Y, Zhang X, Liu J, Zhang Q, Zhao Y, et al. Gut Microbial dysbiosis is associated with altered hepatic functions and serum metabolites in chronic hepatitis B patients. *Front Microbiol*. (2017) 8:2222. doi: 10.3389/fmicb.2017.02222
52. Huang A, Cai R, Wang Q, Shi L, Li C, Yan H. Dynamic change of gut microbiota during porcine epidemic diarrhea virus infection in suckling piglets. *Front Microbiol*. (2019) 10:322. doi: 10.3389/fmicb.2019.00322
53. Chiu CY, Cheng ML, Chiang MH, Kuo YL, Tsai MH, Chiu CC, et al. Gut microbial-derived butyrate is inversely associated with IgE responses to allergens in childhood asthma. *Pediatr Allergy Immunol*. (2019) 30:689–97. doi: 10.1111/pai.13096
54. Houlden A, Hayes KS, Bancroft AJ, Worthington JJ, Wang P, Grencis RK, et al. Chronic trichuris muris infection in C57BL/6 mice causes significant changes in host microbiota and metabolome: effects reversed by pathogen clearance. *PLoS ONE*. (2015) 10:e0125945. doi: 10.1371/journal.pone.0125945
55. Liang H, Dai Z, Liu N, Ji Y, Chen J, Zhang Y, et al. Dietary L-tryptophan modulates the structural and functional composition of the intestinal microbiome in weaned piglets. *Front Microbiol*. (2018) 9:1736. doi: 10.3389/fmicb.2018.01736
56. Jiang S, Xie S, Lv D, Zhang Y, Deng J, Zeng L, et al. A reduction in the butyrate producing species Roseburia spp. and *Faecalibacterium prausnitzii* is associated with chronic kidney disease progression. *Antonie Van Leeuwenhoek*. (2016) 109:1389–96. doi: 10.1007/s10482-016-0737-y
57. Jiang S, Xie S, Lv D, Wang P, He H, Zhang T, et al. Alteration of the gut microbiota in Chinese population with chronic kidney disease. *Sci Rep*. (2017) 7:2870. doi: 10.1038/s41598-017-02989-2
58. Huang C, Chen J, Wang J, Zhou H, Lu Y, Lou L, et al. Dysbiosis of intestinal microbiota and decreased antimicrobial peptide level in paneth cells during hypertriglyceridemia-related acute necrotizing pancreatitis in rats. *Front Microbiol*. (2017) 8:776. doi: 10.3389/fmicb.2017.00776
59. Wang CS, Li WB, Wang HY, Ma YM, Zhao XH, Yang H, et al. VSL#3 can prevent ulcerative colitis-associated carcinogenesis in mice. *World J Gastroenterol*. (2018) 24:4254–62. doi: 10.3748/wjg.v24.i37.4254
60. Tamburini FB, Andermann TM, Tkachenko E, Senchyna F, Banaei N, Bhatt AS. Precision identification of diverse bloodstream pathogens in the gut microbiome. *Nat Med*. (2018) 24:1809–14. doi: 10.1038/s41591-018-0202-8
61. Vernocchi P, Del Chierico F, Russo A, Majo F, Rossitto M, Valerio M, et al. Gut microbiota signatures in cystic fibrosis: Loss of host CFTR function drives the microbiota enterophenotype. *PLoS ONE*. (2018) 13:e0208171. doi: 10.1371/journal.pone.0208171
62. Milani C, Ticinesi A, Gerritsen J, Nouvenne A, Lugli GA, Mancabelli L, et al. Gut microbiota composition and Clostridium difficile infection in hospitalized elderly individuals: a metagenomic study. *Sci Rep*. (2016) 6:25945. doi: 10.1038/srep25945
63. Dinleyici EC, Martinez-Martinez D, Kara A, Karbuz A, Dalgic N, Metin O, et al. Time series analysis of the microbiota of children suffering from acute infectious diarrhea and their recovery after treatment. *Front Microbiol*. (2018) 9:1230. doi: 10.3389/fmicb.2018.01230
64. Zhang X, Yuan J, Zhang X, Liu C, Xiang J, Li F. Genome-wide analysis of alternative splicing provides insights into stress response of the pacific white shrimp *Litopenaeus vanname*. *Front Genet*. (2019) 10:845. doi: 10.3389/fgene.2019.00845
65. Calder PC. Polyunsaturated fatty acids, inflammation, and immunity. *Lipids*. (2001) 36:1007–24. doi: 10.1007/s11745-001-0812-7
66. de Kroon AI, Rijken PJ, De Smet CH. Checks and balances in membrane phospholipid class and acyl chain homeostasis, the yeast perspective. *Prog Lipid Res*. (2013) 52:374–94. doi: 10.1016/j.plipres.2013.04.006
67. Takenami I, de Oliveira CC, Petrilli JD, Machado A, Riley LW, Arruda S. Serum antiphospholipid antibody levels as biomarkers for diagnosis of pulmonary tuberculosis patients. *Int J Tuberc Lung Dis*. (2018) 22:1063–70. doi: 10.5588/ijtld.17.0874
68. Tams RN, Cassilly CD, Anaokar S, Brewer WT, Dinsmore JT, Chen YL, et al. Overproduction of phospholipids by the kennedy pathway leads to hypervirulence in *Candida albicans*. *Front Microbiol*. (2019) 10:86. doi: 10.3389/fmicb.2019.00086
69. Zufferey R, Pirani K, Cheung-See-Kit M, Lee S, Williams TA, Chen DG, et al. The Trypanosoma brucei dihydroxyacetonephosphate acyltransferase TbDAT is dispensable for normal growth but important for synthesis of ether glycerophospholipids. *PLoS ONE*. (2017) 12:e0181432. doi: 10.1371/journal.pone.018143
70. Adebayo AS, Mundhe SD, Awobode HO, Onile OS, Agunloye AM, Isokpehi RD, et al. Metabolite profiling for biomarkers in Schistosoma haematobium infection and associated bladder pathologies. *PLoS Negl Trop Dis*. (2018) 12:e0006452. doi: 10.1371/journal.pntd.0006452
71. Gao X, Guo M, Li Q, Peng L, Liu H, Zhang L, et al. Plasma metabolomic profiling to reveal antipyretic mechanism of Shuang-huang-lian injection on yeast-induced pyrexia rats. *PLoS ONE*. (2014) 9:e100017. doi: 10.1371/journal.pone.0100017
72. Lee HJ, Ko HJ, Song DK, Jung YJ. Lysophosphatidylcholine promotes phagosome maturation and regulates inflammatory mediator production through the protein kinase a-phosphatidylinositol 3 kinase-p38 mitogen-activated protein kinase signaling pathway during *Mycobacterium*

tuberculosis infection in mouse macrophages. *Front Immunol*. (2018) 9:920. doi: 10.3389/fimmu.2018.00920
73. Parra Millan R, Jimenez Mejias ME, Sanchez Encinales V, Ayerbe Algaba R, Gutierrez Valencia A, Pachon Ibanez ME, et al. Efficacy of lysophosphatidylcholine in combination with antimicrobial agents against *Acinetobacter baumannii* in experimental murine peritoneal sepsis and pneumonia models. *Antimicrob Agents Chemother*. (2016) 60:4464–70. doi: 10.1128/AAC.02708-15
74. Yan JJ, Jung JS, Lee JE, Lee J, Huh SO, Kim HS, et al. Therapeutic effects of lysophosphatidylcholine in experimental sepsis. *Nat Med*. (2004) 10:161–7. doi: 10.1038/nm989
75. Hong CW, Kim TK, Ham HY, Nam JS, Kim YH, Zheng H, et al. Lysophosphatidylcholine increases neutrophil bactericidal activity by enhancement of azurophil granule-phagosome fusion via glycine.GlyR alpha 2/TRPM2/p38 MAPK signaling. *J Immunol*. (2010) 184:4401–13. doi: 10.4049/jimmunol.0902814
76. Miyazaki H, Midorikawa N, Fujimoto S, Miyoshi N, Yoshida H, Matsumoto T. Antimicrobial effects of lysophosphatidylcholine on methicillin-resistant *Staphylococcus aureus*. *Ther Adv Infect Dis*. (2017) 4:89–94. doi: 10.1177/2049936117714920
77. Stewart CJ, Mansbach JM, Wong MC, Ajami NJ, Petrosino JF, Camargo CAJr, et al. Associations of nasopharyngeal metabolome and microbiome with severity among infants with bronchiolitis. A multiomic analysis. *Am J Respir Crit Care Med*. (2017) 196:882–91. doi: 10.1164/rccm.201701-0071OC
78. Liu R, Cheng WJ, Tang HB, Zhong QP, Ming ZP, Dong HF. Comparative metabonomic investigations of *Schistosoma japonicum* from SCID mice and BALB/c mice: clues to developmental abnormality of schistosome in the immunodeficient host. *Front Microbiol*. (2019) 10:440. doi: 10.3389/fmicb.2019.00440
79. Maceyka M, Spiegel S. Sphingolipid metabolites in inflammatory disease. *Nature*. (2014) 510:58–67. doi: 10.1038/nature13475
80. Hoehn RS, Seitz AP, Jernigan PL, Gulbins E, Edwards MJ. Ischemia/reperfusion injury alters sphingolipid metabolism in the gut. *Cell Physiol Biochem*. (2016) 39:1262–70. doi: 10.1159/000447831
81. Schutsky K, Portocarrero C, Hooper DC, Dietzschold B, Faber M. Limited brain metabolism changes differentiate between the progression and clearance of rabies virus. *PLoS ONE*. (2014) 9:e87180. doi: 10.1371/journal.pone.0087180
82. Meadows JA, Wargo MJ. Carnitine in bacterial physiology and metabolism. *Microbiology*. (2015) 161:1161–74. doi: 10.1099/mic.0.000080
83. Sharma L, Prakash H. Sphingolipids are dual specific drug targets for the management of pulmonary infections: perspective. *Front Immunol*. (2017) 8:378. doi: 10.3389/fimmu.2017.00378

Conflict of Interest: The authors declare that the research was conducted in the absence of any commercial or financial relationships that could be construed as a potential conflict of interest.

frontiers in Immunology

ORIGINAL RESEARCH
published: 09 October 2020
doi: 10.3389/fimmu.2020.565142

Cruzipain and Its Physiological Inhibitor, Chagasin, as a DNA-Based Therapeutic Vaccine Against *Trypanosoma cruzi*

Natacha Cerny[1,2], *Augusto Ernesto Bivona*[1,2], *Andrés Sanchez Alberti*[1,2], *Sebastián Nicolás Trinitario*[1,2], *Celina Morales*[3], *Alejandro Cardoso Landaburu*[1,2], *Silvia Inés Cazorla*[2,4] *and Emilio Luis Malchiodi*[1,2]*

[1] *Cátedra de Inmunología and Instituto de Estudios de la Inmunidad Humoral Prof. Ricardo A. Margni (IDEHU, UBA-CONICET), Facultad de Farmacia y Bioquímica, Universidad de Buenos Aires, Buenos Aires, Argentina,* [2] *Instituto de Microbiología y Parasitología Médica (IMPaM, UBA-CONICET), Departamento de Microbiología Parasitología e Inmunología, Facultad de Medicina, Universidad de Buenos Aires, Buenos Aires, Argentina,* [3] *Instituto de Fisiopatología Cardiovascular, Departamento de Patología, Facultad de Medicina, Universidad de Buenos Aires, Buenos Aires, Argentina,* [4] *Laboratorio de Inmunología, Centro de Referencia Para Lactobacilos (CERELA-CONICET), Tucumán, Argentina*

OPEN ACCESS

Edited by:
Pedro A. Reche, Complutense University of Madrid, Spain

Reviewed by:
Martin Craig Taylor, University of London, United Kingdom
Michael Lewis, University of London, United Kingdom

***Correspondence:**
Emilio Luis Malchiodi
emalchio@ffyb.uba.ar

Specialty section:
This article was submitted to Vaccines and Molecular Therapeutics, a section of the journal Frontiers in Immunology

Received: *23 May 2020*
Accepted: *24 August 2020*
Published: *09 October 2020*

Citation:
Cerny N, Bivona AE, Sanchez Alberti A, Trinitario SN, Morales C, Cardoso Landaburu A, Cazorla SI and Malchiodi EL (2020) Cruzipain and Its Physiological Inhibitor, Chagasin, as a DNA-Based Therapeutic Vaccine Against Trypanosoma cruzi. Front. Immunol. 11:565142. doi: 10.3389/fimmu.2020.565142

Chagas disease caused by the protozoan parasite *Trypanosoma cruzi* is endemic in 21 Latin American countries and the southern United States and now is spreading into several other countries due to migration. Despite the efforts to control the vector throughout the Americas, currently, there are almost seven million infected people worldwide, causing ∼10,000 deaths per year, and 70 million people at risk to acquire the infection. Chagas disease treatment is restricted only to two parasiticidal drugs, benznidazole and nifurtimox, which are effective during the acute and early infections but have not been found to be as effective in chronic infection. No prophylactic or therapeutic vaccine for human use has been communicated at this moment. Here, we evaluate in a mouse model a therapeutic DNA vaccine combining Cruzipain (Cz), a *T. cruzi* cysteine protease that proved to be protective in several settings, and Chagasin (Chg), which is the natural Cz inhibitor. The DNAs of both antigens, as well as a plasmid encoding GM-CSF as adjuvant, were orally administrated and delivered by an attenuated *Salmonella* strain to treat mice during the acute phase of *T. cruzi* infection. The bicomponent vaccine based on *Salmonella* carrying Cz and Chg (SChg+SCz) was able to improve the protection obtained by each antigen as monocomponent therapeutic vaccine and significantly increased the titers of antigen- and parasite-specific antibodies. More importantly, the bicomponent vaccine triggered a robust cellular response with interferon gamma (IFN-γ) secretion that rapidly reduced the parasitemia during the acute phase and decreased the tissue damage in the chronic stage of the infection, suggesting it could be an effective tool to ameliorate the pathology associated to Chagas disease.

Keywords: Chagas disease, *Trypanosoma cruzi*, cruzipain, chagasin, GM-CSF, therapeutic vaccine

INTRODUCTION

Chagas disease, caused by the protozoan parasite *Trypanosoma cruzi*, is endemic in 21 Latin American countries and the southern United States and now is spreading, due to migration, into several other countries (1, 2). Despite the efforts of the World Health Organization and Pan American Health Organization (3) to control the vector throughout the Americas, currently, there are almost seven million infected people worldwide, causing ∼10,000 deaths per year by complication linked to Chagas disease, and 70 million people at risk to acquire the infection (4).

Although vector control and screening tests before blood transfusions and organ transplantation have successfully achieved substantial reduction in the number of new acute cases in endemic areas (5), complete control of *T. cruzi* is currently unaffordable. Despite vector control programs effectively reducing the level of infestation, when they are not sustained over time, reinfection of treated households reaches levels like the initial one (6). This was mainly seen in rural areas, when constructions are poor or in peridomestic areas with domestic animals (7). Several concerns remain a challenge, namely, disease globalization due to migration (1, 8); the existence of alternative routes of transmission, such as mother-to-child or oral transmission through contaminated food or beverages (9); and the high variability in drug sensitivity across multiple strains of *T. cruzi* (10).

Despite the fact that 100 years has passed since the discovery of Chagas disease, the treatment is restricted only to two parasiticidal drugs, benznidazole, and nifurtimox, developed in the 1970s and 1960s, respectively. The long-course treatments with these therapeutics ensure efficacy during the early stage of the infection (11); however, they have poor success when administered during the chronic phase of the infection. Moreover, they have severe adverse effects, causing up to 40% of dropout of the treatment and resistance issues being described (12, 13). In this context, safer and more effective drugs or therapeutic vaccines are urgently needed (14, 15).

T. cruzi contains a major cysteine proteinase, Cruzipain (Cz), which is expressed by all developmental forms and strains of the parasite; it is secreted and can also be found in the parasite membrane. Parasite virulence and morphogenesis depend on the endogenous activity of the lysosomal Cz (16). In addition, it has been proved that Cz is essential for amastigote replication and plays a crucial role in host–parasite interactions (17). Cz stimulates potent humoral and cellular immune responses during infection (18). Additionally, Cz has been reported as an efficient prophylactic vaccine as both protein and DNA vaccine, in different administration routes and coupled with several adjuvants (19–24). In addition, we had encouraging results using a therapeutic Cz DNA-based vaccine that has been able to decrease parasitemia, inflammatory cell infiltrate, and tissue damage in murine models of *T. cruzi* infection (25).

Cysteine protease inhibitors have been explored as novel anti-*T. cruzi* therapeutic strategies (26–28). Chagasin (Chg), a *T. cruzi* natural protein, is a tight-binding inhibitor of papain-like cysteine proteases. Chg regulates the endogenous activity of Cz, finely modulating proteolytic functions essential for parasite differentiation and invasion to mammalian cells, compromising the virulence and morphogenesis of the parasite. Detailed structural studies showed that Chg is associated with the native cysteine protease in the Golgi compartment (29). However, the proportion of unbound Cz is higher, so only a small amount is found to form the Cz–Chg complex. Actually, this association may be related to the prevention of Cz autocatalysis. It also has been reported that trypomastigotes overexpressing Chg are less infective than wild-type parasites (29). Moreover, Chg is expressed in all developmental stages of *T. cruzi* and can be localized in the flagellar pocket and cytoplasmic vesicles of trypomastigotes and to the cell surface of amastigotes, being an antigen recognized by sera from chronic *T. cruzi*-infected patients (30). The endogenous regulation of Cz by Chg influences important aspects of *T. cruzi* biology, such as morphogenesis, sensitivity to synthetic inhibitors, and infectivity of the parasite (30). These points signal Chg as a relevant antigen to include in a prophylactic or therapeutic vaccine against *T. cruzi* infection, not yet exhaustively investigated.

Based on these backgrounds, we evaluate here a combined strategy with the DNA of both Cz and Chg as therapeutic vaccine, looking for a robust and balanced immune response effective in decreasing blood and tissue parasites and also the characteristic tissue damage of *T. cruzi* infection.

MATERIALS AND METHODS

Parasites

Blood *T. cruzi* trypomastigotes of the RA strain (discrete typing unit (DTU) VI) were isolated from acutely infected mice at the parasitemia peak. Parasite passages were performed weekly in 21-day-old CF1 mice. After 15 days post infection (dpi), parasites were obtained by centrifugation (10,000 × *g*, 30 min) from heparinized blood. Epimastigotes of the same parasite strain were grown in liver infusion tryptose (LIT) medium at 27°C to the exponential phase of growth and centrifuged at 3,000 × *g* for 15 min as previously described (31).

To obtain a soluble antigenic fraction, epimastigotes of *T. cruzi* (RA strain) were centrifuged for 15 min at 5,000 × *g*. The pellet was resuspended in 0.25 M sucrose and 5 mM KCl containing protease inhibitors (2 μM PMSF, 5 μM leupeptin, 5 μM pepstatin, and 5 μM E-64; Sigma, St. Louis, MO), and parasites were lysed by three cycles of freezing and thawing. The homogenate was centrifuged at 105,000 × *g* for 1 h at 4°C, and the supernatant containing *T. cruzi*-soluble antigens was called fraction 105 (F105). The presence of different protein bands in the complex antigen was verified by 10% SDS-PAGE, and F105 was aliquoted and conserved at −20°C.

Antigens

Purified *T. cruzi* epimastigote DNA was used as a template for the amplification of Cz and Chg. Cz gene was cloned as described by Cazorla et al. (19). Chg amplification was performed using the following primers: Fw 5′-gtcatgcatatgggtgcttgtgggtcgaag-3′ and Rev 5′-gtcatggaattctcagtggtggtggtggtggtgcgcgctctccggcacgttg-3′. The PCR was performed at an annealing temperature of 56°C

using a Platinum Taq DNA Polymerase (Invitrogen, Carlsbad, CA). The 333-bp fragment was purified from a 1% agarose gel.

The amplified fragment was digested with the *Nde*I and *Hind*III restriction enzymes, inserted into a pET23a plasmid and transformed in *Escherichia coli* XL2-Blue. The presence of the insert was confirmed by sequence analysis, and the recombinant plasmid was used to transform BL21 cells. Protein expression was induced with 1 mM IPTG ON at 20°C.

rChg was purified under native conditions with growing concentrations of imidazole using a Ni^{+2}-nitrilotriacetic acid–Sepharose matrix. After dialysis in PBS–glycerol 10%, the purity and identity of Chg were analyzed. Endotoxins were removed by a polymyxin B–agarose column (Sigma, St. Louis, MO). Endotoxin levels in the final protein preparations were <100 units/mg, as determined using a *Limulus* amebocyte lysate analysis kit (Whittaker Bioproducts, Walkersville, MD).

The catalytic activity of cysteine proteases was measured in a continuous test using the fluorogenic substrate, Z-Phe-Arg-AMC (Bachem). The fluorescence reading of 7-aminomethyl coumarin (AMC) released was measured with a Victor3 fluorometer (PerkinElmer) every 10 seg ($\lambda_{excitation}$ = 355 nm/$\lambda_{emission}$ = 460 nm). Increasing concentrations of Chg (0.01–10 μg) were evaluated against epimastigote lysates (5 μM) and the N-terminal domain of Cz (NtCz, 6 μg) previously cloned and expressed (20). The synthetic inhibitor E-64 (10 μM) was used as positive control.

Chg gene for DNA vaccination was cloned in the eukaryotic plasmid pcDNA3.1(+), using the primers fw: 5′-tgatgttgaattcgtaatgtcccacaaggtgacg-3′ and rev: 5′-gtcatgggatcctcagtttgccttgagatatacagtg-3′ that contain the cutoff sites for restriction enzymes, the Kozak sequence, the ATG code for proper transcription, and the TCA termination code. The digested fragment, with the enzymes *Eco*RI and *Bam*HI, was ligated to the plasmid pcDNA3.1(+) (Invitrogen, Life Technologies). Positive transformed *E. coli* DH-5α clones were selected on plates with LB–ampicillin medium. In purified DNA (QIAGEN kit), the presence of the insert of interest was confirmed by digestion with the corresponding restriction enzymes and subsequent sequencing.

Additionally, the Chg-pcDNA3.1 plasmid was used for transforming electrocompetent bacteria *Salmonella enterica* serovar Typhimurium aroA SL7207, which were used as a DNA delivery system as described previously (32).

Animals

C3H/HeN mice were maintained in the animal facilities of the Instituto de Microbiología y Parasitología Médica (IMPaM, UBA-CONICET) under standard conditions following the Review Board of Ethics of the School of Medicine, UBA, Argentina (Resol. CD #3721/2014) and the guidelines established by the National Research Council (33). Animal experiments were approved by the Review Board of Ethics of the School of Pharmacy and Biochemistry (UBA, Argentina) and conducted in accordance with the National Institutes of Health guide for the care and use of laboratory animals (NIH Publications No. 8023, 2011). Animal sample size was estimated by a power-based method (34) and following the guidelines established by the National Research Council PREPARE guidelines in the design of experiments (35).

Challenge and Therapy

Immunotherapeutic studies were performed on 6–8-week-old female C3H/HeN mice. Groups of five mice infected with 50 (sublethal dose) or 1,000 (lethal dose) blood trypomastigotes of the RA strain were treated by the oral administration of 10^9 CFU/dose/mouse of aroA-attenuated *Salmonella* transformed with the different plasmids encoding the antigens or the adjuvant (32). The groups are as follows: (I) **SControl**, attenuated *Salmonella* as carriers of granulocyte-macrophage colony-stimulating factor (GM-CSF) DNA (SGM-CSF); (II) **SChg**. two attenuated *Salmonella*, one transformed with Chg DNA and the other with GM-CSF DNA; (III) **SCz**, one *Salmonella* with the Cz gene and SGM-CSF; and (IV) **SChg+SCz**, *Salmonella* transporting the Chg, Cz, and GM-CSF plasmids.

Acute treatments consisted of three doses of the DNA transported by *Salmonella* on 0, 10, and 20 dpi. Chronic treatment was administered on 100, 110, and 120 dpi. Blood and tissue samples from the mice were taken 100 days after the last immunization.

Treatment Efficacy

Parasitemia and Weight Loss

After challenge with trypomastigotes of *T. cruzi*, blood parasites were counted every 2 days, until the end of the acute phase of infection, as previously described (25). Survival and weight of the animals were recorded daily until they were sacrificed.

Specific Immune Response Analyses

Determination of specific antibodies elicited by the vaccines was performed by an indirect ELISA against a complex mixture of soluble *T. cruzi* antigens called F105 (10 μg/ml) or against rCz or rChg (2 μg/ml). Titers were calculated as the inverse of the highest dilution in which the optical density is higher than 0.1.

A delayed-hypersensitivity test (DTH) was performed on day 100 post treatment by measuring the thickness of the footpads prior and 48 h post inoculation of 5 μg of rCz or rChg.

Spleen cell proliferation assays were performed at the end of the experiments in the presence of rCz or rChg (10 μg/ml), F105 (100 μg/ml), Con A (5 μg/ml), or medium alone (control) by triplicate. Eighteen hours before the harvest, 1 μCi per well of thymidine $(H)^3$ (Amersham) was added. Proliferative response was expressed as the difference between cpm values obtained from stimulated and nonstimulated cultures.

Splenocyte stimulation by the different antigens was also measured as the intracellular production of interferon gamma (IFN-γ) in a flow cytometry assay. In the last 12 h of incubation, brefeldin A was added to the cultures. Cells were fixed at room temperature (RT) with PFA 2%, permeabilized in 0.5% saponin, and stained using anti-IFN-γ (e-Bioscience conjugated antibody) in accordance with the manufacturer's instructions. Stained cells were passed through the BD FACS II flow cytometer, and data were analyzed with Flow JoX software 10.0.7.

Muscle Injury

A hundred days after the last immunization (120 dpi), muscle damage was assessed by measuring the serum activity of creatine kinase (CK and CK-MB), following the instructions of the manufacturer (Wiener Lab).

Histological analyses were also performed at the same time, for which the mice were euthanized, and the corresponding necropsy was performed. The section of muscle (quadriceps) and the complete cardiovascular block were removed. Both ventricles and atria were dissected, and the left ventricle (LV) was cut from the apex to base, fixed in phosphate-buffered 10% formaldehyde at pH 7.2, and embedded in paraffin wax.

Tissues were sectioned into multiple, consecutive 5-μm cross sections with a Reichert–Jung micrometer (Nußloch, Germany) for light microscopic observation as previously described (21). For each heart and skeletal muscle, 20 random microscopic fields were counted at 400× magnification. Sections were evaluated under blind conditions. The lesion severity was assessed based on semiquantitative criteria according to the inflammation index: (1) isolated foci; (2) multiple nonconfluent foci; (3) multiple confluent foci; and (4) multiple diffuse foci, as previously described (36). Regarding the heart, histological examinations of the LV, right ventricle, and septum were conducted. The presence of fibrosis in the heart sections was evaluated with Masson's trichrome stain without considering the perivascular collagen for each of the groups.

In addition, on the day of euthanasia, 100 mg of skeletal and cardiac muscles was extracted to quantify the parasite burden in each tissue, as described (37). The DNA extraction was made by a phenol–chloroform–isoamyl alcohol mixture (25:24:1 v/v, Quick-DNA, Kalium Technologies). The template for DNA amplification was adjusted to 25 ng/μl. Specific *T. cruzi* primers were used for the DNA amplification (Pr: 5′-AAGCGGATAGTTCAGGG-3′, Pf: 5′-GGCGGATCGTTTTCGAG-3′). As for the normalized gene, samples were also amplified with mouse TNF-α primers (Pf: 5′-CCCTCTCATCAGTTCTATGGCCCA-3′, Pr: 5′-CAGCAAGCATCTATGCACTTAGACCCC-3′). PCR was performed using HOT FIRE Pol Eva Green qPCR Mix Plus (Solis Biodyne). The standard was performed by mixing 500 mg of noninfected mouse muscle with 1×10^8 *T. cruzi* epimastigotes. After the extraction, the DNA was adjusted to 25 ng/μl. For the curve, 10-fold serial dilution of the standard was made using noninfected mouse muscle DNA (25 ng/μl) as diluent. Parasite burden was expressed as parasite equivalent per 50 ng of total DNA.

Statistical Analysis

Statistical analyses were carried out with GraphPad Prism 6.0 software (San Diego, CA, USA) using one-way analysis of variance (ANOVA) for proliferation, antibody, enzyme activity assays, and parasitemia. Normality was verified using the Shapiro–Wilks test. The specific posttest was indicated in each assay. The log-rank test was used for survival curves, using the Prism 6.0 program (GraphPad, San Diego, CA). The statistical analyses were referred to the control group of each experiment. Values of $p < 0.05$ were considered significant.

RESULTS

Cloning and Characterization of Chg

In order to analyze the humoral and cellular-specific response after the therapeutic treatment, Chg and Cz were produced as recombinant proteins. Cz was previously cloned by Cazorla et al. (19). Chg gene was amplified from epimastigote gDNA and cloned in pET23a$^+$ plasmid. The obtained pET23a$^+$ Chg vector was digested with *Nde*I and *Hind*III restriction enzymes, releasing a 400-bp fragment visualized on a 1% agarose gel (**Figure 1A**). After sequence confirmation, this vector was used to transform *E. coli* BL21. Chg was obtained as a soluble protein and purified under native conditions; a 12-kDa band in SDS-PAGE was observed (**Figure 1B**).

To analyze whether rChg maintains the capacity to inhibit cysteine protease activity of the natural Chg, we analyzed the inhibition of enzymatic activity on the fluorogenic substrate Z-Phe-Arg-AMC. High contents of cysteine proteases, including Cz, are present in the *T. cruzi* replicative epimastigote stage, and we observed that rChg was able to inhibit the activity from lysed epimastigotes with a similar slope to the commercial synthetic inhibitor (E-64) used as positive control (**Figure 1C**). To analyze rChg-specific inhibitory capacity on Cz, the catalytic domain of Cz (rNtCz) was assayed in the presence or absence of rChg, and a well-defined concentration-dependent inhibition was observed (**Figure 1D**).

SChg+SCz as a Therapeutic Vaccine Against a Lethal *T. cruzi* Infection

To improve the therapeutic effect afforded by Cz DNA (25), we evaluated the coadministration with Chg DNA. Mice lethally infected with *T. cruzi* (1,000 RA trypomastigotes/mouse) were treated with three doses of *Salmonella* delivering the DNA encoding for GM-CSF (SGM-CSF) as adjuvant and Chg (SChg), Cz (SCz), or a combination of both (SChg+SCz). The control group was treated with *Salmonella* carrying only the DNA of GM-CSF (SControl) (**Figure 2A**).

During the acute phase of the infection, all treated mice showed an important decrease of the parasitemia across the infection compared to the control group (**Figure 2B**). As the box of **Figure 2B** shows, the area under the curve (AUC) highlights the significant differences between the control group (AUC: 158.60) and treated ones, SChg (AUC: 69.63), SCz (AUC: 87.28), or Chg+SCz (AUC: 54.75) ($p < 0.005$). The reduction in parasitemia was reflected in body weight assessment during this phase, showing substantial differences in all treated mice in comparison to controls (**Figure 2C**). Thus, control mice weight loss correlated with high parasitemia and 100% of mortality at 34 dpi (**Figure 2D**). In contrast, mice receiving the therapeutic vaccine based on *Salmonella*s carrying both Cz and Chg DNAs had a survival rate of 75% ($^*p < 0.05$), while in mice treated with SCz or SChg, the survival rates were 60% and 40%, respectively (**Figure 2D**).

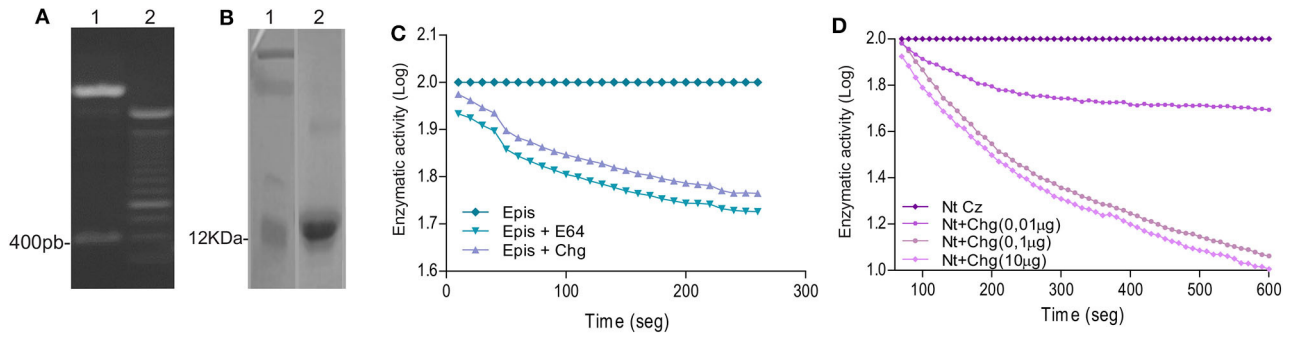

FIGURE 1 | Cloning and characterization of Chg. **(A)** Digestion of pET23a^{+}-Chg construction with the *Nde*I and *Hind*III restriction enzymes released the 400-bp Chg insert. **(B)** SDS-PAGE analysis of rChg expression in *E. coli* BL21 and purification under native condition. Lane 1: MW marker; Lane 2: IMAC Ni-NTA purified rChg (12 kDa) stained with Coomassie Brilliant Blue. **(C)** Relative enzymatic activity of *T. cruzi* epimastigote lysate (5 µM) in the presence of rChg (10 µM) or synthetic inhibitor E-64 (10 µM) on the fluorogenic substrate Z-Gly-Pro-AMC (6 µg) measured as relative fluorescent units (RFUs) and expressed as the log of the percentage of the fluorescence units as a function of time. **(D)** Cysteine protease activity of the rNtCz in the absence or presence of increasing concentrations of rChg (0.01–10 µg).

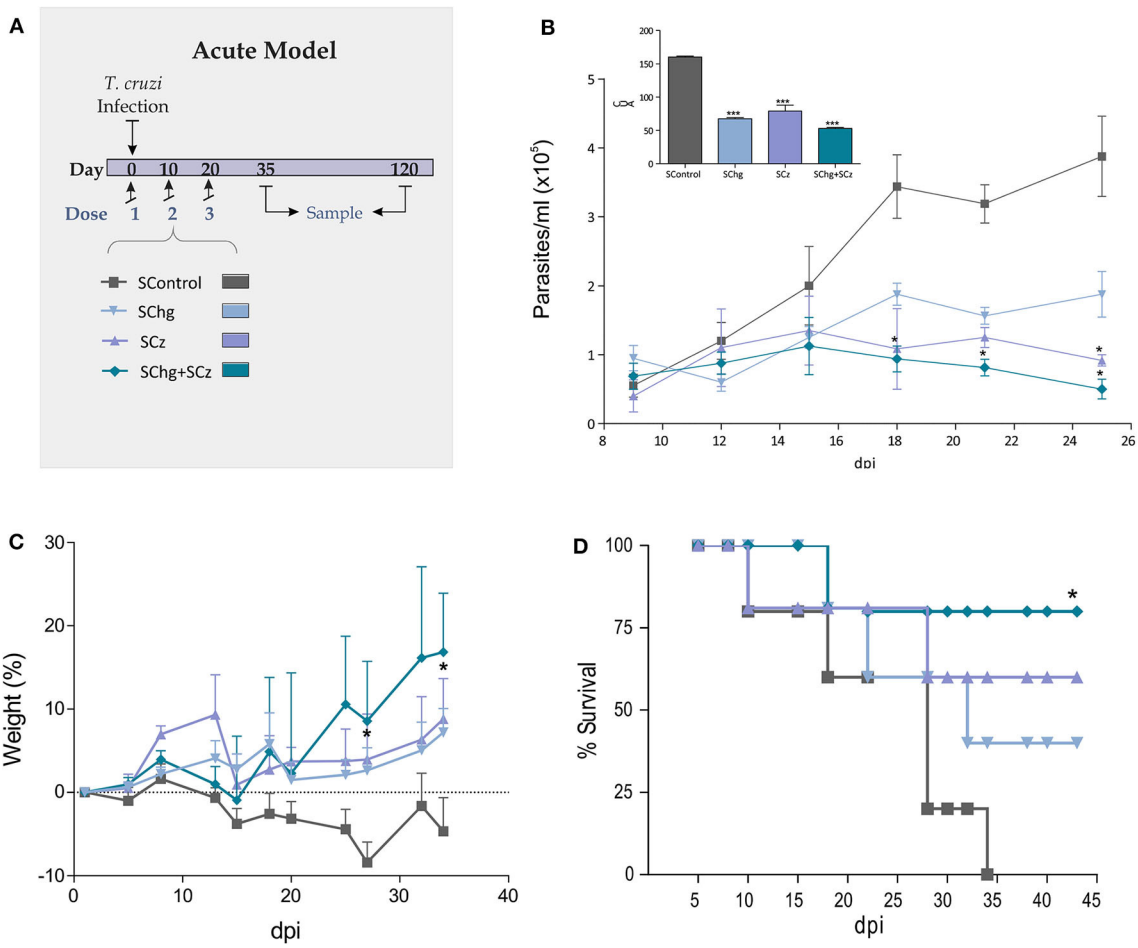

FIGURE 2 | Protection against *T. cruzi* challenge. **(A)** Acute model of infection: C3H/HeN mice infected with *T. cruzi* were treated during the acute phase of infection at 0, 10, and 20 dpi, with three doses of *Salmonella* transporting Cz and/or Chg together with GM-CSF (SCz, SChg, and SChg+SCz, respectively). **(B)** Parasitemia curve after a lethal challenge (insert) AUC of parasitemia. **(C)** Change in body weight of immune-treated mice. **(D)** Survival rate curve evaluated every 2–3 days. These results are representative of at least three independent experiments. One-way ANOVA plus Dunnett's posttest or Tukey's posttest and log-rank test for survival curves were used. Results are expressed as mean ± standard error ($n = 5$ per group), $^{*}p < 0.05$, $^{***}p < 0.001$.

SChg+SCz Therapeutic Vaccine After a Sublethal Infection Enhances *T. cruzi*-Specific Immune Response

To study the effect of the immunotherapies on the specific immune response, at the end of the acute phase (35 dpi) or the chronic phase (120 dpi) of the parasite infection, another set of mice was infected with a sublethal dose (50 RA trypomastigotes per mouse) and treated as previously describe (**Figure 2A**). The presence of specific IgG antibodies against immobilized rCz, rChg, and a *T. cruzi* lysate F105 was monitored when the acute phase of infection was overcome, at 35 dpi (**Figure 3**). At that time, a significant increase in IgG antibodies against rCz and F105 was observed in mice treated with SCz and SChg+SCz (**Figures 3B**,**C**), but not in the SChg-treated mice. By contrast, this group had significant rChg-specific IgG titers compared to controls (**Figure 3A**). Notably, infected and vaccinated mice developed a strong humoral immune response to the immunizing antigen in spite of the ongoing *T. cruzi* infection. When the immune response was analyzed against the natural antigens present in the parasites (F105), a significant antibody titer was observed only in groups that received Cz in the formulation. Just the group that received both antigens (SChg+SCz) had a significant antibody response against all parasite antigens (**Figures 3A**–**C**). The lack of reactivity against F105 in sera from the SChg group could be related with the fact that Chg is much less represented in F105 than Cz, which is a major antigen.

Furthermore, the specific cellular immune response was analyzed *in vivo* by a delayed hypersensitivity test (DTH). As expected, at the end of the acute phase, the groups treated with the different strategies responded in a significant way to the stimulation with their corresponding antigen, rCz or rChg (**Figures 3D**,**E**).

The Immune Response Elicited by the SChg+SCz Therapeutic Vaccine Is Long Lasting and Persists During the Chronic *T. cruzi* Infection

To further characterize the performance of the therapeutic *T. cruzi* vaccines, the elicited immune response was also analyzed during the chronic phase of the infection (120 dpi). We observed that the humoral immune responses against rChg and rCz were slightly increased compared to those observed at the end of the acute phase (35 dpi) for all groups analyzed. This is mainly for SChg+SCz-treated mice which showed significant differences to the control group (**Figures 4A**–**C**).

The DTH at this time point showed a significant increase ($^{*}p < 0.01$) of the *in vivo* specific cellular immune response against the antigens that were administered during the therapy (**Figures 4D**,**E**), according to what was observed at the end of the acute stage of the infection.

In addition, 100 days after last immunization, we evaluated *ex vivo* the lymphoproliferative response of splenocytes from vaccinated mice upon the restimulation with each antigen: rChg, rCz, or F105. Spleen cells from SCz alone or in combination with SChg significantly proliferate in response to rCz and F105 (**Figures 4F**–**H**).

IFN-γ is an inflammatory cytokine crucial for immunity against *T. cruzi*, involved in the control of systematic parasite dissemination (38, 39). At 120 dpi, we observed a significant increase in the percentage of IFN-γ-producing cells in splenocytes from SChg+SCz-treated mice after being stimulated with Cz, Chg, or F105, compared to untreated mice infected with *T. cruzi*. SCz spleen cells responded to Cz or F105 incubation, while SChg only responded to the parasite's lysates (**Figure 4I**).

SChg+SCz Therapeutic Vaccine Prevents Tissue Damage of the Chronic Infection

Then, we analyzed if the therapeutic vaccines administered during the acute phase of the parasite infection were able to prevent the tissue damage associated to the chronic phase of *T. cruzi* infection. To this purpose, at day 100 after the last vaccine doses (120 dpi), three parameters were evaluated: serum levels of CK and CK-MB enzymes, histological analysis of tissue inflammation, and parasitism in skeletal and cardiac tissues.

Serum levels of CK and CK-MB enzymes were assessed as an indicator of muscle injury. As can be seen in **Figure 5A**, the CK and CK-MB values were lower in all mice that received the therapeutic vaccines compared to nontreated controls. However, these differences were only significant compared to SControl (CK: 52.4 ± 13.9 IU/L; CK-MB: 26.4 ± 6.6 IU/L) in the group that received the *Salmonella* with the combination of both antigen DNAs SChg+SCz (CK: 4.7 ± 1.0 IU/L; CK-MB: 6.6 ± 1.1 IU/L), reflecting a significant reduction in muscle damage.

In addition, histological studies of *T. cruzi* target tissues were performed. We observed low levels of pericardial infiltrates mainly in the right ventricular area without significant differences between treated and nontreated control groups when cardiac tissues were analyzed (results not shown). However, histological sections of skeletal muscle showed necrosis of muscle fibers and numerous multifocal and diffuse inflammatory infiltrates in the control group (**Figure 5B**). By contrast, all treated groups presented few necrotic zones and isolated nonspecific inflammatory foci (**Figures 5C**–**E**). The tissue inflammation was analyzed through a semiquantitative comparative analysis of the different groups, showing that this protective effect was observed mainly in those that received SCz as a monocomponent or bicomponent therapeutic vaccine (**Figure 5F**).

To determine *T. cruzi* persistence, the parasite load in target tissues was determined by quantitative PCR (qPCR). *T. cruzi* equivalents in cardiac tissues were very low and presented no significant differences in vaccinated animals compared to control mice. However, when parasite loads were analyzed in skeletal muscles, a significant difference was detected between groups (**Figure 5G**). The control group presented parasite loads between 6 and 10 times higher than those in animals that received the mono-therapeutic vaccine. A striking difference with SControl was observed in animals treated with the combined formulation (SChg+SCz). Importantly, this reduction of parasitic load was more than 100 times. Notably, a significant difference was observed between the groups immunized only with one antigen and the combined treatment (**Figure 5G**), highlighting the higher

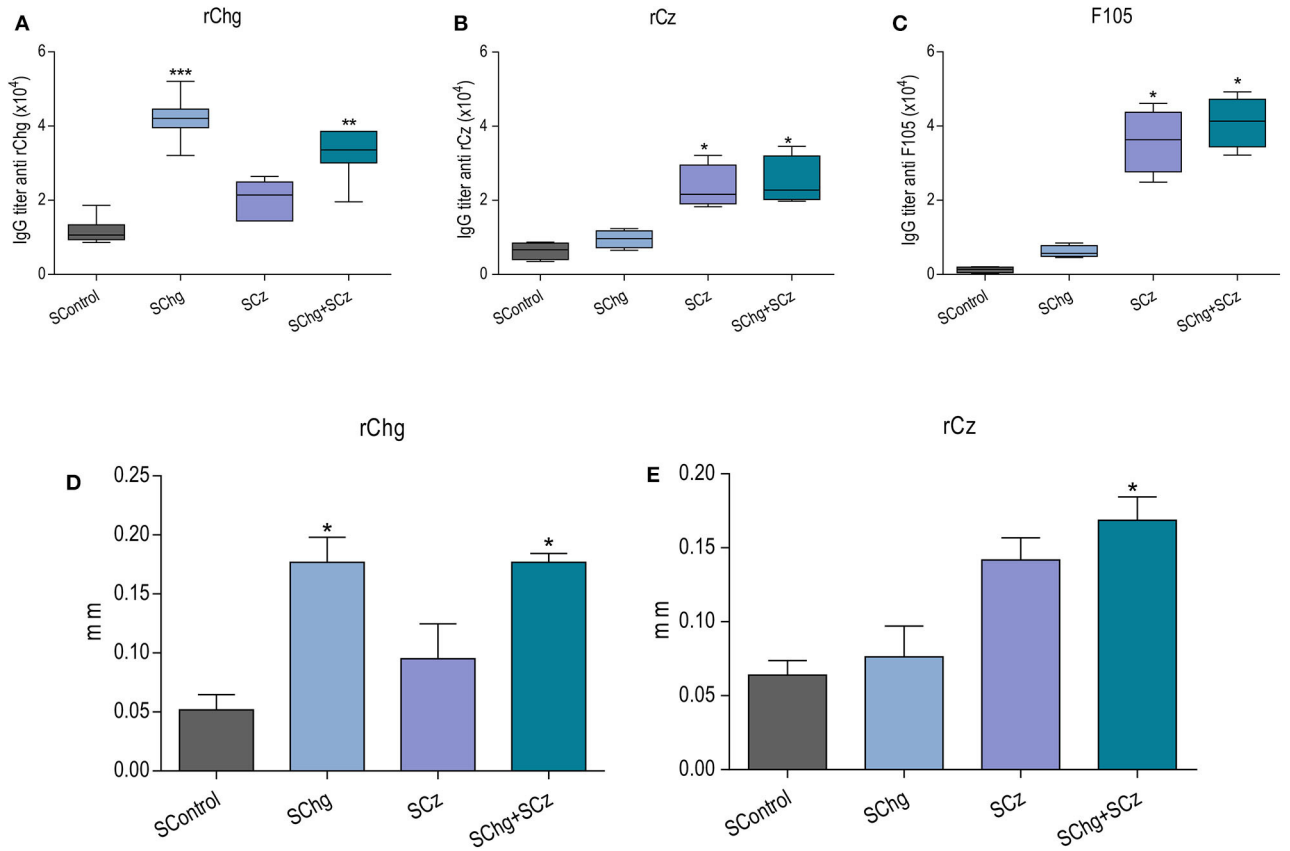

FIGURE 3 | Immune response in mice treated during the acute phase of *T. cruzi* infection. Mice infected with a sublethal dose of *T. cruzi* were treated at 0, 10, and 20 dpi with doses of *Salmonella* carrying the DNA of Chg and/or Cz together with the GM-CSF. Antibody immune response: Total IgG titers of **(A)** anti-rChg, **(B)** anti-rCz, and **(C)** anti-F105 were measured in sera of all groups obtained at 35 dpi. *In vivo* cellular immune response: Footpad thickness was measured before and 48 h after intradermal inoculation of **(D)** rChg or **(E)** rCz. The bars represent the average ($n = 5$ per group) of three representative experiments. $^{*}p < 0.05$, $^{**}p < 0.01$, $^{***}p < 0.001$.

efficacy of the SChg+SCz vaccine compared with the mono-therapeutic vaccines.

Tissue Damage Prevention Is Achieved by SChg+SCz Therapeutic Vaccine Even Administered in the Chronic Phase of *T. cruzi* Infection

After the promising results observed upon the administration of the therapeutic vaccines during the acute phase, conducted using the acute model described in **Figure 2A**, we evaluated the performance of the vaccines when administered during the chronic phase of the infection (**Figure 6A**). *T. cruzi*-infected mice were treated with three doses of the corresponding vaccines on 100, 110, and 120 dpi. At 220 dpi, mice were euthanized, and different parameters were analyzed to assess tissue damage and parasite persistence.

Serum levels of the enzymes CK and CK-MB were significantly lower in SChg+SCz animals (CK: 8.9 ± 3.3 IU/L and CK-MB: 7.0 ± 1.8 IU/L) with respect to control animals (CK: 60.7 ± 17.4 IU/L and CK-MB: 51.2 ± 14.6 IU/L) (**Figure 6B**). In accordance with these results, the histological analysis of skeletal muscle showed confluent foci of mononuclear inflammatory infiltrate with necrosis of the muscle fibers in SControl group (**Figure 6C**). By contrast, in mice treated with the therapeutic vaccines, the foci of mononuclear inflammatory cells were isolated with poor or no necrosis of the skeletal fibers (**Figures 6D–F**). Moreover, animals that received the SChg+SCz vaccine showed isolated inflammatory mononuclear cells with interstitial and perivascular localization. These results are summarized in **Figure 6G**.

To analyze parasite persistence in target tissues, *T. cruzi* equivalents were determined by qPCR. Again, parasite load in cardiac tissues was very low and did not show differences between groups. However, *T. cruzi* equivalents detected in the skeletal muscle of infected mice treated late during the chronic phase of the infection were significantly lower compared to those in SControl (**Figure 6H**).

By contrast, serum enzymatic activity of CK and CK-MB and histopathological analysis of tissue and *T. cruzi* equivalents by qPCR in skeletal and cardiac tissues of 220-day-old noninfected mice are shown in **Supplementary Figure 1**. As expected,

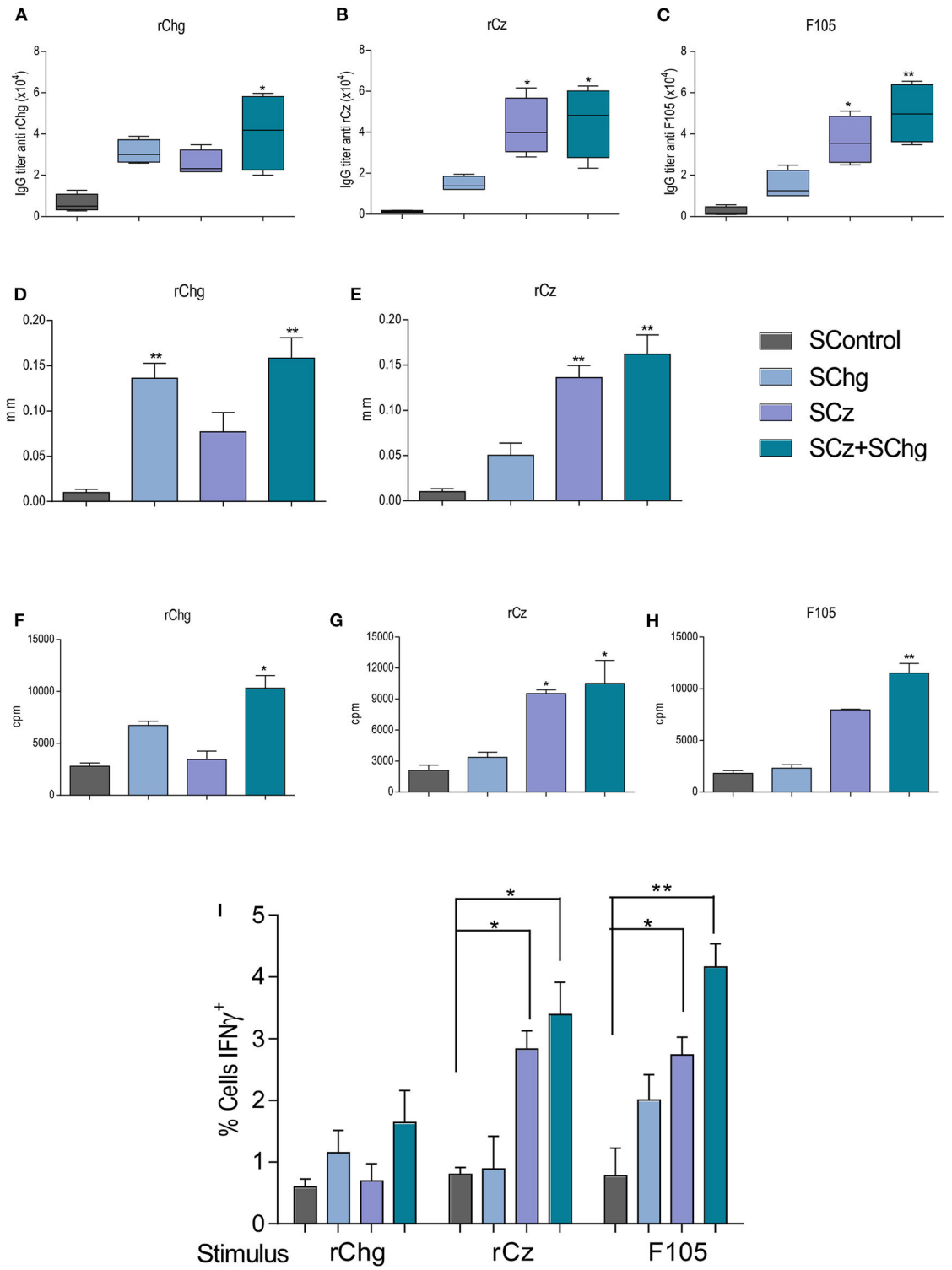

FIGURE 4 | Immune response elicited by the therapeutic vaccine at 120 dpi, in mice treated during the acute phase of *T. cruzi* infection. Mice infected with a sublethal dose of *T. cruzi* were treated with three doses of *Salmonella* at 0, 10, and 20 dpi ($n = 5$ per group), and the immune response generated was analyzed at 120 dpi. The IgG titers **(A)** anti-rChg, **(B)** anti-rCz, and **(C)** anti-F105 were measured in sera at 120 dpi. Cellular response: The *in vivo* DTH assay was performed by measuring the plantar footpad before and 48 h after intradermal inoculation of **(D)** rChg or **(E)** rCz; results are expressed as the differences in thickness. Splenocytes from mice sacrificed at 120 dpi were restimulated with 10 μg/ml **(F)** rCz, **(G)** rChg, or **(H)** F105 for 5 days, and thymidine uptake was determined. The results are expressed as the differences between the cpm of stimulated and baseline cells. **(I)** Intracellular production of INF-γ, determined by flow cytometry, after the stimulation of the splenocytes with the different antigens. These results are representative of at least three independent experiments. $^{*}p < 0.05$, $^{**}p < 0.01$.

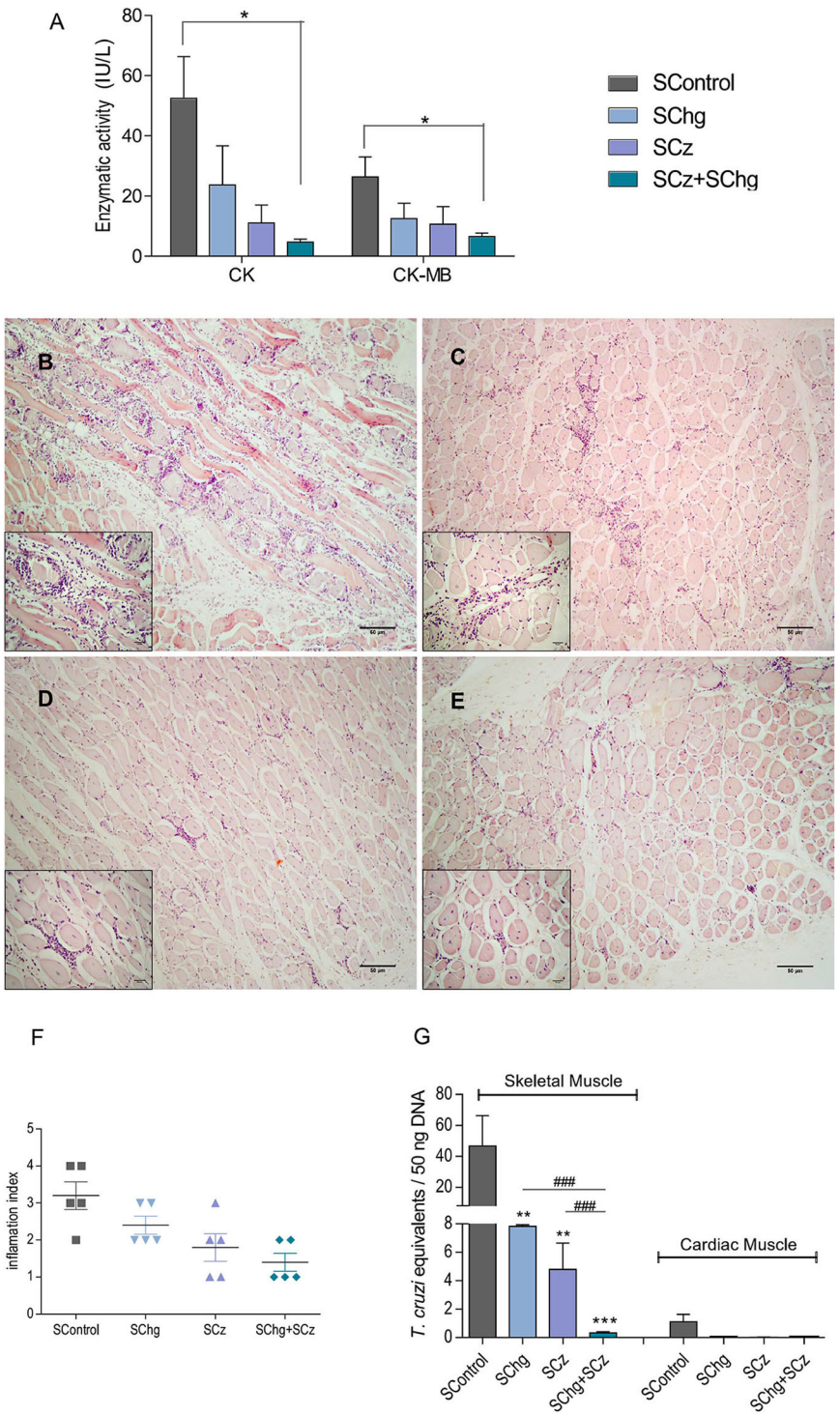

FIGURE 5 | Prevention of tissue damage by vaccine treatment during the acute phase of the parasite infection. **(A)** Enzymatic activity of CK and CK-MB enzymes represented as international units (IU/L). **(B–E)** Representative image of hematoxylin–eosin-stained skeletal muscle samples taken at day 100 after the last immunization; magnification: 40× and the inbox 100×. Animals showed **(B)** multiple confluent foci and necrosis with diffuse distribution (SControl); **(C)** nonconfluent mononuclear inflammatory infiltrate (SChg); **(D)** isolated foci of mononuclear inflammatory infiltrate (SCz); **(E)** few and isolated infiltrates (SChg+SCz). **(F)** Semi-quantified inflammation expressed as inflammation index: (1) isolated foci; (2) multiple nonconfluent foci; (3) inflammatory confluent foci; and (4) multiple diffuse foci (40). **(G)** Parasitism in skeletal and cardiac tissues by qPCR at day 100 after the last immunization. Parasite burden in each tissue was expressed as *T. cruzi* equivalents per 50 ng of total DNA referred to a calibration curve previously constructed containing known concentrations of *T. cruzi* epimastigotes. These results are representative of at least three independent experiments, each one being carried out with five animals per group. $^{*}p < 0.05$, $^{**}p < 0.01$, $^{***}p < 0.001$; $^{\#\#\#}p < 0.01$.

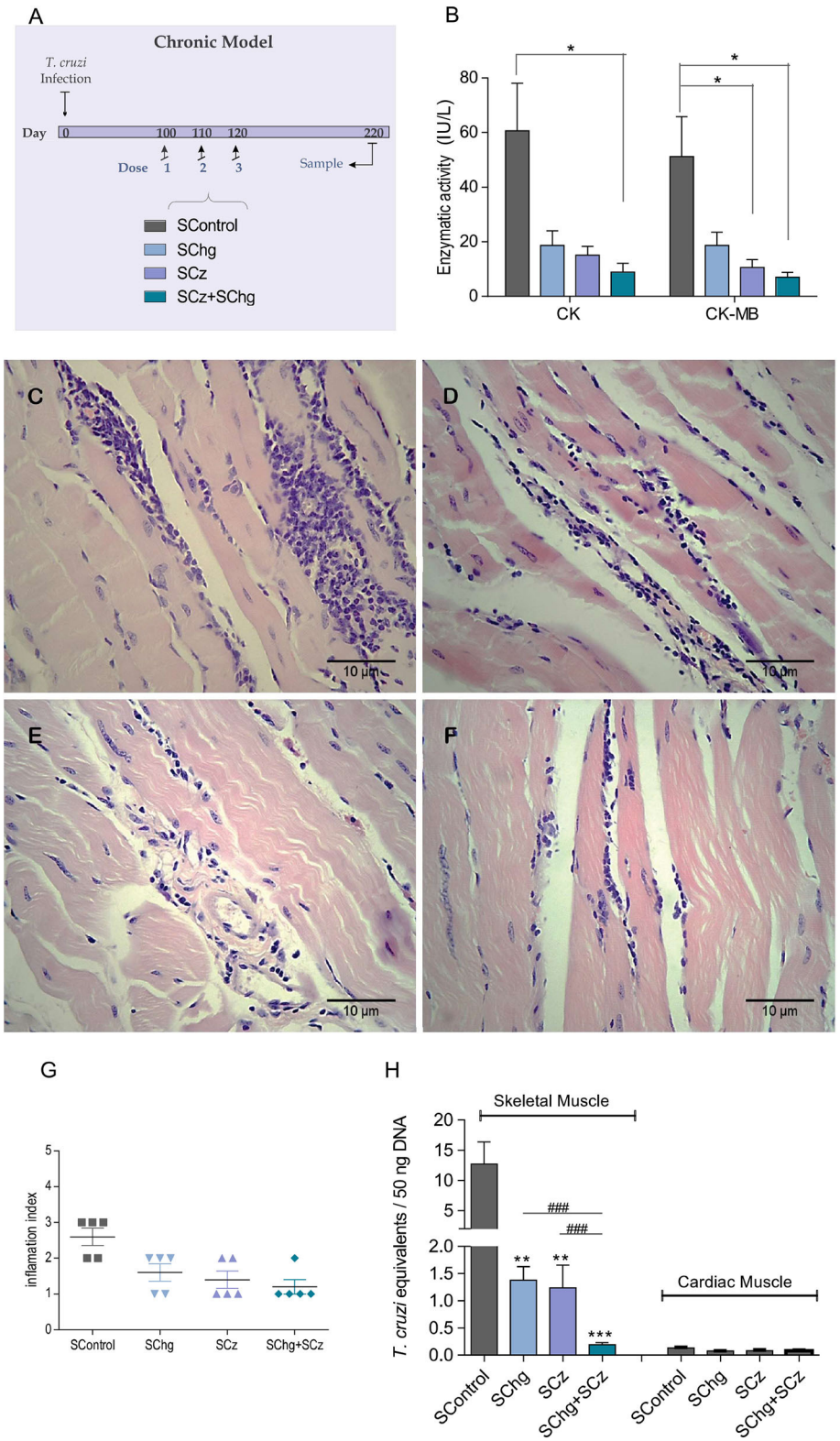

FIGURE 6 | Prevention of *T. cruzi*-associated tissue damage by the vaccines administered at the chronic phase of the parasite infection. **(A)** Scheme of the chronic model of infection: C3H/HeN mice infected with *T. cruzi* received three doses of the SControl, SChg, SCz, or SChg+SCz on 100, 110, and 120 dpi ($n = 5$ per group). **(B)** Enzymatic activity of CK and CK-MB enzymes represented as international units (IU/L). **(C,D)** Histopathological analysis of skeletal tissue samples at 220 dpi showed **(C)** confluent foci of mononuclear inflammatory infiltrate with necrosis of the muscle fibers in SControl; **(D)** isolated foci of mononuclear inflammatory cells with

(Continued)

FIGURE 6 | interstitial and perivascular predominance (SChg); **(E)** nonconfluent mononuclear cells surrounding muscle fibers and interstitial edema (SCz); and **(F)** isolated mononuclear cells at the interstitial and perivascular level (SChg+SCz). **(G)** Inflammation semi-quantified and expressed as an index of inflammation: (1) isolated foci; (2) multiple nonconfluent foci; (3) inflammatory confluent foci; and (4) multiple diffuse foci (40). **(H)** Parasite load in skeletal and cardiac tissues determined by qPCR at 220 dpi. Parasite burden in each tissue was expressed as *T. cruzi* equivalents per 50 ng of total DNA. Results were referred to a calibration curve previously constructed containing known concentrations of *T. cruzi* epimastigotes. These results are representative of at least three independent experiments. $^{*}p < 0.05$, $^{**}p < 0.01$, $^{***}p < 0.001$; $^{\#\#\#}p < 0.01$.

noninfected mice were negative by qPCR. CK and CK-MB values in these mice were similar to those in infected and SChg+SCz-vaccinated mice. In noninfected mice, we observed a conserved architecture of both skeletal and cardiac tissues (**Supplementary Figure 1**), indicating that our treatments were not able to completely avoid skeletal tissue damage. However, the combination of SChg+SCz strongly protected the tissue from damage compared with nontreated mice.

Considering the lack of effective therapeutics during the chronic phase of *T. cruzi* infection, these results suggest that the SChg+SCz-based vaccine would be a promising immunotherapeutic strategy with the potential to decrease the prevalence of Chagas disease.

DISCUSSION

Therapeutic vaccines for indeterminate and chronic Chagas disease not only would provide health benefits but also result in economic benefits (15). Hence, millions of people are waiting for a development of anti-*T. cruzi* vaccines for prophylactic and therapeutic purposes to stop Chagas disease progression. Even though etiologic treatment based on nifurtimox and benznidazole is undisputed in the acute phase, achieving cure rates between 65 and 80%; trypanocidal treatment in the chronic stages of the disease remains controversial because of significant toxicity and the unproven role in preventing progression to cardiomyopathy (11, 12, 41, 42). What worsens the situation is that just a reduced percentage of infections are detected in the acute phase due to mild symptoms.

In the last few years, a better understanding of the protective immune responses that can effectively arrest *T. cruzi* survival in mammalian host provides the fundamentals for a rational design of a prophylactic and therapeutic vaccine against Chagas disease (22). Anti-*T. cruzi* strategies had been focused on targeting specific metabolic biochemical pathways or parasite-specific enzymes, as well as noninvasive immunization routes (23, 24). Most of these strategies need potent adjuvant to obtain the desirable response to improve vaccine efficacy (43). Recently, DNA vaccines have become an effective tool in a wide variety of preclinical models and have been adopted by several researchers. The intramuscular injection of the plasmid DNA encoding several surface antigens or secreted by *T. cruzi* has been studied as DNA vaccine (5, 44, 45). However, it is known that after intramuscular DNA injection, the amount of DNA available for gene expression is very low, which means that high initial amounts of the plasmid must be applied to obtain satisfactory results (25, 46). The difficulties with naked DNA prompted research into DNA delivery systems using attenuated viruses, bacteria and parasites, liposomes, virosomes, microspheres, nanoparticles, and physical delivery systems, such as electroporation, microinjection, gene gun, tattooing, laser, and ultrasound (38, 47–49).

In our laboratory, we took advantage of attenuated *Salmonella enterica* serovar Typhimurium aroA that can be administered orally and is easily produced, facilitating its implementation in vaccination campaigns. We have previously demonstrated the efficacy of this transport system as prophylactic vaccines to *T. cruzi* infection (19, 21, 24, 50, 51). Based on these promising results, we have evaluated the therapeutic effect of *Salmonella* as a DNA delivery system of Cz upon the coadministration with GM-CSF as adjuvant with good performance (25). With the aim to further increase the therapeutic effect of the vaccine, in the present work, we included Chg, a natural inhibitor of cysteine proteases, as a new immunogen against *T. cruzi* infection. A multicomponent therapy might induce a robust parasite-specific immune response even in late infection, controlling tissue damage and preventing Chagas disease progression.

We first cloned Chg DNA in a prokaryotic expression plasmid and expressed the recombinant protein. The activity analysis demonstrated that rChg is properly folded, interacts with rCz, and is active as a protease inhibitor. Then, we cloned Chg in a eukaryotic expression plasmid and evaluated whether its combination with the plasmid encoding Cz was able to control an ongoing acute and chronic *T. cruzi* infection in mice when transported by *Salmonella* as a DNA delivery system. Interestingly, we found that the bicomponent immunotherapeutic vaccine based on *Salmonella* (SChg+SCz) was able to improve the performance obtained by each antigen as a mono-therapeutic vaccine. The efficacy would be due, at least in part, to the high humoral and cellular responses elicited in SChg+SCz not only to the antigens included in the vaccine (Chg and Cz) but also against the whole parasite as observed when immobilizing the F105 lysate in ELISAs or by the IFN-γ production by spleen cells upon restimulation with the same parasite homogenate. In addition, SChg+SCz-treated mice displayed a significant cellular immune response against both antigens compared to untreated mice or mice that receive a mono-therapeutic vaccine, which could decrease parasite replication inside the host.

Our results are in line with diverse approaches exhibiting the efficacy of several *T. cruzi* antigens (ASP-2, enolase, TSA-1, and Tc24) to control *T. cruzi* infection when they are tested as a therapeutic vaccine during the acute phase of the parasite infection (47, 48, 52–54). Nevertheless, only a few groups evaluated the performance of a therapeutic vaccine when it is administered during the chronic phase of *T. cruzi* infection (38, 43, 55–57). In that regard, the effectiveness of the multicomponent therapeutic vaccine SChg+SCz, when it is

orally administered during the chronic phase of the infection, becomes even more relevant. Likewise, like the response observed by a treatment delivered by type 5 recombinant adenoviruses where the IFN-γ-mediated immunity was enhanced (38), treatment of chronically infected mice with DNA of Cz and Chg delivered by *Salmonella* displayed a robust cellular immune response with high levels of IFN-γ secretion upon the restimulation with *T. cruzi* antigens. This is true, particularly, in treatments that include the Cz antigen. Treating mice during the acute phase with the multicomponent vaccine (SChg+SCz) would allow a rapid T-cell response in case of *T. cruzi* reactivation or reinfection and, therefore, a major control of the parasite dissemination to the host tissues. This supports the idea of other authors that IFN-γ is important in mediating an effective immunity against *T. cruzi* (39).

We analyzed the ability of the immunotherapy to prevent or decrease the onset of tissue damage during the chronic stage of parasite infection. Serum activity of the CK enzyme and the cardiac isoform CK-MB, analyzed as highly specific markers of myocardial injury, showed that SChg+SCz-treated mice, independently of the time of administration, presented a mean level 10 times lower than that observed in infected and untreated mice. Importantly, the SChg+SCz immunotherapeutic vaccine administered at the chronic phase of *T. cruzi* infection was able to improve several parameters that were already altered at the start of the treatment. For example, the serum level of CK-MB in infected and nontreated mice at 100 dpi was 26.4 ± 6.6 IU/L (**Figure 5B**). When immunotherapy was administered at the chronic phase, CK-MB levels were reduced to 7.0 ± 1.8 IU/L at 220 dpi, values similar to those in normal tissues (**Supplementary Figure 1A**); otherwise, in the absence of treatment, it reached levels of 51.2 ± 14.6 IU/L (**Figure 6B**). This decrease in tissue damage by chronic immunotherapy, also described by Pereira et al. (38), is really encouraging since current treatment with nifurtimox or benznidazole at the chronic phase of the parasite infection in humans reduces parasite load but does not improve the clinical outcome of Chagas disease (11). As murine and human infections differ in several aspects of the parasite–host relationship, including duration of infection, these results support the evaluation of anti-*T. cruzi* immunotherapy in human clinical trial basis.

Effectively, these results are a clear evidence that SChg+SCz as an oral therapeutic vaccine administered during the acute or chronic stage of infection has potential to delay the progression of Chagas disease and could be an effective tool to mitigate the damage associated to Chagas disease. In addition, despite the fact that tissues of infected-treated mice are not preserved to the same architecture of the organs of noninfected nontreated age-matched mice (**Supplementary Figures 1C,D**), there were only a few and isolated inflammatory foci. These tissue damage parameters have a clear correspondence with the parasitic load analyzed by qPCR in cardiac and mainly skeletal muscles, since mice immunized with the bicomponent vaccine presented the highest reduction compared with infected control and experimental groups. These results reinforce the hypothesis that the reduction in tissue parasitism highly correlates with damage in target tissues. Regarding the performance of SChg+SCz, we demonstrated its immunogenicity, being able to prime a more robust immune response. Moreover, with this multivaccination strategy, we were able to improve the efficacy conferred with the administration of the DNA antigens individually. It is also encouraging since the hopeful SChg+SCz treatment could be administered when an acute *T. cruzi* infection is suspected or confirmed. Interestingly, considering that the diagnosis of a *T. cruzi* infection is usually achieved during the chronic phase of the parasite infection, it is of great importance that a tissue protective effect is displayed by the multicomponent therapeutic vaccine when administered on the chronic stage of infection. The major advantage of this strategy is that it relies on the induction of multiple effector mechanisms against the pathogen that may have higher efficacy than conventional treatments to face the asymptomatic and chronic phase of *T. cruzi* infection. Considering animal model limitations and that this pathology is a dynamic process accounting for organ-specific damage, it would be interesting to analyze the efficacy of the treatment using other mouse models and parasite strains that affect different tissues, such as that made by Francisco et al. (58), in further communications.

A therapeutic vaccine for Chagas disease may improve or even replace the treatment with current drugs which have several side effects and require long-term use that frequently leads to therapeutic withdrawal. The oral therapeutic vaccine SChg+SCz would also be an interesting weapon in combined therapies with parasiticidal drugs, as have been successfully reported in different pathologies (59, 60) and reviewed by Bivona (22). With the active replication of the parasite during the acute *T. cruzi* infection being kept in mind, it would be interesting to evaluate if combined therapy administered during the acute phase of the infection could have a synergism with the host immune response and the drug activity to achieve parasite clearance. This immunotherapeutic vaccine not only would allow targeting different humoral and cellular elements as well metabolic pathways but also would be able to reduce doses and drug exposure periods, thus contributing to the decrease in toxic effects and minimization of the emergence of drug resistance. Not to be underestimated, as has been recently reviewed by Rios et al. (61) and proposed by Dumonteil et al. (62), therapeutic vaccines could be an excellent tool to avoid future congenital transmission, which is estimated at 5% in Latin America, preventing the risk of pregnancy complications like preterm rupture of membranes and preterm delivery. Although available drugs are not approved for use during pregnancy, several studies suggest that reducing maternal parasitemia before conception reduces the risk of congenital transmission (63–65), and it was recently estimated that a therapeutic vaccination of Chagas-positive pregnant women would be cost-effective and cost saving (66).

With the bicomponent therapeutic vaccine SChg+SCz, we were able to improve the efficacy conferred by the administration of the DNA antigens individually. This treatment increased the survival of mice upon a lethal *T. cruzi* challenge and successfully decreased tissue damage associated to *T. cruzi* infection. These

results indicate that SChg+SCz could be a promising strategy in the search of an anti-Chagas therapy to be administered in either the acute or chronic phase of the infection.

DATA AVAILABILITY STATEMENT

All datasets presented in this study are included in the article/ **Supplementary Material**.

ETHICS STATEMENT

The animal study was reviewed and approved by Review Board of Ethics of the School of Pharmacy and Biochemistry (UBA, Argentina) and conducted in accordance with the National Institutes of Health guide for the care and use of Laboratory animals (NIH Publications No. 8023, 2011).

AUTHOR CONTRIBUTIONS

NC, AB, AS, SC, and EM: conceived and designed the experiments. NC, AB, AS, ST, CM, and AC: performed the experiments. NC, AB, AS, CM, SC, and EM: analyzed the data. EM: contributed reagents, materials and analysis tools. NC, SC, and EM: wrote the paper. All authors revised and approved the manuscript.

FUNDING

This work was supported by grants from the Universidad de Buenos Aires (2014–2017 # 20020130100788BA) and National Agency for Promotion of Science and Technology (ANPCyT, PICT-2014-0854, 2015-2018).

ACKNOWLEDGMENTS

We thank Carla Pascuale (Flow Cytometry Unit, INBIRS, UBA-CONICET, Faculty of Medicine, UBA) and Sabrina Soldavini, Valeria Cardozo, and Marianela Lewicki (Animal Facilities and Care IMPaM, Faculty of Medicine, UBA) for all the technical assistance.

SUPPLEMENTARY MATERIAL

The Supplementary Material for this article can be found online at: https://www.frontiersin.org/articles/10.3389/fimmu.2020.565142/full#supplementary-material

Supplementary Figure 1 | Normal tissue analyses at 220 days old animals. **(A)** Serum enzymatic activity of CK and CK-MB represented as International Units (IU/L); **(B)** *T. cruzi* equivalents by qPCR in naïve tissue; Histopathological analysis of non-infected mice, representative image of hematoxylin-eosin stained: **(C)** Cardiac Tissue; **(D)** skeletal muscle. Animals showed a conserved architecture of both tissues. Magnification: 40x.

REFERENCES

1. Gascon J, Bern C, Pinazo MJ. Chagas disease in Spain, the United States and other non-endemic countries. *Acta Trop*. (2010) 115:22–7. doi: 10.1016/j.actatropica.2009.07.019
2. Perez-Molina JA, Poveda C, Martinez-Perez A, Guhl F, Monge-Maillo B, Fresno M, et al. Distribution of *Trypanosoma cruzi* discrete typing units in Bolivian migrants in Spain. *Infect Genet Evol*. (2014) 21:440–2. doi: 10.1016/j.meegid.2013.12.018
3. Pan American Health Organization (2019). Available online at: https://www.paho.org/en/topics/chagas-disease
4. WHO: World Health Organization. *Chagas Disease (American trypanosomiasis)* (2019). Available online at: https://www.who.int/chagas/strategy/en/.
5. Gupta S, Silva TS, Osizugbo JE, Tucker L, Spratt HM, Garg NJ. Serum-mediated activation of macrophages reflects TcVac2 vaccine efficacy against Chagas disease. *Infect Immun.* (2014) 82:1382–9. doi: 10.1128/IAI.01186-13
6. Yoshioka K, Provedor E, Manne-Goehler J. The resilience of *Triatoma dimidiata*: An analysis of reinfestation in the Nicaraguan Chagas disease vector control program (2010-2016). *PLoS ONE.* (2018) 13:e0202949. doi: 10.1371/journal.pone.0202949
7. Juarez JG, Pennington PM, Bryan JP, Klein RE, Beard CB, Berganza E, et al. A decade of vector control activities: Progress and limitations of Chagas disease prevention in a region of Guatemala with persistent *Triatoma dimidiata* infestation. *PLoS Negl Trop Dis.* (2018) 12:e0006896. doi: 10.1371/journal.pntd.0006896
8. Coura JR, Borges-Pereira J. Chagas disease: 100 years after its discovery. A systemic review. *Acta Trop*. (2010) 115:5–13. doi: 10.1016/j.actatropica.2010.03.008
9. Santana RG, Guerra M, Sousa DR, Couceiro K, Ortiz JV, Oliveira M, et al. Oral transmission of *Trypanosoma cruzi*, Brazilian Amazon. *Emerg Infect Dis.* (2019) 25:132–5. doi: 10.3201/eid2501.180646
10. Zingales B. *Trypanosoma cruzi* genetic diversity: Something new for something known about Chagas disease manifestations, serodiagnosis and drug sensitivity. *Acta Trop.* (2018) 184:38–52. doi: 10.1016/j.actatropica.2017.09.017
11. Morillo C, Marin- Neto A, Avenzum S, Sosa- Esstani A, Rassi J, Rosas F, et al. Randomized trial of benznidazole for chronic Chagas' cardiomyopathy. *N Engl J Med*. (2015) 373:1295–306. doi: 10.1056/NEJMoa1507574
12. Molina I, Salvador F, Sánchez-Montalv,á A, Treviño B, Serre N, Avilés AS, et al. Toxic profile of benznidazole in patients with chronic chagas disease: risk factors and comparison of the product from two different manufacturers. *Antimicrob Agents Chemother*. (2015) 59:6125–31. doi: 10.1128/AAC.04660-14
13. Rassi AJr, Marin JA, Neto RA. Chronic Chagas cardiomyopathy: a review of the main pathogenic mechanisms and the efficacy of aetiological treatment following the BENznidazole Evaluation for Interrupting Trypanosomiasis (BENEFIT) trial. *Mem Inst Oswaldo Cruz.* (2017) 112:224–35. doi: 10.1590/0074-02760160334
14. Pinheiro E, Brum-Soares L, Reis R, Cubides JC. Chagas disease: review of needs, neglect, and obstacles to treatment access in Latin America. *Rev Soc Bras Med Trop.* (2017) 50:296–300. doi: 10.1590/0037-8682-0433-2016
15. Bartsch SM, Bottazzi ME, Asti L, Strych U, Meymandi S, Falcón-Lezama JA, et al. Economic value of a therapeutic Chagas vaccine for indeterminate and chagasic cardiomyopathy patients. *Vaccine.* (2019) 37:3704–14. doi: 10.1016/j.vaccine.2019.05.028
16. dos Reis FC, Júdice WA, Juliano MA, Juliano L, Scharfstein J, Lima AP. The substrate specificity of cruzipain 2, a cysteine protease isoform from *Trypanosoma cruzi*. *FEMS Microbiol Lett.* (2006) 259:215–20. doi: 10.1111/j.1574-6968.2006.00267.x
17. Duschak VG, Couto AS. Cruzipain, the major cysteine protease of Trypanosoma cruzi: a sulfated glycoprotein antigen as relevant candidate for vaccine development and drug target. *A review Curr Med Chem.* (2009) 16:3174–202. doi: 10.2174/092986709788802971
18. Schnapp AR, Eickhoff CS, Sizemore D, Curtiss R. 3rd, Hoft DF. Cruzipain induces both mucosal and systemic protection against Trypanosoma cruzi in mice. *Infect Immun.* (2002) 70:5065–74. doi: 10.1128/iai.70.9.5065-5074.2002
19. Cazorla SI, Frank FM, Becker PD, Corral RS, Guzmán CA, Malchiodi EL. Prime-boost immunization with cruzipain co-administered with MALP-2

triggers a protective immune response able to decrease parasite burden and tissue injury in an experimental *Trypanosoma cruzi* infection model. *Vaccine.* (2008) 26:1999–2009. doi: 10.1016/j.vaccine.2008.02.011

20. Cazorla SI, Frank FM, Becker PD, Arnaiz M, Mirkin GA, Corral RS, et al. Redirection of the immune response to the functional catalytic domain of the cystein proteinase cruzipain improves protective immunity against *Trypanosoma cruzi* infection. *J Infect Dis.* (2010) 202:136–44. doi: 10.1086/652872
21. Cazorla SI, Matos MN, Cerny N, Ramirez C, Alberti AS, Bivona AE, et al. Oral multicomponent DNA vaccine delivered by attenuated *Salmonella* elicited immunoprotection against American trypanosomiasis. *J Infect Dis.* (2015) 211:698–707. doi: 10.1093/infdis/jiu480
22. Bivona AE, Alberti AS, Cerny N, Trinitario SN, Malchiodi EL. Chagas disease vaccine design: the search for an efficient *Trypanosoma cruzi* immune-mediated control. *Biochim Biophys Acta Mol Basis Dis.* (2020) 1866:165658. doi: 10.1016/j.bbadis.2019.165658
23. Sanchez Alberti A, Bivona AE, Cerny N, Schulze K, Weißmann S, Ebensen T, et al. Engineered trivalent immunogen adjuvanted with a STING agonist confers protection against Trypanosoma cruzi infection. *NPJ Vaccines.* (2017) 2:9. doi: 10.1038/s41541-017-0010-z
24. Sanchez Alberti A, Bivona AE, Matos MN, Cerny N, Schulze K, Weißmann S, et al. Mucosal heterologous prime/boost vaccination induces polyfunctional systemic immunity, improving protection against *Trypanosoma cruzi*. *Front Immunol.* (2020) 11:128. doi: 10.3389/fimmu.2020.00128
25. Cerny N, Sánchez Alberti A, Bivona AE, De Marzi MC, Frank FM, Cazorla SI, et al. Coadministration of cruzipain and GM-CSF DNAs, a new immunotherapeutic vaccine against *Trypanosoma cruzi* infection. *Hum Vaccin Immunother.* (2016) 12:438–50. doi: 10.1080/21645515.2015.1078044
26. Ferreira RAA, Pauli I, Sampaio TS, de Souza ML, Ferreira LLG, Magalhães Luma G, et al. Structure-based and molecular modeling studies for the discovery of cyclic imides as reversible cruzain inhibitors with potent anti-*Trypanosoma cruzi* activity. *Front Chem.* (2019) 7:798. doi: 10.3389/fchem.2019.00798
27. Da Silva-Junior EF, Barcellos Franca PH, Ribeiro FF, Bezerra Mendonca-Junior FJ, Scotti L, Scotti MT, et al. Molecular docking studies applied to a dataset of cruzain inhibitors. *Curr Comput Aided Drug Des.* (2018) 14:68–78. doi: 10.2174/1573409913666170519112758
28. Mercaldi GF, D'Antonio EL, Aguessi A, Rodriguez A, Cordeiro AT. Discovery of antichagasic inhibitors by high-throughput screening with *Trypanosoma cruzi* glucokinase. *Bioorg Med Chem Lett.* (2019) 29:1948–53. doi: 10.1016/j.bmcl.2019.05.037
29. Santos CC, Sant'anna C, Terres A, Cunha-e-Silva NL, Scharfstein J, de Lima AP. Chagasin, the endogenous cysteine-protease inhibitor of *Trypanosoma cruzi*, modulates parasite differentiation and invasion of mammalian cells. *J Cell Sci.* (2005) 118(Pt 5):901–15. doi: 10.1242/jcs.01677
30. Monteiro AC, Abrahamson M, Lima AP, Vannier-Santos MA, Scharfstein J. Identification, characterization and localization of chagasin, a tight-binding cysteine protease inhibitor in *Trypanosoma cruzi*. *J Cell Sci.* (2001) 114(Pt 21):3933–42.
31. Rojas Córdova M, Torrico MC, Torrico F, Suárez Barrientos EL. Standardization of the technique for obtaining trypomastigotes in 3T3 cells from a local strain of *Trypanosoma cruzi* epimastigotes. *Gaceta Médica Boliviana.* (2015) 38:1.
32. Bivona AE, Cerny N, Alberti AS, Cazorla SI, Malchiodi EL. Attenuated *Salmonella* sp. as a DNA delivery system for *Trypanosoma cruzi* antigens. *Methods Mol Biol.* (2016) 1404:683–95. doi: 10.1007/978-1-4939-3389-1_44
33. National Research Council. *Committee for the Update of the Guide for the Care and Use of Laboratory Animals. Guide for the Care and Use of Laboratory Animals*. 8th ed. Washington, DC: National Academies Press (2011). Available online at: https://grants.nih.gov/grants/olaw/guide-for-the-care-and-use-of-laboratory-animals.pdf
34. Charan J, Kantharia ND. How to calculate sample size in animal studies? *J Pharmacol Pharmacother.* (2013) 4:303–6. doi: 10.4103/0976-500X.119726
35. Smith AJ, Clutton RE, Lilley E, Hansen KEA, Brattelid T. PREPARE: guidelines for planning animal research and testing. *Lab Anim.* (2018) 52:135–41. doi: 10.1177/0023677217724823
36. Martin DL, Postan M, Lucas P, Gress R, Tarleton RL. TGF-beta regulates pathology but not tissue CD8+ T cell dysfunction during experimental *Trypanosoma cruzi* infection. *Eur J Immunol.* (2007) 37:2764–71. doi: 10.1002/eji.200737033
37. Cummings KL, Tarleton RL. Rapid quantitation of *Trypanosoma cruzi* in host tissue by real-time PCR. *Mol Biochem Parasitol.* (2003) 129:53–9. doi: 10.1016/s0166-6851(03)00093-8
38. Pereira IR, Vilar-Pereira G, Marques V, da Silva AA, Caetano B, Moreira OC, et al. A human type 5 adenovirus-based *Trypanosoma cruzi* therapeutic vaccine re-programs immune response and reverses chronic cardiomyopathy. *PLoS Pathog.* (2015) 11:e1004594. doi: 10.1371/journal.ppat.1004594
39. Williams T, Guerrero-Ros I, Ma Y, Dos Santos F, Scherer P, Gordillo R, et al. Induction of effective immunity against *Trypanosoma cruzi*. *Infect Immun.* (2020) 88:e00908–e00919. doi: 10.1128/IAI.00908-19
40. Postan M, Bailey JJ, Dvorak JA, McDaniel JP, Pottala EW. Studies of *Trypanosoma cruzi* clones in inbred mice. III Histopathological and electrocardiographical responses to chronic infection. *Am J Trop Med Hyg.* (1987) 37:541–9. doi: 10.4269/ajtmh.1987.37.541
41. Jackson Y, Alirol E, Getaz L, Wolff H, Combescure C, Chappuis F. Tolerance and safety of nifurtimox in patients with chronic chagas disease. *Clin Infect Dis.* (2010) 51:e69–e75. doi: 10.1086/656917
42. Echeverria LE, Morillo CA. American trypanosomiasis (Chagas disease). *Infect Dis Clin North Am.* (2019) 33:119–34. doi: 10.1016/j.idc.2018.10.015
43. Barry MA, Versteeg L, Wang Q, Pollet J, Zhan B, Gusovsky F, et al. A therapeutic vaccine prototype induces protective immunity and reduces cardiac fibrosis in a mouse model of chronic *Trypanosoma cruzi* infection. *PLOS Negl Trop Dis.* (2019) 13:e0007413. doi: 10.1371/journal.pntd.0007413
44. Brandán CP, Mesías AC, Parodi C, Cimino R, Pérez Brandán C, Diosque P, et al. Effects of IFN-γ coding plasmid supplementation in the immune response and protection elicited by *Trypanosoma cruzi* attenuated parasites. *BMC Infect Dis.* (2017) 17:732. doi: 10.1186/s12879-017-2834-6
45. Villanueva-Lizama LE, Cruz-Chan JV, Aguilar-Cetina A del C, Herrera-Sanchez LF, Rodriguez-Perez JM, Rosado-Vallado ME, et al. *Trypanosoma cruzi* vaccine candidate antigens Tc24 and TSA-1 recall memory immune response associated with HLA-A and -B supertypes in Chagasic chronic patients from Mexico. *PLoS Negl Trop Dis.* (2018) 12:e0006240. doi: 10.1371/journal.pntd.0006240
46. Arce-Fonseca M, Rios-Castro M, Carrillo-Sánchez Sdel C, Martínez-Cruz M, Rodríguez-Morales O. Prophylactic and therapeutic DNA vaccines against Chagas disease. *Parasit Vectors.* (2015) 8:121. doi: 10.1186/s13071-015-0738-0
47. Barry MA, Wang Q, Jones KM, Heffernan MJ, Buhaya MH, Beaumier CM, et al. A therapeutic nanoparticle vaccine against *Trypanosoma cruzi* in a BALB/c mouse model of Chagas disease. *Hum Vaccin Immunother.* (2016) 12:976–87. doi: 10.1080/21645515.2015.1119346
48. Arce-Fonseca M, González-Vázquez MC, Rodríguez-Morales O, Graullera-Rivera V, Aranda-Fraustro A, Reyes PA, et al. Recombinant enolase of *Trypanosoma cruzi* as a novel vaccine candidate against Chagas disease in a mouse model of acute infection. *J Immunol Res.* (2018) 2018:8964085. doi: 10.1155/2018/8964085
49. Hegazy-Hassan W, Zepeda-Escobar JA, Ochoa-García L, Contreras-Ortíz JME, Tenorio-Borroto E, Barbabosa-Pliego A, et al. TcVac1 vaccine delivery by intradermal electroporation enhances vaccine induced immune protection against Trypanosoma cruzi infection in mice. *Vaccine.* (2019) 37:248–57. doi: 10.1016/j.vaccine.2018.11.041
50. Matos MN, Cazorla SI, Bivona AE, Morales C, Guzmán CA, Malchiodi EL. Tc52 amino-terminal-domain DNA carried by attenuated *Salmonella enterica* serovar Typhimurium induces protection against a *Trypanosoma cruzi* lethal challenge. *Infect Immun.* (2014) 82:4265–75. doi: 10.1128/IAI.02190-14
51. Bivona AE, Sánchez Alberti A, Matos MN, Cerny N, Cardoso AC, Morales C, et al. *Trypanosoma cruzi* 80 kDa prolyl oligopeptidase (Tc80) as a novel immunogen for Chagas disease vaccine. *PLoS Negl Trop Dis.* (2018) 12:e0006384. doi: 10.1371/journal.pntd.0006384
52. Biter AB, Weltje S, Hudspeth EM, Seid CA, McAtee CP, Chen WH, et al. Characterization and stability of *Trypanosoma cruzi* 24-C4 (Tc24-C4), a candidate antigen for a therapeutic vaccine against Chagas disease. *J Pharm Sci.* (2018) 107:1468–73. doi: 10.1016/j.xphs.2017.12.014
53. De la Cruz JJ, Villanueva-Lizama L, Dzul-Huchim V, Ramírez-Sierra MJ, Martinez-Vega P, Rosado-Vallado M, et al. Production of recombinant TSA-1 and evaluation of its potential for the immuno-therapeutic control of *Trypanosoma cruzi* infection in mice. *Hum*

Vaccin Immunother. (2019) 15:210–9. doi: 10.1080/21645515.2018.1520581
54. Torrico F, Gascon J, Ortiz L, Alonso-Vega C, Pinazo MJ, Schijman A, et al. Treatment of adult chronic indeterminate Chagas disease with benznidazole and three E1224 dosing regimens: a proof-of-concept, randomised, placebo-controlled trial. *Lancet Infect Dis*. (2018) 18:419–30. doi: 10.1016/S1473-3099(17)30538-8
55. Dumonteil E, Escobedo-Ortegon J, Reyes-Rodriguez N, Arjona-Torres A, Ramirez-Sierra MJ. Immunotherapy of *Trypanosoma cruzi* infection with DNA vaccines in mice. *Infect Immun.* (2004) 72:46–53. doi: 10.1128/iai.72.1.46-53.2004
56. Zapata-Estrella H, Hummel-Newell C, Sanchez-Burgos G, Escobedo-Ortegon J, Ramirez-Sierra MJ, Arjona-Torres A, et al. Control of *Trypanosoma cruzi* infection and changes in T-cell populations induced by a therapeutic DNA vaccine in mice. *Immunol Lett.* (2006) 103:186–91. doi: 10.1016/j.imlet.2005.11.015
57. Gupta S, Smith C, Auclair S, Delgadillo Ade J, Garg NJ. Therapeutic efficacy of a subunit vaccine in controlling chronic *Trypanosoma cruzi* infection and Chagas disease is enhanced by glutathione peroxidase over-expression. *PLoS ONE.* (2015) 10:e0130562. doi: 10.1371/journal.pone.0130562
58. Francisco AF, Jayawardhana S, Taylor MC, Lewis MD, Kelly JM. Assessing the effectiveness of curative benznidazole treatment in preventing chronic cardiac pathology in experimental models of Chagas disease. *Antimicrob Agents Chemother.* (2018) 62:e00832–e00818. doi: 10.1128/AAC.00832-18
59. Chekwube AI, Onyema EI, Ikenna UE, Ezeokonkwo RC. Effect of diminazene aceturate, levamisole and vitamin C combination therapy in rats experimentally infected with *Trypanosoma brucei brucei*. *Asian Pac J Trop Med*. (2014) 7:438–45. doi: 10.1016/S1995-7645(14)60071-7
60. Jones K, Versteeg L, Damania A, Keegan B, Kendricks A, Pollet J, et al. Vaccine-linked chemotherapy improves benznidazole efficacy for acute Chagas disease. *Infect Immun.* (2018) 86:e00876–e00817. doi: 10.1128/IAI.00876-17
61. Rios L, Campos EE, Menon R, Zago MP, Garg NJ. Epidemiology and pathogenesis of maternal-fetal transmission of *Trypanosoma cruzi* and a case for vaccine development against congenital Chagas disease. *Biochim Biophys Acta - Mol Basis Dis.* (2020) 1866:165591. doi: 10.1016/j.bbadis.2019.165591
62. Dumonteil E, Herrera C, Buekens P. A therapeutic preconceptional vaccine against Chagas disease: a novel indication that could reduce congenital transmission and accelerate vaccine development. *PLoS Negl Trop Dis.* (2019) 13:e0006985. doi: 10.1371/journal.pntd.0006985
63. Fabbro DL, Danesi E, Olivera V, Codebó MO, Denner S, Heredia C, et al. Trypanocide treatment of women infected with *Trypanosoma cruzi* and its effect on preventing congenital Chagas. *PLoS Negl Trop Dis*. (2014) 8:e3312. doi: 10.1371/journal.pntd.0003312
64. Murcia L, Simón M, Carrilero B, Roig M, Segovia M. Treatment of infected women of childbearing age prevents congenital *Trypanosoma cruzi* infection by eliminating the parasitemia detected by PCR. *J Infect Dis*. (2017) 215:1452–8. doi: 10.1093/infdis/jix087
65. Álvarez MG, Vigliano C, Lococo B, Bertocchi G, Viotti R. Prevention of congenital Chagas disease by Benznidazole treatment in reproductive-age women. An observational study. *Acta Trop*. (2017) 174:149–52. doi: 10.1016/j.actatropica.2017.07.004
66. Bartsch SM, Stokes-Cawley OW, Buekens P, Asti L, Elena Bottazzi M, Strych U, et al. The potential economic value of a therapeutic Chagas disease vaccine for pregnant women to prevent congenital transmission. *Vaccine.* (2020) 38:3261–70. doi: 10.1016/j.vaccine.2020.02.078

Conflict of Interest: The authors declare that the research was conducted in the absence of any commercial or financial relationships that could be construed as a potential conflict of interest.

frontiers in Microbiology

ORIGINAL RESEARCH
published: 19 October 2020
doi: 10.3389/fmicb.2020.563320

Priming Astrocytes With HIV-Induced Reactive Oxygen Species Enhances Their *Trypanosoma cruzi* Infection

Javier Urquiza[1,2], Cintia Cevallos[1,2], María Mercedes Elizalde[1,2], M. Victoria Delpino[2,3] and Jorge Quarleri[1,2]**

[1]*Instituto de Investigaciones Biomédicas en Retrovirus y Sida (INBIRS), Facultad de Medicina, Universidad de Buenos Aires (UBA), Buenos Aires, Argentina,* [2]*Consejo Nacional de Investigaciones Científicas y Técnicas (CONICET), Buenos Aires, Argentina,* [3]*Instituto de Inmunología, Genética y Metabolismo (INIGEM), Facultad de Farmacia y Bioquímica, Universidad de Buenos Aires, Buenos Aires, Argentina*

Introduction: *Trypanosoma cruzi* is an intracellular protozoa and etiological agent that causes Chagas disease. Its presence among the immunocompromised HIV-infected individuals is relevant worldwide because of its impact on the central nervous system (CNS) causing severe meningoencephalitis. The HIV infection of astrocytes – the most abundant cells in the brain, where the parasite can also be hosted – being able to modify reactive oxygen species (ROS) could influence the parasite growth. In such interaction, extracellular vesicles (EVs) shed from trypomastigotes may alter the surrounding environment including its pro-oxidant status.

Methods: We evaluated the interplay between both pathogens in human astrocytes and its consequences on the host cell pro-oxidant condition self-propitiated by the parasite – using its EVs – or by HIV infection. For this goal, we challenged cultured human primary astrocytes with both pathogens and the efficiency of infection and multiplication were measured by microscopy and flow cytometry and parasite DNA quantification. Mitochondrial and cellular ROS levels were measured by flow cytometry in the presence or not of scavengers with a concomitant evaluation of the cellular apoptosis level.

Results: We observed that increased mitochondrial and cellular ROS production boosted significantly *T. cruzi* infection and multiplication in astrocytes. Such oxidative condition was promoted by free trypomastigotes-derived EVs as well as by HIV infection.

Conclusions: The pathogenesis of the HIV-*T. cruzi* coinfection in astrocytes leads to an oxidative misbalance as a key mechanism, which exacerbates ROS generation and promotes positive feedback to parasite growth in the CNS.

Keywords: astrocytes, *Trypanosoma cruzi*, human immunodeficiency virus, reactive oxygen species, extracellular vesicles

OPEN ACCESS

Edited by:
Rachel Daniels,
Harvard University, United States

Reviewed by:
Matthew H. Collins,
Emory University, United States
Dolores Correa,
National Institute of Pediatrics, Mexico
Phileno Pinge-Filho,
State University of Londrina, Brazil

****Correspondence:***
M. Victoria Delpino
mdelpino@ffyb.uba.ar
orcid.org/0000-0003-2077-8509
Jorge Quarleri
quarleri@fmed.uba.ar
orcid.org/0000-0001-5110-8773

Specialty section:
This article was submitted to Microbial Immunology, a section of the journal Frontiers in Microbiology

Received: *18 May 2020*
Accepted: *22 September 2020*
Published: *19 October 2020*

Citation:
Urquiza J, Cevallos C, Elizalde MM, Delpino MV and Quarleri J (2020) Priming Astrocytes With HIV-Induced Reactive Oxygen Species Enhances Their Trypanosoma cruzi Infection. Front. Microbiol. 11:563320. doi: 10.3389/fmicb.2020.563320

INTRODUCTION

The intracellular protozoan *Trypanosoma cruzi* (*T. cruzi*) causes Chagas disease, which is one of the most important current neglected diseases in the Americas and increasingly widespread worldwide. It is transmitted to humans by *Triatoma infestans* as vector. Current estimations from the World Health Organization (WHO) denote that 8 million people are infected and

other 25 million people are vulnerable of acquiring *T. cruzi* infection worldwide (Perez-Molina and Molina, 2018). Over the last decades of the twentieth century, chronically infected individuals with severe immunosuppression, such as transplant recipients and people living with HIV/AIDS (PLWHA), were at risk of severe forms of reactivation, such as Chagasic meningoencephalitis (Lattes and Lasala, 2014). This condition can arise at chronic stage of infection in immunocompromised hosts including PLWHA (Bern et al., 2011), and it is characterized by brain nodular lesions usually called chagomas involving macrophages, neutrophils, microglia, astrocytes, and perivascular lymphocytic infiltrate in various foci along the central nervous system (CNS; Gomez and Banaei, 2018). Astrocytes are the most abundant brain cells and have multiple functions including maintenance of an adequate environment for neurons by providing metabolic support and modulating synaptic transmission. Moreover, they promote myelination activity of oligodendrocytes and nervous systems repair (Sofroniew and Vinters, 2010; Kiray et al., 2016).

T. cruzi life cycle comprises the trypomastigote as infective bloodstream-form able to infect different nucleated cells. Cell infection is a complex process and includes the parasite-cell uptake, an endocytic process with modification of cellular cytoskeleton, and the growth of a parasitophorous vacuole that encloses trypomastigotes. These trypomastigotes escape into the cytoplasm to be transformed in the amastigote form, able to multiply intracellularly by binary division. Intracellular amastigotes sustain metabolic dependence on cellular energy, nucleotide and fatty acid/glucose metabolites, and survival signaling suggesting a role of host cell metabolism in regulating their intracellular growth (Caradonna et al., 2013). Finally, when the host cell is overwhelmed, amastigotes differentiate into trypomastigotes, host cell is lysed, and infective parasites are released to the bloodstream and eventually could access to the CNS.

Extensive clinical, cerebrospinal fluid (CSF), neuroimaging, and neuropathological data support persistent HIV infection in the CNS (Valcour et al., 2011). We and others have demonstrated that, like other CNS cells, astrocytes can host several infectious agents, including HIV and *T. cruzi* (Blanchet et al., 2010; Vargas-Zambrano et al., 2013; Urquiza et al., 2017) and are regarded as important performers in Chagasic meningoencephalitis development. HIV can infect the brain and impair CNS function. HIV does not directly infect neurons but causes neuronal damage by affecting microglia and other cells in the CNS including astrocytes, causing primary CNS injury (Ellis et al., 2009). This evidence indicated that the cellular response at the local level is altered during HIV infection and the responses to a secondary infection such as *T. cruzi* could be altered favoring the parasite survival and multiplication. Moreover, HIV-infected astrocytes also alter the blood-brain barrier (BBB) permeability due to endothelial cell apoptosis through the disruption of gap junction (Eugenin et al., 2012). This bystander BBB toxicity mediated by HIV-infected astrocytes contributes to understanding not only how the CNS damage caused by HIV has spread but also the increased entry of other pathogens to the CNS. Therefore, Chagas disease may be reactivated in the CNS due to HIV-induced immunosuppression.

As an obligatory intracellular parasite and due to the variety of cellular host environments, *T. cruzi* faces several sources of reactive oxygen species (ROS) including ROS produced by its metabolism and ROS generated by the host's immune responses. Paradoxically, besides the role of ROS in pathogen elimination during the oxidative burst, increasing evidence suggests that ROS production is beneficial to *T. cruzi* infection (Gupta et al., 2009; Paiva et al., 2012, 2018; Goes et al., 2016). This paradoxical role of ROS could be a new target for anti-parasite therapy improvement (Providello et al., 2018). During the cellular invasion, trypomastigotes can activate regulatory pathways using a large number of molecules (Bayer-Santos et al., 2013) carried by extracellular vesicles (EVs), which are small membrane-bound vesicles able to transport secretome components of *T. cruzi* (Retana Moreira et al., 2019). Nevertheless, it remains unclear whether EVs released from parasitized cells and/or by trypomastigotes play any role on *T. cruzi* infection and multiplication by altering the cell host pro-oxidant status.

In the present work, we investigated how the pro-oxidant condition self-promoted by the parasite using its own trypomastigotes derived-EVs or by HIV infection is able to influence *T. cruzi* infection and multiplication in human astrocytes.

MATERIALS AND METHODS

Astrocyte Cultures and *T. cruzi* Strain

Normal human astrocytes (NHA; Lonza®, Pharma&Biotech-Bioscience Solutions) were used. NHA were seeded and grown in AGM™ Bullet Kit™ medium (Lonza®) at 37°C with 5% CO_2.

T. cruzi K98 clone belonging to the discrete typing unit I (DTU I) was used. The clone K98 of the parasite was genetically modified to express the enhanced green fluorescent protein (eGFP). The parasite depicts a homogeneous pattern of GFP fluorescence that allowed to measure both the infection and the multiplication rate in astrocytes. *T. cruzi* was preserved in monolayers of Vero cells (ECACC 84112001). After being released from infected cells, trypomastigotes were collected from supernatants by low-speed centrifugation (500 rpm, 10 min) in order to remove any contaminating cell debris and then counted in a Neubauer chamber.

HIV env-Pseudotyped Production, Titration, and Infection Efficiency Measurement

The pNL4-3 is a full-length infectious molecular clone of HIV that utilizes CXCR4 as a co-receptor. The NL4-3-GFP and pNL4-3-DsRed are two molecular clones that contain the enhanced version of the green fluorescent protein gene (eGFP) or the *Discosoma* sp. red fluorescent protein (DsRed, Clontech), respectively. These viral clones were used alternatively according to fluorochromes requirements for microscopy or flow cytometry evaluation. High-titer stocks of HIV env-pseudotyped with vesicular stomatitis virus envelope glycoprotein (VSV-G) were obtained by cotransfecting 293T cells with a VSV-G expression plasmid (Clontech) at HIV/VSV-G plasmid ratio of 10:1. The concentration of virus stocks was adjusted to a titer of 100 ng/μl

of p24 (HIV capsid protein). Viral infection efficiency was monitored as a function of time using three different approaches: (1) HIV p24 capsid protein in cell culture supernatants (p24 ELISA kit, INNOTEST HIV Antigen mAb), (2) HIV p24 intracellular expression using the KC57 monoclonal antibody labeled with fluorescein isothiocyanate against p24 (p24-FITC) protein (Beckman Coulter, United States; Chassagne et al., 1986; Darden et al., 2000), and (3) HIV gene expression by GFP or DsRed measurement by flow cytometry (FACSCanto II flow cytometer, BD Biosciences, San Jose, CA, United States). Additionally, the identification of productively infected cells for each pathogen, eventual cohabitation of both and neighbor-uninfected cells in a heterogeneous population was measured using flow cytometry analysis of cell fluorescence, by, allows. The measurement of fluorochrome expression sensitivity and performance were checked before data acquisition using Cytometer Setup & Tracking beads (BD Biosciences, San Jose, CA, United States). All experiments were performed in a BSL-3 laboratory at the INBIRS.

HIV and *T. cruzi* Infection of Astrocytes

For infection, human astrocytes were seeded in 48-well culture plates at 3×10^4cells/well. The HIV infection was carried put using an inoculum of 8 μg/ml (measured as p24 antigen), while *T. cruzi* infection with trypomastigotes used a parasite:cell ratio of 5:1. Hence, we used 1.5×10^5 trypomastigotes/well. In these conditions, the release of trypomastigotes began 5-day post-exposure (dpe) from *T. cruzi*-infected astrocytes. To ensure the absence of free HIV particles before inoculating the parasite, astrocytes were washed five times with fresh DMEM.

Evaluation of the *T. cruzi* Infection and Multiplication

The level of infection and multiplication of *T. cruzi* in astrocytes were measured by flow cytometry. For debris exclusion, astrocytes were gated based on side scatter and forward scatter. Quantification of astrocytes with specific fluorescence as well as the mean fluorescence intensity (MFI) in those cells was indicative of infection and multiplication efficiency, respectively. We have collected, stored, and analyzed the data from 5×10^4 cells using Flow Jo X software for Windows 7.0.

T. cruzi infection was also evaluated by fluorescence microscopy. The presence of intracellular amastigotes was evaluated using rabbit polyclonal anti-*T. cruzi* antibody (kindly donated by Dr. Federico Penas, INBIRS, Universidad de Buenos Aires, Argentina). Then, a commercial goat anti-rabbit IgG (H + L) secondary antibody, Alexa Fluor 647 (Invitrogen, Thermo Fisher) was used. The coverslips mounted with DAPI Fluoromount-G (Southern Biotech) were studied in a Nikon Eclipse Ti-S L100 fluorescence microscope using a Plan Apochromat 60 × 1.42 NA oil immersion objective. Images were analyzed using the NIS-Element software.

Finally, a standardized real-time PCR-based method was carried out to quantify intracellular *T. cruzi* DNA (Schijman et al., 2011). For this purpose, after the solvent-based DNA extraction, a Sybr-Green-based real-time PCR targeted to parasite satellite DNA (Sat-DNA) using specific primers TCZ-F (5'-GCTCTTGCCCACAMGGGTGC-3') and TCZ-R (5'-CCAA GCAGCGGATAGTTCAGG-3') was carried out.

Astrocyte Apoptosis Measurement by Flow Cytometry

Using flow cytometry, the percentage of early apoptotic cells was defined based on the plasma membrane permeability and phosphatidylserine cell translocation measurement. For this purpose, dual staining was done with PE or APC-conjugated Annexin-V and 7-amino-actinomycin D (7AAD) using the Annexin-V/7AAD apoptosis detection kit (BD Biosciences).

Isolation, Quantification, and Characterization of Extracellular Vesicles

Free trypomastigotes of *T. cruzi* and human astrocytes were washed with serum-free DMEM. Subsequently, secretion equivalents were obtained from 10^8 parasites and 10^7 astrocytes as was previously described with modifications (Caeiro et al., 2018). For this purpose, such parasite and human cells were incubated in DMEM 10% Gibco Exosome-depleted fetal bovine serum (FBS) at 37°C for 6 h in a humidified atmosphere with 5% CO_2. The products secreted by trypomastigotes and astrocytes were isolated by centrifugation and filtration as follows: (a) 3,000 *g* for 10 min at 4°C to remove the trypomastigotes and apoptotic bodies followed by (b) ultracentrifugation at 100,000 *g* at 4°C to generate the pellet of EVs followed by the second ultracentrifugation with PBS to remove impurities, and finally, (c) the cell-free supernatant was filtered with 0.45 μm syringe filters. The supernatant was wasted, and the exosome pellet was resuspended in 200 μl–1 ml PBS for scanning electron microscopy (SEM) inspection. All ultracentrifugation stages were performed in a 70Ti fixed angle rotor in an Optima XL 100 k ultracentrifuge (Beckman Coulter). For each pellet, protein quantification was spectrophotometrically performed using the Bio-Rad Protein Assay reagent and bovine serum albumin (BSA; 1 mg/ml) as standard.

To assess the biochemical characteristics of EVs by Western Blot, 40 μg of EVs isolated from 100×10^6 of trypomastigotes obtained in Vero cells, and 10×10^6 astrocytes or their equivalent of soluble vesicle secretion (EVs) were electrophoresed in 12% denaturing polyacrylamide gels and transferred to PVDF membranes by standard methodologies. The appropriate transfer was tested by reversible membrane staining with Ponceau Red (5% w/v) in 1% acetic acid (v/v). The membrane was blocked with TBS-3% non-fat milk for 1 h, washed with TBS-0.05% Tween and incubated with primary antibodies. After several washes, membranes were incubated with the secondary antibody horseradish peroxidase-conjugated goat anti-mouse IgG (1 : 4000) and developed with the Supersignal® West Pico Chemiluminescent Substrate (Pierce) according to the manufacturer's instructions. The revealed images were acquired by the MultiDoc-It™ Imaging System. Western blotting of EVs of *T. cruzi* was carried out using primary mouse antibodies anti-TcTASV-C (Trypomastigote Alanine, Serine and Valine protein from *T. cruzi*; 1/400) and anti-SAPA (Shed Acute-Phase Antigen, a trans-sialidase repetitive

domain) kindly provided by Dr. Valeria Tekiel (IIB-INTECH, UNSAM-CONICET, Argentina). Mouse anti-CD9 (clone M-L13; BD Bioscience) and anti-CD63 antibodies (clone H5C6; BD Bioscience) were used for EVs derived from astrocytes. As negative controls, two cytoplasmic proteins were detected: rabbit polyclonal anti-calnexin (1/500; Abcam) and rabbit polyclonal anti-SR62 (1/1000), which must be absent in pure EVs of astrocytes and trypomastigotes, respectively.

For SEM, pellets containing EVs isolated from healthy astrocytes, parasitized cells, and trypomastigotes were vortexed and resuspended in 200 µl–1 ml PBS. EVs were fixed in 2% SEM-quality paraformaldehyde aqueous solution and then diluted in distilled water and added in 1–5 µl vesicle mixtures to clean silicon chips. Samples were mounted on a SEM stage by carbon paste. SEM (Hitachi S-4700) was performed under low beam energies (5.0–10.0 kV). Analysis of EVs sizes was done using the SEM images *via* ImageJ (Wayne Rasband, NIH, United States).

Astrocyte (3×10^4 cells/well) stimulation with free *T. cruzi*-derived EVs was performed using 6 µg/well of protein. Such amount of protein was obtained from EVs extracted from 1.5×10^5 trypomastigotes. Equal protein concentration was used when challenges were performed with EVs from the other two sources (Tc-infected astrocytes and uninfected astrocytes). The EV-treated astrocytes were exposed to *T. cruzi* at three distinguishable conditions such as 24 h before, simultaneous, or 24 h after EVs exposure.

Detection and Scavenging of Cellular Reactive Oxygen Species Generation

Production of cellular and mitochondrial ROS was evaluated using DCFDA and MitoSOX assays, respectively as follows:

a. Cellular ROS production (including hydroxyl, peroxyl, and another ROS) were measured using a DCFDA assay kit (Abcam, United States) according to the manufacturer's protocol. Following a specific timeline after infection, cells were washed twice with PBS, incubated with 25 µM DCFDA in the essential medium at 37°C for 45 min, and evaluated by flow cytometry.
b. Cellular mitochondrial ROS measurement by flow cytometry was made by staining with MitoSOX™ (Thermo Fisher Scientific, United States) following the manufacturer's instructions. Briefly, at the predetermined time points after infection, cells were washed twice with PBS, incubated with 5 µM MitoSOX at the corresponding temperature and time for each reagent, and then evaluated by flow cytometry.

Also, astrocytes were pre-treated for 18 h with the antioxidant ascorbic acid (AA) or with MitoTEMPO® (MT; Sigma-Aldrich), a well-known mitochondria-specific superoxide scavenger, to validate the *in vitro* model and to demonstrate ROS functionality. AA is a non-enzymatic antioxidant, contributing to ROS-scavenging. A stock solution of 100 mM (Sigma) was prepared fresh in a modified Krebs buffer and then diluted in cell culture media until 1 mM final concentration. MT was used in a final concentration of 10 µM.

Tert-Butyl hydroperoxide (TBH) is an organic peroxide used as ROS inducer. Here, three serial dilutions were prepared (100, 50, and 10 µM) from a 70% aqueous solution (Sigma-Aldrich). Astrocytes treated with increased concentrations of TBH (1 h, 37°C) were used as positive controls for ROS generation.

Statistical Analysis

Where applicable, statistical analysis was performed. Multiple comparisons between all pairs of groups were made with Tukey's test, and those against two groups were made with Mann-Whitney U test. Graphical and statistical analyses were performed with GraphPad Prism 5.0 software.

Each experiment was performed in triplicates with different culture preparations on five independent occasions. Data were represented as mean ± SD measured in triplicate from three individual experiments. A $p < 0.05$ is represented as *, $p < 0.01$ as **, and $p < 0.001$ as ***. $p < 0.05$ was the minimum level for accepting a statistically significant difference between groups.

RESULTS

T. cruzi Induces ROS Upregulation in Astrocytes Favoring Its Infection and Multiplication

During *T. cruzi* infection, the macrophages respiratory burst produces ROS. However, the parasite has an antioxidant machinery to deal with the oxidative burst. Moreover, such pro-oxidant environment fuels the *T. cruzi* infection (Gupta et al., 2009; Paiva et al., 2012, 2018; Goes et al., 2016). Here, we have examined whether ROS production occurs during the parasite infection of astrocytes and the impact on its multiplication. For this goal, we performed experiments using MitoSOX and DCFDA, useful for measurement of mitochondrial ROS (mROS) and cellular ROS (cROS) activity by flow cytometry, respectively. Twenty-four hours after *T. cruzi* (trypomastigotes) challenge (**Figure 1A**), significantly higher mitochondrial and cellular ROS positive cells were measured in infected astrocytes to control cells (**Figures 1B,C**). However, these higher levels of ROS observed after *T. cruzi* exposure did not modify the level of programed cell death in comparison with control astrocytes (**Figure 1D**).

Furthermore, to evaluate the ROS impact on *T. cruzi* infection and multiplication, astrocytes were treated with 10, 50, and 100 µM TBH for 1 h before being exposed to trypomastigotes (**Figure 1E**). The level of cell death was evaluated after 48 h in both conditions: control cells (only exposed to TBH) and TBH/*T. cruzi*-infected cells.

In uninfected cells, the level of cell death after TBH treatment did not depict any significant differences according to growing (10, 50, and 100 µM) pro-oxidant concentration respect to untreated control. But the level of cell death on astrocytes was significantly higher in *T. cruzi*-infected cells in the presence of 50 and 100 µM of TBH as shown in **Figure 1F**.

The impact of TBH-induced pro-oxidant level on *T. cruzi* infection and multiplication was measured 48 h post-parasite exposure. The infection rate of astrocytes by *T. cruzi* was directly and dose-dependently influenced by the level of ROS. Cells exposed to growing doses of TBH (10, 50, and 100 µM) showed significantly higher levels of infection compared to unexposed controls (**Figure 1G**). Likewise, a significantly higher

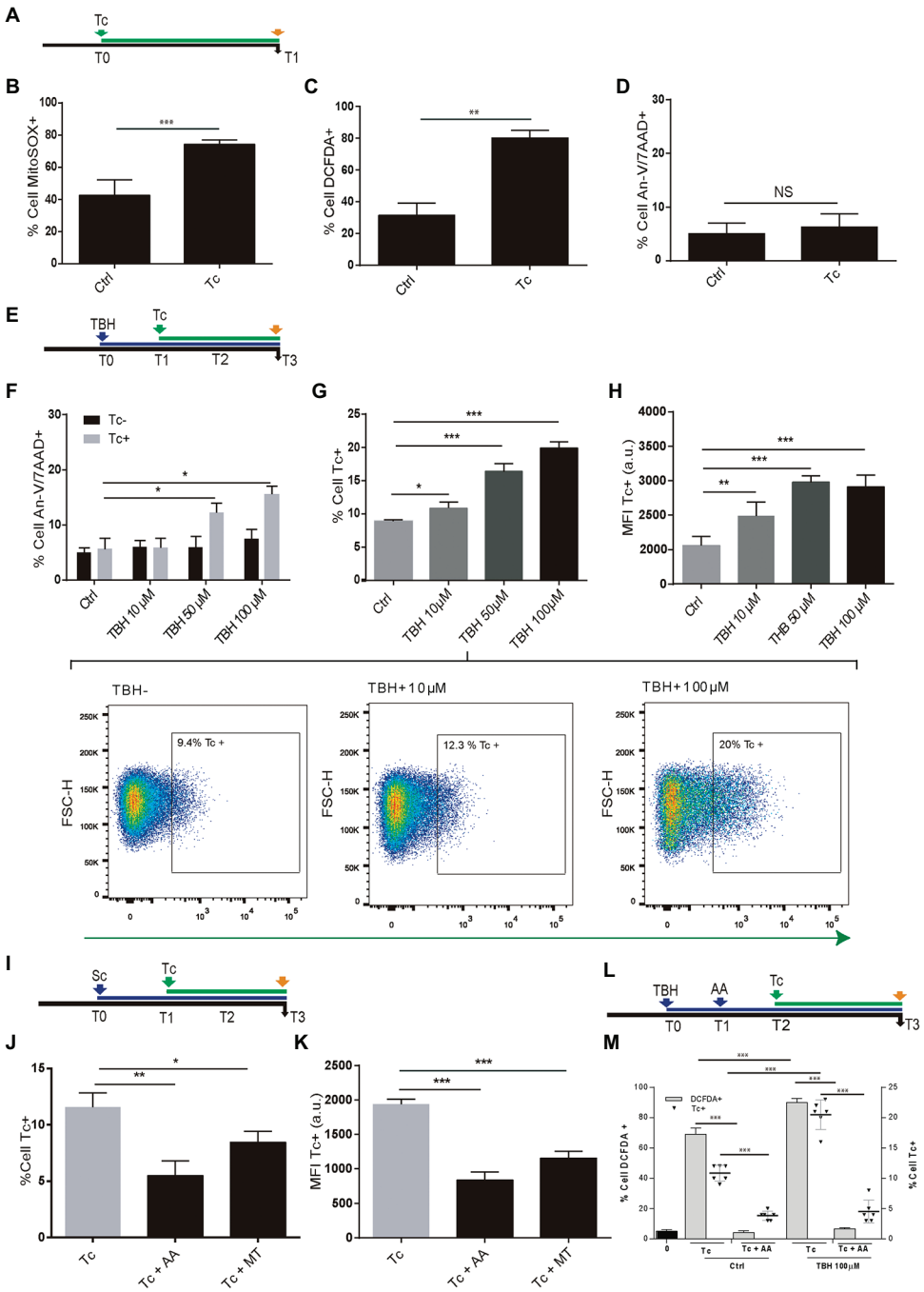

FIGURE 1 | Effect of *Trypanosoma cruzi* infection on astrocyte ROS level and its consequences on parasite infection and multiplication. **(A)** Timeline of the Tc infection of cultured human astrocytes. Parameters were measured at T1 (orange arrow, 24 h after Tc exposure). **(B)** mROS level was measured by flow cytometry using MitoSOX in uninfected astrocytes – Ctrl – and Tc-infected astrocytes. **(C)** cROS level was measured by flow cytometry using DCFDA (assumed to be proportional to the concentration of hydrogen peroxide) in uninfected astrocytes – Ctrl – and Tc-infected astrocytes. **(D)** Cell death levels (positive staining for annexin-V and 7-AAD) in uninfected (Ctrl) and Tc-infected astrocytes analyzed by flow cytometry. **(E)** Timeline of the exposure of cultured astrocytes to tert-Butyl hydroperoxide (TBH; blue arrow) followed by Tc infection (green arrow, 1 h after TBH-exposure). Parameters were measured at T3 (orange arrow, 48 h after Tc exposure). **(F)** Cell death levels by flow cytometry (positive staining for annexin-V and 7-AAD) in unexposed (Ctrl) and TBH-exposed cells (at increasing concentrations as indicated), in non-infected (black columns) and Tc-infected (gray columns) astrocytes. **(G)** Tc-infection rate analysis in unexposed (Ctrl) and TBH-exposed cells (at increasing concentrations as indicated). Three representative dot plots representation are shown. For each diagram, a square depicted the percentage of Tc-infected cells (GFP-positive). **(H)** Tc-multiplication quantification by flow cytometry as mean fluorescence intensity (MFI, expressed in arbitrary units)

(Continued)

FIGURE 1 | in unexposed (Ctrl) and TBH-exposed cells (at increasing concentrations as indicated). **(I)** Timeline of the exposure of cultured astrocytes to ROS scavengers (MT: MitoTEMPO; AA: ascorbic acid; blue arrow) followed by Tc infection (green arrow, 18 h after scavengers exposure). Parameters were measured at T3 (orange arrow, 48 h after Tc exposure). **(J)** Tc-infection rate analysis in non-scavenged and scavenged (with MT, or AA) *T. cruzi*-infected cells. **(K)** Tc-multiplication quantification by flow cytometry as MFI in non-scavenged and scavenged (with MT, or AA) *T. cruzi*-infected cells. **(L)** Timeline of the exposure of cultured astrocytes to pro-oxidant condition (TBH, 100 μM during 1 h), ROS scavenging (AA: ascorbic acid), and Tc infection (green arrow, 18 h after AA exposure). Parameters were measured at T3 (orange arrow, 48 h after Tc exposure). **(M)** Astrocyte ROS level (% cell DCFDA+) and Tc infection rate (% cell Tc+) analysis in control and TBH-treated astrocytes, with and without scavenging (AA). Graphics are showing values obtained from three independent experiments. Data are given as the mean ± SD. NS (not significant), $^{*}p < 0.05$, $^{**}p < 0.01$, and $^{***}p < 0.001$.

level of amastigote multiplication was found when astrocytes were under pro-oxidant condition maintaining a dose-dependent response according to increased TBH level in comparison with unexposed controls (**Figure 1H**).

The incumbency of the pro-oxidant environment on *T. cruzi* infection and multiplication was also evaluated by diminishing the ROS activity using mitochondrial and cytoplasmic scavengers (MT and AA, respectively) before parasite infection (**Figure 1I**). When the ROS level was depleted using scavengers, significantly lower infection and multiplication were observed (**Figures 1J,K**). Finally, the influence of both, the TBH-pro-oxidant environment (using 100 μM) and the ROS scavenging (using AA) on both *T. cruzi* infection rate and ROS level (measured using DCFDA) were simultaneously measured. Thus, the parasite infection rate and the ROS level among astrocytes previously exposed to TBH were significantly higher than control (non-TBH exposed) cells. Although, when ROS scavenging with AA was applied on astrocytes (initially exposed or not to TBH) after their parasite challenge both, Tc infection rate and ROS level appeared significantly reduced (**Figures 1L,M**).

Taken together, our results indicate that astrocytes primed by an oxidative environment or by their oxidative stress – with cellular and mitochondrial ROS production – enhance their *T. cruzi* infection and multiplication.

Extracellular Vesicles Enhance *T. cruzi* Infection by Inducing ROS Upregulation

Considering their role in parasitism increment (Retana Moreira et al., 2019), the capability of EVs released from *T. cruzi* to alter the host-cell oxidant environment was evaluated. EVs were obtained after incubation of 10×10^7 parasite tissue-culture cell-derived trypomastigotes (K98 strain). These EVs were characterized by Scanning Electronic Microscopy (SEM), and the presence of *T. cruzi* trypomastigotes surface molecules (SAPA and Tc-TASV-C antigens) was assessed by western blotting (**Figures 2A,B**). Besides, EVs obtained from 10×10^6 astrocytes parasitized by *T. cruzi* amastigotes as well as from non-infected astrocytes. These EVs were biochemically characterized by detecting cell-derived EVs canonical proteins CD9 and CD63 (**Figure 2C**).

When astrocytes were exposed to EVs released by free trypomastigotes (but not from EVs released from Tc-infected cells and EVs from uninfected cells) during 24 h, a significant increase in the ROS level was observed respect to untreated cells. The influence of this EVs-induced oxidant environment on the *T. cruzi* infection rate was evaluated following an analogous timeline than previous ones (**Figure 2D**). In this condition, the infection rate was increased significantly without infringing significant changes in cell viability (**Figures 2E,F**). This EVs-mediated parasitism augmentation phenomenon showed a dose-dependence since it was significantly reduced when exposures were carried out with 1/10 and 1/100 dilutions of EVs (0.6 and 0.06 μg/well, respectively; **Figure 2G**). The ROS (cellular and mitochondrial) level in astrocytes exposed to trypomastigotes-derived EVs was significantly higher than control cells. In contrast, such ROS levels in astrocytes did not experience any change after exposure to EVs released from uninfected and parasitized astrocytes (**Figure 2H**).

To determine whether the EVs-induced *T. cruzi* infection enhancement keeps a time-dependence, we have evaluated two additional conditions as follows: (i) simultaneous challenge of astrocytes with trypomastigotes-derived EVs and *T. cruzi* (**Figure 2I**) and (ii) astrocytes exposure to free trypomastigotes-derived EVs after their *T. cruzi* exposure (**Figure 2J**). In both conditions, the *T. cruzi* infection rate did not differ significantly from control cells (**Figures 2K,L**, respectively). Likewise, the ROS level was similar in these two conditions (data not shown).

Taken together, these results demonstrate that EVs from free *T. cruzi* trypomastigotes prime astrocytes by raising their ROS level, thus enhancing the parasite infection and multiplication.

T. cruzi Infection and Multiplication in Astrocytes Is Enhanced by HIV Infection

We and others have demonstrated that astrocytes can be productively infected by HIV (Barat et al., 2018; Ojeda et al., 2018; Li et al., 2020) and when *T. cruzi* is concomitantly present, both pathogens may interact (Urquiza et al., 2017). To assess the influence of HIV infection of astrocytes on its posterior *T. cruzi* superinfection and multiplication, primary cultured human astrocytes were exposed subsequently to both pathogens (**Figure 3A**). The parasite infection and multiplication were evaluated 24 h after *T. cruzi* exposure. The rate of parasitism was increased significantly when astrocytes were previously exposed to HIV in comparison with those non-exposed to HIV as shown in **Figure 3B**. Also, the multiplication of *T. cruzi* in astrocytes was also significantly enhanced (**Figures 3C,D**). HIV enhancement of parasite multiplication was also detected by quantifying amastigotes microsatellite DNA sequence (TCZ) using real-time PCR (**Figure 3E**). Furthermore, using both flow cytometry analysis and immunofluorescence microscopy, we coincidentally observed that after challenging astrocytes with both pathogens, monoinfected cells were the most abundant, while the HIV/*T. cruzi* coinfected astrocytes were found to a lesser extent (**Figures 3F–H**). Taken together, these observations pointed out that a previous HIV infection of astrocytes increases their subsequent infection by *T. cruzi* as well as parasite

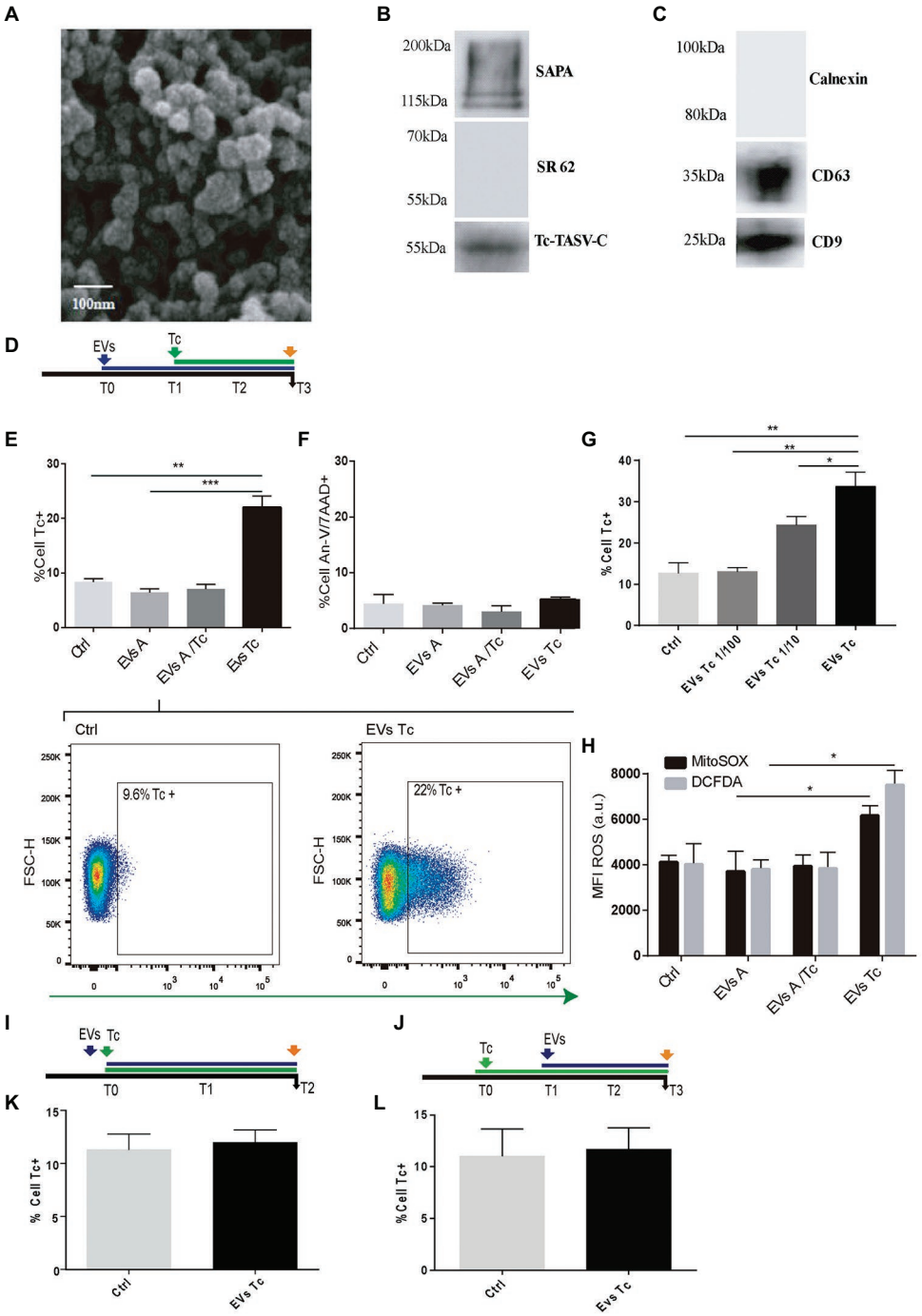

FIGURE 2 | Effect of trypomastigotes-derived extracellular vesicles (EVs) in astrocytes ROS concentration and *Trypanosoma cruzi* infection. **(A)** Scanning electron microscopy (SEM) showing clusters of trypomastigotes-derived EVs formed by ultracentrifugation. The bar size is indicated. **(B)** Biochemical characterization of EVs purified from trypomastigotes by western blot to verify the presence of SAPA (shed acute-phase antigen) and Tc-TASV-C antigens and the absence of SR62 (*T. cruzi* cytoplasmic antigen). **(C)** Biochemical characterization of EVs purified from astrocytes. The presence of CD63, CD9, and absence of calnexin was determined by western blot from astrocyte-derived EVs. **(D)** Timeline of the EVs exposure (blue arrow) in cultured astrocytes followed by Tc infection (green arrow, 24 h after EVs exposure). Parameters were measured at T3 (orange arrow, 48 h after Tc exposure). **(E)** Tc-infection rate measured as GFP+ cells analysis in EVs non-exposed astrocytes followed by Tc infection (Tc), and EVs-exposed cells [EVs from normal astrocytes (EVs A), Tc-infected astrocytes (EVs A/Tc), and EVs from free trypomastigotes (EVs Tc)]. Two representative dot plots obtained by flow cytometry showing EVs non-exposed astrocytes (Ctrl, left panel) and EVs (from trypomastigotes) exposed-astrocytes (EVs-Tc, right panel). In each diagram, a square depicted the percentage of Tc-infected cells (GFP-positive).

(Continued)

FIGURE 2 | (F) Astrocyte death levels (measured as positive staining for annexin-V and 7-AAD) in EVs non-exposed astrocytes followed by Tc infection (Ctrl), and EVs-exposed cells [with EVs obtained from cell sources defined in item **(E)**]. **(G)** Tc-infection rate measured as GFP+ cells analysis in EVs from free trypomastigotes (EVs Tc) at dilutions 1/100 (0.06 μg/well), 1/10 (0.6 μg/well), and pure (6 μ/well). **(H)** Cellular and mitochondrial ROS level (using DCFDA – represented in gray columns and MitoTEMPO – represented in black columns, respectively) as MFI, in astrocytes (exposed to EVs from sources described in **E**). **(I)** Timeline of the EVs exposure (blue arrow) in cultured astrocytes simultaneously infected with Tc (green arrow). Parameters were measured at T2 (orange arrow, 48 h after Tc + EVs exposure). **(J)** Timeline of the cultured astrocytes infected with Tc (green arrow) and stimulated with EVs (blue arrow, 24 h after Tc exposure). Parameters were measured at T3 (orange arrow, 48 h after EVs exposure). **(K)** Tc-infection rate measured as GFP+ cells analysis in EVs non-exposed astrocytes but Tc-infected (Ctrl), and EVs from free trypomastigotes-exposed cells simultaneously with Tc infection. **(L)** Tc-infection rate measured as GFP+ cells in EVs non-exposed astrocytes but Tc-infected (Ctrl), and EVs from free trypomastigotes-exposed cells after infection with Tc. Graphics are showing values obtained from three independent experiments. Data are given as the mean ± SD Significant differences are indicated by $^{*}p < 0.05$, $^{**}p < 0.01$, and $^{***}p < 0.001$, respectively.

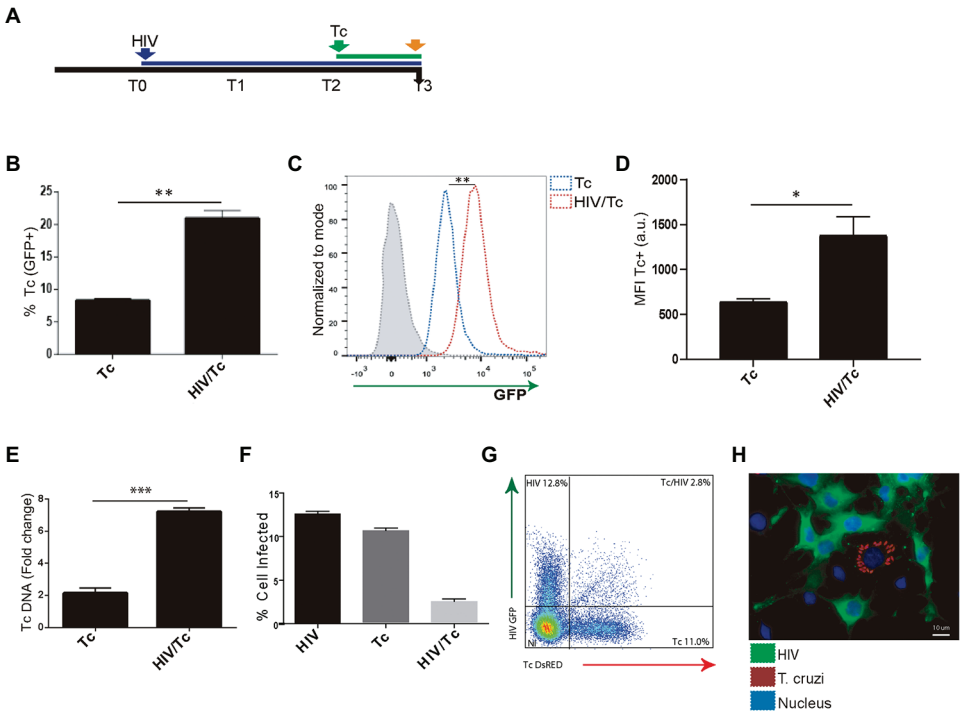

FIGURE 3 | Effect of HIV infection of astrocytes on *Trypanosoma cruzi* infection and multiplication. **(A)** Timeline of the HIV (T0, blue arrow) and Tc (T2 green arrow, after 48 h of HIV exposure) infection of cultured human astrocytes. Parameters were measured at T3 (orange arrow, 24 h after Tc exposure). **(B)** Effect of HIV pre-infection of astrocytes on the Tc-infection rate measured by flow cytometry analysis as percentages of GFP+ cells. **(C)** Histogram example of the quantitative analysis of Tc-GFP positive cells proportion and MFI measured by flow cytometry. The *x*-axis represents the fluorescent signal intensity, and *y*-axis the normalized cell number expressed as a percentage of the maximum. **(D)** Relationship between the geometric mean of MFI of Tc-GFP positive cells in Tc infection (Tc), and astrocytes infected by HIV and superinfected by Tc (HIV/Tc). **(E)** Measurement of variation in the Tc DNA level (as fold change) by qPCR in astrocytes only infected by Tc (Tc), and in astrocytes infected by HIV at first and superinfected by Tc (HIV/Tc). **(F)** Measurement by flow cytometry of HIV (black), Tc (dark gray), and HIV + Tc (light gray)-infected astrocytes by determining the frequencies of HIV-GFP+, Tc-DsRED+, and HIV-GFP+/Tc-DsRED+ cells. **(G)** A representative dot plot diagram obtained by flow cytometry during Tc and/or HIV infection quantification of cultured astrocytes is shown. **(H)** Fluorescence microscopy showing Tc (Red: K98-Alexa fluor 647-labeled intracellular amastigotes) and/or HIV (Green: p24 FITC-labeled) infected-primary human astrocytes. Cell and parasite nucleus were stained by DAPI (blue). Graphics are showing values obtained from three independent experiments. Data are given as the mean ± SD Significant differences are indicated by $^{*}p < 0.05$, $^{**}p < 0.01$, and $^{***}p < 0.001$, respectively.

multiplication, without implying the intracellular cohabitation of both pathogens as *sine-qua-non* condition.

Intracellular HIV-Induced ROS Contributes to Increasing *T. cruzi* Infection and Multiplication in Astrocytes

Recently, we have reported that HIV infection increases ROS generation in astrocytes (Ojeda et al., 2018). Resembling the HIV-mediated enhancement of *T. cruzi* infection described above, we were prompted to study whether HIV-induced ROS production on astrocytes is a dose-dependent phenomenon that may influence susceptibility to *T. cruzi* infection and multiplication (**Figure 4A**). For this goal, astrocytes were challenged with two inoculums of HIV: 8 and 80 μg/ml, thus increasing both the rate of HIV infection and the astrocyte ROS level (**Figure 4B**). After the challenge with *T. cruzi*, these astrocytes exhibiting significantly increased *T. cruzi* infection and multiplication (**Figures 4C,D**). When HIV infection of

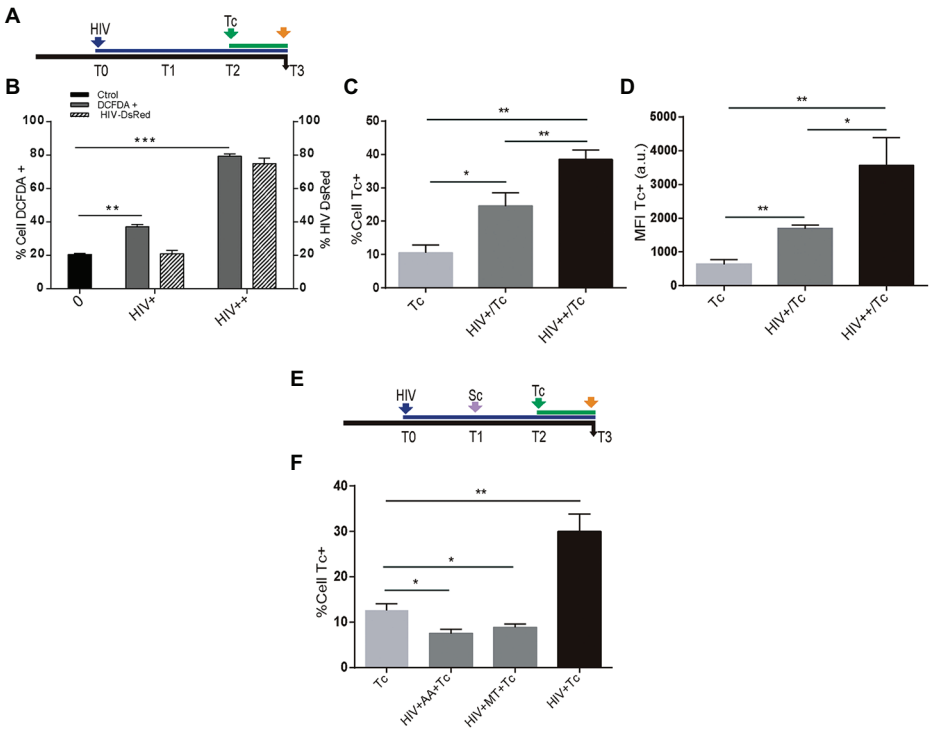

FIGURE 4 | Role of HIV-induced ROS on *Trypanosoma cruzi* infection and multiplication in astrocytes. **(A)** Timeline of the HIV exposure (blue arrow) of cultured astrocytes followed by Tc infection (green arrow, 48 h after HIV exposure). Parameters were measured at T3 (orange arrow, 24 h after Tc exposure). **(B)** Cellular ROS levels (as a percentage of DCFDA-positive cells, on left y-axis) and HIV infection efficiency (measured by flow cytometry as a percentage of GFP-positive cells, on the right y-axis) using two different inoculums at T0 (+: 8 μg/ml, ++: 80 μg/ml of p24 antigen). **(C)** Tc-infection rate measured by flow cytometry analysis in HIV non-exposed (Tc) and HIV-exposed cells (at the two inoculums indicated as HIV+/Tc and HIV++/Tc). **(D)** Tc-multiplication quantification by flow cytometry as mean fluorescence intensity (MFI, expressed in arbitrary units) in HIV non-exposed (Tc) and HIV-exposed astrocytes (at the two inoculums indicated as HIV+/Tc and HIV++/Tc). **(E)** Timeline of the HIV exposure (blue arrow) of cultured astrocytes followed by scavenging (MT: MitoTEMPO; AA: ascorbic acid; violet arrow, 24 h after HIV exposure), and Tc infection (green arrow, 48 h after HIV exposure). Parameters were measured at T3 (orange arrow, 24 h after Tc exposure). **(F)** Tc-infection rate measured by flow cytometry analysis in HIV non-exposed astrocytes followed by Tc infection (Tc) and in HIV-exposed cells (at the two inoculums as indicated), then scavenged (with MT, or AA), and finally exposed to Tc. A control without pretreatment with scavengers is included (HIV + Tc). Graphics are showing values obtained from three independent experiments. Data are given as the mean ± SD Significant differences are indicated by $^{*}p < 0.05$, $^{**}p < 0.01$, and $^{***}p < 0.001$, respectively.

astrocytes was followed by scavenger treatment before *T. cruzi* exposure (**Figure 4E**), the level of parasitism was even significantly lower than untreated cells (**Figure 4F**).

Taken together, these results demonstrate that infection and multiplication of *T. cruzi* in astrocytes increase when cells are previously exposed to HIV, since this raises ROS activity.

DISCUSSION

In immunosuppression conditions, the reactivation of *T. cruzi* infection occurs mainly in the CNS. In this context, neurological involvement is observed is the vast majority of HIV-coinfected patients (Ferreira et al., 1997; Cordova et al., 2008). Astrocytes have been proposed as parasite (Weinkauf et al., 2011; Silva et al., 2015, 2017), and also HIV target cells, as we and others have reported (Urquiza et al., 2017; Chen et al., 2020; Li et al., 2020; Proust et al., 2020).

The ROS are paradigmatically assumed as antimicrobial defense weapons exhibited by phagocytes. It can be generated using both enzymatically and non enzymatically processes being those that occur into the mitochondria one of the main contributors (Nathan et al., 1979). In the CNS, in addition to microglial cells, the activated astrocytes are also source of ROS production (Sharma et al., 2007; Williams et al., 2010; Sheng et al., 2013). Under normal conditions, the ROS produced can be maintained in homeostasis without triggering deleterious effects to the cell host by the coordinated action of antioxidant enzymes and molecules. However, under inflammation among other pathological scenarios, ROS can damage cells (Sheng et al., 2013).

Trypomastigotes can actively infect a variety of non-immune and immune cells and also may be phagocytosed by macrophages (Walker et al., 2014). Such event activates a rapid increased in the production of inflammatory cytokines (Koo et al., 2018), and concomitantly, inducible NADPH oxidase (NOX2) produces superoxide that can be transformed suddenly or enzymatically by superoxide dismutases to H_2O_2, which is also dismutated by cytosolic glutathione peroxidase and peroxidase (Gupta et al., 2011). Likewise, inducible nitric oxide synthetase (iNOS) produces NO that can react with superoxide and generate peroxynitrite

in infected macrophages. Therefore, *T. cruzi* is regularly exposed to ROS throughout its life cycle and needs to effectively manage the antioxidant and reparation systems to overwhelm the toxic effects of oxidative stress. To this goal, this parasite expresses antioxidant enzymes that are crucial to defending against oxidative damage, allowing the parasite to surpass such oxidative conditions (Paiva et al., 2012; Goes et al., 2016; Hugo et al., 2017). Nevertheless, *T. cruzi* produces its own metabolism-derived ROS, and during the intracellular stages of the lifecycle, it must deal with ROS from the host cell oxidative stress. Thus, for its survival *T. cruzi* has developed ROS detoxification and DNA repair pathways (Mesias et al., 2019). Moreover, recent evidence indicates that the amastigotes division in macrophages and cardiomyocytes is stimulated in ROS enriched oxidative environments by increasing iron availability from host's cellular reservoir (Gupta et al., 2009; Paiva et al., 2012, 2018; Goes et al., 2016; Dias et al., 2017). Almost all cells need iron as an essential micronutrient, operating as a cofactor for multiple metabolic enzymes. *T. cruzi* demands a large quantity of iron for growth and differentiation (Dick et al., 2020). When macrophages are exposed antioxidants, then the availability of iron decreased and provokes a higher expression of ferritin (a protein that binds iron) and ferroportin-1 (a channel for iron efflux). A low iron level correlates with a lower parasite cargo. Consequently, the use of an iron chelator such as desferrioxamine has been reported to be useful for reducing parasitemia and mortality in experimentally infected mice (Arantes et al., 2007). Besides, the HIV replication maybe also influenced when the iron is accumulated or depleted, free radical synthesis is promoted, and inflammation and mitophagy is enhanced (Allen et al., 2013; Andersen et al., 2014). In the CNS, it was insinuated that an HIV-associated dysregulation of iron transport in the brain may occur, including the possibility of iron deficiency in neurons and iron overload in astrocytes (Mehta et al., 2017). However, it is still unknown the iron role on *T. cruzi* life cycle in astrocytes. Thus, mechanisms by which ROS promote *T. cruzi* infection are still to be fully explained. Current speculation sustains that two possible evolutionary and interacting pressures that forced the selection of *T. cruzi* proliferative response are the increased availability of micronutrients (such as labile iron) and the decreased activation of efficient microbicide mechanisms under oxidative stress (Paiva et al., 2018). Several research groups have explored the possibility that the oxidative environment is itself a direct stimulus to the growth of *T. cruzi*. As an example, trypomastigotes responded to incubation with H_2O_2 before the infection, giving rise to greater amastigote cargo after they invaded macrophages or fibroblasts (Aguiar et al., 2013). Likewise, cruzipain is a parasite enzyme that increases the susceptibility of macrophages to parasite infection (Stempin et al., 2008) and is a major inducer of NOX2 activation during macrophage infection (Guinazu et al., 2010).

Astrocytes are the most abundant in a location, where the parasite frequently reactivates in immunocompromised patients, as those with AIDS. Here, we demonstrate that ROS produced by astrocyte during parasite infection also fuels significatively its infection and multiplication. Likewise, as the production of mitochondrial ROS can be potentiated by exogenous oxidants (Jou, 2008), we have used an exogenous source of peroxide (TBH) to promote such enhancement. We observed a pronounced augment in the levels of infection and multiplication of the parasite in a concentration-dependent manner. Thus, with the highest concentrations of the pro-oxidant agent, a significant accumulation of amastigotes was observed that may correlate with the increased astrocyte death observed, as occurs among cardiomyocytes at later stages of parasite multiplication (de Souza et al., 2010; Manque et al., 2011). Furthermore, such ROS-dependent exacerbation of the *T. cruzi* infection and multiplication in astrocytes was counteracted when mitochondrial and cellular ROS were scavenged. Likewise, similar findings were reported in macrophages. The incubation of infected macrophages with up to 100 μM H_2O_2 promotes a more intensive amastigote proliferation, but the concentrations of H_2O_2 that reach the cytosol are unknown. During the macrophage respiratory burst, the cytosolic concentration of H_2O_2 would be around 1–4 μM (Paiva et al., 2012). We have observed that astrocytes viability at concentrations of TBH higher than 250 μM was lower than 10% (data not shown). Nevertheless, a concentration of H_2O_2 as high as 300 μM is unlikely to occur *in vivo* (Huang and Sikes, 2014).

Remarkably, other cell types present in the intact CNS could contribute to the regulation of oxidative state experienced by astrocytes. Hence, the progression of HIV infection toward more advanced stages is accompanied by iron accumulation on macrophages and, at the CNS, microglia. The iron excess may enhance the oxidative stress which impairs immune mechanisms. As well, microglial cells are also susceptible to be infected by this parasite, thus generating another cellular scenario for cohabitation. However, astrocytes appear to be more permissive to parasite replication because the activation of the NLRP3 inflammasomes is lower than in microglia-infected cells (Pacheco et al., 2019).

Astrocytes are host-cells for both pathogens (Blanchet et al., 2010; Vargas-Zambrano et al., 2013; Urquiza et al., 2017). Then, in a coinfection – with cellular cohabitation or by bystander effect between monoinfected cells – the progress of the infections can be modified. Such cell-to-cell interactions may involve the participation of EVs, as was reported for *T. cruzi* parasitized cells (Goncalves et al., 1991; Trocoli Torrecilhas et al., 2009). The interaction between *T. cruzi* released EVs and target cells may modulate the host responses against the parasite (Cestari et al., 2012; Ramirez et al., 2017). Similarly, EVs obtained from *T. cruzi* tissue-culture cell-derived trypomastigotes promote functional changes in host-target cells that enhance its infection (Retana Moreira et al., 2019), as well as to modulate the host immune response in favor of the parasite and carry different virulence factors (Ramirez et al., 2017; Caeiro et al., 2018; Lovo-Martins et al., 2018). In line with these reports, we were able to demonstrate that EVs from free trypomastigotes, but not from intracellular amastigotes, were able to increase the host cellular and mitochondrial ROS level which consequently enhanced *T. cruzi* infection in astrocytes, in a concentration-dependent manner. Therefore, this EVs released by the parasite can contain enzymes that increase the ROS production after inducing cell host NADPH oxidase activity (Guinazu et al., 2010), thus increasing the susceptibility to infection (Stempin et al., 2008).

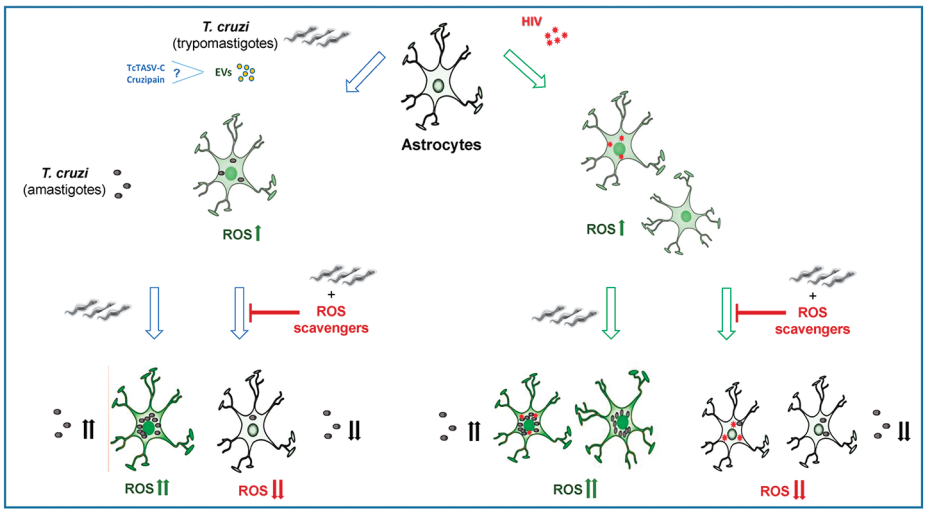

FIGURE 5 | The infection and multiplication of *Trypanosoma cruzi* in astrocytes is influenced by reactive oxygen species (ROS) generated during its infection or by prior HIV exposure.

Moreover, under pro-oxidant conditions, EVs shedding is induced (Benedikter et al., 2018), which also may carry different antioxidant enzymes involved in ROS scavenging (Bodega et al., 2019).

We have previously reported that HIV infection increases intracellular ROS levels in astrocytes. Such oxidative stress was observed among productively and non-productively infected cells, as a bystander effect. Nevertheless, the astrocytes productively infected with HIV but not the non-productively infected ones were able to mitigate ROS production. So, intracellular ROS concentration remained high among non-productive HIV infected cells (Ojeda et al., 2018) as a consequence of its diffusion through channels in the plasma membrane, or promoted by soluble HIV-released proteins released from infected cells (Song et al., 2007). This cellular scenario allows explaining the very low frequency of astrocytes with intracellular coexistence of both pathogens observed in the present study, emphasizing that the synergic interplay between both pathogens may dispense with the intracellular cohabitation.

Currently, the genotypes of *T. cruzi* are assembled in seven discrete typing units (Jansen et al., 2020). It was documented an increased production of ROS and the resulting oxidative damage during both acute and chronic stages of *T. cruzi* infection with strains from different DTUs (Wen et al., 2010, 2014; Dhiman and Garg, 2014). Then, a higher level of parasites was found in the blood, skeletal muscles, and hearts of mice treated with a NADPH oxidase 2 (NOX2) inhibitor during the acute infection with clone Sylvio (DTU-I; Dhiman and Garg, 2011). The opposite was observed in NOX2-deficient mice infected with either Y strain (DTU-II) or clone CL-Brener (DTU-VI), showing a decreased parasite burden in the peritoneal and splenic macrophages (Paiva et al., 2012; Goes et al., 2016). Further comparative studies are deserved considering that it is still unknown whether such differences are related to *T. cruzi* DTU type involved or, to the distinct functions of the ROS enzymes.

In conclusion, the self-sustaining ROS drives astrocyte infection by *T. cruzi*, and involve ROS production from HIV-exposed astrocytes during coinfection, contributing to parasite persistence and CNS pathology. Our original insights shed light on the pathogenesis of the neurologic Chagas disease, offering deeper information that supports the design of new parasite control strategies (**Figure 5**).

DATA AVAILABILITY STATEMENT

The raw data supporting the conclusions of this article will be made available by the authors, without undue reservation.

AUTHOR CONTRIBUTIONS

JU, CC, and ME performed the experiments. All authors analyzed the data. JU, MD, and JQ wrote the article. MD and JQ designed the experiments, revised the article, and obtained research funding. All authors have read and approved the final manuscript.

FUNDING

This work was supported by the Agencia Nacional de Promoción Científica y Tecnológica of Argentina (grant numbers No. PICT-2015-1921 to JQ and No. PICT-2015-0316 to MD).

ACKNOWLEDGMENTS

The authors thank Sergio Mazzini for his assistance and proofreading during the manuscript preparation.

REFERENCES

Aguiar, P. H., Furtado, C., Repoles, B. M., Ribeiro, G. A., Mendes, I. C., Peloso, E. F., et al. (2013). Oxidative stress and DNA lesions: the role of 8-oxoguanine lesions in *Trypanosoma cruzi* cell viability. *PLoS Negl. Trop. Dis.* 7:e2279. doi: 10.1371/journal.pntd.0002279

Allen, G. F., Toth, R., James, J., and Ganley, I. G. (2013). Loss of iron triggers PINK1/parkin-independent mitophagy. *EMBO Rep.* 14, 1127–1135. doi: 10.1038/embor.2013.168

Andersen, H. H., Johnsen, K. B., and Moos, T. (2014). Iron deposits in the chronically inflamed central nervous system and contributes to neurodegeneration. *Cell. Mol. Life Sci.* 71, 1607–1622. doi: 10.1007/s00018-013-1509-8

Arantes, J. M., Pedrosa, M. L., Martins, H. R., Veloso, V. M., de Lana, M., Bahia, M. T., et al. (2007). *Trypanosoma cruzi*: treatment with the iron chelator desferrioxamine reduces parasitemia and mortality in experimentally infected mice. *Exp. Parasitol.* 117, 43–50. doi: 10.1016/j.exppara.2007.03.006

Barat, C., Proust, A., Deshiere, A., Leboeuf, M., Drouin, J., and Tremblay, M. J. (2018). Astrocytes sustain long-term productive HIV-1 infection without establishment of reactivable viral latency. *Glia* 66, 1363–1381. doi: 10.1002/glia.23310

Bayer-Santos, E., Aguilar-Bonavides, C., Rodrigues, S. P., Cordero, E. M., Marques, A. F., Varela-Ramirez, A., et al. (2013). Proteomic analysis of *Trypanosoma cruzi* secretome: characterization of two populations of extracellular vesicles and soluble proteins. *J. Proteome Res.* 12, 883–897. doi: 10.1021/pr300947g

Benedikter, B. J., Weseler, A. R., Wouters, E. F. M., Savelkoul, P. H. M., Rohde, G. G. U., and Stassen, F. R. M. (2018). Redox-dependent thiol modifications: implications for the release of extracellular vesicles. *Cell. Mol. Life Sci.* 75, 2321–2337. doi: 10.1007/s00018-018-2806-z

Bern, C., Kjos, S., Yabsley, M. J., and Montgomery, S. P. (2011). *Trypanosoma cruzi* and Chagas' disease in the United States. *Clin. Microbiol. Rev.* 24, 655–681. doi: 10.1128/CMR.00005-11

Blanchet, F. P., Moris, A., Nikolic, D. S., Lehmann, M., Cardinaud, S., Stalder, R., et al. (2010). Human immunodeficiency virus-1 inhibition of immunoamphisomes in dendritic cells impairs early innate and adaptive immune responses. *Immunity* 32, 654–669. doi: 10.1016/j.immuni.2010.04.011

Bodega, G., Alique, M., Puebla, L., Carracedo, J., and Ramirez, R. M. (2019). Microvesicles: ROS scavengers and ROS producers. *J. Extracell Vesicles* 8:1626654. doi: 10.1080/20013078.2019.1626654

Caeiro, L. D., Alba-Soto, C. D., Rizzi, M., Solana, M. E., Rodriguez, G., Chidichimo, A. M., et al. (2018). The protein family TcTASV-C is a novel *Trypanosoma cruzi* virulence factor secreted in extracellular vesicles by trypomastigotes and highly expressed in bloodstream forms. *PLoS Negl. Trop. Dis.* 12:e0006475. doi: 10.1371/journal.pntd.0006475

Caradonna, K. L., Engel, J. C., Jacobi, D., Lee, C. H., and Burleigh, B. A. (2013). Host metabolism regulates intracellular growth of *Trypanosoma cruzi*. *Cell Host Microbe* 13, 108–117. doi: 10.1016/j.chom.2012.11.011

Cestari, I., Ansa-Addo, E., Deolindo, P., Inal, J. M., and Ramirez, M. I. (2012). *Trypanosoma cruzi* immune evasion mediated by host cell-derived microvesicles. *J. Immunol.* 188, 1942–1952. doi: 10.4049/jimmunol.1102053

Chassagne, J., Verrelle, P., Dionet, C., Clavel, F., Barre-Sinoussi, F., Chermann, J. C., et al. (1986). A monoclonal antibody against LAV gag precursor: use for viral protein analysis and antigenic expression in infected cells. *J. Immunol.* 136, 1442–1445.

Chen, K., Phan, T., Lin, A., Sardo, L., Mele, A. R., Nonnemacher, M. R., et al. (2020). Morphine exposure exacerbates HIV-1 Tat driven changes to neuroinflammatory factors in cultured astrocytes. *PLoS One* 15:e0230563. doi: 10.1371/journal.pone.0230563

Cordova, E., Boschi, A., Ambrosioni, J., Cudos, C., and Corti, M. (2008). Reactivation of Chagas disease with central nervous system involvement in HIV-infected patients in Argentina, 1992-2007. *Int. J. Infect. Dis.* 12, 587–592. doi: 10.1016/j.ijid.2007.12.007

Darden, J. M., Polonis, V. R., Desouza, M. S., Chantakulkij, S., Brown, A. E., Birx, D. L., et al. (2000). A flow cytometric method for measuring neutralization of HIV-1 subtype B and E primary isolates. *Cytometry* 40, 141–150. doi: 10.1002/(SICI)1097-0320(20000601)40:2<141::AID-CYTO8>3.0.CO;2-F

de Souza, W., De Carvalho, T. M., and Barrias, E. S. (2010). Review on *Trypanosoma cruzi*: host cell interaction. *Int. J. Cell Biol.* 2010:295394. doi: 10.1155/2010/295394

Dhiman, M., and Garg, N. J. (2011). NADPH oxidase inhibition ameliorates *Trypanosoma cruzi*-induced myocarditis during Chagas disease. *J. Pathol.* 225, 583–596. doi: 10.1002/path.2975

Dhiman, M., and Garg, N. J. (2014). P47phox−/− mice are compromised in expansion and activation of CD8+ T cells and susceptible to *Trypanosoma cruzi* infection. *PLoS Pathog.* 10:e1004516. doi: 10.1371/journal.ppat.1004516

Dias, P. P., Capila, R. F., Do Couto, N. F., Estrada, D., Gadelha, F. R., Radi, R., et al. (2017). Cardiomyocyte oxidants production may signal to *T. cruzi* intracellular development. *PLoS Negl. Trop. Dis.* 11:e0005852. doi: 10.1371/journal.pntd.0005852

Dick, C. F., de Moura Guimaraes, L., Carvalho-Kelly, L. F., Cortes, A. L., da Silva Lara Morcillo, L., da Silva Sampaio, L., et al. (2020). A ferric reductase of *Trypanosoma cruzi* (TcFR) is involved in iron metabolism in the parasite. *Exp. Parasitol.* 217:107962. doi: 10.1016/j.exppara.2020.107962

Ellis, R. J., Calero, P., and Stockin, M. D. (2009). HIV infection and the central nervous system: a primer. *Neuropsychol. Rev.* 19, 144–151. doi: 10.1007/s11065-009-9094-1

Eugenin, E. A., Basilio, D., Saez, J. C., Orellana, J. A., Raine, C. S., Bukauskas, F., et al. (2012). The role of gap junction channels during physiologic and pathologic conditions of the human central nervous system. *J. Neuroimmune Pharmacol.* 7, 499–518. doi: 10.1007/s11481-012-9352-5

Ferreira, M. S., Nishioka Sde, A., Silvestre, M. T., Borges, A. S., Nunes-Araujo, F. R., and Rocha, A. (1997). Reactivation of Chagas' disease in patients with AIDS: report of three new cases and review of the literature. *Clin. Infect. Dis.* 25, 1397–1400. doi: 10.1086/516130

Goes, G. R., Rocha, P. S., Diniz, A. R., Aguiar, P. H., Machado, C. R., and Vieira, L. Q. (2016). *Trypanosoma cruzi* needs a signal provided by reactive oxygen species to infect macrophages. *PLoS Negl. Trop. Dis.* 10:e0004555. doi: 10.1371/journal.pntd.0004555

Gomez, C. A., and Banaei, N. (2018). *Trypanosoma cruzi* reactivation in the brain. *N. Engl. J. Med.* 378:1824. doi: 10.1056/NEJMicm1703763

Goncalves, M. F., Umezawa, E. S., Katzin, A. M., de Souza, W., Alves, M. J., Zingales, B., et al. (1991). *Trypanosoma cruzi*: shedding of surface antigens as membrane vesicles. *Exp. Parasitol.* 72, 43–53. doi: 10.1016/0014-4894(91)90119-h

Guinazu, N., Carrera-Silva, E. A., Becerra, M. C., Pellegrini, A., Albesa, I., and Gea, S. (2010). Induction of NADPH oxidase activity and reactive oxygen species production by a single *Trypanosoma cruzi* antigen. *Int. J. Parasitol.* 40, 1531–1538. doi: 10.1016/j.ijpara.2010.05.012

Gupta, S., Bhatia, V., Wen, J. J., Wu, Y., Huang, M. H., and Garg, N. J. (2009). *Trypanosoma cruzi* infection disturbs mitochondrial membrane potential and ROS production rate in cardiomyocytes. *Free Radic. Biol. Med.* 47, 1414–1421. doi: 10.1016/j.freeradbiomed.2009.08.008

Gupta, S., Cordeiro, A. T., and Michels, P. A. (2011). Glucose-6-phosphate dehydrogenase is the target for the trypanocidal action of human steroids. *Mol. Biochem. Parasitol.* 176, 112–115. doi: 10.1016/j.molbiopara.2010.12.006

Huang, B. K., and Sikes, H. D. (2014). Quantifying intracellular hydrogen peroxide perturbations in terms of concentration. *Redox Biol.* 2, 955–962. doi: 10.1016/j.redox.2014.08.001

Hugo, M., Martinez, A., Trujillo, M., Estrada, D., Mastrogiovanni, M., Linares, E., et al. (2017). Kinetics, subcellular localization, and contribution to parasite virulence of a *Trypanosoma cruzi* hybrid type a heme peroxidase (TcAPx-CcP). *Proc. Natl. Acad. Sci. U. S. A.* 114, E1326–E1335. doi: 10.1073/pnas.1618611114

Jansen, A. M., Xavier, S., and Roque, A. L. R. (2020). Landmarks of the knowledge and *Trypanosoma cruzi* biology in the wild environment. *Front. Cell. Infect. Microbiol.* 10:10. doi: 10.3389/fcimb.2020.00010

Jou, M. J. (2008). Pathophysiological and pharmacological implications of mitochondria-targeted reactive oxygen species generation in astrocytes. *Adv. Drug Deliv. Rev.* 60, 1512–1526. doi: 10.1016/j.addr.2008.06.004

Kiray, H., Lindsay, S. L., Hosseinzadeh, S., and Barnett, S. C. (2016). The multifaceted role of astrocytes in regulating myelination. *Exp. Neurol.* 283, 541–549. doi: 10.1016/j.expneurol.2016.03.009

Koo, S. J., Szczesny, B., Wan, X., Putluri, N., and Garg, N. J. (2018). Pentose phosphate shunt modulates reactive oxygen species and nitric oxide production controlling *Trypanosoma cruzi* in macrophages. *Front. Immunol.* 9:202. doi: 10.3389/fimmu.2018.00202

Lattes, R., and Lasala, M. B. (2014). Chagas disease in the immunosuppressed patient. *Clin. Microbiol. Infect.* 20, 300–309. doi: 10.1111/1469-0691.12585

Li, G. H., Maric, D., Major, E. O., and Nath, A. (2020). Productive HIV infection in astrocytes can be established via a non-classical mechanism. *AIDS*. doi: 10.1097/QAD.0000000000002512 [Epub ahead of print]

Lovo-Martins, M. I., Malvezi, A. D., Zanluqui, N. G., Lucchetti, B. F. C., Tatakihara, V. L. H., Morking, P. A., et al. (2018). Extracellular vesicles shed by *Trypanosoma cruzi* potentiate infection and elicit lipid body formation and PGE2 production in murine macrophages. *Front. Immunol.* 9:896. doi: 10.3389/fimmu.2018.00896

Manque, P. A., Probst, C. M., Pereira, M. C., Rampazzo, R. C., Ozaki, L. S., Pavoni, D. P., et al. (2011). *Trypanosoma cruzi* infection induces a global host cell response in cardiomyocytes. *Infect. Immun.* 79, 1855–1862. doi: 10.1128/IAI.00643-10

Mehta, S. R., Perez-Santiago, J., Hulgan, T., Day, T. R., Barnholtz-Sloan, J., Gittleman, H., et al. (2017). Cerebrospinal fluid cell-free mitochondrial DNA is associated with HIV replication, iron transport, and mild HIV-associated neurocognitive impairment. *J. Neuroinflammation* 14:72. doi: 10.1186/s12974-017-0848-z

Mesias, A. C., Garg, N. J., and Zago, M. P. (2019). Redox balance keepers and possible cell functions managed by redox homeostasis in *Trypanosoma cruzi*. *Front. Cell. Infect. Microbiol.* 9:435. doi: 10.3389/fcimb.2019.00435

Nathan, C., Nogueira, N., Juangbhanich, C., Ellis, J., and Cohn, Z. (1979). Activation of macrophages in vivo and in vitro, Correlation between hydrogen peroxide release and killing of *Trypanosoma cruzi*. *J. Exp. Med.* 149, 1056–1068. doi: 10.1084/jem.149.5.1056

Ojeda, D. S., Grasso, D., Urquiza, J., Till, A., Vaccaro, M. I., and Quarleri, J. (2018). Cell death is counteracted by Mitophagy in HIV-productively infected astrocytes but is promoted by Inflammasome activation among non-productively infected cells. *Front. Immunol.* 9:2633. doi: 10.3389/fimmu.2018.02633

Pacheco, A. L., Vicentini, G., Matteucci, K. C., Ribeiro, R. R., Weinlich, R., and Bortoluci, K. R. (2019). The impairment in the NLRP3-induced NO secretion renders astrocytes highly permissive to *T. cruzi* replication. *J. Leukoc. Biol.* 106, 201–207. doi: 10.1002/JLB.4AB1118-416RR

Paiva, C. N., Feijo, D. F., Dutra, F. F., Carneiro, V. C., Freitas, G. B., Alves, L. S., et al. (2012). Oxidative stress fuels *Trypanosoma cruzi* infection in mice. *J. Clin. Invest.* 122, 2531–2542. doi: 10.1172/JCI58525

Paiva, C. N., Medei, E., and Bozza, M. T. (2018). ROS and *Trypanosoma cruzi*: fuel to infection, poison to the heart. *PLoS Pathog.* 14:e1006928. doi: 10.1371/journal.ppat.1006928

Perez-Molina, J. A., and Molina, I. (2018). Chagas disease. *Lancet* 391, 82–94. doi: 10.1016/S0140-6736(17)31612-4

Proust, A., Barat, C., Leboeuf, M., Drouin, J., Gagnon, M. T., Vanasse, F., et al. (2020). HIV-1 infection and latency-reversing agents bryostatin-1 and JQ1 disrupt amyloid beta homeostasis in human astrocytes. *Glia* 68, 2212–2227. doi: 10.1002/glia.23833

Providello, M. V., Carneiro, Z. A., Portapilla, G. B., do Vale, G. T., Camargo, R. S., Tirapelli, C. R., et al. (2018). Benefits of ascorbic acid in association with low-dose benznidazole in treatment of Chagas disease. *Antimicrob. Agents Chemother.* 62, e00514–e00518. doi: 10.1128/AAC.00514-18

Ramirez, M. I., Deolindo, P., de Messias-Reason, I. J., Arigi, E. A., Choi, H., Almeida, I. C., et al. (2017). Dynamic flux of microvesicles modulate parasite-host cell interaction of *Trypanosoma cruzi* in eukaryotic cells. *Cell. Microbiol.* 19, 1–15. doi: 10.1111/cmi.12672

Retana Moreira, L., Rodriguez Serrano, F., and Osuna, A. (2019). Extracellular vesicles of *Trypanosoma cruzi* tissue-culture cell-derived trypomastigotes: induction of physiological changes in non-parasitized culture cells. *PLoS Negl. Trop. Dis.* 13:e0007163. doi: 10.1371/journal.pntd.0007163

Schijman, A. G., Bisio, M., Orellana, L., Sued, M., Duffy, T., Mejia Jaramillo, A. M., et al. (2011). International study to evaluate PCR methods for detection of *Trypanosoma cruzi* DNA in blood samples from Chagas disease patients. *PLoS Negl. Trop. Dis.* 5:e931. doi: 10.1371/journal.pntd.0000931

Sharma, V., Mishra, M., Ghosh, S., Tewari, R., Basu, A., Seth, P., et al. (2007). Modulation of interleukin-1beta mediated inflammatory response in human astrocytes by flavonoids: implications in neuroprotection. *Brain Res. Bull.* 73, 55–63. doi: 10.1016/j.brainresbull.2007.01.016

Sheng, W. S., Hu, S., Feng, A., and Rock, R. B. (2013). Reactive oxygen species from human astrocytes induced functional impairment and oxidative damage. *Neurochem. Res.* 38, 2148–2159. doi: 10.1007/s11064-013-1123-z

Silva, R. R., Mariante, R. M., Silva, A. A., Dos Santos, A. L., Roffe, E., Santiago, H., et al. (2015). Interferon-gamma promotes infection of astrocytes by *Trypanosoma cruzi*. *PLoS One* 10:e0118600. doi: 10.1371/journal.pone.0118600

Silva, A. A., Silva, R. R., Gibaldi, D., Mariante, R. M., Dos Santos, J. B., Pereira, I. R., et al. (2017). Priming astrocytes with TNF enhances their susceptibility to *Trypanosoma cruzi* infection and creates a self-sustaining inflammatory milieu. *J. Neuroinflammation* 14:182. doi: 10.1186/s12974-017-0952-0

Sofroniew, M. V., and Vinters, H. V. (2010). Astrocytes: biology and pathology. *Acta Neuropathol.* 119, 7–35. doi: 10.1007/s00401-009-0619-8

Song, H. Y., Ryu, J., Ju, S. M., Park, L. J., Lee, J. A., Choi, S. Y., et al. (2007). Extracellular HIV-1 Tat enhances monocyte adhesion by up-regulation of ICAM-1 and VCAM-1 gene expression via ROS-dependent NF-kappaB activation in astrocytes. *Exp. Mol. Med.* 39, 27–37. doi: 10.1038/emm.2007.4

Stempin, C. C., Garrido, V. V., Dulgerian, L. R., and Cerban, F. M. (2008). Cruzipain and SP600125 induce p38 activation, alter NO/arginase balance and favor the survival of *Trypanosoma cruzi* in macrophages. *Acta Trop.* 106, 119–127. doi: 10.1016/j.actatropica.2008.02.004

Trocoli Torrecilhas, A. C., Tonelli, R. R., Pavanelli, W. R., da Silva, J. S., Schumacher, R. I., de Souza, W., et al. (2009). *Trypanosoma cruzi*: parasite shed vesicles increase heart parasitism and generate an intense inflammatory response. *Microbes Infect.* 11, 29–39. doi: 10.1016/j.micinf.2008.10.003

Urquiza, J. M., Burgos, J. M., Ojeda, D. S., Pascuale, C. A., Leguizamon, M. S., and Quarleri, J. F. (2017). Astrocyte apoptosis and HIV replication are modulated in host cells coinfected with *Trypanosoma cruzi*. *Front. Cell. Infect. Microbiol.* 7:345. doi: 10.3389/fcimb.2017.00345

Valcour, V., Sithinamsuwan, P., Letendre, S., and Ances, B. (2011). Pathogenesis of HIV in the central nervous system. *Curr. HIV/AIDS Rep.* 8, 54–61. doi: 10.1007/s11904-010-0070-4

Vargas-Zambrano, J. C., Lasso, P., Cuellar, A., Puerta, C. J., and Gonzalez, J. M. (2013). A human astrocytoma cell line is highly susceptible to infection with *Trypanosoma cruzi*. *Mem. Inst. Oswaldo Cruz* 108, 212–219. doi: 10.1590/0074-0276108022013014

Walker, D. M., Oghumu, S., Gupta, G., McGwire, B. S., Drew, M. E., and Satoskar, A. R. (2014). Mechanisms of cellular invasion by intracellular parasites. *Cell. Mol. Life Sci.* 71, 1245–1263. doi: 10.1007/s00018-013-1491-1

Weinkauf, C., Salvador, R., and Pereiraperrin, M. (2011). Neurotrophin receptor TrkC is an entry receptor for *Trypanosoma cruzi* in neural, glial, and epithelial cells. *Infect. Immun.* 79, 4081–4087. doi: 10.1128/IAI.05403-11

Wen, J. J., Gupta, S., Guan, Z., Dhiman, M., Condon, D., Lui, C., et al. (2010). Phenyl-alpha-tert-butyl-nitrone and benzonidazole treatment controlled the mitochondrial oxidative stress and evolution of cardiomyopathy in chronic chagasic rats. *J. Am. Coll. Cardiol.* 55, 2499–2508. doi: 10.1016/j.jacc.2010.02.030

Wen, J. J., Nagajyothi, F., Machado, F. S., Weiss, L. M., Scherer, P. E., Tanowitz, H. B., et al. (2014). Markers of oxidative stress in adipose tissue during *Trypanosoma cruzi* infection. *Parasitol. Res.* 113, 3159–3165. doi: 10.1007/s00436-014-3977-7

Williams, R., Yao, H., Peng, F., Yang, Y., Bethel-Brown, C., and Buch, S. (2010). Cooperative induction of CXCL10 involves NADPH oxidase: implications for HIV dementia. *Glia* 58, 611–621. doi: 10.1002/glia.20949

Conflict of Interest: The authors declare that the research was conducted in the absence of any commercial or financial relationships that could be construed as a potential conflict of interest.

frontiers in Immunology

ORIGINAL RESEARCH
published: 23 October 2020
doi: 10.3389/fimmu.2020.552698

Genome-Wide Analysis of the Malaria Parasite *Plasmodium falciparum* Isolates From Togo Reveals Selective Signals in Immune Selection-Related Antigen Genes

Kokouvi Kassegne[1], Komi Komi Koukoura[2], Hai-Mo Shen[3,4,5], Shen-Bo Chen[3,4,5], Hai-Tian Fu[1], Yong-Quan Chen[1,6], Xiao-Nong Zhou[3,4,5], Jun-Hu Chen[3,4,5]* and Yang Cheng[1]**

[1] Laboratory of Pathogen Infection and Immunity, Department of Public Health and Preventive Medicine, Wuxi School of Medicine, Jiangnan University, Wuxi, China, [2] Laboratoire des Sciences Biomédicales, Alimentaires et Santé Environnementale, Département des Analyses Biomédicales, Ecole Supérieure des Techniques Biologiques et Alimentaires, Université de Lomé, Lomé, Togo, [3] National Institute of Parasitic Diseases, Chinese Centre for Disease Control and Prevention, Chinese Centre for Tropical Diseases Research, WHO Collaborating Centre for Tropical Diseases, National Centre for International Research on Tropical Diseases, Ministry of Science and Technology, Key Laboratory of Parasite and Vector Biology, Ministry of Health, Shanghai, China, [4] National Institute of Parasitic Diseases, Chinese Centre for Disease Control and Prevention—Shenzhen Centre for Disease Control and Prevention Joint Laboratory for Imported Tropical Disease Control, Shanghai, China, [5] The School of Global Health, Chinese Centre for Tropical Diseases Research, Shanghai JiaoTong University School of Medicine, Shanghai, China, [6] School of Food Science and Technology, State Key Laboratory of Food Science and Technology, Jiangnan University, Wuxi, China

OPEN ACCESS

Edited by:
Antonio Barragan, Stockholm University, Sweden

Reviewed by:
Akira Kaneko, Karolinska Institutet (KI), Sweden
Yaming Cao, China Medical University, China
Moses Okpeku, University of KwaZulu-Natal, South Africa

***Correspondence:**
Kokouvi Kassegne
ephremk@hotmail.fr
Jun-Hu Chen
chenjh@nipd.chinacdc.cn
Yang Cheng
woerseng@126.com

Specialty section:
This article was submitted to Microbial Immunology, a section of the journal Frontiers in Immunology

Received: *16 April 2020*
Accepted: *02 September 2020*
Published: *23 October 2020*

Citation:
Kassegne K, Komi Koukoura K, Shen H-M, Chen S-B, Fu H-T, Chen Y-Q, Zhou X-N, Chen J-H and Cheng Y (2020) Genome-Wide Analysis of the Malaria Parasite Plasmodium falciparum Isolates From Togo Reveals Selective Signals in Immune Selection-Related Antigen Genes. Front. Immunol. 11:552698. doi: 10.3389/fimmu.2020.552698

Malaria is a public health concern worldwide, and Togo has proven to be no exception. Effective approaches to provide information on biological insights for disease elimination are therefore a research priority. Local selection on malaria pathogens is due to multiple factors including host immunity. We undertook genome-wide analysis of sequence variation on a sample of 10 *Plasmodium falciparum* (Pf) clinical isolates from Togo to identify local-specific signals of selection. Paired-end short-read sequences were mapped and aligned onto > 95% of the 3D7 Pf reference genome sequence in high fold coverage. Data on 266 963 single nucleotide polymorphisms were obtained, with average nucleotide diversity $\pi = 1.79 \times 10^{-3}$. Both principal component and neighbor-joining tree analyses showed that the Togo parasites clustered according to their geographic (Africa) origin. In addition, the average genome-wide diversity of Pf from Togo was much higher than that from other African samples. Tajima's *D* value of the Togo isolates was −0.56, suggesting evidence of directional selection and/or recent population expansion. Against this background, within-population analyses identifying loci of balancing and recent positive selections evidenced that host immunity has been the major selective agent. Importantly, 87 and 296 parasite antigen genes with Tajima's *D* values > 1 and in the top 1% haplotype scores, respectively, include a significant representation of membrane proteins at the merozoite stage that invaded red blood cells (RBCs) and parasitized RBCs surface proteins that play roles in immunoevasion, adhesion, or

rosetting. This is consistent with expectations that elevated signals of selection due to allele-specific acquired immunity are likely to operate on antigenic targets. Collectively, our data suggest a recent expansion of Pf population in Togo and evidence strong host immune selection on membrane/surface antigens reflected in signals of balancing/positive selection of important gene loci. Findings from this study provide a fundamental basis to engage studies for effective malaria control in Togo.

Keywords: *Plasmodium falciparum*, genomes, balancing selection, directional selection, immunity, Togo

INTRODUCTION

Malaria clinical presentation ensues when *Plasmodium* parasites invade and destroy red blood cells (RBCs). Fever and chills occur at the time of rupture of infected RBCs (iRBCs) containing merozoites that are freed to invade uninfected RBCs (1, 2). Failure to receive prompt treatment may lead to dyserythropoietic anaemia or severe malaria. *P. falciparum* (Pf) is the most dangerous malaria parasite because of the high level of mortality with which it is associated, its widespread resistance to antimalarial medicines, and its dominance in the world's most malarious continent, Africa (3–5).

In Togo, malaria transmission occurs most of each year. Although decades of control efforts have reduced the disease burden, the entire country's population is still at risk of falciparum malaria infection (6). In addition, challenges in parasite control would have made the infection a public health concern and may aggravate the difficulty of treatment. Clinical spectrum of malaria in Togo usually ranges from asymptomatic carriage of malaria parasites to a febrile disease that may evolve into a severe, life-threatening illness, making the infection a major cause of morbidity and mortality, especially in children (7, 8). Antimalarial drug resistance (e.g., parasite resistance to chloroquine or pyrimethamine) has been experienced across Africa. In early investigations in Togo, clinical and parasitological therapeutic failure tests of artemether-lumefarine (AL) and artesunate-amodiaquine (ASAQ) for 3% and 3.8%, respectively, have been observed (6), and they drew the entire country's attention to an eventual resistance to artemisinins. However, in a recent study, therapeutic efficacy of **AL** and ASAQ was shown without delay in the clearance of mutant parasites (9). Pf surface-exposed proteins are targets of host immune responses, and repeated exposures to the parasite in endemic areas induce a slow and gradual development of acquired immunity to clinical malaria, which is usually evidenced as a decline in the prevalence of clinical episodes (10, 11). Hence, acquisition of information on both immunity-related antigens and drug resistance genes for effective interventions to sustain and drive forward the struggle against malaria parasite in Togo is therefore a research priority.

Complete sequencing of the Pf genome has boosted post-genomic studies of malaria (12). It provides fundamental knowledge for better understanding of the cellular and molecular mechanisms of infection and immunity to develop new control methods, including new drugs and vaccines, improved diagnostics, and effective vector control techniques. With rapid development of sequencing technologies (13), hundreds of falciparum isolate genomic data worldwide had been investigated and shared by large collaborative initiatives such as the MalariaGEN Pf Community Project and the Pf3k Consortium. Application of the genomic approaches in the analysis of whole genome variations–generated high-density single nucleotide polymorphisms (SNPs) of the parasite has mostly focused on vaccine antigen genes and drug-resistant genes. However, to date, nothing is known on genomes of malaria isolates in Togo, and this could limit the joint research with those in other endemic areas in the sub-Saharan Africa region.

In this study, we performed the first whole-genome sequencing (WGS) of Pf clinical isolates from Togo. With the aim to contribute to accelerating the pursuit of effective malaria control, we applied genomic approaches in the analysis of whole genome variations–generated high-density SNPs to provide biological insights on target genes, especially those under host immune selection.

MATERIALS AND METHODS

Sampling Sites and Ethics Statement

Malaria transmission in Togo occurs for most of each year with seasonal outbreaks (9), and populations are served by health facilities experienced in the management of malaria cases. For this study, clinical samples were collected at health centres in urban areas of Agou-Gadzépé (7°28'01" N; 1°55'01" E) and Atakpamé (7°52'87" N; 1° 13'05" E) in Agou and Ogou prefectures, respectively, in the Plateaux Region (**Figure 1**) in 2017 and 2018. Samples collection was made under a study protocol approved by the Togolese Ministry of Health's Bioethics Committee following institutional ethical guidelines by the ethics committee at National Institute of Parasitic Diseases, Chinese Centre for Disease Control and Prevention. Informed consent was obtained from all subjects prior to sample collection.

Genomic Data

For our analyses, genome and annotation data of Pf 3D7 strain (the most complete whole genome standard reference) from PlasmoDB database (http://plasmodb.org/plasmo/) (14) were downloaded. In addition, raw sequences from 62 genome data of falciparum clinical isolates from Africa [n = 32 (Congo DR, Gambia, Ghana, Guinea, Malawi, Mali, Nigeria, and Senegal)] and Asia [n = 30 (Bangladesh, Cambodia, China-Myanmar

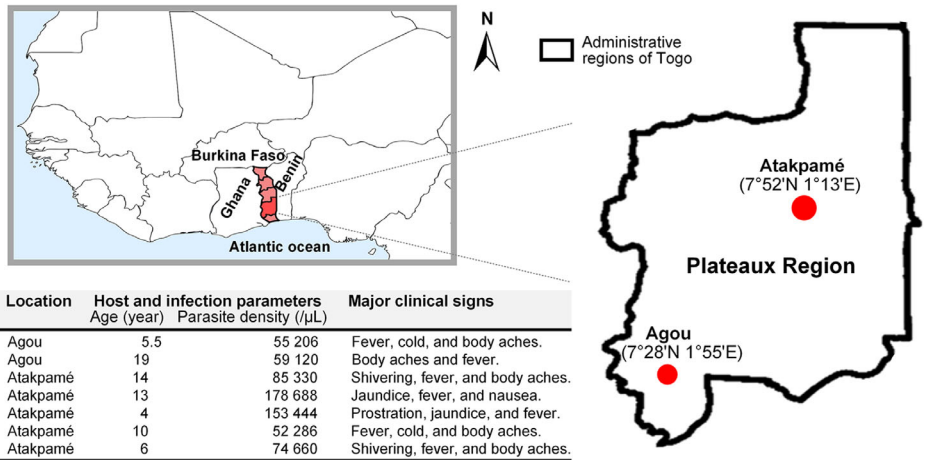

Sample	Location	Host and infection parameters		Major clinical signs
		Age (year)	Parasite density (/µL)	
Ag-022	Agou	5.5	55 206	Fever, cold, and body aches.
Ag-087	Agou	19	59 120	Body aches and fever.
At-005	Atakpamé	14	85 330	Shivering, fever, and body aches.
At-010	Atakpamé	13	178 688	Jaundice, fever, and nausea.
At-017	Atakpamé	4	153 444	Prostration, jaundice, and fever.
At-042	Atakpamé	10	52 286	Fever, cold, and body aches.
At-199	Atakpamé	6	74 660	Shivering, fever, and body aches.

FIGURE 1 | Sampling location in Togo and information about clinical samples used in this study.

Border (CMB), Laos, Myanmar, Thailand, and Viet Nam)] were also referenced (15–17).

Sampling of Malaria Parasites and Extraction of Genomic DNA

Malaria-naturally exposed subjects who received parasitological diagnosis using Giemsa-stained thick blood smear microscopy under 1000x magnification were referred to our study. Whole blood specimens from subjects who were diagnosed with the presence of Pf asexual parasitaemia (parasites counted per 200 leukocytes and parasite density calculated as the number of parasites per microliter by assuming a fixed leukocyte count of 8000 cells/µL of blood) were sampled as dried blood spots (DBSs) on Whatman FTA cards (GE Healthcare) as recommended by the manufacturer. Genomic DNA was extracted [using the QIAGEN DNeasy Blood & Tissue Kit (Qiagen), according to the manufacturer's instructions] from DBSs and monospecies infection was confirmed by polymerase chain reaction (PCR). Ten clinical samples with high parasitaemia (parasite density > 50000/µL), and qualitatively and quantitatively good enough, were selected to ensure the integrity of sequencing.

Whole-Genome Sequencing

WGS of Pf clinical isolates from Togo was performed by OE Biotech (Shanghai). Extracted genomic DNA was sheared into 150 bp fragments using a Covaris instrument. The fragmented DNA molecules were used to construct Illumina-sequencing libraries with TruSeq DNA LT Sample Prep Kit (Illumina). All libraries were sequenced on the Illumina HiSeq X10 platform according to the manufacturer's protocol (18), using the direct sequencing approach, as described previously (17). All reads were filtered by removing the adapter sequences and low quality sequences were removed with Trimmomatic-3.0. (19). The sequencing reads have been submitted to the Short Read Archive of the National Centre for Biotechnology Information.

Identification of SNPs and Population Structure

All sequenced reads from the 10 samples were mapped to the Pf 3D7 genome using Burrows-Wheeler Aligner and Sequence Alignment/Map (SAMtools-1.3) (20). Samples with average coverage < 95% sequences mapping over 3D7 reference genome were removed. For high-quality SNP calling, sequencing reads were genotyped using an in-house pipeline based on GATK best practices and SnpEff workflows (21), with Pf3K known-sites (15).

Principal component analysis (PCA) and neighbor-joining were performed to investigate major geographical division of population structure. PCA and a neighbor-joining tree of all samples were undertaken via SPSS-Ver25 and Mega-Ver6.0 programs, respectively, to compare Pf SNPs from Togo isolates with those from the 62 isolates collected worldwide (15–17).

Tests for Signatures of Selection

For SNPs in all populations, nucleotide diversity (π) was estimated for the whole genome mutation rate in 4 kb sliding window and 2 kb step across each chromosome in Arlequin-Ver3.5 (22). To distinguish between genes evolving neutrally and under selective pressures, or genetic hitchhiking, Tajima's *D* value (TD) for each sliding window and the corresponding gene was also calculated.

In addition, long-range haplotype diversity approach integrated haplotype score (iHS) was employed to identify genes under recent positive selection. iHS compares integrated extended-haplotype homozygosity (EHH) values between alleles at a given SNP (23). iHS computation was based on the Togo clinical isolates by tracking the decay of haplotype homozygosity for both the ancestral and derived haplotypes extending from

every SNP site (24). For this test, we restricted the analyses to SNPs with inferred ancestral states with minor allele frequencies equal to or higher than 5% (25). iHS scores were estimated using Selscan-Ver1.10a (26).

To assess whether genes associated with putative functions were enriched among the group of genes with high Tajima's *D* values (> 1.0) or high |iHS| (top 1% score), gene ontology (GO) term analysis was conducted. Genes with a TD > 1.0 were classed as genes of potential interest for GO analysis. Analysis was performed using GO Enrichment tool of PlasmoDB (http://plasmodb.org/plasmo/, PlasmoDB Ver-46). The adjusted *P* values were also generated from Fisher's exact test, and the statistical significance was set for $P < 0.05$.

RESULTS

Genetic Diversity of *Falciparum* Isolates From Togo

We used a direct sequencing approach that requires only high parasitaemia for malaria parasites without leukocytes filtration (17) to sequence clinical isolates of Pf genomes from Togo. Among the 10 clinical samples that were sequenced, results of seven were good enough and provided enough coverage (> 95% sequences mapping over the 3D7 reference genome) (**Table 1**). The remaining three samples mapped onto only 58.89%, 56.43%, and 46.83% (unshown data) and failed for further analysis. In this study, the Togo isolates generated between 55 and 176 M paired-end reads of 150 bp from each of the samples, globally. All sequencing reads have been deposited to the National Centre for Biotechnology Information (NCBI) Short Read Archive (BioProject Accession Number: PRJNA616298). A variable proportion of reads (3.8–14.2%) from all the isolates were mapped to the reference and aligned onto at least 95% of the reference 3D7 strain genome in high fold coverage (7.2–33.9x).

For analysis of polymorphism, a total of 266963 SNPs common loci were available for analysis after quality filtering (**Table 1**). The list of the SNPs for all the isolates is provided in **Supplementary Table 1**. Of the 266963 SNPs, excluding the low-frequency SNPs (103497 SNPs with minor allele frequency < 5%), a total of 163466 SNPs across the seven isolates were identified and could be mapped to coding sequences. In addition, SNPs were identified across 4614 genes on 14 chromosomes in the samples and 931 genes had more than five SNPs (**Figure 2A**). These genes were considered informative for comparisons of polymorphic nucleotide sites.

Comparison of Genetic Diversity of the Isolates Among Different Endemic Regions

Overall genome-wide π of Pf clinical isolates from Togo were estimated at 1.79×10^{-3}. However, genetic diversity was lower in intronic regions but higher in exonic and intergenic regions (**Supplementary Table 1**). **Supplementary Figure 1** shows the π map of the isolates across 14 chromosomes. Interestingly, we observed that Togo samples have genes with higher SNPs, suggesting a greater genetic diversity than that reported from other African samples ($\pi = 1.03 \times 10^{-3}$) (27), but lower than that of isolates from CMB ($\pi = 2.87 \times 10^{-2}$) (17).

We then performed PCA and neighbor-joining analyses of all strains to assess major geographical difference. As part of Africa isolates, the Togo isolates illustrated a higher discrepancy than the 3D7 strain genome. Neighbor-joining displayed a tree with two distinct branches separating two major clades that correspond to the Asia and Africa geographical groups of samples (**Figure 2B**). There was evidence of clear distinction of the isolates from the two regions, and African isolates displayed sub-clusters to form two (or three) monophyletic clades. Furthermore, we found that the outcome from PCA was similar to that of the neighbor-joining analysis. The major axis of differentiation (F1) of the PCA distinguished clearly two major Asia and Africa groups of isolates, which is in accordance with their geographical origins (**Figure 2C**). Similar observation was noted in recent studies on Pf isolates from CMB (17, 28). In addition, among the Africa samples, Togo samples exhibited greater genetic diversity than has been reported from other African regions. The second and third principal components (F2 and F3) defined a distinct South-Asian cluster and distinguished the African samples better according to their locations, where Togo samples were well differentiated from other African samples (**Figure 2D**). Furthermore, Togo isolates were widely separated in our PCA result, suggesting high diversity of Pf from Togo.

Signatures of Selection in the Isolates From Togo

We investigated signatures of selection of the parasite in this sub-Saharan Africa region. TD of the Togo isolates was −0.56 across the entire genome (**Figure 3A**), indicating a population history

TABLE 1 | Sequencing and mapping summary of Pf genome of seven clinical isolates from Togo.

Samples	Ag-022	Ag-087	At-005	At-010	At-017	At-042	At-199
Sequencing and mapping							
Number of clean reads	95 290 916	56 567 466	55 109 050	135 016 594	132 741 868	141 629 208	176 447 420
Mapped on Pf	3 796 286	3 414 970	7 700 867	6 078 064	5 761 033	6 713 431	6 615 316
Mapped (%)	4.0	6.1	14.2	4.5	4.4	4.8	3.8
Coverage							
Coverage fold	7.2	10.7	33.9	13.1	13.4	13.5	11.8
Genome covered >1 (%)	95.3	97.7	98.7	97.6	98.3	97.8	98.1
Variation							
Filtered SNP	26 091	35 139	57 129	37 065	37 828	35 653	38 058

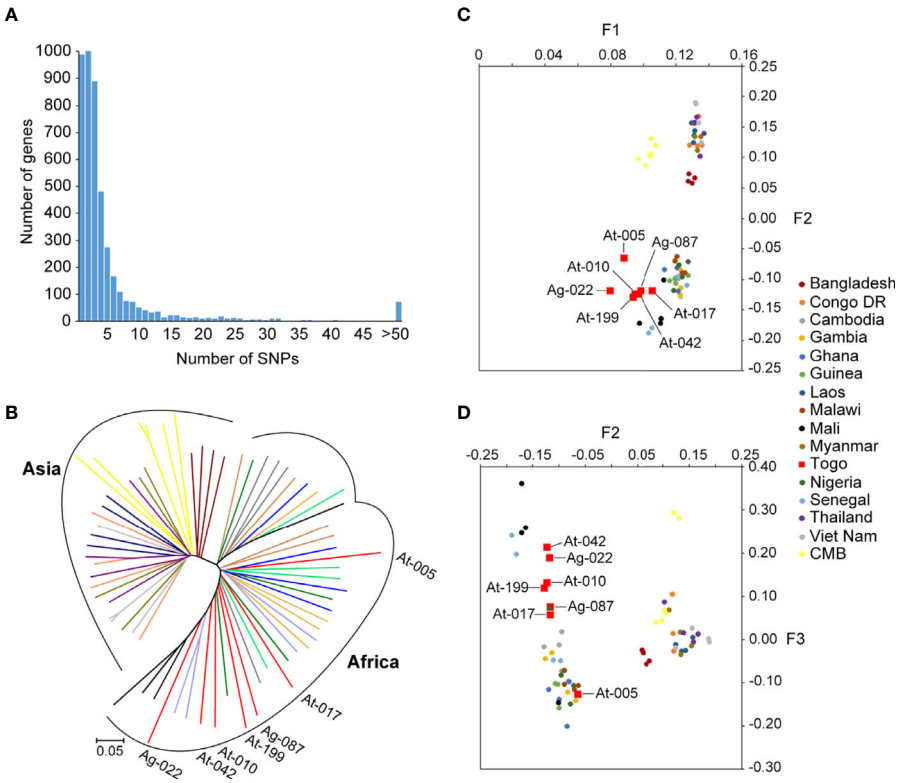

FIGURE 2 | SNPs frequency distribution in samples and genomic relationships among Pf reference strains and Togo isolates. **(A)** Distribution numbers of genes with each given number of SNPs in the population sample of seven Pf clinical isolates from Togo. From the 4614 genes analyzed in total from 14 chromosomes, 20.2% (931/4614) had more than five SNPs. **(B)** Neighbor-joining tree of Pf constructed from the SNPs occurring in at least half of the samples. Lineages are colored according to geographic origin. Branch lengths indicate considerable diversity in Pf strains. Annotated branches represent the Togo isolates. **(C, D)** Principal component analysis based on common SNP loci in Togo clinical isolates and reference strains. Colors correspond to the geographic origin of the samples, of which the Togo isolates are highlighted in red. **(C)** The major fact (F1) of differentiation of the PCA identified clearly the two groups of isolates that clustered according to their geographic origin. **(D)** The second and third facts (F2 and F3) defined a distinct South-Asia cluster and distinguished the African samples better according to their locations.

of purifying selection and/or recent population expansion. To study allele frequency distributions for individual genes, with the gene transfer format file containing information about gene structure, we annotated genes and then calculated TD for the individual genes. Of the 5601 genes analyzed, the TD obtained were mostly negative (3759 genes, average TD = -0.95). Such predominantly negative values are consistent with previous analyses indicating a historical population expansion of Pf in Africa (29), and it suggests that these genes were under selective sweep (directional selection) (17, 28, 30). We found 931 genes that each had at least five SNPs. A list of the top 250 lowest values for genes with at least one SNP (n = 4614) is provided in **Supplementary Table 2**. Against this background, 746/4614 genes (16.2%) had positive TD values (**Supplementary Table 3**), of which 140 genes had values > 1 (87 genes coding proteins with known functions), suggesting signals of balancing selection for these genes (28, 31).

Mean pairwise divergence was higher in a significant representation of genes that encode membrane proteins expressed at the merozoite stage that invades RBCs (for example, merozoite surface proteins, MSPs; serine repeat antigens, SERAs; rhomboid proteases, ROMs; duffy binding-like merozoite surface proteins, MSPDBLs; rhoptry associated adhesins, RA) (32, 33), and parasitized RBC surface proteins that play roles in disease severity—immune evasion, rosetting, or cytoadherence to microvasculature (repetitive interspersed family of polypeptides, RIFINs; erythrocyte membrane protein 1, PfEMP1; and subtelomeric variant open reading frames, STEVORs) (34–37). Importantly, there was evidence of balancing selection on particular genes including antigen genes related to RBC invasion, including those with solid balancing selection (reflected in high TD) [*sera5* (TD = 1.42); apical asparagine-rich protein, *aarp* (TD = 1.34); ferlin-like protein, *flp* (TD=1.29); *msp3* (TD = 1.28); and *msp7* (TD = 1.08)] (**Table 2**) and those with TD < 1 [phospholipase, *pl*; erythrocyte binding antigen-175, *eba175*; reticulocyte binding protein 2 homologue a, *rh2a*; *ra*; 6-cysteine protein, *pf41*; apical membrane antigen 1, *ama1*; *sera4*; glutamate-rich protein, *glurp*; merozoite TRAP-like protein, *mtrap*; *rom4*; membrane associated erythrocyte binding-like protein, *maebel*; rhoptry neck protein 2, *ron2*; subtilisin-like

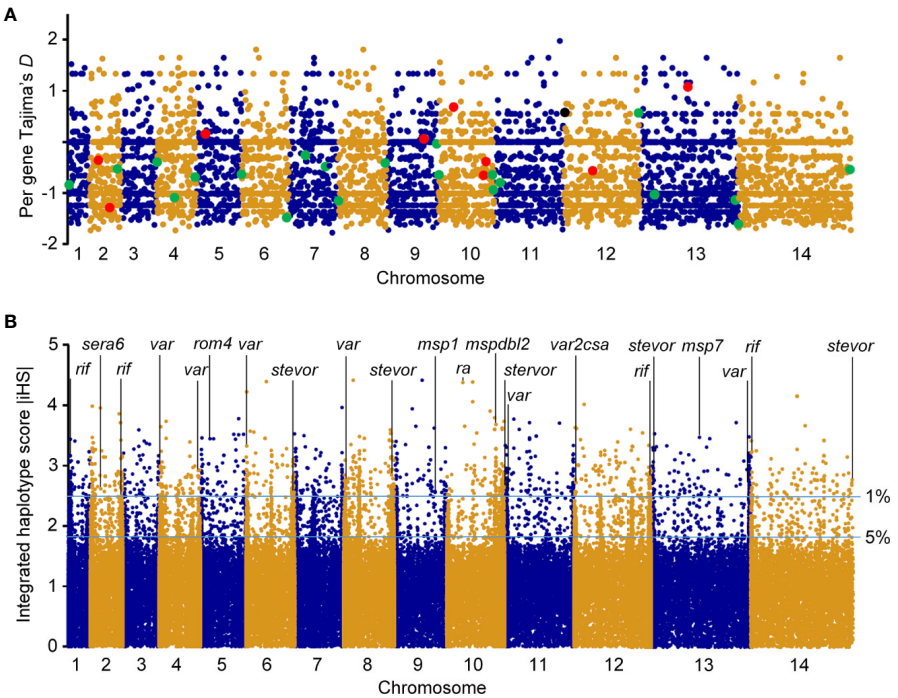

FIGURE 3 | Genomic map of Pf isolates from Togo. Paired-end short-read sequencing produced high-quality data for a population sample of seven falciparum clinical isolates from Togo, with genome-wide average mapping depth to the 3D7 reference strain genome. **(A)** Tajima's *D* values map of falciparum clinical isolates from Togo. Values for all gene SNPs were plotted and arranged according to their chromosomal positions (blue and gold colors indicate consecutive chromosomes numbered from the smallest upwards). TD for RBC invasion-related antigen genes are shown in enlarged red dyes and those for genes implicated in parasite-mediate immunoevasion, cytoadhesion, resetting/sequestration, or deformability of RBC/rigidity, are indicated in enlarged green dyes. Pregnancy malaria-related *var2csa* is also highlighted (black dye). **(B)** Top |iHS| hits in Pf isolates from Togo with SNPs minor allele frequency ⩾ 5%. *x* axis indicates individual chromosomes in alternating colors of their SNPs; *y* axis is the value of |iHS|. Plot of genome-wide |iHS| scores shows regions of the genome that have windows of elevated values with high scoring (top 1% of |iHS| values) for important gene loci highlighted, consistent with the operation of recent positive directional selection. The horizontal lines represent values of 2.49223 and 1.8157 used to define windows containing SNPs with overlapping regions of EHH.

protease 1, *sub1*; and *msp1*] (**Supplementary Table 3**). Most of these antigen genes were reported previously for the balancing selection (28, 31, 38, 39) and were significantly enriched by GO analysis ($P < 0.0001$). Although antigen genes associated with parasite-mediated immune evasion, adhesion, or rosetting were found in the positive TD list [13 *rifs* (PF3D7_1000600, PF3D7_1254800, PF3D7_0713000, PF3D7_0632100, PF3D7_1040900, PF3D7_1300400, PF3D7_1254700, PF3D7_1150300, PF3D7_0808800, PF3D7_0114700, PF3D7_1101300, PF3D7_1100300, and PF3D7_0401300), three *vars* (PF3D7_0302300, PF3D7_1200600, and PF3D7_0601400) and one *stevor* (PF3D7_1479900)] (**Supplementary Table 3**) and were all highly significantly enriched by GO analysis ($P < 0.0001$), only the *var* PF3D7_0302300 is likely under strong balancing selection (TD = 1.33) (**Table 2**). Interestingly, PF3D7_1200600 (TD = 0.57) is the Pf *var* gene (*var2csa*) implicated in pregnancy malaria (34). GO analysis showed significant drug resistance enrichment for amino acid transporter *aat1* and bifunctional farnesyl/geranylgeranyl diphosphate synthase *fpps*/*ggpps*, which got TD > 1.

Antigenic variation within Pf surface-exposed putative proteins is a target of host immune selection. Therefore, we applied iHS for all SNPs from Pf isolate genomes to investigate genome-wide evidence for positive selection (**Figure 3B**). We identified all 14 chromosomal regions with loci above the top 5% value (|iHS| > 1.8157) of the randomly expected distribution including 646 genes (**Supplementary Table 4**). Using |iHS| = 2.49223 (top 1% expected distribution) as a strong hits threshold, we identified 306 genes under significant positive selection (38, 40), of which 296 had at least five SNPs (**Supplementary Table 5**).

This analysis identified the selection signals for important genes with loci above the top 1% iHS score (|iHS| > 2.49223), including 10 RBC invasion-related antigen genes [*msp1*, *msp4*, *msp7*, *msp9*, *ron2*, *mspdbl1*, *mspdbl2*, *ra*, *sera6*, and *rom4*] (**Supplementary Table 6**). From these, *msp1*, *msp7*, *mspdbl1*, *mspdbl2*, *ra*, and *sera6* were highly significantly enriched by GO analysis ($P < 0.0001$) (**Table 3**) and have been reported previously as promising subunit candidates for a malaria multicomponent vaccine (32, 39, 41). Similarly, 134 genes implicated in roles for immune evasion, RBCs aggregation, or cytoadherence to microvasculature (73 *rifs*, 50 *vars*, and 12 *stevors*) were identified (**Supplementary Table 7**), of which six *rifs*, seven *vars*, and eight *stevors* (**Table 3**) were reported

TABLE 2 | Ten Pf genes with Tajima's *D* scores > 1 enriched by GO analysis in Togo isolates.

PlasmoDB accession number	Product description	Genomic location	Tajima's *D*
PF3D7_1128400	bifunctional farnesyl/geranylgeranyl diphosphate synthase, FPPS/GGPPS	Chr11: 1104216 - 1106505 (-)	1.64955
PF3D7_0207600	serine repeat antigen 5, SERA5	Chr02: 303593 - 307027 (-)	1.42303
PF3D7_0423400	apical asparagine-rich protein, AARP	Chr04: 1055665 - 1056318 (+)	1.34164
PF3D7_0302300	erythrocyte membrane protein 1 (PfEMP1), pseudogene	Chr03: 125992 - 130,235(-)	1.32775
PF3D7_0806300	ferlin-like protein, putative, FL	Chr08: 337902 - 343,254 (-)	1.28799
PF3D7_1035400	merozoite surface protein 3, MSP3	Chr10: 1404195 - 1405259 (+)	1.27765
PF3D7_0201600	PHISTb* domain-containing RESA-like protein 1, PHISTb RLP1	Chr02: 77251 - 78808 (-)	1.25357
PF3D7_0629500	amino acid transporter, AAT1	Chr06: 1213948 - 1216005 (-)	1.16843
PF3D7_1335100	merozoite surface protein 7, MSP7	Chr13: 1419086 - 1420141 (-)	1.07565
PF3D7_0629300	phospholipase, putative, PL	Chr13: 1205190 - 1207781 (+)	1.00902

**Plasmodium helical interspersed subtelomeric b.*

TABLE 3 | List of important Pf top 1% |iHS|-related genes enriched by GO analysis in Togo isolates.

PlasmoDB accession number	Product description	Genomic location	Core SNP position	|iHS|	TD
RBC invasion					
PF3D7_0207500	SERA6	Chr02: 298897 - 302564 (-)	302491	2.61685	-1.26953
PF3D7_0930300	MSP1	Chr09: 1201812 - 1206974 (+)	1202025	2.56848	0.01
PF3D7_1012200	RA	Chr10: 470979 - 471933 (+)	471579	4.37817	0.64916
PF3D7_1035700	MSPDBL1	Chr10: 1413200 - 1415293 (+)	1414316	2.90723	-0.38036
PF3D7_1036300	MSPDBL2	Chr10: 1432498 - 1434786 (+)	1434091	3.68371	-0.67735
PF3D7_1335100	MSP7	Chr13: 1419086 - 1420141 (-)	1419448	3.47128	1.07565
Disease severity*					
PF3D7_0100200	RIFIN	Chr01: 38982 - 40207 (-)	39702	3.16652	-0.84159
PF3D7_0223100	RIFIN	Chr02: 904551 - 905775 (+)	905045	2.4995	-0.58835
PF3D7_1040300	RIFIN	Chr10: 1609063 - 1610422 (+)	1610067	2.57465	-0.64439
PF3D7_1041100	RIFIN	Chr10: 1635596 - 1636779 (+)	1636505	2.76899	-0.93846
PF3D7_1254800	RIFIN	Chr12: 2228632 - 2229740 (-)	2229043	2.89538	0.56703
PF3D7_1400600	RIFIN	Chr14: 20897 - 22232 (-)	21300	3.23468	-1.60369
PF3D7_0400400	PfEMP1	Chr04: 45555 - 56860 (-)	45589	2.98694	-0.39466
PF3D7_0412700	PfEMP1	Chr04: 561667 - 569342 (-)	567264	2.67708	-1.12228
PF3D7_0425800	PfEMP1	Chr04: 1156423 - 1167821 (+)	1167689	2.92778	-0.69117
PF3D7_0600200	PfEMP1	Chr06: 3503 - 12835 (+)	4675	3.13913	-0.63996
PF3D7_0800300	PfEMP1	Chr08: 40948 - 50939 (+)	47670	2.76534	-1.15258
PF3D7_1100200	PfEMP1	Chr11: 32666 - 42386 (-)	38595	2.62163	-0.78851
PF3D7_1300300	PfEMP1	Chr13: 33959 - 44742 (-)	38488	2.71192	-1.03834
PF3D7_0631900	STEVOR	Chr06: 1333013 - 1334035 (+)	1333642	2.61356	-1.48024
PF3D7_0700400	STEVOR	Chr07: 36922 - 37927 (-)	37825	2.52706	-0.47579
PF3D7_0732000	STEVOR	Chr07: 1385635 - 1386626 (+)	1386482	2.77924	-0.27519
PF3D7_0832600	STEVOR	Chr08: 1405835 - 1406999 (-)	1406589	2.84218	-0.41204
PF3D7_0900900	STEVOR	Chr09: 55074 - 56081 (-)	55173	2.63821	-0.01639
PF3D7_1040200	STEVOR	Chr10: 1605930 - 1606953 (+)	1606790	2.70068	-0.65842
PF3D7_1300900	STEVOR	Chr13: 62515 - 63547 (-)	62808	2.96459	-1.13878
PF3D7_1479500	STEVOR	Chr14: 3269494 - 3270496 (+)	3270203	2.77831	-0.53876
Pregnancy malaria					
PF3D7_0201600	PHISTb RLP1	Chr02: 77251 - 78808 (-)	78077	3.37438	1.25357
PF3D7_1200600*	VAR2CSA	Chr12: 46788 - 56805 (-)	53438	2.71766	0.57512
Drug resistance					
PF3D7_0319700	ABCI3	Chr03: 820708 - 830802 (+)	821301	2.76481	-1.199
PF3D7_0613800	ApiAP2	Chr06: 566139 - 578993 (+)	571916	2.742	-0.280

***Antigen genes implicated in parasite-mediate immune evasion, deformability of RBC/rigidity of iRBC membrane, rosetting/sequestration, and/or cytoadhesion.*

previously as targets of acquired immunity and may serve to prevent severe malaria (42–46). Furthermore, the *var2csa* that is implicated in pregnancy placental malaria (34, 47) was also observed in the top highest haplotype scores. Overall, iHS values aligned onto those obtained from Tajima's *D* analysis. We also found signals of positive selection in genes that may be related to drug resistance (n = 8) within the top 1% iHS (**Supplementary Table 8**). From these, two genes (abc transporter I family member 1, *abcI3* and AP2 domain transcription factor, *apiap2*) (**Table 3**) were significantly enriched by GO analysis ($P < 0.001$) and were previously reported (48, 49). But, no selection signals were observed around the five known Pf drug resistance genes that include the chloroquine resistance transporter (*crt*), multidrug

resistance-1 (*mdr1*), dihydrofolate reductase (*dhfr*), dihydropteroate synthase (*dhps*), and kelch 13 (*k13*).

DISCUSSION

P. falciparum originated in Africa and spread to other continents as human migration gradually formed new populations (29). In this study, both the PCA and neighbor-joining tree analyses showed that the parasites derived from Togo clustered according to their geographic origin and distinguished two major clades that correspond to the Asia and Africa geographical groups of samples (17, 38). In addition, our data revealed the average nucleotide diversity of Pf from Togo is much higher than that from other African samples, but it is lower than the parasite from the CMB, probably due to the historically different antimalarial drugs used in that area (17). However, locally varying selection on pathogens due to differences in host immunity may be the major factor for the high nucleotide diversity observed in Togo isolates in comparison to other Africa isolates.

The purpose of the Tajima test is to detect deviation from neutrality, in other words, to indicate processes such as balancing selection, selective sweeps, and population expansion. This study revealed that some particular antigen genes that are related to RBC invasion and disease severity, and known to be polymorphic and under balancing selection by host immune system (31, 39), got TD < 0; suggesting selective sweep (directional selection) and/or recent population expansion. Interestingly, previous scans for evidence of positive selection on Pf have clearly identified loci that have undergone selective sweeps (38, 49, 50) as well as loci that are apparently under balancing selection, including those encoding targets of acquired immunity (31). In addition, some other investigations have observed multiple genes under recent positive selection by computation of iHS in other parasite populations (39, 40, 51, 52). Therefore, here, we applied iHS as a complementary analysis to assess signals of host immune selection.

In Pf isolates from Togo, within genes that are likely under signals of recent positive selection, host immunity-related antigen genes have been the major selective agents. In terms of the top outlier genes (top 1% |iHS| as a strong hits threshold and GO enrichment analysis), 31 of the 306 genes with known functions included six RBC invasion-linked antigen genes (*msp1*, *msp7*, *mspdbl1*, *mspdbl2*, *ra*, and *sera6*) (32, 41) and 22 antigen genes (six *rifs*, seven *vars*, and eight *stevors*) that are associated with roles in evasion to host immunity, rosetting or cytoadhesion (35–37), among which is *var2csa*, a pregnancy placental malaria-related gene (34, 47) (**Table 3**). Potential interest for GO analysis for genes under balancing selection by host immune system revealed six genes related to RBC invasion (*aarp*, *flp*, *msp3*, *msp7*, *pl*, and *sera5*) (32), one *var* (PF3D7_0302300) associated with pathogenesis (GO: 0009405), and *phistb rpl1* that is implicated in placental cytoadherence to microvasculature (47).

Interestingly, we found that most of the gene family members with elevated |iHS| are located close to each other on the chromosome. For example, from three *sera* genes that are contiguously arranged on chromosome two, *sera6* was involved in the top 1% SNP locus (|iHS| = 2.61685) and the remaining other two were also included in the 5% iHS list. This was also observed on chromosome two between *mps4* involved in the top 1% |iHS| (|iHS| = 2.83572) and *msp2* included in the 5% |iHS| (|iHS| = 2.08998). Following similar observation with eight serine-repeat antigen genes in *P. vivax* isolates (25), this could be explained by the process of positive natural selection increasing the prevalence of both selected variant as well as of nearby variants, generating local regions of extended haplotypes.

We identified genes that are likely to have been under exceptionally strong recent positive selection. Given these genes encode membrane/surface proteins, they would have been under high selection from the host immune system as potential selective targets of host immunity, and this may explain the high iHS scores that we observed (39, 41, 42). For example, highly elevated |iHS| associated with the gene encoding the MSP1 antigen was consistent with that from a previous report on Pf isolates from Gambia and Guinea, as this gene has a complex pattern of polymorphism that is likely to result from different selective processes (38). The MSP1, a core member of band 3 co-ligand complex during RBC invasion (32), has been validated as one of the leading blood-stage malaria vaccine antigens with sequences incorporated in experimental vaccine trials (41). In addition, highly supported windows of elevated iHS scores were also observed on chromosomes two and 10, incorporating the *sera6* and a cluster of different antigen genes (including *ra*, *mspdbl1*, and *mspdbl2*), respectively. Similarly, genes under high operation of positive selection in the Togo isolates include those encoding known surface antigens such as *vars* (PF3D7_1100200, PF3D7_0425800, PF3D7_1300300, and PF3D7_0400400) and promising targets of immunity that require further studies [members of *rif* (PF3D7_0223100, PF3D7_1400600, and PF3D7_0100200) and *stevor* (PF3D7_1040200, PF3D7_0631900, PF3D7_1300900, and PF3D7_0832600) families]. They are known to bind to cerebral endothelial/RBC surface receptors and have been identified or reported previously as immune targets that may serve to prevent severe malaria (43–45, 53, 54).

This analysis failed to detect selection signals for some important antigen genes such as *lsa3*, *ama1*, *msp2*, *msp3*, *eba175*, or circumsporozoite protein, *csp* [which have been entered vaccine-stage development (39, 41)], and *rif* (PF3D7_0100400, PF3D7_0401600, or PF3D7_1254800), *vars* (PF3D7_1150400, PF3D7_0533100, or PF3D7_0412700), or *stevors* (PF3D7_1254100 or PF3D7_0300400), to mention a few (43, 44, 53, 55), which have been identified or validated as targets of acquired immunity for vaccine development (39, 42). The reason could be that iHS may not be suitable for detecting positive selection for those SNPs that have reached fixation in a local population (28). Another possible explanation could be that they may be less targeted by host immunity in Togo subjects, given malaria transmission intensity and parasite genetic diversity are known to vary greatly among different parts of Africa due to variation in rainfall abundance and seasonality (39). However, immunological investigations using higher numbers of samples are needed in the future.

Positively skewed allele frequency distributions indicating the operation of balancing selection of Pf genes in other parasite populations have been reported (31, 38, 39, 56). In this study, the *phistb rlp1* encoding PHISTb domain-containing RESA-like protein 1 at the surface of iRBCs, which was reported previously as most likely under balancing selection (31, 38), was also identified. It interacts with VAR2CSA and modulates knob-associated heat-shock protein 40 expression on the iRBC surface, and thus may regulate VAR2CSA expression to confer stable chondroitin sulfate A binding capacity and the parasite's cytoadherence (47). The *var2csa* was also detected among genes under strong positive selection in the Togo isolates. It encodes a particular parasite adhesion molecule (PfEMP1) expressed on the surface of iRBCs for roles in sequestration of Pf-iRBCs in the placenta, which occurs as a result of its binding to host receptors such as chondroitin sulphate A. Signals of strong balancing selection were evident in a similar subset of genes in Togo and other West Africa isolates. This is consistent with expectations that balancing selection due to allele frequency-dependent acquired immune responses is likely to operate on antigenic targets in Togo subjects (38). Such evidence could lead to studies for a vaccine to induce antibodies to prevent placental adhesion/sequestration by reducing the maternal anaemia and infant deaths that are associated with malaria in pregnancy (34, 39).

Furthermore, we found high |iHS| for two particularly important antigen genes (*msp7* and *phistb rlp1*), although they appear to being under balancing selection. The *msp7* in association with *msp1*, is important in invasion of mature RBCs and has been reported as a potential target of acquired immunity (32). Following similar observation with *csp* gene in *P. knowlesi* isolates (30), these genes could be targets of both balancing and directional selection due to their location within an elevated window of haplotype homozygosity on chromosomes, or might have hitchhiked to intermediate allele frequencies by a linked locus under selection within population-specific isolates.

Of the eight Pf drug-resistant genes identified within elevated iHS regions in Togo samples, none of the five known drug resistance genes (*crt*, *mdr1*, *dhfr*, *dhps*, and *k13*) were included, suggesting that Togo population is not under important antimalarial drug selection. This is consistent with a recent study in Togo that has shown therapeutic efficacy of AL and ASAQ without delay in the clearance of mutant parasites (9). However, GO analysis for the drug-resistant genes that we identified by iHS computation within the top 1% |iHS| (*abcI3* and *apiap2*) or with TD > 1 (*aat1* and *fpps*/*ggpps*) were highly significantly ($P < 0.001$) enriched. In addition, our study suggested additional drug resistance genes under strong positive selection (**Supplementary Table 8**), which have been reported previously (48, 49).

CONCLUSION

This study assessed the first whole-genome sequences of Pf isolates from Togo. Our results showed that the parasites derived from Togo clustered according to their geographic origin and suggest greater genetic diversity of Pf isolates in Togo than seen in other African countries. In addition, Tajima's *D* values were predominantly negative, consistent with directional selection and/or a history of recent expansion of Pf population in Togo. Against this background, there was evidence of balancing and positive selections on particular genes. Loci showing evidence of recent positive selection and balancing selection attest that host immunity has been the major selective agent. This is reflected in a significant representation of genes that encode membrane proteins expressed at the merozoite stage that invades RBCs and parasitized RBC surface proteins implicated in roles for immunoevasion, rosetting, or cytoadhesion. Our study would contribute with insightful information on the current epidemiological scenario of malaria in Togo and provides a fundamental basis to engage studies for effective malaria control in Togo.

DATA AVAILABILITY STATEMENT

The datasets presented in this study can be found in online repositories. The names of the repository/repositories and accession number(s) can be found below: https://www.ncbi.nlm.nih.gov/, PRJNA616298.

ETHICS STATEMENT

Permission was obtained from all malaria subjects before collecting specimens. Blood collection was made with informed consent from all individuals or their parents, under a study protocol reviewed and approved by the Togo Ministry of Health's Bioethics Committee (Authorisation N°019/2019/MSHP/CBRS), following institutional ethical guidelines by the ethics committee at National Institute of Parasitic Diseases, Chinese Centre for Disease Control and Prevention.

AUTHOR CONTRIBUTIONS

KK, J-HC, and YC conceptualized the study. KK and KKK collected and analyzed the specimens. H-MC performed bioinformatics analysis. S-BC and H-TF participated in the experiments. KK interpreted the data and wrote the manuscript. KK, Y-QC, and Z-NZ revised the manuscript critically for intellectual content. All authors contributed to the article and approved the submitted version.

FUNDING

This work was financially supported in part by the National Research and Development Plan of China (Grant No. 2018YFE0121600 and 2016YFC1202000), the National Natural Science Foundation of China (Grant No. 81601787, 81871681), the Natural Science Foundation of Jiangsu Province (Grant No. BK20160192), the Fundamental Research Funds for the Central

Universities funded by the Ministry of Education of China (Grant No. JUSRP51710A), the Bill & Melinda Gates Foundation (Grant No. OPP1161962), the National First-Class Discipline Program of Food Science and Technology (Grant No. JUFSTR20180101), the Scientific Research Project of Public Health Research Centre of Jiangnan University (Grant No. 1285210162190530), and the Project of Shanghai Science and Technology Commission (Grant No. 18490741100). The sponsor played no roles in the study design or in the collection, analysis, or interpretation of the data, in writing the report, or in the decision to submit the article for publication.

ACKNOWLEDGMENTS

The authors thank Kokou Sepenou Noussougnon and Koffigan Ananou for their help in collecting clinical samples.

SUPPLEMENTARY MATERIAL

The Supplementary Material for this article can be found online at: https://www.frontiersin.org/articles/10.3389/fimmu.2020.552698/full#supplementary-material

REFERENCES

1. Miller LH, Good MF, Milon G. Malaria pathogenesis. *Science* (1994) 264 (5167):1878–83. doi: 10.1126/science.8009217
2. Plewes K, Turner GDH, Dondorp AM. Pathophysiology, clinical presentation, and treatment of coma and acute kidney injury complicating falciparum malaria. *Curr Opin Infect Dis* (2018) 31(1):69–77. doi: 10.1097/QCO.0000000000000419
3. WHO. *World malaria report* (2018). Available at: http://www.who.int/malaria/publications/world-malaria-report-2018/report/en/ (Accessed March 30, 2020).
4. Kassegne K, Zhang T, Chen SB, Xu B, Dang ZS, Deng WP, et al. Study roadmap for high-throughput development of easy to use and affordable biomarkers as diagnostics for tropical diseases: a focus on malaria and schistosomiasis. *Infect Dis Poverty* (2017) 6(1):130. doi: 10.1186/s40249-017-0344-9
5. Uwase J, Chu R, Kassegne K, Lei Y, Shen F, Fu H, et al. Immunogenicity analysis of conserved fragments in Plasmodium ovale species merozoite surface protein 4. *Malar J* (2020) 19(1):126. doi: 10.1186/s12936-020-03207-7
6. WHO. *Malaria profile in Togo* (2018). Available at: https://www.who.int/malaria/publications/country-profiles/profile_tgo_en.pdf?ua=1 (Accessed March 30, 2020).
7. Gbadoé AD, Kini-Caussi M, Koffi S, Traoré H, Atakouma DY, Tatagan-Agbi K, et al. Evolution of severe pediatric malaria in Togo between 2000 and 2002. *Med Mal Infect* (2006) 36(1):52–4. (in French). doi: 10.1016/j.medmal.2005.10.006
8. Eliades MJ, Wolkon A, Morgah K, Crawford SB, Dorkenoo AM, Sodahlon Y, et al. Burden of malaria at community level in children less than 5 years of age in Togo. *Am J Trop Med Hyg* (2006) 75(4):622–9. doi: 10.4269/ajtmh.2006.75.622
9. Dorkenoo AM, Yehadji D, Agbo YM, Layibo Y, Agbeko F, Adjeloh P, et al. Therapeutic efficacy trial of artemisinin-based combination therapy for the treatment of uncomplicated malaria and investigation of mutations in k13 propeller domain in Togo, 2012-2013. *Malar J* (2016) 15:331. doi: 10.1186/s12936-016-1381-8
10. Trape JF, Rogier C, Konate L, Diagne N, Bouganali H, Canque B, et al. The Dielmo project: a longitudinal study of natural malaria infection and the mechanisms of protective immunity in a community living in a holoendemic area of Senegal. *Am J Trop Med Hyg* (1994) 51(2):123–37. doi: 10.4269/ajtmh.1994.51.123
11. Bloland PB, Boriga DA, Ruebush TK, McCormick JB, Roberts JM, Oloo AJ, et al. Longitudinal cohort study of the epidemiology of malaria infections in an area of intense malaria transmission II. Descriptive epidemiology of malaria infection and disease among children. *Am J Trop Med Hyg* (1999) 60(4):641–8. doi: 10.4269/ajtmh.1999.60.641
12. Gardner MJ, Hall N, Fung E, White O, Berriman M, Hyman RW, et al. Genome sequence of the human malaria parasite Plasmodium falciparum. *Nature* (2002) 419(6906):498–511. doi: 10.1038/nature01097
13. Chen SB, Wang Y, Kassegne K, Xu B, Shen HM, Chen JH, et al. Whole-genome sequencing of a *Plasmodium vivax* clinical isolate exhibits geographical characteristics and high genetic variation in China-Myanmar border area. *BMC Genomics* (2017) 18(1):131. doi: 10.1186/s12864-017-3523-y
14. Aurrecoechea C, Brestelli J, Brunk BP, Dommer J, Fischer S, Gajria B, et al. PlasmoDB: a functional genomic database for malaria parasites. *Nucleic Acids Res* (2009) 37(Database issue):D539–43. doi: 10.1093/nar/gkn814
15. Manske M, Miotto O, Campino S, Auburn S, Almagro-Garcia J, Maslen G, et al. Analysis of *Plasmodium falciparum* diversity in natural infections by deep sequencing. *Nature* (2012) 487(7407):375–9. doi: 10.1038/nature11174
16. Lu F, Culleton R, Zhang M, Ramaprasad A, von Seidlein L, Zhou H, et al. Emergence of Indigenous Artemisinin-Resistant *Plasmodium falciparum in* Africa. *N Engl J Med* (2017) 376(10):991–3. doi: 10.1056/NEJMc1612765
17. Shen HM, Chen SB, Cui YB, Xu B, Kassegne K, Abe EM, et al. Whole-genome sequencing and analysis of *Plasmodium falciparum* isolates from China-Myanmar border area. *Infect Dis Poverty* (2018) 7(1):118. doi: 10.1186/s40249-018-0493-5
18. Bentley DR, Balasubramanian S, Swerdlow HP, Smith GP, Milton J, Brown CG, et al. Accurate whole human genome sequencing using reversible terminator chemistry. *Nature* (2008) 456(7218):53–9. doi: 10.1038/nature07517
19. Bolger AM, Lohse M, Usadel B. Trimmomatic: a flexible trimmer for Illumina sequence data. *Bioinformatics* (2014) 30(15):2114–20. doi: 10.1093/bioinformatics/btu170
20. Li H, Handsaker B, Wysoker A, Fennell T, Ruan J, Homer N, et al. The Sequence Alignment/Map format and SAMtools. *Bioinformatics* (2009) 25 (16):2078–9. doi: 10.1093/bioinformatics/btp352
21. McKenna A, Hanna M, Banks E, Sivachenko A, Cibulskis K, Kernytsky A, et al. The Genome Analysis Toolkit: a MapReduce framework for analyzing next-generation DNA sequencing data. *Genome Res* (2010) 20(9):1297–303. doi: 10.1101/gr.107524.110
22. Excoffier L, Lischer HE. Arlequin suite ver 3.5: a new series of programs to perform population genetics analyses under Linux and Windows. *Mol Ecol Resour* (2010) 10(3):564–7. doi: 10.1111/j.1755-0998.2010.02847.x
23. Sabeti PC, Reich DE, Higgins JM, Lohmueller J, Hostetter E, Cotsapas C, et al. Detecting recent positive selection in the human genome from haplotype structure. *Nature* (2002) 419(6909):832–7. doi: 10.1038/nature01140
24. Voight BF, Kudaravalli S, Wen X. Pritchard JK. A map of recent positive selection in the human genome. *PloS Biol* (2006) 4(3):e72. doi: 10.1371/journal.pbio.0040072
25. Shen HM, Chen SB, Wang Y, Xu B, Abe EM, Chen JH, et al. Genome-wide scans for the identification of *Plasmodium vivax* genes under positive selection. *Malar J* (2017) 16(1):238. doi: 10.1186/s12936-017-1882-0
26. Szpiech ZA, Hernandez RD. selscan: an efficient multithreaded program to perform EHH-based scans for positive selection. *Mol Biol Evol* (2014) 31 (10):2824–7. doi: 10.1093/molbev/msu211
27. Nygaard S, Braunstein A, Malsen G, Van Dongen S, Gardner PP, Krogh A, et al. Long- and short-term selective forces on malaria parasite genomes. *PloS Genet* (2010) 6(9):e1001099. doi: 10.1371/journal.pgen.1001099
28. Ye R, Tian Y, Huang Y, Zhang Y, Wang J, Sun X, et al. Genome-Wide Analysis of Genetic Diversity in *Plasmodium falciparum* Isolates From China-Myanmar Border. *Front Genet* (2019) 10:1065. doi: 10.3389/fgene.2019.01065
29. Joy DA, Feng X, Mu J, Furuya T, Chotivanich K, Krettli AU, et al. Early origin and recent expansion of *Plasmodium falciparum*. *Science* (2003) 300 (5617):318–21. doi: 10.1126/science.1081449
30. Assefa S, Lim C, Preston MD, Duffy CW, Nair MB, Adroub SA, et al. Population genomic structure and adaptation in the zoonotic malaria

parasite *Plasmodium knowlesi*. *Proc Natl Acad Sci U S A* (2015) 112 (42):13027–32. doi: 10.1073/pnas.1509534112
31. Amambua-Ngwa A, Tetteh KK, Manske M, Gomez-Escobar N, Stewart LB, Deerhake ME, et al. Population genomic scan for candidate signatures of balancing selection to guide antigen characterization in malaria parasites. *PloS Genet* (2012) 8(11):e1002992. doi: 10.1371/journal.pgen.1002992
32. Cowman AF, Berry D, Baum J. The cellular and molecular basis for malaria parasite invasion of the human red blood cell. *J Cell Biol* (2012) 198(6):961–71. doi: 10.1083/jcb.201206112
33. Kassegne K, Abe EM, Cui YB, Chen SB, Xu B, Deng WP, et al. Contribution of *Plasmodium immunomics*: potential impact for serological testing and surveillance of malaria. *Expert Rev Proteomics* (2019) 16(2):117–29. doi: 10.1080/14789450.2019.1554441
34. Rowe JA, Kyes SA. The role of *Plasmodium falciparum* var genes in malaria in pregnancy. *Mol Microbiol* (2004) 53(4):1011–9. doi: 10.1111/j.1365-2958.2004.04256.x
35. Wahlgren M, Goel S, Akhouri RR. Variant surface antigens of *Plasmodium falciparum* and their roles in severe malaria. *Nat Rev Microbiol* (2017) 15 (8):479–91. doi: 10.1038/nrmicro.2017.47
36. Niang M, Bei AK, Madnani KG, Pelly S, Dankwa S, Kanjee U, et al. STEVOR is a *Plasmodium falciparum* erythrocyte binding protein that mediates merozoite invasion and rosetting. *Cell Host Microbe* (2014) 16(1):81–93. doi: 10.1016/j.chom.2014.06.004
37. Goel S, Palmkvist M, Moll K, Joannin N, Lara P, Akhouri RR, et al. RIFINs are adhesins implicated in severe *Plasmodium falciparum* malaria. *Nat Med* (2015) 21(4):314–7. doi: 10.1038/nm.3812
38. Mobegi VA, Duffy CW, Amambua-Ngwa A, Loua KM, Laman E, Nwakanma DC, et al. Genome-wide analysis of selection on the malaria parasite *Plasmodium falciparum* in West African populations of differing infection endemicity. *Mol Biol Evol* (2014) 31(6):1490–9. doi: 10.1093/molbev/msu106
39. Conway DJ. Paths to a malaria vaccine illuminated by parasite genomics. *Trends Genet* (2015) 31(2):97–107. doi: 10.1016/j.tig.2014.12.005
40. Mu J, Awadalla P, Duan J, McGee KM, Keebler J, Seydel K, et al. Genome-wide variation and identification of vaccine targets in the *Plasmodium falciparum* genome. *Nat Genet* (2007) 39(1):126–30. doi: 10.1038/ng1924
41. Kassegne K, Abe EM, Chen JH, Zhou XN. Immunomic approaches for antigen discovery of human parasites. *Expert Rev Proteomics* (2016) 13 (12):1091–101. doi: 10.1080/14789450.2016.1252675
42. Chan JA, Fowkes FJ, Beeson JG. Surface antigens of *Plasmodium falciparum*-infected erythrocytes as immune targets and malaria vaccine candidates. *Cell Mol Life Sci* (2014) 71(19):3633–57. doi: 10.1007/s00018-014-1614-3
43. Zhou AE, Berry AA, Bailey JA, Pike A, Dara A, Agrawal S, et al. Antibodies to Peptides in Semiconserved Domains of RIFINs and STEVORs Correlate with Malaria Exposure. *mSphere* (2019) 4(2):e00097-19. doi: 10.1128/mSphere.00097-19
44. Travassos MA, Niangaly A, Bailey JA, Ouattara A, Coulibaly D, Lyke KE, et al. Children with cerebral malaria or severe malarial anaemia lack immunity to distinct variant surface antigen subsets. *Sci Rep* (2018) 8(1):6281. doi: 10.1038/s41598-018-24462-4
45. Quintana MDP, Ch'ng JH, Moll K, Zandian A, Nilsson P, Idris ZM, et al. Antibodies in children with malaria to PfEMP1, RIFIN and SURFIN expressed at the *Plasmodium falciparum* parasitized red blood cell surface. *Sci Rep* (2018) 8(1):3262. doi: 10.1038/s41598-018-21026-4
46. Nilsson Bark SK, Ahmad R, Dantzler K, Lukens AK, De Niz M, Szucs MJ, et al. Quantitative Proteomic Profiling Reveals Novel *Plasmodium falciparum* Surface Antigens and Possible Vaccine Candidates. *Mol Cell Proteomics* (2018) 17(1):43–60. doi: 10.1074/mcp.RA117.000076
47. Goel S, Muthusamy A, Miao J, Cui L, Salanti A, Winzeler EA, et al. Targeted disruption of a ring-infected erythrocyte surface antigen (RESA)-like export protein gene in *Plasmodium falciparum* confers stable chondroitin 4-sulfate cytoadherence capacity. *J Biol Chem* (2014) 289(49):34408–21. doi: 10.1074/jbc.M114.615393
48. Cowell AN, Istvan ES, Lukens AK, Gomez-Lorenzo MG, Vanaerschot M, Sakata-Kato T, et al. Mapping the malaria parasite druggable genome by using in vitro evolution and chemogenomics. *Science* (2018) 359(6372):191–9. doi: 10.1126/science.aan4472
49. Park DJ, Lukens AK, Neafsey DE, Schaffner SF, Chang HH, Valim C, et al. Sequence-based association and selection scans identify drug resistance loci in the *Plasmodium falciparum* malaria parasite. *Proc Natl Acad Sci U S A* (2012) 109(32):13052–7. doi: 10.1073/pnas.1210585109
50. Chang HH, Park DJ, Galinsky KJ, Schaffner SF, Ndiaye D, Ndir O, et al. Genomic sequencing of *Plasmodium falciparum* malaria parasites from Senegal reveals the demographic history of the population. *Mol Biol Evol* (2012) 29(11):3427–39. doi: 10.1093/molbev/mss161
51. Ocholla H, Preston MD, Mipando M, Jensen AT, Campino S, MacInnis B, et al. Whole-genome scans provide evidence of adaptive evolution in Malawian *Plasmodium falciparum* isolates. *J Infect Dis* (2014) 210 (12):1991–2000. doi: 10.1093/infdis/jiu349
52. Staff PG. Correction: Imputation-Based Population Genetics Analysis of *Plasmodium falciparum* Malaria Parasites. *PloS Genet* (2016) 12(8): e1006300. doi: 10.1371/journal.pgen.1006300
53. Saito F, Hirayasu K, Satoh T, Wang CW, Lusingu J, Arimori T, et al. Immune evasion of *Plasmodium falciparum* by RIFIN via inhibitory receptors. *Nature* (2017) 552(7683):101–5. doi: 10.1038/nature24994
54. Tan J, Pieper K, Piccoli L, Abdi A, Perez MF, Geiger R, et al. A LAIR1 insertion generates broadly reactive antibodies against malaria variant antigens. *Nature* (2016) 529(7584):105–9. doi: 10.1038/nature16450
55. Turner L, Wang CW, Lavstsen T, Mwakalinga SB, Sauerwein RW, Hermsen CC, et al. Antibodies against PfEMP1, RIFIN, MSP3 and GLURP are acquired during controlled *Plasmodium falciparum* malaria infections in naive volunteers. *PloS One* (2011) 6(12):e29025. doi: 10.1371/journal.pone.0029025
56. Samad H, Coll F, Preston MD, Ocholla H, Fairhurst RM, Clark TG. Imputation-based population genetics analysis of *Plasmodium falciparum* malaria parasites. *PloS Genet* (2015) 11(4):e1005131. doi: 10.1371/journal.pgen.1005131

Conflict of Interest: The authors declare that the research was conducted in the absence of any commercial or financial relationships that could be construed as a potential conflict of interest.

frontiers in Immunology

ORIGINAL RESEARCH
published: 23 October 2020
doi: 10.3389/fimmu.2020.01725

Evaluation of Leishmanization Using *Iranian Lizard Leishmania* Mixed With CpG-ODN as a Candidate Vaccine Against Experimental Murine Leishmaniasis

*Nafiseh Keshavarzian, Mina Noroozbeygi, Mostafa Haji Molla Hoseini and Farshid Yeganeh**

Department of Immunology, School of Medicine, Shahid Beheshti University of Medical Sciences, Tehran, Iran

OPEN ACCESS

Edited by:
Emilio Luis Malchiodi, University of Buenos Aires, Argentina

Reviewed by:
Manuel Soto, Autonomous University of Madrid, Spain
Hira Nakhasi, Center for Biologics Evaluation and Research (FDA), United States

***Correspondence:**
Farshid Yeganeh
fyeganeh@gmail.com; fyeganeh@sbmu.ac.ir

Specialty section:
This article was submitted to Vaccines and Molecular Therapeutics, a section of the journal Frontiers in Immunology

Received: *28 March 2020*
Accepted: *29 June 2020*
Published: *23 October 2020*

Citation:
Keshavarzian N, Noroozbeygi M, Haji Molla Hoseini M and Yeganeh F (2020) Evaluation of Leishmanization Using Iranian Lizard Leishmania Mixed With CpG-ODN as a Candidate Vaccine Against Experimental Murine Leishmaniasis. Front. Immunol. 11:1725. doi: 10.3389/fimmu.2020.01725

Background and Objectives: The live non-pathogenic Leishmania tarantolae has recently provided a promising approach as an effective vaccine candidate against experimental leishmaniasis (ILL). Here, we evaluated the immunoprotective potential of the live Iranian Lizard Leishmania mixed with CpG adjuvant against *L. major* infection in BALB/c mice.

Methods: Four groups of female BALB/c mice were included in the study. The first and second groups received PBS and CpG, respectively. The immunized groups received 2 $\times$ 10^5 ILL promastigotes and the CpG-mixed ILL (ILL+CpG). Injections were performed subcutaneously in the right footpad. Three weeks later, all mice were challenged with 2 $\times$ 10^5 metacyclic promastigotes of *Leishmania major*^{EGFP}; inoculation was done in the left footpad. The measurement of footpad swelling and *in vivo* fluorescent imaging were used to evaluate disease progress during infection course. Eight weeks after challenge, all mice were sacrificed and the cytokines levels (IFN-γ, IL-4, and IL-10) and sera antibodies concentrations (IgG2a and IgG1) using ELISA assay, nitric oxide production using Griess assay, and arginase activity in cultured splenocytes, were measured. In addition, direct fluorescent microscopy analysis and qPCR assay were used to quantify the splenic parasite burden.

Result: The results showed that mice immunized with ILL+CpG were protected against the development of the dermal lesion. Moreover, they showed a significant reduction in the parasite load, in comparison to the control groups. The observed protection was associated with higher production of IFN-γ, as well as a reduction in IL-4 level. Additionally, the results demonstrated that arginase activity was decreased in ILL+CpG group compared to other groups.

Conclusion: Immunization using ILL+CpG induces a protective immunity; indicating that ILL with an appropriate adjuvant would be a suitable choice for vaccination against leishmaniasis.

Keywords: adjuvant, CpG, *Iranian Lizard Leishmania*, live vaccine, immunization, parasite burden

INTRODUCTION

Leishmaniasis is a disease caused by protozoan parasites of the genus *Leishmania*, which is transmitted to mammalian hosts such as humans, dogs, and mice by the bite of an infected female phlebotomine sandfly. *Leishmania* has an obligate intracellular proliferation cycle within phagocytic cells. The consequence of *Leishmania* infection is a chronic disease with diverse clinical manifestations that vary from self-limiting cutaneous leishmaniasis to fatal visceral leishmaniasis (Kala-azar) (1). More than 350 million people are at risk of leishmaniasis in 88 countries, wherein 0.7–1 million new cases occur annually; of which about 90% occurs in middle east countries (2).

Prevention methods or treatment options for leishmaniasis are limited, and each suffers from various shortcomings. Vaccination seems to be the best choice to control leishmaniasis, as patients who recuperate from the disease elicit a complete protective immunity, not only against parasite species causing the primary infection but also against other *Leishmania* species (3). However, there is currently no effective vaccine against leishmaniasis. So far, different strategies have been developed to achieve a safe and protective vaccine for leishmaniasis. Among them, leishmanization is the best way to evoke a protective durable immune response. Leishmanization was performing in the Middle East, which was based on the deliberate inoculation of live infective *Leishmania* parasites into the invisible regions of the body to induce protection against cutaneous leishmaniasis (4). This procedure has been stopped due to safety concerns (5). Therefore, the induction of protective immunity using either inactivated/attenuated or non-pathogenic live vaccines can be an important step toward controlling the disease. It is important to note that, long-term immunity against Leishmania infection needs persistent infection with a low number of parasites in the host cells (6), therefore, vaccination using live infective but non-pathogenic parasites seems to be the proper approach. Recently, leishmanization using *L. tarantolae* that is non-pathogenic to mammals has received much attention (6). Previous results revealed that although *L. tarantolae* is able to infect phagocytic cells, it cannot persist in the cells for a long time, and therefore cannot elicit a potent long-lasting immune response (6, 7). To overcome this problem, researchers have developed several recombinant *L. tarantolae* expressing a range of virulence factors of various Leishmania species (8–10). An alternative approach might be the use of a live, non-pathogenic *Leishmania* along with an adjuvant that promotes more potent immunity (11). The ability of CpG-containing immunostimulatory oligodeoxynucleotides (CpG-ODNs) to induce both innate and adaptive cellular immune responses has made them attractive choices for vaccination against intracellular pathogens (12–15). CpG-ODNs stimulate DCs for making IL-12 and IL-18 and also co-stimulatory molecules, enabling induction of a stronger T_H1 response (16–18). CpG-ODNs also have the ability to induce cytotoxic T cells and antibody responses (14). Thus, they are a good choice for vaccination against intracellular pathogens such as *Leishmania*.

In the present study, we used *Iranian Lizard Leishmania* (*ILL*) as a live vaccine with CpG-ODNs as adjuvants against *L. major*^{EGFP} challenge. The results showed that immunization of BALB/c mice using live ILL mixed with CpG-ODNs induced protective immunity against *L. major* infection, which was confirmed by the absence of lesions at the site of infection and low parasitic load in the draining lymph nodes and spleens.

MATERIALS AND METHODS

Mice and Parasites

Female BALB/c mice (6–8 weeks) were purchased from the Pasture Institute of Iran. The animal care procedures were reviewed and approved by the Institutional Animal Care and Research Advisory Committee of the Shahid Beheshti University of Medical Sciences, Tehran, Iran (IR.SBMU.MSP.REC. 1396.743).

Iranian Lizard Leishmania (a kind gift from Bahram Kazemi[1]) and enhanced green fluorescent protein (EGFP) expressing *L. major* (MRHO/IR/75/ER) were grown in RPMI 1640 medium (Gibco, USA), supplemented with 1% Penstrep (Gibco, USA) and 10% (V/V) heat-inactivated fetal bovine serum (FBS, Gibco, USA) at 26°C.

Vaccine Preparation, Immunization, and Challenge Protocol

Phosphorothioate-modified ODN sequence 1826 containing two CpG motifs (underlined 5′-TCCATGACGTTCCTGACGTT-3′) (Microsynth Group, Switzerland), was reconstituted at 5,000 μg/mL in 1 mL sterile PBS and diluted to 50 μg/μL in sterile and pyrogen-free PBS.

The sample size considering 10 percent attrition was calculated according to the previously described method (19). Mice ($n = 20$) were divided into five groups. Control groups received PBS and CpG ODN (50 μg/mL). The immunized groups received 2×10^5 ILL promastigotes and 2×10^5 ILL plus CpG (50 μg/mL). All injections were done subcutaneously (SC) in the right footpad, in a volume of 40 μL of sterile and non-pyrogenic PBS as a diluent. Three weeks after the immunization, all mice were challenged by inoculation of 2×10^5 infective-stage promastigotes (metacyclic) of *L. major*^{EGFP} (40 μL), subcutaneously in the left footpad. After the challenge, the footpad diameter was measured using a metric caliper twice a week. A group of healthy mice, which received no injections, was also included in the study. Eight weeks after challenge, mice were sacrificed for isolation of spleens and popliteal lymph nodes to determine the parasite burden and evaluate recall antigen-specific, cytokine production. A group of healthy mice, which received no injections, was maintained for 11 weeks to be compared among test groups.

Parasite Quantitation by Fluorescent *in vivo* Imaging

To monitor the infection progress, one mouse from each group (to reduce the risk of any side effects of anesthetizing including stress and death) was selected randomly, and *in vivo*

[1]Cellular and Molecular Biology Research Center, Shahid Beheshti University of Medical Sciences, Tehran, Iran.

fluorescent imaging was performed in the 7 and 8th weeks of post-challenge, using Kodak FX Pro imaging system (Kodak Molecular Imaging Systems, USA). The uninfected (healthy) mouse was used as negative control. To reduce the fluorescence background, the skin of the legs, and feet of mice was epilated. Before imaging, mice were anesthetized with Isoflurane 2% through the inhalation route (20). Semi-quantitative fluorescent intensity was measured for each image using KODAK Molecular Image software.

Parasite Quantitation by Direct Fluorescent Microscopy (DFM)

Eight weeks after infection with *L. major*^{EGFP}, popliteal lymph nodes were isolated and cell suspensions were prepared in RPMI 1640 medium, and the cells infected with the *L. major*^{EGFP} were counted on a hemocytometer using a fluorescent microscope Infection indexes were determined by multiplying the percentage of infected cells by the average number of parasite per cell. Each individual coverslip was first Giemsa stained and then analyzed under a light microscope. To accomplish this, coverslips were divided into four areas, and using 1000X magnitude the number of infected cells was determined in 100 cells in each area. An average of four areas was used to determine the mean percent of the infected macrophages. The average number of parasites per cell was determined by counting the total number of intercellular amastigotes in 400 cells. The infection index, which is the percentage of infected macrophage multiplied by the average number of amastigotes per cell, was also estimated (21).

Briefly, the infection index was calculated by multiplying the percentage of infected macrophages by the average number of Leishmania per cell, which was determined by counting the cells under a fluorescent microscope.

Parasite Quantitation by Real-Time PCR

Real-time PCR was used to quantify parasite burden in the spleen, 8 weeks after challenge. Initially, 1×10^6 cells were isolated from spleen cell suspension and were stored at −20°C. Genomic DNA extraction was performed using a spin column-based nucleic acid purification kit (Parstous DNA Isolation Kit, Iran) according to the manufacturer's protocol. The specific primers were used to amplify a 75 bp fragment of the SODB1 gene of *L. major*. The primers' sequences previously designed, were 5'-TGGTGGACATCATCAAGT-3' and 5'-AGAAGAAGTCGTGGTTGTA-3' (22). The reaction mixture contained 12.5 μL of master mix (Biofact, Korea), 1 μL of 2 pM of each primer, and 10 μL of the template DNA. The real-time PCR reaction was performed on a Rotor-Gene 6000 qPCR machine (Qiagen, Germany). The amplification times and temperatures were previously described (22). The non-template control (NTC) consisting of 10 μL water instead of the template DNA was used in each run. In order to plot a standard curve, a 10-fold serial dilution of *L. major* DNA, corresponding to 1×10^6 parasites to 10^2 parasites was prepared. The average cycle threshold (CT) of each dilution was plotted against the number of parasites. All assays were done in duplicates.

Preparation of Soluble Leishmanial Antigen

The Soluble leishmanial antigen (SLA) was prepared from stationary phase *L. major*^{EGFP} *and ILL* promastigotes using repeated freezing and thawing (10 times), was followed by sonication (23). Briefly, 2×10^8 promastigotes/mL were washed in 5 mL of cold sterile PBS three times. After 10 cycles of freezing and thawing, the suspension was sonicated three times 20 pulls with 40 W on ice then centrifuged at 5,000 × *g* for 20 min at 4°C. The supernatant containing SLA was collected and was stored at −70°C. The SLA protein concentration was determined by using the Bradford reaction (Cibzistfan, Iran).

Anti-leishmania Antibody Level

Total anti-leishmanial antibody measurement was performed twice to confirm immunization. Mice were bled from retro-orbital sinus, 3 weeks after immunization (a day before challenge with *L. major*^{EGFP}), and 8 weeks after challenge (the day before sacrificing). The mice sera were assayed using indirect ELISA for the presence of total IgG against soluble *Leishmania* antigen (SLA). Briefly, to determine anti-SLA IgG titer, ELISA plate (Greiner, Germany) was coated overnight (4°C) with 10 μg/mL of ILL SLA (SLA^{ILL}) or *L. major* SLA (SLA$^{L.major}$) in PBS (pH 7.2). The wells were washed with PBS containing 0.05% Tween-20. The plate was blocked using 200 μL of 1% bovine serum albumin (BSA) in PBS + 0.05% tween 20, for 1 h at room temperature. Then, 100 μL of diluted sera (1:40) was added to each well and followed by 1 h incubation at room temperature. For detection of specific total IgG, peroxidase-conjugated goat anti-mouse antibody (Santa Cruz Biotechnology, Inc., USA) was diluted 1:16000 and added to each well. After 1 h incubation at room temperature, 100 μL tetramethyl benzidine (TMB) (Razibiotech, Iran) was added. The enzymatic reaction was stopped with 100 μL 1 N H_2SO_4. Absorbance was recorded at 450 nm using an ELISA plate reader (Anthos 2020, Austria). The cut-off value was calculated as the mean of healthy controls' OD + 3 standards deviation. Each sample with higher OD than the cut-off value considered as immunized serum.

Serum Levels of IgG1 and IgG2a Subclasses

To determine polarization of immune responses after immunization and after challenge, we evaluated IgG1 and IgG2a subclasses levels among studied groups. The evaluation was done using the commercial ELISA kits (Invitrogen, USA) and was performed according to the manufacturer's instructions.

Cytokine Production Determination

Eight weeks' post-infection with *L. major*^{EGFP}, mice were sacrificed, and single-cell suspensions of splenocytes were prepared in RPMI 1640 supplemented with 10% FBS and 1% Penstrep (Gibco, USA). Splenocytes were plated at 1×10^6 cells/well (SPL, Korea) and re-stimulated by SLA$^{L.major}$ (10 μg/mL). All tests were done in triplicate. Phytohemagglutinin (PHA) 2% was used as positive control. After 72 h incubation at 37°C in 5% CO_2 and humid atmosphere, supernatants were harvested and the concentrations of IFN-γ, IL-4, and IL-10 were

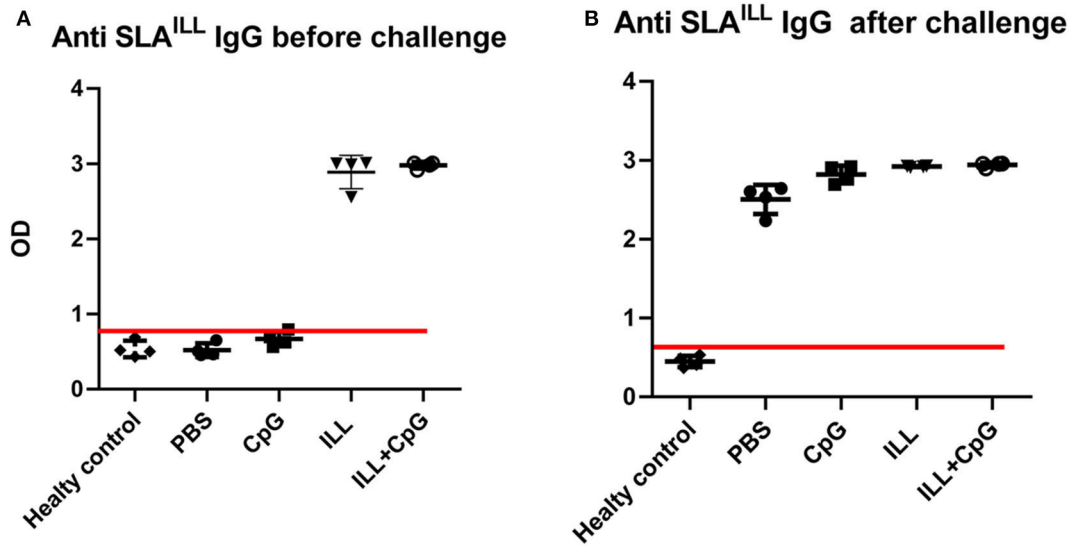

FIGURE 1 | Determination of anti-SLA^{ILL} IgG antibody. **(A)** 3 weeks after immunization and **(B)** 8 weeks after the challenge with *L. major*^{EGFP}, sera of all mice ($n = 20$) were collected. The level of the total anti-SLA^{ILL} IgG was determined using ELISA. Cut-off (red line) was determined using the mean of ODs of healthy controls + three standard deviations. Before challenge; mean + 3 *SD* = 0.866. After challenge; mean + 3 *SD* = 0.576. Each sample with higher OD than the cut-off value was considered as immunized serum. I.L.L (*Iranian Lizard Leishmania*), ILL+CpG (*Iranian Leishmania Lizard*+CpG). Data are shown as median with range.

measured using commercial ELISA kits (respectively R&D, R&D, Biolegend, USA) according to the manufacturer's instructions.

Nitric Oxide Griess Assay

Nitric oxide was measured in the splenocyte culture supernatant by Griess assay (21). Eight weeks after the challenge with *L. major*^{EGFP}, mice were sacrificed and splenocytes (1×10^6 cells/mL) were restimulated with SLA $^{L.major}$. The cultured cells (48 h) and supernatants (72 h) were collected to measure arginase activity and Nitrite concentration, respectively. The Griess assay determines nitrite concentration as a byproduct of the iNOS enzyme which indirectly indicates NO production. Briefly, Griess reagents including 1% sulfanilamide in 5% H_3PO_4, and NED solution including 0.1% naphthyl ethylene diamine (NED) dihydrochloride in distilled water (DW) were prepared. In a 96-well plate, 50 μL of sulfanilamide solution was added to 50 μL of sample and incubated 5 min in a dark place. Then, 50 μL of NED solution was added and incubated again for 5 min in a dark place. The absorbance was measured at 540 nm. Various concentrations (0–100 μM) of sodium nitrite in RPMI 1640 medium were used as standards to plot a standard curve.

Measurement of Arginase Activity

The arginase activity was determined by measuring urea concentration as a byproduct of arginine decomposition using the micro-method (24). Briefly, splenocytes were seeded in 24-well plates (SPL, Korea) at a density of 1×10^6 cells/well, re-stimulated by 10 μg/mL SLA $^{L.major}$ and incubated for 48 h at 37°C in 5% CO_2 humid atmosphere. Then, cells from each well were harvested and mixed with 100 μL lysis buffer (0.02% Triton X100 and 2.5x protease inhibitor cocktail (Santa Cruz Biotechnology, Inc., USA) solution, pH 7.5) for 15 min with shaking. Afterward, the mix was centrifuged, and 25 μL of the supernatant was mixed with 25 μL of arginase activator solution (10 mM $MnCl_2$, 50 mM Tris-HCl, PH = 7.5) followed by incubation at 56°C for 10 min. The activated lysate was incubated with 50 μL of 0.5 M L-arginine (pH = 9.7) at 37°C for 1 h. Reaction was stopped by adding 400 μL acid solution [H_2SO_4 (96%), H_3PO_4 (85%), H_2O (1:3:7, v/v/v)] to each well. Various concentrations of urea (2–60 μg/mL) were prepared as standard, afterward, an acid solution (400 μL) was added to standards. Finally, 25 μL of 6% α-isonitrosopropiophenone (ISPF) (Sigma, USA) was added to samples and standards and incubated at 56°C for 7 min followed by 40 min at 100°C. In the end, all samples were transferred to a microplate, and the absorbance was measured at 540 nm. Arginase activity (mU) was calculated using the following formula:

$$\frac{1000 \times 1000 \times urea\ ug}{time(mins) \times sample\ volume\ (\mu L) \times urea\ molecular\ weight\ (ug)} \quad (1)$$

The calculated arginase activity was divided into the total protein concentration measured using the bicinchoninic acid (BCA) assay kit (DNA biotech, Iran) and reported as mU/mg protein.

Statistical Analysis

The Shapiro-Wilks test was used to detect departures from normality. Mann–Whitney *U*-test was used to compare the mean value of two groups; while for more than two groups Kruskal–Wallis one-way analysis of variance was done. To compare clinical scores data between four groups, repeated measure ANOVA test were used. $P \leq 0.05$ was considered as statistically significant. All data were examined using SPSS (Ver. 24) software. In addition, all graphs were prepared using GraphPad Prism

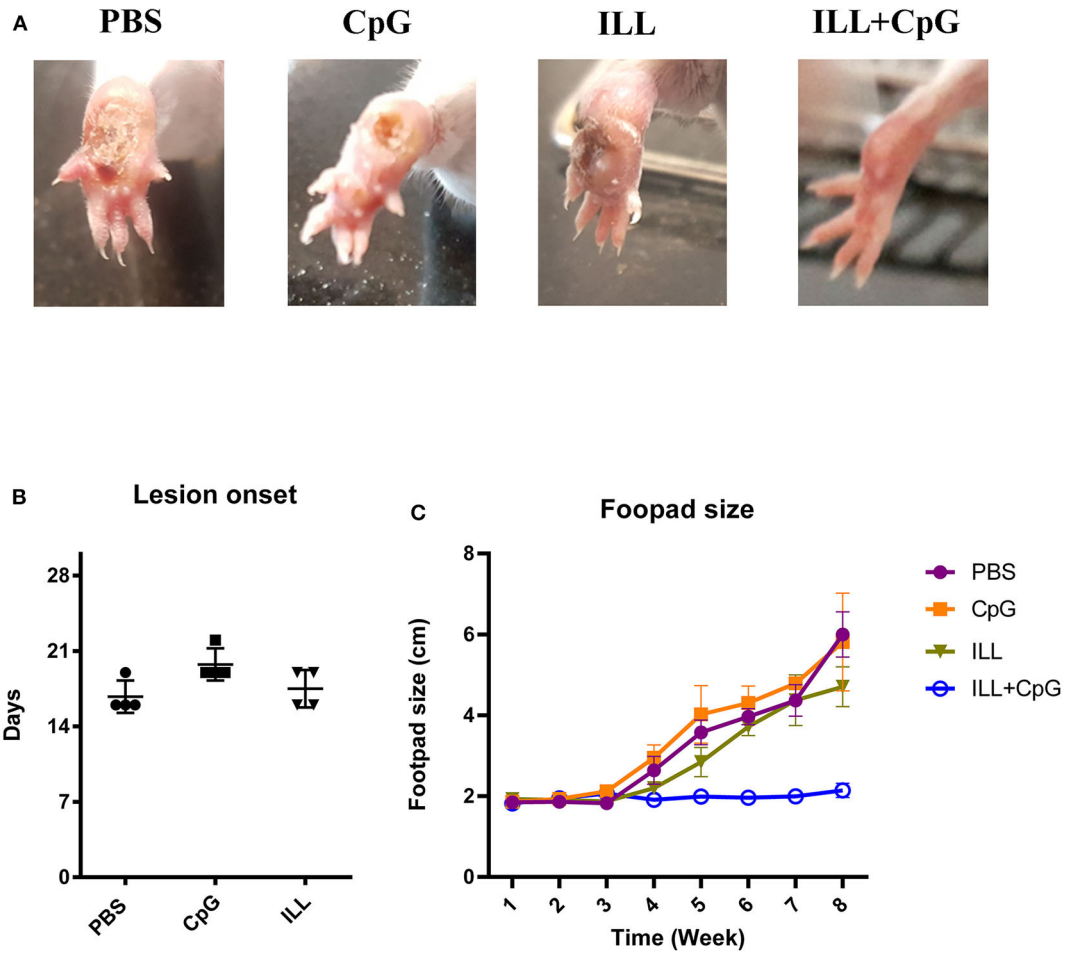

FIGURE 2 | Footpad swelling and lesion onset. **(A)** The footpads of mice were monitored on a daily basis, after challenging with *L. major*^{EGFP}. By the end of the 8th week, unlike the other groups, the ILL+CpG group showed no lesion at the injection site. **(B)** After challenge with *L. major*^{EGFP}, footpad swelling was measured using a metric caliper, twice a week. As shown, the PBS group had the earliest lesion onset. **(C)** In addition, the footpads' diameter of the ILL+CpG group was at the basic level during the 8 weeks follow up. Data are shown as median with range. ($n = 4$ per group). I.L.L (*Iranian Lizard Leishmania*), ILL+CpG (*Iranian Leishmania Lizard*+CpG).

version 8.0.0 for Windows, (GraphPad Software, USA,). The data are presented as the mean ± standard deviation (*SD*).

RESULTS

Immunization

We used live non-pathogenic parasite ILL mixed with CpG as an adjuvant, as a vaccine against *L. major*^{EGFP} infection in susceptible BALB/c mice. All mice groups were challenged 3 weeks after immunization with 2×10^5 stationary phase *L. major*^{EGFP} promastigotes in their left, hind foot pad. Total specific IgG was measured in the serum samples of all groups including healthy mice. All immunized mice that received ILL parasites had specific IgG against SLA^{ILL} (**Figure 1**). Moreover, after challenge with *L. major*^{EGFP}, the anti SLA^{ILL} IgG was detected in all groups expect healthy mice, due to antigenic similarities between ILL and *L. major*.

Immunization With ILL+CpG Protected BALB/c Mice Against L. Major^{EGFP} Challenge

The goal of vaccination is inducing a protective response to restrict the parasite number as well as limit the lesion formation. Therefore, monitoring the clinical manifestations of the disease is an important aspect of the evaluation of vaccine potency. In the present study, the ILL+CpG was the only group that was able to control *L.major*^{EGFP} infection regarding that only a moderate swelling without any open lesion was observed in the site of *L.major*^{EGFP} inoculation during 8 weeks of follow-up (**Figure 2A**). The results showed that in the ILL+CpG group, the lesion onset and footpad diameters ($P = 0.021$ from 4th week) were significantly less than those of the other groups (**Figures 2B,C**). Lesion onset could be considered as a criterion for the formation of a protective response. In addition to examining the clinical signs, protection against infection was

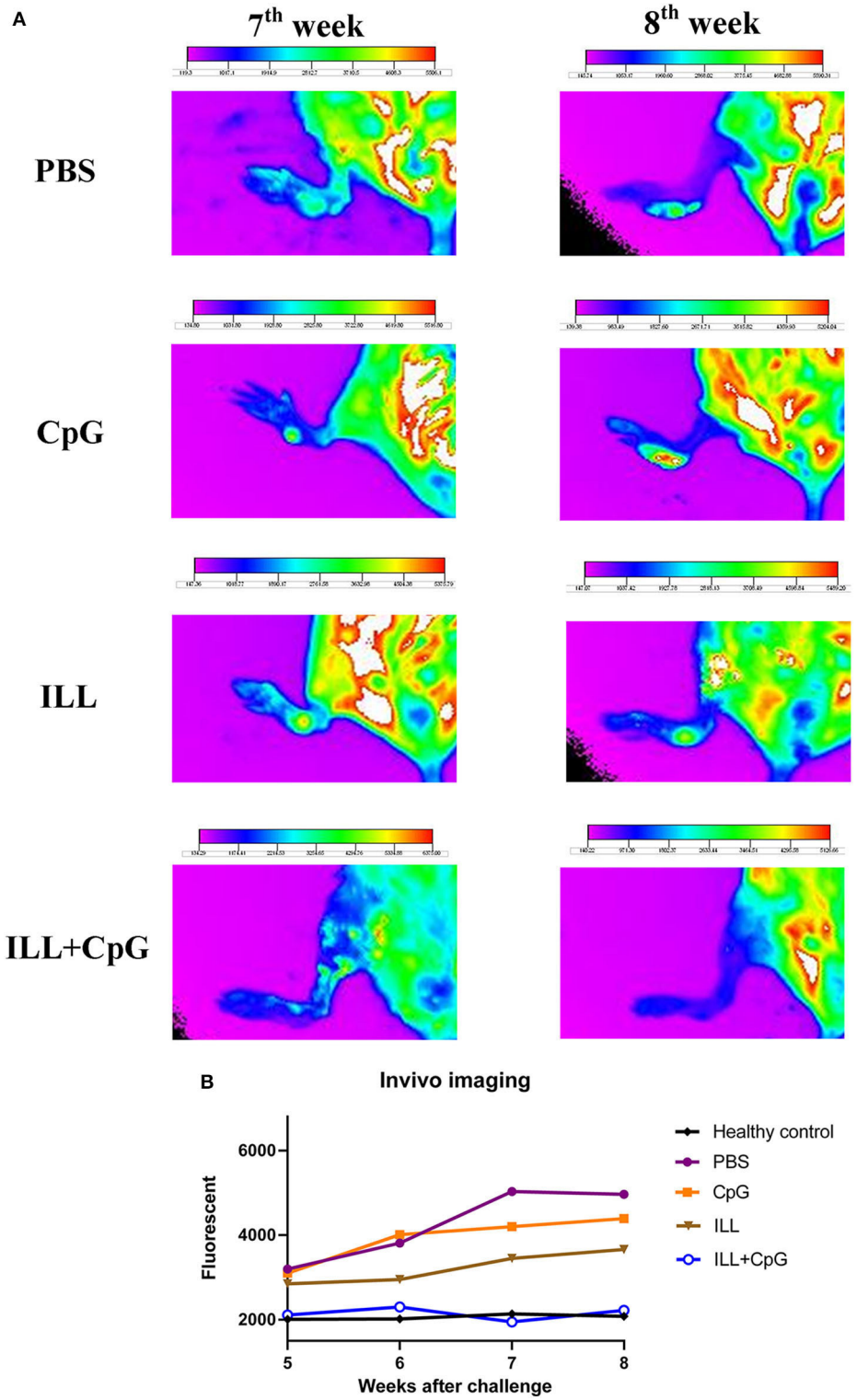

FIGURE 3 | *In vivo* fluorescent imaging. **(A)** Fluorescent imaging was used to evaluate dynamic *L. major*^{EGFP} load at the site of infection (left footpad). Seven-weeks after the challenge with *L. major*^{EGFP}, one mouse from each group was selected randomly and *in vivo*-imaging was performed. The fur of the leg was shaved and the mouse was anesthetized using Isoflurane 2% through the inhalation route, before imaging. The higher fluorescent intensity in the footpad indicates a higher parasitic load at the injection site. The arrows show the lesion site. Fluorescent intensity bar was drawn using Kodak Molecular Imaging software for each photo. **(B)** Considering the intensity bar, results showed that the ILL+CpG group had the lowest parasite load that was similar to the healthy group. Statistical analysis could not be performed because only one mouse per group was imaged. I.L.L (*Iranian Lizard Leishmania*), ILL+CpG (*Iranian Leishmania Lizard*+CpG).

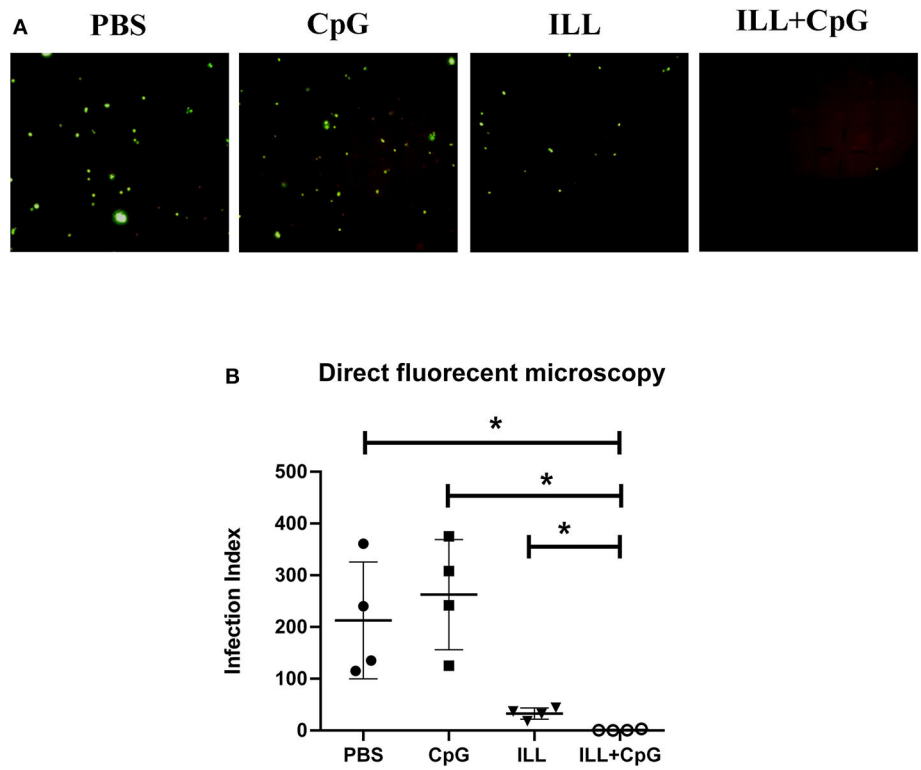

FIGURE 4 | Parasite burden assay in popliteal lymph node using direct fluorescent microscopy. Eight weeks after challenge with *L. major*^{EGFP}, mice were sacrificed and popliteal lymph nodes were isolated. **(A)** The cell suspension was prepared. The parasites expressing green fluorescent protein (GFP) were imaged using a fluorescent microscope. **(B)** To compare parasite burden between groups, the infection index was calculated by multiplying the percentage of infected macrophages by the average number of parasites per cell. The infection index was significantly lower in immunized groups than controls. To compare the means, the Mann–Whitney *U*-test was used. (* $P \leq 0.050$). Data are shown as mean ± *SD*.

determined using *in vivo* imaging. One mouse was randomly selected from each group and *in vivo*-imaging was performed in the 7 and 8th weeks after challenge with *L.major*^{EGFP}. The higher fluorescence intensity in the footpad indicates a higher parasitic load at the inoculation site. Evaluation of fluorescence intensity revealed that parasitic burden increased in all groups except ILL+CpG group (**Figures 3A,B**). Given that a mouse was selected from each group for *in vivo*-imaging, the results of this evaluation were interpreted along with the results of other parasitic load measurements.

In addition, in order to determine the parasitic load in the lymph node, direct fluorescent microscopy was performed and the infection index was calculated (**Figure 4A**). Results showed that mice immunized with ILL+CpG had a significant reduction in infection indexes in comparison to the PBS control group ($P = 0.021$, **Figure 4B**).

Moreover, 8 weeks after the challenge, the amount of parasite dissemination to the spleen was quantified using real-time PCR. As expected, immunization with ILL+CpG significantly reduced parasite burden in comparison to PBS and CpG groups ($P = 0.021$, **Figure 5A**). There is a strong positive correlation between the parasite load measured using the direct fluorescent microscopy on samples taken from draining lymph node and qPCR assay done on splenocytes specimen ($r = 0.78$, $P = 0.0004$, **Figure 5B**).

Immunization With Live ILL Plus CpG Increased IFN-γ and Reduced IL-4 Production

The protection conferred by ILL plus CpG could be due to the potency of CpG-ODN to induce a T_H1 immune response. Therefore, we measured IFN-γ (as the main T_H1 cytokine), IL-4 (as the T_H2 prototype cytokine), and IL-10 (as an immunomodulatory cytokine) in the supernatant of splenocytes re-stimulated with $SLA^{L.major}$. As shown in **Figure 6A**, the ILL+CpG group produced a substantially higher level of IFN-γ in comparison to the PBS control group ($P = 0.021$). The ILL+CpG group also released a lower concentration of IL-4 than the PBS group ($P = 0.021$) (**Figure 6B**). The post-challenge IFN-γ/IL-4 ratio in response to stimulation with $SLA^{L.major}$ is a valuable indicator of vaccine potency. Results showed that IFN-γ/IL-4 ratio was higher in the ILL+CpG group when compared to each of the other groups ($P = 0.021$ in comparison to PBS) (**Figure 6C**). We also measured the secretion of IL-10 as a major anti-inflammatory cytokine. The results showed that the IL-10

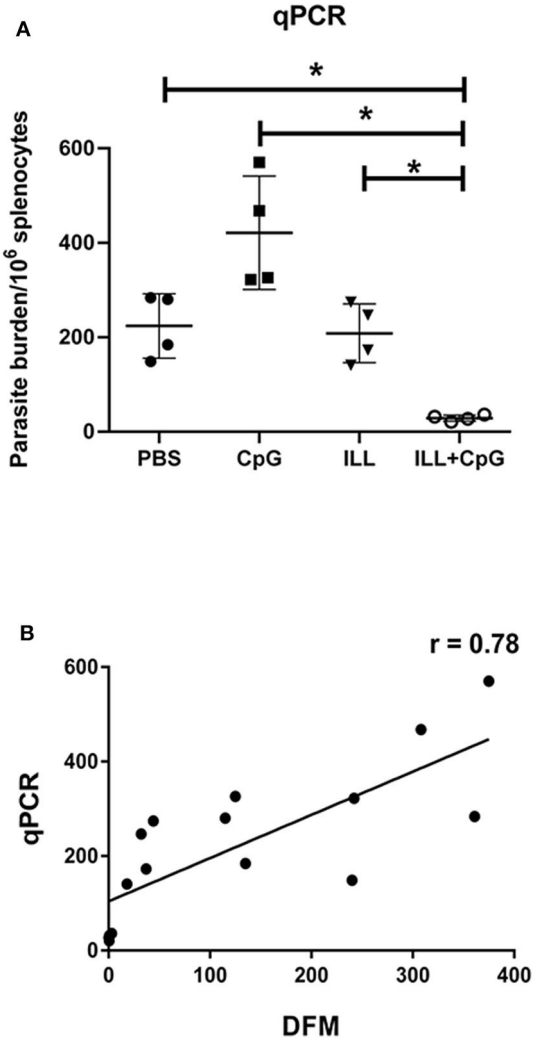

FIGURE 5 | Parasite burden analysis in splenocytes using quantitative real-time PCR assay. **(A)** Eight weeks after challenge all mice ($n = 4$ per group) were sacrificed and spleens were isolated. Genomic DNA was extracted and the amount of *Leishmania* DNA was quantified via amplifying the SODB1 gene of *L. major* using real-time PCR assay. In the ILL+CpG group compared to other groups, parasite burden was significantly decreased. **(B)** In order to determine the correlation coefficient between the direct fluorescent microscopy (DFM) in popliteal lymph node cells and qPCR in splenocytes, statistical analysis was performed. Spearman's correlation coefficient of the parasite burden between the two techniques was 0.78 and was statistically significant ($P = 0.0004$). The asterisks indicate the significant differences between groups as determined by a Mann–Whitney *U*-test (*$P \leq 0.05$). Data are shown as mean ± *SD*.

level in the ILL+CpG group was similar to the other groups ($P > 0.05$) (**Figure 6D**).

We also determined the humoral response through the assessment of IgG subclasses. It has been shown that IgG2a antibody induction is correlated with IFN-γ production and T_H1 responses, while IgG1 production is associated to the T_H2 immune profile (25). The total IgG2a and the total IgG1 levels were determined in mice sera, 3 weeks after immunization, and 8 weeks after challenge. The results showed that before the challenge, there was no difference in the total IgG1 and the total IgG2a levels between the groups (**Figures 7A,B**). However, after the challenge, the PBS group had higher total IgG1 antibody level compared to immunized groups ($P = 0.001$). Moreover, there was a significant difference in IgG2a level between the immunized groups and the PBS group after challenge ($P = 0.021$, **Figure 7B**). Additionally, the results showed that 8 weeks after the challenge, in the ILL+CpG group, the IgG1 level was decreased while the IgG2a level was increased ($P = 0.021$ and $P = 0.021$, respectively). Therefore, IgG2a/IgG1 ratios were increased in ILL+CpG after the challenge in comparison with before the challenge in this group (**Figure 7C**, $P = 0.021$).

Immunization With ILL+CpG Reduced Arginase Activity

Arginase and iNOS are two inducible enzymes that convert arginine as a substrate to active mediators which crucially affect the *Leishmania* infection outcomes. In the current study, the arginase activity and nitrite concentrations were measured in the culture of splenocytes, 8 weeks after the challenge. Regarding the instability of NO, determination of the nitrite concentration which is produced after NO refraction considered as an indicator for iNOS activity and NO level. The results showed that the ILL+CpG group had a lower arginase activity level (4.75 ± 1.7 mU/mg protein) than the PBS group (154 ± 71.91 mU/mg protein, $P = 0.021$, **Figure 8A**). However, no significant difference was observed among the immunized groups and control groups in the levels of nitrite ($P > 0.05$, **Figure 8B**). Nevertheless, the nitrite/arginase activity ratio was significantly higher in the ILL+CpG group mice compared to the controls ($P = 0.021$, **Figure 8C**). These findings confirm that immunization using ILL+CpG is able to limit *L. major* growth by inducing anti-leishmanial responses in host macrophages.

DISCUSSION

In the present study, *Iranian Lizard Leishmania*, mixed with CpG-ODN, was used to induce protective immunity against *L. major*^{EGFP} infection in BALB/c mice. The results showed that subcutaneous inoculation of the live vaccine resulted in a potent protective immunity against *L. major*^{EGFP} infection, which was revealed by the absence of open lesions in the footpad of mice challenged with *L. major*^{EGFP}. The observed protection was associated with mild swelling in the foot-pad and low parasitic load in spleen and draining lymph nodes. The results revealed that the protection was mediated by increased IFN-γ production, decreased IL-4 secretion, as well as decreased arginase activity.

Leishmania produces zoonotic infections. For instance, members of the subgenus *L. Sauroleishmania* can be isolated from reptiles. *Leishmania tarantolae* was detected in the gecko *Tarenola annularis* in Sudan (26). *Iranian lizard Leishmania* was isolated from *Agama caucasica microlepis* captured in Shahrod province in Iran (27). Ultrastructure study using electron microscopy as well as cloning and the enzymatic assay of pteridine reductase-1 showed that *ILL* differs from other *lizard*

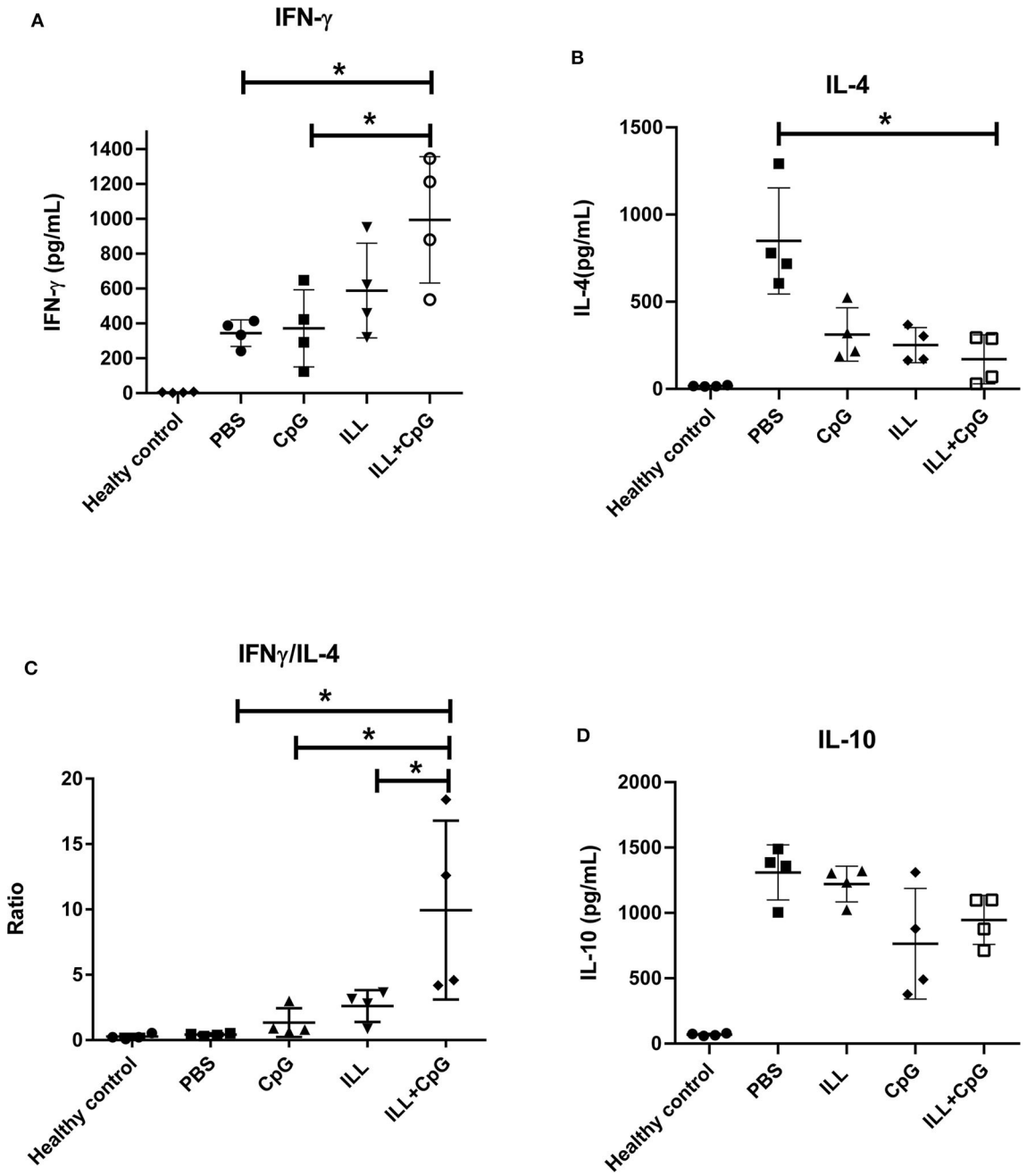

FIGURE 6 | The levels of IFN-γ, IL-4, and IL-10 cytokines in splenocytes culture. Eight weeks after challenge all mice including healthy mice ($n = 4$ per group) were sacrificed and splenocytes were re-stimulated with $SLA^{L.major}$ and PHA. After 72 h, supernatants were collected and cytokines were measured using an ELISA assay. **(A)** IFN-γ level was significantly higher in the ILL+CpG group. **(B)** However, the level of IL-4 was significantly higher in the PBS group **(C)** IFN-γ/IL-4 ratio shows a T_H1 mediated response and in the ILL+CpG group was higher than controls. **(D)** IL-10 levels were not statistically significant differences between studied groups. The asterisks indicate the significant differences between groups as determined by a Mann–Whitney *U*-test (*$P \leq 0.05$). Data are shown as mean ± *SD*. I.L.L (*Iranian Lizard Leishmania*), ILL+CpG (*Iranian Leishmania Lizard*+CpG).

Leishmania promastigotes that previously were isolated in other countries (28, 29). Breton et al. reported that *L. tarentolae* does not persist more than 1 month in infected BALB/c mice and was not able to generate any manifestation of leishmaniasis (6). Therefore, it seems that the main obstacle to using *L. tarentolae* as a live vaccine is its limited infectivity. To overcome this barrier, finding more virulent leishmania strain was considered. Previous studies have shown that not all *lizard Leishmania* are non-pathogenic to humans. For example, *L. adleri* is able to produce a lesion in humans, and some strains of *L. tarentolae*

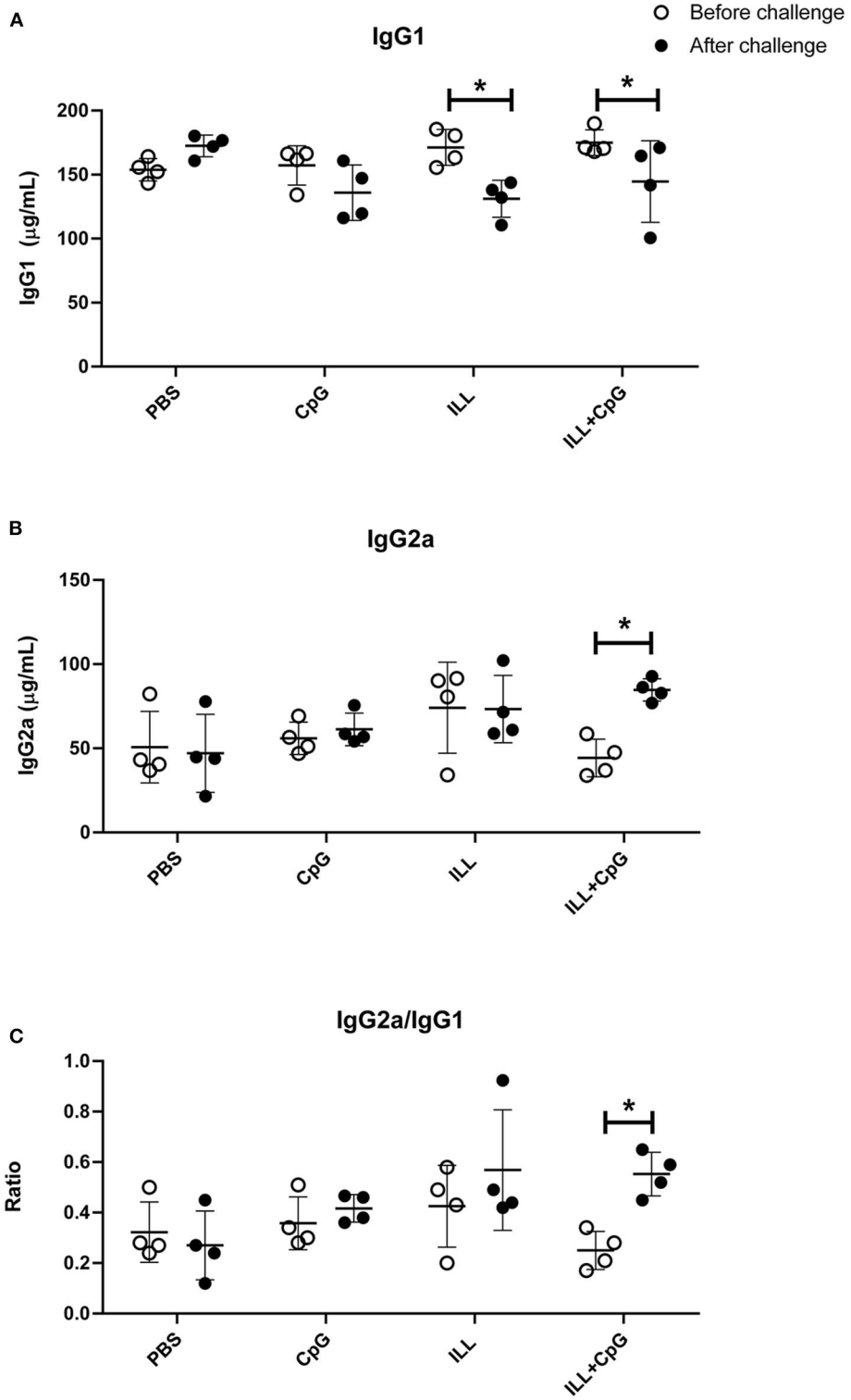

FIGURE 7 | Determination of humoral immune response in mice. Total IgG1 and total IgG2a levels were measured two times using ELISA. Mice were bled 3 and 8 weeks after challenge with *L. major*^{EGFP}. **(A)** IgG1 levels before and after challenge. The level of IgG1 significantly decreased in immunized mice (ILL and ILL+CpG groups), after the challenge. **(B)** IgG2a levels before and after the challenge. After the challenge, the level of IgG2a was increased significantly only in the ILL+CpG group. **(C)** IgG2a/IgG1 ratio levels before and after challenge. The IgG2a/IgG1 ratios were increased in ILL+CpG after challenge. Mann–Whitney *U*-test was performed to compare antibody levels before and after the challenge of each group and significant differences are shown with asterisks (*$P \leq 0.05$). Data are shown as mean ± *SD*. I.L.L (*Iranian Lizard Leishmania*), ILL+CpG (*Iranian Leishmania Lizard*+CpG).

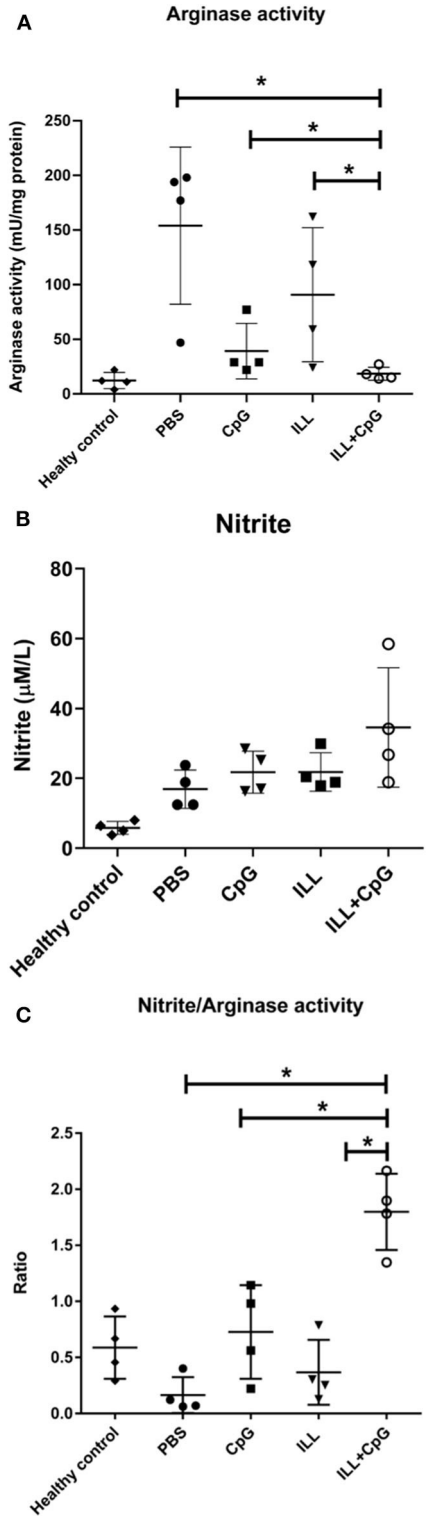

FIGURE 8 | Arginase and iNOS activity in immunized and control groups. Eight weeks after challenge with *L. major*^{EGFP}, mice were sacrificed and splenocytes (1×10^6 cells/mL) were re-stimulated with SLA$^{L.major}$. To measure arginase activity, the cultured cells were collected after 48 h. In addition, to evaluate the nitrite concentration the supernatant of the culture was used.

(Continued)

FIGURE 8 | (A) Arginase activity was significantly lower in the ILL+CpG group in comparison to controls. **(B)** There was no significant difference between nitrite concentration in the studied groups. **(C)** The nitrite concentration/Arginase activity ratio showed immune protective responses. The ratio was significantly higher in the ILL+CpG group than in other groups. $n = 4$ per group. The means were compared with a Mann–Whitney *U*-test and significant differences are shown with asterisks (*$P \leq 0.05$). Data are shown as mean ± *SD*. I.L.L (*Iranian Lizard Leishmania*), ILL+CpG (*Iranian Leishmania Lizard*+CpG).

(LEM 125) could cause a transient infection (7). Our findings showed that in ILL infected mice a transient lesion was detected in the inoculation site and therefore we believed that it sustained longer durability in the body that would elicit more effective immune responses.

Although we did not survey the persistent of ILL in studied groups, our findings showed that in ILL-infected mice a transient lesion was formed at the site of inoculation, therefore we assumed that ILL sustained longer durability in the body than *L. tarantolae*; then it may able to elicit more effective immune responses, which is necessary for long term immunity. Undeniably, the probable higher infectivity increases the concerns about the vaccine biosafety for human use. All of this suggests that further studies are needed.

The results of the present study showed that ILL mixed with CpG-ODN conferred a strong protective response resulting in no open lesion at the site of the challenge with *L. major*^{EGFP}. Mendez et al. showed that using CpG with live *L. major* reduced the size and duration of active lesions very effectively (14). Indeed, inoculation of live *L. major* mixed with CpG induced a T_H1 immune response and long-term immunity (28). Similarly, previous findings revealed that the protection that was achieved by immunizing BALB/c mice with live *L. tarentolae* secreting the sand fly salivary antigen in the presence of CpG-ODN was mediated by T_H1 responses (8). In the present study, immunity induced by ILL+CpG reduced the parasite load in mice. By using *in vivo* imaging, it was observed that the ILL+CpG group had the lowest fluorescent intensity in the challenge site; in addition, the parasite indexes measured in popliteal lymph nodes using the DFM method showed that the ILL+CpG group had ∼190-fold lower parasite burden than the other studied groups. Moreover, the qPCR assay that was used to determine parasite load in spleen cells revealed that the immunized group had about 87% lower parasite burden. Similarly, Breton et al. observed that after vaccination with *L. traentolae* the spleen parasite burden measured by luciferase activity was reduced by 85% (6). Moreover, in another study it was reported that the combination of *L. traentolae* and CpG could reduce the lymph node parasite load (8). It should be added that Real-time PCR and DFM present a snapshot view of parasite burden, so, to get a dynamic view, it is necessary to use live animals. The *in vivo* imaging was performed from the 7th week after challenge with *L.major*^{EGFP} to get a more comprehensive results.

As has been revealed previously, a milieu of T_H1 type cytokines leads to control of *Leishmania* infection while a T_H2 milieu results in the disease progression. Indeed, T_H2 milieu

supports a humoral response, which has little or no effect on intracellular parasites. T_H1 cytokines, mainly IFN-γ, stimulate macrophages to kill *Leishmania* parasites (30). In the current study, ILL+CpG group produced higher quantities of IFN-γ than controls. On the other hand, IL-4 levels were significantly decreased in the ILL+CpG group compared to the PBS control group. Moreover, the highest IFN-γ/IL-4 ratio belonged to the ILL+CpG group while the lowest ratio was observed in the PBS group, which was consistent with the clinical findings.

The results of the current study showed that the immunized mice produced a similar level of IL-10 in comparison with other groups. IL-10 is a principal regulatory cytokine that suppresses the activity of macrophages and T_H1 cells that are essential for parasite control (31). On the other hand, IL-10 plays a pivotal role in the acceleration of the wound healing process (31). The main sources of IL-10 are regulatory T cells and T_H2 cells. Interestingly, IL-10 can also be produced by T_H1 and macrophages that secrete IFN-γ (31). Hence, T_H1 cells and macrophages auto-regulate themselves by IL-10 production. Therefore, a balanced IFN-γ/IL-10 axis could support the clearance of the parasite by macrophages, as well as control the deleterious side-effect of exaggerated inflammation (32). The results of the present study showed that the high production level of IFN-γ in the ILL+CpG group was accompanied by significant IL10 production in this group.

One of the pathways play an important role in the fate of *Leishmania* infection is the arginine metabolic pathway. Arginase catabolizes L-arginine into urea and ornithine. The latter is further catabolized to polyamines that are required for *Leishmania* parasite growth. By contrast, inducible nitric oxide synthase (iNOS) oxidizes L-arginine in a two steps process to nitric oxide (NO), which is a metabolite responsible for the *Leishmania* parasite clearance. Both enzymes use L-arginine as a shared substrate, hence the arginase pathway inhibits the iNOS pathway, and vice versa (33). In the present study, there was no increase in nitrite level in the ILL+CpG group compared to other groups except healthy mice. On the other hand, the lowest arginase activity was observed in the ILL+CpG group, while the highest activity was observed in the PBS controls. The study by Virginia et al. showed that the *L. major* growth increased in macrophages *in vitro* by the induction of arginase-I and that arginase inhibition reduced the number of parasites and delayed lesion onset in infected BALB/c mice (34). By contrast, in resistant mice such as C57BL/6, a protective response caused the arginase activity to be maintained at the baseline level, which was associated with the control of lesions (34).

In the previous studies, it has been well-established that T_H1 cellular responses are associated with a high level of IFN-γ production and increased level of IgG2a antibody subclass (35), whereas T_H2 response augments the production of IL-4 as well as IgG1 subclass (36). In the present study, a considerable decrease in the total IgG1 concentration, along with a significant increase in the total IgG2a level after the challenge was observed in the immunized group. The observed alteration in antibody levels was reflected by a high IgG2a/IgG1 ratio, indicates the induction of a more pronounced T_H1 response. However, since the total IgG subclasses were determined, the determination of specific anti-leishmanial antibodies may prepare more reliable and coordinating results with the cytokines assays.

CONCLUSION

The results demonstrate that ILL+CpG vaccination induced a strong protective response, suggest that *ILL* with an appropriate adjuvant could be a suitable choice for safe leishmanization. Although the observed protective immune response is a short-term response, it could be a step forward to other studies that will be done for inducing long-term immunity.

DATA AVAILABILITY STATEMENT

Data are available from the authors upon reasonable request and with permission of the research deputy of Shahid Beheshti University of Medical Sciences. Requests to access the datasets should be directed to fyeganeh@gmail.com.

ETHICS STATEMENT

The animal study was reviewed and approved by Institutional Animal Care and Research Advisory Committee of the Shahid Beheshti University of Medical Sciences, Tehran, Iran (IR.SBMU.MSP.REC. 1396.743).

AUTHOR CONTRIBUTIONS

FY devised the project, the main conceptual ideas, and proof outline. NK worked out almost all of the technical details with help from MN and performed the statistical analysis for the suggested experiment. MH proposed the methods in discussions with FY and edited the outline. All authors contributed to the article and approved the submitted version.

FUNDING

This study was supported financially by grants from the deputy of research, Shahid Beheshti University of Medical Sciences (Grant No. 11332).

ACKNOWLEDGMENTS

The authors are very thankful to Dr. David Lawrence Sacks (Laboratory of Parasitic Diseases, National Institute of Allergy and Infectious Diseases, National Institutes of Health, Bethesda, Maryland) for his kind technical and editorial advice. We also like to thank Mandana Mohseni Masooleh (Central Research Laboratories, Shahid Beheshti University of Medical Sciences, Tehran, Iran) for *in vivo* imaging technical supports. This article has been extracted from the thesis written by NK in the School of Medicine, Shahid Beheshti University of Medical Sciences.

REFERENCES

1. Novo SP, Leles D, Bianucci R, Araujo A. The process of leishmania infection—disease and new perspectives of paleoparasitology. *Rev Inst Med Trop São Paulo.* (2016) 58:45. doi: 10.1590/S1678-9946201658045
2. Burza S, Croft SL, Boelaert M. Leishmaniasis. *Lancet.* (2018) 392:951–70. doi: 10.1016/S0140-6736(18)31204-2
3. Porrozzi R, Teva A, Amaral VF, Santos da Costa MV, Grimaldi G Jr. Cross-immunity experiments between different species or strains of Leishmania in rhesus macaques (*Macaca mulatta*). *Am J Trop Med Hygiene.* (2004). 71:297–305. doi: 10.4269/ajtmh.2004.71.297
4. Khamesipour A, Dowlati Y, Asilian A, Hashemi-Fesharki R, Javadi A, Noazin S, et al. Leishmanization: use of an old method for evaluation of candidate vaccines against leishmaniasis. *Vaccine.* (2005) 23:3642–8. doi: 10.1016/j.vaccine.2005.02.015
5. Gillespie PM, Beaumier CM, Strych U, Hayward T, Hotez PJ, Bottazzi ME. Status of vaccine research and development of vaccines for leishmaniasis. *Vaccine.* (2016) 34:2992–5. doi: 10.1016/j.vaccine.2015.12.071
6. Breton M, Tremblay MJ, Ouellette M, Papadopoulou B. Live nonpathogenic parasitic vector as a candidate vaccine against visceral leishmaniasis. *Infect Immun.* (2005) 73:6372–82. doi: 10.1128/IAI.73.10.6372-6382.2005
7. Klatt S, Simpson L, Maslov DA, Konthur Z. Leishmania tarentolae: taxonomic classification and its application as a promising biotechnological expression host. *PLoS Negl Trop Dis.* (2019) 13:e0007424. doi: 10.1371/journal.pntd.0007424
8. Katebi A, Gholami E, Taheri T, Zahedifard F, Habibzadeh S, Taslimi Y, et al. Leishmania tarentolae secreting the sand fly salivary antigen PpSP15 confers protection against Leishmania major infection in a susceptible BALB/c mice model. *Mol Immunol.* (2015) 67:501–11. doi: 10.1016/j.molimm.2015.08.001
9. Mizbani A, Taheri T, Zahedifard F, Taslimi Y, Azizi H, Azadmanesh K, et al. Recombinant Leishmania tarentolae expressing the A2 virulence gene as a novel candidate vaccine against visceral leishmaniasis. *Vaccine.* (2009) 28:53–62. doi: 10.1016/j.vaccine.2009.09.114
10. Zahedifard F, Gholami E, Taheri T, Taslimi Y, Doustdari F, Seyed N, et al. Enhanced protective efficacy of nonpathogenic recombinant leishmania tarentolae expressing cysteine proteinases combined with a sand fly salivary antigen. *PLoS Negl Trop Dis.* (2014) 8:e2751. doi: 10.1371/journal.pntd.0002751
11. Raman V, Reed S, Duthie M, Fox C, Matlashewski G. Adjuvants for leishmania vaccines: from models to clinical application. *Front Immunol.* (2012) 3:144. doi: 10.3389/fimmu.2012.00144
12. Giunchetti RC, Corrêa-Oliveira R, Martins-Filho OA, Teixeira-Carvalho A, Roatt BM, Aguiar-Soares RDdO, et al. A killed leishmania vaccine with sand fly saliva extract and saponin adjuvant displays immunogenicity in dogs. *Vaccine.* (2008) 26:623–38. doi: 10.1016/j.vaccine.2007.11.057
13. Giunchetti RC, Corrêa-Oliveira R, Martins-Filho OA, Teixeira-Carvalho A, Roatt BM, de Oliveira Aguiar-Soares RD, et al. Immunogenicity of a killed leishmania vaccine with saponin adjuvant in dogs. *Vaccine.* (2007) 25:7674–86. doi: 10.1016/j.vaccine.2007.08.009
14. Lipford GB, Bauer M, Blank C, Reiter R, Wagner H, Heeg K. CpG-containing synthetic oligonucleotides promote B and cytotoxic T cell responses to protein antigen: a new class of vaccine adjuvants. *Eur J Immunol.* (1997) 27:2340–4. doi: 10.1002/eji.1830270931
15. Mendez S, Tabbara K, Belkaid Y, Bertholet S, Verthelyi D, Klinman D, et al. Coinjection with CpG-containing immunostimulatory oligodeoxynucleotides reduces the pathogenicity of a live vaccine against cutaneous leishmaniasis but maintains its potency and durability. *Infect Immun.* (2003) 71:5121–9. doi: 10.1128/IAI.71.9.5121-5129.2003
16. Jakob T, Walker PS, Krieg AM, Udey MC, Vogel JC. Activation of cutaneous dendritic cells by CpG-containing oligodeoxynucleotides: a role for dendritic cells in the augmentation of Th1 responses by immunostimulatory DNA. *J Immunol.* (1998) 161:3042–9.
17. Bohle B, Jahn-Schmid B, Maurer D, Kraft D, Ebner C. Oligodeoxynucleotides containing CpG motifs induce IL-12, IL-18 and IFN-gamma production in cells from allergic individuals and inhibit IgE synthesis *in vitro*. *Eur J Immunol.* (1999) 29:2344–53. doi: 10.1002/SICI1521-4141199907290:072344::AID-IMMU23443.0.CO;2-R
18. Hartmann G, Weiner GJ, Krieg AM. CpG DNA: a potent signal for growth, activation, and maturation of human dendritic cells. *Proc Natl Acad Sci USA.* (1999) 96:9305–10. doi: 10.1073/pnas.96.16.9305
19. Arifin WN, Zahiruddin WM. Sample size calculation in animal studies using resource equation approach. *Malays J Med Sci.* (2017) 24:101–5. doi: 10.21315/mjms2017.24.5.11
20. Chuzel T, Sanchez V, Vandamme M, Martin S, Flety O, Pager A, et al. Impact of anesthesia protocols on *in vivo* bioluminescent bacteria imaging results. *PloS ONE.* (2015) 10:e0134048. doi: 10.1371/journal.pone.0134048
21. Dehghani F, Hoseini MHM, Memarnejadian A, Yeganeh F, Rezaie AM, Khaze V, et al. Immunomodulatory activities of chitin microparticles on leishmania major-infected murine macrophages. *Arch Med Res.* (2011) 42:572–6. doi: 10.1016/j.arcmed.2011.11.005
22. Ghotloo S, Mollahoseini MH, Najafi A, Yeganeh F. Comparison of parasite burden using real-time polymerase chain reaction assay and limiting dilution assay in leishmania major infected mouse. *Iran J Parasitol.* (2015) 10:571–6.
23. Scott P, Pearce E, Natovitz P, Sher A. Vaccination against cutaneous leishmaniasis in a murine model. I. Induction of protective immunity with a soluble extract of promastigotes. *J Immunol.* (1987) 139:221–7.
24. Iyamu EW, Asakura T, Woods GM. A colorimetric microplate assay method for high-throughput analysis of arginase activity *in vitro*. *Anal Biochem.* (2008) 383:332–4. doi: 10.1016/j.ab.2008.08.016
25. Snapper C, Paul W. Interferon-gamma and B cell stimulatory factor-1 reciprocally regulate Ig isotype production. *Science.* (1987) 236:944–7. doi: 10.1126/science.3107127
26. Elwasila M. Leishmania tarentolae wenyon, 1921 from the gecko tarentola annularis in the sudan. *Parasitol Res.* (1988) 74:591–2. doi: 10.1007/BF00531640
27. Kazemi B, Gh T-B, Hashemi Feshareki SR, Javadian EE. Isolation a lizard leishmania promastigote from its natural host in Iran. *J Biol Sci.* (2004) 4:623. doi: 10.3923/jbs.2004.620.623
28. Kazemi B, Heidari M, Naderi M, Piryaei A, Nazari-Pouya M-R, Iran RI. Study on ultrastructure of leishmania major and lizard leishmania. *J Cell Anim Biol.* (2008) 2:129–33.
29. Kazemi B, Tohidi F, Bandehpour M, Yarian F. Molecular cloning, expression and enzymatic assay of pteridine reductase 1 from iranian lizard leishmania. *Iran Biomed J.* (2010) 14:97–102.
30. Foti M. Chapter 1 - introduction to cytokines as tissue regulators in health and disease. In: Foti M, Locati M, editors. *Cytokine Effector Functions in Tissues.* Milan: University of Milano-Bicocca. (2017). p. 3–30. doi: 10.1016/B978-0-12-804214-4.00019-1
31. Mingomataj EÇ, Bakiri AH. Regulator versus effector paradigm: interleukin-10 as indicator of the switching response. *Clin Rev Allergy Immunol.* (2016) 50:97–113. doi: 10.1007/s12016-015-8514-7
32. Azizi M, Yousefi R, Yeganeh F, Mami S, Haji Molla Hoseini M. Co-administration of chitin micro-particle and leishmania antigen proposed a new immune adjuvant against experimental leishmaniasis. *Parasite Immunol.* (2019) 41:e12676. doi: 10.1111/pim.12676
33. da Silva MF, Floeter-Winter LM. Arginase in leishmania. *Sub Cell Biochem.* (2014) 74:103–17. doi: 10.1007/978-94-007-7305-9_4
34. Iniesta V, Carcelén J, Molano I, Peixoto PMV, Redondo E, Parra P, et al. Arginase I induction during Leishmania major infection mediates the development of disease. *Infect Immun.* (2005) 73:6085–90. doi: 10.1128/IAI.73.9.6085-6090.2005
35. Bossie A, Vitetta ES. IFN-gamma enhances secretion of IgG2a from IgG2a-committed LPS-stimulated murine B cells: implications for the role of IFN-gamma in class switching. *Cell Immunol.* (1991) 135:95–104. doi: 10.1016/0008-8749(91)90257-C

36. Hasbold J, Hong JS-Y, Kehry MR, Hodgkin PD. Integrating signals from IFN-γ and IL-4 by B cells: positive and negative effects on CD40 ligand-induced proliferation, survival, and division-linked isotype switching to IgG1, IgE, and IgG2a. *J Immunol.* (1999) 163:4175–81.

Conflict of Interest: The authors declare that the research was conducted in the absence of any commercial or financial relationships that could be construed as a potential conflict of interest.

frontiers in Microbiology

ORIGINAL RESEARCH
published: 17 November 2020
doi: 10.3389/fmicb.2020.559255

Asymptomatic Malaria Infection Is Maintained by a Balanced Pro- and Anti-inflammatory Response

Augustina Frimpong[1,2,3], Jones Amponsah[2], Abigail Sena Adjokatseh[4], Dorothy Agyemang[4], Lutterodt Bentum-Ennin[2], Ebenezer Addo Ofori[1,2], Eric Kyei-Baafour[2], Kwadwo Akyea-Mensah[2], Bright Adu[2], Gloria Ivy Mensah[5], Linda Eva Amoah[1,2] and Kwadwo Asamoah Kusi[1,2,4]**

[1] West African Centre for Cell Biology of Infectious Pathogens (WACCBIP), University of Ghana, Accra, Ghana, [2] Department of Immunology, Noguchi Memorial Institute for Medical Research, College of Health Sciences, University of Ghana, Accra, Ghana, [3] African Institute for Mathematical Sciences, Accra, Ghana, [4] Department of Biochemistry, Cell and Molecular Biology, College of Basic and Applied Sciences, University of Ghana, Accra, Ghana, [5] Department of Bacteriology, Noguchi Memorial Institute for Medical Research, College of Health Sciences, University of Ghana, Accra, Ghana

OPEN ACCESS

Edited by:
Rachel Daniels,
Harvard University, United States

Reviewed by:
Xianzhu Wu,
Penn State Hershey Children's Hospital, United States
Adrian John Frederick Luty,
Institut de Recherche pour le Développement (IRD), France

***Correspondence:**
Augustina Frimpong
afrimpong@noguchi.ug.edu.gh;
tinafrimp@gmail.com
Kwadwo Asamoah Kusi
akusi@noguchi.ug.edu.gh

Specialty section:
This article was submitted to Microbial Immunology, a section of the journal Frontiers in Microbiology

Received: 05 May 2020
Accepted: 19 October 2020
Published: 17 November 2020

Citation:
Frimpong A, Amponsah J, Adjokatseh AS, Agyemang D, Bentum-Ennin L, Ofori EA, Kyei-Baafour E, Akyea-Mensah K, Adu B, Mensah GI, Amoah LE and Kusi KA (2020) Asymptomatic Malaria Infection Is Maintained by a Balanced Pro- and Anti-inflammatory Response. Front. Microbiol. 11:559255. doi: 10.3389/fmicb.2020.559255

Background: Pro- and anti-inflammatory cytokines are important mediators of immunity and are associated with malaria disease outcomes. However, their role in the establishment of asymptomatic infections, which may precede the development of clinical symptoms, is not as well-understood.

Methods: We determined the association of pro and anti-inflammatory cytokines and other immune effector molecules with the development of asymptomatic malaria. We measured and compared the plasma levels of pro-inflammatory mediators including tumor necrosis factor-alpha (TNF-α), interferon-gamma (IFN-γ), interleukin (IL)-6, IL-12p70, IL-17A, and granzyme B, the anti-inflammatory cytokine IL-4 and the regulatory cytokine IL-10 from children with asymptomatic malaria infections (either microscopic or submicroscopic) and uninfected controls using Luminex.

Results: We show that individuals with microscopic asymptomatic malaria had significantly increased levels of TNF-α and IL-6 compared to uninfected controls. Children with either microscopic or submicroscopic asymptomatic malaria exhibited higher levels of IFN-γ, IL-17A, and IL-4 compared to uninfected controls. The levels of most of the pro and anti-inflammatory cytokines were comparable between children with microscopic and submicroscopic infections. The ratio of IFN-γ/IL-10, TNF-α/IL-10, IL-6/IL-10 as well as IFN-γ/IL-4 and IL-6/IL-4 did not differ significantly between the groups. Additionally, using a principal component analysis, the cytokines measured could not distinguish amongst the three study populations. This may imply that neither microscopic nor submicroscopic asymptomatic infections were polarized toward a pro-inflammatory or anti-inflammatory response.

Conclusion: The data show that asymptomatic malaria infections result in increased plasma levels of both pro and anti-inflammatory cytokines relative to uninfected persons. The balance between pro- and anti-inflammatory cytokines are, however, largely

maintained and this may in part, explain the lack of clinical symptoms. This is consistent with the generally accepted observation that clinical symptoms develop as a result of immunopathology involving dysregulation of inflammatory mediator balance in favor of pro-inflammatory mediators.

Keywords: microscopic, *Plasmodium*, anti-inflammatory cytokines, pro-inflammatory cytokines, asymptomatic malaria, submicroscopic

INTRODUCTION

Malaria is a protozoan infectious disease that puts more than 3 billion of the world's population at risk (WHO, 2018). Infection with *Plasmodium* may cause different manifestations of the disease based on several factors, including the quality of host acquired immunity. Manifestations of the disease range from microscopic or submicroscopic asymptomatic infections to symptomatic uncomplicated complicated malaria. A significant number of parasite-infected persons in malaria-endemic areas are asymptomatic (Bousema et al., 2014; Snow et al., 2017). These asymptomatic infections are loosely defined as individuals who present with parasites over a period of time but have no clinical symptoms of the disease and have not recently been treated with anti-malarial drugs (Lindblade et al., 2013). These infections manifest as a result of repeated exposure to the parasite over a period resulting in the acquisition of anti-disease immunity. In addition, tolerance to the infection may be multi-factorial based on parasite and host factors (Laishram et al., 2012; Galatas et al., 2016). Nevertheless, investigating the immunological mechanisms that explain asymptomatic infections remains important in order to understand disease etiology (Langhorne et al., 2008; Wammes et al., 2013). Aside the presence of parasites in the host, a significant portion of the clinical symptoms of the disease are believed to be caused by parasite-induced host immune responses, typically those that promote inflammation (Othoro et al., 1999; Prakash et al., 2006).

Naturally acquired antibody responses to key parasite antigens have been noted to play significant roles in the acquisition of anti-malarial immunity despite being shown to be short-lived (White et al., 2014; Partey et al., 2018). In addition, cellular responses to malaria, which may involve various lymphocyte subsets and the cytokines they secrete, have been found to either mediate protection or impede the acquisition of immunity by down-regulating protective immune responses (Frimpong et al., 2018, 2019; Nlinwe et al., 2018; Kurup et al., 2019).

These cytokines may also be secreted by other immune cell subsets such as monocytes or macrophages. Pro-inflammatory cytokines such as IFN-γ and TNF-α produced by Th1 cells are signaling molecules that also help in the recruitment of other cell subsets such as monocytes to phagocytose infected erythrocytes (Akdis et al., 2011). In addition, IL-12p70 produced mainly by macrophages and dendritic cells aid in the activation of T cells and polarizing the immune response to pro-inflammatory responses (Kumar et al., 2019). Also, other pro-inflammatory cytokines like IL-17A produced by Th17 cells and other cell types have been observed to be upregulated during *P. vivax* infection and aid in the recruitment of neutrophils to sites of inflammation (Bueno et al., 2012). In malaria, an early increase in the levels of these pro-inflammatory cytokines has been associated with parasite clearance and plays an important role in resistance to infections (Angulo and Fresno, 2002; Ibitokou et al., 2014). Nevertheless, subsequent uncontrolled levels have been associated with the development of immunopathology which is often found in severe forms of the disease (Mshana et al., 1991; Gimenez et al., 2003; Mackintosh et al., 2004). Therefore, to circumvent the impact of high levels of pro-inflammatory cytokines, anti-inflammatory cytokines such as IL-4, IL5, and IL-13 are secreted to regulate inflammation (Torre et al., 2002). Also, the immunoregulatory cytokines IL-10 and tumor growth factor-beta (TGF-β) have been shown to regulate the levels of both pro- and anti-inflammatory mediators in an effort to restore homeostatic balance (Kumar et al., 2020). On these basis, several studies have proposed that the ratio of pro-inflammatory to anti-inflammatory cytokines as significant predictors of disease outcome (Kurtzhals et al., 1998; Othoro et al., 1999; Kidd, 2003; Sinha et al., 2010; Farrington et al., 2017). While these are well-described for individuals who are symptomatic (Mshana et al., 1991; Kurtzhals et al., 1998; Gimenez et al., 2003; Farrington et al., 2017), there have been no distinctive studies on characterizing the ratio of pro-inflammatory:anti-inflammatory cytokines to determine if asymptomatic infections, whether microscopic or submicroscopic, are polarized by pro-inflammatory or anti-inflammatory responses.

In addition, previous studies have associated asymptomatic malaria with relatively decreased levels of pro-inflammatory responses, relative to the regulatory cytokine IL-10 (Wilson et al., 2010; Ibitokou et al., 2014; de Jong et al., 2017). In pregnant women, it was observed that high levels of IL-10 was a good predictor of infection and maternal anemia (Ibitokou et al., 2014). IL-10 is an immunoregulatory cytokine produced by Th1, Th2, B cells, and some innate cells (Wilson et al., 2010; Ibitokou et al., 2014; de Jong et al., 2017). This regulatory cytokine plays important role in regulating the detrimental effect of most pro-inflammatory cytokines such as TNF-α and IL-12 in a dose-dependent manner and being a significant predictor of parasitemia levels (Kumar et al., 2019). Despite these findings which have led to the postulation that asymptomatic malaria is largely associated with anti-inflammatory responses (Ochola-Oyier et al., 2019), others have reported a suppressed regulatory immune response in asymptomatic malaria (Wammes et al., 2013; de Jong et al., 2017). These together imply that understanding the immune mechanisms associated with asymptomatic malaria needs to be investigated.

In this study, we tested the hypothesis that asymptomatic infections are characterized by increased levels of regulatory or anti-inflammatory cytokines compared to the levels of pro-inflammatory mediators. We determined the levels of pro- and anti-inflammatory mediators as well as that of the regulatory cytokine IL-10 in children with microscopic or submicroscopic asymptomatic malaria and compared to levels in uninfected controls. Additionally, we estimated pro-inflammatory: anti-inflammatory cytokine ratios to determine whether asymptomatic infections are skewed toward any one of these inflammatory mediators.

MATERIALS AND METHODS

Ethics Statement

Ethical approval for the study was obtained from the Institutional Review Board at the Noguchi Memorial Institute for Medical Research, University of Ghana (No. 089/14-15). Written informed consent and assent were properly obtained from participants before sample collection.

Study Site

Participants for the study were recruited from Obom, a semi-rural community in the Ga South Municipality of the Greater Accra Region of Ghana. Malaria transmission in the community is perennial with peak transmission occurring from May to September. The parasite prevalence in the area as estimated by microscopy is about 35% (Amoah et al., 2016).

Study Design and Sample Collection

This was a cross-sectional study where archived samples obtained from community children under 15 years of age were used. About 5 ml of peripheral venous blood was collected from each volunteer into EDTA tubes. Parasite density was determined using Giemsa-stained thick blood smears by counting the number of parasites per 200 white blood cell counts. Samples were processed and plasma aliquots were stored in Eppendorf tubes at −80°C until needed for the experiment. Participants who were positive for *Plasmodium* infection via microscopy but showed no clinical symptoms were classified as having microscopic asymptomatic infections, whereas, children who were negative via microscopy but positive via PCR were classified as having a submicroscopic asymptomatic infection. Additionally, children who were negative for microscopy and PCR were classified as uninfected and used as controls.

Identification of Submicroscopic Infections

Genomic DNA was extracted using the Zymo DNA Kit (Zymo Research, Irvine, United States) according to the manufacturer's protocol for whole blood samples. Briefly, 100 μl of whole blood was lysed with 400 μl of lysis buffer before running over the spin column. The DNA was eluted using 100 μl of elution buffer and stored at 4°C for immediate use.

The *P. falciparum* 18s rRNA was amplified from 20 to 40 ng of the extracted DNA in a 15 μl reaction volume. The PCR reaction was made up of 2.5 mM $MgCl_2$, 200 nM deoxynucleoside triphosphate mix (dNTPs), 1 U of Onetaq^{TM}, DNA polymerase (NEB, United Kingdom) and 250 nM each of forward and reverse primers (rPLUS and rPLU; Ayanful-Torgby et al., 2018) and rFAL1(F) and rFAL2(R) for the nested reaction (Adjah et al., 2018). Genomic DNA from 3D7 strain from *P. falciparum* (MRA 102G) and double distilled water was used as positive and negative controls, respectively, for the amplification.

The PCR amplification products were resolved on 2.0% agarose gels stained with 0.5 μg/ml ethidium bromide. The gels were observed under ultraviolet light after electrophoresis. The gel image was captured using Vilber Lourmat Gel Dock System (Vilber Wielandstrasse, Germany).

Multiplex Immunoassay

Plasma samples were defrosted on ice. Plasma was diluted twofold for the assay. The levels of cytokines were determined using a magnetic bead-based multiplex assay, which enables the quantification of multiple cytokines/analytes in the same plasma sample using a 96 well plate format. A human 8-plex assay kit was used to quantify levels of pro-inflammatory mediators (granzyme B, IFN-γ,-6, IL-12p70, IL-17A, and TNF-α), the anti-inflammatory cytokine IL-4 and the regulatory cytokine IL-10 (R&D Systems, United States). Sample dilutions, reagents, and standards were all prepared according to the manufacturer's protocol. All blanks and standards were prepared in duplicate on each plate to determine uniformity in the assay. The plates were read using the LUMINEX® 200^{TM} system, running on the Xponent 3.1 software. Analyte levels were reported as the median fluorescent intensity values.

Statistical Analysis

All data analyses were performed using the Prism version 6.01 (GraphPad Software, Inc.) and the R statistical software version 3.5.2 (R Foundation for Statistical Computing). Categorical data variables were analyzed using the Chi-square test. Continuous variables were analyzed using Kruskal–Wallis or One-way ANOVA, for data involving three groups, whereas, Mann–Whitney *U*-test was used for data comparison between two groups. Both Kruskal–Wallis and Mann–Whitney *U*-tests were used to analyze data that were not normally distributed. Comparison between three groups was followed by a Dunn's *post-hoc* test or a Bonferroni test to correct for multiple comparisons. The association between cytokines was determined using Spearman's rank correlation test. Multivariate analyses were performed using a generalized additive model using the mgcv package in R (Wood and Wood, 2015) with a likelihood ratio test to determine cytokines that were predictive of age and parasitemia. A principal component analysis was used to determine if the cytokine profiles could be used to distinguish the study population; uninfected children, children who had microscopic or submicroscopic infection. Statistical significance was set at $P < 0.05$.

RESULTS

Demographic and Baseline Characteristics of Participants

Samples from a total of 78 participants, consisting of 18 uninfected controls and 60 children with asymptomatic malaria infections (22 with submicroscopic and 38 microscopic parasite densities) were used in this study. After diagnosis via microscopy and PCR, the proportion of males to females was not different among participants in the various groups ($p = 0.84$). The age distribution differed significantly between the study cohorts ($p = 0.021$); children with submicroscopic asymptomatic malaria were significantly older than uninfected children ($p = 0.017$) but not children with microscopic asymptomatic malaria. Also, hemoglobin levels were comparable among the study participants ($p = 0.98$). Likewise, no statistically significant difference was observed in the temperatures measured among the participants in the various groups (**Table 1**).

Elevated Levels of TNF-α and IL-6 in Children With Microscopic Asymptomatic Malaria

High levels of pro-inflammatory cytokines have been associated with the development of clinical disease whereas increased levels of IL-6 have been observed in submicroscopic malaria in pregnancy. In this study we observed that the levels of pro-inflammatory cytokines TNF-α and IL-6 were increased significantly only in children with microscopic asymptomatic malaria compared to uninfected controls ($p = 0.0006$; $p = 0.027$, respectively), whereas, levels in children with microscopic parasitemia were comparable to levels in children with submicroscopic parasitemia. Also, levels of both TNF-α and IL-6 in children with submicroscopic infections were comparable to levels in uninfected controls ($p > 0.05$; **Figures 1A,B**).

Levels of IFN-γ and IL-17A Are Increased in Children With Microscopic and Submicroscopic Asymptomatic Malaria

For infected children with either microscopic or submicroscopic asymptomatic malaria, levels of the pro-inflammatory cytokine IFN-γ were significantly higher compared to levels in uninfected controls (**Figure 1C**). However, levels in children with microscopic asymptomatic parasitemia did not differ significantly from levels in children with submicroscopic asymptomatic parasitemia ($p > 0.05$). Similarly, levels of the pro-inflammatory mediator IL-17A (**Figure 1D**) were increased significantly in children with microscopic and submicroscopic infections compared to controls ($p = 0.027$ and $p = 0.027$, respectively).

Meanwhile, levels of IL-12p70 did not differ between any of the groups ($p = 0.53$; **Figure 1E**), whereas, levels of granzyme B were found to be significantly lower in children with microscopic ($p = 0.027$) and submicroscopic ($p = 0.003$; **Figure 1F**) parasitemia compared to uninfected controls.

Increased Levels of IL-4 in Children With Microscopic and Submicroscopic Asymptomatic Malaria

The levels of anti-inflammatory cytokines, IL-4 and IL-10 in children with microscopic asymptomatic malaria, submicroscopic asymptomatic malaria and uninfected controls were compared (**Figure 2**). It was observed that levels of IL-4 were increased significantly in children with either microscopic or submicroscopic asymptomatic malaria compared to uninfected controls ($p = 0.006$; $p = 0.006$) However, levels of IL-4 were comparable between children with microscopic and submicroscopic asymptomatic infections ($p = 0.57$). For levels of IL-10, there was no significant difference between the various groups ($p = 0.23$).

IL-6 and IL-10 Are Major Predictors of Parasitemia in Children With Microscopic Asymptomatic Malaria

To identify cytokines that may correlate with each other during infection, we compared the interrelationship between the cytokines in both microscopic (**Table 2**) and submicroscopic asymptomatic malaria (**Supplementary Table S1**). For children with microscopic asymptomatic malaria, IL-6 was found to positively correlate with TNF-α ($r = 0.59$, $p < 0.0001$), IL-4 ($r = 0.39$, $p = 0.017$), and IL-10 ($r = 0.50$, $p = 0.002$). Similarly, TNF-α also positively correlated with anti-inflammatory cytokines IL-4 ($r = 0.41$, $p = 0.011$) and IL-10 ($r = 0.39$,

TABLE 1 | Demographic and clinical characteristics of the study participants.

Characteristics	Controls	Submicroscopic	Microscopic	*P*-value
Sample size (n)	18	22	38	
Sex (n)				
Male	8	11	16	0.84[a]
Female	10	11	22	
Age (IQR) years	9 (6.75–11)	11.5 (9–13.25)	10.5 (9–12)	**0.021**[b]
Parasitemia (IQR), /μl	NA	NA	935.5 (269.3–1990)	NA
Hemoglobin, level (IQR), g/dl	10.85 (10.68–12.0)	11.05 (10.65–12.03)	11.05 (10.5–12.7)	0.98[b]
Temperature (IQR), °C	36.8 (36.55–36.85)	36.80 (36.6–36.9)	36.9 (36.6–36.9)	0.49[b]

IQR, interquartile range; NA, not applicable. [a]Chi square test. [b]Kruskal–Wallis test.

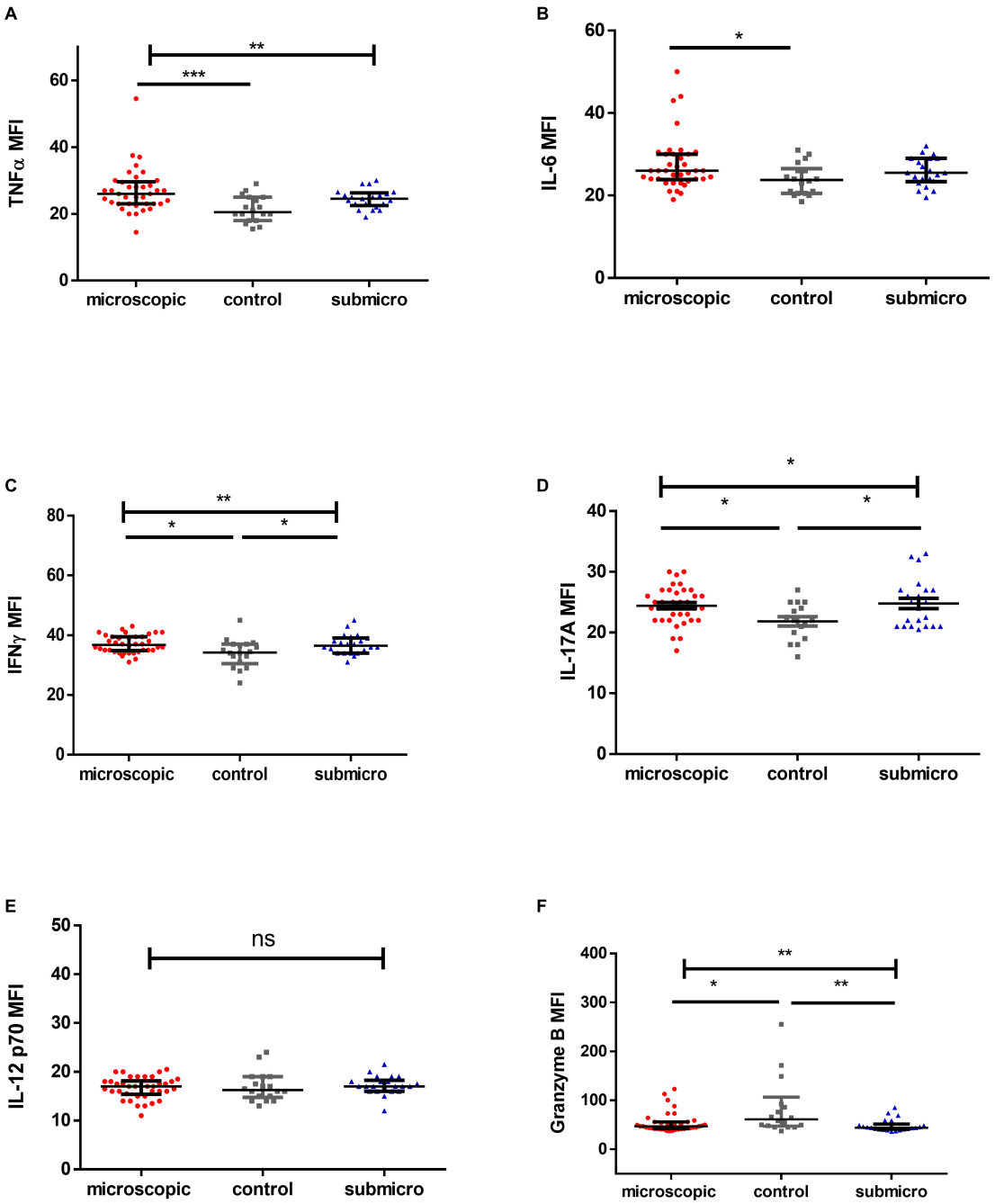

FIGURE 1 | Profile of pro-inflammatory mediators during microscopic and submicroscopic malaria. Scatter plot graphs are plotted showing the median fluorescence intensities (MFI) of **(A–F)** TNF-α, IL-6, IFN-γ, IL-17A, IL-12p70, and Granzyme B in plasma samples collected from uninfected controls ($n = 18$), patients with microscopic asymptomatic malaria ($n = 38$) and submicroscopic malaria ($n = 22$). Plots show median and interquartile ranges. Significant differences are denoted by $^{*}p < 0.05$, $^{**}p < 0.01$, $^{***}p < 0.001$, ns = not significant.

$p = 0.016$). Also, IL-4 and IL-10 were positively correlated ($r = 0.49$, $p = 0.003$). However, only granzyme B correlated negatively with IL-17A ($r = -0.35$, $p = 0.032$). In addition, in children with submicroscopic infections, IL-12p70 correlated negatively with IL-10 ($r = -0.52$, $p = 0.012$), whereas, granzyme B correlated positively with IL-4 ($r = 0.62$, $p = 0.002$) (**Supplementary Table S1**). However, we observed that using principal component analysis, the cytokine profiles could not differentiate children with either microscopic or submicroscopic asymptomatic malaria from uninfected controls (**Figure 3**).

Also, to determine the impact of parasitemia on these cytokines, we initially determined if parasitemia correlated

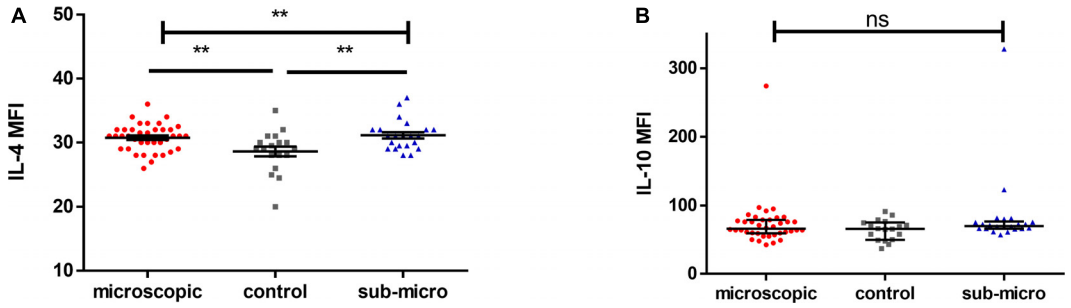

FIGURE 2 | Evaluating the levels of anti-inflammatory cytokines. Scatter plots showing the median fluorescence intensities (MFI) of **(A,B)** IL-4 and IL-10 in plasma samples collected from uninfected controls (n = 18) and patients with microscopic asymptomatic malaria (n = 38) and submicroscopic malaria (n = 22). Plots show median and interquartile ranges. Significant differences are denoted by $p < 0.01$**, ns = not significant.

TABLE 2 | Correlation between the pro- and anti-inflammatory cytokines in children with microscopic asymptomatic infections.

	Granzyme B	IFN-γ	TNF-α	IL-6	IL-12 p70	IL-4	IL-10	IL-17A
Granzyme B	1							
IFN-γ	−0.07	1						
TNF-α	−0.11	0.22	1					
IL-6	−0.11	0.15	**0.59******	1				
IL-12 p70	0.04	−0.02	−0.19	−0.14	1			
IL-4	−0.07	0.21	**0.41***	**0.39***	0.30	1		
IL-10	−0.08	−0.25	**0.39***	**0.50****	0.16	**0.47****	1	
IL-17A	**−0.35***	0.25	−0.10	0.17	−0.01	0.14	−0.05	1

*Significant associations are in bold and denoted by *$p < 0.05$, **$p < 0.01$, ****$p < 0.0001$.*

with any of the cytokines measured and only IL-6 correlated significantly with parasitemia ($r = 0.36$, $p = 0.029$; **Supplementary Figure S1**). Furthermore, using a generalized additive model and a likelihood ratio test to determine the impact of parasitemia on the secretion of these cytokines, parasitemia seems to be a major predictor of IL-10 and IL-6 levels (**Table 3**).

Association Between Cytokine Levels and Age

It has been reported that cytokine levels during infection may vary with age (Mshana et al., 1991; Farrington et al., 2017) and since age differed significantly in our study population, we determined whether cytokine responses are impacted by age. It was observed that none of the cytokine levels were significantly associated with age in children with microscopic or submicroscopic malaria infection. However, in a multivariate analysis using a generalized additive model, age was a good predictor of granzyme B ($p = 0.002$) and IL-6 ($p = 0.04$) levels (**Supplementary Table S2**).

Pro-inflammatory/Anti-inflammatory Ratio Does Not Differ Between Asymptomatic Children and Uninfected Controls

To determine whether pro-inflammatory cytokines or regulatory cytokines dominate asymptomatic infections, the ratio of IFN-γ, TNF-α and IL-6 to IL-4 and IL-10 were measured and compared with that in uninfected controls. We first compared the ratio of IFN-γ/IL-4, TNF-α/IL-4, and IL-6/IL-4. There were no significant differences in IFN-γ/IL-4 and IL-6/IL-4 ratios when compared between microscopic or submicroscopic asymptomatic children and controls ($p > 0.05$ in all cases). The only exception was for TNF-α/IL-4 which was significantly increased in children with microscopic asymptomatic malaria compared to uninfected controls using the Mann-Whitney test ($p = 0.044$). Secondly, we also compared the ratio of IFN-γ/IL-10, TNF-α/IL-10, and IL-6/IL-10. It was observed that the ratios of IFN-γ/IL-10, TNF-α/IL-10, and IL-6/IL-10 did not differ between children with microscopic asymptomatic malaria, submicroscopic asymptomatic malaria and uninfected controls (**Figure 4**). Thus, although most cytokine levels were increased in response to infection, the balance between pro- and anti-inflammatory cytokines was largely maintained in the infected group when compared to the uninfected controls.

DISCUSSION

Asymptomatic malaria remains a major challenge in malaria control elimination programs due to its significant impact on disease transmission (Alves et al., 2005; Schneider et al., 2007). Even though it has been noted that asymptomatic malaria may confer partial immunity against malaria (Tran et al., 2013), it can also be a precursor to the development of clinical disease (Njama-Meya et al., 2004). Cytokines produced by

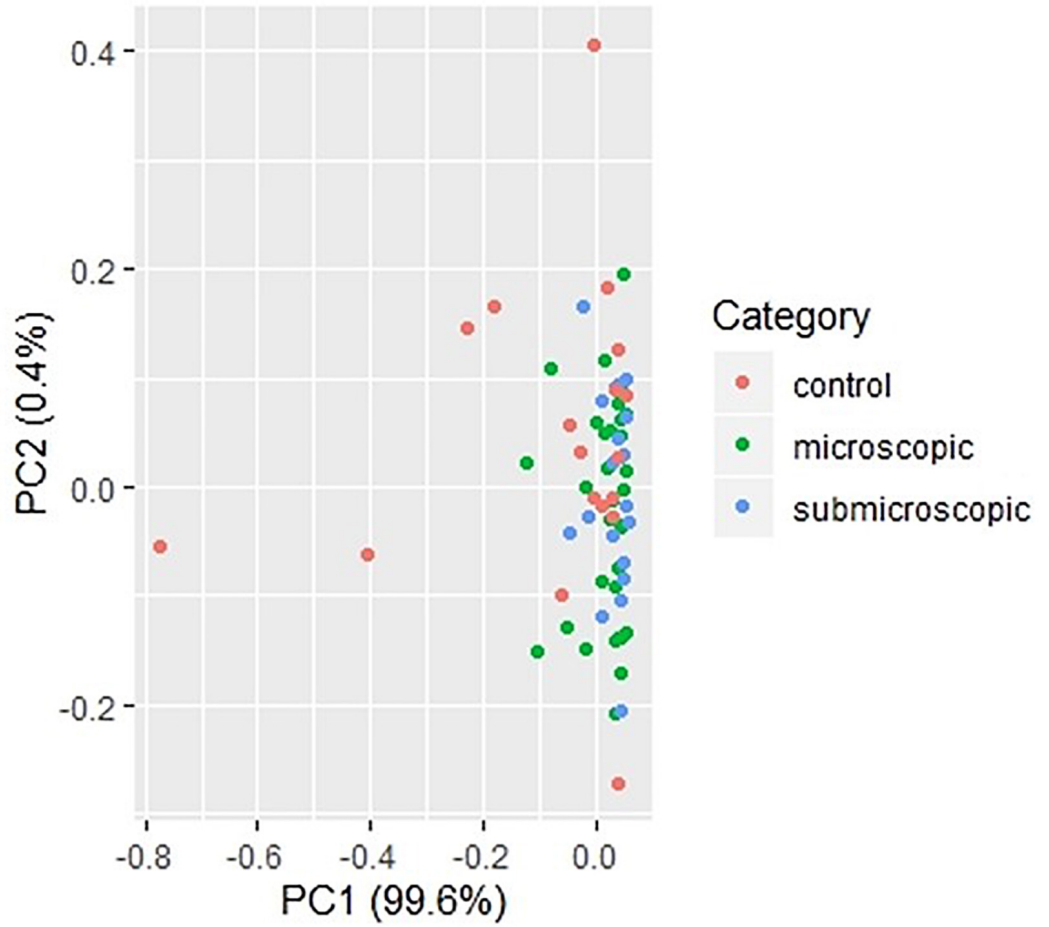

FIGURE 3 | Principal component analysis of cytokine responses in children with microscopic, submicroscopic infections, and uninfected controls. A principal component analysis of cytokine profiles in uninfected (n = 18), microscopic asymptomatic infection (n = 38) and submicroscopic asymptomatic infected (n = 22) children. Uninfected controls are indicated with the red dots, microscopic with green dots and submicroscopic asymptomatic malaria with blue dots.

different cell types are the normal expected immune response against invading pathogens but can also drive immunopathology. Various studies have shown that a disproportionate increase in the levels of pro-inflammatory cytokines can lead to an immune-associated pathology and cause the progression of asymptomatic infections to febrile and severe forms (Othoro et al., 1999; Jagannathan et al., 2014; Mandala et al., 2017). In this study, we determined the impact of asymptomatic malaria infections on the secretion of pro- and anti-inflammatory cytokines and how this may affect disease outcome. We observed increased levels of cytokines such as TNF-α and IL-6 in children with microscopic asymptomatic malaria, whereas, IFN-γ, IL-17A, and IL-4 levels were increased in infected children with microscopic or submicroscopic asymptomatic malaria compared with uninfected controls. Also, levels of granzyme B were decreased in children with either microscopic or submicroscopic infections compared to uninfected controls whilst levels of IL-10 and IL-12p70 were comparable between infected and uninfected children.

TABLE 3 | The association between inflammatory mediators and parasitemia for children with microscopic asymptomatic infection.

Covariates	*P*-value in model	Deviance explained (%)	LR test *p*-value
Granzyme B	0.84	60.3	0.82
IFN-γ	0.96	60.4	0.96
TNF-α	0.84	60.3	0.82
IL-6	**0.019**	51.9	**0.007**
IL-12p70	0.77	60.2	0.73
IL-4	0.22	58.3	0.16
IL-10	**0.004**	47.4	**0.001**
IL-17A	0.98	60.4	0.98

Significant associations are in bold.

TNF-α induces reactive oxygen species, cell death and the secretion of other cytokines such as IL-1 and IL-6. In addition, it regulates the production of IL-12 by macrophages, primes neutrophils and serves as a cofactor for IL-12 induced IFN-γ production (Malaguarnera and Musumeci, 2002). Studies have shown that increasing levels of TNF-α and IL-6 in malaria

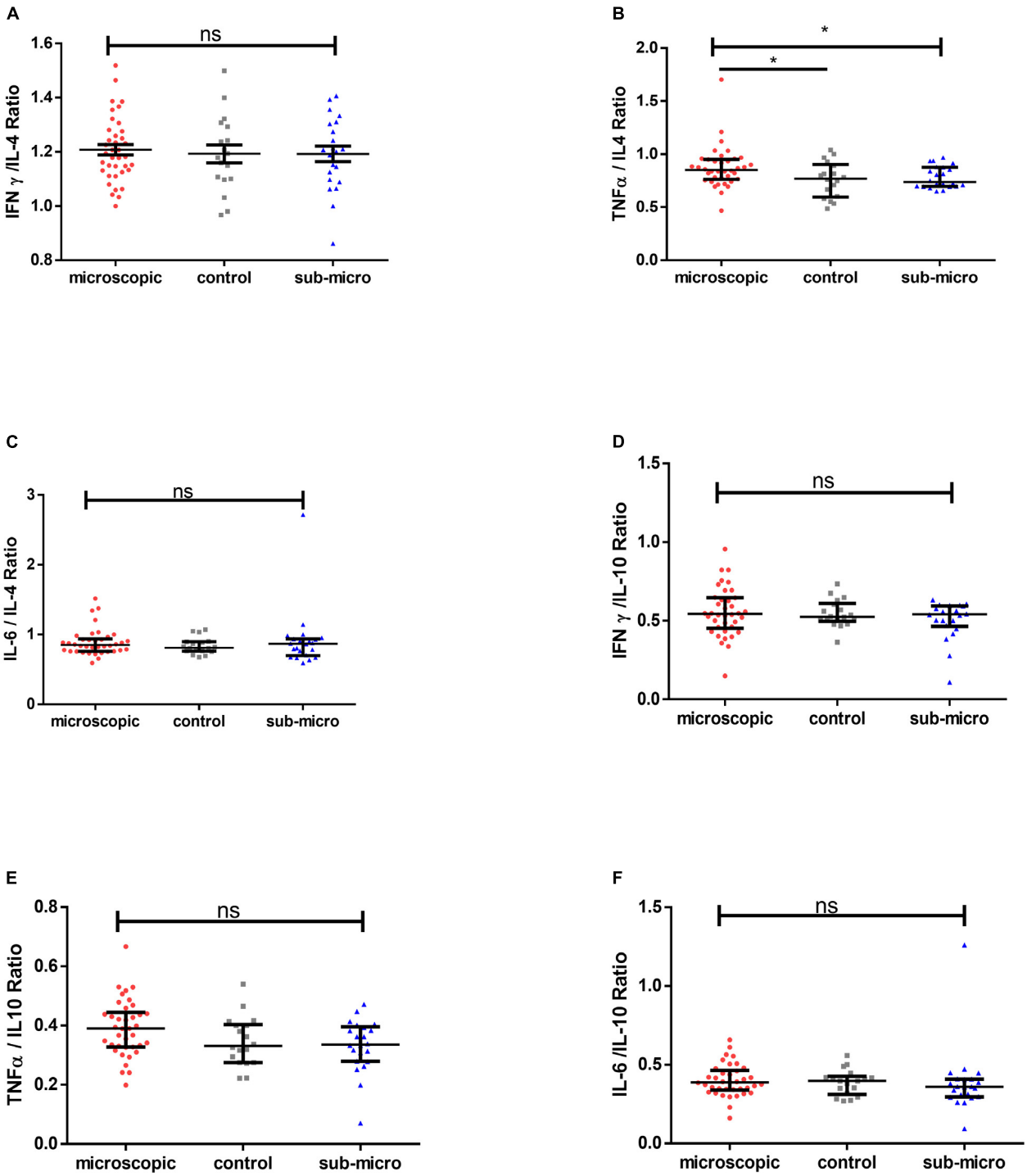

FIGURE 4 | Comparable pro-inflammatory/anti-inflammatory cytokine ratios in microscopic, submicroscopic asymptomatic infected and uninfected controls. The graphs **(A–F)** shows the ratio of IFN-γ/IL-4, TNF-α/IL-4, IL-6/IL-4 and IFN-γ/IL-10, TNF-α/IL-10, IL-6/IL-10 in uninfected controls (n = 18), microscopic (n = 38), and submicroscopic asymptomatic malaria infection (n = 22). Data are displayed as scatter plots showing median and interquartile ranges. Significant values are indicated by $^*p < 0.05$.

are associated with the cytoadherence of infected erythrocytes leading to the development of febrile disease (Lyke et al., 2004; Robinson et al., 2009; Cruz et al., 2016). Also, increasing IL-6 levels mediates the production of acute-phase reactant proteins such as C-reactive proteins (CRP) and secretory phospholipase A2 (sPLA2) (Juffrie et al., 2001) whereas moderate levels can

reduce parasitemia (Lyke et al., 2004). However, it remains to be understood whether TNF-α association with immune pathology is due to its ability to induce IL-1, IL-6, and IFN-γ secretion. In addition, others have reported moderate levels of TNF-α to be associated with parasite control by stimulating monocyte to phagocytose infected erythrocytes as well as activate calcium signaling in human malaria parasites (Aggarwal, 2003; Cruz et al., 2016; Oyegue-Liabagui et al., 2017). In our study, we observed that children with microscopic infections had increased levels of TNF-α and IL-6 compared to uninfected controls and children with submicroscopic infections. Probably denoting that with increasing parasitemia, TNF-α as well as IL-6 may work synergistically to decrease parasitemia levels.

Protective mechanisms induced by IFN-γ have been reported during liver-stage and blood-stage infections (D'Ombrain et al., 2008; Robinson et al., 2009) with predominant sources of this cytokine being T cells and NK cells (Dodoo et al., 2002; D'Ombrain et al., 2008; Jagannathan et al., 2017). In addition, Increasing levels of IL-17A have been associated with inflammation in malaria and mediating protection in various infectious diseases through the recruitment of immune cells such as neutrophils and mediate the production of several pro-inflammatory cytokines (Kelly et al., 2005; Oyegue-Liabagui et al., 2017). Here, we show that asymptomatic infection with *Plasmodium* is associated with higher levels of IFN-γ and IL-17A. However, neither of these cytokines correlated with age or parasitemia. Nonetheless, the increased levels observed in the asymptomatic malaria group may indicate that IFN-γ and IL-17A are associated with on-going inflammation which has a significant impact on disease pathogenesis as well as the development of anti-disease immunity.

It has previously been shown that asymptomatic infections are characterized by limited T cell activation and regulation (Frimpong et al., 2018). Likewise, levels of regulatory T cells (Tregs) (Boyle et al., 2015) and activated Tregs did not differ significantly between children with asymptomatic malaria and uninfected controls (Frimpong et al., 2018). Interestingly, other studies have observed that individuals with asymptomatic *P. vivax* infections had lower levels of the Treg cytokine IL-10 compared to controls (Jangpatarapongsa et al., 2008; Bueno et al., 2012) whereas, a study by Othoro et al. (1999) found no significant difference in levels between asymptomatic cases and uninfected controls. Also, IL-10 levels have been noted to decrease with increasing age (Boyle et al., 2017). Therefore, the lack of significant difference observed in the levels of IL-10 in the current study may be as a result of the age differences. Probably, it could indicate that IL-10 may not be the sole anti-inflammatory cytokine in mediating inflammation in asymptomatic malaria and its production may be transient during asymptomatic malaria. It may also suggest that IL-10 production is directly affected by levels of parasitemia since IL-10 was the only anti-inflammatory cytokine that was a good predictor of parasitemia and it may be secreted in a dose dependent manner. This could also imply that increasing IL-10 levels may be associated with the development of febrile disease (Farrington et al., 2017; Oyegue-Liabagui et al., 2017). Even though both IL-10 and IL-12p70 levels did not differ among the study population, they were negatively correlated in children with submicroscopic infections indicating the inhibitory effect of IL-10 on IL-12p70.

On the other hand, IL-4 was found to increase significantly in children with microscopic and submicroscopic malaria compared to controls. IL-4 like IL-10 has an important role in immunoregulation by downregulating the secretion and activity of pro-inflammatory cytokines like TNF-α, IL-6, and IL-17A (Riley et al., 2006). The positive relationship between IL-4 and IL-10 and these pro-inflammatory cytokines (TNF-α and IL-6) in children with microscopic infections, supports the counter-regulatory activity of these anti-inflammatory cytokines on TNF-α and IL-6. Also, IL-4 has been reported to suppress the upregulation of granzyme B in T cells, thereby reducing induced cell death (Riou et al., 2006). Additionally, decreasing levels of granzyme B has been associated with a Th2 response (Devadas et al., 2006), whereas, increasing levels in malaria have been observed in children with severe and uncomplicated infections (Kaminski et al., 2019). Here the lower levels of granzyme B observed in children with malaria infection and the upregulation of IL-4 support the immunoregulatory activity of IL-4 on granzyme B. Furthermore, the positive correlation observed between both IL-4 and granzyme B in children with submicroscopic infections may indicate that probably at the sub-patent level of infection, the effect of IL-4 on regulating granzyme B expression is reduced. Likewise, the negative correlation observed between Granzyme B and IL-17A may have resulted from the low levels of granzyme B observed in malaria-infected children.

The outcome of various diseases in humans may largely be based on a pro- or anti-inflammatory response balance, since these produce cytokines with diverse functions and outcome. Asymptomatic malaria has been proposed to be associated with anti-inflammatory responses (Ochola-Oyier et al., 2019). We tested the hypothesis whether there is a polarization toward immunoregulatory cytokines during asymptomatic infection. The data, however, demonstrated that both pro-inflammatory and anti-inflammatory cytokines are upregulated in asymptomatic infections, however, the ratios of pro-inflammatory/anti-inflammatory responses were comparable between the study groups. This may suggest that a balance between pro- and anti-inflammatory cytokines may be responsible for the absence of clinical disease symptoms despite the presence of parasites.

The study had some limitations since it was cross-sectional and participants were sampled at a single time point. Also, participants were not followed to determine if any of them progressed to febrile disease and to assess trends in the cytokine profile during asymptomatic infection and disease onset in the same individuals. Also, the presence of other infectious diseases such as helminth co-infections which were unaccounted for may account for some of the differences in the cytokine profile since they are common in children of school-going age (Brooker et al., 2007; Salazar-Castañón et al., 2018). Nevertheless, we have been able to show that asymptomatic malaria infections are characterized by a concomitant upregulation of both pro- and anti-inflammatory cytokines, specifically TNF-α, IFN-γ, IL-6, IL-17A, and IL-4 as assessed in this study. The observed maintenance of a balance between pro- and anti-inflammatory

mediators may in part explain the asymptomatic status of infected children. Thus, disease symptoms will only develop when there is a perturbation of this balance, especially toward an increased pro-inflammatory response which has been severally shown to have immunopathological consequences.

CONCLUSION

The data show that despite the increase in both pro- and anti-inflammatory mediators in children with asymptomatic microscopic and submicroscopic infections, there is a homeostatic maintenance of the balance between pro- and anti-inflammatory cytokines. This outcome is very consistent with the numerously reported observations that an imbalance in the levels of pro- and anti-inflammatory cytokines are an essential trigger of febrile disease in infected persons.

DATA AVAILABILITY STATEMENT

The raw data supporting the conclusions of this article will be made available by the authors, without undue reservation.

ETHICS STATEMENT

The studies involving human participants were reviewed and approved by the Institutional Review Board of the Noguchi Memorial Institute for Medical Research at the University of Ghana. Written informed consent to participate in this study was provided by the participants' legal guardian/next of kin.

AUTHOR CONTRIBUTIONS

KK and AF conceived the idea and designed the experiments and supervised the work. JA, AA, DA, and LB-E performed the experiments in the study and were assisted by EO, EK-B, and KA-M. AF, BA, GM, LA, and KK wrote the manuscript. All authors read and approved the final manuscript.

FUNDING

AF and EO were both supported by a WACCBIP-World Bank African Centres of Excellence Ph.D. and Masters Fellowship Grant (ACE02-WACCBIP: Awandare).

ACKNOWLEDGMENTS

We are grateful to the children, parents, and guardians who participated in this study. We are also grateful to the Obom Health Directorate, Sophia Ampah, and members of the Gametocytogenesis team at the Immunology Department, NMIMR.

SUPPLEMENTARY MATERIAL

The Supplementary Material for this article can be found online at: https://www.frontiersin.org/articles/10.3389/fmicb.2020.559255/full#supplementary-material

REFERENCES

Adjah, J., Fiadzoe, B., Ayanful-Torgby, R., and Amoah, L. E. (2018). Seasonal variations in *Plasmodium falciparum* genetic diversity and multiplicity of infection in asymptomatic children living in southern Ghana. *BMC Infect. Dis.* 18:432. doi: 10.1186/s12879-018-3350-z

Aggarwal, B. B. (2003). Signalling pathways of the TNF superfamily: a double-edged sword. *Nat. Rev. Immunol.* 3, 745–756. doi: 10.1038/nri1184

Akdis, M., Burgler, S., Crameri, R., Eiwegger, T., Fujita, H., Gomez, E., et al. (2011). Interleukins, from 1 to 37, and interferon-γ: receptors, functions, and roles in diseases. *J. Allergy Clin. Immunol.* 127, 701–721.e70.

Alves, F. P., Gil, L. H., Marrelli, M. T., Ribolla, P. E., Camargo, E. P., and Da Silva, L. H. (2005). Asymptomatic carriers of *Plasmodium* spp. as infection source for malaria vector mosquitoes in the Brazilian Amazon. *J. Med. Entomol.* 42, 777–779. doi: 10.1093/jmedent/42.5.777

Amoah, L. E., Opong, A., Ayanful-Torgby, R., Abankwa, J., and Acquah, F. K. (2016). Prevalence of G6PD deficiency and *Plasmodium falciparum* parasites in asymptomatic school children living in southern Ghana. *Malaria J.* 15:388.

Angulo, I., and Fresno, M. (2002). Cytokines in the pathogenesis of and protection against malaria. *Clin. Diagn. Lab. Immunol.* 9:1145. doi: 10.1128/cdli.9.6.1145-1152.2002

Ayanful-Torgby, R., Quashie, N. B., Boampong, J. N., Williamson, K. C., and Amoah, L. E. (2018). Seasonal variations in *Plasmodium falciparum* parasite prevalence assessed by varying diagnostic tests in asymptomatic children in southern Ghana. *PLoS One* 13:e0199172. doi: 10.1371/journal.pone.0199172

Bousema, T., Okell, L., Felger, I., and Drakeley, C. (2014). Asymptomatic malaria infections: detectability, transmissibility and public health relevance. *Nat. Rev. Microbiol.* 12:833. doi: 10.1038/nrmicro3364

Boyle, M. J., Jagannathan, P., Bowen, K., McIntyre, T. I., Vance, H. M., Farrington, L. A., et al. (2017). The development of *Plasmodium falciparum*-specific IL10 CD4 T cells and protection from Malaria in children in an Area of high malaria transmission. *Front. Immunol.* 8:1329. doi: 10.3389/fimmu.2019.01329

Boyle, M. J., Jagannathan, P., Farrington, L. A., Eccles-James, I., Wamala, S., McIntyre, T. I., et al. (2015). Decline of FoxP3+ regulatory CD4 T cells in peripheral blood of children heavily exposed to malaria. *PLoS Pathog.* 11:e1005041. doi: 10.1371/journal.pone.1005041

Brooker, S., Akhwale, W., Pullan, R., Estambale, B., Clarke, S. E., Snow, R. W., et al. (2007). Epidemiology of plasmodium-Helminth co-infection in Africa: populations at risk, potential impact on anemia, and prospects for combining control. *Am. J. Trop. Med. Hyg.* 77, 88–98. doi: 10.4269/ajtmh.2007.77.88

Bueno, L. L., Morais, C. G., Lacerda, M. V., Fujiwara, R. T., and Braga, ÉM. (2012). Interleukin-17 producing T helper cells are increased during natural Plasmodium vivax infection. *Acta Trop.* 123, 53–57. doi: 10.1016/j.actatropica.2012.02.071

Cruz, L. N., Wu, Y., Ulrich, H., Craig, A. G., and Garcia, C. R. S. (2016). Tumor necrosis factor reduces *Plasmodium falciparum* growth and activates calcium signaling in human malaria parasites. *Biochim. Biophys. Acta* 1860, 1489–1497. doi: 10.1016/j.bbagen.2016.04.003

de Jong, S. E., Asscher, V. E. R., Wammes, L. J., Wiria, A. E., Hamid, F., Sartono, E., et al. (2017). Longitudinal study of changes in γδ T cells and CD4(+) T cells upon asymptomatic malaria infection in Indonesian children. *Sci. Rep.* 7:8844.

Devadas, S., Das, J., Liu, C., Zhang, L., Roberts, A. I., Pan, Z., et al. (2006). Granzyme B is critical for T Cell receptor-induced cell death of Type 2 helper T cells. *Immunity* 25, 237–247. doi: 10.1016/j.immuni.2006.06.011

Dodoo, D., Omer, F., Todd, J., Akanmori, B., Koram, K., and Riley, E. (2002). Absolute levels and ratios of proinflammatory and anti-inflammatory cytokine production in vitro predict clinical immunity to *Plasmodium falciparum* malaria. *J. Infect. Dis.* 185, 971–979. doi: 10.1086/339408

D'Ombrain, M. C., Robinson, L. J., Stanisic, D. I., Taraika, J., Bernard, N., Michon, P., et al. (2008). Association of early interferon-gamma production with immunity to clinical malaria: a longitudinal study among Papua New Guinean children. *Clin. Infect. Dis.* 47, 1380–1387. doi: 10.1086/592971

Farrington, L., Vance, H., Rek, J., Prahl, M., Jagannathan, P., Katureebe, A., et al. (2017). Both inflammatory and regulatory cytokine responses to malaria are blunted with increasing age in highly exposed children. *Malaria J.* 16:499.

Frimpong, A., Kusi, K. A., Adu-Gyasi, D., Amponsah, J., Ofori, M. F., and Ndifon, W. (2019). Phenotypic evidence of T cell exhaustion and senescence during symptomatic *Plasmodium falciparum* Malaria. *Front. Immunol.* 10:1345. doi: 10.3389/fimmu.2019.01345

Frimpong, A., Kusi, K. A., Tornyigah, B., Ofori, M. F., and Ndifon, W. (2018). Characterization of T cell activation and regulation in children with asymptomatic *Plasmodium falciparum* infection. *Malaria J.* 17:263.

Galatas, B., Bassat, Q., and Mayor, A. (2016). Malaria parasites in the asymptomatic: looking for the hay in the haystack. *Trends Parasitol.* 32, 296–308. doi: 10.1016/j.pt.2015.11.015

Gimenez, F., De Lagerie, S. B., Fernandez, C., Pino, P., and Mazier, D. (2003). Tumor necrosis factor α in the pathogenesis of cerebral malaria. *Cell. Mol. Life Sci. CMLS* 60, 1623–1635.

Ibitokou, S. A., Boström, S., Brutus, L., Ndam, N. T., Vianou, B., Agbowaï, C., et al. (2014). Submicroscopic infections with *Plasmodium falciparum* during pregnancy and their association with circulating cytokine, chemokine, and cellular profiles. *Clin. Vac. Immunol.* 21, 859–866. doi: 10.1128/cvi.00009-14

Jagannathan, P., Eccles-James, I., Bowen, K., Nankya, F., Auma, A., Wamala, S., et al. (2014). IFNγ/IL-10 co-producing cells dominate the CD4 response to malaria in highly exposed children. *PLoS Pathog.* 10:e1003864. doi: 10.1371/journal.ppat.1003864

Jagannathan, P., Lutwama, F., Boyle, M. J., Nankya, F., Farrington, L. A., McIntyre, T. I., et al. (2017). Vδ2+ T cell response to malaria correlates with protection from infection but is attenuated with repeated exposure. *Sci. Rep.* 7, 1–12.

Jangpatarapongsa, K., Chootong, P., Sattabongkot, J., Chotivanich, K., Sirichaisinthop, J., Tungpradabkul, S., et al. (2008). Plasmodium vivax parasites alter the balance of myeloid and plasmacytoid dendritic cells and the induction of regulatory T cells. *Eur. J. Immunol.* 38, 2697–2705. doi: 10.1002/eji.200838186

Juffrie, M., Meer, G. V., Hack, C., Haasnoot, K., Veerman, A., and Thijs, L. (2001). Inflammatory mediators in dengue virus infection in children: interleukin-6 and its relation to C-reactive protein and secretory phospholipase A2. *Am. J. Trop. Med. Hyg.* 65, 70–75. doi: 10.4269/ajtmh.2001.65.70

Kaminski, L.-C., Riehn, M., Abel, A., Steeg, C., Yar, D. D., Addai-Mensah, O., et al. (2019). Cytotoxic T cell-derived granzyme B is increased in severe *Plasmodium Falciparum* Malaria. *Front. Immunol.* 10:2917. doi: 10.3389/fimmu.2019.2917

Kelly, M. N., Kolls, J. K., Happel, K., Schwartzman, J. D., Schwarzenberger, P., Combe, C., et al. (2005). Interleukin-17/interleukin-17 receptor-mediated signaling is important for generation of an optimal polymorphonuclear response against *Toxoplasma gondii* infection. *Infect. Immun.* 73, 617–621. doi: 10.1128/iai.73.1.617-621.2005

Kidd, P. (2003). Th1/Th2 balance: the hypothesis, its limitations, and implications for health and disease. *Altern. Med. Rev.* 8, 223–246.

Kumar, A., Schmidt, B. R., Sanchez, Z. A. C., Yazar, F., Davis, R. W., Ramasubramanian, A. K., et al. (2020). Automated motion tracking and data extraction for red blood cell biomechanics. *Curr. Protoc. Cytom.* 93:e75.

Kumar, R., Ng, S., and Engwerda, C. (2019). The role of IL-10 in Malaria: a double edged sword. *Front. Immunol.* 10:229. doi: 10.3389/fimmu.2019.00229

Kurtzhals, J. A., Adabayeri, V., Goka, B. Q., Akanmori, B. D., Oliver-Commey, J. O., Nkrumah, F. K., et al. (1998). Low plasma concentrations of interleukin 10 in severe malarial anaemia compared with cerebral and uncomplicated malaria. *Lancet* 351, 1768–1772. doi: 10.1016/s0140-6736(97)09439-7

Kurup, S. P., Butler, N. S., and Harty, J. T. (2019). T cell-mediated immunity to malaria. *Nat. Rev. Immunol.* 19, 457–471.

Laishram, D. D., Sutton, P. L., Nanda, N., Sharma, V. L., Sobti, R. C., Carlton, J. M., et al. (2012). The complexities of malaria disease manifestations with a focus on asymptomatic malaria. *Malaria J.* 11:29. doi: 10.1186/1475-2875-11-29

Langhorne, J., Ndungu, F. M., Sponaas, A.-M., and Marsh, K. (2008). Immunity to malaria: more questions than answers. *Nat. Immunol.* 9:725. doi: 10.1038/ni.f.205

Lindblade, K. A., Steinhardt, L., Samuels, A., Kachur, S. P., and Slutsker, L. (2013). The silent threat: asymptomatic parasitemia and malaria transmission. *Expert Rev. Antiinfect. Ther.* 11, 623–639. doi: 10.1586/eri.13.45

Lyke, K. E., Burges, R., Cissoko, Y., Sangare, L., Dao, M., Diarra, I., et al. (2004). Serum levels of the proinflammatory cytokines interleukin-1 beta (IL-1beta), IL-6, IL-8, IL-10, tumor necrosis factor alpha, and IL-12(p70) in Malian children with severe *Plasmodium falciparum* malaria and matched uncomplicated malaria or healthy controls. *Infect. Immun.* 72, 5630–5637. doi: 10.1128/iai.72.10.5630-5637.2004

Mackintosh, C. L., Beeson, J. G., and Marsh, K. (2004). Clinical features and pathogenesis of severe malaria. *Trends Parasitol.* 20, 597–603. doi: 10.1016/j.pt.2004.09.006

Malaguarnera, L., and Musumeci, S. (2002). The immune response to *Plasmodium falciparum* malaria. *Lancet Infect. Dis.* 2, 472–478. doi: 10.1016/s1473-3099(02)00344-4

Mandala, W. L., Msefula, C. L., Gondwe, E. N., Drayson, M. T., Molyneux, M. E., and MacLennan, C. A. (2017). Cytokine profiles in Malawian children presenting with uncomplicated malaria, severe malarial anemia and cerebral malaria. *Clin. Vac. Immunol.* 24, e533–e516.

Mshana, R., Boulandi, J., Mshana, N., Mayombo, J., and Mendome, G. (1991). Cytokines in the pathogenesis of malaria: levels of IL-I beta, IL-4, IL-6, TNF-alpha and IFN-gamma in plasma of healthy individuals and malaria patients in a holoendemic area. *J. Clin. Lab. Immunol.* 34, 131–139.

Njama-Meya, D., Kamya, M. R., and Dorsey, G. (2004). Asymptomatic parasitaemia as a risk factor for symptomatic malaria in a cohort of Ugandan children. *Trop. Med. Intern. Health* 9, 862–868. doi: 10.1111/j.1365-3156.2004.01277.x

Nlinwe, O. N., Kusi, K. A., Adu, B., and Sedegah, M. (2018). T-cell responses against Malaria: effect of parasite antigen diversity and relevance for vaccine development. *Vaccine* 36, 2237–2242. doi: 10.1016/j.vaccine.2018.03.023

Ochola-Oyier, L. I., Kimenyi, K. M., Wamae, K., and Understanding, P. (2019). falciparum asymptomatic infections: a proposition for a transcriptomic approach. *Front. Immunol.* 10:2398. doi: 10.3389/fimmu.2019.2398

Othoro, C., Lal, A. A., Nahlen, B., Koech, D., Orago, A. S., and Udhayakumar, V. (1999). A low interleukin-10 tumor necrosis factor-α ratio is associated with malaria anemia in children residing in a holoendemic malaria region in western Kenya. *J. Infect. Dis.* 179, 279–282. doi: 10.1086/314548

Oyegue-Liabagui, S. L., Bouopda-Tuedom, A. G., Kouna, L. C., Maghendji-Nzondo, S., Nzoughe, H., Tchitoula-Makaya, N., et al. (2017). Pro- and anti-inflammatory cytokines in children with malaria in Franceville. *Gabon. Am. J. Clin. Exp. Immunol.* 6, 9–20.

Partey, F. D., Castberg, F. C., Sarbah, E. W., Silk, S. E., Awandare, G. A., Draper, S. J., et al. (2018). Kinetics of antibody responses to PfRH5-complex antigens in Ghanaian children with *Plasmodium falciparum* malaria. *PLoS One* 13:e0198371. doi: 10.1371/journal.pone.0198371

Prakash, D., Fesel, C., Jain, R., Cazenave, P.-A., Mishra, G. C., and Pied, S. (2006). Clusters of cytokines determine malaria severity in *Plasmodium falciparum*-infected patients from endemic areas of Central India. *J. Infect. Dis.* 194, 198–207. doi: 10.1086/504720

Riley, E. M., Wahl, S., Perkins, D. J., and Schofield, L. (2006). Regulating immunity to malaria. *Par. Immunol.* 28, 35–49. doi: 10.1111/j.1365-3024.2006.00775.x

Riou, C., Dumont, A. R., Yassine-Diab, B., Haddad, E. K., and Sekaly, R.-P. (2006). IL-4 influences the differentiation and the susceptibility to activation-induced cell death of human naive CD8+ T cells. *Intern. Immunol.* 18, 827–835. doi: 10.1093/intimm/dxl019

Robinson, L. J., D'Ombrain, M. C., Stanisic, D. I., Taraika, J., Bernard, N., Richards, J. S., et al. (2009). Cellular tumor necrosis factor, gamma interferon, and interleukin-6 responses as correlates of immunity and risk of clinical *Plasmodium falciparum* malaria in children from Papua New Guinea. *Infect. Immun.* 77, 3033–3043. doi: 10.1128/iai.00211-09

Salazar-Castañón, V. H., Juárez-Avelar, I., Legorreta-Herrera, M., Govezensky, T., and Rodriguez-Sosa, M. (2018). Co-infection: the outcome of *Plasmodium*

infection differs according to the time of pre-existing helminth infection. *Parasitol. Res.* 117, 2767–2784. doi: 10.1007/s00436-018-5965-9

Schneider, P., Bousema, J. T., Gouagna, L. C., Otieno, S., van de Vegte-Bolmer, M., Omar, S. A., et al. (2007). Submicroscopic *Plasmodium falciparum* gametocyte densities frequently result in mosquito infection. *Am. J. Trop. Med. Hyg.* 76, 470–474. doi: 10.4269/ajtmh.2007.76.470

Sinha, S., Qidwai, T., Kanchan, K., Jha, G. N., Anand, P., Pati, S. S., et al. (2010). Distinct cytokine profiles define clinical immune response to *falciparum* malaria in regions of high or low disease transmission. *Eur. Cytok. Netw.* 21, 232–240.

Snow, R. W., Sartorius, B., Kyalo, D., Maina, J., Amratia, P., Mundia, C. W., et al. (2017). The prevalence of *Plasmodium falciparum* in sub-Saharan Africa since 1900. *Nature* 550, 515–518. doi: 10.1038/nature24059

Torre, D., Speranza, F., Giola, M., Matteelli, A., Tambini, R., and Biondi, G. (2002). Role of Th1 and Th2 cytokines in immune response to uncomplicated *Plasmodium falciparum* malaria. *Clin. Diagn. Lab. Immunol.* 9, 348–351. doi: 10.1128/cdli.9.2.348-351.2002

Tran, T. M., Li, S., Doumbo, S., Doumtabe, D., Huang, C. Y., Dia, S., et al. (2013). An intensive longitudinal cohort study of Malian children and adults reveals no evidence of acquired immunity to *Plasmodium falciparum* infection. *Clin. Infect. Dis.* 57, 40–47. doi: 10.1093/cid/cit174

Wammes, L. J., Wiria, A. E., Toenhake, C. G., Hamid, F., Liu, K. Y., Suryani, H., et al. (2013). Asymptomatic plasmodial infection is associated with increased tumor necrosis factor receptor II-expressing regulatory T cells and suppressed Type 2 immune responses. *J. Infect. Dis.* 207, 1590–1599. doi: 10.1093/infdis/jit058

White, M. T., Griffin, J. T., Akpogheneta, O., Conway, D. J., Koram, K. A., Riley, E. M., et al. (2014). Dynamics of the antibody response to *Plasmodium falciparum* infection in African children. *J. Infect. Dis.* 210, 1115–1122. doi: 10.1093/infdis/jiu219

WHO (2018). *World Malaria Report 2018*. Geneva: World Health Organization.

Wilson, N. O., Bythwood, T., Solomon, W., Jolly, P., Yatich, N., Jiang, Y., et al. (2010). Elevated levels of IL-10 and G-CSF associated with asymptomatic malaria in pregnant women. *Infect. Dis. Obstetr. Gynecol.* 2010:317430.

Wood, S., and Wood, M. S. (2015). Package 'mgcv'. *R Pack. Ver.* 1:29.

Conflict of Interest: The authors declare that the research was conducted in the absence of any commercial or financial relationships that could be construed as a potential conflict of interest.

frontiers in Immunology

ORIGINAL RESEARCH
published: 10 December 2020
doi: 10.3389/fimmu.2020.590934

Resistance to Experimental Visceral Leishmaniasis in Mice Infected With *Leishmania infantum* Requires Batf3

Manuel Soto[1], Laura Ramírez[1], José Carlos Solana[1†], Emma C. L. Cook[2], Elena Hernández-García[2], Sara Charro-Zanca[2], Ana Redondo-Urzainqui[2], Rosa M. Reguera[3], Rafael Balaña-Fouce[3] and Salvador Iborra[2]*

[1] Centro de Biología Molecular Severo Ochoa (CSIC-UAM), Departamento de Biología Molecular, Nicolás Cabrera 1, Universidad Autónoma de Madrid, Madrid, Spain, [2] Department of Immunology, Ophthalmology and ENT, School of Medicine, Universidad Complutense de Madrid, Madrid, Spain, [3] Departamento de Ciencias Biomédicas, Universidad de León, León, Spain

OPEN ACCESS

Edited by:
Emilio Luis Malchiodi,
University of Buenos Aires, Argentina

Reviewed by:
Malcolm Scott Duthie,
HDT Biotech Corporation,
United States
Bhaskar Saha,
University of Poitiers, France

***Correspondence:**
Salvador Iborra
siborra@ucm.es

†Present address:
José Carlos Solana,
WHO Collaborating Centre for Leishmaniasis, National Centre for Microbiology, Instituto de Salud Carlos III, Madrid, Spain

Specialty section:
This article was submitted to Microbial Immunology, a section of the journal Frontiers in Immunology

Received: 03 August 2020
Accepted: 09 November 2020
Published: 10 December 2020

Citation:
Soto M, Ramírez L, Solana JC, Cook ECL, Hernández-García E, Charro-Zanca S, Redondo-Urzainqui A, Reguera RM, Balaña-Fouce R and Iborra S (2020) Resistance to Experimental Visceral Leishmaniasis in Mice Infected With Leishmania infantum *Requires Batf3. Front. Immunol. 11:590934. doi: 10.3389/fimmu.2020.590934*

Unveiling the protective immune response to visceral leishmaniasis is critical for a rational design of vaccines aimed at reducing the impact caused by this fatal, if left untreated, vector-borne disease. In this study we sought to determine the role of the basic leucine zipper transcription factor ATF-like 3 (Batf3) in the evolution of infection with *Leishmania infantum*, the causative agent of human visceral leishmaniasis in the Mediterranean Basin and Latin America. For that, Batf3-deficient mice in C57BL/6 background were infected with an *L. infantum* strain expressing the luciferase gene. Bioluminescent imaging, as well as *in vitro* parasite titration, demonstrated that Batf3-deficient mice were unable to control hepatic parasitosis as opposed to wild-type C57BL/6 mice. The impaired microbicide capacities of *L. infantum*-infected macrophages from Batf3-deficient mice mainly correlated with a reduction of parasite-specific IFN-γ production. Our results reinforce the implication of Batf3 in the generation of type 1 immunity against infectious diseases.

Keywords: ***Leishmania*, Batf3, visceral leishmaniasis, dendritic cells, Batf3 DC+, Th1 responses**

INTRODUCTION

Human leishmaniases are a group of poverty-related neglected diseases caused by an infection with parasites of the genus *Leishmania*, which are transmitted by infected sand flies. Depending on the infectious parasitic species, patients may develop different pathologies. In the Old World, cutaneous leishmaniasis (CL) is mainly caused by *L. major* infection. Visceral leishmaniasis (VL) usually develops after infection with *L. infantum* (Mediterranean countries and South America) or *L. donovani* (Indian Subcontinent and East Africa) (1). Even though patients who have recovered from leishmaniasis develop immunity against reinfection (2), suggesting that an effective vaccine should be feasible, to date there are no vaccines or specific immunotherapies against the human forms of the disease.

The existence of murine models of infection for different parasitic species is contributing to the development of vaccines or more effective and advanced therapeutic strategies (3, 4). In addition, these models have been fundamental to understand the generation, maintenance and, eventually, failure of those immune responses underlying either resistance or susceptibility to infection. Different studies performed on mice experimentally infected with *L. major* have allowed the

establishment of an association between resistance and susceptibility, and the cellular response induced after challenge. The susceptibility to infection shown by BALB/c mice correlates with the induction of a dominant Interleukin (IL)-4–producing $CD4^+$ Th2 response, and to the generation of parasite-dependent IL-10 responses (5). As a result, the parasite multiplies in the site of infection and subsequently spreads to the viscera (6). Alternatively, resistant C57BL/6 mice develop a response mediated by Interferon (IFN)-γ-producing $CD4^+$ Th1 cells, thus activating infected macrophages to produce nitric oxide (NO), which mediates the intracellular killing of the parasite (5).

Infection of both BALB/c or C57BL/6 strains with *Leishmania* viscerotropic species results in parasite multiplication in the liver, spleen and bone marrow (6). During the first weeks after challenge (initial phase) parasites multiply in the liver, but in the late phase infected Kupffer cells are activated to produce NO resulting in a decrease of hepatic parasitic burdens. This inflammatory response is unable to control parasite multiplication in either the spleen or the bone marrow, resulting in a chronic infection (7, 8). The immune response concomitant to this parasitosis evolution after challenge with *L. infantum* has been mainly studied in the BALB/c model and results in the generation of both Th1 and Th2 responses (9–11). This mixed Th1/Th2 response has been also recently reported in the C57BL/6-*L. infantum* model of infection (12).

AP-1 (activator protein-1) constitutes a family of transcription factors endowed with a basic region-leucine zipper (bZIP) belonging to different families (JUN, FOS, ATF, basic leucine zipper transcriptional factor ATF-like and MAF) that form heterodimers to regulate transcription. Development and function of myeloid and lymphoid cell populations is regulated by different basic leucine zipper transcriptional factor ATF-like (BATF) proteins (13). BATF proteins can act as negative regulators of the AP-1 complex or interact with IFN regulatory factor (IRF) family member to regulate transcription (14). Batf3 is a BATF member that was firstly identified in human T cells and is required for the development of the of a subset of conventional dendritic cells (DC) (15). To determine the role of Batf3 in visceral leishmaniasis (VL), we have employed C57BL/6 wild-type and $Batf3^{-/-}$ animals challenged with an infective genetically-modified strain expressing red-shifted luciferase (luc) gene (16). We have followed the presence of parasites in internal organs *in vivo* throughout the course of the infection. We have analyzed the presence of viable parasites in liver, spleen and bone marrow in the initial (fourth week) and late phases (tenth week). We have also examined the immune response in animals in both phases, studying the humoral and cellular responses against the parasite. We found an enhanced susceptibility along with a decrease in the parasite-specific $CD4^+$ Th1 response in *L. infantum*-infected Batf3-deficient mice, while the proportions of IL-4, IL-17, or IL-10–producing $CD4^+$ T cells remained unaffected. These results suggest the involvement of Batf3-dependent conventional type 1 DC (cDC1) in resistance to VL, but further studies will be required to directly demonstrate their role in the susceptibility to this infectious disease. Thus, we show that, although the absence of Batf3 critically impairs Th1 immunity, it might have a differential impact on other T cell subsets or not, depending on the pathogen.

MATERIALS AND METHODS

Mice and Parasites

Mice were bred under specific pathogen-free conditions at the National Centre for Cardiovascular Research (CNIC) and transported to the Severo Ochoa Molecular Biology Centre (CBMSO) to conduct the research. $Batf3^{-/-}$ mice kindly provided by Dr. Kenneth M. Murphy, (Washington University, St. Louis, MO. USA), were backcrossed more than ten times to establish WT and $Batf3^{-/-}$colonies from the heterozygotes. The animal research complies with EU Directive 2010/63EU, Recommendation 2007/526/EC and Spanish Royal Decree (RD 53/2013) regarding the protection of animals used for experimental and other scientific purpose. Procedures were approved by the Animal Care and Use Committee at the Centro de Biología Molecular Severo Ochoa (CEEA-CBMSO 23/243), the Bioethical Committee of the CSIC (under reference 795/2019), Bioethical Committees of the CNIC and Universidad Complutense de Madrid as well as the Government of the Autonomous Community of Madrid (Spain) under the references PROEX 115/19, PROEX 121/14, and PROEX134/19. All animal procedures conformed to EU Directive 2010/63EU and Recommendation 2007/526/EC regarding the protection of animals used for experimental and other scientific purposes, enforced in Spanish law under Real Decreto 1201/2005. All experimentation was performed with female mice.

The *PpyRE9h*$^+$*L. infantum* strain expressing red-shifted luc gene was employed to infect the mice (16). Promastigotes were cultured at 26°C in M3 medium supplemented with 10% fetal calf serum (FCS; Sigma. St. Louis MO. USA), 100 U/ml of penicillin, 100 µg/ml of streptomycin and 100 µg/ml of puromycin (all purchased from Thermo Fischer Scientific, Waltham, MA, USA). Animals were challenged intravenously (i.v.) with 1×10^7 stationary phase promastigotes. For soluble leishmania antigen (SLA) preparation, *L. infantum* (strain MCAN/ES/96/BCN150) promastigotes were employed. This strain was grown in the same medium indicated above but in the absence of puromycin.

Follow-Up of *In Vivo* Infections by Bioluminescent Imaging and *In Vitro* Quantification in Internal Organs of the Parasitic Burdens

After challenging the mice with *PpyREh9+L. infantum* promastigotes, animals were monitored weekly in a Charge-Coupled Device (CCD) IVIS 100 Xenogen system (Caliper Life Science, Hopkinton, MA, USA) as described in (16). Briefly, images were acquired for 10 min from animals anesthetized with isoflurane that were previously intraperitoneally injected with D-luciferin (150 mg/Kg) purchased from Perkin Elmer (Waltham, MA, USA). The estimation of the parasitic burden in living mice

was performed by the quantification of the regions of interest (ROIs) around liver and femur in ventral position using Living Image v.4.3. The values of BLI are expressed as radiance (p/s/cm^2/sr).

At the indicated time points post-challenge, parasitic burden in liver, spleen and bone marrow (BM) were determined by limiting dilution as described in (17). Briefly, approximately 20 mg of liver, the whole spleen, and BM samples perfused from the femur cavities of each mouse, were individually homogenized in M3 medium supplemented with 20% FCS, 100 U/ml of penicillin, 100 µg/ml of streptomycin and 100 µg/ml of puromycin and filtered through 70 µm cell strainers (Corning Gmbh, Kaiserslautern, Germany) to obtain a cell suspension. Cells were serially diluted (1/3) in 96-well flat-bottomed microtiter plates (Thermo Fischer Scientific) containing the same medium employed for homogenization (in triplicates). The number of viable parasites was determined from the highest dilution at which promastigotes could be observed after 10 days of incubation at 26°C and is indicated per whole spleen, per gram of liver, or parasites per 1×10^7 BM cells.

Analysis of the *Leishmania*-Specific Humoral Responses

The reactivity against parasite proteins was determined by ELISA as described in (18) using NUNC MaxySorp plates. Briefly, plate wells were coated with freeze-thawed *L. infantum* SLA (1.2 µg per well) and incubated with 1/2 dilutions (starting at 1/100). The serum of each infected mouse was analyzed independently. Anti-IgG1, or anti-IgG2c horseradish peroxidase-conjugated anti-mouse immunoglobulins from Nordic (BioSite Täby, Sweden) were used as secondary antibodies at 1/2,000 dilution. Orto-phenylenediamine was employed for color development and the optical densities were read at 490 nm in an ELISA microplate spectrophotometer (Model 680, Bio-Rad Laboratories). Sera reactivity was calculated as the reciprocal end-point titer defined as the inverse value of the highest serum dilution factor giving an absorbance > 0.1 absorbance unit.

In Vitro Cell Stimulation, Determination of Cytokine Concentration in Culture Supernatants, and Analysis of IFN-γ Production by T Cells

Primary cultures from the spleen of infected mice were established in RPMI complete medium: RPMI medium (Sigma) supplemented with 10% heat-inactivated FCS, 20 mM L-glutamine, 200 U/ml penicillin, 100 µg/ml streptomycin and 50 µg/ml gentamicin (Thermo Fischer Scientific). GMCSF BM-derived $CD11c^+$ cells (GM-BM) were used as antigen presenting cells. They were derived from BM suspensions cultured for 7 days in RPMI complete medium supplemented with 20 ng/ml recombinant GMCSF (Peprotech, London, UK). Cells were loaded with *L. infantum* SLA (3 µg/ml) the last 24 h to obtain stimulated cells. For *in vitro* stimulation, spleen cells (2×10^6 cells/ml) were co-cultured at 37°C and 5% CO_2 with GM-BM cells (4×10^5 cell/ml) (stimulated or not with SLA) in RPMI complete medium.

For the analysis of cytokine secretion to culture supernatants, spleen cells were stimulated as indicated above for 72 h. Afterwards, supernatants were obtained and analyzed by sandwich ELISA using commercial kits (Thermo Fisher Scientific). The levels of IFN-γ, IL-17, IL-10, IL-4, or IL-13 in culture supernatants were determined.

For the analysis of cells producing IFN-γ, spleen cells were stimulated as indicated above for 48 h. For the last 6 h, cultures were treated with brefeldin A (10 µg/ml; Sigma). Then, cells were harvested, washed in PBS with 1% heat-inactivated FCS (PBSw) and incubated with Fc block (BD Bioscience, San José, CA, USA) prior to staining. Next, cell surface markers: CD3 (clone 145-2C11; APC), CD4 (clone RM4-5; BV570) and CD8 (clone 53–6.7; FITC) were stained for 30 min at 4°C. After washing in PBSw, cells were fixed and permeabilized with Cytofix/Cytoperm (BD Bioscience). Next, the PE/Cy7 anti-mouse IFN-γ (clone XMG1.2) antibody was added for 30 min at 4°C. Finally, cells were washed and analyzed. Antibodies were purchased from BioLegend (San Diego, CA, USA). Samples were acquired using a FACS Canto II flow cytometer and FACSDiva Software (BD Bioscience) and processed and plotted with FlowJo Software (FlowJo LLC, Ashland, Oregon, USA).

Nitrite Determination

Release of nitrite was determined in the supernatant of spleen cell cultures (5×10^6 cell/ml) stimulated or not with Concanavalin A (ConA;1 µg/ml) or SLA (12 µg/ml) for 72 h in complete RPMI medium. For nitrite determination, 50 µl of culture supernatant were mixed with an equal volume of Griess reagent. Nitrite concentration was calculated from a sodium nitrite linear standard curve (1–100 µM). Absorbance was measured at 540 nm.

Statistical Analysis

Statistical analysis was performed using the Graph-Pad Prism 5 program. Data were analyzed by a two-tailed Student *t*-test. Differences were considered significant when $P < 0.05$.

RESULTS

Batf3 Deficiency Impacts on VL Progression in Mice Infected With *L. infantum*

To analyze the role of Batf3 deficiency in the evolution of VL, we carried out a comparative analysis of the development of the infection in the liver with parasites expressing the luc gene between $Batf3^{-/-}$ mice and their corresponding littermate controls. No differences were observed in hepatic bioluminescence values between $Batf3^{-/-}$ and control mice at the initial phase of the infection (weeks 1–6; **Figure 1A** and **Supplementary Figure 1**). However, as can be deduced from the radiance values from week 7 to the end of the assay, at the late phase of the infection, parasite burden reached a plateau in $Batf3^{-/-}$ mice, suggesting that they have an impaired ability to control hepatic parasite multiplication (weeks 7–10; **Figures 1A, B** and **Supplementary Figure 1**). From week 6

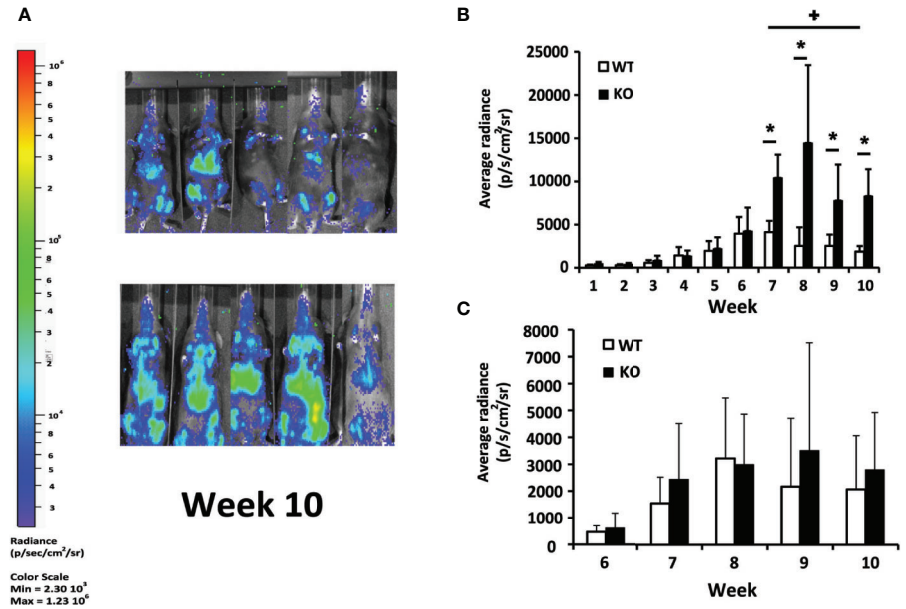

FIGURE 1 | *In vivo* evaluation of *L. infantum* infection. *Batf3*$^{-/-}$ (KO; n= 9, weeks 1–3; n = 5, weeks 4–10) and wild-type (WT; n= 10, weeks 1–3; n = 5, weeks 4–10) mice were infected intravenously with 1 × 10^7 PpyREh9+ *L. infantum* stationary phase promastigotes. **(A)** Representative bioluminescent images of infected mice. **(B, C)** The graphs show the mean (+ SD) of the quantification of ventral bioluminescence corresponding to the liver **(B)** or femurs **(C)** from the experiment shown in the **Supplementary Figure 1**. Symbol * shows the statistical differences between KO and WT mice data ($P < 0.05$). Symbol + shows the statistical differences between WT data taken at week 7 and at week 10 ($P < 0.05$). Results are representative of two independent experiments.

onwards, similar parasite numbers were detected in the bone marrow of both groups (**Figure 1C** and **Supplementary Figure 1**). We could not detect parasites in the spleen with either the front view or the lateral view, except for some Batf3-deficient mice that, during the last two weeks, presented dispersion of parasites to other internal organs (**Supplementary Figure 1**).

Differences in hepatic parasitic burdens between *Batf3*$^{-/-}$ and control mice were confirmed by using a limiting dilution assay. *Batf3*$^{-/-}$ mice showed an increase of two orders of magnitude in hepatic parasitic load compared to controls at week 10 post-challenge. The ability to control parasite multiplication in the liver was only observed in wild-type mice, since there was a decrease in the number of parasites from the early to the late phase. However, mice deficient for Batf3 exhibit an increase in the number of parasites (**Figure 2**). We also determined the parasitic burden in the spleen. Although *Batf3*$^{-/-}$ mice presented higher parasite numbers than control mice in this organ, the increase was not found to be significantly different in any of the two repeat experiments. In both groups, we found splenic chronic progressive infection, since the number of parasites increased significantly in the spleen with infection time (**Figure 2**). Similar parasite numbers were found in the bone marrow from both groups at week 4 and week 10 post-challenge (**Figure 2**). All these results allowed us to conclude that the deficiency in Batf3 transcription factor prevents the control of parasite multiplication in the liver, without affecting the establishment of a chronic infection in the spleen or bone marrow. We found in some Batf3-deficient mice signs of illness around weeks 7 to 9 post-challenge: i.e. lethargy and unkempt coats, so we decided to establish a humane endpoint at 10 weeks to prevent unnecessary animal distress.

Batf3 Deficiency Impairs the Generation of *Leishmania*-Specific IgG2c Humoral Response in Mice Infected With *L. infantum*

Next, we analyzed the humoral immune response against leishmanial antigens in the *L. infantum* infected mice. We evaluated the titer of IgG2c and IgG1 anti-SLA antibodies in the sera of infected mice as an indication of the in vivo induction of Th1- or Th2-mediated responses respectively. The analysis was performed at week 4 after challenge (initial phase, **Figure 3A**) and at the end of the experiment 10 weeks after infection (late phase, **Figure 3B**). At both time points, mice of the control group showed a mixed response, with titers of IgG1 and IgG2c anti-SLA antibodies that were not significantly different. *Batf3*$^{-/-}$ mice showed very low, although detectable, titers of the IgG2c subclass antibodies throughout the infection process. These titers were significantly lower than those found in mice of the control group (**Figures 3A, B**). No differences were observed for the titer of anti-SLA IgG1 antibodies between both groups (**Figures 3A, B**). This diminished IgG2c response, which depends on IFN-γ (19), suggests that *Batf3*$^{-/-}$ mice have an impaired capacity to induce Th1 responses against the parasite that did not result in an increased parasite-specific Th2-mediated humoral response.

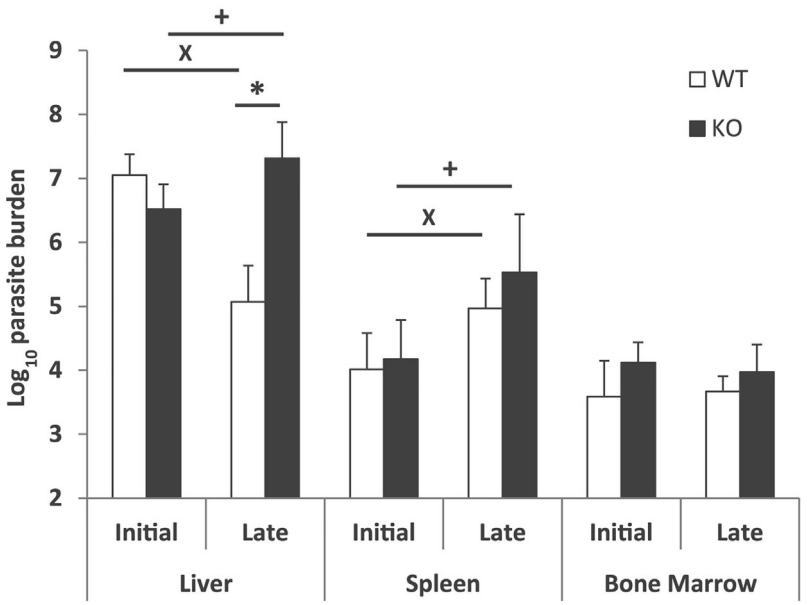

FIGURE 2 | Evolution of parasite burden. The presence of viable parasites in *Batf3*$^{-/-}$ (KO) and wild-type (WT) mice infected intravenously with 1 × 10^7 *PpyREh9*$^+$*L. infantum* stationary phase promastigotes was determined at week 4 (initial; n= 4 KO, n = 5 WT) or at week 10 (late; n = 5 both groups) by limiting dilution. Data are represented as the mean (+ SD) of the parasite loads from each group. Samples from each mouse were independently determined in the liver (parasites per gr), spleen (parasites per organ) or bone marrow (parasites per 1 × 10^7 cells). * ($P < 0.05$) shows the statistical differences in liver parasite loads from WT and KO groups. $^+$ ($P < 0.05$) shows the statistical differences in liver or spleens from mice of the KO group at week 4 and at week 10 post-challenge. $^×$ ($P < 0.05$) shows the statistical differences in liver or spleens from mice of the WT group at week 4 and at week 10 post-challenge.

Batf3 Deficiency Impairs the Generation of *Leishmania*-Specific Cellular Immune Responses in Mice Infected With *L. infantum*

To investigate the cellular immune response elicited against the parasite, we analyzed *Leishmania*-specific cytokine secretion by spleen cells taken at week 4 and at week 10 post-infection ex vivo. For stimulation, we used CD11c$^+$ GMCSF bone marrow-derived cells (GM-BM) loaded or not with *L. infantum* SLA were employed. The SLA-specific production of IFN-γ was higher in wild-type animals at the initial and at the late phase of infection, (**Figure 4A**). A similar profile was obtained when determining the presence of IL-10 in culture supernatants (**Figure 4B**). The only difference was the absence of IL-10 in the supernatant of the cultures established from the *Batf3*$^{-/-}$ mice independently of the stimuli at the initial phase (**Figure 4B**). Regarding Th2-related cytokines, SLA-dependent secretion of IL-4 (**Figure 4C**) and IL-13 (**Figure 4D**) was observed at the late phase for both cytokines and also at the initial phase for IL-13. At the late phase of the infection we did not detect significant differences between the amount of these cytokines in both mice groups. We did not detect a SLA-dependent secretion of IL-17 in any group (**Supplementary Figure 2**).

Since the predominant IFN-γ-mediated response found in the infected wild-type animals was decreased, although not absent, in *Batf3*$^{-/-}$ mice, we analyzed the frequency of CD4$^+$ and CD8$^+$ T cells producing this cytokine in both mice groups. **Supplementary Figure 3** shows the gating strategies and FMO controls. The frequency of IFN-γ-producing CD4$^+$ and CD8$^+$ T cells was analyzed both at the initial (**Figure 5A**), and at the late phase of the infection (**Figure 5B**). We detected a statistically significant higher production of FN-γ-producing only for CD4$^+$ T cells stimulated with SLA at the final phase of the infection.

To complement these findings, we measured the amounts of nitrites, derived from NO production in macrophages, by Griess reaction in the culture supernatants of spleen cells established from *Batf3*$^{-/-}$ and control mice. Our results showed the presence of nitrites in cell supernatants from WT mice upon stimulation with SLA, in greater magnitude in the late phase of infection (**Figure 6**). This metabolite was almost absent in cultures generated from Batf3-deficient mice stimulated with SLA, but produced in similar levels than in WT mice upon Concanavalin A treatment, reflecting the limited leishmanicidal capacity of their macrophages in response to parasite stimuli.

DISCUSSION

Batf3 transcription factor may play different roles in the development and function of myeloid and lymphoid populations. For example, it inhibits the differentiation of regulatory T cells in the periphery (20). Very recently, a role

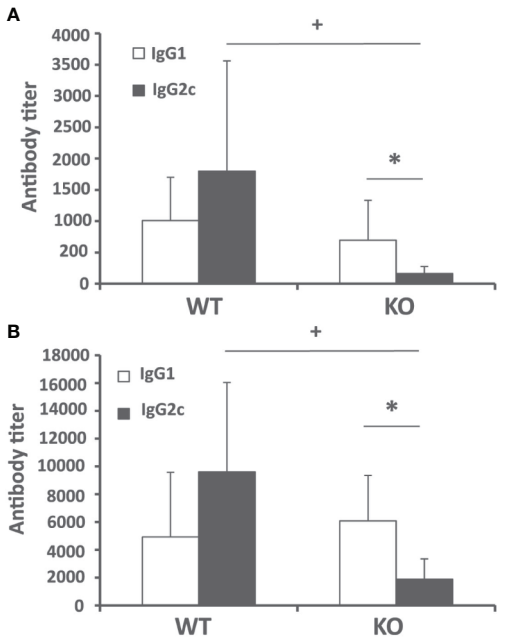

FIGURE 3 | Humoral response against *Leishmania* after challenge. *Batf3*$^{-/-}$ (KO) and wild-type (WT) mice were infected intravenously with 1×10^7 *PpyREh9*$^+$ *L. infantum* stationary phase promastigotes. The IgG1 and IgG2c reciprocal end-point titers against *L. infantum* SLA were calculated by ELISA at week 4 **(A)** (n = 9 KO, n = 10 WT) or week 10 **(B)** (n = 5 per group). Data are represented as mean + SD. * ($P < 0.05$) shows the statistical differences between IgG1 and IgG2c titers in the KO group. $^+$ ($P < 0.05$) shows the statistical differences of the IgG2c titers between WT and KO groups. Results are representative of two independent experiments.

for Batf3 in memory CD8$^+$ T cell differentiation has been revealed (21, 22). Importantly, Batf3 selectively determines acquisition of CD8α^+ DC phenotype and function in lymphoid organs, and CD103$^+$ in non-lymphoid organs (15, 23–25). Both subsets comprise conventional type 1 DCs (cDC1), which play important roles in viral and cancer immunity (26).

The chronic self-healing *L. major* infection model in C57BL/6 mice contributed to unveiling the role of the different DC subsets in the priming and maintenance of the anti-*Leishmania* response [reviewed in (27, 28)]. DC comprise a heterogenous population, and are further classified into distinct subtypes according to ontogeny, differential expression of surface proteins, cell localization, and immunological function. Intradermal infection of a C57BL/6 mouse strain deficient in Batf3, resulted in an exacerbated evolution of the CL disease (29, 30). In this model, it was demonstrated that Batf3-dependent DCs are essential for the control of CL due to *L. major* infection. Batf3-deficient mice presented unresolved lesions and higher parasitic burdens, because of their inability to produce IL-12, a cytokine which is critical for the maintenance of Th1 immunity (29). In contrast to the mouse model of *L. major*-induced CL, less is known about the role of the different DC subsets in VL. We hypothesized that absence of cDC1, due to Batf3-deficiency, might impact on cross-priming of IFN-γ CD8$^+$ T cells (15, 31, 32), which play a major role in experimental VL (32, 33) and/or maintenance of IFN-γ-producing CD4$^+$ T cell responses (29, 35).

Murine models of VL have been extensively employed to elucidate the interaction of the host's immune system and viscerotropic parasite species (36, 37). Using *in vivo* bioimaging techniques we have been able to follow the evolution of the parasite colonization in C57BL/6 mice infected by *L. infantum*. According to previous reports (16, 38, 39) we have employed the pseudocolor heat-map signals to analyze the evolution of the parasitic burden in liver, spleen and bone marrow (**Figure 1** and **Supplementary Figure 1**). We have also determined the parasite loads in these organs by titration assays at two time points corresponding to the initial phase, when the immune response is primed in the spleen, and to the late phase of infection, when hepatic resistance is observed and parasites are present chronically in the spleen and BM (**Figure 2**) (7, 40). Although C57BL/6-*L. infantum* is not the most frequent murine model of VL, the data collected in this work are roughly consistent with published reports (12). Data show a similar evolution of the disease in this model of VL to that occurring in BALB/c mice infected by *L. infantum* or *L. donovani*, or in C57BL/6 mice infected with *L. donovani*; namely if comparing the control of parasitic burdens in the liver and development of a chronic infection in the spleen or the bone marrow (7, 8, 11, 41). Regarding the evolution of the hepatic parasite burden, bioluminescence reached its peak in weeks 6 to 7 and showed a progressive decline from those weeks until the end of the trial in wild-type mice. Interestingly, deficiency in Batf3 protein altered this evolution of hepatic parasitic load, which was progressively increased in *Batf3*$^{-/-}$ mice resulting in a chronic hepatic infection. It is noteworthy that in the last two weeks a dispersion of bioluminescence to other internal organs was observed in some *Batf3*$^{-/-}$ deficient mice, thus demonstrating a lack of control of the disease in Batf3-deficient animals. Contrary to the data shown by Alvarez et al. where they use the same *Leishmania* strain for infection of BALB/c mice (16), we were not able to detect bioluminescent signal in the spleen (except in some of the *Batf3*$^{-/-}$ animals at the end of the assays, as depicted above). Interestingly, a positive signal was obtained in the bone marrow (of the femur) in both animal groups. The higher concentration of parasites in the bone marrow is likely to allow their visualization, while in the spleen the luminescence remains below the detection threshold. The lower parasitic load observed in the spleen of C57BL/6 mice compared to BALB/c animals infected with the same *L. infantum* strain (10, 16) is consistent with previous data indicating that, although both strains are considered susceptible to VL, C57BL/6 mice show an intermediate phenotype of infection, less susceptible than BALB/c mice (2, 12, 42, 43). However, and as reported previously for C57BL/6 infected with *L. infantum* (12) or *L. donovani* (42), an increase of splenic parasite burdens with time was observed in both wild-type and *Batf3*$^{-/-}$ animals.

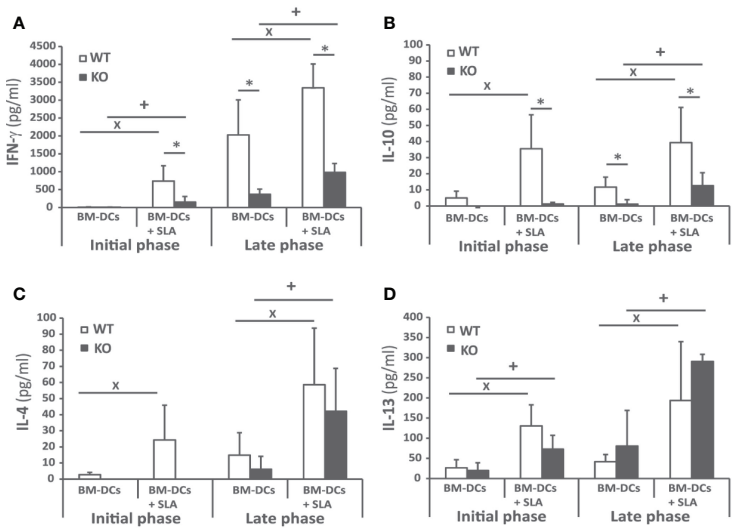

FIGURE 4 | Cytokine production against the parasite after challenge. *Batf3*$^{-/-}$ (KO) and wild-type (WT) mice were infected intravenously with 1 × 10^7 *PpyREh9*$^+$ *L. infantum* stationary phase promastigotes. Spleen cells cultures from each mouse were independently established at week 4 (Initial phase; n= 4 KO, n = 5 WT) or at week 10 (Late phase; n = 5 both groups) and stimulated for 72 h with BM-DCs pulsed or not with SLA. IFN-γ **(A)**, IL-10 **(B)**, IL-4 **(C)**, or IL-13 **(D)** levels were measured in culture supernatants by quantitative sandwich ELISA. Data are represented as the mean + SD. * ($P < 0.05$) shows the statistical differences between WT and KO mice groups. $^+$ ($P < 0.05$) shows the statistical differences between the SLA stimulated and unstimulated cells from mice of the KO group. ^{x} ($P < 0.05$) shows the statistical differences between the SLA stimulated and unstimulated cells from mice of the WT group. Results are representative of two independent experiments (Late phase).

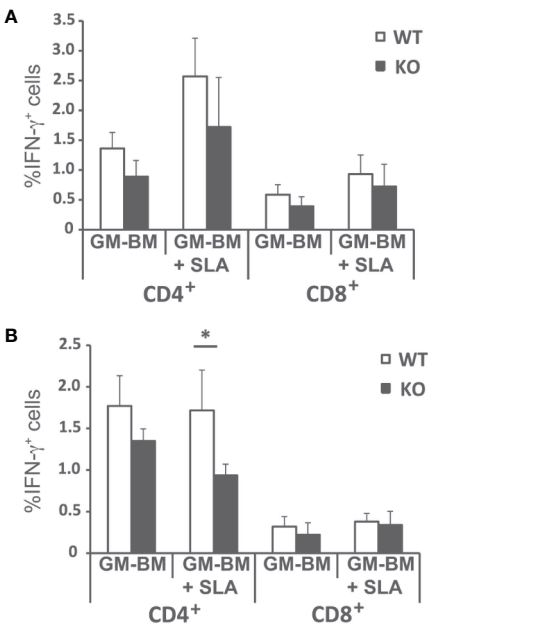

FIGURE 5 | Percentages of T cell producing IFN-γ. *Batf3*$^{-/-}$ (KO) and wild-type (WT) mice were infected intravenously with 1 × 10^7 PpyREh9$^+$ *L. infantum* stationary phase promastigotes. Spleen cells cultures from each mouse were independently established at week 4 (**A**; Initial phase; n= 4 KO, n = 5 WT) or at week 10 (**B**; Late phase; n = 5 both groups) and stimulated for 48 h with BM-DCs pulsed or not with SLA. Afterwards cells were processed for flow cytometry. Analyses are gated on CD3$^+$ cells. Data are represented as the mean (+ SD) of the percentage of CD4$^+$ or CD8$^+$ T cells positive for IFN-γ. * ($P < 0.05$) shows the statistical differences between WT and KO mice groups.

The self-resolving liver infection of the murine VL models mainly relies on the development of a CD4$^+$ Th1 response specific for the parasite that is primed in the spleen and is implicated in the formation of inflammatory granulomas in the liver (40). The activation of this CD4$^+$ Th1 cell response mounted by DCs occurs in the spleen in a IL-12–dependent manner (7, 11, 37). Here, we present different evidence about the existence of a dampened inflammatory response in *Batf3*$^{-/-}$ mice both at the initial and late phases of the disease compared to wild-type mice. The first evidence is the limited presence of anti-SLA IgG2c subclass antibodies in the serum of knockout mice at both phases of infection. Thus, we found significantly reduced titers of this antibody subclass in *Batf3*$^{-/-}$ animals compared to wild-type mice (**Figures 3A, B**). The second evidence is related to the observation that *Batf3*$^{-/-}$ mice exhibit reduced production of parasite-specific IFN-γ by CD4$^+$ T cells. This cytokine, that is essential for the activation of infected macrophages (37, 44), was found at significantly lower levels in the supernatants of cultures established from Batf3-deficient mice than in those of wild-type controls (**Figure 4A**). This finding correlates to the low NO production found in Batf3$^{-/-}$ mice (**Figure 6**). Thus, Batf3-deficiency resulted in a decrease in global leishmanicidal capacity, since NO promotes the destruction of parasites that infect macrophages (45). Others and we (29, 30) have shown that, in the absence of Batf3-depedendent cDC1, there is a poor IFN-γ response in the murine model of CL due to infection with *L. major*. This highlights the involvement of Batf3 in the generation of Th1 immunity against different *Leishmania* species, as also happens with other protozoan parasites such as *Toxoplasma gondii* (35), or in mucosal or systemic bacterial infections (46). Although

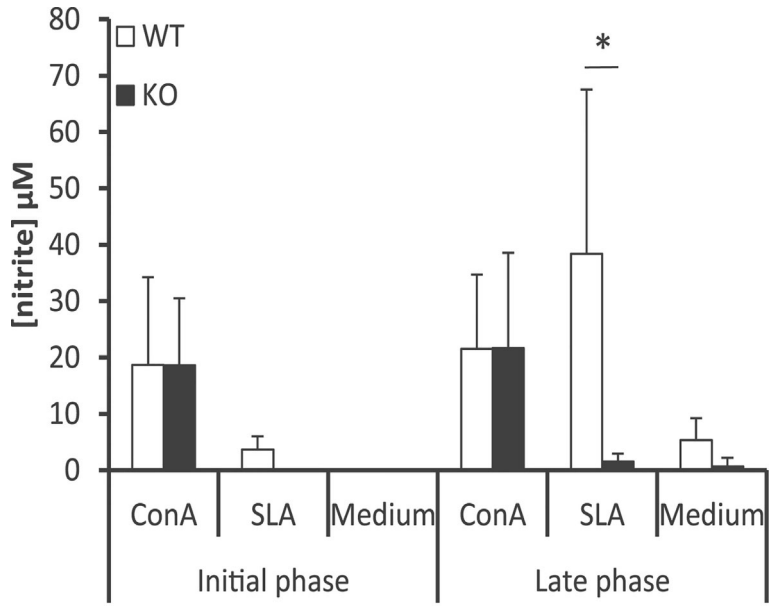

FIGURE 6 | Determination of the amounts of nitrite in the supernatants of splenic cell cultures. *Batf3*$^{-/-}$ (KO) and wild-type (WT) mice were infected intravenously with 1 × 10^7 PpyREh9$^+$ *L. infantum* stationary phase promastigotes. Spleen cells cultures from each mouse were independently established at week 4 (Initial phase; n= 4 KO, n = 5 WT) or at week 10 (Late phase; n = 5 both groups) and grown for 72 h without stimulus (Medium), treated with ConA or pulsed with SLA. Mean (+ SD) of nitrite levels is shown. * ($P < 0.05$) shows the statistical differences between WT and KO mice groups. Data shown are representative of two independent experiments with similar results (Late phase).

there is evidence indicating that CD8$^+$ T cells can also contribute to the production of IFN-γ in murine models of VL (47, 48), and that Batf3-dependent DC are critical for CD8$^+$ T cell crosspriming (15, 31, 32), we did not detect statistically significant differences in the percentages of CD8$^+$ T cells producing IFN-γ between wild-type and Batf3-deficient animals (**Figures 5A, B**). We have not detected the generation of Th17 responses against *L. infantum* proteins (**Supplementary Figure 2**). This result contrasts with what has previously been reported for the CL murine model in *Batf3*$^{-/-}$ mice, where the defect in Th1 response was compensated by the induction of parasite-dependent IL-17–mediated responses (30).

Contrary to what occurs upon *L. major* infection, the negative effect of the absence of Batf3-dependent DC in the generation of Th1 responses does not correlate with an increase in Th2-type responses (29, 30). Thus, we show that parasite-specific IL-4 (**Figure 4C**) and IL-13 production (**Figure 4D**) and the titers of SLA-specific IgG1 circulating antibodies (**Figures 3A, B**) did not differ between the two mice groups, which could be related with the paucity of splenic Tfh cells observed in *L. infantum* C57BL/6 mice (12). Finally, IL-10 has been described as an immunoregulatory molecule in human and murine experimental VL that can suppress antiparasitic immunity but also contributes to tissue damage prevention (49–51). As occurred for Th2-related cytokines, the absence of Batf3 resulted in an increased production of IL-10 after *L. major* infection (28, 29), that is not reproduced in the VL model employed for this work (**Figure 4B**). Since IL-10 production by CD4$^+$ Th1 cells could act as a feedback control of IFN-γ-mediated inflammation (51–53), the decreased production of IL-10 detected in Batf3$^{-/-}$ mice splenocytes could be an indirect effect of the diminished IFN-γ responses observed in these animals.

In summary, our results suggest that Batf3-dependent DCs are essential for controlling VL induced by *L. infantum* infection. Notwithstanding, our results imply, but do not directly demonstrate the role of cDC1 in resistance to VL, and further studies are needed to address this important limitation. In the absence of this population, the induction of CD4$^+$ Th1 responses against the viscerotropic *L. infantum* species is severely impaired, as has been described for CL. In contrast to *L. major*-infected Batf3-deficient mice, enhanced susceptibility to VL did not correlate with increased production of IL-10, Th2-type (29) or Th17-mediated responses (30). Thus, the crucial role of Batf3-dependent DCs, differentially imprinting Th responses in the different forms of leishmaniasis, reinforces the possibility of designing vaccines or targeted immunotherapies based on delivery of parasite antigens to this type of DCs.

DATA AVAILABILITY STATEMENT

The raw data supporting the conclusions of this article will be made available by the authors, without undue reservation.

ETHICS STATEMENT

The animal study was reviewed and approved by Animal Care and Use Committee at the Centro de Biología Molecular Severo Ochoa (CEEA-CBMSO 23/243), the Bioethical Committee of the CSIC (under reference 795/2019) Bioethical Committees of the CNIC and Universidad Complutense de Madrid as well as the Government of the Autonomous Community of Madrid (Spain) under the references PROEX 115/19, PROEX 121/14 and PROEX134/19.

AUTHOR CONTRIBUTIONS

Conceptualization: MS and SI. Methodology: MS, SI, LR, JS, and RR. Investigation, MS, LR, JS, SC-Z, AR-U, EH-G, EC, and SI. Writing—Original Draft: MS and SI. Writing—Review and Editing: MS, LR, JS, SC-Z, AR-U, EH-G, EC, and SI. Funding Acquisition: MS and SI. Resources: RR and RB-F. Supervision: MS and SI. All authors contributed to the article and approved the submitted version.

FUNDING

The research made for this study was supported in Spain by grants from Ministerio de Ciencia e Innovación FISPI11/00095 and FISPI14/00366 (FEDER FUNDING) and the Fondo de Investigaciones Sanitarias (ISCIII-RETICRD16/0027/0008-FEDER). SI is funded by RYC-2016-19463 and RTI2018-343 094484-B-I00 from Ministerio de Ciencia e Innovación (FEDER FUNDING). Institutional grants from the Fundación Ramón Areces and Banco de Santander to the CBMSO are also acknowledged. The funders had no role in study design, data collection and analysis, decision to publish, or preparation of the manuscript.

SUPPLEMENTARY MATERIAL

The Supplementary Material for this article can be found online at: https://www.frontiersin.org/articles/10.3389/fimmu.2020.590934/full#supplementary-material

REFERENCES

1. Steverding D. The history of leishmaniasis. *Parasit Vectors* (2017) 10:82. doi: 10.1186/s13071-017-2028-5
2. Gillespie PM, Beaumier CM, Strych U, Hayward T, Hotez PJ, Bottazzi ME. Status of vaccine research and development of vaccines for leishmaniasis. *Vaccine* (2016) 34:2992–5. doi: 10.1016/j.vaccine.2015.12.071
3. Uliana SRB, Trinconi CT, Coelho AC. Chemotherapy of leishmaniasis: present challenges. *Parasitology* (2018) 145:464–80. doi: 10.1017/S0031182016002523
4. Iborra S, Solana JC, Requena JM, Soto M. Vaccine candidates against *Leishmania* under current research. *Expert Rev Vaccines* (2018) 17(4):323–34. doi: 10.1080/14760584.2018.1459191
5. Scott P, Novais FO. Cutaneous leishmaniasis: immune responses in protection and pathogenesis. *Nat Rev Immunol* (2016) 16:581–92. doi: 10.1038/nri.2016.72
6. Sacks DL, Melby PC. Animal models for the analysis of immune responses to leishmaniasis. *Curr Protoc Immunol* (2015) 10819(2):1–24. doi: 10.1002/0471142735.im1902s108
7. Engwerda CR, Kaye PM. Organ-specific immune responses associated with infectious disease. *Immunol Today* (2000) 21:73–8. doi: 10.1016/S0167-5699(99)01549-2
8. Loeuillet C, Banuls AL, Hide M. Study of *Leishmania* pathogenesis in mice: experimental considerations. *Parasit Vectors* (2016) 9:144. doi: 10.1186/s13071-016-1413-9
9. Rolao N, Cortes S, Gomes-Pereira S, Campino L. *Leishmania infantum*: mixed T-helper-1/T-helper-2 immune response in experimentally infected BALB/c mice. *Exp Parasitol* (2007) 115:270–6. doi: 10.1016/j.exppara.2006.09.013
10. Carrion J, Nieto A, Iborra S, Iniesta V, Soto M, Folgueira C, et al. Immunohistological features of visceral leishmaniasis in BALB/c mice. *Parasite Immunol* (2006) 28:173–83. doi: 10.1111/j.1365-3024.2006.00817.x
11. Nieto A, Dominguez-Bernal G, Orden JA, De La Fuente R, Madrid-Elena N, Carrion J. Mechanisms of resistance and susceptibility to experimental visceral leishmaniosis: BALB/c mouse versus syrian hamster model. *Vet Res* (2011) 42:39. doi: 10.1186/1297-9716-42-39
12. Perez-Cabezas B, Cecilio P, Gaspar TB, Gartner F, Vasconcellos R, Cordeiro-da-Silva A. Understanding Resistance vs. Susceptibility in Visceral Leishmaniasis Using Mouse Models of *Leishmania infantum* Infection. *Front Cell Infect Microbiol* (2019) 9:30. doi: 10.3389/fcimb.2019.00030
13. Murphy TL, Tussiwand R, Murphy KM. Specificity through cooperation: BATF-IRF interactions control immune-regulatory networks. *Nat Rev Immunol* (2013) 13:499–509. doi: 10.1038/nri3470
14. Li P, Spolski R, Liao W, Wang L, Murphy TL, Murphy KM, et al. BATF-JUN is critical for IRF4-mediated transcription in T cells. *Nature* (2012) 490:543–6. doi: 10.1038/nature11530
15. Hildner K, Edelson BT, Purtha WE, Diamond M, Matsushita H, Kohyama M, et al. Batf3 deficiency reveals a critical role for CD8alpha+ dendritic cells in cytotoxic T cell immunity. *Science* (2008) 322:1097–100. doi: 10.1126/science.1164206
16. Alvarez-Velilla R, Gutierrez-Corbo MDC, Punzon C, Perez-Pertejo MY, Balana-Fouce R, Fresno M, et al. A chronic bioluminescent model of experimental visceral leishmaniasis for accelerating drug discovery. *PLoS Negl Trop Dis* (2019) 13:e0007133. doi: 10.1371/journal.pntd.0007133
17. Buffet PA, Sulahian A, Garin YJ, Nassar N, Derouin F. Culture microtitration: a sensitive method for quantifying *Leishmania infantum* in tissues of infected mice. *Antimicrob Agents Chemother* (1995) 39:2167–8. doi: 10.1128/AAC.39.9.2167
18. Solana JC, Ramirez L, Corvo L, de Oliveira CI, Barral-Netto M, Requena JM, et al. Vaccination with a *Leishmania infantum* HSP70-II null mutant confers long-term protective immunity against *Leishmania major* infection in two mice models. *PLoS Negl Trop Dis* (2017) 11:e0005644. doi: 10.1371/journal.pntd.0005644
19. Gracie JA, Bradley JA. Interleukin-12 induces interferon-gamma-dependent switching of IgG alloantibody subclass. *Eur J Immunol* (1996) 26:1217–21. doi: 10.1002/eji.1830260605
20. Lee W, Kim HS, Hwang SS, Lee GR. The transcription factor Batf3 inhibits the differentiation of regulatory T cells in the periphery. *Exp Mol Med* (2017) 49:e393. doi: 10.1038/emm.2017.157
21. Qiu Z, Khairallah C, Romanov G, Sheridan BS. Cutting Edge: Batf3 Expression by CD8 T Cells Critically Regulates the Development of Memory Populations. *J Immunol* (2020) 205:901–6. doi: 10.4049/jimmunol.2000228
22. Ataide MA, Komander K, Knopper K, Peters AE, Wu H, Eickhoff S, et al. BATF3 programs CD8(+) T cell memory. *Nat Immunol* (2020) 21:1397–407. doi: 10.1038/s41590-020-0786-2
23. Edelson BT, Bradstreet TR, Wumesh KC, Hildner K, Herzog JW, Sim J, et al. Batf3-dependent CD11b(low/-) peripheral dendritic cells are GM-CSF-independent and are not required for Th cell priming after subcutaneous immunization. *PLoS One* (2011) 6:e25660. doi: 10.1371/journal.pone.0025660
24. Seillet C, Jackson JT, Markey KA, Brady HJM, Hill GR, MacDonald KPA, et al. CD8α+ DCs can be induced in the absence of transcription factors Id2, Nfil3, and Batf3. *Blood* (2013) 121:1574–83. doi: 10.1182/blood-2012-07-445650
25. Waithman J, Zanker D, Xiao K, Oveissi S, Wylie B, Ng R, et al. Resident CD8(+) and Migratory CD103(+) Dendritic Cells Control CD8 T Cell Immunity

during Acute Influenza Infection. *PLoS One* (2013) 8:e66136. doi: 10.1371/journal.pone.0066136
26. Böttcher JP, Reis e Sousa CR. The Role of Type 1 Conventional Dendritic Cells in Cancer Immunity. *Trends Cancer* (2018) 4(11):784–92. 10.1016/j.trecan.2018.09.001
27. von Stebut E, Tenzer S. Cutaneous leishmaniasis: Distinct functions of dendritic cells and macrophages in the interaction of the host immune system with *Leishmania major*. *Int J Med Microbiol* (2017) 308:2206–214. doi: 10.1016/j.ijmm.2017.11.002
28. Martinez-Lopez M, Soto M, Iborra S, Sancho D. *Leishmania* Hijacks Myeloid Cells for Immune Escape. *Front Microbiol* (2018) 9:883. doi: 10.3389/fmicb.2018.00883
29. Martinez-Lopez M, Iborra S, Conde-Garrosa R, Sancho D. Batf3-dependent CD103+ dendritic cells are major producers of IL-12 that drive local Th1 immunity against *Leishmania major* infection in mice. *Eur J Immunol* (2015) 45:119–29. doi: 10.1002/eji.201444651
30. Ashok D, Schuster S, Ronet C, Rosa M, Mack V, Lavanchy C, et al. Cross-presenting dendritic cells are required for control of *Leishmania major* infection. *Eur J Immunol* (2014) 44:1422–32. doi: 10.1002/eji.201344242
31. den Haan JM, Lehar SM, Bevan MJ. CD8(+) but not CD8(-) dendritic cells cross-prime cytotoxic T cells in vivo. *J Exp Med* (2000) 192:1685–96. doi: 10.1084/jem.192.12.1685
32. Theisen DJ, Davidson JTT, Briseno CG, Gargaro M, Lauron EJ, Wang Q, et al. WDFY4 is required for cross-presentation in response to viral and tumor antigens. *Science* (2018) 362:694–9. doi: 10.1126/science.aat5030
33. Polley R, Stager S, Prickett S, Maroof A, Zubairi S, Smith DF, et al. Adoptive immunotherapy against experimental visceral leishmaniasis with CD8+ T cells requires the presence of cognate antigen. *Infect Immun* (2006) 74:773–6. doi: 10.1128/IAI.74.1.773-776.2006
34. Stager S, Rafati S. CD8(+) T cells in leishmania infections: friends or foes? *Front Immunol* (2012) 3:5. doi: 10.3389/fimmu.2012.00005
35. Mashayekhi M, Sandau MM, Dunay IR, Frickel EM, Khan A, Goldszmid RS, et al. CD8alpha(+) dendritic cells are the critical source of interleukin-12 that controls acute infection by Toxoplasma gondii tachyzoites. *Immunity* (2011) 35:249–59. doi: 10.1016/j.immuni.2011.08.008
36. Kaye PM, Aebischer T. Visceral leishmaniasis: immunology and prospects for a vaccine. *Clin Microbiol Infect* (2011) 17:1462–70. doi: 10.1111/j.1469-0691.2011.03610.x
37. Faleiro RJ, Kumar R, Hafner LM, Engwerda CR. Immune regulation during chronic visceral leishmaniasis. *PLoS Negl Trop Dis* (2014) 8:e2914. doi: 10.1371/journal.pntd.0002914
38. Tavares J, Costa DM, Teixeira AR, Cordeiro-da-Silva A, Amino R. In vivo imaging of pathogen homing to the host tissues. *Methods* (2017) 127:37–44. doi: 10.1016/j.ymeth.2017.05.008
39. Thalhofer CJ, Graff JW, Love-Homan L, Hickerson SM, Craft N, Beverley SM, et al. In vivo imaging of transgenic *Leishmania* parasites in a live host. *J Vis Exp* (2010) (41):e1980. doi: 10.3791/1980
40. Kaye PM, Svensson M, Ato M, Maroof A, Polley R, Stager S, et al. The immunopathology of experimental visceral leishmaniasis. *Immunol Rev* (2004) 201:239–53. doi: 10.1111/j.0105-2896.2004.00188.x
41. Wilson ME, Jeronimo SM, Pearson RD. Immunopathogenesis of infection with the visceralizing *Leishmania* species. *Microb Pathog* (2005) 38:147–60. doi: 10.1016/j.micpath.2004.11.002
42. Bodhale NP, Pal S, Kumar S, Chattopadhyay D, Saha B, Chattopadhyay N, et al. Inbred mouse strains differentially susceptible to *Leishmania donovani* infection differ in their immune cell metabolism. *Cytokine* (2018) 112:12–5. doi: 10.1016/j.cyto.2018.06.003
43. Perez-Cabezas B, Cecilio P, Robalo AL, Silvestre R, Carrillo E, Moreno J, et al. Interleukin-27 Early Impacts *Leishmania infantum* Infection in Mice and Correlates with Active Visceral Disease in Humans. *Front Immunol* (2016) 7:478. doi: 10.3389/fimmu.2016.00478
44. Kaye P, Scott P. Leishmaniasis: complexity at the host-pathogen interface. *Nat Rev Microbiol* (2011) 9:604–15. doi: 10.1038/nrmicro2608
45. Olekhnovitch R, Bousso P. Induction, Propagation, and Activity of Host Nitric Oxide: Lessons from *Leishmania* Infection. *Trends Parasitol* (2015) 31:653–64. doi: 10.1016/j.pt.2015.08.001
46. Arnold IC, Zhang X, Artola-Boran M, Fallegger A, Sander P, Johansen P, et al. BATF3-dependent dendritic cells drive both effector and regulatory T-cell responses in bacterially infected tissues. *PLoS Pathog* (2019) 15:e1007866. doi: 10.1371/journal.ppat.1007866
47. Tsagozis P, Karagouni E, Dotsika E. CD8(+) T cells with parasite-specific cytotoxic activity and a Tc1 profile of cytokine and chemokine secretion develop in experimental visceral leishmaniasis. *Parasite Immunol* (2003) 25:569–79. doi: 10.1111/j.0141-9838.2004.00672.x
48. Joshi T, Rodriguez S, Perovic V, Cockburn IA, Stager S. B7-H1 blockade increases survival of dysfunctional CD8(+) T cells and confers protection against *Leishmania donovani* infections. *PLoS Pathog* (2009) 5:e1000431. doi: 10.1371/journal.ppat.1000431
49. Bunn PT, Montes de Oca M, de Labastida Rivera F, Kumar R, Ng SS, Edwards CL, et al. Distinct Roles for CD4(+) Foxp3(+) Regulatory T Cells and IL-10-Mediated Immunoregulatory Mechanisms during Experimental Visceral Leishmaniasis Caused by *Leishmania donovani*. *J Immunol* (2018) 201:3362–72. doi: 10.4049/jimmunol.1701582
50. Montes de Oca M, Kumar R, de Labastida Rivera F, Amante FH, Sheel M, Faleiro RJ, et al. Blimp-1-Dependent IL-10 Production by Tr1 Cells Regulates TNF-Mediated Tissue Pathology. *PLoS Pathog* (2016) 12:e1005398. doi: 10.1371/journal.ppat.1005398
51. Nylen S, Sacks D. Interleukin-10 and the pathogenesis of human visceral leishmaniasis. *Trends Immunol* (2007) 28:378–84. doi: 10.1016/j.it.2007.07.004
52. Stager S, Maroof A, Zubairi S, Sanos SL, Kopf M, Kaye PM. Distinct roles for IL-6 and IL-12p40 in mediating protection against *Leishmania donovani* and the expansion of IL-10+ CD4+ T cells. *Eur J Immunol* (2006) 36:1764–71. doi: 10.1002/eji.200635937
53. Cope A, Le Friec G, Cardone J, Kemper C. The Th1 life cycle: molecular control of IFN-gamma to IL-10 switching. *Trends Immunol* (2011) 32:278–86. doi: 10.1016/j.it.2011.03.010

Conflict of Interest: The authors declare that the research was conducted in the absence of any commercial or financial relationships that could be construed as a potential conflict of interest.

frontiers in Microbiology

ORIGINAL RESEARCH
published: 20 January 2021
doi: 10.3389/fmicb.2020.579929

Population Genetic Analysis of the *Theileria annulata* Parasites Identified Limited Diversity and Multiplicity of Infection in the Vaccine From India

*Sonti Roy[1,2], Vasundhra Bhandari[1], Madhumanti Barman[1], Pankaj Kumar[3], Vandna Bhanot[4], Jaspreet Singh Arora[5], Satparkash Singh[5] and Paresh Sharma[1]**

[1]National Institute of Animal Biotechnology, Hyderabad, India, [2]Manipal Academy of Higher Education, Manipal, India, [3]Division of Livestock and Fisheries Management, ICAR-Research Complex for Eastern Region, Patna, India, [4]Disease Investigation Laboratory, Lala Lajpat Rai University of Veterinary and Animal Sciences, Ambala, India, [5]School of Animal Biotechnology, Guru Angad Dev Veterinary and Animal Sciences University, Punjab, India

Background: Apicomplexan parasite *Theileria annulata* causes significant economic loss to the livestock industry in India and other tropical countries. In India, parasite control is mainly dependent on the live attenuated schizont vaccine and the drug buparvaquone. For effective disease control, it is essential to study the population structure and genetic diversity of the *Theileria annulata* field isolates and vaccine currently used in India.

Methodology/Results: A total of 125 *T. annulata* isolates were genotyped using 10 microsatellite markers from four states belonging to different geographical locations of India. Limited genetic diversity was observed in the vaccine isolates when compared to the parasites in the field; a level of geographical substructuring was evident in India. The number of genotypes observed per infection was highest in India when compared to other endemic countries, suggesting high transmission intensity and abundance of ticks in the country. A reduced panel of four markers can be used for future studies in these for surveillance of the *T. annulata* parasites in India.

Conclusion: High genetic variation between the parasite populations in the country suggests their successful spread in the field and could hamper the disease control programs. Our findings provide the baseline data for the diversity and population structure of *T. annulata* parasites from India. The low diversity in the vaccine advocates improving the current vaccine, possibly by increasing its heterozygosity. The reduced panel of the markers identified in this study will be helpful in monitoring parasite and its reintroduction after *Theileria* eradication.

Keywords: genotyping, schizont stage vaccine, *Theileria annulata*, population genetics, genetic diversity

OPEN ACCESS

Edited by:
Jun-Hu Chen,
National Institute of Parasitic Diseases, China

Reviewed by:
Prashant Khare,
All India Institute of Medical Sciences Bhopal, India
Vijay Kumar Prajapati,
Central University of Rajasthan, India
Hem Chandra Jha,
Indian Institute of Technology Indore, India
Kerry Woods,
University of Bern, Switzerland

***Correspondence:**
Paresh Sharma
paresh@niab.org.in;
pareshsharma21@gmail.com

Specialty section:
This article was submitted to Microbial Immunology, a section of the journal Frontiers in Microbiology

Received: *03 July 2020*
Accepted: *15 December 2020*
Published: *20 January 2021*

Citation:
Roy S, Bhandari V, Barman M, Kumar P, Bhanot V, Arora JS, Singh S and Sharma P (2021) Population Genetic Analysis of the Theileria annulata Parasites Identified Limited Diversity and Multiplicity of Infection in the Vaccine From India. Front. Microbiol. 11:579929. doi: 10.3389/fmicb.2020.579929

INTRODUCTION

Bovine theileriosis, a tick-borne infectious disease, remains a severe problem for livestock in tropical countries affecting millions of animals, especially crossbreed and exotic cattle annually. The dominant *Theileria* species, linked to economic loss and mortality worldwide, are *Theileria annulata* and *Theileria parva*. *Theileria annulata* is responsible for the majority of theileriosis cases in India, while there are no reports of *T. parva* from the country (George et al., 2015). The management of the disease is mainly dependent on a live attenuated *T. annulata* schizont vaccine and a hydroxynaphthoquinones class of drug Buparvaquone. High prevalence rates (3–41%) of *T.annulata* were reported from different states of India (Kundave et al., 2015; Kumar et al., 2016; Dandasena et al., 2018). The attenuated vaccine is 100% effective against the homologous parasite challenge; however, the efficiency decreases in the presence of heterologous parasites in the field (Gill et al., 1980; Hashemi-Fesharki, 1988; Darghouth et al., 1996). There is limited information on the genetic diversity and population structure of the *T. annulata* parasites prevalent in field and in vaccine from India. The present study was designed to study the population genetics of the *T. annulata* parasites in the country.

Hyalonmma anatolicum transmits *T. annulata* sporozoites in the host and causes a lymphoproliferative disease similar to cancer (Ghosh and Azhahianambi, 2007; Tretina et al., 2015). The *T. annulata* sporozoites transform to the schizont stage and reside inside the host lymphocyte and macrophage cells (Sager et al., 1998). Among the different parasite stages in the host, the schizont stage is the symptomatic stage, based on which attenuated schizont vaccines were designed. The cell culture-based attenuated vaccines have been used in countries, like India (Gupta et al., 1998), China (Zhang, 1997), Russia (Stepanova and Zablotskii, 1989), Turkey (Sayin et al., 1997), Spain (Viseras et al., 1997), Israel (Pipano and Tsur, 1966), Iran (Hashemi-Fesharki, 1988), Tunisia (Darghouth, 2008), and Morocco (Ouhelli et al., 1997) for controlling the *T. annulata* infection. The attenuation of the vaccine line because of the long term passage results in loss of genotypes, decreasing the diversity of the parasites (Darghouth et al., 1996; Pipano and Shkap, 2006; Bilgic et al., 2019). Previous studies in *T. parva* have also shown limited genetic and antigenic diversity in the Muguga cocktail vaccine, recommending modification in the current vaccine by enhancing its diversity (Hemmink et al., 2016). Genetic diversity studies have been shown to be important for dissecting important information about protozoan parasites, like epidemiology, control, evolution, virulence, antigenicity, infectivity, drug sensitivity, and host preference (Majewska and Sulima, 1999; Sivakumar et al., 2014).

The multilocus genotyping technique has been used for studying the genetic diversity, transmission dynamics, and population structure of *T. annulata* parasites from other endemic countries, like China, Oman, Turkey, Tunisia, Portugal, and Sudan (Weir et al., 2007, 2011; Al-Hamidhi et al., 2015; Gomes et al., 2016; Yin et al., 2018). High genetic diversity, presence of multiple genotypes per sample, and geographical sub-structuring were the highlighting feature of the *T. annulata* populations reported till now (Weir et al., 2007, 2011; Al-Hamidhi et al., 2015; Gomes et al., 2016; Yin et al., 2018). Recently using a small number of samples, our group has shown high allelic and antigenic diversity in the clinical strains of *T. annulata* from India (Roy et al., 2019). However, comparative population genetic analysis among the *T. annulata* vaccine and the field isolates from different geographical locations of India is not known.

In the present study, microsatellite-based genotyping has been used for understanding the genetic diversity, population structure, and geographical substructuring of the *T. annulata* vaccine and parasite isolates collected from the four different locations in India. The genotyping results were also compared with similar data from other endemic countries. The results provide the first insight into the population genetics and diversity of the *T. annulata* parasites in India.

MATERIALS AND METHODS

Parasite Sample Collection

Blood samples were collected from the suspected animals from four different geographical locations of India (Telangana, Gujarat, Haryana, and Bihar). Approximately 3 ml of blood was collected in EDTA coated vacutainer tubes (BD) with the help of trained veterinarians. A total of 125 blood samples, including the *T. annulata* vaccine, were collected. DNA was isolated from the blood using the standard phenol chloroform isoamyl alcohol method. DNA concentration and integrity were checked using nanodrop, and by running 0.8% agarose gel in TAE buffer. Diagnosis of the *T. annulata* infection was done based on microscopic analysis of Giemsa stained smears and PCR using *T. annulata* specific primers. The primers used were specific to the *T. annulata* Surface protein (*TaSP*) gene of the parasite (Roy et al., 2019).

Microsatellite Genotyping

Genotyping was done using the 10 microsatellite markers previously described for *T. annulata* (Weir et al., 2007). The forward primer used for amplifying the markers was labeled with FAM at the 5' end for detection in capillary electrophoresis. The DNA samples (N = 125) were used as a template for amplifying the 10 markers from each sample using a previously described protocol (Roy et al., 2019). Amplified PCR products were purified using the Qiagen PCR clean-up kit and stored in an amber tube to reduce the fluorescence loss. The amplified products were separated on the ABI 3730Xl electrophoresis instrument, with Liz500 as the standard internal marker for the fragment size analysis.

Data Analysis

The file generated from capillary electrophoresis was imported into Gene marker 2.7.0 software (SoftGenetics, LLC) for further analysis. Allele scoring for each marker was done in the previously described range for *T. annulata*. The alleles were scored based on the predominant peak, and only peaks above 25% of this peak were recorded for analysis. Stutter peak filter

was applied to remove stutter peaks within 2.5 base pairs of the primary peak. Plus A filter was used to prevent calling two alleles in case of a split peak, which is one base pair apart. The total number of alleles was counted and averaged for each sample across 10 loci to estimate the multiplicity of infection (MOI). Multilocus genotype (MLG) data for each sample were generated using the predominant peak (Weir et al., 2007). For comparative population study, publicly available similar data from other endemic countries were used for analysis (Weir et al., 2011; Al-Hamidhi et al., 2015). The MLG data were used to estimate the allele frequency, number of effective alleles (Ne), and expected heterozygosity (He) using GenAlEx 6.503 (Peakall and Smouse, 2012) as an excel add-in tool kit. The proportion of shared alleles was calculated using PopGenReport package in R software (Adamack and Gruber, 2014). Mean allele number and allele richness (R_s) were calculated for all the markers using the FSTAT 2.9.4 program (Goudet, 2003). Lian 3.7 Program (Haubold and Hudson, 2000) was used to calculated I^A_S, V_D, and V_{para} to predict linkage disequilibrium (LD) in the population using the MLG data. Population genetic differentiation (Fst) was calculated on the Genepop 4.2 Web Server (Raymond, 1995; Rousset, 2008) using the MLG data to understand the population differentiation. Bayesian analysis was done using the STRUCTURE 2.3.4 software (Pritchard et al., 2000; Evanno et al., 2005). Twenty iterations were run for each group (K = 1–12) with a burn-in of 50,000 steps and then 500,000 Bayesian Markov Chain Monte Carlo (MCMC) steps using the admixture model. The optimal number of clusters was identified using method described by Evanno et al. (2005). Discriminant Analysis of Principal Components (DAPC) was done by R software using the Adegenet 2.0.1 package (Jombart, 2008) for understanding the geographical substructuring between the populations using the MLG data.

The complete allelic profile of each sample was next used to prepare a binary data set for the presence and absence of alleles for understanding the genotypic diversity considering multiple parasite genotypes in each sample. A similarity matrix and dendrogram were created based on the allelic data by Jaccard's similarity index using online server DendroUPGMA (Garcia-Vallve et al., 1999). Interactive Tree Of Life (iTOL) software was used for visualization of the tree (Letunic and Bork, 2007).

Bottleneck Analysis

The Bottleneck analysis was done using the allele frequency data for assessing the change in the population size by measuring excess or deficit in heterozygosity by Bottleneck software version 1.2.02 (Piry et al., 1999). The two-phase model (TPM) with 1,000 iterations was used to compare the number of loci in population that present heterozygosity excess or deficiency under the mutation drift equilibrium (Cornuet and Luikart, 1996; Luikart and Cornuet, 1998). Sign test and Wilcoxon test were used for identifying the statistical significance of the data generated using TPM model.

Recent effective population size reductions (genetic bottlenecks) were studied using allele frequency data and BOTTLENECK software (Version 1.2.02; Cornuet and Luikart, 1996). To determine whether a population exhibits a significant number of loci with heterozygosity excess, BOTTLENECK proposes three tests: sign test, standardized differences test (minimum 20 loci), and Wilcoxon sign-rank test. Finally, the allele frequency distribution was established in order to see whether it is approximately L-shaped (as expected under mutation-drift equilibrium) or not (recent bottlenecks provoke a mode shift). As recommended by Piry et al. (1999), the TPM with 95% proportion of the Stepwise Mutation Model (SMM) and 5% of the Multistep mutations was used.

Optimal Set of Marker for Population Differentiation

For identifying a minimum number of microsatellite markers for differentiating the parasite population, sequential removal of markers was done for counting haplotypes based on the He values starting from low to high. The optimal set of markers needed for population differentiation and the correlation between the populations of different states was done using Genalex 6.503 software (Peakall and Smouse, 2012; Kittichai et al., 2017).

Ethics Statement

Collection of less than 5 ml of blood, in accordance with national legislation, is exempt from ethical approval requirements. The animal study was reviewed and approved by Institutional Animal Ethics committee, National Institute of Animal Biotechnology, Hyderabad.

RESULTS

High Genetic Diversity and MOI in the *Theileria annulata* Isolates From India

A total of 125 samples were collected from four different states (Telangana, Haryana, Gujarat, and Bihar), including the vaccine for assessing genotypic diversity of *T. annulata* parasites in India (**Figure 1A**). The parasite infection was confirmed by Giemsa stained smears and PCR in all the samples. The genotypic diversity was studied using a panel of 10 micro and minisatellite markers in *T. annulata*. The diversity of the isolates was assessed based on their; allelic profile, MOI, allelic richness, the proportion of shared alleles, effective number of alleles, expected heterozygosity, and minor allele frequency. The allelic profile of the vaccine showed less than five alleles in most of the markers except TS6 and TS31 (**Figure 1B**). The genotyping showed the presence of mixed parasite infections in each isolate based on the presence of multiple alleles at each locus. The allelic data per locus were used for calculating MOI for each sample from all the states. The MOI values for Gujarat (16.77), Haryana (13.03), and Telangana (11.64) were found to be significantly higher when compared to Bihar (**Table 1**). The genotypes per infection in the vaccine line based on the MOI values (6) were substantially less than the parasite population from all the states (**Figure 1C**). The comparative MOI analysis between the different endemic countries showed very high number of genotypes per infection in Indian population (**Figure 1C**). Since multiple alleles

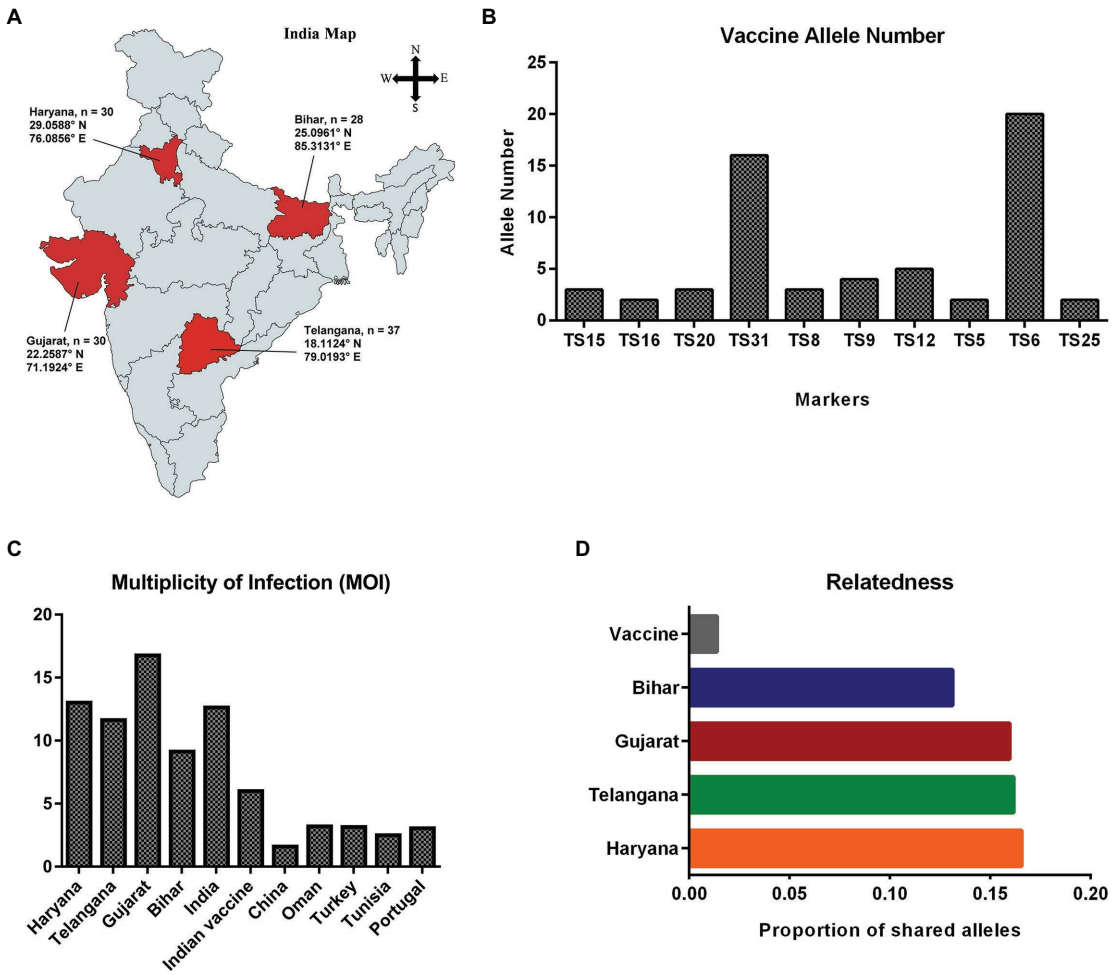

FIGURE 1 | Sample collection map and genetic diversity: **(A)** Sampling locations of *Theileria annulata* are indicated on the map of India; **(B)** Graph showing total number of alleles detected for the 10 markers in vaccine; **(C)** Comparative analysis of multiplicity of infection (MOI) in *T. annulata* isolates from India and other endemic countries; and **(D)** Proportion of shared alleles between the *T. annulata* isolates of different states and vaccine.

TABLE 1 | Population Diversity.

Population	N	MOI[#]	Ne	Mean number of alleles	Mean allelic richness[a]	Mean H_E
Haryana	30	13.03	10.465	15.2	15.17	0.850
Telangana	37	11.64	12.114	19.1	18.42	0.876
Gujarat	30	16.77	9.126	13.5	13.48	0.856
Bihar	28	9.15	10.895	15.1	15.10	0.872
Total	125	12.64	10.650	15.72	22.84[b]	0.864

[a]*Allelic richness based on a minimum sample size of 28 haploid individual samples.*

[b]*Allelic richness based on a minimum sample size of 125 haploid individual samples.*

[#]*Significant by one-way ANOVA between Haryana and Gujarat, Haryana and Bihar, Telangana and Gujarat, Telangana and Bihar, and Gujarat and Bihar.*

Expected Heterozygosity (H_E) is high for all the population. Expected H_E measures will range from zero (no heterozygosity) to nearly 1.0.

were found in the samples, the MLG profile was created by selecting the predominant allele from each locus for all the samples. The MLG data identified 125 unique haplotypes with no sharing between or within the states. High polymorphism was found in all the markers in the field samples, with an overall number of alleles ranging from 26 (TS12) to 8 (TS25, TS15) per marker. Allele comparison between the vaccine and the regional isolates showed little proportion of alleles shared among them (**Figure 1D**). Out of 10 markers, TS8, TS9, TS12, and TS31 showed no shared allele with the vaccine, while TS5, TS6, TS15, TS16, TS20, and TS25 showed some shared alleles within the population.

We next calculated mean allele number and allele richness using the MLG data (**Table 1**). Telangana showed the highest allele number (19.1) and allele richness (18.42) among the regional population, followed by Haryana, Bihar, and Gujarat. TS6, TS8, TS9, TS12, and TS31 markers showed more number of alleles per locus and also had high allele richness consistently in all the population (**Figure 2A**).

The number of effective alleles ranged from 9.1 (Gujarat) to 12.1 (Telangana; **Table 1**). The MLG data were next used for calculating the expected heterozygosity between the states and in the total population. The expected He was found to be high (0.864) in samples across India (**Table 1**). We also compared expected He of parasite population from India to previously reported *T. annulata* isolates from countries, like Oman, Portugal, Sudan, Tunisia, China, and Turkey (**Figure 2B**). The high genetic diversity of Indian parasites was similar to other countries, like Oman, Turkey, Tunisia, and Sudan. Further allele frequency was calculated from the allelic data per locus for segregating the common and rare alleles, which in turn helps in identifying the diversity of the parasite population. The allele count was highest for Gujarat in the frequency range of 0–0.02 and 0.02–0.04, followed by Haryana, Telangana, and then Bihar suggesting high diversity in the former state (**Figure 2C**). As the frequency range increases, there is not much difference between the populations.

Geographical Sub-structuring in the Indian *Theileria annulata* Parasite Population

For understanding the genetic variance among the Indian *T. annulata* parasite population, pairwise Fst values were calculated using the MLG profiles. Based on the Fst data, genetic divergence was found higher in the Bihar parasite population when paired to Gujarat (0.046), Haryana (0.046), and Telangana (0.0326; **Table 2**). While low variance was observed between the parasite population of Haryana, Gujarat, and Telangana with Fst values ranging from 0.0081 to 0.0156. Next, we compared the Indian parasite population with the previously reported parasite population from countries like Oman, Turkey, Tunisia, and Sudan using their MLG profiles. The Fst data showed high genetic variance between the Indian and Tunisia (0.0850) parasite population. While moderate variation was seen when the pairwise comparison was made between the India and Sudan (0.0691), India and Oman (0.0647), and India and Turkey (0.0573) parasite populations.

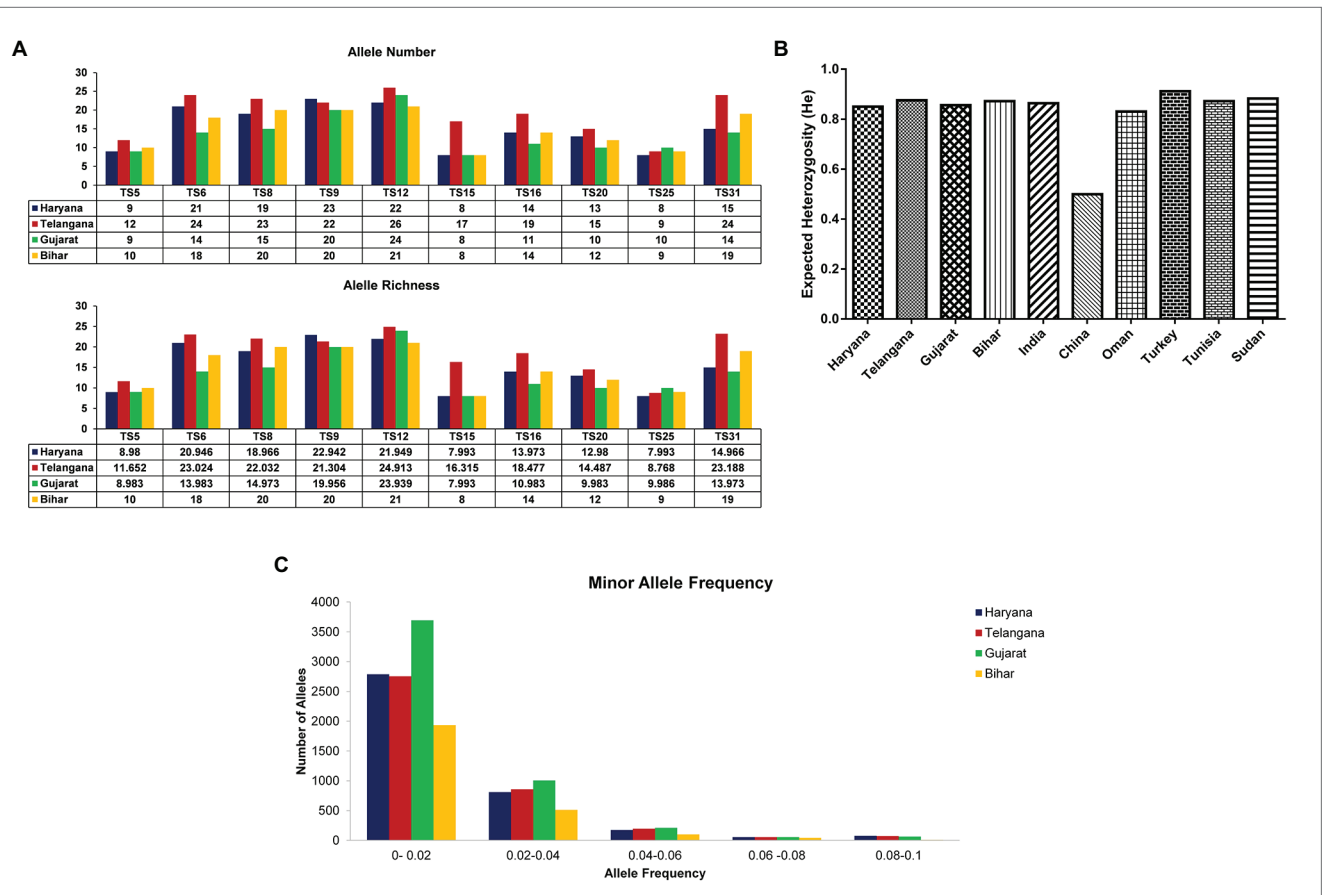

FIGURE 2 | Allelic Number and Allele richness, Expected heterozygosity (He), and Minor allele frequency: **(A)** Graph showing number of alleles and allele richness of 10 markers in *T. annulata* isolates from four states in India; **(B)** Comparative analysis of expected heterozygosity (He) values between the *T. annulata* population of India and other endemic countries; and **(C)** The graph shows distribution of number of alleles against different frequency range in *T. annulata* isolates from four states in India.

Next, we calculated Nei's genetic distance between Indian populations for finding the relation between genetic and geographic distance. No significant correlation was observed when pairwise Nei genetic distance or Fst values were plotted against geographic distance in kilometer, with R^2 value of 0.2889 and 0.2297, respectively (**Figure 3A**). Structure analysis using the Bayesian iterative algorithm did not show any clear pattern of distribution among the Indian parasite populations at K values ranging from $K = 1$ to $K = 12$ (**Figures 3B,C**). However, the DAPC analysis showed clustering between the parasite populations of different states, suggesting a level of geographical distribution in India (**Figure 3D**). The Indian vaccine clustered near to the Bihar and Telangana parasites in the analysis. The *T. annulata* parasite population was next compared using similar data to parasites from other endemic countries, like Tunisia, Turkey, and Oman. The DAPC analysis supported a high genetic differentiation between populations in India, Tunisia, Turkey, and Oman (**Figure 3E**). The differentiation analysis done until now is based on the predominant allele of the isolates and might miss other relevant alleles that might show differentiation between the populations. Therefore, we constructed a phylogenetic tree based on the complete allelic profiles of all the samples to understand the genetic differentiation pattern. The analysis showed regional clustering in the samples from Haryana, Telangana, and Gujarat, although some samples had mixed distribution within other regions (**Figure 3F**). The vaccine strain was found near to the isolates from state of Bihar and Telangana, suggesting some level of similarity among the parasites.

LD and Nonbottlenecked Parasite Population in India

The MLG data was next used for identifying LD in the Indian parasite population by calculating the standard index of association (I^S_A). We found significant LD in parasite population of Telangana ($I^S_A = 0.0545$, $p < 0.001$), Bihar ($I^S_A = 0.0313$, $p < 0.001$) and in total Indian population ($I^S_A = 0.0263$, $p < 0.001$; **Supplementary Table S1**). However, in the state of Haryana and Gujarat, I^S_A values were found to be statistically insignificant to conclude anything [$I^S_A = -0.0022$, $p = 6.70 \times 10^{-01}$, $I^S_A = 0.0156$, $p = 1.10 \times 10^{-01}$, respectively (**Figure 4A**)]. We observed LD when comparing Indian parasite population in combination with other countries population, like Oman ($I^S_A = 0.0313$, $p < 0.001$), Turkey ($I^S_A = 0.0313$, $p < 0.001$), Tunisia ($I^S_A = 0.0313$, $p < 0.001$), Sudan ($I^S_A = 0.0313$, $p = < 0.001$), and India and other countries ($I^S_A = 0.0429$, $p < 0.001$). Further bottleneck analysis was done using allele frequency data for checking the recent population size reduction in the Indian parasites under the TPM model. Statistical analysis of the data was carried out, under the assumption of mutation-drift equilibrium, by Sign rank test and the Wilcoxon test. A significant heterozygosity deficit was seen in the population, indicating nonbottlenecked parasite population in India (**Supplementary Table S2**).

TABLE 2 | Pairwise Fst values between all geographically isolated populations.

Comparison between	N	Fst
Haryana and Telangana	67	0.0081
Haryana and Gujarat	60	0.0156
Haryana and Bihar	58	0.046
Telangana and Gujarat	67	0.0160
Telangana and Bihar	65	0.0326
Gujrat and Bihar	58	0.046
India and Oman	356	0.0647
India and Turkey	138	0.0573
India and Tunisia	174	0.0850
India and Sudan	129	0.0691

N, Number of Individuals; Fst, Fixative Index (measure of Genetic Differentiation).

Minimum Four Microsatellite Markers Can Be Used for Differentiating the Parasite Population

The next question we asked was whether less than 10 markers could be used for differentiating the parasite populations in these states of India. The microsatellite markers were removed from each sample sequentially based on their He values from low to high, keeping the highly diverse markers for counting the number of haplotypes (**Supplementary Table S3**). We found that four markers (TS6, TS8, TS9, and TS12) were sufficient for detecting 100% haplotypes in the Indian population (**Figure 4B**). However, in a regional population of Gujarat (TS6, TS9, and TS12), three markers were enough, while Telangana (TS12, TS31), Haryana (TS9, TS12), and Bihar (TS9, TS12) two markers were able to detect all haplotypes.

DISCUSSION

This study is the first comprehensive analysis of the *T. annulata* diversity and population structure from India using microsatellite typing. The samples ($N = 125$) for the study were collected from four different geographical locations, including the *T. annulata* vaccine from India. The genotyping analysis identified high diversity among the microsatellite makers and the presence of multiple genotypes in all the samples. Based on the analysis, we found less genetic diversity in the *T. annulata* vaccine when compared to the parasite population from the field.

The total number of alleles per locus was found to be very low in the vaccine in comparison to the field isolates indicating limited diversity. High genetic diversity (H_E; 0.864) was found in the parasite population of all four locations; similar diversity was reported from other endemic countries, like Turkey, Tunisia, Oman, and Sudan (Weir et al., 2007, 2011; Al-Hamidhi et al., 2015). However, diversity was very high when compared to the parasite population from China and Portugal (Gomes et al., 2016; Yin et al., 2018). Based on the previous reports where a direct relationship has been shown between genetic diversity and effective population size, it can be concluded that the effective population size of *T. annulata* is high in India (Al-Hamidhi et al., 2015). The MOI values (9.15–16.77) indicated the presence of mixed genotypes in each sample, including vaccine (MOI = 6). Among the four states, Bihar has the

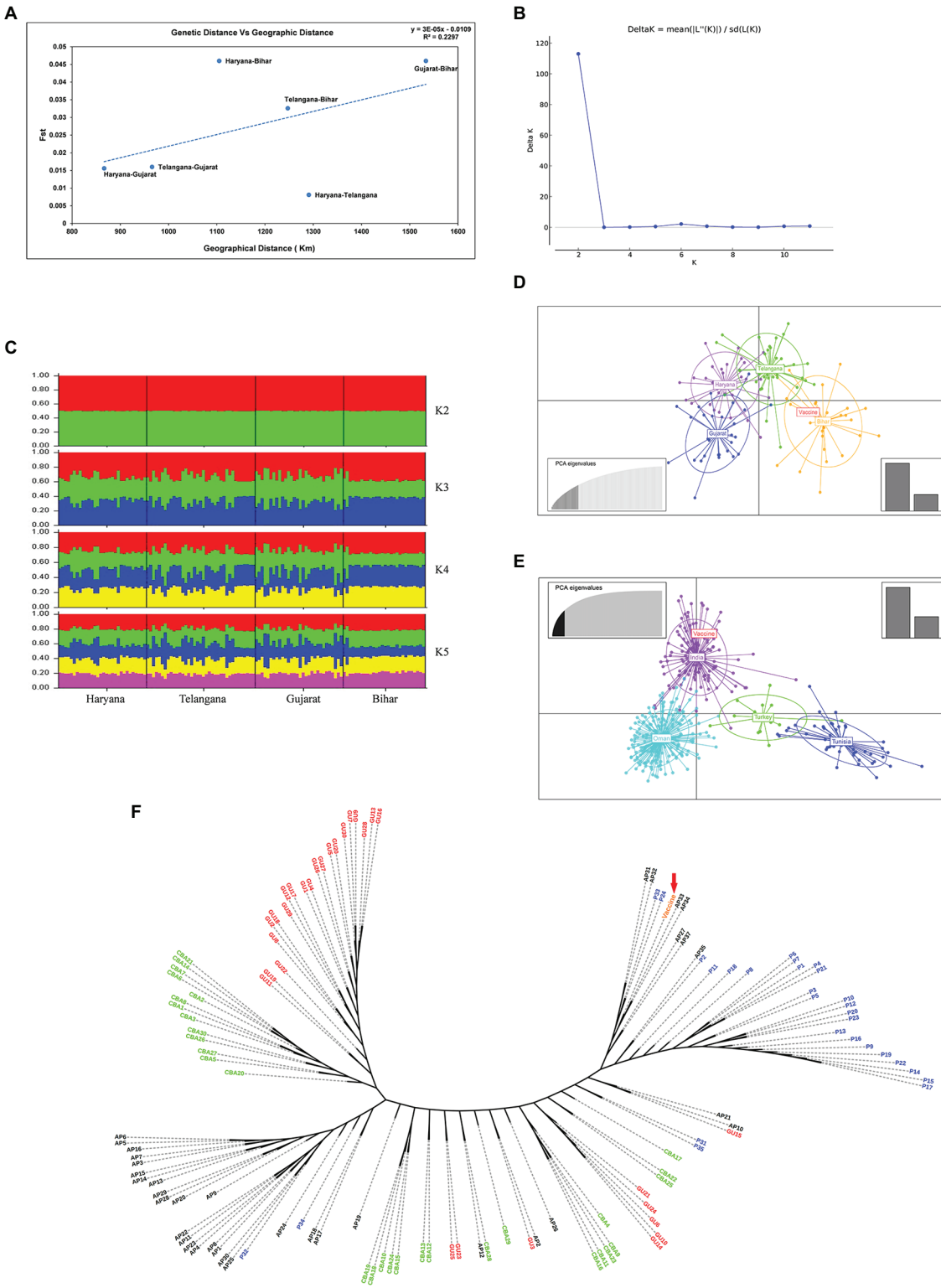

FIGURE 3 | Population structure: **(A)** Graph showing correlation between pairwise genetic distance and geographic distance based on the Fst values among the four states; **(B)** The graph shows optimal number of clusters from the STRUCTURE analysis; **(C)** STRUCTURE analysis from $K = 2$ to $K = 5$ with isolates from the four states of India; **(D)** Discriminant Analysis of Principal Components (DAPC) analysis showing the genetic structure of *T. annulata* populations from four states; **(E)** DAPC analysis showing the genetic structure of *T. annulata* populations from India, Turkey, Tunisia, and Oman; and **(F)** A phylogenetic tree was drawn to show complete allelic profiling between the samples from Bihar (P1–P35), Haryana (CBA1–CBA30), Gujarat (GU1–GU30), and Telangana (AP1–AP30).

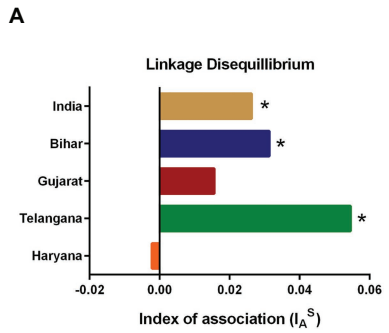

B

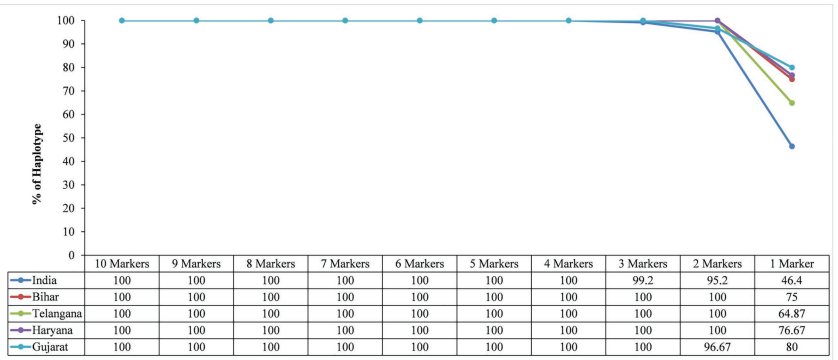

	10 Markers	9 Markers	8 Markers	7 Markers	6 Markers	5 Markers	4 Markers	3 Markers	2 Markers	1 Marker
India	100	100	100	100	100	100	100	99.2	95.2	46.4
Bihar	100	100	100	100	100	100	100	100	100	75
Telangana	100	100	100	100	100	100	100	100	100	64.87
Haryana	100	100	100	100	100	100	100	100	100	76.67
Gujarat	100	100	100	100	100	100	100	100	96.67	80

FIGURE 4 | Linkage Disequilibrium (LD) and Minimum number of Markers for complete Haplotype Detection: **(A)** The graph shows the standardized index of association I_A^S values of the *T. annulata* population from the states of Haryana, Telangana, Bihar, and Gujarat. Higher I_A^S indicates non-random association between loci. (*$p < 0.01$). **(B)** The figure shows percentage of haplotypes detected in the *T. annulata* populations by sequential removal of markers based on the He values.

lowest, and Gujarat has the highest MOI, followed by Haryana and Telangana. Compared to the MOI values reported from the other endemic countries, the number of genotypes present in a single infection was highest in India (Weir et al., 2007, 2011; Al-Hamidhi et al., 2015; Gomes et al., 2016; Yin et al., 2018). The significantly different MOI values inside India and when compared to other countries might be linked to factors, such as an abundance of the tick vector, time of sample collection, and transmission intensity. The high MOI in India points toward high transmission intensity and vector abundance in the country (Al-Hamidhi et al., 2015). The allele frequency data based on the presence of less frequent alleles indicated that parasite population in Gujarat is highly diverse among the four states with Bihar having the lowest diversity (Manske et al., 2012). The MOI values of the clinical samples were found to be very high when compared to the Indian vaccine strain (MOI = 6), suggesting less parasite diversity in the vaccine. The presence of multiple parasites in the infected sample points toward random mating in the tick host; however, the level of cross mating and recombination could not be determined (Hill et al., 1995). We then estimated the inbreeding coefficient 0.08 (f = 1/ne) and extent of outcrossing (>50%) for the *T. annulata* population in India using the mean number of clones per infection (ne = 12.64). This method is prevalidated in similar kinds of studies on *T. annulata* and *Plasmodium falciparum* (Hill et al., 1995; Al-Hamidhi et al., 2015). High outcrossing events found in our study have been previously linked to the formation of new genotypes different from the vaccine types, leading to its reduced efficacy in the field.

Despite high genetic diversity in samples from all the four sites, significant LD was found in the *T. annulata* populations from the states of Telangana and Bihar. The significant LD was also observed when all the samples were considered as one population. Although LD was observed in India, its values were not in the range where population structure can be considered to be clonal. The high genetic diversity and LD have been previously reported for *T. annulata* from other endemic countries and other similar apicomplexan parasites, like *T. parva*, and *P. falciparum* (Muleya et al., 2012; Al-Hamidhi et al., 2015; Wei et al., 2015; Yin et al., 2018). Observed LD can be because of multiple reasons, such as genetic drift, gene flow, and population size change. To detect population size change, we performed a bottleneck analysis, which showed no recent size reduction in India.

The level of genetic differentiation was found to be low when the pairwise comparison was done between state-wise parasite populations in India (Fst < 0.05). Moderate to high genetic differentiation was observed when the Indian parasite population was compared with other countries, like Oman, Turkey, Tunisia, and Sudan. The parasite population from Bihar was found to be genetically distant based on the Fst analysis when compared to the other three states. The low genetic differentiation between the parasites may be connected to the free movement of the animals in the country for commercial purposes. No correlation was found between the parasites based on the geographic and genetic distance (Fst). There was some evidence of regional distribution in the parasite population based on the clusters formed in the DAPC analysis. The current vaccine should ideally comprise of sufficient genotypic diversity for protection in all the states; however, it clustered near to the Bihar and Telangana population, signifying the presence of heterologous parasites in the field. The heterologous parasites in the field might be due to the frequent movement of animals inside and between the states, which provides an opportunity for the development of diverse parasites, making the population highly complex in India. The DAPC analysis reconfirmed the high genetic differentiation of the parasite population from India and other countries (Oman, Tunisia, and Turkey), which is evident as the animal movements between the countries are zero to none. As multiple parasites were present in every infection, an analysis based on the predominant allele might be biased. The phylogenetic analysis based on the complete allelic profiles of each sample also identified regional clustering in India. This implies that the genotype circulating in a particular region is similar and did not exactly match with other areas. This also proves that even though there is an allelic similarity

among different states based on MLG, the genotypes circulating in different states are different. It might have a significant implication in parasite control as different genotypes may respond differently to control measures, and in the future, state-wise control strategies should be adopted. Therefore, diversity and genotypes circulating in a particular region have to be considered while implementing control measures.

The previous studies from other countries, have utilized 10 microsatellite markers for understanding the *T. annulata* population diversity. However, in the future, if we plan to track the parasite control measures in these states, such studies might not be feasible due to time and economics involved. Based on our genotyping data, we next checked whether it is possible to use a smaller number of markers for future genetic diversity studies. We identified that a minimum of four markers could be used to study the population structure of the parasite without missing the critical information and reducing the cost of the assay.

CONCLUSION

Our study helps to understand the population structure of *T. annulata* parasites in India. The low genetic diversity observed in the vaccine highlights the scope for improvement in the current vaccine. The detection of multiple unique genotypes other than the vaccine, calls for increased efforts for *Theileria* control. We hypothesize that using a cocktail of parasites having sufficient genetic and antigenic diversity might be a good idea for the future vaccine. For a better understanding of the genotypic and antigenic composition of the parasite populations in the country, sample numbers and sites will have to be increased substantially in future studies. Our results can be used as the baseline data for future studies and will be helpful in monitoring the parasite population in the country. Our findings for the use of a smaller number of markers for genotype allocation in these states will be useful for the *Theileria* control programs.

DATA AVAILABILITY STATEMENT

The original contributions presented in the study are included in the article/**Supplementary Material**, further inquiries can be directed to the corresponding author.

AUTHOR CONTRIBUTIONS

PS and SR designed the experiments. SR, MB, and VBd have done the experiments and data analysis. VBo, PK, JA, and SS have helped in sample collection, designing study, data analysis, and manuscript editing. PS, SR, and VBd edited the paper. All authors have given approval to the final version of the manuscript.

FUNDING

This work was supported by the intramural funds from National Institute of Animal Biotechnology. SR is supported by DBT JRF fellowship program. The funding agency had no role in study design, data collection and analysis.

ACKNOWLEDGMENTS

We would like to thank the Animal Husbandry Departments and veterinarians of the four states for providing blood samples.

SUPPLEMENTARY MATERIAL

The Supplementary Material for this article can be found online at: https://www.frontiersin.org/articles/10.3389/fmicb.2020.579929/full#supplementary-material

REFERENCES

Adamack, A. T., and Gruber, B. (2014). PopGenReport: simplifying basic population genetic analyses in R. *Methods Ecol. Evol.* 5, 384–387. doi: 10.1111/2041-210X.12158

Al-Hamidhi, S., Tageldin, M. H., Weir, W., Al-Fahdi, A., Johnson, E. H., Bobade, P., et al. (2015). Genetic diversity and population structure of *Theileria annulata* in Oman. *PLoS One* 10:e0139581. doi: 10.1371/journal.pone.0139581

Bilgic, H. B., Aksulu, A., Bakırcı, S., Unlu, A. H., Kose, O., Hacılarlıoglu, S., et al. (2019). Infection dynamics of *Theileria annulata* over a disease season following cell line vaccination. *Vet. Parasitol.* 265, 63–73. doi: 10.1016/j.vetpar.2018.11.012

Cornuet, J. M., and Luikart, G. (1996). Description and power analysis of two tests for detecting recent population bottlenecks from allele frequency data. *Genetics* 144, 2001–2014.

Dandasena, D., Bhandari, V., Sreenivasamurthy, G. S., Murthy, S., Roy, S., Bhanot, V., et al. (2018). A real-time PCR based assay for determining parasite to host ratio and parasitaemia in the clinical samples of bovine Theileriosis. *Sci. Rep.* 8:15441. doi: 10.1038/s41598-018-33721-3

Darghouth, M. A. (2008). Review on the experience with live attenuated vaccines against tropical theileriosis in Tunisia: considerations for the present and implications for the future. *Vaccine* 26, G4–G10. doi: 10.1016/j.vaccine.2008.09.065

Darghouth, M. A., Miled, L. B., Bouattour, A., Melrose, T. R., Brown, C. G. D., and Kilani, M. (1996). A preliminary study on the attenuation of Tunisian schizont-infected cell lines of *Theileria annulata*. *Parasitol. Res.* 82, 647–655. doi: 10.1007/s004360050179

Evanno, G., Regnaut, S., and Goudet, J. (2005). Detecting the number of clusters of individuals using the software structure: a simulation study. *Mol. Ecol.* 14, 2611–2620. doi: 10.1111/j.1365-294X.2005.02553.x

Garcia-Vallve, S., Palau, J., and Romeu, A. (1999). Horizontal gene transfer in glycosyl hydrolases inferred from codon usage in *Escherichia coli* and *Bacillus subtilis*. *Mol. Biol. Evol.* 16, 1125–1134. doi: 10.1093/oxfordjournals.molbev.a026203

George, N., Bhandari, V., Reddy, D. P., and Sharma, P. (2015). Molecular and phylogenetic analysis revealed new genotypes of *Theileria annulata* parasites from India. *Parasit. Vectors* 8:468. doi: 10.1186/s13071-015-1075-z

Ghosh, S., and Azhahianambi, P. (2007). Laboratory rearing of Theileria annulata-free *Hyalomma anatolicum* anatolicum ticks. *Exp. Appl. Acarol.* 43, 137–146. doi: 10.1007/s10493-007-9100-3

Gill, B. S., Bansal, G. C., Bhattacharyulu, Y., Kaur, D., and Singh, A. (1980). Immunological relationship between strains of *Theileria annulata* Dschunkowsky and Lihs 1904. *Res. Vet. Sci.* 29, 93–97. doi: 10.1016/S0034-5288(18)32692-4

Gomes, J., Salgueiro, P., Inácio, J., Amaro, A., Pinto, J., Tait, A., et al. (2016). Population diversity of *Theileria annulata* in Portugal. *Infect. Genet. Evol.* 42, 14–19. doi: 10.1016/j.meegid.2016.04.023

Goudet, J. (2003). Fstat (ver. 2.9.4), a program to estimate and test population genetics parameters. Available at: http://www2.unil.ch/popgen/softwares/fstat.htm (Accessed: June 2020).

Gupta, S. K., Sharma, R. D., Rakha, N. K., Sudhan, N. A., and Nichani, A. K. (1998). Immune response to *Theileria annulata* (Hisar) cell culture vaccine under the field conditions in bovines. *Indian Vet. J.* 75, 405–411.

Hashemi-Fesharki, R. (1988). Control of *Theileria annulata* in Iran. *Parasitol. Today* 4, 36–40. doi: 10.1016/0169-4758(88)90062-2

Haubold, B., and Hudson, R. R. (2000). LIAN 3.0: detecting linkage disequilibrium in multilocus data. *Bioinformatics* 16, 847–849. doi: 10.1093/bioinformatics/16.9.847

Hemmink, J. D., Weir, W., MacHugh, N. D., Graham, S. P., Patel, E., Paxton, E., et al. (2016). Limited genetic and antigenic diversity within parasite isolates used in a live vaccine against *Theileria parva*. *Int. J. Parasitol.* 46, 495–506. doi: 10.1016/j.ijpara.2016.02.007

Hill, W. G., Babiker, H. A., Ranford-Cartwright, L. C., and Walliker, D. (1995). Estimation of inbreeding coefficients from genotypic data on multiple alleles, and application to estimation of clonality in malaria parasites. *Genet. Res.* 65, 53–61. doi: 10.1017/S0016672300033000

Jombart, T. (2008). Adegenet: a R package for the multivariate analysis of genetic markers. *Bioinformatics* 24, 1403–1405. doi: 10.1093/bioinformatics/btn129

Kittichai, V., Koepfli, C., Nguitragool, W., Sattabongkot, J., and Cui, L. (2017). Substantial population structure of *Plasmodium vivax* in Thailand facilitates identification of the sources of residual transmission. *PLoS Negl. Trop. Dis.* 11:e0005930. doi: 10.1371/journal.pntd.0005930

Kumar, B., Maharana, B. R., Prasad, A., Joseph, J. P., Patel, B., and Patel, J. S. (2016). Seasonal incidence of parasitic diseases in bovines of south western Gujarat (Junagadh), India. *J. Parasit. Dis.* 40, 1342–1346. doi: 10.1007/s12639-015-0686-9

Kundave, V. R., Patel, A. K., Patel, P. V., Hasnani, J. J., and Joshi, C. G. (2015). Detection of theileriosis in cattle and buffaloes by polymerase chain reaction. *J. Parasit. Dis.* 39, 508–513. doi: 10.1007/s12639-013-0386-2

Letunic, I., and Bork, P. (2007). Interactive tree of life (iTOL): an online tool for phylogenetic tree display and annotation. *Bioinformatics* 23, 127–128. doi: 10.1093/bioinformatics/btl529

Luikart, G., and Cornuet, J. (1998). Empirical evaluation of a test for identifying recently bottlenecked populations from allele frequency data. *Conserv. Biol.* 12, 228–237. doi: 10.1111/j.1523-1739.1998.96388.x

Majewska, A. C., and Sulima, P. (1999). Source and significance of genetic polymorphism of selected parasitic protozoa. *Wiad. Parazytol.* 45, 293–307.

Manske, M., Miotto, O., Campino, S., Auburn, S., Almagro-Garcia, J., Maslen, G., et al. (2012). Analysis of *Plasmodium falciparum* diversity in natural infections by deep sequencing. *Nature* 487, 375–379. doi: 10.1038/nature11174

Muleya, W., Namangala, B., Simuunza, M., Nakao, R., Inoue, N., Kimura, T., et al. (2012). Population genetic analysis and sub-structuring of *Theileria parva* in the northern and eastern parts of Zambia. *Parasit. Vectors* 5:255. doi: 10.1186/1756-3305-5-255

Ouhelli, H., Kachani, M., Flach, E., Williamson, S., El Hasnaoui, M., and Spooner, R. (1997). Investigations on vaccination against theileriosis in Morocco. *Trop. Anim. Health Prod.* 29:103S. doi: 10.1007/BF02632945

Peakall, R., and Smouse, P. E. (2012). GenAlEx 6.5: genetic analysis in excel. Population genetic software for teaching and research--an update. *Bioinformatics* 28, 2537–2539. doi: 10.1093/bioinformatics/bts460

Pipano, E., and Shkap, V. (2006). Vaccination against tropical Theileriosis. *Ann. N. Y. Acad. Sci.* 916, 484–500. doi: 10.1111/j.1749-6632.2000.tb05328.x

Pipano, E., and Tsur, I. (1966). Experimental immunization against *Theileria annulata* with a tissue culture vaccine. *Refuah. vet.* 23, 186–194.

Piry, S., Luikart, G., and Cornuet, J. M. (1999). BOTTLENECK: a computer program for detecting recent reductions in the effective population size using allele frequency data. *J. Hered.* 90, 502–503. doi: 10.1093/jhered/90.4.502

Pritchard, J. K., Stephens, M., and Donnelly, P. (2000). Inference of population structure using multilocus genotype data. *Genetics* 155, 945–959.

Raymond, M. (1995). GENEPOP (version 1.2): population genetics software for exact tests and ecumenicism. *J. Hered.* 86, 248–249. doi: 10.1093/oxfordjournals.jhered.a111573

Rousset, F. (2008). genepop'007: a complete re-implementation of the genepop software for windows and Linux. *Mol. Ecol. Resour.* 8, 103–106. doi: 10.1111/j.1471-8286.2007.01931.x

Roy, S., Bhandari, V., Dandasena, D., Murthy, S., and Sharma, P. (2019). Genetic profiling reveals high allelic diversity, heterozygosity and antigenic diversity in the clinical isolates of the *Theileria annulata* from India. *Front. Physiol.* 10:673. doi: 10.3389/fphys.2019.00673

Sager, H., Bertoni, G., and Jungi, T. W. (1998). Differences between B cell and macrophage transformation by the bovine parasite, *Theileria annulata*: a clonal approach. *J. Immunol.* 161, 335–341.

Sayin, F., Dinçer, S., Çakmak, A., Inci, A., Yukari, B. A., Vatanserver, Z., et al. (1997). Tick-borne diseases in Turkey. *Trop. Anim. Health Prod.* 29:53S. doi: 10.1007/BF02632925

Sivakumar, T., Hayashida, K., Sugimoto, C., and Yokoyama, N. (2014). Evolution and genetic diversity of Theileria. *Infect. Genet. Evol.* 27, 250–263. doi: 10.1016/j.meegid.2014.07.013

Stepanova, N. I., and Zablotskii, V. T. (1989). Bovine theileriosis in the USSR. *Rev. Sci. Tech.* 8, 89–92. doi: 10.20506/rst.8.1.396

Tretina, K., Gotia, H. T., Mann, D. J., and Silva, J. C. (2015). Theileria-transformed bovine leukocytes have cancer hallmarks. *Trends Parasitol.* 31, 306–314. doi: 10.1016/j.pt.2015.04.001

Viseras, J., García-Fernández, P., and Adroher, F. J. (1997). Isolation and establishment in in vitro culture of a *Theileria annulata*—infected cell line from Spain. *Parasitol. Res.* 83, 394–396. doi: 10.1007/s004360050270

Wei, G., Zhang, L., Yan, H., Zhao, Y., Hu, J., and Pan, W. (2015). Evaluation of the population structure and genetic diversity of *Plasmodium falciparum* in southern China. *Malar. J.* 14:283. doi: 10.1186/s12936-015-0786-0

Weir, W., Ben-Miled, L., Karagenç, T., Katzer, F., Darghouth, M., Shiels, B., et al. (2007). Genetic exchange and sub-structuring in *Theileria annulata* populations. *Mol. Biochem. Parasitol.* 154, 170–180. doi: 10.1016/j.molbiopara.2007.04.015

Weir, W., Karagenç, T., Gharbi, M., Simuunza, M., Aypak, S., Aysul, N., et al. (2011). Population diversity and multiplicity of infection in *Theileria annulata*. *Int. J. Parasitol.* 41, 193–203. doi: 10.1016/j.ijpara.2010.08.004

Yin, F., Liu, Z., Liu, J., Liu, A., Salih, D. A., Li, Y., et al. (2018). Population genetic analysis of *Theileria annulata* from six geographical regions in China, determined on the basis of micro- and mini-satellite markers. *Front. Genet.* 9:50. doi: 10.3389/fgene.2018.00050

Zhang, Z. H. (1997). A general review on the prevention and treatment of *Theileria annulata* in China. *Vet. Parasitol.* 70, 77–81. doi: 10.1016/S0304-4017(96)01127-2

Conflict of Interest: The authors declare that the research was conducted in the absence of any commercial or financial relationships that could be construed as a potential conflict of interest.

Advantages of publishing in Frontiers

OPEN ACCESS
Articles are free to read for greatest visibility and readership

FAST PUBLICATION
Around 90 days from submission to decision

HIGH QUALITY PEER-REVIEW
Rigorous, collaborative, and constructive peer-review

TRANSPARENT PEER-REVIEW
Editors and reviewers acknowledged by name on published articles

Frontiers
Avenue du Tribunal-Fédéral 34
1005 Lausanne | Switzerland

Visit us: www.frontiersin.org
Contact us: frontiersin.org/about/contact

REPRODUCIBILITY OF RESEARCH
Support open data and methods to enhance research reproducibility

DIGITAL PUBLISHING
Articles designed for optimal readership across devices

FOLLOW US
@frontiersin

IMPACT METRICS
Advanced article metrics track visibility across digital media

EXTENSIVE PROMOTION
Marketing and promotion of impactful research

LOOP RESEARCH NETWORK
Our network increases your article's readership